ISSN 0289-842X

RIKEN Accelerator Progress Report

1990

vol. 24

理化学研究所
the Institute of Physical and Chemical Research

RIKEN Accelerator Progress Report 1990
January-December

理化学研究所
the Institute of Physical and Chemical Research
Wako-shi, Saitama, 351-01 JAPAN

Editors

S. Ambe	Y. Gono
M. Hara	A. Hashizume
T. Kambara	Y. Miyazawa
N. Sakai	I. Shimamura
I. Tanihata	E. Yagi
S. Yamaji	Y. Yano
F. Yatagai	

CONTENTS

II. OPERATION OF ACCELERATORS

III. RESEARCH ACTIVITIES

1. Nuclear Physics

2. Atomic and Solid-State Physics

3. Radiochemistry and Nuclear Chemistry

4. Radiation Chemistry and Radiation Biology

5. Instrumentation

6. Material Analysis

IV. NUCLEAR DATA

V. DEVELOPMENT OF ACCELERATOR FACILITIES

1. Ion Accelerator Development

2. Synchrotron Radiation Source Development

VI. RADIATION MONITORING

AUTHOR INDEX

I. INTRODUCTION

M. Ishihara

This annual report covers the activities of the RIKEN Accelerator Facility for the year of 1990. The Facility possesses an intermediate-energy heavy-ion accelerator complex composed of a central booster accelerator, RIKEN Ring Cyclotron (RRC), and two injectors, a heavy-ion linear accelerator (RILAC) and an AVF cyclotron (AVF). The accelerators were constructed under a longterm project starting in 1974: The RILAC brought out the first beam in 1980, the RRC in December 1986, and the AVF in April 1989. The two injectors may also be used in stand-alone modes. In addition, a 1-MeV Tandetron is in operation. The heavy ions so far accelerated are ranged from deuterons to xenon, with beam energies up to 135 MeV/u. They have been served for research work of a variety of disciplines including nuclear physics, atomic physics, nuclear and radiation chemistry, condensed matter physics, and radiation biology. The users range over 11 laboratories of 50 in the whole RIKEN. There is also a large involvement of outside users. For the period 198 staff researchers and 68 graduate students from other domestic and foreign institutions contributed to the activities at the Facility.

The report also covers activities associated with two major projects which have newly started. One is the joint project between RIKEN and Japan Atomic Energy Research Institute (JAERI) to build an 8-GeV synchrotron radiation source (SPring-8) at the site of Harima Science Garden City, Hyougo Prefecture. The Construction has started in April 1990 and will be completed in several years. The other is an international project between RIKEN and RAL (U. K.) on muon science research. An intense pulsed muon beam is to be facilitated at RAL in combination with the synchrotron. The construction work was initiated, recently.

With respect to the RRC complex, this annual period may be marked as the first full year in which the AVF was employed for routine operation. The entry of AVF as an injector brought a significant increase in the capability of the RRC complex. The maximum energies of lighter ions reached goal values; 35 new beams were added to the list of accomplishment in the past year. A dual injector system also contributes to elongation of beam hours. The RRC was operated for 178 days during December 2, 1989, to November 10, 1990. This number will be further increased in coming years. Among other developments in the RRC complex, the installation of a Neomafios ECR ion source in place of a PIG source at RILAC started in September 1990. The new source will become available in the early 1991 and contribute to grade up the energies of RILAC-injected beams. Another effort was directed to lower energy bounds. Operation of RRC at 7 MeV/u was established beyond the original limit. This was to enhance the access to studies using fusion-like reactions. The fabrication of a polarized ion source of hydrogen for AVF has started and the completion is scheduled in the next summer. The device aims at gaining a broader prospect for the beams of 210-MeV protons and 270-MeV deuterons.

There were also remarkable efforts to develop the experimental apparatus at RRC beam channels. In particular a projectile-fragment separator called RIPS started its full operation providing high-energy beams of radioisotopes. The apparatus yields intense beams, which are about two orders of magnitudes stronger than the other existing analogues. This encourages the studies on nuclear reactions with unstable nuclei. In this connection a large acceptance magnetic spectrometer for the secondary reactions is in preparation to be located downstream of RIPS. An on-line mass separator of the GARIS-IGISOL type has also become employed for experiments. It is primarily used to study heavy unstable nuclei including possible super-heavy elements (SHE). We have another magnetic spectrometer called SMART, which is a tandem-type high-precision charged-particle analyzer with broad angular and momentum acceptances. It has an access to neutron spectroscopy as well. It is under the process of debugging and tuning and is scheduled to be completed in the early summer of 1991.

During the past year, heavy ion beams from the RIKEN accelerators have been serving for various studies. RRC has run for 116 days for experiments among which about 70 % went to nuclear physics and the rest to the other research fields by covering 17 subjects for the former and 20 subjects for the latter. RILAC has run for 89 days by itself for its own users. They were primarily used for studies on atomic physics and other fields of science.

Studies on and with unstable nuclei were extensively pursued. Experiments with RIPS are directed to three major categories. Studies on anomalous properties of extremely neutron-rich nuclei by observing the secondary reactions were upgraded; High-energy Coulomb dissociation mechanism among other processes were exploited to measure unstable-nucleus reaction cross sections of astrophysical interests; Attempts to produce spin-polarized unstable nuclei were pursued through dynamical and optical methods. It has been shown that the projectile fragmentation reaction by itself offers a useful means to produce polarized isotopes. The setups for laser spectroscopy have been developed, and an optical pumping method for polarization was tested for isotopes in semi-conductors.

A challenging program to search for SHE isotopes has started using GARIS-IGISOL. A possible new scheme based on a particular type of reaction process is to be used to enhance the production and survival probabilities. A preliminary experiment indicated a promising result.

The group of nuclear theorists was strengthened this year by inviting three visiting professors and five post doctoral fellows. The activity now covers nuclear phenomena from low to relativistic energies.

Experiments on atomic physics were made by using RRC, RILAC, and a section of the AVF ECR ion source. Electron capture and loss cross sections and δ-ray emission processes in high energy atomic collisions were investigated with RRC. A detailed study of collision mechanism was performed through observation of spin alignment effects at RILAC. Beam foil spectroscopy steadily continued with RILAC Ti beams. Two-electron capture processes at low energies were studied with ECR.

Muon beam channels at RRC was completed and an effort was extended to a new beam channel at RAL. Meanwhile the target dependence of a surface muon yield was studied.

Studies of nuclear and radiation chemistry have continued with various methodologies. Mossbauer and perturbed angular correlation techniques were used to study the properties of magnetic and high-T_c superconducting materials. Rutherford scattering and PIXE techniques were applied to the analysis of impurities contained in high-purity industrial materials and in the compositions of medical environmental and geological samples. Positron annihilation analysis proved the dislocation in semiconductors. A systematic study on the production cross sections in high-energy heavy-ion reactions continued by using various ions. On this basis a multi-tracer technique is being developed to be applied, *e.g.*, to oceanography problems.

Studies of radiation biology were performed in two aspects, space biology and radiotherapy. Effects of irradiation of high-energy heavy ions were studied on biological samples such as spores, beans, and shrimp eggs to simulate the effects of cosmic rays. Basic studies on heavy-ion cancer therapy were carried out by irradiating mice and mammal culture cells with RRC.

While new developments continued, one accelerator has ceased operation. The 160-cm cyclotron was shut down in April 1990 after a successful service for more than 25 years. A special volume entitled the 160-cm Cyclotron was issued as a supplement of this Report to summarize and memorize the research accomplishments obtained with the accelerator.

RIKEN Accel. Prog. Rep. **24** (1990)

II. OPERATION OF ACCELERATORS

1. RRC Operation

Y. Yano, A. Goto, M. Kase, T. Kageyama, T. Nakagawa, H. Isshiki,* R. Abe,*
S. Otsuka,* H. Akagi,* T. Ishikawa,* R. Ichikawa,* and T. Maie*

For nearly one year December 2, 1989, through November 10, 1990, the RRC machine time scheduled for user's experiments totaled 178 days, which excludes the periods spent in carrying out long and short term regular machine overhauls and in developing and improving the machine. Among 178 days, relatively large part of 48 days (27%) were spent in preparing beams, because almost half of the beams demanded by the users were new ones. The shut-down time due to machine trouble amounted to 14.5 days (8%). Eventually 115.5 days (65%) were devoted to proceed nuclear (70% in portion) and non-nuclear (30% in portion) experiments. The AVF cyclotron-injected beam time exceeded the linac-injected beam time in a ratio of 7 to 3. Regular long-term overhauls were carried out for 3 weeks in the winter and for 8 weeks in the summer.

An extensive improvement were made for almost the whole parts of the machine during the summer overhaul; the improvement was very effective in quick starting up, stable operation, and easy maintenance of the machine.

In Fig. 1 the new beams were shown in the space of the acceleration energy per nucleon versus the atomic mass number of ion, together with the beams accelerated so far. Almost the whole region of beams, except for 210 MeV protons and 185 MeV/u ^{3}He particles obtainable by AVF injection, have been covered this year. Since the summer overhaul the linac was shut down for replacing the old PIG ion source with an ECR ion source. The new source will grade up the linac performance greatly, and thereby the energies of the linac-injected beams will be pushed up to the maximum design values. This is scheduled at the beginning

Table 1. RRC beams during April 1987 – November 1990.

Particle	Charge	RF F (MHz)	h	Energy (MeV/u)	Intensity (nA)
d	*1*	*24.6*	5	*70*	*50* (*)
^{12}C	5	35	9	42	200
	6	*32.6*	*5*	*135*	*350* (*)
^{13}C	6	35	9	42	50
^{14}N	6	28	9	26	200
	6	35	10	34	200
	6	32	9	35	300 (*)
	6	35	9	42	200
	7	*26*	*5*	*80*	*700* (*)
	7	*32.6*	*5*	*135*	*500*
^{15}N	5	20.187	10	10.65	100
	6	35	10	34	50
	6	35	9	42	50
	7	*24.6*	*5*	*70*	*1,100* (*)
	7	*30.5*	*5*	*115*	*200* (*)
^{16}O	5	25	9	20.6	—
	8	*32.6*	*5*	*135*	*500* (*)
^{18}O	7	35	9	42	20
	8	*29*	*5*	*100*	*600*
^{20}Ne	9	33	9	37	150
^{22}Ne	8	28	10	21	40
^{24}Mg	*11*	*29*	*5*	*100*	*30* (*)
^{27}Al	*13*	*29*	*5*	*100*	*60* (*)
^{40}Ar	11	20	10	10.3	1,500
	12	28	10	21	200
	13	28	9	26	600
	16	*26*	*5*	*80*	*40* (*)
	17	*28.1*	*5*	*95*	*40* (*)
^{40}Ca	14	28	9	26	10
^{64}Zn	20	25	9	20.6	10
^{65}Cu	18	25	10	17	10
^{84}Kr	18	20	10	10.3	70
^{132}Xe	24	20	11	8.5	— (*)
	21	18	11	7	50 (*)

---

* Sumijyu Accelerator Service, Ltd.

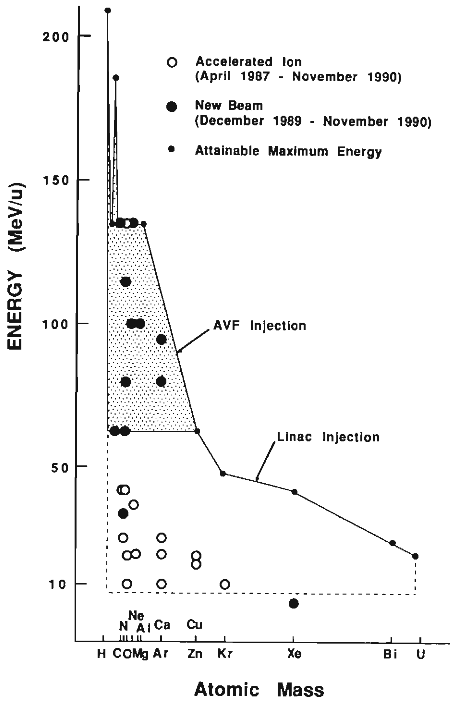

Fig. 1. RRC beams during April 1987–November 1990.

of next year. We successfully operated the RRC rf system at 18 MHz which is lowered from the nominal value of 20 MHz; thus the lowest beam energy of 7 MeV/u in the linac injection has been available in the acceleration harmonics of 11. This acceleration mode was applied to a xenon beam. Table 1 lists the acceleration parameters and the maximum intensities used during each experiment run for the beams accelerated so far. New beams are denoted by asterisks.

RIKEN Accel. Prog. Rep. 24 (1990)

II-2. RILAC Operation

Y. Chiba, M. Hemmi, M. Yanokura, M. Kase, E. Ikezawa, T. Aihara,* T. Ohki,* H. Hasebe,* T. Chiba, and Y. Miyazawa

This year, the PIG ion source, which had been used for many years, of RILAC was replaced with a new ECR ion source. For the replacement, regular RILAC operation was discontinued by the end of July. The remaining period of the year was devoted to the modification of the injector high voltage station and the installation of the ECR ion source on it. Tables 1 to 3 show the operation statistics for the calendar year 1990. The "overhaul and improvement" in Table 1 includes the ion source renewal. During regular operation, there arose no serious trouble except carelessly mistaking $^{66}Zn^{5+}$ ions for $^{64}Zn^{5+}$ ions gave a loss in beam time to RIKEN Ring Cyclotron.

Table 1. Statistics of the operation for Jan. 1 – Dec. 31, 1990.

	Day	%
Beam time	123	33.7
Frequency change	6	1.6
Overhaul and improvement	95	26.0
Periodic inspection and repair	21	5.8
Machine trouble	0	0.0
Scheduled shut down	120	32.9
Total	365	100

Table 2. Beam time for individual research groups.

	Day	%
Atomic physics	33	26.8
Solid-state physics	21	17.1
Nuclear chemistry	24	19.5
Radiation chemistry	7	5.7
Accelerator research	4	3.3
Beam transportation to RRC	34	27.6
Total	123	100

Table 3. List of ions used in this year.

Ion	Mass	Charge state	Day
N	14	2	3
Ne	20	2	7
Al	27	3	4
Si	28	3	5
Ar	40	3	19
Ar	40	4	45
Ti	48	3	8
Cr	52	5	2
Cu	63	4	9
Zn	64	3	1
Zn	64	5	6
Kr	84	5	5
Kr	84	8	2
Xe	132	6	5
Xe	132	9	2

The newly installed ECR ion source, called NEOMAFIOS, developed and manufactured by C.E.N.-G., France, arrived at our facilities in February 1990. Performance tests[1] and operation training for the new ion source were repeated on a test bench until the end of July. August through the middle of November, we successively carried out the removal of the old PIG ion source system from the injector high voltage station, the installation of the ECR ion source system, and the preparation of peripheral equipments. Most of the instruments on the station were replaced with new ones designed for the ECR ion source system.

Adjustment of the ECR ion source combined with beam transport in the injector system was started in the middle of November and acceleration test of RILAC using an $^{40}Ar^{8+}$ beam in the end.

Beam acceleration will be reopened for users in the middle of January 1991.

References

1) E. Ikezawa *et al.*: This Report, p. 133.

---

* Sumijyu Accelerator Service, Ltd.

RIKEN Accel. Prog. Rep. **24** (1990)

II-3. AVF Cyclotron Operation

A. Goto, M. Kase, Y. Yano, T. Kageyama, S. Kohara, M. Nagase, K. Hatanaka,*
H. Isshiki,** R. Abe,** S. Otsuka,** H. Akagi,** T. Ishikawa,**
R. Ichikawa,** and T. Maie**

We have routinely operated the AVF cyclotron since we began beam service for users last October. The cyclotron has been exclusively used as an injector for RIKEN Ring Cyclotron (RRC). We accelerated various ions from deuteron to argon in a total of sixteen cases as shown in Table 1. The designed maximum energies from RRC have been achieved for these ions except for deuteron.

Table 1. AVF beams accelerated in September 1989 – November 1990.

Ion	RF Frequency (MHz)	Energy * (MeV/u)	Main coil current (A)	Average field (T)	External current (enA)
d	12.3	4.0 (70)	303	0.80	500
d	13.8	5.0 (---)**	343	0.90	1000
$^{12}C^{4+}$	16.3	7.0 (135)	810	1.60	-----
$^{14}N^{4+}$	12.0	3.8 (67)	578	1.37	1000
$^{14}N^{4+}$	12.3	4.0 (70)	604	1.41	800
$^{14}N^{4+}$	13.0	4.4 (80)	680	1.49	2500
$^{14}N^{5+}$	16.3	7.0 (135)	685	1.50	5000
$^{15}N^{4+}$	12.3	4.0 (70)	699	1.51	2000
$^{15}N^{5+}$	15.25	6.1 (115)	690	1.50	1300
$^{16}O^{6+}$	16.3	7.0 (135)	616	1.43	2500
$^{18}O^{6+}$	14.5	5.5 (102)	615	1.42	1700
$^{18}O^{6+}$	14.85	5.8 (---)*	646	1.46	300
$^{24}Mg^{7+}$	14.5	5.5 (102)	856	1.63	-----
$^{27}Al^{8+}$	14.5	5.5 (102)	824	1.60	200
$^{40}Ar^{11+}$	13.0	4.4 (80)	747	1.55	300
$^{40}Ar^{11+}$	14.05	5.2 (95)	935	1.67	700

* The values in the parentheses show the energies obtained by the coupled operation with RRC.

** These ions were accelerated only with the AVF cyclotron.

The vacuum chamber of the cyclotron was opened three times for repairs of a phase defining slit and a joint of a cooling pipe on a dummy dee and for a scheduled overhaul in summer. At the overhaul time we checked rf contacts, driving mechanism systems and others, and found no problems on them. We also replaced the septum of the deflector and the electrodes of the inflector with new ones. These new ones are in an essential sense spairs for these elements, though some modifications were made to the original ones: the vertical clearance of the septum in the region where last few revolutions pass through was widened from 12 mm to 14 mm, and the gap of the infector was also widened from 5 mm to 8 mm.

The performance of the cyclotron has been good as a whole, but there are still some problems with respect to beam transmission, which have not been resolved. At the moment the beam transmission through the cyclotron is around 10 % for beams of up to several tens of eμA. A beam loss in the injection beam transport line is among the losses, when a beam intensity is very high. The problem of a beam loss near and during extraction is rather serious: at a high beam intensity, more than half of the beam is lost in the outermost region just before extraction (20 or 30 mm in radial width).

Because a high intensity beam of deuterons is planned to be used for isotope production in the near future, the radiation shield effect of the cyclotron vault was checked by accelerating deuterons at 5 MeV/u. The result suggests that we should strengthen the shield of the hole in the ceiling which is just above the cyclotron and through which the injection beam line passes.

---

* Research Center for Nuclear Physics, Osaka University.

** Sumijyu Accelerator Service, Ltd.

RIKEN Accel. Prog. Rep. **24** (1990)

II-4. Cyclotron Operation

K. Ogiwara, T. Kageyama, S. Kohara, and I. Kohno

The 160 cm cyclotron was operated on a 24 h-a-day basis during the period XXV from Jan. 1 to Apr. 30, 1990. The statistics of the machine operaton time is shown in Table 1.

Table 1. Cyclotron operation in the period XXV.

	Oscillator	Ion source	Beam
Reading of the time meter on Jan. 06 1990 (h)	99,107.6	105,423.5	61,453.9
Reading of the time meter on Apr. 30 1990 (h)	99,753.5	106,148.4	61,909.9
Difference (h)	645.9	724.9	456
Schedule in this period:			
Beam-time		57 d	
Overhaul and installation		12	
Periodical inspection and repair		5	
Schedule shutdown		31	
Machine trouble		3	

Table 2 shows the beam-time allotment to various activities during this period. Table 3 shows the distribution of the scheduled beam time among various particles.

The cyclotron was shut down on Apr. 30, 1990. The overall net operation time of the oscillator and the ion source over past 23 years attained to 99,753.5 and 106,148.4 hours, respectively. Over all net beam time attained to 61,909.9 hours since 1973.

Table 2. Scheduled beam-time and research subjects in period XXV.

Subject	Heavy ion	Light ion	Total
RI production for nuclear and solid physics	8 h	64 h	72 h
Nuclear chemistry	0	368	368
Radiation biology	24	24	48
Radiation chemistry	120	24	144
Radiation damage of polymer	0	16	16
Radiation damage of semiconductor	0	24	24
Test of radiation detector	0	16	16
Outside users			
Radiochemical analyses	0	96	96
Radiation damage of device for sattelite	0	16	16
Test of single even upset	24	0	24
Proton irradiation on thyristor	0	80	80
Total	176 h	728 h	904 h
Percentage in total	19.5%	80.5%	100%

Table 3. Distribution of the beam-time among particles accerated.

Particle	(h)	(%)
p	296	32.7
$^{3}He^{2+}$	96	10.6
$^{4}He^{2+}$	336	37.2
$^{12}C^{4+}$	8	0.9
$^{14}N^{4+,5+}$	168	18.6
Total	904	100.0

RIKEN Accel. Prog. Rep. **24** (1990)

II-5. Tandetron Operation

T. Kobayashi, H. Sakairi, E. Yagi, and T. Urai

The Tandetron was operated for 106 days for 11 months from Nov. 1, 1989 to Sep. 31, 1990, during which ^{1}H, ^{4}He, and ^{11}B were accelerated.

The machine was shut down a few times by following causes; leakage of air through a metal-insulator bond of the duoplasmatron housing, leakage of SF_6 (insulating) gas at the high voltage terminal, and burn of a variable transformer for the electric power supply to an einzel lens.

The Tandetron was used for the experimental studies on the following subjects.

(1) Rutherford backscattering spectroscopy
  a) Analysis of the Tb distribution and damage in Tb-implanted CaF_2 (Semiconductor Lab. and Surface Characterization Center)
  b) Ion irradiation effect on Bi-Sr-Ca-Cu-O system, MoS_2, and $SrTiO_3$ (Surface Characterization Center and Surface and Interface Lab.)
  c) Characterization of AlN_x (Surface Characterization Center)
  d) RBS analysis of aluminum-titanium nitrides and tantalum oxides. (Metal Physics Lab.)
  e) Behavior of Kr atoms implanted into aluminum by a channeling method. (Metal Physics Lab.)
(2) Nuclear reaction analysis
  a) Lattice location of hydrogen in niobium alloys by a channeling method. (Metal Physics Lab.)
(3) Particle induced X-ray emission (PIXE)
  a) Application of PIXE to medical, environmental, archaeological, and materials science (Inorganic Chemical Physics Lab.)
(4) Sputtered neutral mass spectrometry (SNMS)
  a) Development of a new type of SNMS for ultra-high sensitive detection (Plasma Physics Lab. and Surface Characterization Center)
  b) Development of a multi-use high current ion source for accelerators (Plasma Physics Lab. and Surface Characterization Center)

RIKEN Accel. Prog. Rep. 24 (1990)

III. RESEARCH ACTIVITIES

1. Nuclear Physics

1. Measurement of Total Interaction Cross Section for $^{11}Li+^{12}C$ at 45 MeV/u

N. Inabe, S. Shimoura, T. Nakamura, H. Okuno, H. Okamura,
H. Sakai, T. Kubo, T. Nakagawa, H. Kumagai,
I. Tanihata, and M. Ishihara

(Nuclear density distribution, secondary nuclear reaction, heavy ion-collision, neutron halo.)

In the past several years, total interaction cross sections (σ_I) of various nuclei have been measured in 0.8 GeV/u region and found for extremely neutron rich nuclei such as ^{11}Li or ^{14}Be to have very large radii by fitting σ_I with a Glauber type calculation[1-3]. Figure 1 shows the energy dependence of σ_I obtained by the Glauber type calculation in three cases of matter distribution of ^{11}Li. These results suggest that the measurement of σ_I of ^{11}Li is important in an energy region of tens of million electronvolts per nucleon, where σ_I is particularly sensitive to neutron halo.

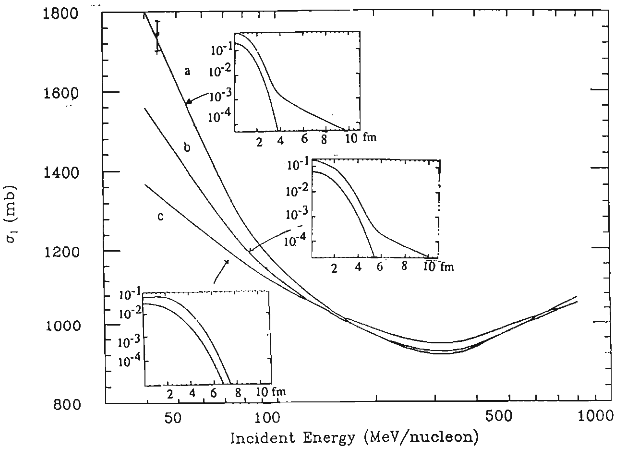

Fig. 1. Energy dependence of σ_I for $^{11}Li+^{12}C$ by Glauber Type calculation. Curve a, ^{11}Li with two neutron halo; c, ^{11}Li with no halo; b, intermediate of a and c. Insets illustrate the density distributions for each line; inner curves show a proton distribution and an outer curves a matter distribution of ^{11}Li.

We thus measured σ_I of ^{11}Li at 45 MeV/u by a transmission method in the RIKEN Ring Cyclotron radioactive beam line RIPS[4] with the setup shown in Fig. 2. We used ^{18}O (102 MeV/u) as a primary beam and ^{9}Be (2.22 g/cm^2) as a production target for ^{11}Li. ^{11}Li beams were separated from other fragments with an achromatic degrader, and identified by measuring an energy loss in SSD (F3SSD) and the time-of-flight (TOF) between scintillators at F2 (f2pl) and at F3 (f3pl). The purity of ^{11}Li as a secondary beam was about 98%. The image of the ^{11}Li beams was defined by using a position sensitive SSD

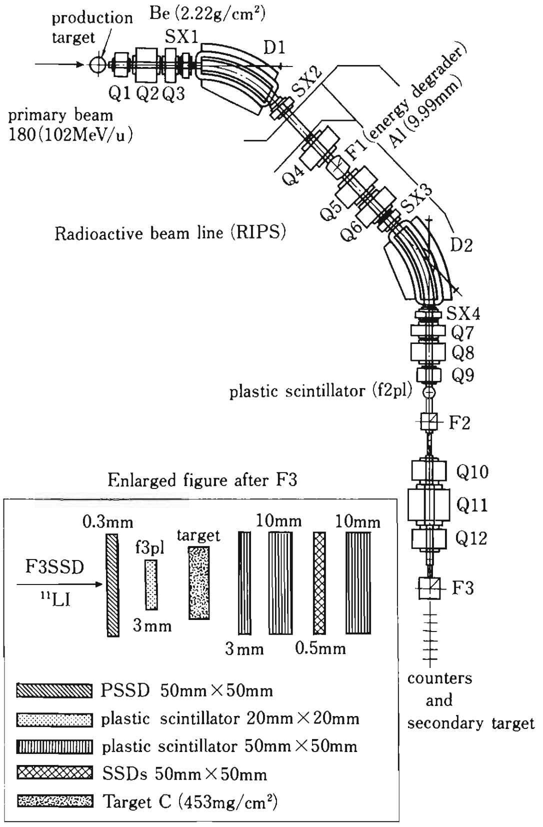

Fig. 2. Experimental setup. Because all ^{11}Li nuclei are stopped in the last plastic scintillator, their ranges can be analyzed.

(F3SSD). Setting a counter telescope composed of SSD's and plastic scintillators downstream of a secondary target (^{12}C 453 mg/cm^2), we made particle identification after secondary reactions by range and ΔE-E analysis.

σ_I is deduced from

$$\sigma_I = (1/N_t) \log (R_{out}/R_{in})$$

where R_{out} and R_{in} are the ratios of the counts of incident nuclides after and before entering the counter telescope. The suffix "in" stands for target-in-run and "out", target-out-run, and N_t is the number of a secondary target per unit area.

A preliminary value of σ_I (in Fig. 1) is 1740 ± 30 mb, which suggests that ^{11}Li has neutron halo.

References

1) I. Tanihata *et al.*: *Phys. Lett. B*, **206**, 592 (1988).
2) I. Tanihata *et al.*: *ibid.*, **160**, 380 (1985).
3) I. Tanihata *et al.*: *Phys. Rev. Lett.*, **55**, 2676 (1985).
4) T. Kubo *et al.*: This Report, p. 96.

RIKEN Accel. Prog. Rep. **24** (1990)

III-1-2. Three α Disintegration of ^{12}C in the Field of ^{208}Pb Nucleus at 35 MeV/u

T. Motobayashi, S. Kox, C. Perrin, F. Merchez, D. Rebreyend,
S. Kubono, T. Ichihara, and M. Ishihara

NUCLEAR REACTIONS $^{208}Pb(^{12}C, 3\alpha)^{208}Pb$, E = 35 MeV/u; measured $\sigma(\theta)$.
CsI(Tl) scintillator array, MWPC.

A projectile breakup process was studied for a $^{12}C + ^{208}Pb$ reaction by measuring outgoing three α particles in coincidence. A 35 MeV/u carbon beam was provided by the separate sector cyclotron of SARA facility at ISN Grenoble. Complete kinematical conditions of four body final state (3α and ^{208}Pb) were determined from the energies and scattering angles of the three α particles obtained by a multi-detector system consisting of 3 planes of MWPC and 24 CsI(T1) scintillators based on the EMRIC device developed at ISN Grenoble.[1]

Figure 1 shows a spectrum for the relative energy of the three outgoing α particles (or the excitation energy measured from the 3-α threshold of ^{12}C). The prominent peak corresponds to the second 0^+ state of ^{12}C at E_{ex} = 7.65 MeV. The 3^-state at 9.68 MeV is weakly excited. No evidence is seen for possible excitation of the 10.3 MeV state, where the spin assignment is still uncertain and strong effects on the elastic scattering channel is predicted by CDCC calculations.[2]

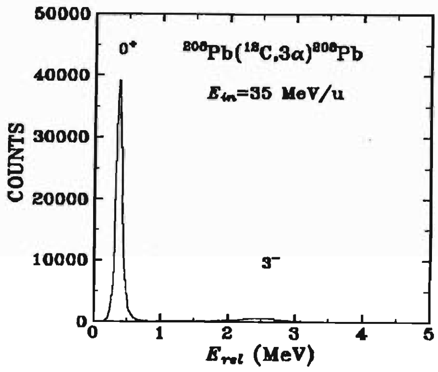

Fig. 1. Relative energy spectrum for outgoing three α particles. The horizontal axis represents the excitation energy from the three α threshold at 7.27 MeV above the ground state of ^{12}C. Two peaks correspond to the second 0^+ state at E_{ex} = 7.65 MeV and the 3^- state at 9.64 MeV.

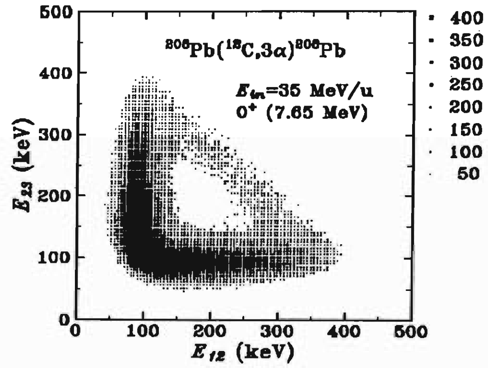

Fig. 2. Dalitz plot for three α particles decaying from the second 0^+ state of ^{12}C. The events are concentrated on three lines showing that two α particles out of three are in the ^{8}Be ground state with E_{rel} = 92 keV.

Figure 2 shows a Dalitz plot for the decay of the 0^+ state. The state decays with almost 100% probability to the $^{8}Be(0^+)+\alpha$ channel and few counts are seen for the decay to the 3-α continuum. This indicates that the decay width of the second 0^+ state of ^{12}C is dominated by the $^{8}Be(0^+)+\alpha$ channel. That is consistent with the present understanding of the helium burning process in stars, where the process $^{8}Be(0^+)+\alpha \rightarrow {}^{12}C(0^+; 7.65\ MeV) \rightarrow {}^{12}C(0^+; 0.0\ MeV)$ is assumed to play a dominant role in producing ^{12}C nucleus.[3]

References

1) F. Merchez, S. Kox, C. Perrin, J. Mistretta, J.C. Gondrand, L.N. Imouk, P. Gretillat, and E. Schwarz: *Nucl. Instrum. Methods*, **A275**, 133 (1989).
2) Y. Sakuragi, M. Kamimura, M. Yahiro, and Y. Fukushima: *J. Phys. Soc. Jpn.*, **54**, Suppl. II, p.88 (1985).
3) C. Rolf and H.P. Trautvetter: *Ann. Rev. Nucl. Part. Sci.*, **28**, 115 (1978).

RIKEN Accel. Prog. Rep. **24** (1990)

III-1-3. Coulomb Breakup Reaction of 90 MeV/u ^{14}O

T. Takei, T. Motobayashi, K. Ieki, H. Murakami, Y. Ando, N. Iwasa,
M. Kurokawa, C. Perrin, F. Merchez, S. Kox, D. Rebreyend,
S. Kubono, M. Ishihara, S. Shimoura, T. Kubo, and N. Inabe

NUCLEAR REACTIONS, ^{208}Pb(^{14}O, ^{13}Np), $E(^{14}O)/A$ = 91 MeV/u; measured correlation between proton and ^{13}N, CsI(Tl) scintillator array, position sensitive Si detectors, plastic hodoscopes.

The Coulomb breakup process, $^{14}O \rightarrow {}^{13}N+p$, in the field of ^{208}Pb nucleus was studied at 91 MeV/u. It can be related to the inverse reaction $^{13}N(p,\gamma)^{14}O$, which is of great astrophysical interest, because it is a key reaction for the hot CNO cycle. The process via the 1^- state of ^{14}O (E_{ex}=5.14 MeV) is important, and our purpose is to determine the transition probability between the ground 0^+ and 1^- states or the radiative width Γ_γ of the 1^- state.

Unstable ^{14}O ions of 91 MeV/u were provided by the RIPS facility at RIKEN. Outgoing proton and ^{13}N were detected in coincidence with the EMRIC device.[1] It consisted of plastic hodoscopes for angle measurement of protons, 24 two-dimensional position-sensitive silicon detectors for the angle determination and particle identification of heavy ions, and 24 CsI(Tl) crystals coupled with PMTs for the identification of protons and total energy measurement (Fig. 1).

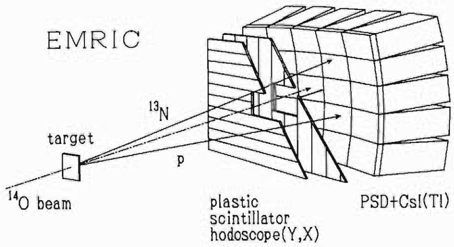

Fig. 1. Schematic view of the experimental setup.

Figure 2 shows a two dimensional plot of the energies of the proton and ^{13}N in coincidence. Events are concentrated on the line of Q_r=0, where Q_r denotes the excitation energy of the residual nucleus ^{208}Pb. About 4×10^4 events were collected and they are to be used to deduce Γ_γ after correcting for an experimental back ground.

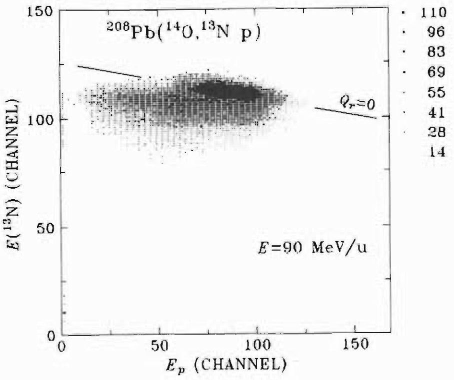

Fig. 2. Correlation between the energies of proton and ^{13}N. The kinematical locus of Q_r = 0 is shown by the solid line.

References

1) F. Merchez, S. Kox, C. Perrin, J. Mistretta, J.C. Gondrand, L.N. Imouk, P. Gretillat, and E. Schwarz: *Nucl. Instrum. Methods,* **A275**, 133 (1989).

RIKEN Accel. Prog. Rep. **24** (1990)

III-1-4. Tensor Analyzing Powers of $^1H(d,^2He)n$ Reaction at 200 MeV

T. Motobayashi, C. Perrin, J. Carbonell,*1 C. Wilkin,*2 S. Kox, F. Merchez,
Nguyen van Sen,*1 D. Rebreyend, G. Guillaume,*3 J. Arvieux,*4 J. Yonnet,*4
B. Bonin,*5 A. Boudard,*5 M. Garcon,*5 J. Guillot,*6 and G. Gaillard*7

[NUCLEAR REACTION $^1H(d,2p)$, E = 200 MeV; measured $A_{xx}(\theta)$, $A_{yy}(\theta)$.]

Tensor analyzing powers A_{xx} and A_{yy} have been obtained for the $^1H(d,^2He)n$ reaction at 200 MeV in the region of momentum transfer q=0–500 MeV/c and excitation energy of the final two proton system E_{ex}=0–8 MeV. The experiment was performed by using the synchrotron Saturne II at Saclay. A part of the results has been reported,[1] where the excitation energy was limited to 0–1 MeV and the data of A_{xx} at high momentum transfers were missing.

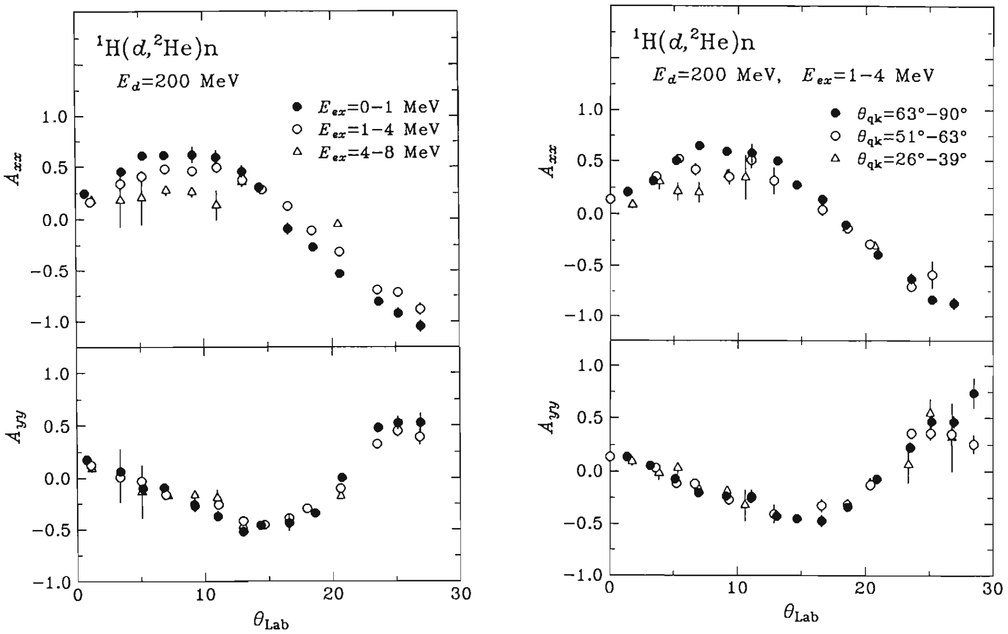

(a) (b)

Fig. 1. Tensor analyzing powers A_{xx} and A_{yy} for different E_{ex} (a) and θ_{qk} (b). The analyzing powers in (a) are averaged over the direction of the relative momentum $\boldsymbol{k}$.

Examples of the results are shown in Fig. 1. Only the tensor analyzing powers A_{xx} at around θ_{lab}=9° (corresponding to q=120 MeV/c) depend on both E_{ex} and θ_{qk}, where θ_{qk} is the angle between $\boldsymbol{q}$ and $\boldsymbol{k}$, relative momentum of the two protons. A plane wave impulse approximation (PWIA) calculation[2] predicts larger admixture of P-wave into the dominant $^1S_0$ state at higher excitation energies E_{ex}. The P-wave contamination results the reduction of A_{xx} values at around q=200 MeV/c depending on θ_{qk} by the form, $A_{xx}=a-b\cos^2\theta_{qk}$, where a is a constant independent of E_{ex}, whereas b increases with E_{ex}. These features are consistent with our observations.

---

*1 Institute des Sciences Nucleaires, 38026 Grenoble Cedex, France.
*2 University College London, London WC1E 6BT, U.K.
*3 Centre de Recherches Nucleaires, 67037 Strasbourg Cedex, France.
*4 Laboratoire National Saturne, 91191 Gif-sur-Yvette Cedex, France.
*5 DPhN/ME-Saclay, 91191 Gif-sur-Yvette Cedex, France.
*6 Institute de Physique Nucleaire, 91406 Orsay Cedex, France.
*7 DPNC Universite de Geneve, 1211 Geneve 4, Switzerland.

References

1) T. Motobayashi, C. Perrin, J. Carbonell, C. Wilkin, S. Kox, F. Merchez, Nguyen Van Sen, D. Rebreyend, G. Guillaume, J. Arvieux, J. Yonnet, B. Bonin, A. Boudard, M. Garçon, J. Guillot, and G. Gaillard: *Phys. Lett.*, **B233**, 69 (1989); *RIKEN Accel. Prog. Rep.*, **23**, 8 (1989).
2) J. Carbonell and C. Wilkin: in preparation.

RIKEN Accel. Prog. Rep. **24** (1990)

III-1-5. Polarization Measurement of ^{12}B and ^{13}B in the Reaction $^{15}N+^{197}Au$ at 112MeV/u

H. Okuno, K. Asahi, T. Nakamura, M. Adachi, H. Miyatake,
T. Shimoda, N. Takahashi, T. Ichihara, N. Inabe, T. Kubo, A. Yoshida,
D. Mikolas,* D. Morrisey,* D. Beaumel,** and M. Ishihara

NUCLEAR REACTION $^{197}Au+^{15}N$, $E=112MeV/nucleon$; measured β-ray asymmetry of ^{12}B and ^{13}B nuclei; deduced spin polarization ^{12}B and ^{13}B.

Spin polarization of ^{12}B and ^{13}B were measured in the reaction $^{15}N+^{197}Au$ (target thickness 200 μm) at 112MeV/u by using a radioactive beam line RIPS.[1] The beam swinger of RIPS was used to collect fragments at 2, 4, and 6 degrees. ^{12}B and ^{13}B were seperated from other fragments with RIPS, and implanted into a Pt stopper placed at the final focus of RIPS (Fig. 1). Spin polarization was deduced from the observed up/down asymmetry in the beta decay of ^{12}B ($T_{1/2}=20.2$ ms) and ^{13}B ($T_{1/2}=17.4$ ms).

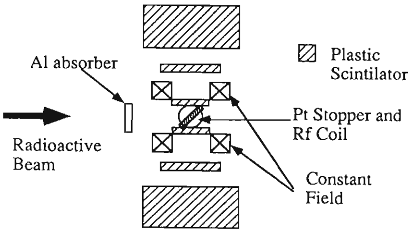

Fig. 1. Setup at the final focus of RIPS.

Experimental results are presented in Fig. 2. The momentum distribution of ^{12}B shown in the upper part exhibits a single broad peak with a maximum located closed to the momentum corresponding to the incident beam velocity. The spin polarization observed is shown in the lower part of Fig. 2, as a function of the momentum. The size of polarization takes a maximum value near the peak of the momentum distribution while the sign stays negative in the whole range of momentum. The result for ^{13}B is similar to that for ^{12}B. This momentum dependence of the polarization is different from that obtained. $^{14}N+^{197}Au$ at 40MeV/u.[2] Up to now we have not yet attained a full understanding of the observed behaviors of polarization. Clearly, futher extent ion of measurement at, *e.g.*, different reaction channels and energies is necessary. Recently, we measured spin polarization of ^{12}B and ^{13}B in $^{15}N+X$ reactions (X=Al, Nb, Tb, Au) at 70 MeV/u. Data Analysis is now in progress.

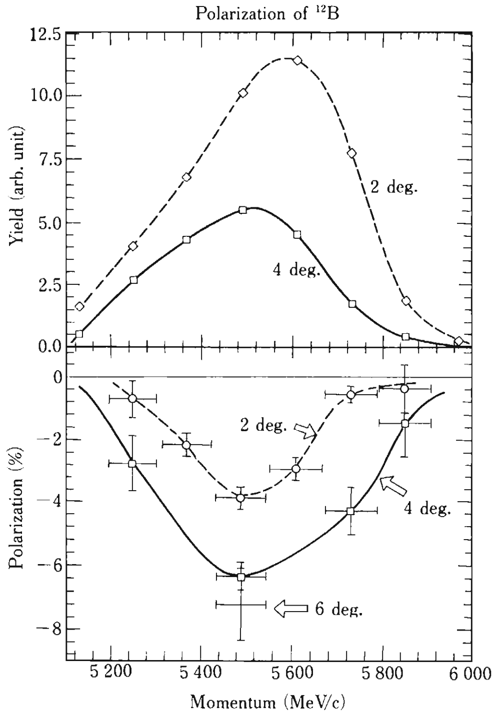

Fig. 2. Experimental result. The spin polarization (lower part) and the yield (upper part) ^{12}B are shown as a function of outgoing momentum.

References

1) T. Kubo *et al.*: This Report, p. 96.
2) K. Asahi *et al.*: *RIKEN Accel. Prog. Rep.*, **23**, 18 (1989).

---

* NSCL, Michigan State University, East Lansing, MI 48824, U.S.A.

** Institut de Physique Nucleaire, B.P. 1, 91406 Orsay, France.

RIKEN Accel. Prog. Rep. **24** (1990)

III-1-6. Negative Pion Production in Subthreshold Nuclear Collisions

T. Suzuki, N. Inabe, T. Nakagawa, K. Yoshida, and I. Tanihata

〔NUCLEAR REACTION, ^{14}N(C,π^-)X, measured σ_{π}-(E); deduced slope factor.〕

Inclusive π^- spectra have been measured for ^{14}N+C collisions at 67A, 80A and 135A MeV. Experimental details can be found in Ref. 1. Lorentz-invariant cross sections, $(1/p)d^2\sigma/d\Omega dE$, depend exponentially upon the pion energy in the nucleon-nucleon c.m. frame with a inverse slope T_0 as indicated in Fig. 1. In Fig. 2 we plot the slope factors T_0, for π^- produced at $\theta_{c.m.}=90°$, over a wide range of the mass and beam energy.[3] The slope factor T_0 decreases monotonously as the beam energy decreases down to around 100A MeV. However, the behavior seems to change below 100A MeV, where T_0 appears to flatten out down to 25A MeV. Although a slight decrease in the slope factor with beam energy is indeed observed within a error bar, energy distributions below 100A MeV are less steep than expected from the monotonous decrease in the slope factor down to 100A MeV. A recent BUU calculation which includes both the $\Delta \rightarrow N\pi$ channel and the tail portion of the momentum distribution originating from short range correlations reproduces above behavior.[4]

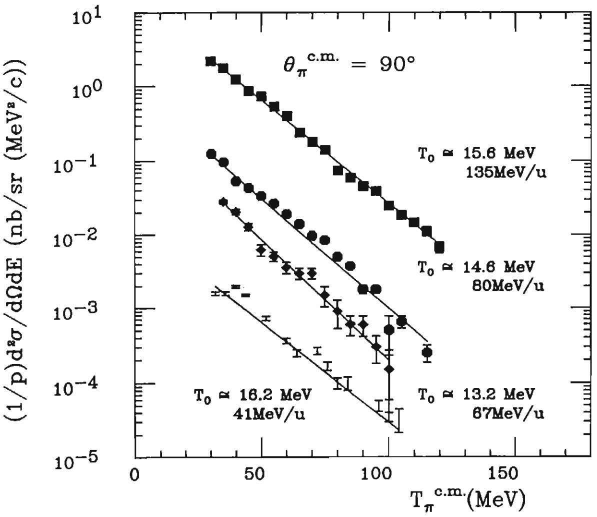

Fig. 1. Lorentz-invariant cross sections, $(1/p)d^2\sigma/d\Omega dE$, for inclusive π^- production in ^{14}N + C collision, at energies indicated. Only statistical errors are shown in the plot. T_0 is the slope factor when the cross sections are parameterized by $\exp(-T_\pi/T_0)$.

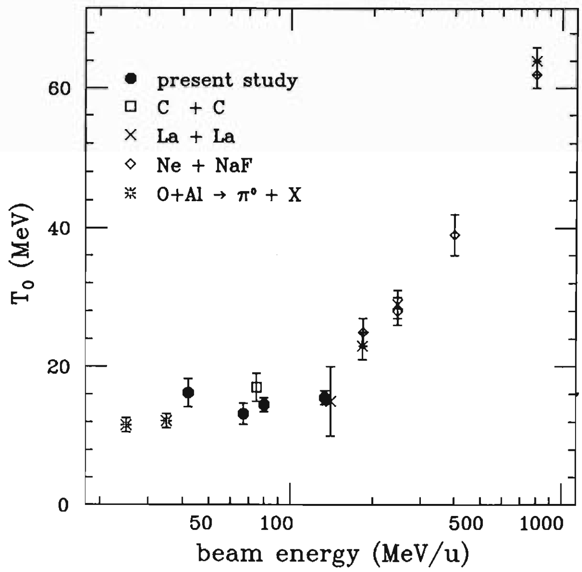

Fig. 2. Slope factor, T_0, for π^- spectra at $\theta_{c.m.}$ = 90°, plotted as a function of beam energy for a variety of targets and projectiles, at beam energies between 41 and 800A MeV. For comparison, the apparent temperature deduced from π^0 transverse momentum spectrum, $(d\sigma/dp_\perp)$, assuming the isotropic emission with $d^3\sigma/dp^3 \propto \exp(-T_\pi/T_0)$ in the frame where the pion source is at rest, are also plotted. The π^- data are from Refs. 1,2, and the present study. The π^0 data are taken from Ref. 2.

References

1) T. Suzuki *et al.*: *Phys. Lett. B*, (1991), in press.
2) G.R. Young *et al.*: *Phys. Rev.*, **C33**, 742 (1986); J. Stachel *et al.*: *ibid.*, p.1420.
3) I. Tanihata *et al.*: *Phys. Lett.*, **87B**, 349 (1979); S. Nagamiya *et al.*: *Phys. Rev.*, **24**, 971 (1981); *Phys. Rev. Lett.*, **48**, 1780 (1982); T. Johansson *et al.*: *ibid.*, **48**, 732 (1982); V. Bernard *et al.*: *Nucl. Phys.*, **A422**, 511 (1984); J. Miller *et al.*: *Phys. Rev. Lett.*, **58**, 2408 (1987); *ibid.*, **59**, 519 (1987).
4) K. Niita *et al.*: *Nucl. Phys.*, (1991), in press.

RIKEN Accel. Prog. Rep. 24 (1990)

III-1-7. Target Dependence of Surface Muon Yields in Heavy Ion Reactions

K. Ishida, T. Matsuzaki, K. Nagamine, R. Kadono, A. Matsushita,
H. Kitazawa, Y. Miyake, and E. Torikai

[NUCLEAR REACTION, pion production, measured surface muon yield.]

Muon is an elementary particle that has many applied fields such as μSR and μCF. We started to investigate the production of surface muons in various targets using a ^{14}N beam of 135 MeV/u from RIKEN Ring Cyclotron. Since surface muons are produced from decay of positive pions produced in nuclear reactions and stopped near the surface skin of a production target, low-energy pions (below 10 MeV) mostly contribute to the surface muon production. Thus surface muon is a sensitive probe for the investigation of low-energy pion production.

In this experiment, muons were transported through a "Large Ω" beam course and were identified by a counter system reported in Ref. 1. Experimental muon yield divided by the number of target nuclei is expected to give a value which is almost proportional to the cross section of low-energy (<10 MeV) pion production. The result is shown in Fig. 1.

In order to understand the target mass dependence of the muon yield, we carried out a Monte-Carlo calculation on the yield of surface muons on the basis of the following model of pion production.[1-4]

(1) The total pion-production cross section depends on the projectile mass number and the target mass number, $S_\pi(A_P A_T)^{2/3}$, where S_π is a normalized cross section.

(2) Pion is emitted from a hot nucleus produced as a result of projectile-target collision, where the number of participating nucleons can be obtained from the values listed in Table 1 of Ref. 2. A pion emission angle is isotropic in the frame moving with a pion source (PS frame).

(3) Pion kinetic energy distribution is an exponentially decreasing function with an inverse slope constant T_0 in the PS frame.[3] Three different values of T_0 (15, 25, and 35 MeV) were used to cover the uncertainty of this value. The Coulomb interaction of positive pion with the pion source was included as a final pion energy shift.[4]

Result of the calculation is shown in Fig. 1. The scale of the lines calculated relative to the experimental data was chosen arbitrarily with $S_\pi = 9\,\mu$b. We found that the conversion efficiency of the produced pions into surface muons is almost independent of the target mass number, as far as T_0 is taken independent of the target, and, thus, the surface muon yield calculated is almost proportional to the pion production cross section. The measured muon yield is flattened for heavier targets, while it seems consistent with $A_T{}^{2/3}$ dependence for lighter targets. Although this tendency is in qualitative agreement with π^0 and π^+ data obtained at lower projectile energies,[3,4] the descrepancies from $A_T{}^{2/3}$ seems to be more pronounced in our case. This might indicate the effects characteristic of low energy pion emission such as pion reabsorption.

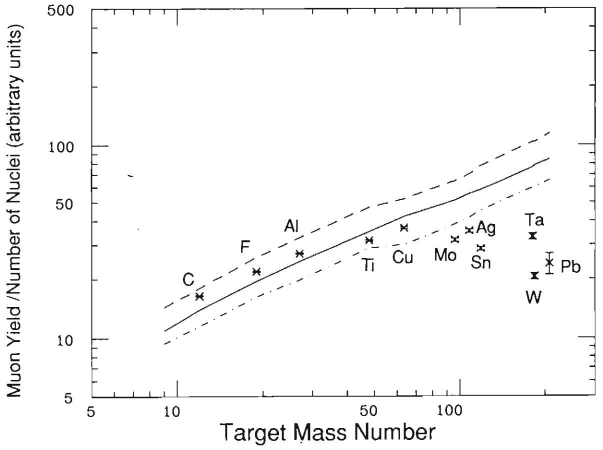

Fig. 1. Number of detected muons normalized by the number of nuclei in a target. The three lines show calculated results for three values of inverse slope constant T_0 of 15 MeV (dashed line), 25 MeV (solid line), and 35 MeV (dashed dotted line) with an arbitrarily chosen value of $S_\pi = 9\,\mu$b.

References

1) K. Ishida *et al.*: *RIKEN Accel. Prog. Rep.*, **23**, 26 (1989).
2) M. Prakash *et al.*: *Phys. Rev.*, **C33**, 937 (1986).
3) J. Stachel *et al.*: *ibid.*, p. 1420.
4) V. Bernard *et al.*: *Nucl. Phys.*, **A423**, 511 (1984).

RIKEN Accel. Prog. Rep. **24** (1990)

III-1-8. Identification of *Z* near 30 Nuclei

M. Yanokura, H. Xu, C. Alok, X. Bai, M. Fujimaki,
N. Inabe, K, Kimura, T. Kubo, H. Kumagai,
T. Nakagawa, T. Suzuki, M. Tapan, and I. Tanihata

〔NUCLEAR REACTIONS 20 A MeV ^{64}Zn + Be, particle identification.〕

A Be target of 17.2 mg/cm^2 was bombarded with a beam of 20.11A MeV and 20 enA $^{64}Zn^{20+}$ provided by RRC with RILAC as an injector. The purpose of the experiment is to observe $T_Z = -1/2$ exotic nuclei such as ^{61}Ga, ^{63}Ge, and ^{65}As. In this *Z* region, it is difficult to get good particle identification. Our detecting system and the identification abilities of the system are briefly presented as follows.

To determine the charge state, atomic numbers, and masses of the reaction products, we used a detector telescope with RIPS$^{1)}$ at the RRC facility. The detector telescope, consisting of a PPAC, a MUSIC,$^{2)}$ and a Position Sensitive Silicon Detector (PSSD) was positioned behind the F3 plane of RIPS. The Time-of-Flight (TOF) was measured by using the RF signal of the cyclotron and PPAC. The flight path was 2,779.6 cm. A ΔE detector is a MUSIC operated in an ionization chamber mode. The chamber was 50 cm in sensitive length and was filled with 76 Torr P10 gas. Remaining energy was measured with a PSSD of 45 mm × 45 mm × 300 μm after MUSIC.

The identification abilities of this detecting system were shown in Figs. 1 and 2.

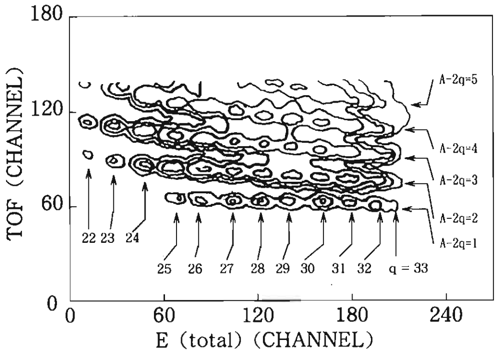

Fig. 1. TOF *vs.* *E* (total) contour plot. It shows the resolution of charge states. From outside to inside, the counts are 2, 4, 10, 50, and 360 respectively. Both $A-2q$ line and q line are indicated on the plot.

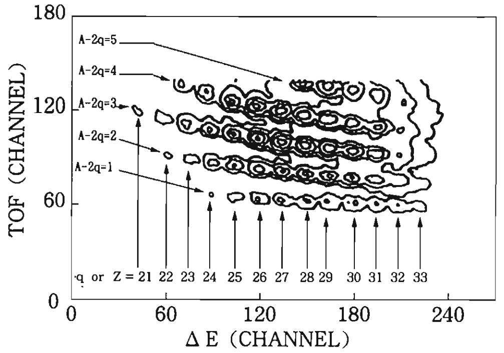

Fig. 2. TOF *vs.* ΔE contour plot. It shows the resolution of atomic numbers. The scales are similar to Fig. 1. Both $A-2q$ line and Z line are indicated on the plot.

Figure 1 refers to the contour plot of TOF *vs.* *E* (total). Here a slight conversion of plot was made so that all the events for each q or Z appear almost on a vertical line. A similar treatment was also made in Fig. 2, which shows a TOF *vs.* ΔE contour plot which stands for Z distribution. The calibration points of q, Z, and A on the contour plots were obtained from a wedge shaped Al target run using the primary beam. Under the conditions mentioned above, an atomic number resolution of $\sigma_z = 0.24e$ at $Z = 30$ and a charge state resolution of $\sigma_q = 0.26e$ at $q = 30$ were obtained. The resultant A resolution in conbination with RIPS was about $\sigma_A \sim 0.26$.

In conclusion, the identification has been carried out successfull for the nuclei of Z near 30.

References

1) T. Kubo, M. Ishihara, *et al.*: Proc. 1st Int. Conf. on Radioactive Nucl. Beams, Univ. California at Berkeley and Lawrence Lab., Berkeley, California, Oct., p. 563 (1989).
2) K. Kimura *et al.*: *RIKEN Accel. Prog. Rep.*, **23**, 97 (1989).

RIKEN Accel. Prog. Rep. **24** (1990)

III-1-9. First Observation of a Proton-Rich Isotope ^{65}As

H. Xu, M. Yanokura, C. Alok, X. Bai, M. Fujimaki,
N. Inabe, K. Kimura, T. Kubo, H. Kumagai,
T. Nakagawa, T. Suzuki, M. Tapan, and I. Tanihata

NUCLEAR REACTIONS 20*A* MeV ^{64}Zn + Be, particle identification; search for proton-rich isotope ^{65}As.

Establishing the limits of the particle stability for nuclei has been a goal of experimentalists for many years. Theoretical estimates predicated that up to 8,000 nuclides might lie within the boundaries of the particle stability of nuclei. Among them, only about 2,000 nuclides have been identified. This field still receives an increasing amount of attention.

A number of exotic nuclei were observed with the advent of the intermediate and high energy heavy ion accelerators.$^{1-4)}$ Most of them were produced by projectile fragmentation. However, it is now widely recognized that in the energy domain of tens to a hundred MeV per nucleon, the clean picture of high energy fragmentation can not yet be applied. Mean field effcts are still important and a so-called fragmentation peak originates in fact from the superposition of various processes: transfer reactions, direct breakup, sequential breakup, and mixtures of these mechanisms. As for the nuclei of $30 < Z < 34$, moreover, there seem no suitable stable nuclei for the projectiles to produce their unobserved isotopes in a proton-rich side via projectile fragmentation. This is because the isotopes to be searched lie far from the stability line. In the present work, the relatively proton-rich stable nucleus ^{64}Zn was chosen as a projectile to produce unobserved proton-rich isotopes in this Z region by few-nucleon transfer reactions.

The experiment was carried out on RIPS.$^{5)}$ A Be target of 17.2 mg/cm^2 was bombarded with a beam of 20.11*A* MeV ^{64}Zn^{20+} provided by RRC with RILAC as an injector. Under these conditions, an atomic number resolution of $\sigma_Z = 0.24$ at $Z = 30$ and a mass resolution of $\sigma_A = 0.26$ at $A = 60$ were obtained. Data were accumulated in a 4-h period, during which a primary beam intensity was $\sim 6 \times 10^9$ particle/s.

By taking the data corresponding to $Z = 33$ and $A - 2q = 1$, we have a histogram of E (total) as displayed in Fig. 1. There appear only two peaks which are ^{65}As^{32+} and ^{67}As^{33+}, respectively. This is the first observation of a proton-rich isotope ^{65}As.

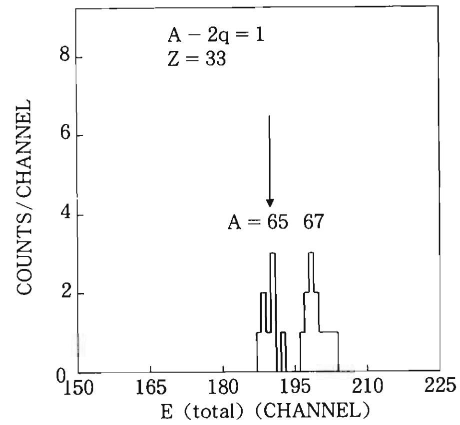

Fig. 1. Histogram of the data from only $A - 2q = 1$ line and $Z = 33$ corresponding to TOF *vs.* E (total) contour plot. Only two peaks appear due to the ±5% rigidity acceptance. They are ^{65}As^{32+} and ^{67}As^{33+}. Isotope ^{65}As are observed first time (as indicated by the arrow).

For clarifying the faithfulness of the ovservation, consideration should be given to a possible contaminant arising from the neighboring peak of $Z = 32$. If a Gaussian distribution is assumed to hold for each Z, the contamination infiltrated into the peak of $Z = 33$ accounts for 2.7% of the peak of $Z = 32$ according to the Z resolution. It is much less than the events of $Z = 33$.

References

1) V.V. Volkov: *Treatise of Heavy-Ion Science*, **8**, 101 (1989).
2) A.C. Muller *et al.*: *Nucl. Phys. A*, **455**, 149 (1986).
3) J.A. Musser and J.D. Stevenson: *Phys. Rev. Lett.*, **53**, 2544 (1984).
4) F. Pougheon *et al.*: *Z. Phys. A*, **327**, 17, (1987).
5) T. Kubo, M. Ishihara *et al.*: Proc. 1st Int. Conf. on Radioactive Nucl. Beam, Univ. of California at Berkeley and Lawrence Lab. Berkeley, California, 16–18 Oct., p. 563 (1989).

RIKEN Accel. Prog. Rep. **24** (1990)

III-1-10. Coulomb Excitation of Unstable Nucleus ^{76}Kr

Y. Gono, M. Oshima, H. Kusakari, T. Murakami, and M. Sugawara

NUCLEAR REACTIONS ^{9}Be(^{70}Ge,3n)^{76}Kr, ^{208}Pb(^{76}Kr, ^{76}Kr$'\gamma$), E(^{70}Ge) = 320 MeV; measured E_{γ}.

γ Rays from the Coulomb excitation of an unstable nucleus ^{76}Kr were observed for the first time. The nucleus ^{76}Kr was produced by the ^{9}Be(^{70}Ge,3n)^{76}Kr reaction under the conditions as follows; (1) A ^{70}Ge beam of 320 MeV was delivered by JAERI tandem accelerator. (2) Targets were 1.5 mg/cm^2 ^{9}Be for production and 2 mg/cm^2 ^{208}Pb for Coulomb excitation. (3) The ^{9}Be target was surrounded with 19 BaF$_2$ crystals. (4) The annular plastic detector (PS) segmented into four was used to detect ^{76}Kr scattered by Pb. (5) γ Rays emitted from Coulomb-excited ^{76}Kr were measured by 4 HPGe's shielded with a 20 cm Pb from the ^{9}Be target. Under these conditions the kinetic energy of the secondary beam of ^{76}Kr was estimated as 185±21 MeV. The γ rays emitted by Coulomb excitation were measured in coincidence with TOF signals between PS and BaF$_2$.

The 424 keV γ ray of the $2^+ \rightarrow 0^+$ transition in ^{76}Kr is clearly seen in Fig. 1. This peak is concluded to originate from Coulomb excitation of ^{76}Kr on the basis of the facts that (1) the peak energy was 424 keV after the reasonable Doppler shift correction (424 keV γ rays from other origins should have different Doppler shift) and (2) the yield of this peak was consistent with that estimated for the present experimental setup using a known half-life.[1)]

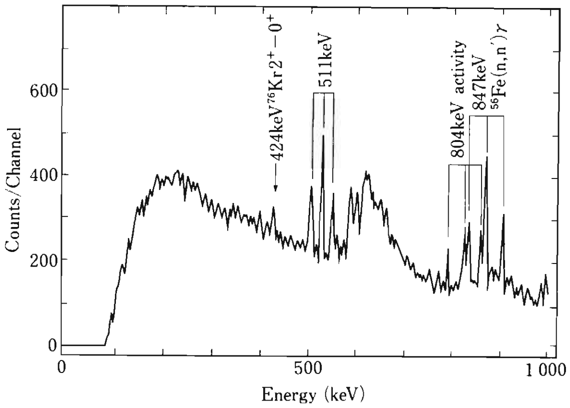

Fig. 1. Doppler corrected γ-ray spectrum of Coulomb-excited ^{76}Kr. Peaks from activities, 511, 804, and 847 keV, resulted in three peaks because of the Doppler shift corrections made for three different angles between Ge's and PS's.

This is a first successfull experiment of Coulomb excitation of unstable nucleus and may open a new possibility of an application of unstable nucleus beams.

References

1) E. Nolte *et al.*: *Z. Phys.*, **268**, 267 (1974).

RIKEN Accel. Prog. Rep. **24** (1990)

III-1-11. Isomer Decay of ^{136}Ce Studied by GARIS

Y. Gono, T. Murakami, H. Kusakari, M. Oshima,
K. Morita, A. Yoshida, and H. Kumagai

NUCLEAR REACTIONS ^{9}Be(^{132}Xe, 5n), $E/A=7.0$ MeV; Gas Filled Recoil Ion Separator; measured $E\gamma$, $I\gamma$, γ γ-coin, deduced $B(E1)/B(E2)$.

Delayed γ rays in ^{136}Ce were measured by using the ^{9}Be(^{132}Xe,5n)^{136}Ce reaction. A 7.0 MeV/u ^{132}Xe beam was delivered by RRC. The reaction product ^{136}Ce was collected to a Pb catcher after the separation of the ^{132}Xe beam by a gas-filled ion separator, GARIS.[1]

γ-Ray spectra taken at a ^{9}Be target and the catcher positions are shown in Fig. 1(A) and (B), respectively. The 683.1 keV peak in (B) was found for the first time and was assigned as the transition between the 8^+ and 7^- states in ^{136}Ce, as shown in Fig. 2, on the basis of a γ-γ coincidence measurement. The intensity of the γ ray was found to be 1.2% of the 552.1 keV γ ray of the $2^+ \rightarrow 0^+$ transition. The yield corresponds to ~ 0.3% of the total yield of ^{136}Ce since the isomer ratio of the 10^+ isomer was obtained to be 0.22 in the present experiment. This γ ray yield is the same order of magnitude as that of the weakest γ ray so far observed even with the elaborated compton suppressed multidetector system.

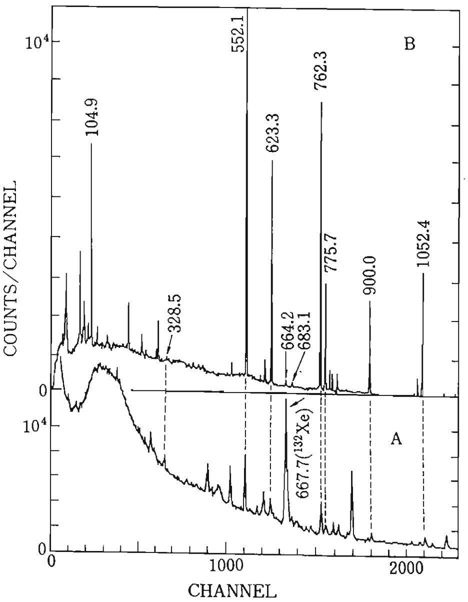

Fig. 1. γ-ray spectra taken at the target position (A) and the catcher position (B).

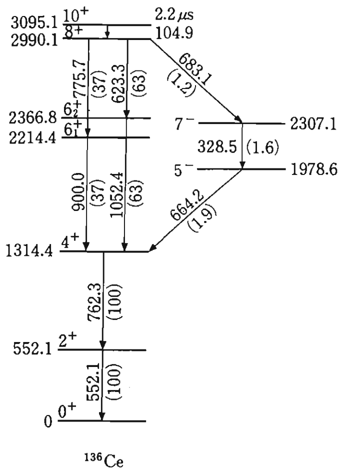

Fig. 2. Partial level scheme of ^{136}Ce.

The ratios $B(E1$: $8^+ \rightarrow 7^-)/B(E2$: $8^+ \rightarrow 6_1{}^+)$ and $B(E1$: $8^+ \rightarrow 7^-)/B(E2$: $8^+ \rightarrow 6_2{}^+)$ were deduced to be 4.3×10^{-5} and 2.2×10^{-4} fm^{-2}, respectively. They are relatively large compared with those of other nuclei.[2] This point will be discussed in a forthcoming paper.[3]

References

1) K. Morita *et al.*: *RIKEN Accel. Prog. Rep.*, **21**, 155 (1987).
2) *e.g.* Y. Gono *et al.*: *Phys. Lett.*, **49B**, 338 (1974).
3) T. Murakami *et al.*: submitted to *J. Phys. Soc. Jpn.*

RIKEN Accel. Prog. Rep. **24** (1990)

III-1-12. γ-Vibrational States in ^{164}Dy

M. Oshima, H. Kusakari, M. Sugawara, T. Inamura, A. Hashizume,
H. Kumagai, S. Ichikawa,* and H. Iimura*

NUCLEAR REACTIONS ^{164}Dy(^{58}Ni, ^{58}Ni'γ), $E=240$ MeV; measured $E\gamma$, particle-γ angular correlation.

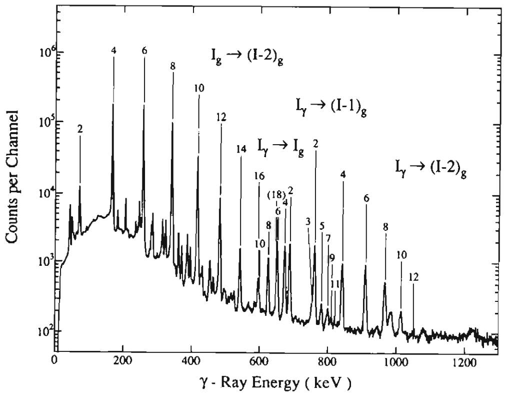

Fig. 1. Doppler-corrected γ-ray spectrum observed in coincidence with backward-scattered projectiles in multiple Coulomb excitation ^{164}Dy(^{58}Ni, ^{58}Ni') at $E=$ 240 MeV.

The ^{164}Dy nucleus is known to be well deformed and to have a one-phonon γ-vibrational state at the lowest excitation energy in this mass region. Thus this nucleus is best suited for the study of the γ-vibrational mode in deformed nuclei. An important question is whether two phonon γ-vibrational states exist or not.[1-4] No definite evidence for two phonon γ-vibrational states in deformed nuclei have so far been provided experimentally. Because of this, we have made a multiple-Coulomb-excitation experiment on ^{164}Dy.

^{164}Dy was multiply Coulomb-excited with a beam of 240-MeV ^{58}Ni obtained from the JAERI tandem accelerator. The target ^{164}Dy was a self-supporting metallic foil of 1.8 mg/cm^2 in thickness (95% isotopically enriched). Deexcitation γ rays were observed with four Compton-suppressed γ-ray spectrometers (RIKEN BGO-ACS)[5] in coincidence with recoiled target atoms and scattered projectiles detected with four PPACs (Parallel Plate Avalanche Counter). PPACs were placed symmetrically with respect to the beam, surrounding the target, so that they covered forward as well as backward angles. The size of PPAC was 10 cm×10 cm, and the distance between the center of the PPAC window and the target was 7 cm. PPACs detected recoiled particles as well as scattered ones, and provided the position signals of the particles. The timing signals from PPACs were used to distinguish between the two. The observed γ-ray spectra were corrected for Doppler shifts kinematically by using the position signals.

Figure 1 shows a Doppler-corrected spectrum corresponding to the backward scattering of the projectiles. We observed members of the ground-state rotational band up to 18$^+$ and of the γ band up to 12$^+$. The transition from a two-phonon γ-vibrational state to a one-phonon state is, however, not observed in the energy range of 750–1100 keV, which corresponds to the excitation energy of the two-phonon state at 2.0–2.5 times higher than that of the one-phonon state.

Because the Coulomb-excitation cross section is a direct function of B (E2), the upper limit of the unobserved γ-ray intensity gives that of the B (E2; $4_{\gamma\gamma} \rightarrow 2_\gamma$) value. The estimation shows that B (E2; $4_{\gamma\gamma} \rightarrow 2_\gamma) \leq 2.5$ W.u. Several theoretical investigations predicted rather large B (E2) values for a neighboring well-deformed nucleus ^{168}Er: for example, self-consistent collective-coordinates analysis done by Matsuo *et al.* predicted 9 W.u. for this value;[1] also Yoshinaga *et al.* predicted 7 W.u. based on an interacting boson model.[2] In ^{164}Dy, however, it can be said that a two-phonon γ-vibrational state with large collectivity does not exist in the energy region between 2.0 and 2.5 times that of the one-phonon γ-vibrational state.

A large scale analysis[6] is under way to determine precisely the β- and γ-deformations for the ground and γ band as a function of spin.

References

1) M. Mastuo and K. Mastuyanagi: *Prog. Theor. Phys.*, **74**, 1227 (1985); **76**, 93 (1986); and **78**, 591 (1987).
2) N. Yoshinaga *et al.*: *Phys. Rev. Lett.*, **56**, 1116 (1986).
3) V.G. Soloviev: E4-87-795, Dubna (1987).
4) M.K. Jammari and R. Piepenbring: *Nucl. Phys.*, **A487**, 77 (1988).
5) M. Fukuda *et al.*: *RIKEN Accel. Prog. Rep.*, **18**, 152 (1984).
6) for example, D. Cline: *Ann. Rev. Nucl. Part. Sci.*, **36**, 681 (1986).

---

* Japan Atomic Energy Research Institute at Tokai.

RIKEN Accel. Prog. Rep. **24** (1990)

III-1-13. Study of the Decay Property of ^{20}Na

—Onset Mechanism of the Rapid-Proton Process—

S. Kubono, Y. Funatsu, N. Ikeda, M.H. Tanaka, T. Nomura, T. Kubo,
N. Inabe, T. Ichihara, M. Ishihara, M. Ohura, H. Orihara, S. Kato,
H. Okuno, S. Shimoura, K. Asahi, H. Ohnuma, and T. Kajino

[NUCLEAR STRUCTURE, ^{20}Na, Radioactive beam of ^{20}Mg, Explosive hydrogen burning.]

The rapid-proton (rp) process,[1)] which will take place in high-temperature, hydrogen-rich stellar sites such as in novae and super novae, is expected to involve many proton-rich unstable nuclei. However, the nuclear structures are often not well known of these nuclei. It should be worthwhile to check experimentally the key nuclear reactions for nucleosynthesis scenarios in nuclear astrophysics. Some scenarios are still standing on rather fragile bases in a sense of nuclear physics.

Recently,considerable efforts have been made for investigating experimentally the breakout process from the hot-CNO cycle,[2)] which leads to the onset of the rp-process. The main sequence of the breakout process is considered to be ^{15}O(α, γ)^{19}Ne(p, γ)^{20}Na.[1,3)] Although the nuclear structure of ^{20}Na is so crucial for this process, it was almost unknown until recently.[4)] We have identified[5–7)] many new levels by the (^{3}He, t) and (p, n) reactions on ^{20}Ne, including a possible s-wave resonant state (1^+) at 2.637 MeV which is the first excited state above the proton threshold. The stellar reaction rate of the ^{19}Ne(p, γ) ^{20}Na process calculated[6)] based on these experimental results is about two orders of magnitude larger than the previous theoretical predictions,[1,3)] suggesting the onset temperature of the rp-process to be about a factor of two smaller than those predicted before. However, these are some assumptions made for this estimate which are the same as in Ref. 3. To learn the mechanism and the absolute temperature of the onset of the rp-process, the decay property of ^{20}Na has to be studied, especially the widths for proton and gamma decays as well as the total widths of the states near and above the proton threshold.

A test experiment was performed to investigate the decay property of the threshold states in ^{20}Na by using the projectile fragment separator RIPS in the RIKEN Ring Cyclotron Facility. Specifically, the decay property of the crucial threshold state, the 2.637 MeV 1^+ state, was partly studied.

The secondary beam of ^{20}Mg was produced from the ^{24}Mg induced fragmentation process, and separated by using the RIPS. The primary beam energy was set to 100 MeV/u. The secondary beam had high contaminations of other beams, especially of ^{18}Ne. On the focal plane F3 of the RIPS, ^{20}Mg particles were stopped in an array of silicon detectors of 100 μm, in which the decay protons were measured. Two Ge detectors were also set for gamma decay measurement at 90°. The beta counter made of three sets of ΔE-E plastic-scintillator telescopes covers about 70% around the silicon detector array. Because of the low intensity of the secondary beam and the severe contamination of other particles, only the proton decay was measured.

In the preliminary result of the experiment, Several sharp peaks were observed in the proton spectrum. Even the proton decay information will give an insight to the nuclear structure as well as the resonance property of the states of interest.

To confirm these preliminary results, a final experiment will be performed soon with better setups.

References

1) R. Wallace and S.E. Woosley: *Astrophys. J., Suppl.*, **45**, 389 (1981).
2) R.R. Caughlan and W.A. Fowler: *Nature Phys. Sci.*, **238**, 23 (1972).
3) K. Langanke *et al.*: *Astrophys. J.*, **301**, 629 (1986).
4) F. Ajzenberg-Selove: *Nucl. Phys.*, **A475**, 1 (1987).
5) S. Kubono *et al.*: *Z. Phys.*, **A331**, 359 (1988).
6) S. Kubono *et al.*: *Astrophys. J.*, **344**, 460 (1989).
7) S. Kubono *et al.*: Proc. Int. Symp. on Heavy Ion Physics and Nuclear Astrophysical Problems, World Scientific Pub. (Singapore), ed. S. Kubono *et al.*, p. 83 (1989).

RIKEN Accel. Prog. Rep. **24** (1990)

III-1-14. Nuclear Polarization of ^{33}Si with Optical Pumping in Solids

K. Shimomura, T. Nakamura, H. Okuno, M. Koizumi, S. Hamada,
N. Inabe, I. Ogawa, K. Suzuki, M. Wada, H. Sunaoshi,
Y. Fukashiro, T. Murayama, T. Kohmoto, T. Shinozuka,
T. Kubo, K. Asahi, T. Inamura, M. Ishihara,
M. Fujioka, and S. Matsuki

NUCLEAR REACTION ^{40}Ar+^{9}Be, $E(^{40}\text{Ar})=80$ MeV/nucleon; optical pumping in solids GaAs; measured β-ray asymmetry from ^{33}Si nuclei; deduced nuclear polarization of ^{33}Si.

Recently much interests have been focussed onto the structure of light neutron-rich isotopes (Ne to Si) with neutron numbers N around 20; it has been suggested from a number of experimental and theoretical investigations that, in this region, the neutron magic number may not be 20 and some nuclei with N around 20 may be deformed.

In order to clarify the situation on this interesting suggestion, it is important to accumulate more detailed experimental data on the nuclei in this region. As part of the experimental program to study the structure of nuclei around this region, we tried to polarize ^{33}Si isotopes implanted into GaAs crystal by optical pumping in solids,[1] thereby measuring the nuclear magnetic moment from the radiation-detected magnetic resonance.

Schematic diagram of the experimental system for the optical pumping in soilds is shown in Fig. 1. The isotopes ^{33}Si were produced by a projectile fragmentation process with the interaction of a 80 MeV/n Ar beam and a Be target. After mass separated with the mass separator RIPS at RIKEN, the isotopes ^{33}Si were implanted into a GaAs crystal cooled to about 20 K by contact with liquid He. The implantation rate of the isotope was about 3,400 s^{-1}.

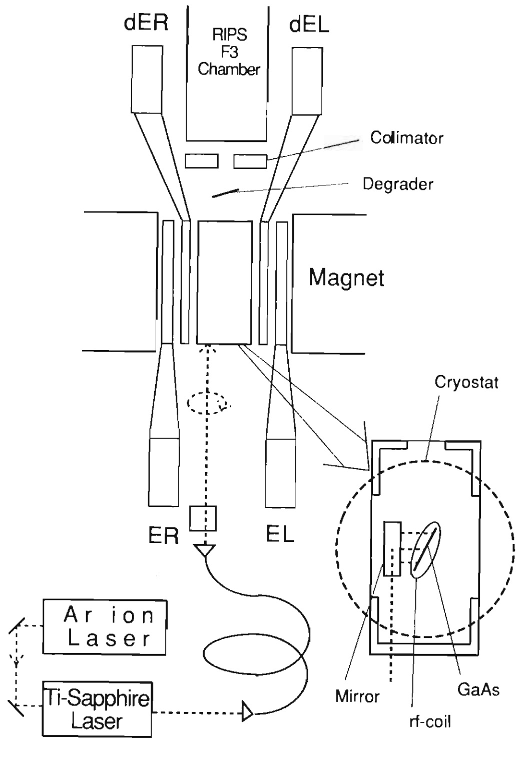

Fig. 1. Schematic diagram of the experimental system OPERA for on-line optical pumping in solids.

The GaAs crystal containing the implanted ^{33}Si was irradiated with circularly polarized laser light to get the spin polarization of electrons excited from the valence band to the conduction band. Through the hyperfine interactions between the excited electrons and the donor nucleus of implanted ^{33}Si, the nuclear spin of ^{33}Si can also be polarized.[2] The pumping source used for this optical pumping is a Ti-sapphire laser excited with an Ar-ion laser. The degree of polarization was measured by detecting the asymmetry of emitted beta-rays distribution with a pair of CaF$_2$(Eu) scintillation-counter telescope set along the magnetic field, one in front of and the other behind the sample. The asymmetry measured under a 2.5 KOe magnetic field is shown in Fig. 2 as a function of the wavelength of the exciting light. Nuclear polarization was achieved only at a narrow region of laser wavelength, consistent with the expectation that only the laser light in that wavelength region can reach the implanted ^{33}Si isotopes. The measured asymmetry corresponds to the nuclear polarization of about 2%. This value is appreciable and

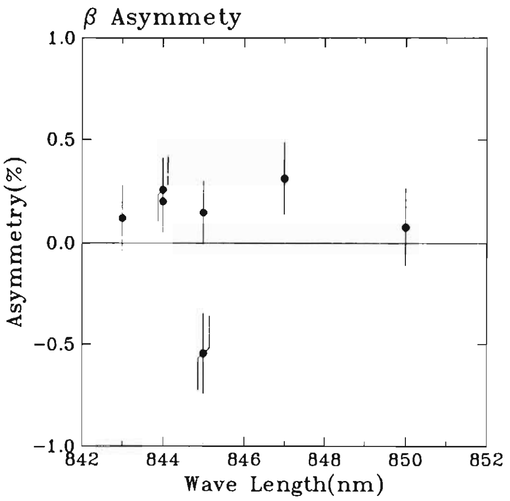

Fig. 2. β-rays asymmetry from ^{33}Si measured as a function of the wavelength of exciting laser light.

was obtained for the first time for unstable isotopes by the optical pumping in semiconductor materials.

References

1) K. Shimomura *et al.*: *Phys. Rev.* **C42**, R487 (1990).
2) Optical Orientation, eds., F. Meier and B. Zakharchenya, North-Holland (1984).

RIKEN Accel. Prog. Rep. **24** (1990)

III-1-15. Cross Sections of ^{209}Bi(^{40}Ar, αxn)$^{245-x}$Es Reactions

T. Nomura, K. Morita, T. Inamura, A. Yoshida, M. Koizumi,
Y. Nagai, T. Toriyama, H. Miyatake, Y. Fujita, M. Fujioka,
T. Shinozuka, M. Wada,* H. Kudo, K. Sueki, Y. Hatsukawa,
S. Kubono, N. Ikeda, and R. Saintola

NUCLEAR REACTION ^{209}Bi+^{40}Ar, $E(^{40}$Ar$)=5.2$ MeV/nucleon; collected reaction products with gas-filled separator; measured α decays; deduced σ for (^{40}Ar, αxn) and (^{40}Ar, α2n).

The (HI, αxn) reaction, in which precompound α particle emission takes place, is shown to occur significantly even near the Coulomb barrier in an ^{40}Ar induced reaction on ^{209}Bi. Becasue the α emission can efficiently cool down a highly excited nucleus both in energy and angular momentum, it is considered to be very effective for production of fissile nuclei like superheavy elements (SHE).

The above phenomenon has been known to occur significantly when relatively light heavy ions up to $A=22$ are bombarded. In the case of an ^{40}Ar projectile, the heaviest system known so far is the ^{181}Ta (^{40}Ar, αxn)$^{217-x}$Ac reaction, in which the cross sections of interest have been comparable to the case of the lighter projectiles. However, the residual nuclei produced in this reaction are located at the beginning of the actinide species far from the SHE region in which we are interested in. Therefore, we have considered it worthwile to measure cross sections of the ^{209}Bi-(^{40}Ar, αxn)$^{245-x}$Es reactions in order to see whether this type of reaction can be promising for the search of SHE.

The present measurement has been done by using the gas-filled separator (GARIS) at the RIKEN Ring Cyclotron. A ^{209}Bi target of about 1 mg/cm^2 thickness backed with a thin Al plate was placed 70 cm upstream from the field boundary of a dipole magnet of the GARIS and was bombarded with pulsed 10 MeV/u ^{40}Ar ions. A typical pulse duration was 10 s with a repition frequency of 0.05 Hz. The effective bombarding energy after the target backing was set to be 5.2 MeV/u. A Si-detector having a 2,000 mm^2 effective area was positioned at the focal plane of the GARIS. Alpha decays of the residual nuclei implanted onto the Si detector were measured during a beam-off period. The assignment of the observed α decays was done on the basis of the measured energies and lifetimes.

Figure 1 shows a part of the observed α spectra.

The 7.893 MeV peak has been assigned to ^{243}Es produced in the ^{209}Bi(^{40}Ar, α2n) reaction, while two peaks with $E_\alpha=7.163$ and 7.213 MeV have been assigned to ^{244}Cf produced by the EC decay of ^{244}Es made in the (^{40}Ar, αn) reaction. The present result yields the following cross sections; $\sigma_{\alpha n}=44\pm15$ nb and $\sigma_{\alpha 2n}=36\pm15$ nb.

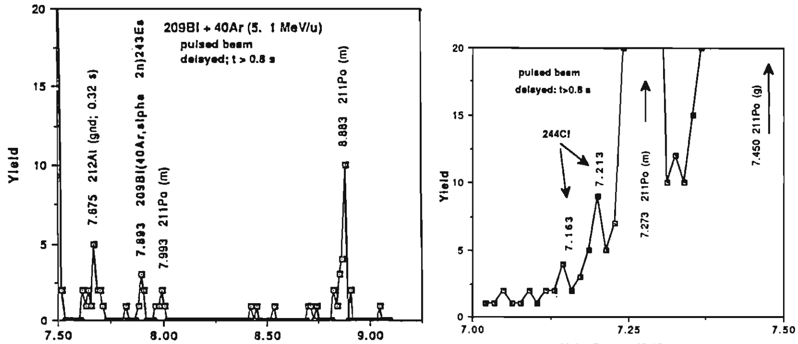

Fig. 1. A part of α spectra observed in the ^{209}Bi+^{40}Ar reaction.

---

* Cyclotoron and Radioisotope Center, Tohoku Univ.

RIKEN Accel. Prog. Rep. **24** (1990)

III-1-16. A Measurement of Pion Absorption at 1 GeV/c on a Few-Nucleon System

I. Nomura, I. Arai,*[1] T. Fukuda, H. Kitayama,*[1] P. Kitching,*[2]
T. Kobayashi, K. Maeda, H. Matsuyama,*[3] T. Nagae,*[4] Y. Nagasaka,*[1]
M.A. Prokhvatilov,*[5] V.I. Rasin,*[5] D. Rowntree,*[6] M. Sekimoto,*[4]
T. Suda, K. Tomizawa,*[1] S. Ueno,*[1] and K. Waki*[1]

[NUCLEAR REACTION ^{4}He, ^{12}C(π^+, pp), (π^+, pn), Pπ= 1 GeV/c, pion absorption.]

Pion absorption on a nucleon pair (two-body absorption) in the GeV region can be a good probe to study short range correlations in nuclei due to the large momentum transfer. In this energy region, however, the measurement has been made only for a deuteron target. The (π^+, pp) and (π^+, pn) cross sections for ^{4}He and ^{12}C have been measured at Pπ=1GeV/c. We intend to obtaion information about short range correlations for T=1 pairs as well as T=0 pairs. We chose ^{4}He as a target because of its high density compared with other nuclei, expecting higher momentum components between two nucleons.

The experiment was done at the π2 beam line (internal target) of the KEK 12GeV Proton Synchrotron, which delivers 10^5 π^+/spill with energies higher than those at existing meson factories (up to 500 MeV). Figure 1 shows the experimental setup, and the angular ranges measured in this experiment are given in Table 1. Forward-going protons with high momentum were measured by using a spectrometer consisting of a dipole magnet, five drift chambers (W1-5), and a hodoscope (FH). Backward-going protons and neutrons were detected with two TOF walls, one made of 10 cm-thick plastic scintillators and the other composed of a stack of scintillators with a total thickness of 15 cm. Flight paths were 2~3 m, and the angular resolution for backward nucleons was better than ±3 degrees. The thicknesses of the ^{4}He and ^{12}C targets were 3.9 g/cm^2 and 6.6 g/cm^2, respectively. The ^{4}He target was a cylindrical container made of stainless steel, whose diameter and window thickness were 230 mm and 0.5 mm, respectively.

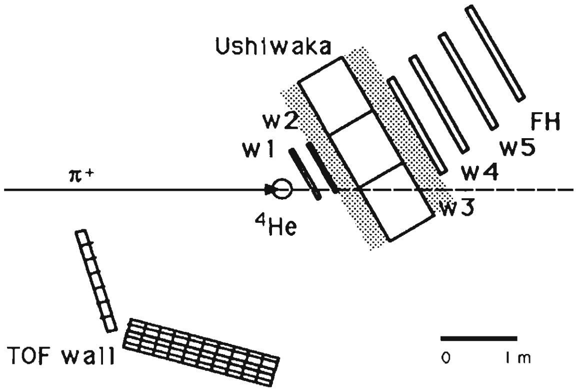

Fig. 1. Schematic view of an experimental setup.

Table. 1. Angular ranges measured with setup 1 and 2.

	foward	backward	
setup 1	5-23 degrees	110-170	degrees
setup 2	17-35 degrees	80-140	degrees

The measurement has been finished, and data analysis is in progress.

---

*[1] Institute of Physics, University of Tsukuba.

*[2] Nuclear Research Center, University of Alberta and TRIUMF.

*[3] Laboratory of Nuclear Science, Tohoku University.

*[4] Institute for Nuclear Study, University of Tokyo (INS).

*[5] Institute for Nuclear Research, Academy of Science (INR) and INS.

*[6] Department of Physics and Laboratory for Nuclear Science, Massachusetts Institute of Technology (MIT).

RIKEN Accel. Prog. Rep. 24 (1990)

III-1-17. Yields of Long-Lived Isotopes around $A=169$ Produced in the $^{14}N+^{181}Ta$ Reaction at $E_{^{14}N}=35$ MeV/u

I. Nakamura, M. Azuma, T. Ishizuka, T. Inamura, H. Katsuragawa,
M. Koizumi, H. Kosuga, K. Shimomura, I. Sugai, M. Takami,
S. Matsuki, T. Murayama, K. Morita, and A. Yoshida

〔Experimental result, Target fragmentation, Yield of the isotopes.〕

For our future experiments, collinear laser spectroscopy, the knowledge of the yields of the radioactive products formed by nuclear reactions is very important. This paper reports the yields of the radioactive products around the mass number $A=169$ produced by target fragmentation in the $^{14}N+^{181}Ta$ reaction at $E_{^{14}N}=35$ MeV/u, measured with the RIKEN GARIS system.[1)]

The experimental setup basically uses a thin-target and an Al-catcher foil technique. The identification of radioactive isotopes produced were made from the energies of γ rays and half-lives of the products. The GARIS system was tuned so as to get maximum transmission efficiency for ^{169}Hf. The transmission efficiency of GARIS was $0.49\pm0.11\%$ for the above mentioned target fragmentation ($^{14}N+^{181}Ta\rightarrow^{169}Hf$). The target thickness was 8.3 mg/cm^2.

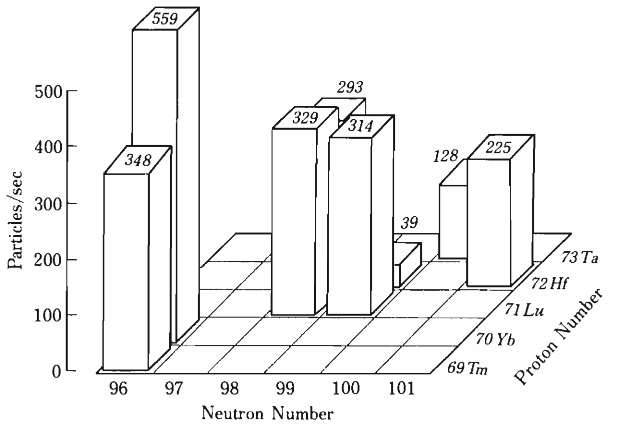

Fig. 1. Distribution of the yields of long-lived isotopes produced by target fragmentation in the $^{14}N+^{181}Ta$ reaction at $E_{^{14}N}=35$ MeV/u. An average beam intensity was 183 nA. The yields were given by the height on the N-Z plane.

Here we present the yields of isotopes produced at the GARIS focus point of long-lived isotopes with half-lives longer than 1 hour. Figure 1 shows the distribution of the yields of long-lived isotopes; the number at each top of the column shows the yield (particles/s) of each isotope. In this illustration, no feeding correction for a sequential decay is included. For the reason of above no feeding correction, the yields of ^{166}Yb, ^{165}Tm are larger than that of ^{169}Lu.

The result that the neighbouring isotopes of a mass difference $\Delta A=12$ ($\Delta A=A_{\mathrm{target}}-A_{\mathrm{isotope}}$), for example ^{169}Lu, are most probable to be produced is in agreement with a previously reported result that the isotopes with $\Delta A=10$ are most probable in the $^{14}N+^{124}Sn$ reaction at $E_{^{14}N}=30$ MeV/u.[2)] However, isotopes with atomic numbers larger than that of the target were not produced in the present target fragmentation.

Finally, the cross section for the $^{14}N+^{181}Ta\rightarrow^{169}Lu$ reaction is about 124 mb.

A further analysis including feeding correction and the yield of short-lived isotopes is in progress.

References

1) K. Morita, T. Inamura, K. Valli, T. Nomura, J. Tanaka, H. Miyatake, K. Sueki, Y. Hatsukawa, M. Fujioka, T. Shinozuka, K. Taguchi, H. Kudo, Y. Nagai, T. Toriyama, H. Hama, M. Yoshii, and K. Furuno: *RIKEN Accel. Prog. Rep.*, **21**, 155 (1987).
2) J. Blachot, J. Crancon, B. deGoncourt, A. Gizon, and A. Lleres: *Z. Phys. A: At. Nucl.*, **321**, 645 (1985).

RIKEN Accel. Prog. Rep. **24** (1990)

III-1-18. Dynamical Collective Properties of Nuclei at Finite Temperature

S. Yamaji, H. Hofmann,* and A.S. Jensen**

〔Large Scale Collective Motion, Linear Response Theory.〕

We derived a selfconsistent transport equation for the nuclear collective motion, computed transport coefficients for a fission, process, and found that a Markovian approximation is a fairly good approximation for temperatures around 2 MeV.[1)] We then studied the validity of the Markovian approximation in more detail.[2)]

In the present paper, we report a study of the temperature-dependence of the collective vibrational motion of ^{208}Pb within the frame work of our theory.

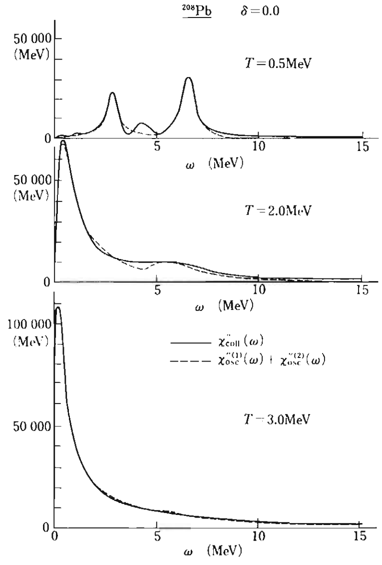

Fig. 1. Strength Function for the quadrupole oscillation of ^{208}Pb. The sum of the strength functions of harmonic oscillator type $\chi''^{(1)}{}_{osc}(\omega)$ and $\chi''^{(2)}{}_{osc}(\omega)$ (dashed curves) is fitted to the strength functions numerically calculated $\chi''_{coll}(\omega)$ (solid curve).

We calculate the collective response function whose imaginary part is the strength function. We plot the strength function of ^{208}Pb with spherical shape as a function of the excitation energy ω for temperatures $T=0.5$, 2, and 3 MeV in Fig. 1, and the energy-weighted sum as a function of temperature in Fig. 2. To get the energy-weighted sum, we fit the sum of two strength functions of harmonic oscillator type $\chi''^{(1)}{}_{osc}(\omega)$ and $\chi''^{(2)}{}_{osc}(\omega)$ to the strength function $\chi''_{coll}(\omega)$. We then calculate the energy-weighted sum S_i by the relation $S_i=\hbar^2/2M_ik^2$, M_i and k being the inertia of the i-th harmonic vibration and the coupling constant, respectively.[1)]

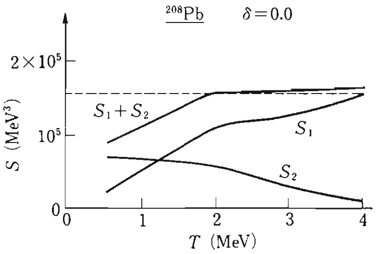

Fig. 2. Energy-weighted sum of ^{208}Pb as a function of temperature. S_1 and S_2 correspond to the low and high modes of collective oscillations, respectively. The dashed line shows the sum rule limit given by $\hbar^2/2M_{\mathrm{irrot}}k^2$, where M_{irrot} is the inertia of an irrotational flow.

We find that the energy-weighted sum for a high mode (iso-scalar quadrupole resonance) decreases with increasing temperature and that all strength is concentrated in a low frequency mode. This means that the vibrational inertia of the slow motion becomes the one of irrotational flow. Thus we can get rid of the defect that we somtimes have a negative inertia at high temperature in the Markovian approximation.

References

1) S Yamaji, H. Hofmann, and R. Samhammer: *Nucl. Phys.*, **A475**, 487 (1988).
2) H. Hofmann, R. Samhammer, and S. Yamaji: *Phys. Lett.*, **B229**, 309 (1989).

---

* Dep. Physics, Technical University of Munich, Germany.
** Insitute of Physics, University of Aarhus, Denmark.

RIKEN Accel. Prog. Rep. **24** (1990)

III-1-19. Dissociation Cross Sections of ^{11}Li

K. Soutome, S. Yamaji, and M. Sano

[dissociation of ^{11}Li, target-charge dependence, Glauber approximation.]

Recently, Kobayashi *et al.*[1] measured cross sections for the reaction $^{11}\mathrm{Li} + \mathrm{T}(A_\mathrm{T}, Z_\mathrm{T}) \rightarrow {}^{9}\mathrm{Li} + \mathrm{X}$ where T = C, Cu, and Pb and reported unusual target-charge dependence of the Coulomb dissociation cross section $\sigma_\mathrm{C}^{(\mathrm{exp})}$. In extracting $\sigma_\mathrm{C}^{(\mathrm{exp})}$ from experimental data $\sigma^{(\mathrm{exp})}$, they assumed that (i) the nuclear dissociation cross section $\sigma_\mathrm{N}^{(\mathrm{exp})}$ takes the form $\sigma_\mathrm{N}^{(\mathrm{exp})} = \gamma\{R(^{11}\mathrm{Li}) + R(\mathrm{T})\}$, where $R(\mathrm{A})$ is the "interaction radius"[2] of a nucleus A and (ii) Coulomb-nuclear interference can be neglected and hence $\sigma^{(\mathrm{exp})} = \sigma_\mathrm{C}^{(\mathrm{exp})} + \sigma_\mathrm{N}^{(\mathrm{exp})}$, and (iii) $\sigma_\mathrm{C}^{(\mathrm{exp})} = 0$ for T = C. With these assumptions they first fixed γ using the value of $\sigma^{(\mathrm{exp})}$ for T = C and then calculated $\sigma_\mathrm{N}^{(\mathrm{exp})}$ for T = Cu and Pb from which $\sigma_\mathrm{C}^{(\mathrm{exp})} = \sigma^{(\mathrm{exp})} - \sigma_\mathrm{N}^{(\mathrm{exp})}$ can be estimated. In this way, they obtained the target-charge dependence $\sigma_\mathrm{C}^{(\mathrm{exp})} \propto Z_\mathrm{T}^{1.41\pm0.22}$, which deviates largely from Z_T^2.

Assuming that ^{11}Li consists of a ^{9}Li core and two valence neutrons and the core remains in its ground state after collision, we can calculate the dissosciation cross section for the above process using Glauber's formalism. Computational details are given in Ref. 3 and here we show only numberical results in Fig. 1. Our nuclear cross section σ_N (dotted curve) shows a qualitative agreement with $\sigma_\mathrm{N}^{(\mathrm{exp})}$, while the total cross section σ (dashed curve) overestimates for a Pb target. This is due to the fact that the effect of Coulomb-nuclear interference is — as expected — small and hence $\sigma - \sigma_\mathrm{N}$ is almost equal to the pure Coulomb cross section σ_C, which rises as Z_T^2.

As discussed in detail in Ref. 4, however, the exponent of the Coulomb cross section σ_C is suppressed for a high-Z_T target if we take account of the bending of a trajectory. The solid curve in Fig. 1 includes this effect. In this case the Z_T dependence of the Coulomb cross section becomes $Z_\mathrm{T}^{1.75}$, closer to the experimental Z_T dependence. This shows the limits of the straight-line approximation, or the importance of the bending effect.

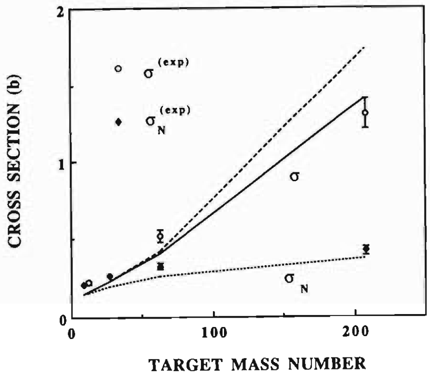

Fig. 1. Dissociation cross sections calculated and measured for ^{11}Li. The dashed curve represents the total dissociation cross section σ calculated by a harmonic oscillator model,[3] and open circles are the cross sections measured $\sigma^{(\mathrm{exp})}$. Cross sections due to pure nuclear interaction σ_N are also shown (dotted curve) together with the experimental $\sigma_\mathrm{N}^{(\mathrm{exp})}$. The solid curve represents the cross section σ which takes bending effects into account.[4]

References

1) T. Kobayashi *et al.*: *Phys. Lett.*, **232B**, 51 (1990).
2) I. Tanihata *et al.*: *Phys. Rev. Lett.*, **55**, 2676 (1985).
3) K. Soutome, S. Yamaji, and M. Sano: RIKEN-AF-NP-96 (1990).
4) K. Soutome, S. Yamaji, and M. Sano: in preparation.

RIKEN Accel. Prog. Rep. **24** (1990)

III-1-20. Induced Fission Studied with a Multi-Dimensional Langevin Equation

T. Wada, Y. Abe, and N. Carjan*

[Fission, multi-dimensional Langevin equation, kinetic energy distribution.]

Nuclear dissipative phenomena, such as deep inelastic collisions, have been treated as non-equilibrium statistical problems. Slow collective degrees of freedom with heavy masses are treated as Brownian particles and fast nucleon degrees of freedom as a heat bath. It is shown in Ref. 1) that recent developments in computers enabled us to practically solve a Langevin equation. As is well known, nuclear fission is a multi-dimensional collective motion. Some observable quantities are expected to reflect multi-dimensional dissipative dynamics. Thus it is very important to extend Langevin approach to multi-dimensional cases.

A multi-dimensional Langevin equation is given by

$$\frac{d}{dt}p_i = -\frac{\partial V}{\partial q_i} - \frac{1}{2}p_j\frac{\partial}{\partial q_i}(m^{-1})_{jk}p_k - \gamma_{ij}(m^{-1})_{jk}p_k + g_{ij}R_j(t)$$

$$\frac{d}{dt}q_i = (m^{-1})_{ij}p_j \qquad (1)$$

where m_{ij} and γ_{ij} are the mass and friction tensor, respectively. The multi-dimensional random force $R_j(t)$ is assumed to be a white noise and its strength g_{ij} is given by $g_{ik}g_{jk} = T\gamma_{ij}$, where T is the temperature of a compound nucleus.

A characteristic aspect of the Brownian picture for nuclear fission is a fluctuation of the fissioning coordinate in the course of the descent from saddle to scission, which are expected to strongly affect observable quantities of fragments, such as kinetic energy distrubution. The fragment kinetic energy is calculated as the sum of the pre-scission kinetic energy and the Coulomb energy between two fragments at scission. In one-dimensional treatment, the variance of the kinetic energy comes only from the fluctuation of the pre-scission kinetic energy, because the scission point is fixed. Calculated variance was found to be too small to explain experimental data. On the other hand, in a multi-dimensional treatment, the fluctuation of the scission point causes the fluctuation of the Coulomb energy. Several authors have already tried to explain the large variance by solving a multi-dimensional Fokker-Planck equation approximately and obtained rather satisfactory results.[2] Here we directly solve the multi-dimensional Langevin equation (1) without any approximations. The potential $V(q)$, the mass tensor $m_{ij}(q)$, and the friction tensor $\gamma_{ij}(q)$ are calculated with a liquid drop model.[3] We adopt two-body dissipation mechanism in calculating $\gamma_{ij}(q)$ with a viscosity coefficient μ = 0.02 TP = 1.25 × 10^{-23} MeV·s/fm^3. Figure 1 shows the calculated average value of the fragment kinetic energy and its variance as a function of the nuclear temperature for the symmetric fission of ^{213}At. The agreement between the theory and the experiment[4] is very good for the average value of the kinetic energy. The calculated variance is found to be dominated by the fluctuation of the Coulomb energy.

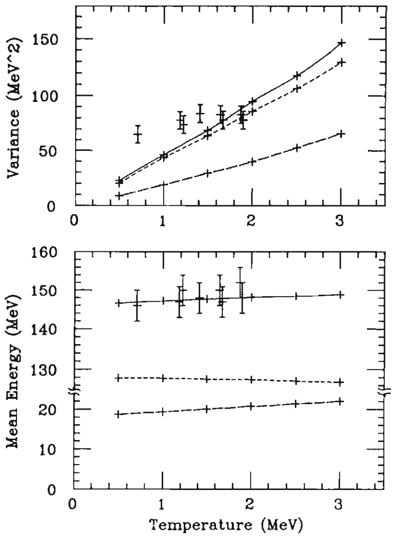

Fig. 1. Average value of the fragment kinetic energy and its variance are compared with experiment for the symmetric fission of ^{213}At. Long dashed lines are for the pre-scission kinetic energy, short dashed lines are for the Coulomb energy, and solid lines are for the total kinetic energy. Experimental values are taken from Ref. 4).

References

1) Y. Abe *et al.*: *J. de Phys. (Paris)*, **47**, C4-329 (1986).
2) F. Scheuter *et al.*: *Phys. Lett.*, **149B**, 303 (1984); G.D. Adeev and V.V. Pashkevich: *Nucl. Phys.*, **A502**, 405c (1989).
3) K.T.R. Davies *et al.*: *Phys. Rev.*, **C13**, 2385 (1976); H.J. Krappe *et al.*: *ibid.*, **C20**, 992 (1979).
4) F. Plasil *et al.*: *ibid.*, **142**, 696 (1966).

---

* Centre d'Etudes Nucléaires, Bordeaux-Gradignan, France.

RIKEN Accel. Prog. Rep. **24** (1990)

III-1-21. Approximate Ground State of the Lipkin Model Hamiltonian in Density-Matrix Formalism

M. Tohyama, P. Schuck,* and S.J. Wang**

〔Density matrix theory, ground state calculation, Lipkin model.〕

Recently realistic calculations based on an extended time-dependent Hartree-Fock theory, called the time-dependent density-matrix theory (TDDM), have been reported by one of the present authors for the damping of giant resonances[1] and for low-energy heavy-ion collisions.[2] The results of the numerical calculations are quite encouraging: TDDM reproduces the damping widths of isoscalar quadrupole resonances and gives much larger mass fluctuations in deep-inelastic heavy-ion collisions than TDHF does. These numerical calculations, however, contain an inconsistency in the treatment of the ground state: the HF ground state, which is not compatible with the equations of motion of TDDM, was used as an initial ground state. The aim of this paper is to show the possibility of finding a stationary solution of TDDM using the Lipkin model as a model hamiltonian.

In the case of a stationary problem the TDDM equations become the following equations for the occupation matrix $n_{\alpha\beta}$ and the two-body correlation matrix $C_{\alpha\beta\alpha'\beta'}$:

$$(\varepsilon_{\alpha'} - \varepsilon_{\alpha})n_{\alpha\alpha'} = \sum_{\beta\gamma\delta} \{C_{\beta\gamma\alpha'\delta} <\alpha\delta|v|\beta\gamma> - C_{\alpha\gamma\beta\delta} <\beta\delta|v|\alpha'\gamma>\}.$$

$$(\varepsilon_{\alpha'} + \varepsilon_{\beta'} - \varepsilon_{\alpha} - \varepsilon_{\beta})C_{\alpha\beta\alpha'\beta'} = B_{\alpha\beta\alpha'\beta'} + P_{\alpha\beta\alpha'\beta'} + H_{\alpha\beta\alpha'\beta'},$$

where B, P, and H describe the Born, particle-particle and particle-hole interaction terms, respectively.[1,2] It is important to note that the above equations of motion are not sufficient to determine all the matrix elements of $n_{\alpha\beta}$ and $C_{\alpha\beta\alpha'\beta'}$. We used additional conditions and constraints from eigenvalue-eigenstate problems and from the properties of reduced density matrices, which will be discussed elsewhere.

Our method was tested for the Lipkin model. In Fig. 1 the ground-state energy for an $N = 4$ system is compared with the exact value. The TDDM ground state is better that the HF one. However, a substantial part of the total energy is missing in the TDDM result as compared with the exact one. The difference between the TDDM result and the exact one may be attributed to the omission of a three-body correlation function C_3.

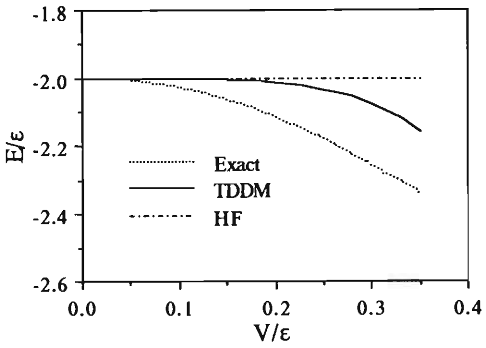

Fig. 1. Total energy of the Lipkin model as a function of V/ε for an $N = 4$ system.

References

1) M. Gong and M. Tohyama: *Z. Phys.*, **A335**, 153 (1990).
2) M. Gong, M. Tohyama, and J. Randrup: *ibid.*, p. 331.

---

* Institut des Science Nucleaires, Grenoble, France.

** Department of Modern Physics, Lanzhou University, China.

RIKEN Accel. Prog. Rep. **24** (1990)

III-1-22. Energy and Baryon Number Densities in Ultrarelativistic Heavy Ion Collisions

S. Daté

〔multiple scattering model, event simulator, multiparticle production.〕

Heavy ion collisions at incident energies of 10 GeV/nucleon and above offer an unique opportunity to study hadronic systems under extreme conditions. Lattice QCD simulations and effective theories show existence of color liberated and chiral symmetry restored phase in equilibrated hadronic systems at high energy density, ε, and at high baryon number density, ρ. The critical values of these densities have been estimated as $\varepsilon_c=(2\pm1)$ GeV/fm^3 and $\rho_c=(5\pm5)\ \rho_0$, respectively, where ρ_0 is the normal nuclear density.[1] Realization and detection of the new phase of matter, quark-gluon plasma, is one of the most stimulative subject in recent heavy ion studies.

It is however a highly nontrivial problem to define signatures of the new phase formation and relate ε and ρ with experimentally observable quantities. The nontriviality is mainly due to the fact that, regardless of the new phase formation, final state particles are coming out from the system only after suffering many interactions. We have no direct way of observing intermediate states of the system. Obviously, we need a concrete base to predict background samples and see through space-time evolution of the system.

To approach the problem mentioned above, we employ multichain model (MCM)[2] as our base. This model is a most conservative one in a sense that nuclear collision process is described not in quark-string level but in nucleon level and that elementary nucleon-nucleon collision data are superposed as multiple scattering process proceeds inside colliding nuclei. The superposition is independent except for the energy momentum conservation and that inelasticity of leading nucleons is treated as a free parameter. The model has proved its validity for proton-nucleus collisions and its power to study space-time structure of the collision process.[3]

In this report, we briefly discuss our calculations and results[4] on ε and ρ achieved in heavy ion collisions. All calculations have been done with a simulator version of MCM. At very high energies above 100 GeV/nucleon, hadronic systems produced in the central region are mainly composed of secondary mesons and nucleons are far aside in the fragmentation regions. This is due to finite formation time for secondary particles. Under this decoupling of mesonic and baryonic contributions, the unique way of getting large values of ε is to increase incident energy above 10 TeV/nucleon, which corresponds to RHIC energies, so that the number of secondaries per each collisions becomes sufficiently large. In particular, we have shown[4] that the densities achieved in 200 GeV/nucleon S + S collisions are not sufficient to be critical. At lower energies than 50 GeV/nucleon, a finite contribution of nucleons is expected and large values of ε and ρ may be achieved. Amount of the contribution depends, however, strongly on the space-time structure of hadronic scattering processes. In the most naive space-time picture within the framework of a multiple scattering model, colliding two nucleons complete momentum transfer immediately after they collide with each other. If it was the case, the maximum ε and ρ values exceed their critical values even in S + S collisions at 50 GeV/nucleon. Contrary to this picture, Regge field theory[5] suggests that a time of order of incident energy is necessary to complete the momentum transfer. This reduces ε and ρ considerably. We take a picture with finite completion time for momentum transfers to make rather pessimistic estimation of the densities. In our picture, a nucleon completes its momentum transfer when the last secondary meson from the collision emerges into on-shell state after a finite formation time. As a result, we have obtained 90 events which achieve $\rho>5\rho_0$ and satisfy $\rho>5\rho_0/3$ during a time period of 3 fm among 1000Pb + Pb events at 50 GeV/nucleon. We have not observed such events in S + S collisions at the same energy. Values of ε in these events are found to be rather moderate around 1.5 GeV/fm^3. In summary, it is hopeful to realize high density matter in heavy ion collisions at 50 GeV/nucleon. High energy density near to the critical value is also achievable. It is crucial to use quite heavy nuclei to realize the extreme conditions.

References

1) For reviews, see F. Karsch: CERN Report No. CERN-TH-5498/89; G. Baym: in Proc. 'Quark Matter Formation and Heavy Ion Collisions,' Bielefeld (1982).
2) A. Capella *et al.*: *Phys. Lett.*, **81B**, 68 (1979).
3) S. Daté, M. Gyulassy, and H. Sumiyoshi: *Phys. Rev.*, **D32**, 619 (1985).
4) S. Daté: Proc. 'Int. Workshop on High-Density Nuclear Matter,' KEK (1990).
5) J. Koplik and A. H. Mueller: *Phys. Rev.*, **D12**, 3638 (1975).

RIKEN Accel. Prog. Rep. **24** (1990)

III-2. Atomic and Solid-State Physics

1. Ionization of Helium Atoms by Proton Impact

H. Fukuda, I. Shimamura, L. Vĕgh, and T. Watanabe*

The collision system of proton and helium is suitable for studying ionization in detail by comparing experiments with theories. Recent papers report proton (p) angular distribution for ionization of He[1-3] and coincidence measurements of the scattered protons and the recoil He^+ ions[4] or ejected electrons.[5]

We applied to p-He collisions an eikonal distorted-wave approximation (EDWA) that accounts for the distortion of the proton motion from the plane wave due to the collisions; the eikonal approximation is used for the distorted waves in the distorted-wave Born approximation.[6]

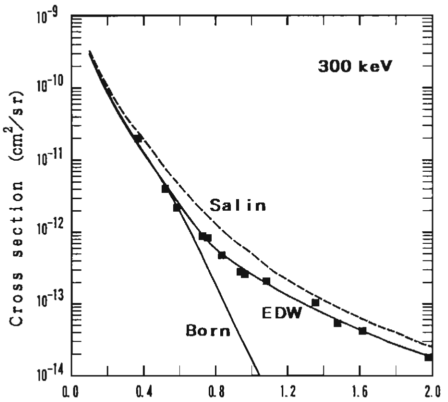

Fig. 1. Angular distribution of protons (E=300 keV). Salin: Ref. 7. ■: experiments.[1]

The proton angular distribution in the EDWA (denoted by EDW) is compared in Fig. 1 with that in the plane-wave Born approximation (PWBA, denoted by Born), experiments,[1] and Salin's theory.[7] The EDWA reproduces the experiments best among all the theories. Calculations at 500 keV, 1 MeV, and 3 MeV also reproduce the experimental results remarkably well, the latter ranging over 3-4 orders of magnitude over a wide angular region.

A recent experiment of coincidence measurements[4] of p and He^+ prompted us to compare the measured average recoil energy in the perpendicular direction and the results of the theories referred to above (Fig. 2). Classical-trajectory Monte-Carlo (CTMC) calculations are also included in Ref. 4. With the thermal motion of He taken into account, the CTMC method agrees well with experiments. However, the EDWA and PWBA give results far below the CTMC results at small angles where the former two should be accurate, even when compared at $T=0$ K. In fact, we were informed that the CTMC results of Ref. 4 were revised recently and now agree well with our results.

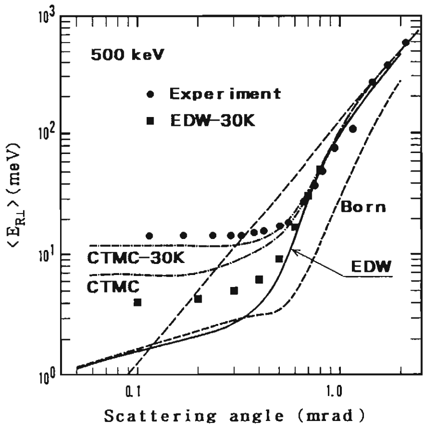

Fig. 2. Average transverse energy $\langle E_{R\perp} \rangle$ of He^+ as a function of the p scattering angle (E=500 keV). ●: measurements at 30 K.[4] CTMC: Ref. 4. EDW-30K and CTMC-30K: with the thermal motion of He at 30 K.

References
1) J.P. Giese and E. Horsdal: *Phys. Rev. Lett.*, **60**, 2018 (1988).
2) E.Y. Kamber, C.L. Cocke, S. Cheng, and S.L. Varghese: *ibid.*, p. 2026.
3) E.Y. Kamber, C.L. Cocke, S. Cheng, J.H. McGuire, and S.L. Varghese: *J. Phys.*, **B21**, L455 (1988).
4) R. Dörner, J. Ullrich, H. Schmidt-Böcking, and R.E. Olson: *Phys. Rev. Lett.*, **63**, 147 (1989).
5) G. Schiwietz: *Phys. Rev.*, **A37**, 370 (1988).
6) H. Fukuda, I. Shimamura, L. Vĕgh, and T. Watanabe: submitted to *Phys. Rev. A*.
7) A. Salin: *J. Phys.*, **B22**, 3901 (1989).

---

* Present address: Department of Physics, International Christian University.

RIKEN Accel. Prog. Rep. **24** (1990)

III-2-2. Atomic Effects on Nuclear Beta Decay

M.R. Harston and N.C. Pyper*

In the beta decay process, a nucleus, of charge Z and mass number A, decays to a daughter nucleus, of charge $Z+1$ and mass number A, with the simultaneous creation of an electron and antineutrino:

$$(Z, A) \rightarrow (Z+1, A) + e^- + \bar{\nu} \qquad (1)$$

For many high energy β^- decays, this process can be viewed to a very good approximation as a purely nuclear decay which takes place independently of the atomic electron cloud surrounding the nucleus. However, the ever-increasing accuracy achieved in measurements of β-particle spectra and β-decay half-lives has led to interest in the role of atomic electrons in the β-decay process[1-3] particularly for the case of low energy β^--emitters. These atomic electrons may affect the β-emission probability, for instance, through their screening effect on the β-particle wavefunction, through their effect on the decay energy and through exchange processes involving bound and continuum electrons.

The present work is concerned with the calculation of the exchange effects in the continuum β-decay. A final state arising from the β-decay process in which there is one continuum electron (β-particle) may be produced either by direct creation of the β-electron in the continuum orbital, or by creation of the β-electron in a bound orbital with an electron simultaneously exciting from a bound orbital to the continuum. The former process is known as the direct process whilst the latter process is called an exchange process.

The continuum decay constant, λ_c, for allowed beta transitions, including exchange processes, is given approximately by

$$\lambda_c = C\int_0^{E_0}\left\{ P^2_{E\mathrm{s}'}(R)\left[1 - \sum_n \frac{\langle E\mathrm{s}'|n\mathrm{s}\rangle\, P_{n\mathrm{s}'}(R)}{\langle n\mathrm{s}'|n\mathrm{s}\rangle\, P_{E\mathrm{s}'}(R)}\right]^2 + Q^2_{E\bar{\mathrm{p}}'}(R)\left[1 - \sum_n \frac{\langle E\bar{\mathrm{p}}'|n\bar{\mathrm{p}}\rangle\, Q_{n\bar{\mathrm{p}}'}(R)}{\langle n\bar{\mathrm{p}}'|n\bar{\mathrm{p}}\rangle\, Q_{E\bar{\mathrm{p}}'}(R)}\right]^2\right\} pW(E_0 - E)^2 \mathrm{d}E \qquad (2)$$

where C is a constant and $P_{E\mathrm{s}'}(R)$ and $Q_{E\bar{\mathrm{p}}'}(R)$ are the large and small components of the Dirac wavefunction for a continuum s or $\bar{\mathrm{p}}$ electron of energy E evaluated at the nuclear radius R. $P_{n\mathrm{s}'}(R)$ and $Q_{n\bar{\mathrm{p}}'}(R)$ are the corresponding quantities for bound orbitals of principal quantum number n. A prime superscript on an orbital label indicates that the wavefunction refers to an orbital of the final state atom. Orbital labels lacking primes refer to orbitals of the inital state atom. The ki-netic energy of the continuum electron runs from zero to a maximum value E_0, the end-point energy, which is a known experimental parameter of the decay. The factor W is the electron energy including the rest mass contribution and p is the electron momentum. The summation over n runs over all s or $\bar{\mathrm{p}}$ orbitals present in the initial state. The factors of unity in the square braces correspond to the direct terms whilst the terms in the summation over n correspond to exchange terms.

The aim of the work in progress is to obtain estimates of the magnitude of the exchange terms compared to the direct terms. A good approximation to the bound wavefunctions in Eq. 2 can be obtained using the multiconfiguration Dirac-Fock method.[2] The continuum wavefunctions, evaluated at the nuclear radius, can be obtained from unscreened hydrogenic Dirac wavefunctions with suitable corrections for screening.[3] Since the exchange effect arises because of the non-orthogonality of initial and final state wavefunctions, it is essential in evaluating overlap integrals of the kind $\langle E\mathrm{s}'|n\mathrm{s}\rangle$ or $\langle E\bar{\mathrm{p}}'|n\bar{\mathrm{p}}\rangle$, to use continuum wavefunctions which are orthogonal to bound final state wavefunctions. In the present work, these continuum wavefunctions are being calculated as solutions to the Hartree-Fock equations using a frozen core approximation for the bound orbitals.[4]

References

1) B. Eman and D. Tadic: *Phys. Rev. C*, **33**, 2128 (1986).
2) O. Fackler, B. Jeziorski, W. Kolos, H. Monkhorst, and K. Szalewicz: *Phys. Rev. Lett.*, **55**, 1388 (1985).
3) N.C. Pyper and M.R. Harston: *Proc. R. Soc. A*, **420**, 277 (1988).
4) G.N. Bates: *Comput. Phys. Commun.*, **8**, 220 (1974).

---

* Department of Chemistry, University of Cambridge, Lensfield Road, Cambridge CB2 1EW, England.

RIKEN Accel. Prog. Rep. **24** (1990)

III-2-3. Electron Screening in the dtμe Molecule

M.R. Harston, I. Shimamura, and M. Kamimura*

A key step in the muon-catalyzed fusion cycle in D_2/T_2 mixtures is the formation of the molecule $(dt\mu)_{11}$ dee in which the three-body dtμ system is in the $J=1$, $v=1$ state (where J is the total angular momentum and v the vibrational quantum number) and effectively substitutes for a deuterium nucleus in the D_2 molecule.[1] This molecule is produced predominantly by collisions of tμ atoms and D_2 molecules in a resonant process:

$$t\mu + D_2 \rightarrow (dt\mu)_{11}dee \qquad (1)$$

The calculated formation rate of the muonic molecule is very sensitive to the precise value of the molecular binding energy and an accuracy of about 1 meV in this energy is necessary in order to obtain reasonable theoretical estimates of the formation rate.[2] In this work, the effect of electron screening in the related molecule $(dt\mu)_{11}e$ is evaluated in order to obtain an estimate of the corresponding screening effect in the molecule $(dt\mu)_{11}$dee.

The total Hamiltonian for the four-body dtμe system may be written in the form

$$H = H_{dt\mu} + H_e + \Delta V \qquad (2)$$

with

$$\Delta V = V_{\mu e} + V_{de} + V_{te} - U \qquad (3)$$

where $H_{dt\mu}$ is the Hamiltonian of the isolated three-body dtμ system, H_e is the Hamiltonian for an electron moving in the potential U due to the spherically averaged charge distribution of the $(dt\mu)_{11}$ state and $V_{\mu e}$, V_{de} and V_{te} are the electro-static potentials between the electron and μ, d and t respectively. The origin of the coordinate system is chosen to be at the centre of mass of the dtμ system. With this splitting of the Hamiltonian, the energy of the dtμe system can be calculated conveniently by perturbation theory using the eigenfunctions of $H_{dt\mu}$ and H_e as zeroth order wavefunctions. For $(dt\mu)_{11}e$ with the electron in its ground state, this yields an energy

$$E_{(dt\mu)11e} = E_{(dt\mu)11} + E_{1s} + \Delta E^{(2)} \qquad (4)$$

where $E_{(dt\mu)11}$ and E_{1s} are the eigenenergies of $H_{dt\mu}$ and H_e corresponding to the $(dt\mu)_{11}$ and 1s states respectively and $\Delta E^{(2)}$ is the second order perturbation energy arising from the perturbing potential ΔV. The first order perturbation energy vanishes by parity considerations.

Table 1. Contribution to the second order perturbation energy $\Delta E^{(2)}(J,v)$ from different dt$\mu(J,v)$ states.

J	v	$\Delta E^{(2)}(J,v)$ (meV)
0	0	0.00
0	1	−0.29
0	$v>1$	−5.04
1	0	0.00
1	$v>0$	−1.75
2	0	−0.02
2	$v>0$	−10.10
3	$v\geq0$	−0.20
Total $\Delta E^{(2)}$:		−17.41

The contributions to $\Delta E^{(2)}$ from different J, v states summed over all electron states are shown in Table 1. The value of $\Delta E^{(2)}$ obtained was −17.41 meV. Diagonalizing H_e using a Gaussian basis set yields $E_{1s}=-13.58646$ eV. If dtμ is treated as a point charge, then $U=1/r$ and the energy of the 1s state is −13.60425 eV. The shift of the 1s energy due to the finite extent of the $(dt\mu)_{11}$ state is then 17.78 meV. The shift in the total energy of $(dt\mu)_{11}e$ due to the finite size effect is then equal to $-17.41+17.78=0.37$ meV. The corresponding shift in the molecule $(dt\mu)_{11}$dee can be estimated from this shift by multiplying by the ratio (1.45) of the electron density at the deuteron in the D_2 molecule and the D atom. The result is a shift of +0.54 meV. These results can be compared with a recent calculation based on a similar approach,[3] but with the origin of the coordinate system located on the deuteron. In this latter calculation the shift in $(dt\mu)_{11}e$ was estimated to be +0.20 meV and that in $(dt\mu)_{11}$dee +0.29 meV. However, this calculation omitted contributions to $\Delta E^{(2)}$ arising from quadrupole terms in the perturbation potential ΔV which have been included in the present calculation.

References

1) W.H. Breunlich, P. Kammel, J.S. Cohen, and M. Leon: *Ann. Rev. Nucl. Part. Sci.*, **39**, 311 (1989).
2) M. Leon: *Phys. Rev. Lett.*, **52**, 605 (1984).
3) A. Scrinzi and K. Szalewicz: *Phys. Rev. A*, **39**, 4983 (1989).

---

* Department of Physics, Kyushu University, Fukuoka.

RIKEN Accel. Prog. Rep. 24 (1990)

III-2-4. Calculation for $(\mu^+\mu^-)$ Formation by Collision of μ^- on (μ^+e)

T. Watanabe,* A. Ohsaki,** and K. Ishida

The Production of exotic atom $(\mu^+\mu^-)$ is a pioneering subject in atomic physics using accelerators. Recently, the formation of thermal muonium is successfully produced at the muon production facilities (Booster Meson facility) attached to a proton synchrotron at the National Laboratory for High Energy Physics (KEK) in Japan.[1] In connection with this success, it becomes probable to produce a $(\mu^+\mu^-)$ atom by using thermal muonium as target.

Using a classical trajectory Monte Carlo (CTMC) method, we are calculating the cross section for this process. Although the complete validity for the CTMC method has not yet been established, there are many examples which show good agreement with experimental results empirically.[2] The CTMC method considers that all the particles participated in the process are regarded as classical particles. Initial states are selected in proportion to the statistical weight in a phase space obtained from quantum mechanical conditions. The motion of these particles is assumed to follow the Newtonian equation and is solved numerically by using the Hamilton's canonical equation. Figure 1 shows a preliminary calculation for the total cross section for the process of $(\mu^+e^-)+\mu^-\rightarrow(\mu^+\mu^-)+e^-$ as a function of the impact velocity in atomic unit.

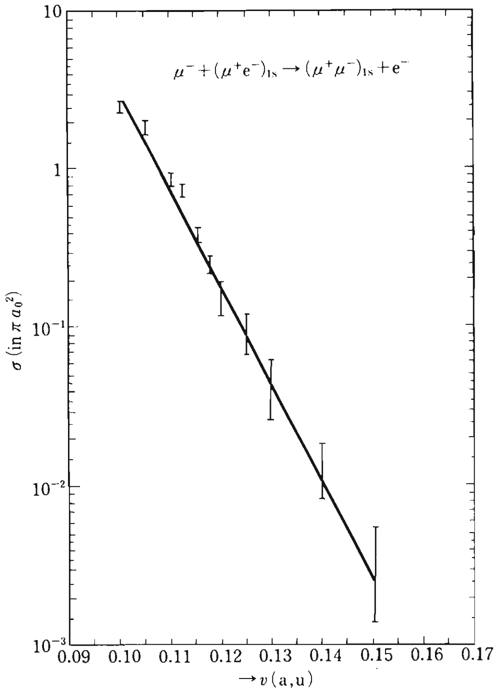

Fig. 1. Preliminary cross sections calculated by the CTMC method for the process of $(\mu^+e^-)+\mu^-\rightarrow(\mu^+\mu^-)+e$ as a function of the impact velocity v in atomic unit. Error bars in the figure mean the HVW obtained from the statistical mean-square deviations.

References

1) A.P. Mills, Jr., J. Imazato, S. Saitoh, A. Uedono, Y. Kawashima, and K. Nagamine: *Phys. Rev. Lett.*, **56**, 1463 (1986).
2) R. Olson and A. Salap: *Phys. Rev.*, **A16**, 531 (1977).

---

* Present address: Department of Physics, International Christian University.

** Department of Applied Physics, Miyazaki University.

RIKEN Accel. Prog. Rep. **24** (1990)

III-2-5. Cross Sections for Positronium Formation from He and Ar, Calculated by the Eikonal Method

X. Liu,* Y. Sun,* Z. Zhou,* Y. Liu,* and
T. Watanabe**

Cross sections for positronium (Ps) formation by collision of e^+ with rear gas atoms have been obtained theoretically and experimentally.[1)] Agreement between theory and experiment is reasonable for a He target, but for an Ar target there is considerable discrepancy. The cross section for Ps formation measured by Fornari[2)] is one order of magnitude larger than that calculated by Gillepie and Thompson[3)] using DWBA (distorted wave Born approximation). We have developed an expansion method in the Eikonal approximation for the treatment of a rearrangement process concerning many-electron atoms. Results obtained by this method for $e^+ + \mathrm{He}$ and for $e^+ + \mathrm{Ar}$ are compared with the results by other theories and experiments.

The most important point in the present approach lies in the application of the Eikonal method to the electron capture process of a projectile particle from a "many-electron" target atom. The matrix element needs to estimated in the Jacobi coordinate description. The bound state wavefunctions of initial and final-states, a plane-wave operator and an eikonal phase-shift factor are expanted in terms of spherical harmonics in order to perform a multi-fold integration analytically. We have obtained a formula which can be applied to many-electron atoms. For a He target, we have obtained cross sections in reasonable agreement with experiments and other theoretical calculations in an impact energy region above 80 eV. Cross sections calculated for an Ar target are of the same order of experiments in an impact energy region of 60–80 eV. Figure 1 shows that results of calculation for $e^+ + \mathrm{He} \rightarrow \mathrm{Ps} + \mathrm{He}^+$ together with other calculation and experiments. In the present approach, we employed a Hartree-Fock type wavefunction as a target wavefunction.

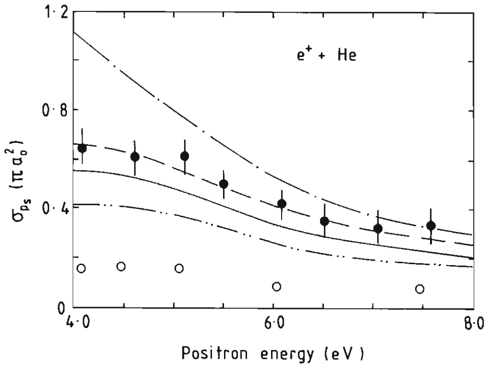

Fig. 1. Results of calculation for $e^+ + \mathrm{He} \rightarrow \mathrm{Ps} + \mathrm{He}^+$ and comparison with other data. Experiments: ●, Fornari *et al.* (1983); ○, Chariton *et al.* (1983); Theory: — • — • —, first Born approximation by Mandal *et al.* (1975); ———, distorted wave approximation by Mandal *et al.* (1979); —••—••, polarized orbital approximation by Khan and Ghosh (1983); ———, present calculation using the Eikonal method. These reference are found in Ref. 1.

References

1) M. Chariton: *Rep. Prog. Phys.*, **48**, 737 (1986).
2) L.S. Fornari, L.M. Diana, and P.G. Coleman: *Phys. Rev. Lett.*, **51**, 2276 (1983).
3) E.S. Gillespie and D.G. Thompson: *J. Phys. B. At. Mol. Phys.*, **10**, 3543 (1977).

---

* Department of Modern Physics, University of Science and Technology of China, Hefei, Anhui, 320026, China.

** Present address: Department of Physics, International Christian University.

RIKEN Accel. Prog. Rep. **24** (1990)

III-2-6. Calculation of the Correlation Diagram of the Ne^{7+}-Ne System

K. Fujima,* Y. Naito,* T. Watanabe,**
T. Kambara, and Y. Awaya

Recently some of present authors have made measurements on the azimuthal angle dependence of emitted X-rays coincidence with scattered ions into particular angles,[1] using 10 and 26 MeV a Ne^{7+} ions and 22 MeV Al^{10+} ions on a neutral Ne gas target. An Impact velocity range is comparable to the velocity of the K-shell orbital of a Ne target, and the process can be considered to take place following a molecular orbital scheme. The electronic configurations of the projectile ion and of the target atom are assumed to be $(1s)^2(2s)$ and $(1s)^2(2s)^2(2p)^6$. Many of the occupied electronic atomic orbitals of neutral Ne are far from the highest occupied atomic orbitals of the projectile ion and many unoccupied atomic orbitals of the ion exist below the occupied orbitals of the neutral when two species get close to each other. As a result of collision, a vacancy in the K-shell of the projectile is formed and an excited electron is in the 2p orbit of the ions due to either of a direct process (direct coulomb excitation) or electron promotion processes between the molecular orbital levels.

As the first step, we planned to obtain the correlation diagram of the Ne^{7+}-Ne system which is sufficiently reliable for the calculation of present specific excitation processes. And then we were going to calculate the radial as well as rotational matrix elements between these electronic levels. Finally we plan to estimate cross sections for respective excitation processes by solving the coupled-channel equations.

For a practical reason, we take one-electron energy scheme in a diatomic molecular system. We use a DV-Xα method,[2,3] in which exchange integrals are replaced by the 1/3 power of simple density integrals,[4] *i.e.* non-local interaction potentials are approximated by local interactions. Figure 1 shows the energy diagram of sigma states in a Ne^{7+}-Ne system, calculated by using the DV-Xα method as a function of the internuclear distance.

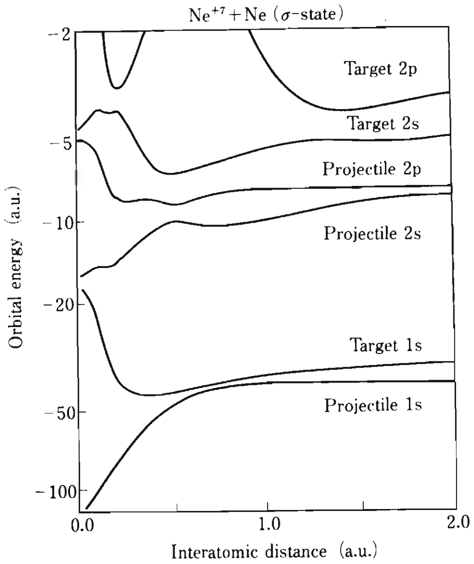

Fig. 1. Energy diagram of the sigma states in a Ne^{7+}-Ne system, calculated by using the DV Xα method as a function of the internuclear distance.

References

1) Preliminary reports, T. Kambara, Y. Kanai, Y. Awaya, H. Vogt and H. Schmidt-Böcking: Abstract of 16th ICPEAC, ed. by A. Dargarro, R.S. Freund, M. S. Lubell, and T.B. Lucatorto (New York) 483 (1989); T. Kambara, Y. Awaya, Y. Kanai, T. Mizogawa, M. Terasawa, H. Schmidt-Böcking, R. Dörner, and H. Vogt: *Proc. At. Coll. Res. Jpn.*, **15**, 32 (1989).
2) H. Adachi, M. Tsukada, and C. Satoko: *J. Phys. Soc. Jpn.*, **3**, 875 (1976).
3) A. Rosen *et al.*: *Chem. Phys.*, **65**, 3085 (1976).
4) J.C. Slater: Quantum Theory of Molecules and Solids (McGraw-Hill, New York) Vol. 4 (1974).

---

* Faculty of Engineering, Yamanashi University.
** Depertment of Physics, International Christian University.

RIKEN Accel. Prog. Rep. **24** (1990)

III-2-7. Theoretical Study of High-Energy Ion-Atom Collisions

N. Toshima

(1) Relativistic collisions

We have analyzed several distorted-wave approximations[1] that have been recently applied to relativistic ion-atom collisions and found that the symmetric treatment of distortions in initial and final channels does not necessarily represent an improvement over a description in which one of channels is left undistorted. The relativistic version of the symmetric eikonal approximation contains unphysically large contribution of spin-flip transitions, which makes the foundation of this theory unreliable.

The importance of Coulomb boundary conditions are widely recognized for perturbative treatments both in relativistic and nonrelativistic ion-atom collisions. On the other hand, it is known that a coupled-channel approach is free from this effect for nonrelativistic collisions since the correction factor arising from the asymptotic residual interaction can be completely absorbed into time-dependent expansion coefficients. However this is not true for relativistic collisions. As we have discovered recently in relativistic coupled-channel calculations, the long-range couplings of a monopole type exist even for neutral atom collisions and the leading term depends on electronic states. We treated this long-range interaction by using coupled equation formalism based on distorted-wave basis expansion and found that the results are strongly affected by this manipulation.[2]

(2) Non-relativistic collisions

A Thomas double scattering mechanism has been studied by many theoreticians using a variety of methods over tens of years. However all the theories are based on perturbative treatments up to the second order and nobody has confirmed quantitatively the convergence of the perturbation series and the reliability of the second-order calculations. We have studied this mechanism by using two non-perturbative approaches, a classical trajectory Monte-Carlo (CTMC) method[3] and a coupled-channel formalism based on pseudo-state expansion.[4] These are the first non-perturbative studies of the Thomas mechanism.

CTMC has been widely used successfully for various charge transfer processes. Though CTMC is based on purely classical mechanics, it rigorously solves the equations of motion of a three-body system. Hence we can investigate three-body effects that are absent in perturbative treatments. It was shown that the trajectories are somewhat deformed from the idealized picture of double scattering, especially at small impact parameters. Two other types of captures, knock-on capture, and OBK-type capture also play important roles.

Since the Thomas mechanism occurs via a high-lying continuum state as an intermediate state, it is rather difficult to treat this process by the coupled-channel formalism. In addition an accurate calculation of coupling matrix elements also becomes difficult because of the rapid oscillation of the integrand caused by the electron translation factor. We have overcome these difficulty by using a GTO expansion technique and succeeded in obtaining a differential cross section that has a sharp Thomas peak around the critical angle in good agreement with experimental data.

We studied the orientation and alignment of the atomic states induced by collisions with negatively and positively charged projectiles by the CTMC method and investigated how well the classical theory works in comparison with quantum theoretical calculations.[5]

References

1) N. Toshima and J. Eichler: *Phys. Rev.*, **A41**, 5221 (1990).
2) N. Toshima and J. Eichler: *ibid.*, **A42**, 3896 (1990).
3) N. Toshima: *ibid.*, p.5739.
4) N. Toshima and J. Eichler: *Phys. Rev. Lett.* (in press).
5) N. Toshima and C.D. Lin: unpublished.

RIKEN Accel. Prog. Rep. **24** (1990)

III-2-8. Investigation of a HD$^+$ Energy Level in Hyper-Radial Adiabatic Approximation

S. Hara, T. Ishihara,* N. Toshima, and H. Fukuda

The Schroedinger equation for a HD$^+$ system is given by (in units of $e = \hbar = 1$)

$$[H(\boldsymbol{r}, \boldsymbol{R}) - E]\Psi(\boldsymbol{r}, \boldsymbol{R}) = 0 \qquad (1)$$

where

$$H(\boldsymbol{r},\boldsymbol{R}) = -(\tfrac{1}{2}M)\nabla^2_R + (\tfrac{1}{2}m)\nabla^2_r + V(\boldsymbol{r},\boldsymbol{R}) \qquad (2)$$

is the total Hamiltonian, E the total energy, and Ψ the total wave function; M and m are the reduced masses for a proton p and deuteron d system, and for a (p + d) and electron e system, respectively, thus

$$1/M = 1/M_p + 1/M_d$$

and

$$1/m = 1/m_e + 1/(M_p + M_d)$$

In Eqs. 1 and 2, $\boldsymbol{R}$ represents the position vector of d relative to p, $\boldsymbol{r}$ that of electron e with respect to the centre of mass of (p+d), and V the Coulomb interaction between the three particles

$$V(\boldsymbol{r}, \boldsymbol{R}) = -1/r_p - 1/r_d + 1/R$$

The hyper-radius X for the three-body system can be defined by

$$M_0X^2 = MR^2 + mr^2$$

where M_0 is an arbitrary mass constant. We choose $M_0 = M$ in the following. In practical application of the hyper-radial approach, a set of five coordinates Ω other than the hyper-radius can be chosen in many ways. Matveenko[1)] proposed the hyper-spheroidal coordinates for molecular type three-body problems. In this coordinates, the set of variables Ω is $(\xi, \eta, \varphi, \Theta, \Phi)$, where (ξ, η, φ) are the spheroidal coordinates for the electron, Θ and Φ, the polar and azimuthal angles for $\boldsymbol{R}$ measured from space-fixed coordinates. By using the hyperradius thus defined, the total Hamiltonian H reduces to the following form

$$H(\Omega, X, J) = -\frac{1}{2M}\frac{1}{X^5}\frac{\partial}{\partial X}X^5\frac{\partial}{\partial X} + h(\Omega, X, J)$$

where h is the adiabatic Hamiltonian which includes X as a parameter and dependent on the total angular momentum J of the system.

The eigen function $\Phi_n(\Omega, X, J)$ and eigen values $\varepsilon_n(X, J)$ of the adiabatic Hamiltonian h are obtained by solving the following Schroedinger equation

$$[h(\Omega, X, J) - \varepsilon_n(X, J)]\Phi_n(\Omega, X, J) = 0$$

This equation has been solved variationally. The total wave function Ψ in the adiabatic approximation is then expressed by

$$\Psi = X^{-5/2}\Phi_n(\Omega, X)F_n(X)$$

The radial wave function $F_n(X)$ satisfies the following hyper-radial equation

$$\left[-\frac{1}{2M}\frac{d^2}{dX^2} + U_n(X) - E_v\right]F_n(X) = 0 \qquad (3)$$

where

$$U_n(X) = \varepsilon_n(X) + 15/(8MX^2) + W_{nn}(X)$$

and

$$W_n(X) = -(1/2M) < \Phi_n \frac{\partial^2}{\partial X^2} \Phi_n >$$

where the bracket denotes integration over coordinates Ω.

We have solved differential (eigenvalue) equation 3 numerically and obtained E_v. The results[2)] are presented in Table 1, the hyper-radial adiabatic approximation gives energies better (lower) than a conventional Born-Oppenheimer approximation.

Table 1. Dissociation energies E_v of HD$^+$ (in cm^{-1}) relative to the 1S state of the D atom.

v	J = 0	J = 1	J = 2
0	21515.9	21472.1	21384.7
1	19602.8	19561.0	19477.6
2	17785.9	17746.0	17666.4
3	16062.2	16024.2	15948.4

References

1) A.V. Matveenko: *Phys. Lett.*, **B129**, 11 (1983).
2) S. Hara, H. Fukuda, and T. Ishihara: *Phys. Rev. A*, **39**, 35 (1989).

---

* Institute of Applied Physics, University of Tsukuba.

RIKEN Accel. Prog. Rep. **24** (1990)

III-2-9. Charge State Distribution Measurements of 77 MeV/u Ar Ions Which Have Passed through a Carbon Foil

Y. Kanai, T. Kambara, Y. Awaya, A. Hitachi,
T. Niizeki, Y. Zou, and K. Shima

We measured the charge-state distributions of 77 MeV/u Ar ions which have passed through a carbon foil with varying the foil thickness (10 μg/cm^2 - 4.27 mg/cm^2) and incident charge states (16+ - 18+). The study aims to get (1) the equilibrium mean charge distribution of Ar ions which have passed through a carbon foil and (2) the charge changing cross sections (capture and loss cross sections) of Ar ions which collide with carbon atoms. Projectiles of 77 MeV/u Ar^{16+} ions were obtained from RIKEN Ring Cyclotron. Projectiles of Ar$^{17+,18+}$ ions were produced by using Al foils and then selected by a magnet. The experiment was performed at the atomic physics beam line (E2B); the targets were placed in the general purpose experimental chamber on the E2B beam line. The charge states of the Ar ions which have passed through the target were analyzed with a charge analyzing magnet and a position-sensitive parallel-plate avalanche counter (PPAC).

When the target was thicker than about 1 mg/cm^2, the charge-state distributions did not depend on the target thickness. We concluded therefore that the distribution is equilibrated as shown in Table 1. Shima proposed a semi-empirical formula for the equilibrium charge-state distribution of high energy ions (>10 MeV/u) after passing through the carbon foil.[1)] Our previous results for 26 MeV/u Ar ions[2)] are in good agreement with the values obtained from Shima's formula. However, the Ar^{17+} fraction of our present results is larger than the value obtained from Shima's formula. This difference may be due to the difference in a dominant process of the electron capture of the Ar ions between 26 MeV/u and 77 MeV/u.[3)]

Table 1. Equilibrium charge-state distributions of 77 MeV/u Ar ions after passing through carbon targets. The numbers in parentheses stand for the power of ten.

	Charge state fraction		
Mean charge	16+	17+	18+
17.9994	5±5(-7)	5.6±0.1(-4)	9.994±0.001(-1)

Using the charge-state distributions for thin targets (10 - 38.5 μg/cm^2), we obtained the electron capture and loss cross sections of 77 MeV/u Ar ions which collide with carbon atoms. Preliminary results are shown in Table 2. Precise analysis is in progress.

Table 2. Preliminary charge changing (electron capture and loss) cross sections of 77 MeV/u Ar ions collide with carbon atoms. Numbers in parentheses stand for the power of ten.

Initial charge state	Final charge state	Cross section (cm^2)
16+	17+	5.9±0.5 (-20)
17+	18+	2.9±0.5 (-20)
17+	16+	1.3±0.5 (-23)
18+	17+	3.0±1.0 (-23)

References

1) K. Shima, N. Kuno, and M. Yamanouchi: *Phys. Rev.*, **A40**, 3557 (1989).
2) Y. Kanai, T. Kambara, T. Mizogawa, A. Hitachi, K. Shima, and Y. Awaya: *RIKEN Accel. Prog. Rep.*, **22**, 54 (1988).
3) Y. Kanai, T. Kambara, Y. Awaya, A. Hitachi, T. Niizeki, Y. Zou, and K. Shima: This Report, p. 42 (1990).

RIKEN Accel. Prog. Rep. **24** (1990)

III-2-10. Ratio of the Radiative to the Total Electron Capture Cross Section of 77 MeV/u Ar^{18+} Ions on a Carbon Target

Y. Kanai, T. Kambara, Y. Awaya, A. Hitachi,
T. Niizeki, Y. Zou, and K. Shima

We measured the ratio of the radiative electron caprure cross section (σ(REC)) to the total electron capture cross section (σ(total)) of 77 MeV/u Ar^{18+} ions in carbon foils (23 and 44 μg/cm^2). Projectile Ar^{18+} ions were produced through an Al stripper foil at RIKEN Ring Cyclotron. Experiments were performed on the atomic-physics beam line (E2B). X rays emitted from the projectile Ar ions in the target were measured with a pure-Ge detector at 90° to the beam direction. The charge states of Ar ions after passing through the target were determined with a charge analyzing magnet and a position-sensitive parallel-plate avalanche counter (PPAC). An X-ray spectrum measured with the Ge detector is shown in Fig. 1a, in which a broad peak around 44 keV is due to the X-rays emitted by REC. A huge background due to the primary and secondary bremsstrahlung was reduced by using a coincidence technique. An X-ray spectrum in coincidence with Ar^{17+} ions is shown in Fig. 1b, in which almost all the background is vanished. We can find two peaks, K- and L-REC (radiative electron capture into projectile K- and L-shell), as indicated in Fig. 1b. The width of each peak is caused by the momentum distribution of target electrons captured by the projectile.$^{1)}$

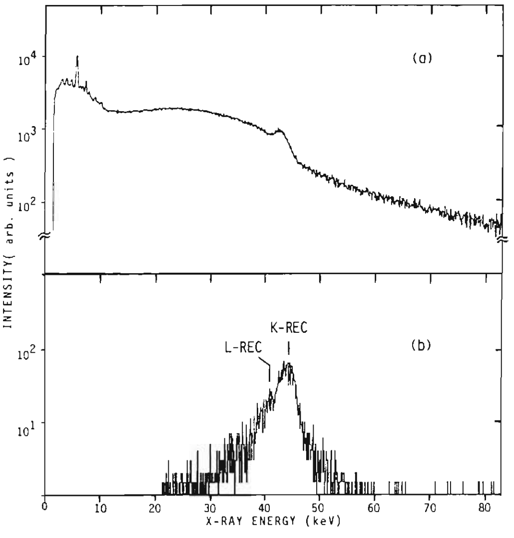

Fig. 1. X-ray spectra from 77 MeV/u Ar^{18+} on a C foil (44μg/cm^2). a, Spectrum measured with the Ge detector without coincidence; b, Spectrum measured with the Ge detector in coincidence with Ar^{17+} ions.

We estimated the ratio of σ(REC) to σ (total) by using the X-ray spectra obtained by coincidence with Ar^{17+}as $\sigma(\text{total}) = I(17+)/(I_0 \times N)$, $\sigma(\text{REC}) = X(\text{REC})/(I_0 \times N)$, and $\sigma(\text{REC})/\sigma(\text{total}) = X(\text{REC})/I(17+)$. Here I_0 is the number of incident Ar^{18+}, $I(17+)$ the number of Ar^{17+} after the target, N the target number density, and X(REC) the number of photons emitted by REC. We observed the X rays at only 90°. We estimated $X(\text{REC})/I(17+)$ by assuming the $\sin^2\theta$ angular dependence of the REC X rays, where θ is the emission angle of the REC X rays. This assumption is reasonable in our case.$^{1)}$ From this measurement, we obtained the ratio $\sigma(\text{REC})/\sigma(\text{total}) = 58\%$ in both targets.

References

1) Y. Awaya, K. Hino, A. Hitachi, Y. Kanai, K. Kawatsura, K. Kuroki, H. Vogt, Y. Yamazaki, and T. Watanabe: High-Energy Ion-Atom Collisions, Springer-Verlag, Berlin Heidelberg, p. 185 (1988).

RIKEN Accel. Prog. Rep. **24** (1990)

III-2-11. Multiple Inner-Shell Ionization of Target Atoms by 92 MeV/u Ar-Ion Impact

Y. Awaya, T. Kambara, Y. Kanai, and A. Hitachi

We have studied simultaneous single K- and multiple L-shell ionization of target atoms for high-velocity nearly symmetric ion-atom collisions by diffraction of K_α-satellite X rays. This is an extension of previous systematic studies to a higher collision velocity and near-symmetric collision systems.

Previously we made systematic studies of simultaneous single K- and multiple L-shell ionization of target atoms in asymmetric heavy ion-atom collisions, using 0.8-26 MeV/u He, C, N, and O ions from the cyclotron, the RILAC, and RIKEN Ring Cyclotron.[1,2] The K-sattelite X rays from various target elements (Al, Ar, Ti, Cr, Fe, Ni, Kr, and Y) were resolved with crystal spectrometers. From the intensity distribution among the satellites, we obtained the probability of L-shell ionization simultaneous to a K-shell ionization P_L, assuming a binomial satellite distribution. The P_L values thus obtained for different collision systems and a wide range of collision velocity agree well with a universal scaling based on a binary-encounter approximation (BEA),[3] except for low-velocity regions where the projectile velocity v_1 is nearly equal to the target electron orbital velocity v_n.

Although applied mainly to asymmetric collisions, the BEA model is expected to be also valid for near-symmetric system if a collision velocity is very high. In order to check the validity, we carried out measurements with an Ar^{17+} beam at 92 MeV/u from RIKEN Ring Cyclotron incident on solid targets of Ti, V, Fe, Ni, and Cu at a collision velocity of about 0.41c or 56.8 atomic unit. The scaled velocity v_1/v_n range between 7 and 10.4 for the target L-shell electrons. The K-X rays from the targets were measured with a broad-range crystal spectrometer[4] with a crystal of LiF(200) for the V and Ti and a LiF(220) for the other targets.

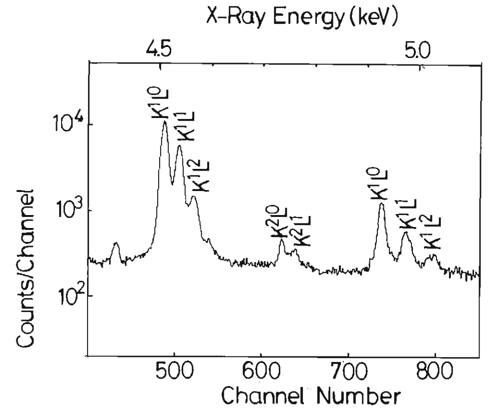

Fig. 1. Spectrum of Ti K-X rays from a 92 MeV/u Ar-ion impact. A group of peaks around 4.5 keV correspond to the K_α satellites, those around 4.7 keV to the K_α hypersatellites, and those around 5 keV to the K_β satellites.

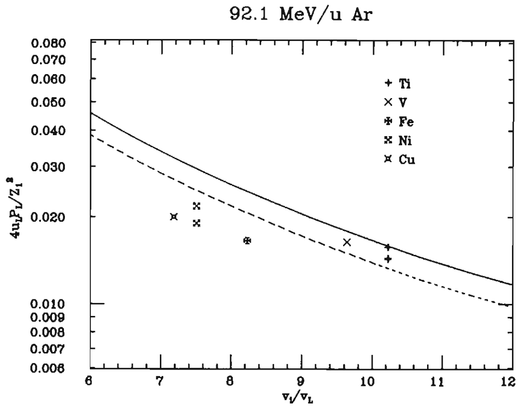

Fig. 2. Scaled ionization probability $4u_LP_L/Z_1^2$ is plotted against a scaled velocity v_1/v_L, where u_L is the binding energy of the target L electron in atomic unit and Z_1 is the atomic number of the projectile. The solid curve shows the universal BEA curve, and the dashed curve shows the curve multiplied by 0.84.

Figure 1 shows a spectrum of the Ti K-X rays, where K^mL^n shows a satellite component with m K- and n L vacancy configuration before K X-ray emission. We fitted the experimental K_α-satellite spectra by Gaussian curves and obtained the intensity distribution of the satellites, $I(n)$. The values of P_L are obtained from the K_α satellites by assuming a binomial distribution, $I(n) \propto (8!/n!(8-n)!)P_L^n(1-P_L)^{8-n}$, and are plotted in Fig. 2 according to the BEA scaling. The experimental P_L agrees well with the universal curve for the Ti and V targets and is smaller than that for the heavier targets. In the previous studies,[1,2] we found that a universal curve multiplied by 0.84 better fits experimental results. If the same factor is multiplied to the universal curve, it better fits the present experimental results.

By combining the present results and the previous ones, we found that the values of P_L fit within 30% the universal curve multiplied by 0.84. We conclude that the simple BEA scaling can be applied to collision systems with a wide range of collision velocity when $v_1 > v_n$, and that it can also be applied to near-symmetric systems at very high velocities.

References

1) Y. Awaya: Electronic and Atomic Collisions, Proc. XI ICPEAC (eds. N. Oda and T. Takayanagi), North Holland Pub. Co., Amsterdam, p. 325 (1979).
2) Y. Awaya, T. Kambara, Y. Kanai, T. Mizogawa, A. Hitachi, and B. Sulik: *RIKEN Accel. Prog. Rep.*, **22**, 55 (1988).
3) J.H. McGuire and P. Richard: *Phys. Rev.*, **A8**, 1374 (1973).
4) A. Hitachi, H. Kumagai, and Y. Awaya: *Nucl. Instrum. Methods*, **195**, 631 (1982).

RIKEN Accel. Prog. Rep. **24** (1990)

III-2-12. A Trial of Doppler Beam-Foil Spectroscopy Using Relativistic Heavy (95 MeV/u Ar^{17+}) Ion Beams

K. Komaki, Y. Yamazaki, T. Azuma, K. Kuroki, K. Kawatsura,
Y. Kanai, T. Kambara, and Y. Awaya

Beam-foil spectroscopy has been used as a reliable and unique technique for the measurements of the energy levels and lifetimes of excited states of highly charged ions. Here we propose to measure decay curves of 2p → 1s transition of 95 MeV/u Ar^{17+} using RIKEN Ring Cyclotron. Although the real lifetime of this transition is of the order of sub-pico seconds, an appearing decay time is often in the order of ~ns owing to the slow feeding of 2p states from highly excited high-*l* Rydberg states via an yrast line. In other words, information on the initial (n, l) distribution is obtainable by measuring the decay curve between deep bound states.

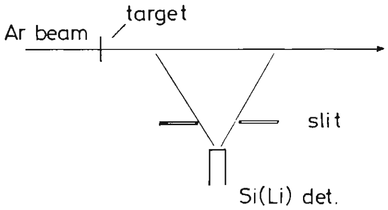

Fig. 1. A schematic drawing of the experimental setup.

Figure 1 shows a schematic diagram of the experimental setup. A Si(Li) X-ray detector was installed to observe a part of the beam downstream from a target foil. As the velocity of the beam is ~$0.4c$, the X-ray evergy of the 2p → 1s transition of Ar^{17+} should show a strong Doppler shift depending on the position where the X ray is emitted. Since we know the velocity, the decay curve of the transition is obtained.

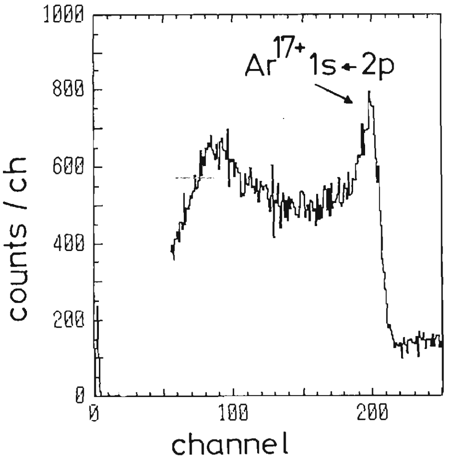

Fig. 2. An example of the "delayed" spectrum of Ar^{17+} (1s ← 2p) transitions.

Figure 2 shows an example of preliminary results. Although a continuum background is very high, it is clearly seen that the transition line (Ar^{17+} 2p → 1s) skews to the lower energy side, indicating the production of a considerable amount of delayed (~ns) X rays as expected.

RIKEN Accel. Prog. Rep. **24** (1990)

III-2-13. Angular Correlation between K-X Rays and Scattered Particles in 10 and 20 MeV Ne^{7+}-Ne Collisions

T. Kambara, Y. Awaya, Y. Kanai, T. Mizogawa, and M. Terasawa

We measured the angular correlation between K X-ray emission and scatered particles in Ne-Ne collisions to study the alignment in inner-shell excitation processes in heavy ion-atom collisions. In the experiments, a Ne-ion beam from RILAC was collimated and was incident on a Ne gas target. The scattered ions were charge-state analyzed and then counted with a two-dimensional position-sensitive particle detector (PPAD), in coincidence with the K-X rays measured at the target. We obtained the K X-ray emission probability as a function of the charge state of the scattered ions q, scattering angle θ, and the angle between the scattering plane and the X-ray emission direction ϕ. The experimental setup[1] and the first measurements with 10 and 26 MeV Ne^{7+} ions[2] were reported previously.

We have made the following improvements on the measurement system: (1) We found that the measurement at 26 MeV reported before was contaminated by lower-energy particles scattered at the edges of the collimators. Therefore the slits of the beam collimation system was changed from knifeedge plates to mirror-polished round-shape bars to avoid the edge scattering. A remote-controlled pulse motor system was introduced for the driving system of the slits, which saved the time to adjust the collimators. (2) Since the position of the scattered particles was measured after the charge-state analysis, the stability of the field of the analyzer magnet is essential to the precision of the results. An NMR gaussmeter for the magnetic field measurement of the charge-state analyzing magnet after the target was connected to a CAMAC register, thus the field can be monitored continuously throughout a measurement.

Two new measurements were performed with Ne^{7+} ions (Li-like) of 10.5 and 20 MeV on a Ne target. The charge states of the scattered ions were analyzed from 4+ to 8+ at 10.5 MeV and from 5+ to 9+ at 20 MeV,and the coincidence with the K-X rays were measured for ions of 6+ and 7+ at 10.5 MeV and those from 6+ to 9+ at 20 MeV. The scattering angle θ ranged up to 2.6×10^{-3} rad with an angular resolution of 8×10^{-5} rad.

The ϕ-dependence of X-ray emission probabilities at different regions of impact parameter b was fitted to a function $A\ \sin^2\phi+B$ and an anisotropy parameter $R=A/2B$ was calculated. The impact parameter b was calculated from θ with a screened Coulomb potential after correction for focusing with the charge-state analyzing magnet. In Fig. 1, an example of the b-dependence of R is shown. The obtained R is small and positive at incident energies of 20 MeV and 10.5 MeV, being consistent with previous measurements. A theoretical investigation of the alignment with a molecular-orbital model is reported by Dr. Fujima *et al.*[3]

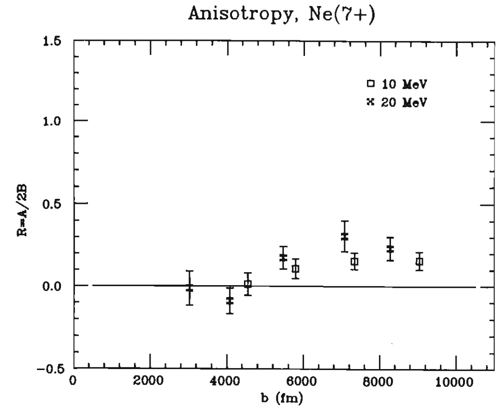

Fig. 1. Examples of impact parameter (b) dependence of the anisotropy parameter $R=A/2B$ for scattered Ne^{7+} ions.

References

1) T. Kambara, Y. Awaya, Y. Kanai, H. Schmidt-Böcking, and H. Vogt: *RIKEN Accel. Prog. Rep.*, **22**, 72 (1988).
2) T. Kambara, Y. Awaya, Y. Kanai, T. Mizogawa, M. Terasawa, H. Schmidt-Böcking, R. Dörner, and H. Vogt: *ibid.*, **23**, 48 (1989).
3) K. Fujima *et al.*: This Report, p. 38.

RIKEN Accel. Prog. Rep. **24** (1990)

III-2-14. Angular Distribution Measurement of K-X Rays Emitted from an Ar Beam Passing through C Foil

T. Papp, Y. Awaya, A. Hitachi, T. Kambara,
Y. Kanai, and T. Mizogawa

In ion-solid foil interaction, the symmetry of the collision geometry is reflected in the angular and polarization distribution of collision-induced fluorescence. When the beam axis coincides with the axis of the normal to the foil, in beam-foil spectroscopy, the collision geometry has cylindrical symmetry. When the foil is tilted with respect to the beam axis, the collision geometry loses its axis of symmetry. This lower degree of symmetry is mirrored by a correspondingly lower degree of symmetry in the angular distribution of emitted radiation.[1,2]

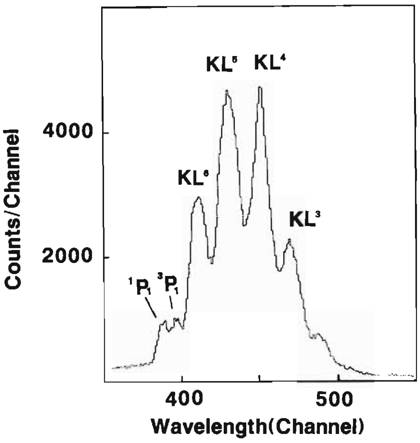

Fig. 1. K_α-satellite X-ray spectrum of Ar measured at 30°, relative to the incoming beam, when the foil was tilted by 45° with respect to the beam axis.

In the experiment, a 1 MeV/u Ar beam obtained from the RILAC was passed through a carbon foil target of 20 $\mu g/cm^2$ in thickness. Angular distributions of Ar KL^n X-ray lines were measured at two target angles, tilted at 90° and 45° relative to the beam direction. The spectra of Ar X rays were measured with a broad-range crystal spectrometer[3] using a flat Ge (111) crystal with a Bragg angle at its center $2\theta = 76°$. The spectra were fitted by a quadratic background and an appropriate number of pseudo-Voigt peaks simultaneously, by using a computer code EWA.[4] The spectra were analyzed by a Gaussian-peak shape too, and a better fitting was obtained when a pseudo-Voigt peak shape was used. From the analysis the intensity ratio of the well resolved peaks were determined as a function of the detection angle. At a 90° target angle, all the ratios were found to be isotropic within error limits. At a 45° target angle the $^3P_1/^1P_1$ intensity ratio had a definite anisotropy.

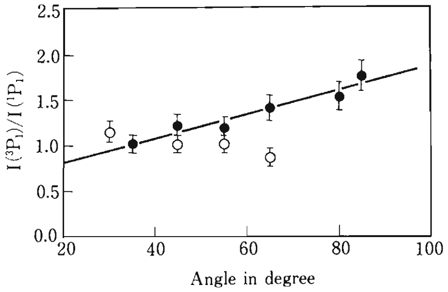

Fig. 2. Intensity ratio of the $^1P_1$ and $^3P_1$ transitions as a function of the detector angle. ○, beam axis was perpendicular to the foil surface; ●, angle of beam axis and foil was 45°. The line is drawn to guide the eyes.

References

1) J. Macek and D. Burns: Beam Foil Spectroscopy (ed. S. Bashkin), Springer Verlag, Berlin, Heidelberg, and New York, p. 237 (1976).
2) D. A. Church, R. A. Kenefick, D. -W. Wang, and R. L. Watson: *Phys. Rev.*, **A26**, 3093 (1982).
3) A. Hitachi, H. Kumagai, and Y. Awaya: *Nucl. Instrum. Methods*, **195**, 631 (1982).
4) J. Vêgh: Thesis ATOMKI Debrecen 1990 (unpublished).

RIKEN Accel. Prog. Rep. 24 (1990)

III-2-15. High Resolution L X-Ray Angular Distribution Measurement on Terbium

T. Papp, Y. Awaya, A. Hitachi, T. Kambara,
Y. Kanai, and T. Mizogawa

It was found, in the L_3-subshell angular correlation[1] and angular distribution[2,3] studies, that the angular distribution of X rays reflects the effect of magnetic quadrupole (M2) mixing into the electric dipole (E1) transition. The M2/E1 mixing ratios experimentally obtained deviate significantly from theory[4] around $Z \sim 60$. In these experiments semiconductor detectors were used to detect X rays. This type of detectors well resolve the L_l and L_α peak; however the tail of the intense L_α peak lies under the L_l peak, causing a systematic error in the evaluation of the mixing ratio. The large discrepancy between theory and experiments would be verified from an angular distribution measurement by a higher-resolution detection technique.

Thus we carried out such a measurement, detecting X rays with a crystal spectrometer in which a position-sensitive proportional counter was incorporated.[5] N^{2+} ions of 0.553 MeV/amu obtained from the RILAC were allowed to impinge on a Tb target of 4 μm in thickness, tilted by 45° to an incoming beam, and the angular distribution was measured at eight different angles in the range of 95°-155°.

Usually, the $L_{\beta 1,3}$-X ray emission is regarded as isotropic and is used for a normalization standard in angular distribution measurements. However, in heavy ion-atom collisions with a simultaneous multiple outer-shell ionization, the isotropic angular distribution of the $L_{\beta 1,3}$-X ray has to be verified experimentally. Therefore the angular distribution measurement was performed in two steps: First the ratio of $L_{\beta 1,3}$ to L_α transitions was studied using a LiF (220) crystal. Since the Bragg angle for the L_α transition is 44° and the polarization sensitivity is very close to unity, the L_α intensity measured has an isotropic angular distribution, and can be used for normalization. From the measurement, the ratio of $L_{\beta 1,3}$ to L_α transitions and thus the $L_{\beta 1,3}$ transition were found to have an isotropic angular distribution. In the second step the angular distribution of the L-X rays was studied with a LiF(200) analyzer crystal. The intensity of the L_3-X rays were normalized to the $L_{\beta 1,3}$ transitions.

Figure 1 shows an example of the L X-ray spectra. The spectra were evaluated by assuming a Voigt peak shape.

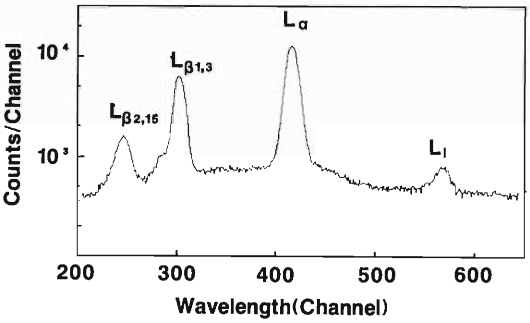

Fig. 1. L X-ray spectrum of Tb, ionized by 0.553 MeV N-ion impact, and measured with a crystal spectrometer using a LiF(200) crystal.

A large anisotropy was observed for the L_3 X-ray lines. By assuming that the crystal was perfect, a value of -0.20 ± 0.04 was obtained for the anisotropy parameter for the L_l transition normalized to the $L_{\beta 1,3}$. The anisotropy was found two times larger for the $L_{\beta 2,15}$ transition than for the L_α. The ratio of the anisotropy parameters of the normalized L_l and L_α transitions was evaluated to be 2.76 ± 1.5 and 3.25 ± 1.9, assuming perfect and mosaic crystal structure respectively. These results verify the disagreement with the theory observed in the earlier measurement carried out with semiconductor detectors.

References

1) A.L. Catz: *Phys. Rev.*, **A2**, 634 (1970); E.S. Macias and M.R. Zalutsky: *ibid.*, **A9**, 2356 (1974).
2) T. Papp: High Energy Ion-Atom Collisions (eds. D. Berényi and G. Hock), Lecture Notes in Physics, **294**, Springer-Verlag, Berlin Heidelberg, p. 204 (1988).
3) T. Papp and J. Pálinkás: *Phys. Rev.*, **A38**, 2686 (1988).
4) J.H. Scofield: *ibid.*, **179**, 9 (1969); J.H. Scofield: *ibid.*, **A10**, 1507 (1974).
5) A. Hitachi, H. Kumagai, and Y. Awaya: *Nucl. Instrum. Methods*, **195**, 631 (1982).

RIKEN Accel. Prog. Rep. **24** (1990)

III-2-16. Atomic Bremsstrahlung in the MO Process

K. Ishii, K. Maeda, Y. Sasa, J. Kawai,
M. Takami, M. Uda, and S. Morita[*]

Adiabatic collisions of an incident heavy ion with a target atom forms a united atom and produces molecular orbital (MO) X rays. It is expected that the production cross section of MO X rays becomes maximum when the atomic number of a projectile (z_p) is equal to that of target atom (z_t).[1)]

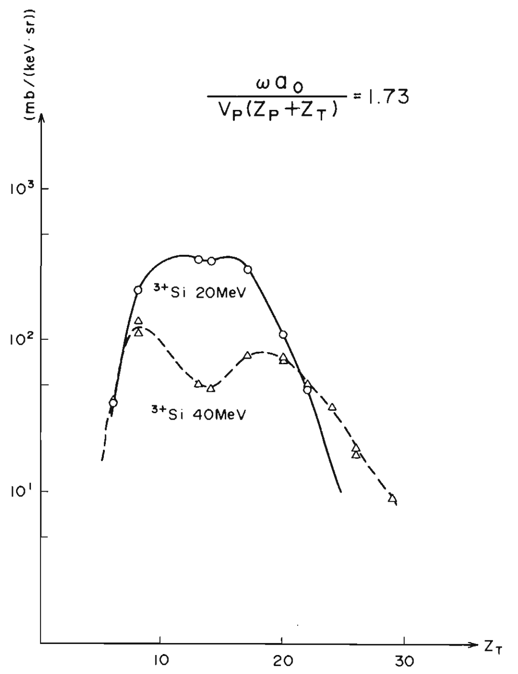

Fig. 1. Incident energy dependence of the production cross sections of continuous X rays by Si^{3+} ion bombardment.

Up to the present, many workers have studied the MO process, but not enough on this effect.

On the other hand, secondary electron bremsstrahlung (SEB), quasi-free electron bremsstrahlung (QFEB), and atomic bremsstrahlung (AB) are expected in light-ion bombardments.[2)] Among these processes, a considerable contribution of AB in heavy ion collisions is theoretically expected,[3)] though not yet confirmed. In symmetric collision, the cross section of AB is almost zero because of a dipole transition process. In order to search such characteristics of MO and AB, we have measured continuous X rays produced from the targets of $z_t = 6 - 29$ by bombardment of Si^{3+} ions accelerated at 20 MeV and 40 MeV with the RIKEN RILAC.

Figure 1 shows the absolute cross sections of continuous X rays at the scaling parameter[4)] $\omega a_0/(v_p(z_p + z_t)) = 1.73$ (ω is the frequency of X-ray, a_0 is the Bohr radius, and v_p is the projectile velocity) for Si^{3+} 20 MeV and Si^{3+} 40 MeV bombardments. For 20 MeV, the cross section forms a peak at symmetric collision, but that of 40 MeV shows a dip. This is the first confirmation for the above-described characteristics of MO and AB.

References

1) R. Anholt: *Z. Phys. A*, **289**, 41 (1978).
2) K. Ishii and S. Morita: *Int. J. PIXE*, **1**, 1 (1990).
3) K. Ishii and S. Morita: *Phys. Rev. A*, **30**, 2278 (1984).
4) K. Ishii *et al.*: *RIKEN Accel. Prog. Rep.*, **23**, 47 (1989).

---

[*] Laboratory for Materials Science and Technology, Waseda University.

RIKEN Accel. Prog. Rep. **24** (1990)

III-2-17. Nickel *Lα* X-ray Emission Spectra of Nickel Compounds

J. Kawai, K. Maeda, Y. Sasa, M. Takami, and M. Uda

Multiplet structures in X-ray emission spectra of transition metal compounds are usually interpreted in terms of splittings due to the exchange interaction between unpaired *3d* electrons ($S=1$ for Ni^{2+}) and X-ray hole in the initial and the final states of the X-ray emission. Thus, X-ray line profiles can be calculated by using multiplet wave functions in an *LS* or *jj* coupling scheme in a spherical symmetry field or in a crystal field.[1] However the agreement between these theoretical calculations and experiment are unsatisfactory.[2]

We have measured the Ni *Lα* spectra of $NiI_2(S=1)$, Ni(salen) ($S=0$) and Ni(metal) with a Bragg spectrometer equipped with a RAP(100) crystal by fluorescent excitation (Rh-anode tube) and proton bombardment (1.6 MeV). The spectral line shape of the fluorescent excitation was identical to that of the proton excitation for the same compound within an experimental error. The spectra of fluorescent excitation are presented in Fig. 1. We found the existence of a structure on the high-energy shoulder of NiI_2Ni*Lα* line (Peak *b* in Fig. 1). The *Lα* line width of Ni(salen) is narrow since it has no unpaired electrons ($S=0$). The width of the main line of NiI_2(Peak *a* in Fig. 1) is not significantly broader than that of Ni(salen) in spite that NiI_2 has two unpaired electrons in the *3d* orbital in the ground state ($S=1$). Comparing the present X-ray emission spectra with the X-ray photoelectron spectra of Zaanen *et al.*,[3] we assigned that the *Lα* main line of NiI_2 (Peak *a*) corresponds to the $\underline{2p}3d^{10}\underline{L}^2 \rightarrow 3d^9\underline{L}^2({}^2P \rightarrow {}^2D)$ transition [transition between well-screened states, which are due to charge transfer (CT) from ligands], while the high-energy structure (Peak *b*) is assigned to the $\underline{2p}3d^{8,9}\underline{L}^{0,1} \rightarrow 3d^{7,8}\underline{L}^{0,1}$ transition (transition between poorly screened states). Here the underline denotes hole(s) and *L* denotes a linear combination of ligand orbitals. Therefore the spectrum of NiI_2 is not broadened corresponding to its spin state in the ground state.

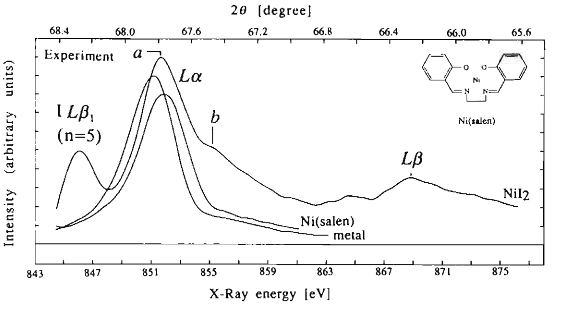

Fig. 1. Measured Ni *Lα* ($\underline{2p} \rightarrow \underline{3d}$) spectra of NiI_2 ($S=1$), Ni(salen) ($S=0$) and Ni(metal) of fluorescent excitation.

To clarify the CT effect theoretically, we calculated the X-ray multiplet structure of NiI_2 by the *LS* coupling and CT effect (Fig. 2). The agreement between theory (Fig. 2) and experiment (NiI_2 in Fig. 1) is satisfactory after the inclusion of the CT mechanism.

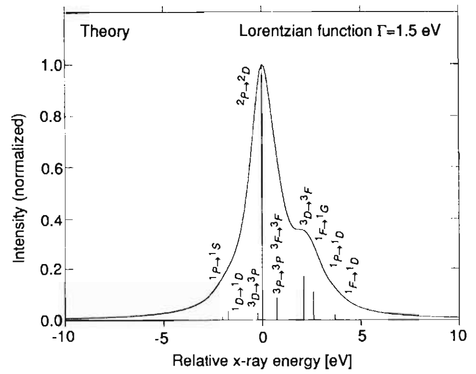

Fig. 2. Calculated Ni *Lα* spectrum of NiI_2.

In summary, though the doublet structures of peaks *a* and *b* were believed to originate from the splitting by the exchange interaction between the X-ray hole and *3d* holes, the present result indicates that the splitting originates from the screening effect by the CT from ligands. The main line of NiI_2 (Peak *a* in Fig. 1) is the CT peak and thus narrower than that expected from the spin state of the ground state. The multiplet structure in X-ray emission spectra of CT semiconductors[4] could be interpreted in the same manner.[5]

Thanks are due to Dr. K. Miyamura (Univ. Tokyo) for providing us with the Ni(salen) compound.

References

1) K. Tsutsumi: *J. Phys. Soc. Jpn.*, **14**, 1696 (1959).
2) K.S. Srivastava, S. Singh, A.K. Srivastava, R.S. Nayal, A. Chaubey, and P. Gupta: *Phys. Rev.*, **A25**, 2838 (1982).
3) J. Zaanen, C. Westra, and G.A. Sawatzky: *ibid.*, **B33**, 8060 (1986).
4) J. Zaanen, G.A. Sawatzky, and J.W. Allen: *Phys. Rev. Lett.*, **55**, 418 (1985).
5) J. Kawai, M. Takami, and C. Satoko: *ibid.*, **65**, 2193 (1990).

RIKEN Accel. Prog. Rep. **24** (1990)

III-2-18. Two-Photon Decay of a He-Like Ge^{30+} Excited State Produced by Resonant Transfer and Excitation (RTE)

P.H. Mokler,[*1] S. Reusch,[*1] Z. Stachura,[*2] A. Warczak,[*3] T. Kambara, A. Müller,[*4] R. Schuch,[*5] and M. Schulz[*6]

We have investigated the resonant transfer and excitation (RTE) processes in collisions between hydrogen-like Ge^{31+} ions and an H_2 target at collision energies between 12 and 19 MeV/u at the UNILAC facility of GSI in Darmstadt, Germany. Since the intermediate doubly-excited states of He-like Ge^{30+} ions produced by KLL RTE have two K-vacancies and emit two K-X ray photons, we utilized an X-ray/X-ray coincidence technique. The experimental setup and some of the results were reported previously.[1)]

Among the different overlapping KLL-RTE resonances in He-like ions, there is one leading to the doubly-excited 2s2p $^1P_1$ state which decays promptly to the 1s2s $^1S_0$ state, and this can only decay via a two-photon decay (2E1) into the $1s^2$ $^1S_0$ ground state. In the decay of the 2s2p $^1P_1$ state, three X rays are emitted: One K-X ray from the decay into the 1s2s $^1S_0$ state and two photons of continuous energy, where the sum of both is the binding energy difference between the 1s2s $^1S_0$ and the $1s^2$ $^1S_0$ state.

The signature of the two-photon decay was clearly observed as a diagonal ridge with E_1+E_2 $\sim$10.3 keV in the X-ray/X-ray energy correlation diagram (Fig. 3 in Ref. 1). Integrating the intensity in the two-photon spectrum along the diagonal ridge, we obtained the total cross section for the two-photon emission, where the KLL resonance was clearly separated from higher-shell resonances KLn with $n \geq 3$ (Fig. 5 in Ref. 1).

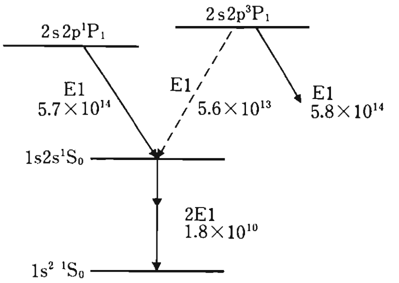

Fig. 1. Level scheme of the He-like Ge^{30+}. States which are accessible via KLL-RTE processes and may decay via the 1s2s $^1S_0$ state are marked in the LS-coupling scheme. Radiative transition rates are given in s^{-1}.

Figure 1 shows a decay diagram for the relevant levels in the He-like Ge^{30+} restricted to levels accessible for KLL-RTE processes. The radiative decay rates given in Fig. 1 are calculated using a multiconfiguration Dirac-Fock program. According to the radiative decay rates and Auger rates relevant for the production of the intermediate states, one finds that for the KLL region the resonance leading to the doubly-excited 2s2p $^1P_1$ state is with 98% the dominant one populating the 1s2s $^1S_0$ level. Therefore the 2 E1 decay of this state provides means to isolate the RTE resonance via the 2s2p $^1P_1$ level for heavy projectiles. For He-like Ge ions, the 2E1 decay is fast enough for detection near the reaction volume. It is estimated that the 1s2s $^1S_0$ state decays within the accessible time window of our experimental arrangement.

The energy spectrum of one of both the photons obtained from the diagonal ridge is shown in Fig. 2. Due to the uncertainties in coincidence detection efficiency, the spectrum is cut off in both sides, *i.e.* below 2 keV and beyond 8 keV; in between the spectrum is efficiency

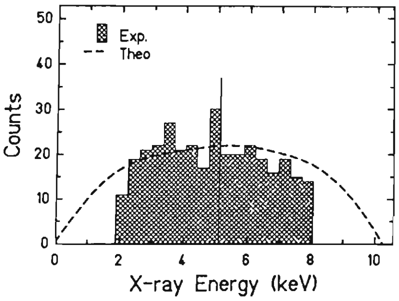

Fig. 2. Energy distribution of one of the two photons from the 2E1 decay measured in coincidence each other. The expected shape for the corresponding transition in hydrogen is displayed as a dashed curve.

[*1] GSI, D-6100 Darmstadt, Germany

[*2] Inst. of Nuclear Physics, 31-342 Kraków, Poland

[*3] Inst. of Physics, Jagiellonski University, 30-059 Kraków, Poland

[*4] Strahlenzentrum, Universität Gießen, D-6300 Gießen, Germany

[*5] Manne-Siegbahn Institute of Physics, S-10405 Stockholm, Sweden

[*6] Physics Department, Kansas State University, Manhattan, KS 66506, USA

corrected. The spectrum should be symmetric around $(E_1+E_2)/2\sim5.2$ keV which is fulfilled within the available low statistics. In Fig. 2, we plot also the energy spectrum expected for the two-photon decay for hydrogen as a simple test. However, in order to get a reliable comparison with theory, dedicated experiments with better statistics and with possibly heavier projectiles are needed.

It is demonstrated that the 2E1 decay of the 1s2s $^1S_0$ state in heavy He-like ions can effectively be studied by means of an X-ray/X-ray coincidence technique and that RTE is the dominant production mechanism populating the state. Detained studies of the shape of an X-ray continuous spectrum will yield information on relativistic and correlation effects in very heavy two-electron ions.

References

1) S. Reusch, P.H. Mokler, T. Kambara, R. Schuch, G. Wintermeyer, A. Müller, Z. Stachura, and A. Warczak: *RIKEN Accel. Prog. Rep.*, **22**, 57 (1988).

RIKEN Accel. Prog. Rep. **24** (1990)

III-2-19. Multiply Charged Ions and Cluster Ions Produced from Frozen Targets under Energetic Heavy Ion Impact

H. Tawara, T. Tonuma, H. Kumagai, T. Matsuo, and H. Shibata

In the present work we have measured positive as well as negative ions produced under the impact of a few picoampere 60 MeV Ar^{q+} ($q=4$, 12, 13) ions provided from RIKEN linear accelerator on frozen gas targets. The target (molecular) gases are frozen on thin foils cooled at the liquid nitrogen temperature. The gas pressure measured at a vacuum chamber wall is about $(5\text{-}7) \times 10^{-7}$ Torr, with a background pressure of 1×10^{-7} Torr.

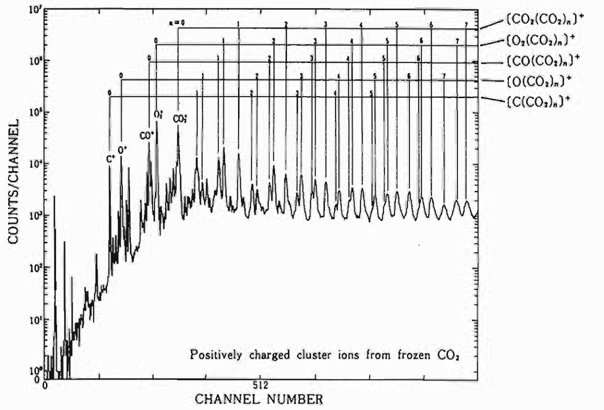

Fig. 1. A typical positive ion spectrum obtained from frozen CO_2 target under 60 MeV Ar^{4+} ion impact.

A typical example of positive ion spectra from a frozen CO_2 target is shown in Fig. 1. In addition to singly as well as multiply charged atomic ions and molecular ions, a variety of cluster ions are observed at fairly high intensities. These cluster ions are clearly formed from different core ions produced in preceding collisions with energetic heavy ions. In the present case, the following singly charged cluster ions are dominant: $[CO_2(CO_2)_n]^+$, $[CO(CO_2)_n]^+$, $[O_2(CO_2)_n]^+$, $[C(CO_2)_n]^+$, and $[O(CO_2)_n]^+$. Surprisingly the most intense peak is found to be due to O_2^+ ions, which have never been observed in gaseous targets, followed by the cluster ions with O_2^+ ion core. In the frozen CO_2 targets, the O_2^+ ion is formed probably through recombination of O^+ ion with another O atom, both being the dissociation products in the frozen target, during migration to the surface. It is also noted that the intensities of these cluster ions decrease smoothly with a little fluctuation as the number of molecules clustered around the core, n, increases, but the "magic number" indicating cluster ions with special stabilities could be hardly observed. This is in contrast to cluster ion produced in expanding gas targets.[1]

A similar sharp difference is also observed in the production of multiply charged ions: relatively intense peaks corresponding to O^{i+} ($i=1\text{-}4$) ions and even a trace of O^{5+} ions are seen in a spectrum, meanwhile only very weak C^{2+} and practically no C^{3+} ions are observed. On the other hand, in a previous gaseous target spectrum,[2] multiply charged carbon ions are more intense by an order of magnitude than corresponding multiply charged oxygen ions.

A more dramatic difference is seen in negatively charged cluster ion spectra. In the present frozen target experiment, most intense peaks correspond to O^- and $[O(CO_2)_n]^-$ cluster ions, whereas only a series of $[CO_2(CO_2)_n]^-$ cluster ions are observed in expanding gas targets.[3]

Similar measurements are under way for other frozen gas targets. Presently, the detailed production mechanisms and stabilities of ions involving cluster ions from frozen targets are not well understood, though the stabilities of the ions seem to be strongly influenced by the density of targets depending on gas or frozen phases.

It is concluded that the frozen targets can provide a variety of cluster ions as well as atomic and molecular ions, sharply different from those produced in gaseous targets, some of which have been observed only in space but not in laboratories.

References

1) O. Echt, K. Sattler, and E. Recknagel: *Phys. Lett.*, **90A**, 185 (1982).
2) T. Matsuo, T. Tonuma, M. Kase, T. Kambara, H. Kumagai, and H. Tawara: *Chem. Phys.*, **121**, 93 (1988).
3) M.L. Alexander, M.A. Johnson, N.E. Levinger, and W.C. Lineberger: *Phys. Rev. Lett.*, **57**, 976 (1986).

RIKEN Accel. Prog. Rep. **24** (1990)

III-2-20. Search for Relativistic Electron Emission in Relativistic Heavy Ion Atom Collisions

Y. Yamazaki, K. Komaki, T. Azuma, K. Kuroki, K. Kawatsura,
Y. Kanai, T. Kambara, and Y. Awaya

The energy and angular distributions of "secondary" electrons emitted in 95 MeV/u Ar^{17+} + C, Ni, Au collisions have been measured with RIKEN Ring Cyclotron. High energy electrons ($\gtrsim$ MeV) were observed with surprisingly high cross sections ($\sim 10^{-24}$ cm^2).

High energy electrons were measured with a detector assembly consisting of four-fold surface barrier detectors (SSD), each having a depletion layer of ~500 μm. Comparison of partial energy deposition to each SSD with total energy deposition allows us to identify electrons from heavier energetic particles like fragment ions. The detector assembly can be rotated around the target from θ = 30° to 150° with respect to the beam.

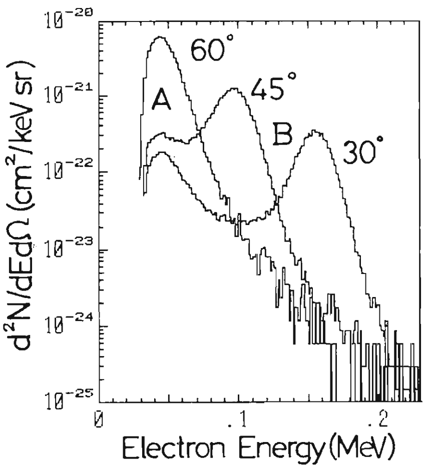

Fig. 1. Doubly differential cross sections $d^2N/dEd\Omega$ of electron production as a function of electron energy measured at 30°, 45°, and 60° with respect to the incident ion beam, 95 MeV/u Ar^{17+}, on a carbon foil (~4,000A).

Figure 1 shows electron spectra in th region of a few hundreds keV for a carbon foil of ~4,000 Å at θ = 30° to 60°. At θ = 45° and 60°, two peaks (A and B of the figure) are clearly visible. The appearance of the peak at ~45 keV independently of the ejection angle is specific to the electron loss to the continuum ($E_e = (m_e/M)E_p$), where E_e is the electron energy, E_p the projectile energy, m_e the electron mass, and M the projectile mass). On the other hand, the peak B appears at $E_e \sim 4(m_e/M) \cdot E_p \cos^2\theta$, indicating that knock-on collisions are responsible for the formation of the peak. Figure 2 shows higher energy part, the principal interest of this experiment, which was obtained by inserting an absorber foil (~1 mm Al sheet) in front of the detector assembly to discriminate huge number of low energy electrons. The observations are summarized as (i) electrons in ~MeV region are detected with surprisingly high cross section, (ii) the angular distribution of these electrons are almost isotropic, and (iii) the differential cross section either in its absolute value or in its shape depends very weakly on the target material. A further experiment is in progress to confirm these observations.

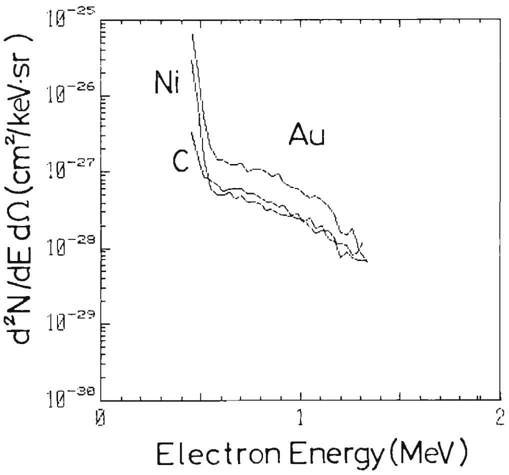

Fig. 2. Higher energy part of the doubly differential cross section $d^2N/dEd\Omega$ at 45° on carbon, nickel, and gold foils.

RIKEN Accel. Prog. Rep. **24** (1990)

III-2-21. Convoy Electron Excitation by Glancing Angle Incident Heavy Ion Impact on Thick Metal Targets

H. Ishikawa,* Y. Sasa, and A. Koyama

In a previous report, it was shown that two kinds of convoy electrons were induced by glancing angle incident fast Xe^{9+} ion impact, that is, the one was a usual convoy electron with a velocity equal to that of inducing ions, and the other a convoy electron accelerated by a dynamic surface image potential induced by a projectile.$^{1)}$ It has not been elucidated whether the usual convoy electrons are produced by projectiles impinging into or those emerging from the surface. In the present report, it is shown that they are produced by emerging projectriles.

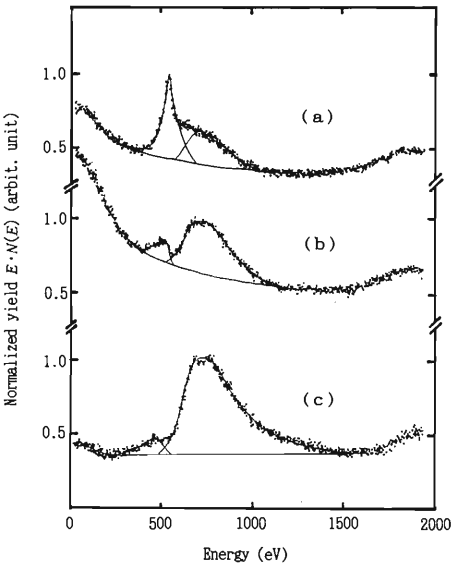

Fig. 1. Energy spectra of electrons from Al induced by glancing angle incident Xe^{27+} ions of 0.98 MeV/amu. Detection angle is 1.5° with respect to the incident beam direction. Incident angle with respect to the target surface is (a) 0.5°, (b) 0.8°, and (c) 1.0°. Solid curves are to guide the eye.

Figure 1 shows the energy spectra of electrons induced from Al by 0.98 MeV/amu Xe^{27+} ions. The incident angles are (a) 0.5° with respect to the target surface, (b) 0.8°, and (c) 1.0°. The detection angle is 1.5° with respect the incident beam direction.

Rather narrow peaks of usual convoy electrons as well as broad peaks of accelerated ones are seen. An important point is that most probable energy of these usual convoy electron peaks is decreased with increasing incident angle; 530 eV for 0.5°, 507 eV for 0.8°, and 460 eV for 1.0°. This means that the energy of projectiles inducing usual convoy electrons is also decreased with increasing incident angle. Energy loss of a projectile which penetrates the target and is scattered out of the surface becomes more prominent as the incident angle is increased. Therefore, it is concluded that these usual convoy electrons are produced by projectiles emerging from the surface after transportation inside a target. Quantitative deduction of energy loss of glancing angle incident ions is now in progress. Such usual convoy electrons are observed because of the presence of narrow steps on the target surface; they are not accelerated by an image force, because the time of the interaction between the image potential and the produced convoy electrons is too short.

References

1) H. Ishikawa, A. Koyama, and Y. Sasa: *RIKEN Accel. Prog. Rep.*, **23**, 51 (1989).

---

* Science University of Tokyo.

RIKEN Accel. Prog. Rep. **24** (1990)

III-2-22. Electron Spectra from Doubly Excited Boron Ions Produced by Double Electron Capture

H.A. Sakaue, Y. Kanai, T. Nabeshima, N. Nakamura, I. Yamada,*
S. Ohtani, K. Wakiya, H. Suzuki, T. Takayanagi, T. Kambara,
A. Danjo, M. Yoshino, and Y. Awaya

We measured spectra of electrons ejected by the following double-electron transfer collisions at varying collision energies (37.5, 50, and 65 keV);

$$\begin{aligned}B^{5+}+\mathrm{He}(1s^2)\longrightarrow\ & B^{3+}(2lnl')\,^1L+\mathrm{He}^{2+}\\ & \hookrightarrow B^{4+}(1s)+e^-.\end{aligned}$$

$^{11}B^{5+}$ ions were produced with the ECRIS (Electron Cyclotron Resonance Ion Source) constructed as an ion source for the RIKEN AVF cyclotron. Spectra of ejected electrons were measured by zero-degree electron spectroscopy.[1)]

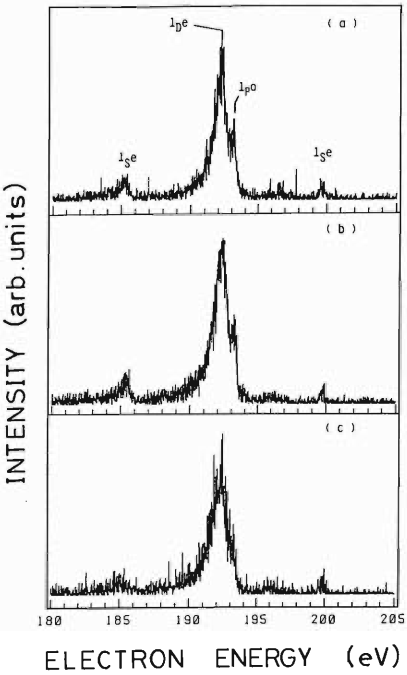

Fig. 1. High resolution ejected electron spectra from the $2l2l'$ configuration of B^{3+}. Each peak is tentatively identified as shown. Collision energy is (a) 65 keV; (b) 50 keV; and (c) 37.5 keV.

High resolution spectra of ejected electrons from $2l2l'$ and $2l3l'$ states are shown in Figs. 1 and 2, respectively. We tentatively identify each peak as denoted in the figures. The relative-intensity ratio of the peaks in $2l2l'$ does not change with collision energy, but that of the peaks in $2l3l'$ changes. Possible explanations for this phenomena are (1) the position of the reaction window changes with collision energy and (2) the magnetic sublevel distribution m_L of each angular momentum state (L) produced by double electron capture changes with collision energy.[1)]

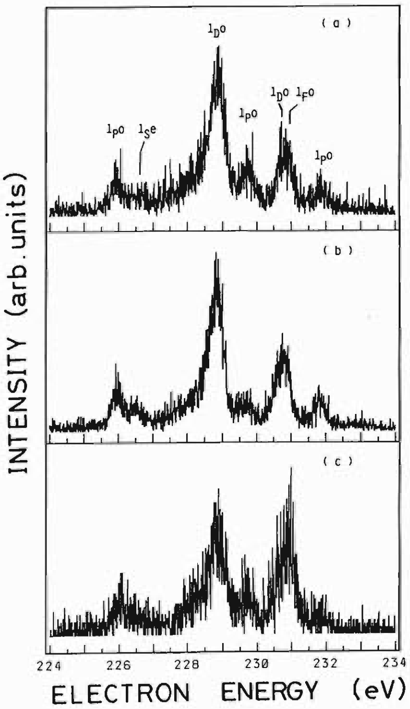

Fig. 2. High resolution ejected electron spectra from the $2l3l'$ configuration of B^{3+}. Each peak is tentatively identified as shown. Collision energy is (a) 65 keV; (b) 50 keV; and (c) 37.5 keV.

Since the observed electron peaks are shifted by a post collision interaction (PCI) effect, so we cannot directly compare the observed peak energies with theoretical values. Precise analysis is in progress.

References

1) H.A. Sakaue, Y. Kanai, Y. Ohta, K. Kushima, M. Inaba, S. Ohtani, K. Wakiya, H. Suzuki, T. Takayanagi, T. Kambara, A. Danjo, M. Yoshino, and Y. Awaya: *J. Phys.*, **B23**, L401 (1990).

---

* National Institute for Fusion Science.

RIKEN Accel. Prog. Rep. **24** (1990)

III-2-23. Beam-Foil Lifetime Measurements of the $2p^5 3p$ and $2p^5 3d$ Levels in Ti XIII

K. Ando, Y. Zou, S. Kohmoto, T. Kambara, Y. Awaya, T. Tonuma, T. Niizeki, and S. Tsurubuchi

Beam-foil decay curve measurements were performed at RILAC by using a 2.2 m grazing incidence spectrometer (McPherson 247) with a grating of 600 grooves/mm. Decay curves measured were analyzed by multiexponential fitting using a program DISCRETE.[1] For the decays of 3p $^1D_2$ and 3p $^3P_2$, cascading from upper states were corrected by performing an ANDC (Arbitrary Normalized Decay Curve) analysis using a program CANDY.[1] The results of the ANDC analysis and multiexponential fitting are displayed in Table 1 with other experiments[2] and the theoretical calcuation.[3-5] All the decay curves of the 3d levels, with the exception of 3d $^1F_3$, include a short lived cascade of lifetime of 11 - 24 ps. The level of 3p $^3D_3$ is repopulated not only by long lived 3d cascades, but also by long lived 4d $^3D_2$ and 4d $^1F_3$ cascades. The lifetimes of 3d levels obtained by multiexponential fitting should be reliable since all direct cascades to 3d levels are very fast.

Table 1. Lifetimes (ns) of levels in Ti XIII.

Upper level	Experiment		Theory
	This work	Ref. 2	
$2p^5 3d\ ^3F_4$	$0.188 \pm 0.006 (0.015)^a$	0.115 ± 0.010	0.158^d 0.113^e
$2p^5 3d\ ^3F_3$	$0.173 \pm 0.015 (0.019)^a$	0.112 ± 0.010	0.156^d 0.105^e
$2p^5 3d\ ^1F_3$	0.181 ± 0.006^a	0.115 ± 0.012	0.147^d 0.105^e
$2p^5 3d\ ^3D_3$	0.137 ± 0.009^a $(0.011,\ 0.006,\ 2.25)^a$	0.111 ± 0.010	0.147^d 0.108^e
$2p^5 3d\ ^1D_2$	$0.153 \pm 0.009 (0.013)^a$	0.105 ± 0.010	0.142^d 0.101^e
$2p^5 3d\ ^3P_2$	$0.212 \pm 0.015 (0.024)^a$	0.115 ± 0.010	0.154^d 0.113^e
$2p^5 3p\ ^1D_2$	0.279 ± 0.013^b $[0.312 \pm 0.042 (0.055)]^a$	0.215 ± 0.020	0.225^c 0.329^d 0.210^e
$2p^5 3p\ ^3P_2$	0.370 ± 0.037^b $[0.48 \pm 0.16 (0.092)]^a$	0.218 ± 0.020	0.202^c 0.181^d 0.230^e
$2p^5 3p\ ^3D_3$	$0.359 \pm 0.060 (0.146)^a$	0.240 ± 0.030	0.236^c 0.290^d 0.227^e

a) Results of multiexponential fitting with cascade lifetimes are given in parentheses.
b) Results of ANDC analysis.
c) Results of Crance.[3]
d) Results of Bureeva.[4]
e) Results of MCDF.[5]

References

1) L. Engström: *Nucl. Instrum. Methods*, **202**, 369 (1982).
2) E. Träbert: *Z. Phys. D*, **1**, 283 (1986).
3) M. Crance: *At. Data*, **5**, 185 (1973).
4) L.A. Bureeva and U.I. Safronova: *Phys. Scri.*, **20**, 81 (1979).
5) I.P. Grant, B.J. McKenzie, and P.H. Norrington: *Comp. Phys. Commun.*, **21**, 207 (1980).

RIKEN Accel. Prog. Rep. **24** (1990)

III-2-24. Neutral Atomic Beam Source with a Pulsed Heater

T. Minowa, H. Komatsu,* H. Katsuragawa, and T. Inamura

In a previous report we described a novel method to produce neutral atomic beams of metal elements.[1] This method is based on low-bias pulsed discharge; plasma generated heats up metal elements to be evaporated. We successfully carried out resonance ionization spectroscopy of Fe and Al by this method.[2] Although the pulsed discharge method is simple, low-cost, and capable of making intense atomic beams of metal elements, several drawbacks were found. The most troublesome was an increase in background due to charged particles produced at pulsed discharge.

We have developed a pulsed heating method to produce neutral atomic beams for such a case as no intense atomic beam is needed but an extremely clean atomic flux is required. The experimental setup was the same as that described in Ref. 1 except for an atomic beam source. A Mo filament (diameter 30 μm, effective length 1 cm) was connected periodically to a charged capacitor (330 μF) with an electrical relay. An advantage of this pulsed heating method is in that no extra technique is required for cooling the filament and its support, and in that the lifetime of the filament is considerably prolonged.

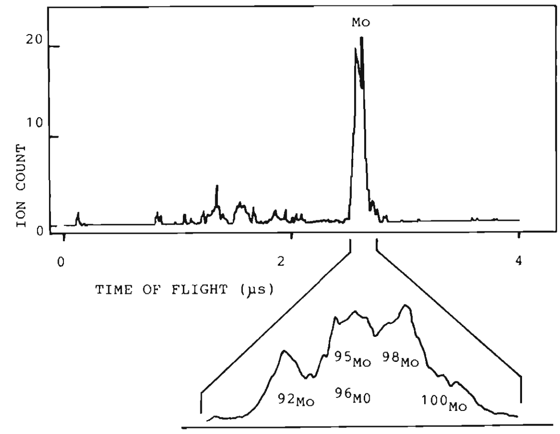

Fig. 1. Time-of-flight spectrum of Mo ions. The wavelength of radiation of the pulsed dye laser was kept at 386.4 nm.

We carried out resonance ionization spectroscopy of a Mo atomic beam produced by the pulsed heating method. In Fig. 1 a time-of-flight spectrum of Mo^+ and a plot expanded around the Mo^+ peak are shown. Here Mo^+ isotope peaks are partly resolved. Mo-ion counts are plotted as a function of the wavelength of laser radiation in Fig. 2. The ionization peak corresponds to the $z^7P_3{}^o-a^7S_3$ transition in Mo atom.

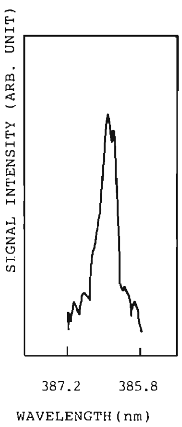

Fig. 2. Resonance ionization spectrum of Mo. The ionization peak corresponds to the $z^7P_3{}^o-a^7S_3$ (386.4 nm) transition in a Mo atom.

The rate of Mo atoms evaporated from a unit surface is given by

$$\log m = 27.81 - 33.25\times10^3/T + 5.50\times10^6/T^2 \qquad (1)$$

where log denotes a general logalithm, m is the evaporation rate in $cm^{-2}s^{-1}$, and T is the temperature of the Mo surface.[3] Mo atoms flew away from the filament uniformly into the space in a vacuum chamber, so that, if evaporation is stationary, the density of Mo atoms at a distance r apart from the Mo source is given by

$$n(r) = mS/4\pi vr^2 \qquad (2)$$

where the Mo filament is assumed to be a point source, $n(r)$ is the density of Mo atoms, S is the surface area of the Mo filament, and v is the mean velocity of Mo atoms. The mean velocity of Mo atoms can be estimated at hundreds of meters per second. The ionization volume in this work was placed 10 cm apart from the Mo source; therefore evaporation was considered to

---

* Tokyo Gakugei University.

be stationary because firing of the laser was delayed by few milliseconds after the rise of evaporation and its fall time was 70 ms.

For Mo the saturation condition was easily fulfilleld by a relatively low-power laser radiation, *i.e.*, tens of microjoules per pulse. Under the saturation condition almost all the Mo atoms in the volume irradiated by the laser is ionized and the linear dependence of an ionization signal upon the laser power is obtained. We confirmed by this linear dependence that the saturation condition was fulfilled.

The pulse duration time of the laser was 10 ns. In this time scale Mo atoms can be considered to be at rest. The Mo^+ counting rate was nearly unity per pulse at an application voltage of 15 V to the capacitor. Therefore following equation holds

$$mSV/4\pi vr^2=1 \tag{3}$$

where V is the volume where resonance ionization took place. We took the following formula for the mean velocity

$$v=\sqrt{3kT/M} \tag{4}$$

where k is the Boltzmann constant and M is the mass of Mo. Combining Eq. (1), (3), and (4) and substituting the value 10^{-4} cm^3 into V, we obtained values of 6×10^{13} $cm^{-2}s^{-1}$ and 2,200 K for m and T, respectively.

Upon the application of voltage pulses to the Mo filament, light emission occurs simultaneously with evaporation. We measured the light intensity with a photodiode (HAMAMATSU S1227-66BQ). The output current of the photodiode is proportional to radiated light intensity when the current is lower than 0.1 A. Using Planck's radiation formula, the output current of the photodiode was approximately related to the evaporation rate of the Mo filament as follows

$$m=B\cdot I^{1.8} \tag{5}$$

where B is the constant determined by experimental conditions and I is the output current in A. With the value $m=6\times10^{13}$ that of B is determined to be 1×10^{20}. The temporal dependence of the output current was converted to that of the evaporation rate of the Mo filament and is plotted in Fig. 3. From this measurement it is found that the pulsed heating prolongs the lifetime of the Mo filament by one order of magnitude compared with continuous heating with a direct current.

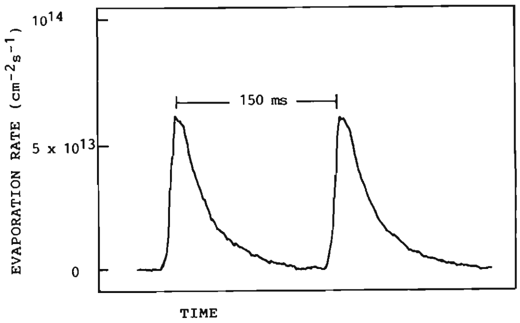

Fig. 3. Evaporation rates of a Mo filament plotted *vs.* time. The diameter and the effective length of the filament is 30 μm and 1 cm, respectively.

References

1) M. Otsuki, T. Minowa, H. Katsuragawa, and T. Inamura: *RIKEN Accel. Prog. Rep.*, **22**, 176 (1988).
2) T. Hoshino, M. Otsuki, T. Minowa, H. Katsuragawa, and T. Inamura: *ibid*, p. 178.
3) G. Czak, G. Kirshstein, D. Koschel, H.K. Kugler, and P. Kuhm: "Gmelin Handbook of Inorganic Chemistry," Springer Verlag, Tokyo, Mo suppl. A2a, p. 462 (1985).

RIKEN Accel. Prog. Rep. **24** (1990)

III-2-25. Magnetic Property of $BiPbSr_2FeO_6$

T. Okada, K. Asai, and T. Yamadaya*

The physical properties of compounds $Bi_2M_{1+n}Fe_nO_y$ (M=Sr, Ca; n=1, 2, 3) are of great interest in view of their crystallo-graphical isostructure with high-T_c superconductors $Bi_2Sr_2Ca_{n-1}Cu_nO_y$ for n=1, 2, 3.

A sample of $BiPbSr_2FeO_6$ (n=1) was prepared by heating starting materials Bi_2O_3, PbO, $SrCO_3$, and α-Fe_2O_3 in air at 815°C for five days. One of the Bi atoms of $Bi_2M_{1+n}Fe_nO_y$ for n=1 was replaced with a Pb atom so as to keep the charge balance. The resulting compound, isostructural with a one layer superconductor $Bi_2Sr_2Cu_2O_6$, is found to be orthorhombic (a = 5.42 Å, b = 5.49 Å, c = 23.20 Å).

The static magnetization of $BiPbSr_2FeO_6$ in the temperature range between 77 K and 298 K was measured using a vibrating sample magnetometer. The magnitude of the magnetization in an applied magnetic field of 1.6 T was very small ($\sim 10^{-1}$ emu/g) at 77 K and monotonously decreased with increasing temperature.

The Mössbauer measurements of ^{57}Fe were carried out at temperatures from 5 K to 295 K. Two typical Mössbauer spectra are shown in Fig. 1. The spectrum at 295 K [Fig. 1 (a)] was composed of a doublet arising from quadrupole splitting. The hyperfine magnetic field (H_{hf}) was observed in the spectrum at 80 K [Fig. 1 (b)]. The temperature dependence of H_{hf} is shown in Fig. 2. The value of H_{hf} decreased with increasing temperature, and reduced to zero at 210 K. Extrapolation suggests that the hyperfine magnetic field disappears at 190 K, indicating that the magnetic transition takes place at this temperature.

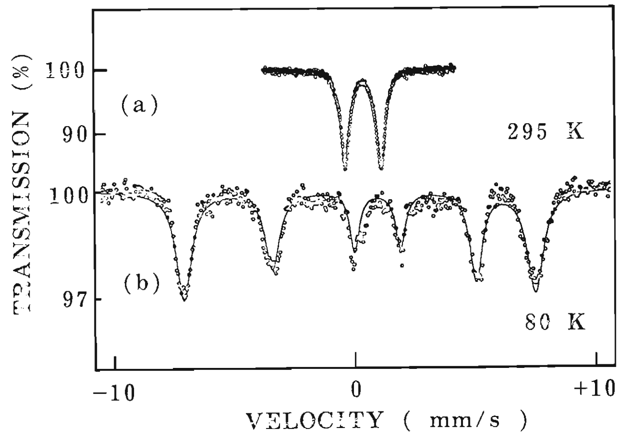

Fig. 1. ^{57}Fe-Mössbauer spectra of $BiPbSr_2FeO_6$ at (a) 295 K and (b) 80 K.

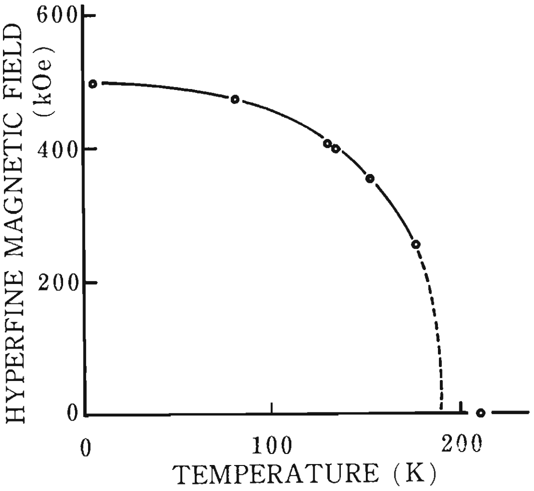

Fig. 2. Temperature dependence of the hyperfine magnetic field at ^{57}Fe obtained from Mössbauer spectra.

---

* Faculty of Literature and Science, Yokohama City University.

RIKEN Accel. Prog. Rep. **24** (1990)

III-2-26. Behavior of Kr Atoms Implanted into Aluminum

E. Yagi

It has been demonstrated that heavy inert gas atoms (Ar, Kr, and Xe) implanted into metals at ambient temperature precipitate into a solid phase (often referred to as solid inert gas bubbles) at high implantation doses, and that they have an epitaxial face-centered cubic (fcc) structure in fcc matrices.[1,2] The growth of such bubbles has been extensively studied mainly by transmission electron microscopy and by an X-ray diffraction method. Since these methods are sensitive to bubbles greater than a certain minimum size, usually after the interesting initial growth of bubbles has occurred, they are more effective to the study on bubble growth rather than that on nucleation. On the other hand, a channeling method is useful to study phenomena such as bubble nucleation, because it provides direct information on the lattice location of implanted atoms.

In the present study the implantation-dose dependence of lattice location of Kr atoms implanted in Al at room temperature has been investigated by the ion-channeling method with a 1 MeV He^+ beam in more detail than in previous studies.[3-6] From the channeling angular profiles we observed, as shown in Fig. 1, that, at an implantation dose lower than $2\times10^{15}/cm^2$, Kr atoms are distributed over random (R), substitutional (S), tetrahedral (T) and octahedral (O) sites. At a dose higher than $2\times10^{15}/cm^2$ a fraction of the Kr atoms come to be located at O*-sites displaced from O-sites by about 0.03 nm. The T- and O-site occupancies are considered to result from the multiple trapping of vacancies by Kr atoms, because large-sized impurity atoms tend to interact strongly with vacancies. The Kr atoms are displaced to the T- and O-sites by trapping 4 and 6 vacancies, respectively. On annealing the T- and O-site configurations (KrV_4 and KrV_6) became unstable between 380 and 470 K. The R-site occupancy can be ascribed to the Kr atoms associated with larger vacancy clusters (cavities) consisting of more than 6 vacancies. This interpretation is supported by the previously reported result that with increasing dose from 4×10^{14} to $1\times10^{15}/cm^2$ the number density of the R-site occupancy increases and, correspondingly, cavities come to be observed.[6] The O*-site occupancy is considered to be due to the clustering of the Kr atoms located at the O-sites. The Kr atoms are displaced slightly from the O-sites due to the mutual interaction.

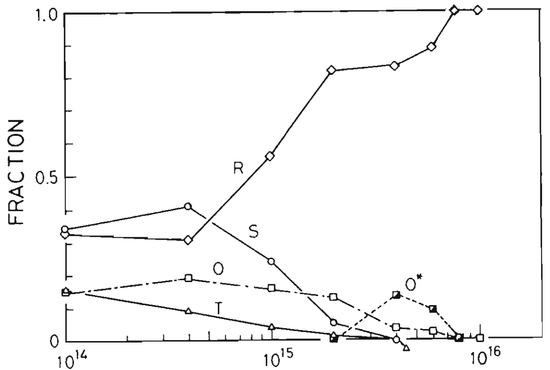

Fig. 1. Implantation-dose dependence of the fractions of Kr atoms located at various kinds of sites.

From these results we proposed that for the Kr implantation at room temperature Kr-vacancy complexes such as KrV_4, KrV_6, and larger ones are formed in the early stage of implantation, and these complexes act as nucleation centers for the precipitation of Kr atoms.

References

1) A. vom Felde, J. Fink, Th. Müller-Heinzerling, J. Plüger, B. Scheerer, G. Linker, and D. Kaletta: *Phys. Rev. Lett.*, **53**, 922 (1894).
2) C. Templier, C. Jaouen, J.-P. Rivière, J. Delafond, and J. Grilhé: *C. R. Acad. Sci. Paris*, **299**, 613 (1884).
3) E. Yagi: *Phys. Stat. Solidi*, **A104**, K13 (1987).
4) E.Yagi, M. Iwaki, K. Tanaka, I. Hashimoto, and H. Yamaguchi: *Nucl. Instrum. Methods*, **B33**, 724 (1988).
5) E. Yagi: *ibid.*, **B39**, 68 (1989).
6) E. Yagi, I. Hashimoto, and H. Yamaguchi: *J. Nucl. Mater.*, **169**, 158 (1989).

RIKEN Accel. Prog. Rep. **24** (1990)

III-2-27. RBS Investigation of Ar implanted AlN$_x$ Thin Films on Glassy Carbon

K. Kobayashi, T. Fujihana,* and M. Iwaki

A study has been made of the compositions of AlN$_x$ thin films on glassy carbon (G.C) substrates before and after Ar-implantation.

AlN$_x$ thin films of approximately 100 nm in thickness were deposited on G.C by means of an activated reactive evaporation in a nitrogen atmosphere.

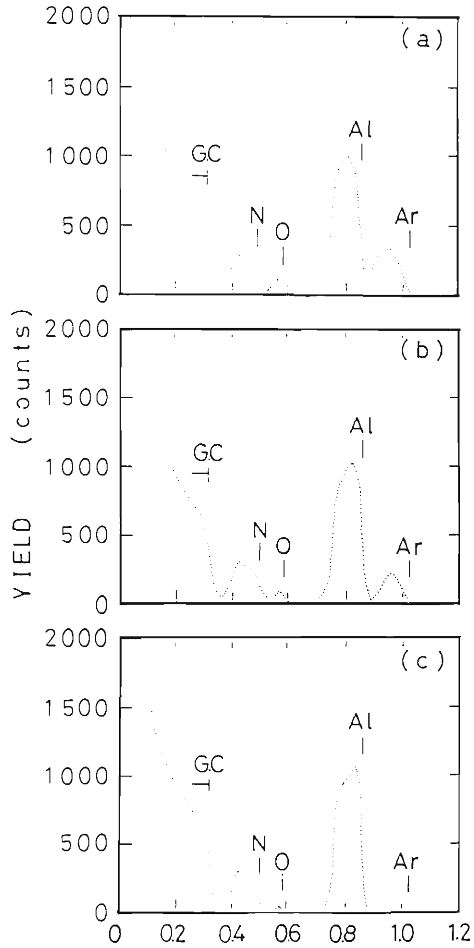

Fig. 1. RBS spectra before and after Ar-implantation into AlN$_x$ thin films on a G.C substrate.
(a), spectrum after Ar-implantation with 1×10^{17} Ar$^+$/cm^2 at 150 keV;
(b), spectrum after Ar-implantation with 5×10^{16} Ar$^+$/cm^2 at 150 keV;
(c), spectrum before Ar-implantation.

Air-implantation into AlN$_x$ thin films was performed to the doses ranging from 5×10^{16} to 1×10^{17} Ar$^+$/cm^2 at 150 keV near room temperature. The compositions of the films on G.C substrates before and after Ar-implantation were evaluated by He$^+$ Rutherford backscattering spectroscopy (RBS) using a 1.5 MeV ^{4}He$^+$ beam. The dose of He$^+$ was 2.4×10^{15} He$^+$/cm^2 throughout the study.

Figure 1 shows the RBS spectra before and after Ar-implantation into the films on the G.C substrates. Figure 1 (c) shows the spectrum before Ar-implantation. The doses for Figs. 1 (b) and (a) were 5×10^{16} and 1×10^{17} Ar$^+$/cm^2, respectively. The surface edges of Al, N, O, and Ar are indicated by short lines; the position of G.C is also indicated.

The spectrum for an as-deposited specimen shows a uniform concentration of O atoms. The ratio of N/Al in the as-deposited film is estimated as 0.8, according to a surface energy approximation.

It was found from Figs. 1 (b) and (a) that Ar atoms were retained into the specimens. The depth position of the maximum concentration of Ar is located at the depth of about 80 nm from the surface. As the dose of Ar-implantation increases, the backscattering yield height from Ar atoms increases. It is estimated that the amount of the Ar atoms in the specimen (a) is twice as large as that in the specimen (b), in proportion to the dose of Ar-implantation.

It is also found in Figs. 1 (b) and (a) that O atoms invaded the surface layers of the films after Ar-implantation. The yields from the O atoms increases as the dose of Ar-implantation increases. The O atoms included in the residual gas (for example, gas of H_2O and CO_2) would invade the films by cascade mixing during Ar-implantation.

Thus, it is concluded that Ar atoms are retained in the films, in proportion to the dose of Ar-implantation. The O atoms invaded the films during Ar-implantation.

---

* Advanced Technology Inc.

RIKEN Accel. Prog. Rep. **24** (1990)

III-2-28. Development of Nuclear Track Microfilters

N. Nakanishi, S. Nakajima, and S. Wakasa*

Energetic charged particles leave their latent tracks in a polymer, polycarbonate Makrofol, irradiated with them. Pierced pores can be observed in it after chemical etching. The phenomenon is applicable to the production of microfilters for industrial uses.

The etch phenomenon is considered geometrically as shown in Fig. 1. In this simplified case, the surface A before etch is corroded to go to the surface B at a balk etching rate V_b after an etching time T. On the other hand, as etching goes on, an etch pit is formed along the latent track at a track etching rate V_t. Until docking, etch pits in both sides of the films proceed a the cone angle δ, for which we can get a relation of $\delta=\sin^{-1}\left(\frac{V_b}{V_t}\right)$ It is desirable to get pores with δ as small as possible.

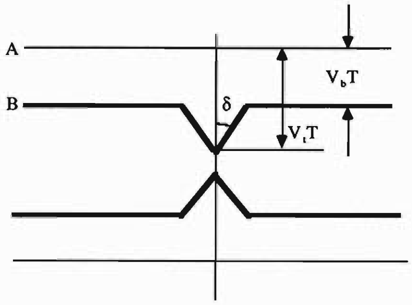

Fig. 1. Schematic cross section of etch pits.

We have examined irradiating and etching conditions for thin polycarbonate Makrofol films.[1] The present goals are to realize pores of less than 0.05 μm and to find the best conditions for polyimid films. Figure 2 shows an example of etched pores in a 10 μm film irradiated with 1 MeV/u $^{84}Kr^{8+}$. We have also tried to observe cross sections of etch pits.

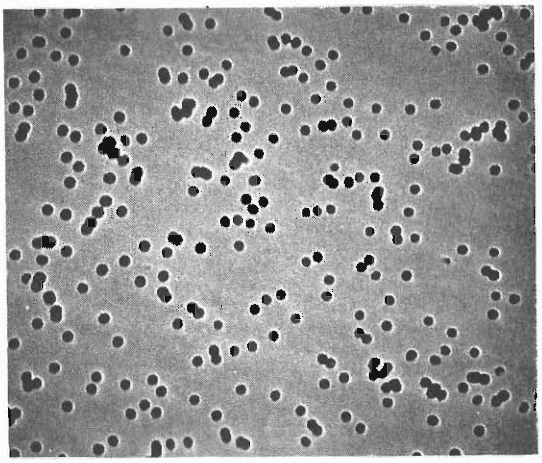

Fig. 2. Scanning electron micrograph of etched pores in a 10 μm Makrofol irradiated by 1 MeV/u $^{84}Kr^{8+}$ ions. Magnification × 10,000. Diameter is 0.2 μm.

References

1) N. Nakanishi *et al.*: *RIKEN Accel. Prog. Rep.*, **23**, 88 (1989).

---

* Japan Steel Work Ltd.

RIKEN Accel. Prog. Rep. **24** (1990)

III-2-29. Temperature Measurement of Solid Surface during 50 MeV Ar^{4+} Beam Bombardment

K. Yano, H. Oyama, M. Yanokura, M. Aratani, and M. Minami

Elastic recoil detection (ERD) is a powerful method for the prompt determination and profiling of atomic species, especially light elements such as hydrogen atoms, near the surface. We have measured the depth profiles of hydrogen and deuterium atoms in thin carbon films prepared by chemical vapor deposition by ERD using an Ar^{4+} beam from the RILAC, whose incidence angle and energy were 30° and 50 MeV, respectively.[1] A decrease in hydrogen atoms in the films was found during measurement as the bombarding time proceeds. This decrease is attributed to the heating of the surface by the bombardment of high energy Ar^{4+} beams. It is well known from a thermal desorption spectrum that hydrogen atoms are desorbed from the surface and/or diffuse into substrate at about 300°C. Therefore, we observed a local-surface temperature during 50 MeV Ar^{4+} beam bombardment. Figure 1 shows the schematic arrangement of the experimental setup. The specification of a radiation thermometer used is as follows: the measurable temperature range, 200–600°C and the spot area measured, 1 mmϕ, where a beam-spot size bombarded is 2×2 mm^2 to 4×7 mm^2. Radiation ($\lambda = 1.8$–2.5μm) from the heated surface was conducted to a PbS detector from a vacuum chamber through a lens (ϕ6) and an optical fiber. Figure 2 shows the surface temperatures of Si and stainless steel targets as a function of the Ar^{4+} beam current. The dimensions of the Si and the stainless steel are $12 \times 8.5 \times 0.4$ mm and $12 \times 9 \times 1$ mm, respectively. These targets and others (see Fig. 2) were mounted at a time on a holder of a large heat capacity. With increasing 50 MeV Ar^{4+} beam current, the target surface is heated and its temperature reaches near 200°C at a beam current of about 100 nA including secondary electrons. A further increase in beam current results in a linear increase in the surface temperature. Finally the surface temperature of Si reaches near 400°C at 200 nA after bombardments of other targets as shown in Fig. 2.

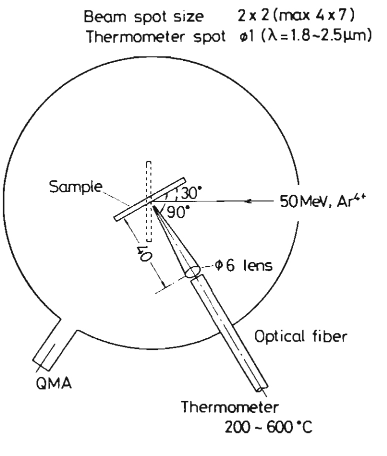

Fig. 1. Schematic arrangement of the experimental setup.

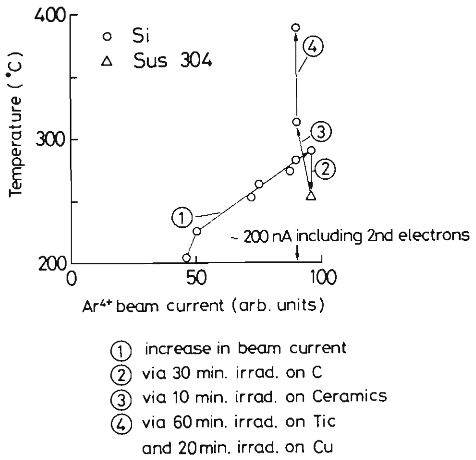

Fig. 2. Dependence of surface temperature on the Ar^{+} beam current.

However, the beam current used in the present study is higher than that of a usual ERD measurement by a factor of about 10. The surface temperature is thought to be less than 200°C, although it could not be measured with this thermometer under the conditions of ERD measurement. It is deduced from Fig. 2 that the surface temperature lies below 150°C at practical ERD measurements.

References

1) K. Yano, H. Oyama, Y. Sakamoto, M. Yanokura, I. Kohno, and K. Sugiyama: *RIKEN Accel. Prog. Rep.*, **20**, 73 (1986).

III-3. Radiochemistry and Nuclear Chemistry

1. Mössbauer Emission Spectroscopy of ^{57}Fe Arising from ^{57}Mn in Chromium Metal and its Oxides

M. Nakada, Y. Watanabe,* K. Endo, H. Nakahara,* H. Sano,* K. Mishima,
K. Kubo, Y. Sakai,** T. Tominaga, K. Asai, M. Iwamoto, Y. Kobayashi,
T. Okada, N. Sakai, I. Kohno, and F. Ambe

Mössbauer emission spectroscopy using the short-lived ^{57}Mn produced by the ^{54}Cr(α, p)^{57}Mn reaction was continued. In this period, several improvements were achieved in experimental details. Among them are the use of a ^{57}Fe-enriched absober with a larger area than that of the former one, the temperature control of an actuator, and the calibration with ^{57}Co embedded in iron.

The emission Mössbauer spectra of ^{57}Fe arising from ^{57}Mn in α-irradiated ^{54}Cr metal, ^{54}CrO$_3$, and ^{54}Cr$_2$O$_3$ are shown in Fig. 1. The isomer shift is given relative to iron metal at room temperature.

As seen from Fig. 1(A), the emission spectrum of ^{57}Mn in ^{54}Cr-metal consists of a singlet. The isomer shift is in good agreement with that of ^{57}Co doped in chromium. A clearly split doublet was observed for ^{57}Fe arising from ^{57}Mn in ^{54}CrO$_3$ (Fig. 1(B)). The isomer shift indicates high-spin ferric ions coordinated with oxide ions. In the case of ^{54}Cr$_2$O$_3$, the spectrum was decomposed into two sets of quadrupole doublets, as seen from Fig. 1(C). The doublet with a smaller isomer shift is assigned to high spin ferric species, while the other to high spin ferrous ones.

Detailed discussion on the observations will be given elsewhere.

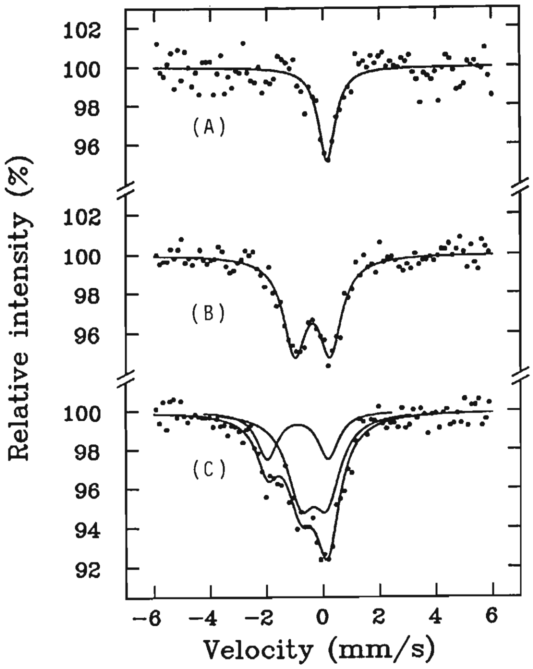

Fig. 1. Emission Mössbauer spectra of ^{57}Fe arising from ^{57}Mn produced by the ^{54}Cr(α,p)^{57}Mn reaction in (A) ^{54}Cr-metal, (B) ^{54}CrO$_3$, and (C) ^{54}Cr$_2$O$_3$. The temperature of measurement was about 30°C.

---

* Faculty of Science, Tokyo Metropolitan University.

** Faculty of Science, the University of Tokyo.

RIKEN Accel. Prog. Rep. **24** (1990)

III-3-2. ^{99}Ru Mössbauer Spectroscopy on Adducts of Ruthenocene with Halogens

Y. Kobayashi, M. Watanabe,* T. Okada, M. Katada,
H. Sano, and F. Ambe

The physicochemical properties of ferrocene derivatives have extensively been studied by ^{57}Fe Mössbauer spectroscopy. No ^{99}Ru Mössbauer spectra of ruthenocene derivatives seem to have been published. In this period, we applied ^{99}Ru Mössbauer spectroscopy to the study of the adducts of ruthenocene with halogens, expressed as $[Ru(C_5H_5)_2X]Y$ (X = Cl, Br, I; Y = PF_6, BF_4, I_3), using a source nuclide ^{99}Rh produced by irradiating 97% enriched ^{99}Ru metal with 12 MeV protons accelerated by the cyclotron.$^{1)}$

The samples were prepared by the method described in the literature,$^{2)}$ and the results of their elemental analysis were in good agreement with calculation.

The Mössbauer spectra obtained at 5K of $[Ru(C_5H_5)_2Cl]PF_6$, $[Ru(C_5H_5)_2Br]PF_6$ and ruthenocene are shown in Fig. 1. The spectra were fitted well to a theoretical curve assuming an electric field gradient, while those of the adducts containing iodine were analyzed with two Lorentzian curves since the relative intensity of absorption was small. It was found that both the isomer shift and the electric quadrupole splitting of the adducts with halogens are large compared with those of ruthenocene. The results obtained in the present work lead us to the conclusion that ruthenocene gives halogen adducts containing direct chemical bonding between Ru and Cl (or Br, I) and that the Ru ion in each adducts is in a higher oxidation state, probably 4+ resulting from a two-electron process, than 2+ in ruthenocene. Such behavior described above has not been observed in ferrocene and its derivatives.

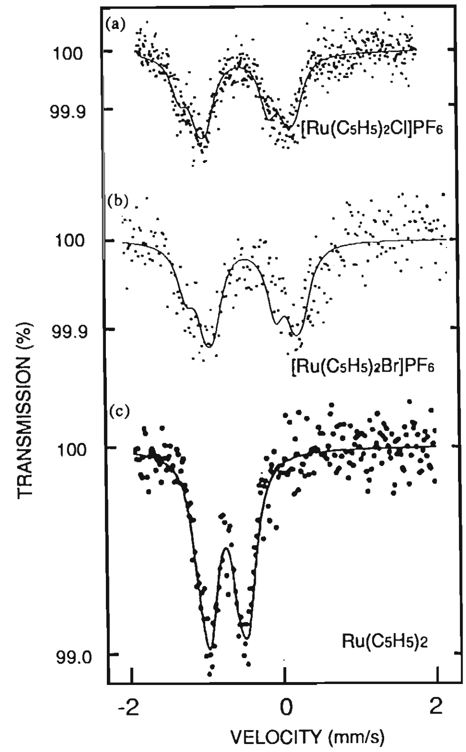

Fig. 1. ^{99}Ru Mössbauer spectra at 5K of (a) ruthenocene-Cl adduct, (b) ruthenocene-Br adduct, and (c) ruthenocene (relative to ruthenium metal).

References

1) Y. Kobayashi, M. Katada, H. Sano, T. Okada, K. Asai, S. Ambe, and F. Ambe: *RIKEN Accel. Prog. Rep.*, **20**, 111 (1986).
2) T.P. Smith, K.S. Kwan, H. Taube, A. Bino, and S. Cohen: *Inorg. Chem.*, **23**, 1943 (1984).

---

* Tokyo Metropolitan University.

RIKEN Accel. Prog. Rep. **24** (1990)

III-3-3. Measurements of Time-Differential γ-Ray Perturbed Angular Correlation (TDPAC) and Emission Mössbauer (EM) Effects for ^{99}Ru in α-Fe$_2$O$_3$ Using ^{99}Rh as a Source Nuclide

Y. Ohkubo, Y. Kobayashi, K. Asai, Y. Yanagida,
M. Iwamoto, and F. Ambe

In this period, we finished measuring TDPAC and EM spectra for ^{99}Ru in α-Fe$_2$O$_3$, using ^{99}Rh ($t_{1/2}$=15 days) as its parent. The employed γ-Rays were 353–90 keV cascade ones through the intermediate level 3/2+ with $t_{1/2}$=20.5 ns for TDPAC and 90 keV (3/2+ → 5/2+) for EM spectroscopy. α-Fe$_2$O$_3$ has the corundum structure. Since the point symmetry of the Fe^{3+} site is not cubic, there is an electric field gradient (EFG). α-Fe$_2$O$_3$ is antiferromagnetic below T_N = 950 K (the Néel point). Thus, below T_N, the nuclei of ^{99}Ru ions replacing Fe^{3+} experience a hyperfine magnetic field H_{hf} in addition to the EFG.

The preparation procedure for α-Fe$_2$O$_3$(^{99}Rh) was described before.[1] In this period, we prepared two α-Fe$_2$O$_3$(^{99}Rh) samples by heating Fe$_2$O$_3$·nH$_2$O(^{99}Rh) at 1,173 K or at 1,023 K. We used four BaF$_2$ (1.5 in ϕ × 1 in) detectors to set up a PAC spectrometer. Coincidence counts for detector combinations of 90 and 180 degrees were measured as a function of delay time between the emissions of 353 and 90 keV γ rays. In this measurement, four spectra (two for 90° and two for 180°) were taken simultaneously, though eight spectra could be taken in principle.

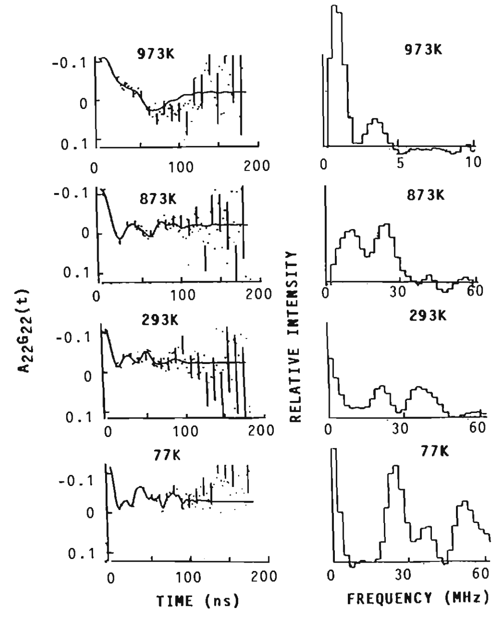

Fig. 1. TDPAC spectra of ^{99}Ru (3/2+) in α-Fe$_2$O$_3$ measured below and above its magnetic transition temperature (left) and their Fourier transformed spectra (right).

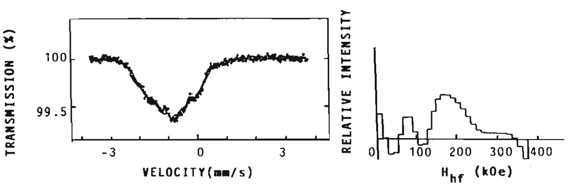

Fig. 2. Emission Mössbauer spectrum of ^{99}Ru (3/2+ → 5/2+) in α-Fe$_2$O$_3$ measured at 5 K (left) and the spectrum of the hyperfine magnetic field calculated from it (right).

Measurements of TDPAC spectra were made in the temperature range from 10 K over T_N to 1,023 K. An EM spectrum was taken at 5 K. The measured TDPAC spectra were identical for the two samples heated at the two different temperatures. Figure 1 shows a part of the measured TDPAC spectra (left) and their Fourier transformed spectra (right). Figure 2 shows the measure EM spectrum (right) and the H_{hf} spectrum calculated from it (left). The saturated H_{hf} obtained from TDPAC was about 190 kOe, the value of which is consistent with that obtained from the EM spectrum of about 180 kOe. These values are preliminary; detailed analysis is in progress.

References

1) Y. Ohkubo and F. Ambe: *RIKEN Accel. Prog. Rep.*, **23**, 75 (1989).

RIKEN Accel. Prog. Rep. **24** (1990)

III-3-4. Time-Differential γ-Ray Perturbed Angular Correlation (TDPAC) and Emission Mössbauer (EM) Spectroscopy of ^{99}Ru in Fe_3O_4 Using ^{99}Rh as a Source Nuclide

Y. Ohkubo, Y. Kobayashi, K. Asai, T. Okada, and F. Ambe

This year we measured TDPAC and EM spectra for ^{99}Ru in Fe_3O_4, using ^{99}Rh ($t_{1/2}$ = 15 days) as its parent. Fe_3O_4 has the inverse spinel structure and is ferrimagnetic below T_C = 858 K.

Fe_3O_4(^{99}Rh) was prepared by heating α-Fe_2O_3(^{99}Rh), obtained by the method described before,[1,2] under a reduced pressure of about 3 Pa at 1,423 K for 2 h. We used the same PAC spectrometer as described in the previous report.[2]

Measurements of TDPAC spectra were made in the temperature range from 10 K over T_C to 873 K. An EM spectrum was taken at 5 K. With the method used by Asai *et al.*[3] we confirmed that ^{99}Rh ions are in the octahedral sites. Figure 1 shows a part of measured TDPAC spectra (left) and their Fourier transformed (FT) spectra (right). The FT spectrum has two components because the directions of the H_{hf} are distrubuted. Figure 2 shows the measured EM spectrum (left) and the H_{hf} spectrum calculated from it (right). Asymmetry of the former is ascribed to electric quadrupole interactions. The saturated H_{hf} field obtained from TDPAC was about 160 kOe, the value of which is consistent with that obtained from the EM spectrum of about 140 kOe. Figure 3 shows the temperature dependence of H_{hf}. These results are preliminary; detailed analysis is in progress.

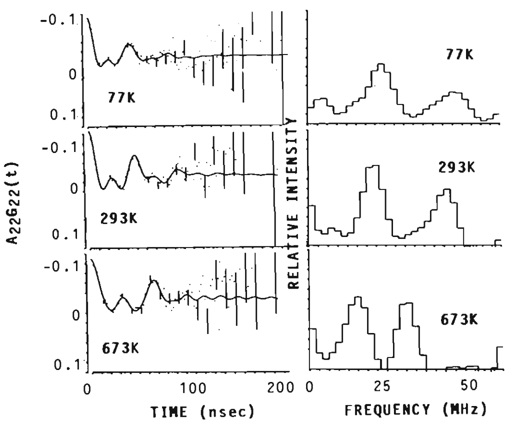

Fig. 1. TDPAC spectra of ^{99}Ru (3/2+) in Fe_3O_4 measured at 77 K, 293 K, and 673 K (left) and their Fourier transformed spectra (right).

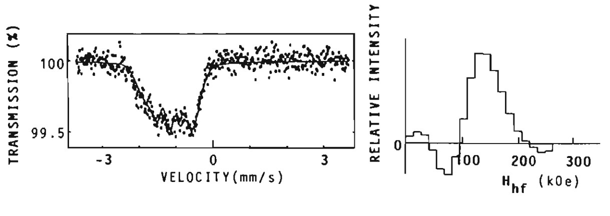

Fig. 2. Emission Mössbauer spectrum of ^{99}Ru (3/2+ → 5/2+) in Fe_3O_4 measured at 5 K (left) and the spectrum of the hyperfine magnetic field calculated from it (right).

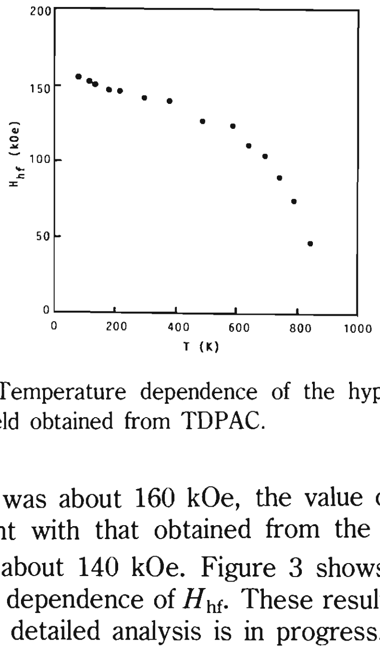

Fig. 3. Temperature dependence of the hyperfine magnetic field obtained from TDPAC.

References

1) Y. Ohkubo and F. Ambe: *RIKEN Accel. Prog. Rep.*, **23**, 75 (1989).
2) Y. Ohkubo, Y. Kobayashi, K. Asai, Y. Yanagida, M. Iwamoto, and F. Ambe: This Report, p. 67.
3) K. Asai, T. Okada, and H. Sekizawa: *J. Phys. Soc. Jpn.*, **54**, 4325 (1985).

RIKEN Accel. Prog. Rep. **24** (1990)

III-3-5. Angular-Momentum Effect in Heavy Ion-Induced Fusion Reactions

H. Kusawake, T. Saito, N. Takahashi, A. Yokoyama,
H. Baba, Y. Ohkubo, and A. Shinohara

According to a Bass model,[1] the cross section for evaporation residue formation was predicted to be reciprocally proportional to the incident energy in the region higher than a specific energy.[2] In order to confirm validity of the prediction, we aim to measure the cross sections directly both for evaporation residues and fission and their dependence on energy by a nuclear-chemical method.

We studied the reaction of a ^{141}Pr target with 24.8- and 23.5-MeV/u ^{40}Ar projectiles. Experimental details were described in previous reports.[3,4]

The total chain yields of fission fragments were deduced from the cumulative and independent yields of gamma-emitting radioactive products on the assumption of a Gaussian charge dispersion with the width parameter $\sigma = 1.5$. The cross sections of evaporation residues were deduced from the average of cumulative yields of isobaric products because primary products were very unstable. The results are shown in Fig. 1. If each emitted light particle carries off 12 MeV, the mass number of the resulting evaporation residue is estimated to be 125, which agrees with the peak position of measured evaporation residues.

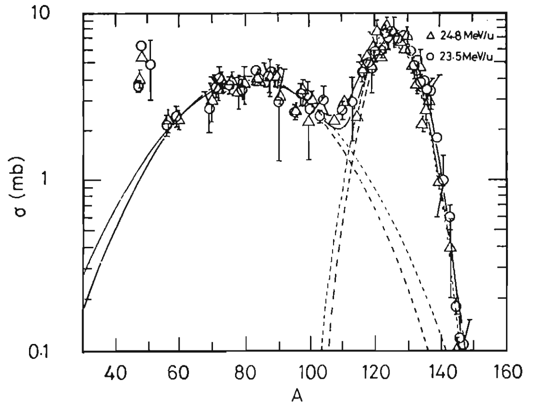

Fig. 1. Total chain yields of the reaction products in the most downstream catcher.

The total cross sections deduced for evaporation residues and the values measured by Zank *et al.*[5] are plotted versus $1/E_{\mathrm{CM}}$ in Fig. 2 as compared with the Bass model. The L_{ER} values deduced in this work were 69 and 67 at 24.8 and 23.5 MeV/u, respectively. They are larger than that predicted from a rotating finite range model.

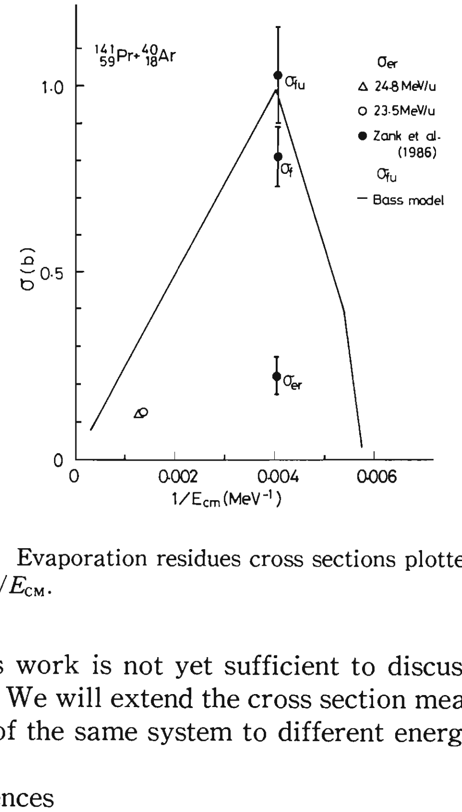

Fig. 2. Evaporation residues cross sections plotted versus $1/E_{\mathrm{CM}}$.

This work is not yet sufficient to discuss the result. We will extend the cross section measurement of the same system to different energies.

References

1) R. Bass: "Nuclear Reaction with Heavy Ions", Springer-Verlag, Berlin (1980).
2) S. Baba *et al.*: *Z. Phys.*, **A331**, 53 (1988).
3) M. Yanokura *et al.*: *RIKEN Accel. Prog. Rep.*, **22**, 150 (1988).
4) H. Baba *et al.*: *ibid.*, **23**, 76 (1989).
5) W.P. Zank *et al.*: *Phys. Rev.*, **C33**, 519 (1986).

RIKEN Accel. Prog. Rep. **24** (1990)

III-3-6. Heavy-Ion Reactions of Copper with ^{14}N and ^{40}Ar Ions of Intermediate Energies

A. Shinohara, E. Taniguchi, M. Narita, M. Furukawa, S. Kojima, T. Saito,
H. Kusawake, Y. Ohkubo, F. Ambe, and S. Shibata

We studied interactions of a given target with different types of projectile. Copper foils (25 μm thick) covered with aluminum catcher foils were irradiated with the ^{14}N (0.49 and 1.89 GeV) and ^{40}Ar(1.04 and 3.80 GeV) ions in the beam course E3. After irradiation, γ rays from the targets and catchers were measured. Recoil properties of the products were obtained by measuring the ratios of radioactivity in the target to those in the catchers.

Figure 1 shows a mass-yield distribution of products in 1.04-GeV ^{40}Ar irradiation, obtained from the cross sections and charge dispersion. The dependence of mean recoil ranges on the mass number in two types of reactions is presented in Fig. 2. The results show that the ranges decrease with increasing bombarding energy. Reaction products heavier than the target have larger recoil ranges, indicating the contribution of fusion or dumped-collision types of interactions. The reaction mechanism will be obtained from detailed analysis of the experimental data.

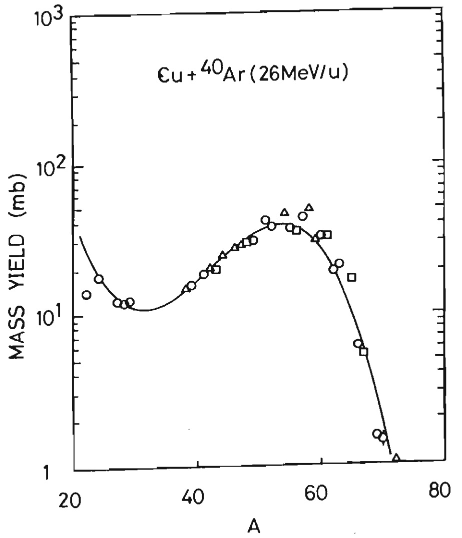

Fig. 1. Mass-yield distribution in the interaction of copper with 1.04 GeV ^{40}Ar ions. Symbols indicate the fraction of each measured yield. (□, >70%; ○, 40–70%; △, <40%)

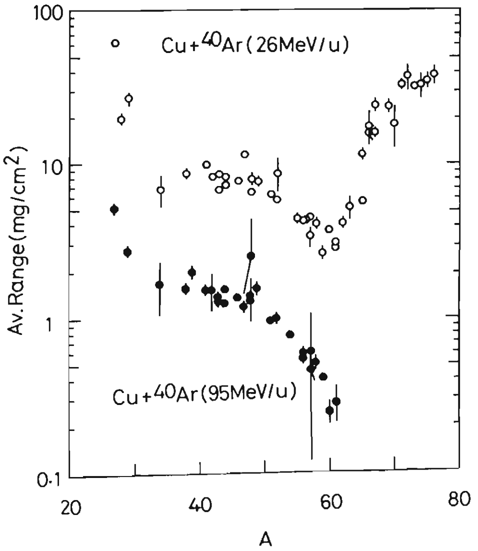

Fig. 2. Dependence of the mean recoil ranges of the products on mass number. (○, 1.04 GeV ^{40}Ar; ●, 3.80 GeV ^{40}Ar)

RIKEN Accel. Prog. Rep. **24** (1990)

III-3-7. Yields of Nuclear Reaction Products Induced by 95 MeV/u-^{40}Ar Ions

M. Furukawa, E. Taniguchi, M. Narita, A. Shinohara, S. Kojima,
T. Saito, H. Kusawake, Y. Ohkubo, F. Ambe, and S. Shibata

Nuclear reactions induced by intermediate-energy heavy ions have intensively been studied. The results of the present study are compared with those of proton induced reactions to find relations among various reaction mechanisms such as fission, quasi-elastic transfer, deep inelastic transfer, fusion, and fragmentation.

We aim to measure formation cross sections of many nuclides with a radiochemical technique, in order to offer fundamental data of intermediate energy heavy-ion reactions and to obtain detailed information on the reaction systems.

We studied interactions of various target nuclides with a single projectile. Irradiations were performed with 3.80 GeV ^{40}Ar ions on the E3 course of RIKEN Ring Cyclotron. Targets were natural foils of odd Z elements (V, Cu, Nb, Pr, Ho, Au, *etc.*) together with aluminum catcher foils. After irradiation, targets were submitted to gamma-ray spectrometry, and various gamma-ray emmitting nuclide were assayed. Long-lived nuclides were measured at the Radioisotope Center of Nagoya University, where a low background gamma-ray spectrometer has been installed and a well-type germanium detector is easily accessible.

Figure 1 shows the distributions of formation cross sections for V and Nb targets obtained in this experiment. The results will be converted to mass yield curves by using information on charge dispersion, and comparison among different reaction systems will be performed to obtain detailed information on the reaction mechanism. Recoil ranges measured in this experiment are also helpful for a better understanding.

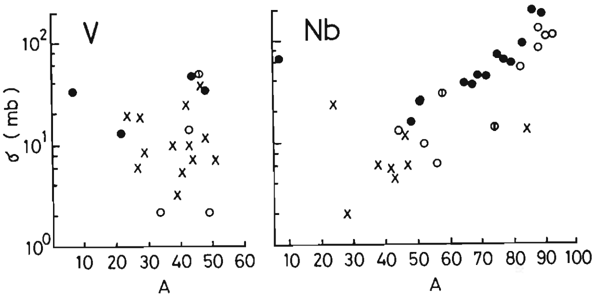

Fig. 1. Dependences of formation cross sections on the mass number in the interaction of V and Nb with 3.80 GeV ^{40}Ar. (×, yields for neutron rich nuclides; ○, fractional yields for neutron deficient nuclides; ●, cumulative yields for neutron deficient nuclides; ⦶, independent yields)

RIKEN Accel. Prog. Rep. **24** (1990)

III-3-8. Dry Separation of Radioactive Nuclides from a Gold Target Irradiated with 135 MeV/u ^{14}N Ions

M. Iwamoto, S. Ambe, S.Y. Chen, Y. Ohkubo,
Y. Kobayashi, and F. Ambe

We started in this period a series of experiments on the preparation of multitracer solutions from targets irradiated with heavy ions accelerated with RIKEN Ring Cyclotron.[1] Solutions containing a large variety of radioactive nuclides are to be used in chemical, geochemical, and biochemical investigations. This report describes the separation of radioactive nuclides obtained from a gold target by heating under a reduced pressure.

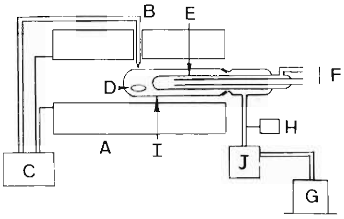

Fig. 1. Apparatus for dry separation. A, electric furnace; B, thermocouple; C, temperature controller; D, irradiated gold foil; E, cold finger; F, cooling water; G, rotary pump; H, Pirani gauge; I, quartz tube; J, charcoal trap.

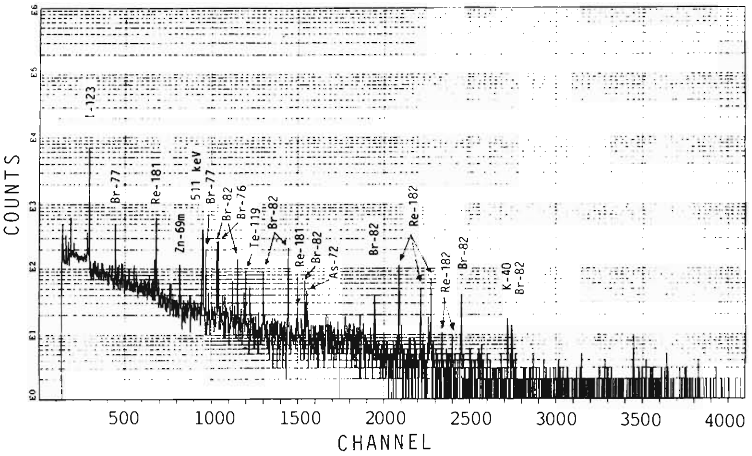

Fig. 2. Gamma-ray spectrum of the nuclides dissolved from the cold finger into (1:1) hydrochloric acid.

A stack of gold foil was irradiated with a 135 MeV/u ^{14}N-ion beam by using the falling ball irradiation system.[2] A piece of the gold foil was heated at 1,050°C (melting point of gold: 1,064°C) in a quartz tube under a pressure of about 1 Pa (Fig. 1). The nuclides evaporating from the foil were collected on a Pyrex cold finger cooled with water. The finger was successively immersed into (1:1) nitric acid and (1:1) hydrochloric acid solutions. The dissolved radioactive nuclides were identified by γ-ray spectrometry with a pure Ge detector. The spectrum of the hydrochloric acid solution is shown in Fig. 2.

γ-Ray spectra were analyzed by the computer program BOB developed by Baba *et al.*[3] The nuclides of following elements were found to have been dissolved in acid solutions:

(1:1) Nitric acid: Zn, As, Te, Tb, Re
(1:1) Hydrochloric acid: Zn, As, Br, Te, I, Re

A more quantitative experiment is now in progress.

References

1) S. Ambe, S.Y. Chen, Y. Ohkubo, Y. Kobayashi, M. Iwamoto, and F. Ambe: This Remort, p. 73.
2) M. Yanokura, Y. Ohkubo, S. Ambe, M. Iwamoto, and F. Ambe: *RIKEN Accel. Prog. Rep.*, **22**, 150 (1988).
3) H. Baba: JAERI-M, 7017.

RIKEN Accel. Prog. Rep. **24** (1990)

III-3-9. Preparation of a Radioactive Multitracer Solution from Gold Foil Irradiated with 135 MeV/nucleon ^{14}N Ions

S. Ambe, S.Y. Chen, Y. Ohkubo, Y. Kobayashi,
M. Iwamoto, and F. Ambe

Simultaneous use of a number of radioactive tracers enables us not only to aquire data efficiently on various elements at once but also to determine the characteristic behavior of different elements precisely under identical experimental conditions. The advance in solid state detectors, counting circuits, and computers has made it possible to measure and analyze complex γ-ray spectra of samples containing many radioactive nuclides. We have established a separation procedure of a radioactive multitracer from a gold target.

A stack of gold foil (22 mmϕ) was irradiated with a ^{14}N beam of 135 MeV/nucleon. The beam intensity was about 100 nA and the irradiation time was 150 min. The irradiated target was dissolved in aqua regia. The solution was evaporated to dryness under a reduced pressure of about 4 kPa in a closed vessel with a trap. The residue was dissolved in conc. hydrochloric acid. Gold ions in the solution were reduced to metal with hydrogen peroxide and filtered out. The evaporation, dissolution, reduction, and filtration were repeated several times to ensure complete removal of gold from the solution. Finally, the residue was dissolved in 6 mol dm^{-3} hydrochloric acid to yield a carrier- and salt-free multitracer solution containing a large va-riety of radioactive nuclides produced from the gold target.

The γ-ray spectra of the solution and the precipitated gold metal were measured with a pure Ge-detector of 18% relative efficiency. The complicated spectra of the solution were analyzed by means of a program BOB[1] on a FACOM M780 computer of the institute. Essentially no peaks assignable to radionuclides of elements other than gold were detected in the fraction of precipitated gold and no γ-rays due to radioactive nuclides of gold were found in the multitracer solution obtained. These observations prove the completeness of the separation carried out. The kind of elements traceable by the nuclides in the solution depends on time after irradiation, because the radionuclides of different half-lives are produced. The dominant peaks in the γ-ray spectrum of the tracer solution measured 4 days after irradiation are those due to ^{67}Ga, ^{89}Zr, ^{87}Y, ^{99}Mo, ^{103}Ru, ^{111}In, ^{131}Ba, ^{145}Eu, ^{146}Eu, ^{146}Gd, ^{147}Gd, ^{149}Gd, ^{152}Tb, ^{153}Tb, ^{155}Tb, ^{166}Tm, ^{167}Tm, ^{169}Lu, ^{171}Lu, ^{170}Hf, ^{173}Hf, ^{181}Re, ^{183}Os, ^{195m}Hg, and so on.

It is noteworthy that a multitracer solution containing neither carriers nor salts is obtained by the present radiochemical procedure. This is a great advantage in applying it to a variety of chemical problem.[2] Now, the application of this procedure to a model experiment on marine chemistry is in progress. We also plan to prepare multitracer solutions covering elements in different ranges of atomic number by using other heavy ions and target materials in combination with appropriate radiochemical procedures.

References

1) H. Baba: JAERI-M 7017.
2) S.Y. Chen, S. Ambe, Y. Ohkubo, M. Iwamoto, Y. Kobayashi, N. Takematsu, and F. Ambe: This Report, p. 74; p. 75.

RIKEN Accel. Prog. Rep. **24** (1990)

III-3-10. A Multitracer Study of the Adsorption of Metal Elements on Hydrated Ferric Oxide

S.Y. Chen, S. Ambe, Y. Ohkubo, M. Iwamoto,
Y. Kobayashi, N. Takematsu, and F. Ambe

Adsorption is one of the most important processes in geochemical behavior of metal elements. A multitracer technique using radioactive nuclides produced by heavy-ion irradiation is especially effective in studying the characteristic behavior of different elements simultaneously. This report describes a multitracer study on the adsorption of various metal elements on hydrated ferric oxide.

Carrier- and salt-free radioactive multitracer solutions were prepared from gold foil irradiated with a ^{14}N beam of 135 MeV/nucleon as described elsewhere.[1)]

Eight milliliters of artificial seawater and 10 μl of a multitracer solution was put into a polyethylene bottle. After pH was adjusted to 7.5 with a 1 mol dm^{-3} Na_2CO_3 solution, 0.5 ml of adsorbent suspension (2 mg/ml) was added to the solution. The volume of the suspension was then adjusted to 10 ml with artificial seawater, and its pH to 7.5. Shaken in an 8-shape mode with a shaker at 25°C, the suspension was found to attain the adsorption equilibrium within 60 min. After centrifugation, 5 ml of the solution was pipetted from the supernatant solution. The γ-ray spectrum of radioactive nuclides in the solution was measured with a Ge detector.

The distribution coefficients (K_d) of Y, Zr, Hf, Mo, Re, Ru, Rh, Cu, Hg, In, Eu, Gd, Tb, Tm, Yb, Sn, and Nb were determined from the activities of their radioactive isotopes. The results are shown in Table 1. The logarithmic plot of K_d against the electron binding energy I_2 of M^{+2} is given in Fig. 1.

These data provide a basis for understanding the removal mechanism of metal elements from seawater.[2)]

Table 1. Distribution coefficients of metal elements for hydrated ferric oxide ($ml \cdot mg^{-1}$).*

	$Fe(OH)_3$
Y	2.63×10^5
Zr	9.12×10^4
Hf	1.07×10^5
Mo	6.46×10^3
Re	1.35×10^4
Ru	1.50×10^4
Rh	8.32×10^3
Cu	1.41×10^6
Hg	1.26×10^5
In	1.58×10^4
Eu	2.51×10^5
Gd	5.75×10^5
Tb	1.05×10^5
Tm	3.72×10^5
Lu	2.63×10^5
Yb	5.27×10^4
Sn	2.27×10^4
Nb	5.39×10^4

* The concentration of a sorbent is 0.1 $mg \cdot ml^{-1}$.

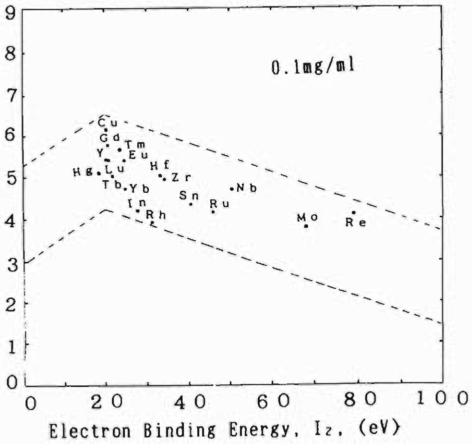

Fig. 1. Logarithmic distribution coefficients K_d of metal elements are plotted against electron binding energies.

References

1) S. Ambe, S.Y. Chen, Y. Ohkubo, Y. Kobayashi, M. Iwamoto, and F. Ambe: This Report, p. 73.
2) S.Y. Chen, S. Ambe, Y. Ohkubo, M. Iwamoto, Y. Kobayashi, N. Takematsu, and F. Ambe: *ibid.*, p. p. 75.

RIKEN Accel. Prog. Rep. **24** (1990)

III-3-11. A Multitracer Study of Adsorption of Metal Elements on Clay Minerals and Marine Sediments

S.Y. Chen,* S. Ambe, Y. Ohkubo, M. Iwamoto,
Y. Kobayashi, N. Takematsu, and F. Ambe

A leading model for the removal mechanism of metal elements from the ocean is a surface complextion model.[1] However, it is based not on stability constants of surface complexes of the elements, but on their hydrolysis constants or dissociation constants of acids they form in solution. It is assumed that the adsorption affinity of cationic elements is dependent on their hydrolysis constants, while that of oxyanionic elements is dependent on the dissociation constants of their acids. This is a point of the model criticized by its opponents.[2] In order to clarify this essentially by important problem, we started an adsorption study of metal elements on various marine samples making use of a multitracer produced with RIKEN Ring Cyclotron.

The details of the experiment are referred to a preceding report describing a similar adsorption study on hydrated ferric oxide.[3]

The distribution coeffients (K_d) of Y, Zr, Hf, Mo, Ru, Rh, Cu, Ag, Hg, In, Eu, Gd, Tb, Tm, Lu, Yb, Sn, and Nb were calculated from γ-ray spectra. For the metal elements, the order of K_d for each adsorbent is summarized as follows: Hy-drated ferric oxide[3] > deep-sea sediment > montmorillonite ⩾ nearshore sediment ⩾ kaolinite. It is inferred from these observations that hydrated ferric oxide plays an important role in removing metal elements from seawater.

The logarithmic plot of adsorption coefficients K_d versus electron binding energy I_2 for deep-sea and nearshore sediments is shown in Fig. 1. A correlation is seen similar to that observed for the concentration ratio of elements in oceanic pelagic clay sediments and seawater.[1]

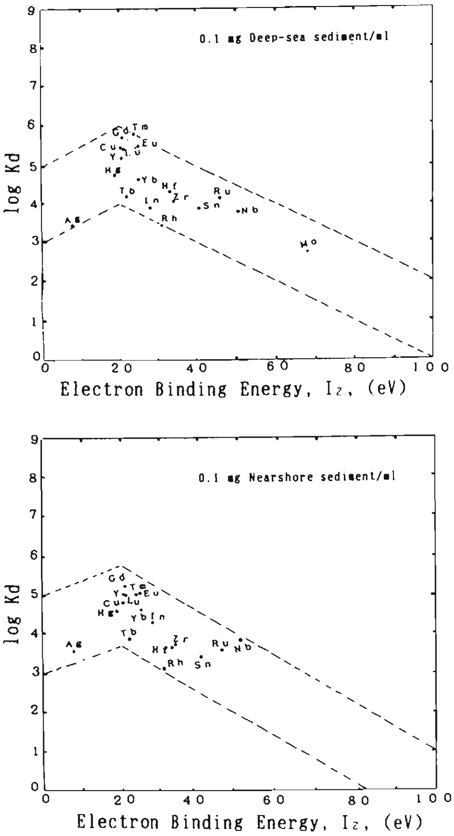

Fig. 1. Logarithmic plot of distribution coefficients K_d of metal elements for deep-sea and nearshore sediments as a function of the electron binding energies.

References

1) Yuan-Hui Li: *Geochim. Cosmochim. Acta*, **45**, 1659 (1981).
2) M. Whitfield and D.R. Turner: *ibid.*, **46**, 1989 (1982).
3) S.Y. Chen, S. Ambe, Y. Ohkubo, M. Iwamoto, Y. Kobayashi, N. Takematsu, and F. Ambe: This Report, p. 74.

---

* South China Sea Institute of Oceanology, Academia Sinica.

RIKEN Accel. Prog. Rep. **24** (1990)

III-3-12. Preparation of No-Carrier-Added ^{105}Ag and ^{106m}Ag and Their Chemical Behavior

S. Ambe, Y. Ohkubo, M. Iwamoto, and Y. Kobayashi

In this study we have established a procedure of preparing no-carrier-added ^{105}Ag (half-life: 41.3 d) and ^{106m}Ag (half-life: 8.46 d) (hereafter we refer to as Ag*) by using the cyclotron, that is, by the Pd(α, pxn)Ag* reactions.

Pd foils (8 μm) were irradiated with 40 MeV α particles accelerated in the cyclotron. The Pd foils were heated in a quartz tube with a cold finger under a reduced pressure (~10 Pa). Ag* deposited on the cold finger was dissolved in a hot 1 : 1 HNO_3 or 1 : 1 HCl solution, yielding no-carrier-added and salt-free Ag* solutions. The solutions thus obtained were used for adsorption and coprecipitation experiments.

Figure 1 shows that the sublimation of Ag* starts at around 900°C and is accelerated with temperature. We adopted 1,050°C as the temperature for routine sublimation. The Sublimation is an excellent separation method, because dissolution of Pd foils is not necessary and separation time can be greatly saved in comparison with wet separation methods.

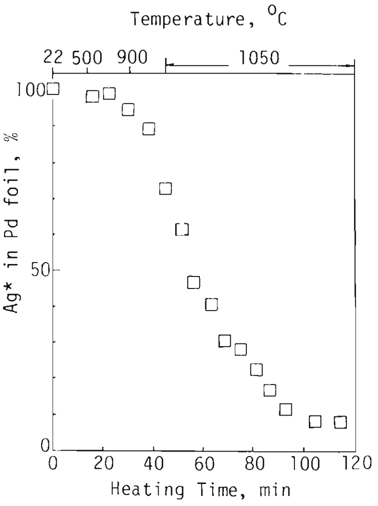

Fig. 1. Sublimation of Ag* from α-irradiated Pd foils heated upto 1,050°C under a reduced pressure of about 10 Pa.

The adsorption yield of Ag*(I) on α-Fe_2O_3 from 0.5 mol dm^{-3} $NaNO_3$ increased with pH, while only a slight increase was observed for the adsorption from 0.5 mol dm^{-3} NaCl at pH 3–12.

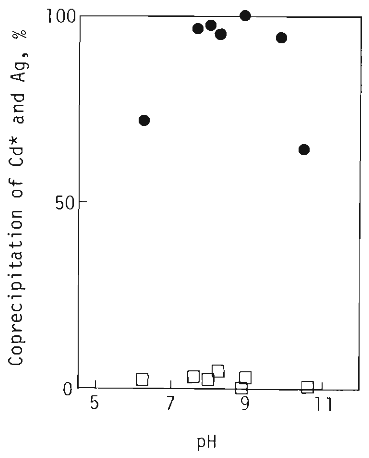

Fig. 2. Coprecipitation of no-carrier-added Cd*(II)(●) and Ag*(I)(□) with ferric hydroxide precipitated with NH_4OH.

Figure 2 shows the coprecipitation of Ag*(I) and Cd*(II) with ferric hydroxide precipitated with NH_4OH. Almost all the Cd*(II) ions were coprecipitated, while Ag*(I) was scarcely coprecipitated at pH 7.5-9. This result shows that Ag*(I) and Cd*(II) are separated by means of ferric hydroxide coprecipitation in the presence of NH_4OH.

RIKEN Accel. Prog. Rep. **24** (1990)

III-3-13. Proton Irradiation-Induced Defects in LEC-GaAs Studied by Positron Annihilation

Y. Itoh and T. Takahashi

Irradiation-induced defects in GaAs with electrons and protons have been investigated from their electrical or optical properties.[1,2] Recently, the defects in GaAs have been studied by positron annihilation.[3,4] We have performed positron Doppler broadening measurements to investigate fluence effects on the vacancy in undoped and Si-doped liquid encapsulated Czochralski (LEC)-GaAs.

Wafer samples of GaAs were irradiated with protons of 15 MeV and of about 0.5-0.8 μA for 60-1800 s in a helium atmosphere at room temperature. A ^{48}V positron source produced in 1 μm Ti film was sandwiched with two wafers of $30 \times 30 \times 0.7$mm^3. Doppler broadening spectra of 0.511 MeV positron annihilation were measured with a high-resolution pure Ge detector (1.05 keV at ^{106}Ru 0.512 MeV). S parameters represent the ratio of the area of a sharp narrow energy peak range symmetrical around 511 keV to the sum of the areas of the "wings" of the peak. The narrower spectrum with the smaller "wing" gives the larger S parameter. The sharpness of the spectrum corresponds to the annihilation sites for the positrons, that is, the vacancy defects generation.[5]

Figure 1 shows the temperature dependence of undoped and si-doped LEC-GaAs irradiated with various proton fluences. For as-irradiated samples, the undoped one gives a smaller S-parameter than that of the Si-doped one. For the undoped samples, the S-parameters increases with proton fluence at three temperatures investigated, whereas the S-parameters of Si-doped samples show no significant change at low fluences except for 10^{15} proton cm^{-2}.

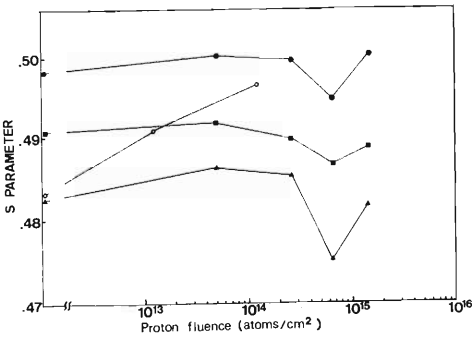

Fig. 1. Temperature dependence of undoped and Si-doped LEC-GaAs irradiated with various proton fluences. Undoped sample at room temperature (○), Si-doped, room temerature (●), Si-doped, liquid temperature (■), and Si-doped, liquid helium temperature (▲).

The annealing studies are in progress.

References

1) M. Bugajski, K.H. Ko, J. Lagowski, and H.C. Gatos: *J. Appl. Phys.*, **65**, 596 (1989).
2) S. Danneffarer, P. Mascher and D. Kerr: *ibid.*, **60**, 1313 (1986).
3) C. Corbel, F. Pierre, P. Hautojarvi, K. Saarinen, and P. Moser: Int. Conf. on Defects in Semiconductor Crystals, Yokohama, Sept. (1989).
4) A. Sen Gupta, S.V. Naidu, R.K. Bhadari, and P. Sen: *Phys. Lett. A*, **104**, 117 (1984).
5) W. Branct: "Positron Solid-State Physics," Enlico-Fermi, International School of Physics, p. 89 (1983).

RIKEN Accel. Prog. Rep. **24** (1990)

III-3-14. Generation of Slow Positron Beam from $^{nat}B(p, xn)^{11}C$ Reaction

Y. Itoh, M. Takai, and K. Ogiwara

Techniques of mono-energetic positron beams with variable energy have recently been developed.[1,2] Positrons from a radioactive source (^{22}Na or ^{58}Co) or from a high energy electron accelerator are injected into a single-crystal metal moderator. In the moderator the positrons are slowed down. A few of them thermalize in the region close to the moderator surface. They may then diffuse back to the surface before they annihilate having a certain probability of being re-emitted from the surface with an energy equal to the negative value of the work function of the positron in the metal. This is of the order of an electron-volt. Mono-energetic positrons from the moderator can then be accelerated to a desired energy and injected into a sample.

A mono-energetic, low energy positron beam can be also obtained by the $^{11}B(p, n)^{11}C$ reaction which has a threshold energy of 3.0 MeV. The half-life of ^{11}C is 20.3 min, and the maximum positron energy is 0.97 MeV. An advantage of this technique is the emission of low-energy positrons from an irradiated boron target itself with no additional moderating materials.

A 5 MeV proton beam from a 160 cm cyclotron was used to bombard a boron nitride target. The positron activity of the ^{11}C source was determined with a 2 inch × 2 inch BGO (Bismuth Germanium Oxide) detector by detecting gamma rays produced by annihilation of positrons in a target chamber. A proton bombardment with a current of approximately 1 μA for 20 min produced a positron source having an activity which was approximately the same as the activity reported by Stein.[3]

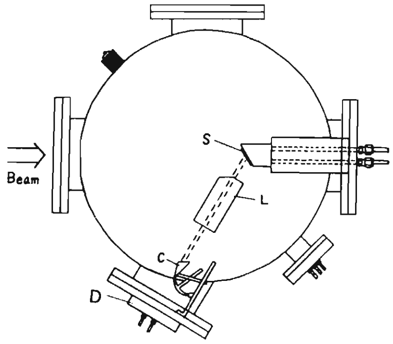

Fig. 1. Schematic diagram of the apparatus for the production of slow positron. C, Channeltron; S, Target (Boron Nitride), L, Focusing Lens Elements; Beam, 5 MeV Proton Beam; D, BGO Detector.

A low energy positron-beam apparatus, as shown in Fig. 1, is now under construction to study defects in the surface layers of semiconductor samples. The target is biased at some appropriate positive potential and an electrostatic lens system is used to extract and focus energy positrons from a boron nitride target into a beam. We are planning to test the apparatus with an electron source instead of a positron source by reversing all potentials applied to the lens assembly.

References

1) A. Vehanen, P. Huttunen, J. Makinen, and P. Hautojarvi: *J. Vac. Sci. Technol.*, **A5**(**4**), 1142 (1987).
2) C.D. Beling and M. Charlton: *Contemp. Phys.*, **28**, 241 (1987).
3) T.S. Stein, W.E. Kauppila, V. Pol, J.H. Smart, and G. Jesion: *Phys. Rev.*, **A17**, 1600 (1978).

RIKEN Accel. Prog. Rep. **24** (1990)

III-3-15. Positron Annihilation Study on Defects in LEC-GaAs Grown from Ga-rich Melt

Y. Itoh and T. Takahashi

A positron annihilation technique which is well established to investigate defect properties in metals[1] has been applied to a study on the defects in liquid-encapsulated Czochralski (LEC)-GaAs grown from a Ga-rich melt. Recent several studies have revealed that positrons are trapped by grown-in vacancy defects in GaAs.[2–4] Although the vacancy-related positron traps in GaAs are attributed to Ga vacancies, Ga vacancies-impurity complexes, As vacancies and $V_{As}V_{Ga}$ divacancies, the microscopic properties of these vacancy defects are not clear.

An LEC-GaAs ingot was grown from a Ga rich melt and cut into wafers of 30×30×0.7 mm^3 from the front, the middle and the tail portions. The wafers with a (100)-orientation were polished. A ^{48}V positron source prepared by bombarding a 1 μm Ti foil was sandwiched with two wafers. Doppler broadening spectra of 0.511 MeV positron annihilation were measured with a high-resolution pure Ge detector. After annealing the front and the tail samples, at 850°C for 20 min in an arsenic atmosphere the Doppler broadening was re-measured. S parameter which is related to positron trapped defects[1] was calculated from the spectrum.

The results are shown in Fig. 1. In as-annealed samples, the S parameter for the wafer taken from the tail portion gives a value higher than that of the front one. After annealing, the S parameter of the tail wafer decreased, whereas, the parameter of the front one slightly increased. These results are under further study.

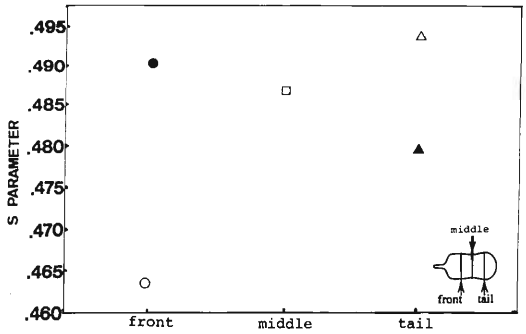

Fig. 1. S parameters of the positron annihilation in LEC-GaAs cut from the front, middle and tail portions of the ingot grown from Ga-rich Melt. As-annealed: front (○), middle (□) and tail (△). Annealed at 850°C, for 20 min in AsH$_3$ atmosphere: front (●) and tail (▲).

References

1) W. Brandt and A. Dupasquier: Positrons-Solid State Physics, Proc. Int. School of Phys. “Enrico Fermi”, Varenna 1981, North-Holland Publ. Co. (1983).
2) G. Dlubek, O. Brummer, F. Plazaola, and P. Hautojarvi: J. Phys. C: *Solid State Phys.,* **19**, 331 (1986).
3) S. Dannefaer and D. Kerr: *J. Appl. Phys.,* **60**, 591 (1986).
4) C. Corbel, F. Pierre, P. Hautojarvi, K. Sarrinen, and P. Moser: Defect Control in Semiconductors, North-Holland, Yokohama, p. 915 (1989).

RIKEN Accel. Prog. Rep. **24** (1990)

III-3-16. Development of an Ion Beam Sputtering Method to Prepare Long-Lived Carbon Stripper Foils

I. Sugai,* M. Oyaizu,* M. Aratani, M. Minami, and M. Yanokura

Carbon stripper foils with long lifetimes are very important for accelerating cascade-type protons and heavy ions. We have developed various methods suited to prepare long-lived carbon stripper foils and improved them to give high reproducibility and creditability. A controlled AC and DC arc discharge (CADAD) method[1] and an ion-beam sputtering (IBS) method were found to be useful compared with an electron-beam heating and an old DC arc discharge method as discussed previously.[2] The foils made by the CADAD method are widely used at several institutes and universities in this country.

Hitherto, the IBS technique has not been popular, because of its low sputtering yield of carbon small-scale productivity. Previously[3] we investigated the lifetimes of carbon stripper foils made by using various kinds of gas ions for sputtering carbon source materials, and suggested that a foil made by the IBS method may possibly a super long-lived carbon stripper foil. We have established highly reliable and reproducible conditions for the preparation of long-lived carbon foils by improving the IBS method.

The experimental apparatus for the measurement of lifetimes of carbon foils (about 15 $\mu g/cm^2$) was almost the same as that described in Ref. 1. Experiments were performed in a high-vacuum chamber (10^{-4} Pa), using a 3.2 MeV Ne^+ ion beam of 2–3 μA of 3.5 mm in diameter obtained by a Van de Graaff accelerator at the Tokyo Institute of Technology.

The lifetime of foil is conventionally defined as an integrated beam current of ions passing through it before it breaks. We investigated lifetimes of all the foils made by using various kinds of noble gas ions for sputtering carbon source materials. Commercially available (CM) foils showed only a short lifetime of 2.5 mC in average. Figure 1 shows the lifetimes of carbon foils versus the mass of noble gas ions. As seen from Fig. 1, lifetime of carbon foils depends on the atomic mass of noble gas ions.

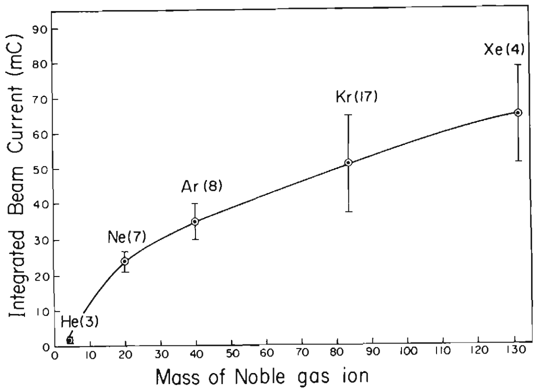

Fig. 1. Dependence of lifetime of carbon stripper foils versus the mass of noble gas ion employed for sputtering during preparation. Error bars represent mean-squares errors and the numbers in parentheses denote the numbers of samples investigated.

For a light atomic mass such as ^4He, the lifetime is short, 1.2 mC, only half of the lifetime of the CM-foil (2.5 mC). For ^{131}Xe, the heaviest atomic mass investigated in the present work, the lifetime is very long, 64 mC in average and 26 times longer than that of the CM-foil. From the dependence of the lifetime of the atomic mass of noble gas employed for sputtering during preparation, we found that foils made by Kr and Xe shows long lifetimes compared with foils made by light atomic mass ions such as Ne and Ar. A key point in producing long-lived foils with Kr or Xe is to make the amount of oxygen in a foil as low as possible.

References

1) I. Sugai and T. Hattori *et al.*: *Nucl. Instrum. Methods Phys. Res.*, **A265**, 376 (1988).
2) I. Sugai and T. Hattori *et al,*: *ibid.*,**A236**,576 (1985).
3) I. Sugai, M. Aratani, M. Minami, and M. Yanokura: *RIKEN Accel. Prog. Rep.*, **23**, 85 (1989).

---

* Institute for Nuclear Study, University of Tokyo.

RIKEN Accel. Prog. Rep. **24** (1990)

III-3-17. Hydrogen Desorption from Diamond-like Carbon Film during Ion Beam Irradiation

M. Minami, M. Aratani, and M. Yanokura

In measuring hydrogen contents in diamond-like carbon (DLC) films by elastic recoil detection analysis, we observed a decrease in hydrogen contents with the irradiation time.

The DLC films (about 200 nm thick) were prepared from methane on silicon wafers by the electron cyclotron resonance (ECR) chemical vapor deposition (CVD) method. The size of each film was 20 mm × 10 mm.

The scattering chamber (100 cm in diameter, 2 × 10^{-6} Torr) located at the RILAC A-1 beam line was employed. At the center of the chamber, the DLC films were set up at 30° to a 50 MeV incident argon beam of 2 nA. Two surface barrier semiconductor detectors (SSD) were arranged at 35° (SSD-1) and at 50° (SSD-2) to the beam. In front of the SSD-1, an aluminium foil (10 μm thick) was set up to detect only hydrogen and carbon ions in the specimens.

Figure 1 shows the decrease in hydrogen content of the DLC film during ion-beam irradiation; no such a decrease was observed for hydrogenated amorphous silicon (a-Si:H) films.[1] The preparation methods for the DLC and a-Si:H films are very similar in chemical forms of starting materials and decomposition processes. Starting gas was CH_4 for the DLC films and SiH_4 for the a-Si:H films.

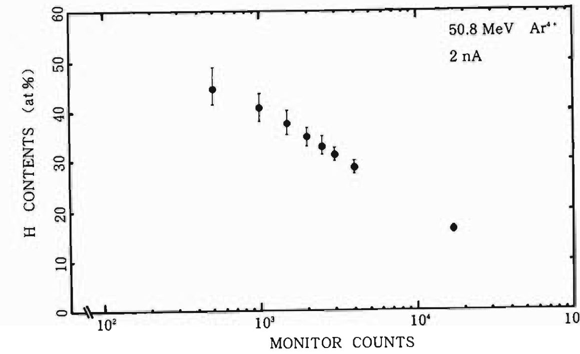

Fig. 1. Hydrogen desorption from DLC film during ion-beam irradiation.

The decrease in hydrogen content may be considered due to the temperature rise in the film resulting from energy deposited by heavy ions. Temperature measurements, however, suggested no desorption of hydrogen.[2] Thus, it could be considered that hydrogen behaves in the DLC films very differently from that in the a-Si:H films. This interesting phenomenon is should be further investigated.

References

1) M. Aratani and T. Nozaki: Unpublished data.
2) K. Yano, H. Oyama, M. Yanokura, M. Aratani, and M. Minami: This Report, p. 64.

RIKEN Accel. Prog. Rep. **24** (1990)

III-3-18. Elastic Recoil Detection and the Forward Scattering Analysis of Nitride Films

K. Onoe, M. Aratani, M. Minami, A. Kaburagi, and M. Yanokura

Transition-metal nitrides and carbides have been used extensively as protective coating materials on cutting tools because of their extremely high hardness. In addition, such nitrides have been increasingly used as the diffusion barrier in integrated circuits.1) In the PVD (physical vapor deposition) process, the properties of the films produced such as composition, microstructures, and crystal structures are greatly influenced by process conditions.2) Therefore it is important for practical applications to understand the film properties in relation to the deposition parameters.

Recent quantitative surface analyses, especially AES (Auger Electron Spectroscopy) and XPS (X-ray Photoelectron Spectroscopy), have improved considerably.3) However, it is often difficult to obtain a reference sample with known composition, thus limiting the accuracy of quantification. Moreover, the emission lines of TiN, TiL_l and NK_α, are too close to be separated in AES and EPMA (Electron Probe Microanalysis). As a result, quantification of nitrogen in TiN films becomes somewhat difficult. Thus cross check of results from several analytical methods based on various principles is needed to provide an accurate analysis.

Results of preliminary compositional analyses of BN, TiN, CrN, and ZrN films by ERDA (Elastic Recoil Detection Analysis) are briefly described below.

TiN, CrN, and ZrN were deposited onto stainless steel plates by the HCD-ARE (Activated Reactive Evaporation using Hollow Cathode Discharge) method. BN was deposited on a Si wafer by the same technique. Details of the HCD-ARE method have been reported.4) The thicknesses of the films ranged from 0.5 to 0.9 μm.

Argon ions, Ar^{4+}, accelerated up to 50 MeV with RILAC were used as a primary beam. The measurement apparatus used was described by H. Nagai *et al.* in detail.5) The beam current was 3 to 4 nA in this experiment. Energy spectra of recoil and forward scattered particles from film samples are shown in Figs. 1 and 2. θ_1 is an angle between the target plane and the scattering plane and θ_2 is a detector angle with respect to the incident beam.

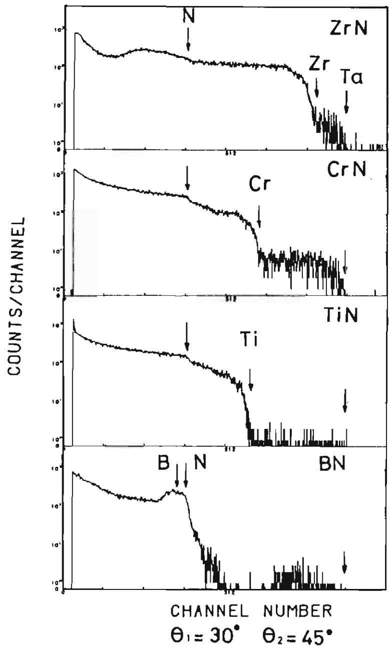

Fig. 1. Energy spectra of recoil and scattered particles. Target angle, $\theta_1=30°$; detector angle, $\theta_2=45°$; incident particles, Ar^{4+} 50 MeV: samples, BN, TiN, CrN, and ZrN films.

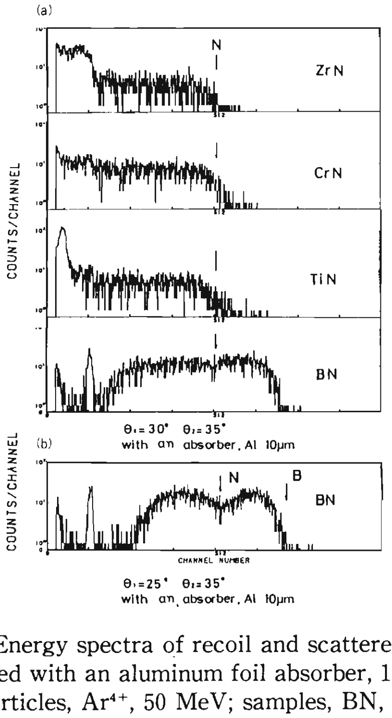

Fig. 2. Energy spectra of recoil and scattered particles measured with an aluminum foil absorber, 10 μm. Incident particles, Ar^{4+}, 50 MeV; samples, BN, TiN, CrN, and ZrN films. a) target angle, $\theta_1=30°$, and detector angle, $\theta_2=35°$. b) target angle, $\theta_1=25°$; detector angle, $\theta_2=35°$.

In Fig. 1 arrows show the energy of the recoiled particles measured at $\theta_1 = 30°$ and $\theta_2 = 45°$. Heavy element impurities, mainly tantalum, were also detected. The tantalum may originate from a tantalum cathode used during the deposition. The nitrogen peaks apparently overlap with the metallic element and boron ones owing to the thicknesses of the present samples. Here it is difficult to quantify the nitrogen concentration.

The nitrogen peaks can be observed when aluminum foil was placed in front of the detector as an absorber (see Fig. 2a). The use of an aluminum absorber appears to provide better analytical results for the nitrogen in the films. Furthermore, separation of nitrogen and boron was improved when the target angle was changed from 30° to 25° (see Fig. 2b).

Further investigations are being carried out based on these results.

References

1) M. Wittmer: *J. Vac. Sci. Technol.*, **A3**, 1797 (1985).
2) R.F. Bunshaw: Vacuum and Thin Film Technology, Pergamon Press, p. 353 (1978).
3) C.J. Powell and M.P. Seah: *J. Vac. Sci. Technol.*, **A8**, 735 (1990).
4) K. Inagawa *et al.*: *Plating and Coating*, **4**, 34 (1984).
5) H. Nagai *et al.*: *Nucl. Instrum. Methods.*, **B28**, 59 (1987).

RIKEN Accel. Prog. Rep. **24** (1990)

III-3-19. Analysis of Contamination Processes during Vacuum Deposition of Thin TiN$_x$ Films

A. Kaburagi, M. Minami, M. Yanokura, M. Aratani, K. Onoe, and I. Sugai

Recently, films of titanium nitride or oxide are widely used as coating and coloring materials. Contamination of impurities has an influence on brightness especially as coloring materials. So, characterization for impurities is required. We examined a thin TiN$_x$ film prepared by activated reactive evaporation using hollow cathode discharge (HCD-ARE) which was an entirely new preparation method. We paid attention to mainly heavy-element impurities using heavy ion Rutherford scattering (HIRS).$^{1-4)}$

A sample was set at an angle of 15° to an incident beam and surface-barrier detectors were set at angle of 30°, 40°, and 60° to the incident beam. The sample was bombarded with a 50.77 MeV Ar beam from RILAC at an intensity of less than 5 nA. Forward scattering spectra for thin TiN$_x$ film and a tantalum standard are shown in Fig. 1. The thick line spectrum is for the thin TiN$_x$ film; the thin line is for the tantalum standard. High energy end corresponding to the heaviest impurity in TiN$_x$ agreed with high energy end of tantalum. Thus, the main impurity is interpreted as tantalum. Total content of impurities heavier than titanium including tantalum in TiN$_x$ was calculated to be 0.07 at.%.

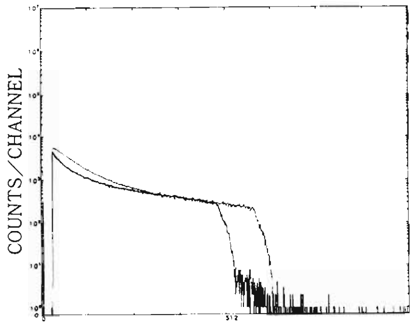

Fig. 1. Forward scattering spectra for thin TiN$_x$ film and tantalum using 50.77 MeV Ar^{4+} beam of less than 5nA.

These results are inconceivable from high melting point and low vapor pressure of tantalum in case of TiN$_x$ prepared by usual methods. The tantalum contaminant in the titanium nitride film prepared by HCD-ARE, however, may be attributed to the method itself. Namely contaminating tantalum may result from fabricating materials of hollow cathode. Titanium cathode should be tried for preparation of high-purity TiN$_x$.

Our next plan is determination of x and trace amount of oxygen in TiN$_x$.

References

1) O. Kuboi, M. Hashimoto, Y. Yatsurugi, H. Nagai, M. Aratani, M. Yanokura, S. Hayashi, I. Kohno, and T. Nozaki: *Appl. Phys. Lett.,* **45**, 543 (1984).
2) M. Aratani, M. Yanokura, B.G. Yu, Q. Qiu, and T. Nozaki: 10th Conf. on the Appl. of Accel. in Res. and Industry, Denton, U.S.A., Nov. (1988).
3) K. Tachi, M. Aratani, T. Kato, M. Yanokura, T. Sato, M. Ohtsuka, M. Tsujiguchi: Proc. 7th Symp. on Ion Beam Technol. Hosei Univ., p. 151 (1988).
4) R. Imura, R. Suzuki, M. Aratani, M. Yanokura, and T. Nozaki: Int. Magnetic Conf. BE07 (1987).

RIKEN Accel. Prog. Rep. **24** (1990)

III-3-20. Depth Profile of Hydrogen in the Volcanic Glass Studied by Heavy-Ion Rutherford Scattering

Kazue Tazaki, M. Aratani, M. Yanokura, and M. Minami

Electron microscopy, low-angle X-ray diffraction (XRD), differential thermal analysis (DTA) and heavy-ion Rutherford scattering (HIRS) play an important role in elucidating the crystal structure of glass materials, especially, of a hydrated phase in a matrix. Amorphous materials can usually be investigated with reasonable confidence from XRD, density measurements, and various chemical techniques. HIRS is a powerful technique for chemical and structural analysis of glassy materials, and their hydrated phase. Electron microscopy has a potential advantage of providing real lattice-fringe imagings of about 3, 4, 5 Å separations in a small region.[1)]

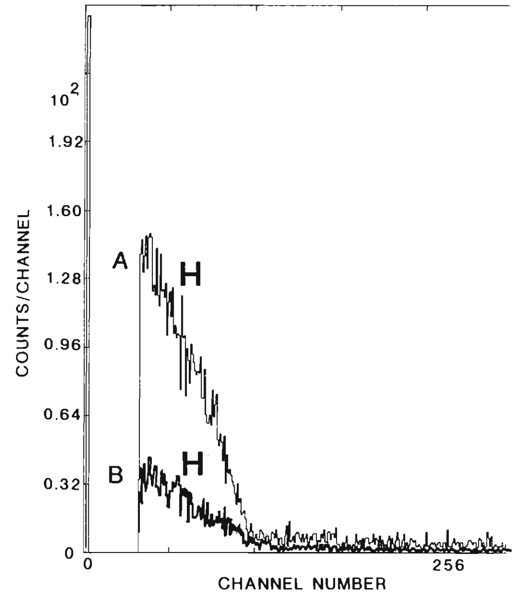

Fig. 1. Depth profile of hydrogen in volcanic glasses. A, volcanic glass fragments from Daisen volcanic ash at Daisen-ike, Tottori; B, volcanic glass fragments from Aira volcanic ash soil at Asahi tunnel, Ito, Kokubu, Kagoshima. The hydrogen contents are different five times between the two origins.

Dacitic volcanic glass samples were collected from Daisen volcanic ash soil at Daisen-ike, Tottori, and Aira volcanic ash soil at Asahi tunnel, Kagoshima. The glass samples were examined by forward recoil measurement[2)] or HIRS[3)] using the RIKEN heavy-ion linear accelerator (RILAC). The energy spectra of hydrogen ions recoiled forward (35° to an incident Ar^{4+} ion beam) from the glass samples are shown in Fig. 1. The highest end in spectra corresponds to the surface position, where no significant peak is seen. This result indicates that hydrogen atoms in these samples are located at the structural sites, but not on the surface. The shape of the hydrogen peaks is attributed to the uniform distribution of hydrogen atoms in the glass fragments, which are microscopically small beads and incident Ar^{4+} ions hit a hemispherical surface of each bead. Daisen volcanic glass fragments (A) contain five times hydrogen compare with Aira volcanic glass fragments (B). The results suggest that the hydrogen content in a volcanic glass samples may provide a measure to distinguish between different volcanic sources.

References

1) Kazue Tazaki, W.S. Fyfe, and S.J. van Der Gaast: *Clays Clay Miner.*, **37**, 348 (1989).
2) H. Nagai, S. Hayashi, M. Aratani, T. Nozaki, M. Yanokura, I. Kohno, O. Kuboi, and Y. Yatsurugi: *Nucl. Instrum. Methods Phys. Res.*, **B28**, 59 (1987).
3) M. Aratani: *Radioisotopes*, **37**, 43 (1988).

RIKEN Accel. Prog. Rep. **24** (1990)

III-3-21. Side Determination of Weathered Egg Shell by Heavy-Ion Rutherford Scattering

M. Aratani, M. Yuyatani, Kazue Tazaki, M. Minami, and M. Yanokura

When we perform nondestructive measurement of a small piece of so intensely weathered egg shell that we cannot tell which is outside or inside, how can we distinguish outside from inside? Before we examine the sample of the weathered egg shell of a dinosaur, preliminary measurements have been made by using egg shell of a hen. Hen egg shell was cut into pieces of a size of 19 mm × 9 mm, followed by soft pressing so as to get rid of curvature with or without boiling. As for an inside sample, two kinds of pieces were prepared. One is a piece as cut with a thin film attached to the inside and the other is a piece without a thin film by peeling from the inside. These three kinds of samples were examined by heavy-ion Rutherford scattering. A 62 MeV Cu^{4+} beam of tens of nanoamperes was employed as the incident. A target angle was 20° to the beam. Detector angles were 35°, 45°, and 120°. After the measurement of the egg shell of a hen, the intensely weathered egg shell was examined.

The main constituents of the egg shell of a hen were observed to be C, O, Si, Ca, Fe, and some other heavy elements, as shown in Figs. 1 to 3.

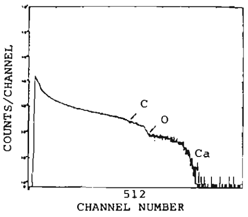

Fig. 1. Outside of hen egg shell.

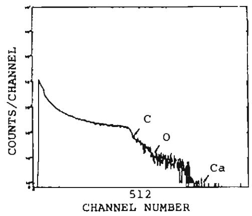

Fig. 2. Inside of hen egg shell.

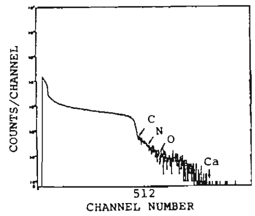

Fig. 3. Inside with thin film of hen egg shell.

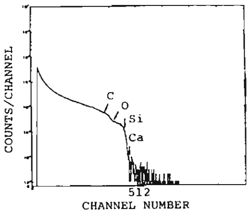

Fig. 4. Light brown side of dinosaur egg shell.

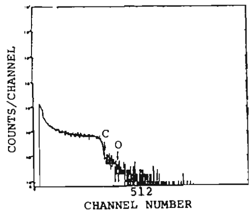

Fig. 5. Dark brown side of dinosaur egg shell.

The results obtained for dinosaur egg shell at a detector angle of 45° are shown in Figs. 4 and 5. In comparison with hen egg shell, three samples of a dinosaur reveal a significant difference between outside and inside. The inside contains many carbon atoms and some nitrogen atoms; this result may be attributed to protein contained in the thin film. The sample of the weathered egg shell of a dinosaur is light brown in one side and dark brown in another side. From the spectra for a hen egg and those for a dinosaur egg, the light brown side may be attributed to outside and the dark brown side to the inside. A difference was also seen in some heavy elements. These results may lead us to the relationship between original constituent of the egg shell and any other environmental-origin elements, and mechanism of weathering.

RIKEN Accel. Prog. Rep. **24** (1990)

III-3-22. Heavy Ion Probe Rutherford Scattering Applied to Pathological Samples

Y. Qiu,* T. Kobayashi,* M. Minami, M. Aratani, and M. Yanokura

Although some rare metals are considered to play an important role in the pathophysiological process in some intractable human diseases such as amyotrophic lateral sclerosis (ALS) and Duchenne muscular dystrophy (DMD), there are few analytical studies of rare heavy metals in these diseases because of technical difficulties.[1] The heavy ion probe Rutherford scattering method[2] is very useful to detect all rare elements in a thin material; however so far it has been applied only to metal and electronic materials. We report for the first time the application of this method to biological materials.

Frozen muscle tissues (−25°C) from mdx and scn mice, which are animal models of DMD and control, and paraffin blocks of the autopsied spinal cord from patients with ALS, and controls were used. These tissues were sliced into 6 μm sections, and nine slices were mounted on a ladder-type holder installed at the center of a scattering chamber at 30° angles to an incident beam. Detectors were located at forward angles (35° and 45°) for ions recoiled and scattered by 50 MeV Ar^{4+} and incident Cu^{4+} of about 60 MeV from RILAC. Figure 1 is an energy spectrum of ions scattered forward from a thin slice of an mdx-mouse. The incident ion is Ar. Heavier ions appear in the high energy side. Figure 2 is an energy spectrum of a diamond-like carbon (DLC) film of 300 nm in thickness.[3] The carbon peak of muscle from the mdx-mouse (Fig. 1) is almost the same as that of the DLC film, indicating that the number of carbon atoms in a 6 μm muscle section is almost the same as that in the DLC film. We also used thin films of W, Pd, Zn, and Cd, as standard samples. We used acrylic resin as a phantom model for the mammalian tissue and drew the amount of rare heavy metals in these biological materials (for example: 0–200 at. ppm of Cd-Sn in an mdx mouse). Now we calculate and compare rare metals in mdx and scn mice and also ALS and control spinal cords.

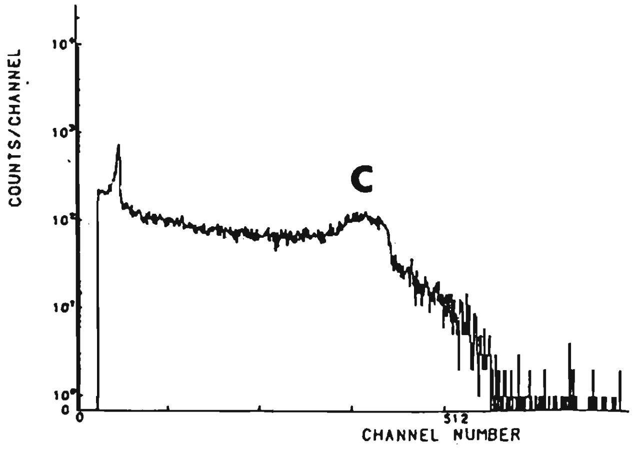

Fig. 1. Energy spectrum of Ar ions scattered and light element ions recoiled from mdx muscle.

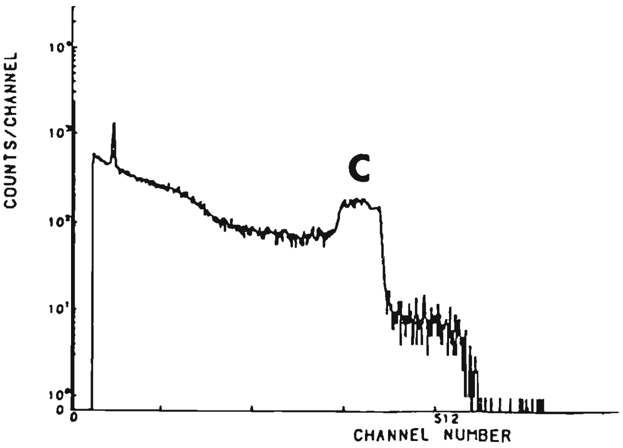

Fig. 2 Energy spectrum of Ar ions scattered and carbon ions recoiled from the DLC film.

References

1) J.F. Ziegler (Eds.): Handbook of Stopping Cross Sections for Energetic Ions in All Elements, Pergamon Press, New York (1980).
2) H. Nagai, S. Hayashi, M. Aratani, T. Nozaki, M. Yanokura, I. Kohno, O. Kuboi, and Y. Yatsurugi: *Nucl. Instrum. Methods B*, **28**, 59 (1987).
3) S. Okada, M. Hayakawa, S. Morishima, and S. Kunishima: 11th Vacuum Congr. Koln, Sep. (1989).

---

* Department of Neurology, Tokyo Medical and Dental University.

RIKEN Accel Prog. Rep. **24** (1990)

III-4. Radiation Chemistry and Radiation Biology

1. High-Density Excitation by Heavy Ions: Track-Depth Resolved Luminescence of N-ions Injected-Helium Gas and Liquid

K. Kimura, J. Wada, and M. Arai

Ions of few MeV/amu show characteristic radiation effects such as charge exchange, wake field, and convoy electrons. Furthermore, in their tracks, electronic excited states are contained at an extremely high density. Our studies aim to find characteristic phenomena caused by above effects and elucidate them. For these purposes, space- and time-resolved luminescence measurements were done.

A space-resolved or track-depth resolved luminescence were measured using a following equipment named a tack scope. The track scope was composed of a quartz imaging fiber and a position detective photon-counter. One end of the fiber was mounted in a cryostat and thereby temperature and pressure of sample helium were adjusted. The image projected from the other end, namely, luminescence intensities along the path of ion tracks, was digitized by a position-detective photon-counter. (See Ref. 1.) Also, depth-resolved luminescence spectra were measured by the change of a section of the full image which enters into a monochromator through a monochromator-slit.

Figure 1 shows helium-density dependent specific luminescence, *dL*/*dx*, as a function of track-depth. Luminescence spectra were changed scarcely except for their intensities; peaks were assigned to be due to the d-b, D-B, H-C, and J-C transitions between excimer states (Fig. 2). The most important finding is a splitting of Bragg-like curve of *dL*/*dE* *vs.* excitation density. Namely, the first peak positioned at the high energy side of the maximum stopping power and in addition to it the second peak was observed at the low energy side. The positions of the first peaks were invariant with variation in the helium density. These peaking were explained by the effect of excitation density. On the other hand, the positions of the second ones varied with variation in the helium density and excitation density, but they appeared at a given ionic velocity with variation of helium density as shown in Fig. 3. The second peaking may be attributable to charge exchanges or direct excitations.

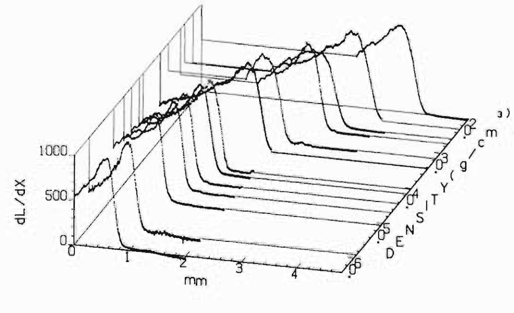

Fig. 1. Specific luminescence, *dL*/*dx*, *vs.* the depth of N-ion tracks and its helium density dependence. All the curves are illustrated in equiheight.

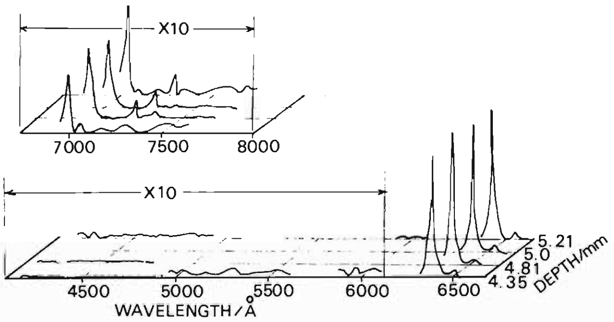

Fig. 2. Depth-resolved and density-dependent luminescence spectra.

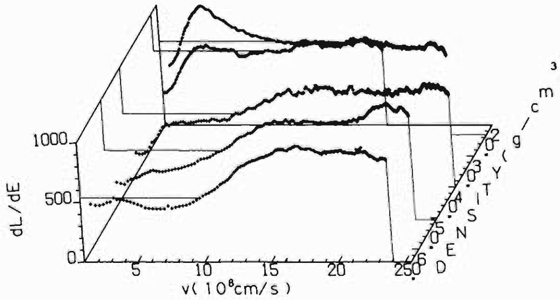

Fig. 3. Luminescence efficienty, *dL*/*dE*, *vs.* ionic velocity and its helium density dependence. All the curves are illustrated in equiheight.

References

1) K. Kimura: *Nucl. Instrum. Methods B*, in press.

RIKEN Accel. Prog. Rep. **24** (1990)

III-4-2. Analytical Formula for the Dose around the Path of an Ion and Its Application

T. Takahashi, F. Yatagai, K. Nakano, and K. Izumo

In an earlier paper,[1)] we applied Butts and Katz's formula (D_{KZ}) of the density of energy delivery (dose) as a function of the distance from the trajectory of an ion to the analysis of inactivation cross sections of *B. subtilis spores, E. coli* B_{s-1}, and *E. coli* B/r. The formula D_{KZ} is very useful, but is based on too simple an assumption that the range of secondary electrons x in a medium is given by $x = kw$, where k is a constant and w is the electron energy. To get a more reliable dose, we used Tabata and Ito's energy deposition algorithm for electrons in water and succeeded in calculating the dose D_T around the path of an ion.[2)] However, the calculation is time consuming, and it is impossible to use the dose D_T, *e.g.*, for the least-squares analysis of the inactivation cross sections of bacteria. We tried to get a formula which gives the dose D_T for heavy ions of energy E between 1 MeV/u and 6 MeV/u. A preliminary formula which gives the dose with sufficient accuracy is as follows:

$$D(r) = \frac{A(E)Z^{*2}}{\beta^2 r(r+\theta)}\left(1 - \frac{r+\theta}{R+\theta}\right)^{P(E)}. \qquad (1)$$

Here, $A(E)$ and $P(E)$ are the energy dependent parameters to be so determined as to reproduce the dose D_T, and r is the distance from the path of an ion. R is the maximum range of δ-electrons, Z^* is the effective charge of the ion, β is the speed of the ion relative to the light velocity, and θ is a constant (4.17×10^{-8} g/cm^2). A value of 1.43 was chosen as $P(E)$ for ions of 1 MeV/u – 6 MeV/u. $A(E)$ was obtained by interpolation so as to fulfil the following relation: the value of $\ln(A(E)/\beta^2)$ is -11.52 at $E = 1$, -12.06 at $E = 1.6$, -12.627 at $E = 2.5$, -13.095 at $E = 4$, and -13.46 at $E = 6$, where E is in MeV/u. The digits at every E are the best values of the quantity to reproduce the dose D_T at corresponding E.

By using the dose distribution given by Eq. 1 the inactivation cross sections of *E. coli* K-12 (*rec*$^+$, *uvr*$^+$) AB1157[3)] was analyzed. Line (1) in Fig. 1 shows a result of least sqares analysis, which was made by the procedure essentially same as that for *B. subtilis* spores in Ref. 1. The radiosensitivity of the strain for nitrogen ion's core $1/E_{in}$ was found to be $3.3/E_\delta$, where E_δ was assumed to be equal to D_{37} for gamma-rays (11.8 krad). This result means that the core of a nitrogen ion is about three times effective in inactivating the bacteria (AB1157) compared with that of δ-electrons. Line (2) shows the result of analysis based on Katz's theory in its original form. Details will be discussed in Ref. 4.

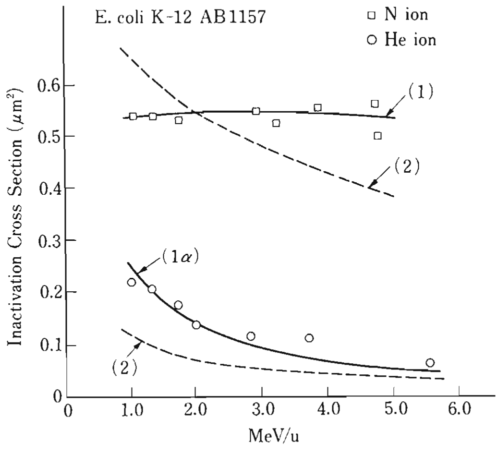

Fig. 1. Inactivation cross sections of *E. coli* K-12 AB1157 as a function of energy of ions. Least squares analysis was made by the dose distribution of Eq. 1. Lines (1) and (1α) were obtained by essentially the same method as in Ref. 1 for the spores, and the optimum geometrical cross section was found to be 0.50 μm^2. Line (2) was obtained from the analysis based on Katz's theory in its original form, and the geometrical cross section was found to be 0.97 μm^2.

References

1) T. Takahashi, F. Yatagai, K. Izumo, S. Konno, and T. Katayama: *RIKEN Accel. Prog. Rep.*, **19**, 138 (1985).
2) T. Takahashi, F. Yatagai, S. Konno, T. Katayama, and I. Kaneko: *Adv. Space Res.*, **6**(11), 117 (1986).
3) F. Yatagai and A. Matsuyama: *Radiat. Res.*, **71**, 259 (1977).
4) T. Takahashi, F. Yatagai, and K. Izumo: Accepted for publication in *Adv. Space Res.*

RIKEN Accel. Prog. Rep. **24** (1990)

III-4-3. Chromosome Fragmentation in Syrian Golden Hamster Embryo Cells Irradiated with Heavy Ions

M. Watanabe, M. Suzuki, K. Suzuki,* and K. Nakano

A conventional chromosome assay can not directly detect chromatin damage in interphase. On the other hand, a premature chromosome condensation (PCC) technique is very sensitive for detecting chromatin damages in interphase cells.[1] Previous reports suggest that the contribution of interphase cell death to the biological effects of heavy ions is larger than in low LET radiations.[1-3] Therefore, we undertook to detect chromosome aberrations as chromatin breaks in interphase cells using a PCC technique and compare with the data obtained by conventional methods.

We used primary Syrian golden hamster embryo (SHE) cells obtained by trypsinization of 13- to 14-old embryos and cultured as previously reported.[4] The procedure for polyethylene glycol (PEG) mediated cell fusion and induction of PCC have been described in detail elsewhere.[1] As far as irradiation with IPCR Cyclotron beam, dosimetry and irradiation procedures were carried out according to methods described elsewhere.[2,3]

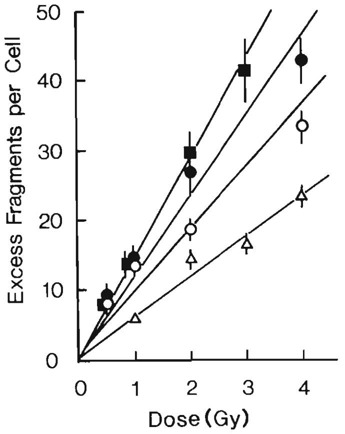

Fig. 1. Dose-response curves for the induction of PCC in SEH cells irradiated with ^{14}N ions (LET=530 keV/μm) (■), ^{4}He ions with a 100-μm Al absorber (LET=77 keV/μm)(●), ^{4}He ions without an absorber (LET=36 keV/μm)(○), and ^{137}Cs gamma rays (△).

The induction rate of chromatin breaks with heavy ions in PCC was higher than that with ^{137}Cs gamma rays (Fig. 1). The relative biological effectiveness (RBE) to ^{137}Cs gamma rays was 2.4 for ^{14}N ions (LET=530 keV/μm), 1.8 for ^{4}He ions with a 100-μm Al absorber (LET=77 keV/μm), and 1.4 for ^{4}He ions without an absorber (LET=36 keV/μm). The rejoining kinetics of the PCC fragments with heavy ions clearly differs from that with gamma rays (Fig. 2). About 95% of the PCC fragments induced by gamma rays rejoined within 8 hours of post-irradiation incubation. For heavy ions, however, only 35 to 45% of fragments rejoined. These results suggest a qualitative difference in chromatin damage caused between heavy ions and gamma rays.

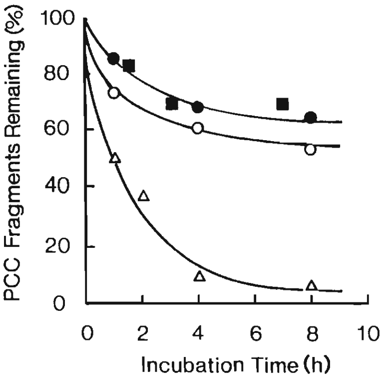

Fig. 2. Repair kinetict of PCC breaks as a function of post-irradiation incubation in SHE cells irradiated with 2 Gy of radiations. Symbols are the same as Fig. 1.

References

1) C.A. Waldren and R.T. Johnson: *Proc. Natl. Acad. Sci. USA*, **71**, 1137 (1974).
2) M. Suzuki, M. Watanabe, K. Suzuki, K. Nakano, and I. Kaneko: *Radiat. Res.*, **120**, 468 (1989).
3) K. Suzuki, M. Suzuki, K. Nakano, I. Kaneko, and M. Watanabe: *Int. J. Radiat. Biol.*, **58**, 781 (1990).
4) M. Watanabe, M. Horikawa, and O. Nikaido: *Radiat. Res.*, **98**, 274 (1984).

---

* Yokohama City University.

RIKEN Accel. Prog. Rep. 24 (1990)

III-4-4. Studies on Induced Mutations by Ion Beams in Plants

H. Nakai, H. Watanabe, Y. Kobayashi, T. Asai,* and S. Kitayama

We have been engaged in studies on radiobiological effects of thermal neutrons on higher plants. We found that the relative bioligical effectiveness (RBE) of thermal neutrons relative to γ-rays is more than 10 and that the mutagenic effects of thermal neutrons on various agronomic traits in rice is significantly higher than that of low LET radiations, *e.g.* γ rays.[1,2] Referring to the above results, this study was started to make clear the mechanism of mutations induced by ion beams and to evaluate the use of ion beams for mutation breeding of crop plants.

A preliminary investigation was conducted to find the ion-beam sensitivity of rice and the appropriate dosage of an ion beam for induction of mutations for practically useful traits. Dry seeds of rice, *Oryza sativa* L., a variety Harebare, were irradiated with an ion beam of O_2^+ of 135 MeV/n from the Ring Cyclotron to a dose of 0-100Gy. Irradiated seeds were sown to be germinated in petri-dishes at room temperature. Two weeks later, the root length and seedling height were measured; the result is presented in Fig. 1. The dose-response curves for both root length and seedling height were of a typical one-hit type, which is generally seen for high LET radiations. The Degree of M_1 (the first generation after mutagen treatment) damage in root length was found to be higher than that in seedling height. This result is explained on the basis that the damage for root length was caused mainly by chromosome aberration, whereas that for seedling height was caused mainly by some physiological event. All the seedlings were killed by irradiation to a dose exceeding 100 Gy. M_1 plants survived were grown in an experimental rice field of the Shizuoka University and are currently analyzed of damage at their mature stage. Analysis of mutations on the M_2 plants is conducted next year.

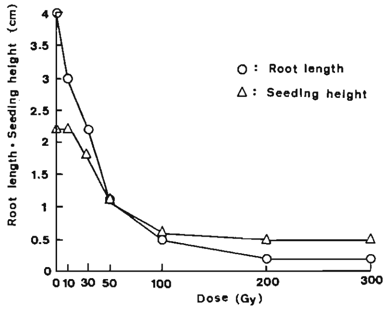

Fig. 1. Effects of irradiation of O_2^+ to seeds of rice variety Harebare on the root length and seedling height in M_1 generation.

References

1) H. Nakai, M. Saito, and H. Yamagata: *Environ. Exp. Bot.*, **20**, 191 (1980).
2) H. Nakai and M. Saito: *ibid.*, **25**, 385 (1985).

---

* Faculty of Agriculture, Shizuoka University.

RIKEN Accel. Prog. Rep. **24** (1990)

III-5. Instrumentation

1. Design of a Microbeamline for a Compact Cyclotron

N. Nakanishi and H. Y. Yoshida*

As extensions of the particle induced X-ray emission analysis (PIXE) and the Rutherford backscattering spectrometry (RBS), which have been extensively used as typical ion beam analysis methods, a micro PIXE and an RBS become more popular recently because of their high space resolution. The installation of microbeamlines have been required in many facilities.[1]

A microbeamline was designed for 1.8 MeV protons and 7.2 MeV alpha particles from the compact cyclotron produced by JSW. The goal of the design was to obtain a beam intensity of 100 pA in a beam spot size of $10\mu m \times 10\mu m$ under constrains (1) the whole length of the system was less than about 3500 mm, and (2) the working space between the last element and the target was more than 200 mm.

So far, a number of microbeamlines have been constructed in many research laboratories; however few microbeamlines were constracted for cyclotron beams. It is mainly due to the difficulty for using poor quality beams from cyclotron relative to that from electrostatic acceleraters.

Before the calculation we measured horizontal and vertical emittances of proton and alpha beams from the cyclotron to know the relation between the resultant beam emittance and the intensity included in phase ellipses. We then surveyed a magnet setting possibility to satisfy the present goal by first-order ion optics calculations. The ion optics computer code TRANSPORT was used.[2]

With a quadrupole doublet, the desirable demagnification factors could not obtained. Because of the poor emittance of the beams, resultant intensity was much lower than required. In order to realize the goal, we investigated systems composed of three quadrupole magnets. A large acceptance being indispensable for the system, it was difficult to get small 2nd-order intrinsic aberrations. In order to get the 1st-order abberation coefficients as small as possible, we used a triplet consisted of quadrupole magnets with a different effective length and a different field gradient. The field gradient of these quadrupole magnets was set to be less than 3 KG/cm in view of technical considerations. Calculated beam envelopes in horizontal and vertical planes are shown Fig. 1. The objective aperture is formed by two pairs of slits and beams are defined by subsidiary slits at 2.5 m from the object point. Figure 2 shows the beam intensity as a function of the vertical half width of the beam spot at the target position. We obtain a result that the beam intensity is 100 pA in a beam spot of 8.5 μm(H)×9.2 μm(V). The whole length of the system and the image distance are 3550 mm and 220 mm, respectively. The specification of the beamline are summarized in Table 1, and the layout of the system is shown in Fig. 3. The beamline will be completed by the end of 1990.

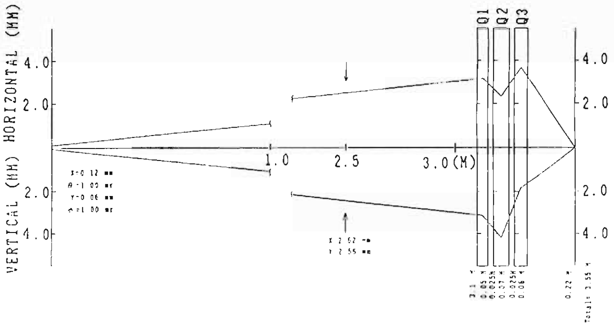

Fig. 1. Beam envelopes in horizontal and vertical planes.

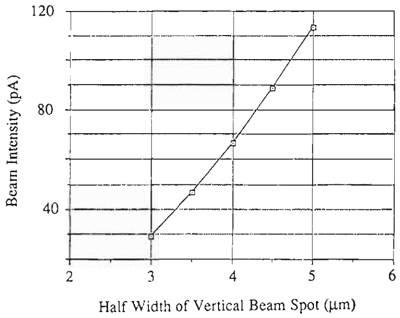

Fig. 2. Expected beam intensity as a function of their vertical half width a of beam spot at a target.

---

* Japan Steel Work Ltd. (JSW).

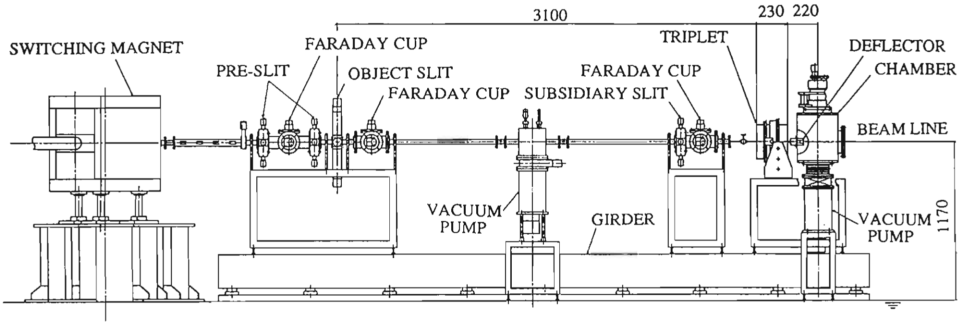

Fig. 3. Schematic diagram of the microbeamline system.

Table 1. Specification of the microbeamline.

Beam characteristics	
Accelerater	cyclotron
Ion	1.8 MeV p 7.2 MeV alpha
Acceptance	0.12 mm mrad(H) 0.06 mm mrad(V)
Momemtum spread	0.1%
Microbeamline characteristics	
Beam width	8.5 μm(H) 9.2 μm(V)
Beam intensity	100 pA
Q-magnet length	500 mm(Q1), 70 mm(Q2), 60 mm(Q3)
Field gradient	1.46 Kg/cm(Q1), 2.90 KG/cm(Q2), 2.97 KG/cm(Q3)
Object distance	3100 mm
Image distance	220 mm
Whole length	3550 mm

References

1) G.W. Grime and F. Watt: Beam Optics of Quadrupole Probe-Forming Systems, Adam Hilger, Bristol (1984).

2) K.L. Brown, F. Rothacker, D.C. Carey, and Ch. Iselin: SLAC91 Rev. 2 UC-28.

RIKEN Accel. Prog. Rep. **24** (1990)

III-5-2. Design of a Decay Muon Channel Using an Axially Symmetric Magnetic Field for a Pion Injector

K. Ishida, T. Matsuzaki, and K. Nagamine

A beam transportation system with an axially symmetric magnetic field may be used for achieving one order larger solid angle than conventional systems using magnetic dipoles and quadrupoles. We have designed a powerful decay muon channel which uses superconducting coils producing this type of symmetric field as a pion injector and a superconducting solenoid as a $\pi\mu$ decay section. One example of the design calculation is shown in Fig. 1. The pion momentum was set to be 150 MeV/c. The pion source distribution (square of 2 cm×2 cm), the pion emission angle (10-45 degree), and the time and the angle of $\pi\mu$ decay were Monte-Carlo generated. The number of transmitted muons originating from pions with a large emission angle in the range of 10-45 degrees ("large solid angle injection") was compared with that from pions with a small emission angle of 0-10 degree ("small angle injection"). The latter case was intended to simulate a small divergence injection with conventional systems. Figure 2 shows the calculated muon intensity at the exit of the solenoid decay section as a function of the muon emission angle for both cases. We can conclude that the large solid angle system can be used for generating nearly one order more muons than conventional ones. More detailed design work aiming at reducing stray field on a pion production target and reducing neutron background is now in progress.

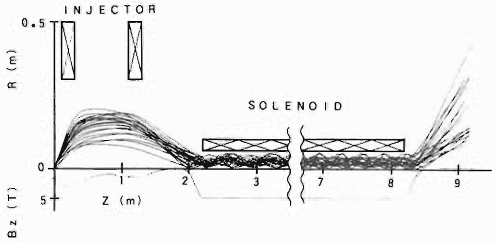

Fig. 1. An example of the design calculation of a high acceptance pion injecetor for decay muon channel. The field distribution is shown on the lower side. Trajectories of pions (emission angle 10-45 degrees) surviving as muons are shown on the upper side.

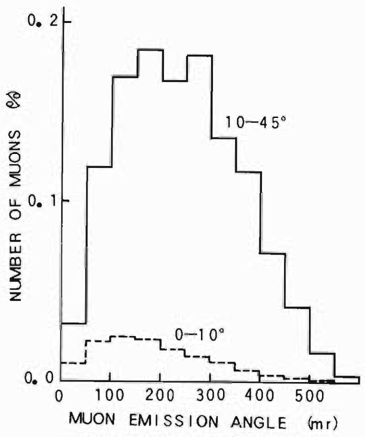

Fig. 2. Angular distribution of muons at the exit of the solenoid decay section. Vertical axis shows the number of muons divided by the pion intensity at the source. The solid line is the case for the muons originating from pions with an emission angle in the range of 10-45 degree. The broken line is for those from pions in the range of 0-10 degree.

RIKEN Accel. Prog. Rep. **24** (1990)

III-5-3. Development of an Induction Accelerator for the Heidelberg Test Storage Ring

C. Ellert,* D. Habs,* E.Jaeschke,* T. Kambara,
W. Petrich,* D. Schwalm,* P. Sigray,** and A. Wolf*

An induction accelerator was constructed and employed at a heavy-ion storage ring (Test Storage Ring: TSR) in the Max Planck Institute for Nuclear Physics, Heidelberg, as a universal device for energy tuning of stored ions, beam diagnostics, and storage-ring optimization. The accelerator was designed to vary the energy of ions within the acceptance of the TSR. The induction accelerator is especially suitable for experiments with cooled ion beams because its quasistationary accelerating field does not change the energy distribution during acceleration.

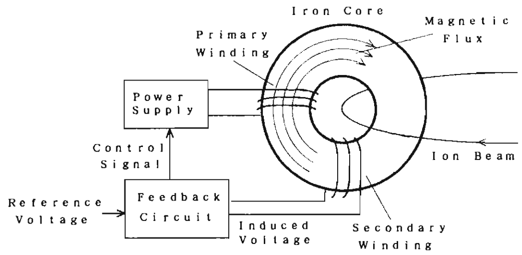

Fig. 1. Schematic drawing of the induction accelerator.

A schematic representation of the induction accelerator is shown in Fig. 1. Its principle of operation is similar to that of a transformer: A stored ion beam represents the secondary winding. A change in the current in the primary winding, which encloses a doughnut-shaped core, gives rise to a change in the magnetic flux Φ in the core. An electric field V_{acc} is induced along a closed path passing through the hole of the core:

$$V_{acc} = \oint \vec{E}\, d\vec{s} = -\frac{d\Phi}{dt} \qquad (1)$$

The stored ions repeatedly pass through the hole of the core and changes their energy by qeV_{acc} per each turn. When the flux varies from Φ_1 to Φ_2 during a time interval T and the change of the orbital frequency f is negligible, the energy gain dE is given by

$$dE = qe\int_0^T f\frac{d\Phi}{dt}dt = qef \times (\Phi_2 - \Phi_1) \qquad (2)$$

The energy gain is independent of the specific way that the flux Φ is changed. The maximum relative energy change dE/E is between 5×10^{-2} and 5×10^{-3} in the present case.

The induction accelerator consists of an iron core, a power supply, and a feedback system. The core is made of isolated and glued 1 mm-thick iron sheets with an octagonal shape with a hole with the same shape. The outer radius is about 0.64 m, the hole radius is about 0.15 m, and the length along the beam line is 0.3 m. This gives an estimate of the total flux change of about 0.4 Vs if the magnetic flux density is swung between saturations at ±1.5 T. The beam tube of the TSR passes through the hole of the core, interrupted by a ceramic gap in order to isolate the two sides of the beam tube from each other. The primary coil is wound around two opposite sides of the core, with the number of winding between 10 and 100 and is connected to a remote-controllable regulated power supply.

In many applications, it is important to induce a constant acceleration voltage for a given period of time. Since the magnetic flux is a strongly nonlinear function of the primary current, it is necessary to regulate the current to induce a constant voltage. We fabricated a feedback system which compares an induced voltage picked up by a secondary winding to a reference voltage and controls the power supply.

The first test of the induction accelerator showed that it offers a simple way to tune the energy of a stored ion beam within a moderate time and without a change of the velocity distribution.

The induction accelerator has been used successfully in the laser-cooling experiments of Li^+ and Be^+, and in the measurement of the cooling force of an electron cooler.

---

* Physikalisches Institut der Universität Heidelberg and Max-Planck-Institut für Kernphysik, D-6900 Heidelberg, Germany.

** Manne Siegbahn Institutet För fysik, S-104 05 Stockholm, Sweden.

RIKEN Accel. Prog. Rep. **24** (1990)

III-5-4. Status of the Radioactive Beam Facility RIPS

T. Kubo, M. Ishihara, N. Inabe, T. Nakamura, H. Okuno, K. Yoshida,
H. Kumagai, S. Shimoura, K. Asahi, and I. Tanihata

We have completed a radioactive beam facility names RIPS (RIKEN Projectile-fragment Separator)[1,2] in order to facilitate experimental studies on and using radioactive nuclei.

RIPS has been designed to be an achromatic beam line so that it can analyze and transport secondary radioactive beams. The projectile fragmentation mechanism is used to convert a primary beam into radioactive beams, because it has various useful features such as large cross sections and good kinematical properties. In addition to magnetic analysis, a technique called momentum loss achromat[3] is used to separate radioactive beams, a technique which allows separation by the combination of magnetic analysis and energy loss.

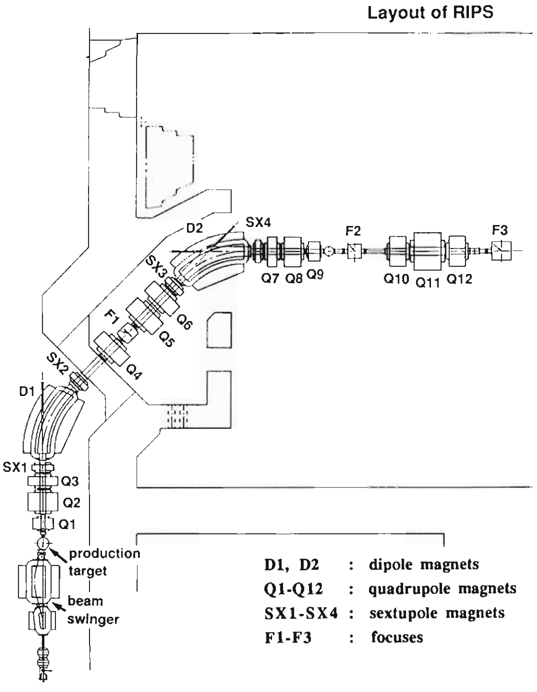

Fig. 1. Layout of the Radioactive Beam Facility RIPS.

Figure 1 schematically shows the layout of the beam line, whose configuration can be abbreviated as Q-Q-Q-SX-D-SX-Q-Q-Q-SX-D-SX-Q-Q-Q-Q-Q-Q, where Q, D, and SX represent quadrupole, dipole, and sextupole magnets, respectively. The beam line can be divided into three sections by intervening focuses. The first analyzing section, consisting of Q-Q-Q-SX-D-SX-Q, gives dispersive focusing at F1. The velocity conservation in projectile fragmentation allows the separation at F1 according to A/Z of radioactive nuclei. The second section, consisting of Q-Q-SX-D-SX-Q-Q-Q, serves as a dispersion compensating section and gives doubly achromatic focusing at F2. The use of an energy degrader at F1 provides an additional separation scheme according to the energy loss difference depending on $A^{2.5}/Z^{1.5}$ of radioactive nuclei. The property of the momentum loss achromat is achieved by using an achromatic energy degrader.[3] The quadrupole triplet Q-Q-Q at the final section gives the third focus (F3) at an open space of downstream, where experimental devices can be easily accomodated under better shielding conditions. The sextupole magnets at the entrance and exit of each dipole magnet correct optical aberrations to optimize isotopic separation power and beam size.

The basic characteristics of RIPS are summarized in Table 1. In comparison with the existing facilities,[4] RIPS has two improved features so as to enlarge the capability of radioactive beams. The first feature is the capability of producing a strong beam intensity, which is achieved by adopting wide acceptances and large magnetic rigidity ($B\rho$). The acceptances in angle and momentum are taken to be 80 mr (circle) and 6%, respectively, corresponding to more than half of spreading widths of typical projectile fragments. The maximum $B\rho$ is taken to be about 165% compared with that of RIKEN Ring Cyclotron. This large $B\rho$ allows us to use the maximum incident energy even for extremely neutron-rich nuclei, so that we can take an advantage of the thickest possible targets and better kinematical conditions. The second characteristic feature of RIPS is the possibility to produce spin-polarized radioactive beams by means of the reac-

Table 1. Basic characteristics of RIPS.

Configuration	Q-Q-Q-SX-D-SX-Q (first stage) Q-Q-SX-D-SX-Q-Q-Q (second stage) Q-Q-Q (third stage)
Angular acceptance	80 mr, circle
Solid angle	5 msr
Momentum acceptance	6 %, for full angular acceptance
Max. magnetic rigidity	5.76 Tm, 65% larger than that of the cyclotron
Focuses	F1, dispersive, 2.4cm/%, end of first stage F2, double achromatic, end of second stage F3, double achromatic, end of third stage
Flight path length from production target	10.4 m to F1, 21.3 m to F2, 27.5m to F3
Isotopic separation	A/Z and energy loss
Goal of mass resolution (F2)	$A/\Delta A$ > 100, for achromatic energy degrader
Beam swinger	max. 15 degrees

tion process itself. For this purpose, a beam swinger has bean installed ahead of a production target, enabling us the collection at finite angles.

The construction of RIPS was completed in the summer of 1989. After test experiments to confirm the basic performance, it started to provide radioactive beams for a variety of experiments in the beginning of 1990.

Two characteristic features of RIPS have been already confirmed. The intensity of radioactive beams was found to be more than 100 times stronger than that of the existing facilities. We expect the intensity of the order of 10^4 pps even for neutron dripline nuclei such as ^{11}Li. Such intense beam will certainly enable a new regime of experiments such as secondary reaction studies on radioactive nuclei. The production of spin-polarized radioactive beams through the reaction process has also been found to be possible and universal at intermediate energies. The observed spin-polarization is fairly large, reaching about 5–20%. This feature of RIPS, together with a strong beam intensity, will open up new fields using spin-polarized radioactive nuclei.

More detailed reports on RIPS are given in this volume.

References

1) T. Kubo *et al.*: Proc. 1st Int. Conf. on Radioactive Nucl. Beams, World Scientific, Singapore, p. 563 (1989).
2) T. Kubo and M. Ishihara: Proc. 2nd IN2P3-RIKEN Symp. on Heavy-ion Collisions, World Scientific, Singapore, p. 40 (1990).
3) J.P. Dufour *et al.*: *Nucl. Instrum. Methods*, **A248**, 267 (1986).
4) R. Anne *et al.*: *ibid.*, **A257**, 215 (1987) and see references in Proc. 1st Int. Conf. on Radioactive Nucl. Beams, World Scientific, Singapore (1989).

RIKEN Accel. Prog. Rep. **24** (1990)

III-5-5. Characteristics of Magnetic Elements in RIPS

T. Nakamura, T. Kubo, H. Takebe, K. Yoshida, I. Tanihata, and M. Ishihara

Magnets in the radioactive beam line RIPS[1)] are composed of 2 dipole magnets, 12 quadrupole magnets, and 4 sextupole magnets. The magnetic system is designed to bend and focus charged particles with a magnetic rigidity up to 5.76 T•m. Specifications of the magnets are determined to satisfy required optics and acceptances (angular acceptance: 5 msr., momentum acceptance: 6%).

Table 1. Characteristics of dipole magnets in RIPS.

	Pole gap (cm)	Central trajectory radius (m)	Bending angle (degree)	Pole tilted angle(degree)		Max. field (kG)
				entrance	exit	
D1	14.0	3.6	45.0	0.0	+19.6	16.0
D2	14.0	3.6	45.0	0.0	0.0	16.0

The dipole magnets are identical H-type magnets except for a tilted angle at the exit. Their specifications are shown in Table 1. In order to minimize the change in the effective boundaries of the magnets due to excitation characteristics, the pole edges of the magnets are cut according to Rogowski's curve. The effective boundary of each dipole is made equal to its real boundary by adjusting field clamps.

The specifications of the quadrupole magnets are shown in Table 2. The pole shapes are determined to avoid saturation effects in iron caused by high magnetic fields to attain a strong focus.

Table 2. Characteristics of quadrupole magnets in RIPS.

Magnet	Bore radius (mm)	Real length (mm)	Effective length (mm)	Max. field gradient (kG/cm)	Polarity
Q1	62.0	500	542	1.41	H
Q2	86.0	800	857	1.05	V
Q3	86.0	400	459	0.98	H
Q4	120.0	600	673	0.55	H
Q5	120.0	700	769	0.64	V
Q6	120.0	600	673	0.55	H
Q7	86.0	400	459	0.94	V
Q8	86.0	700	755	0.94	H
Q9	62.0	500	542	1.21	V
Q10	86.0	700	764	0.94	V
Q11	120.0	1100	1168	0.65	H
Q12	86.0	700	764	0.94	V

The specifications of the sextupole magnets are shown in Table 3; the magnets are geometrically identical to each other.

The excitation characteristics and the effective lengths of all the magnets are obtained by measurements using a hall probe calibrated by

Table 3. Characteristics of sextupole magnets in RIPS.

Magnet	Bore radius (mm)	Real length (mm)	Effective length (mm)	Max. field gradient (G/cm^2)
SX1	125.0	250	286	10.0
SX2	125.0	250	286	22.0
SX3	125.0	250	286	30.0
SX4	125.0	250	286	18.5

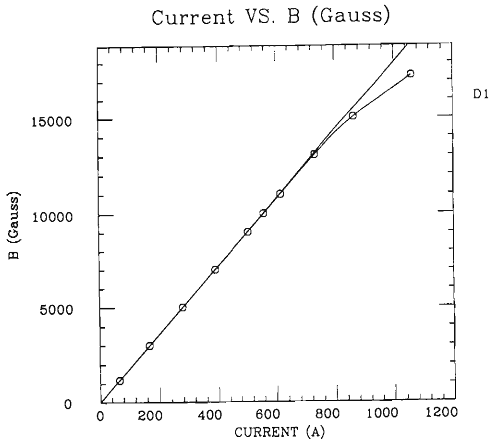

Fig. 1. Excitation curve for D1 magnet (the upstream dipole magnet).

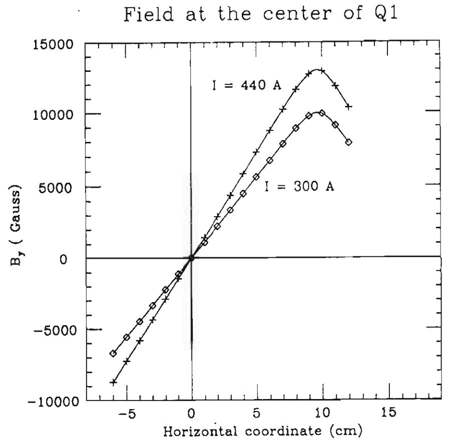

Fig. 2. Field distribution at the center of Q1.

an NMR probe. Designed specifications are found to be satisfied for all the magnets. Figures 1 and 2 show some results from the measurements. Figure 1 shows the excitation curve for the D1 magnet, indicating that the maximum field reaches 1.7 T which is higher than the designed value (1.6 T). Figure 2 shows the field distribution of the Q1 magnet. In an operational region which is less than 70mm in the x coordinate, linearity is guaranteed. These parameters are used for optics calculation and for initial setting of currents in the magnets.

References

1) T. Kubo *et al.*: This Report, p. 96.

RIKEN Accel. Prog. Rep. **24** (1990)

III-5-6. Control System of RIPS

N. Inabe, T. Kubo, I. Tanihata, and M. Ishihara

The computer control system of the radioactive beam line RIPS[1] has been developed. By the system, we control all devices of RIPS summarized in Table 1.

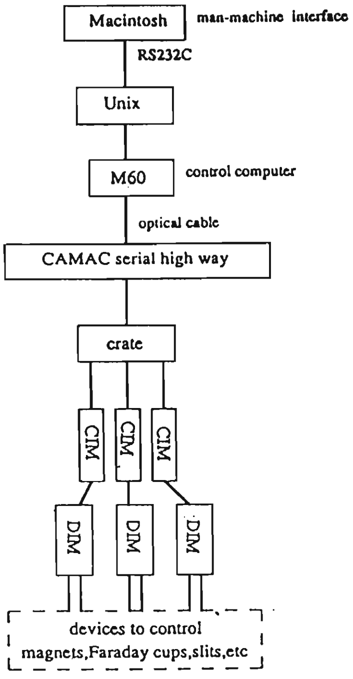

Fig. 1. Block diagram of computer control system of RIPS.

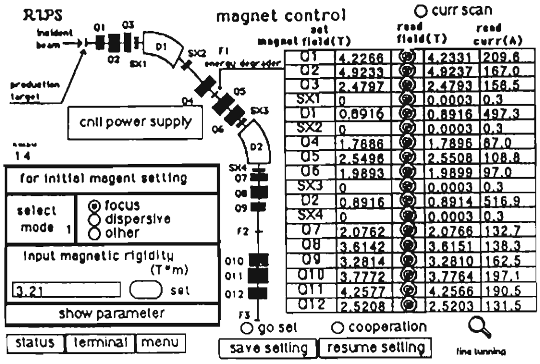

for initial magent setting

select mode 1
◉ focus
○ dispersive
○ olher

input magnetic rigidity (T*m)
3.21
set

show parameter

status | terminal | menu

	set magnet field(T)		read field(T)	read curr(A)
Q1	4.2266	◉	4.2331	209.6
Q2	4.9233	◉	4.9237	167.0
Q3	2.4797	◉	2.4793	156.5
SX1	0	◉	0.0003	0.3
D1	0.8916	◉	0.8916	497.3
SX2	0	◉	0.0003	0.3
Q4	1.7886	◉	1.7896	87.0
Q5	2.5496	◉	2.5508	108.8
Q6	1.9893	◉	1.9899	97.0
SX3	0	◉	0.0003	0.3
D2	0.8916	◉	0.8914	516.9
SX4	0	◉	0.0003	0.3
Q7	2.0762	◉	2.0766	132.7
Q8	3.6142	◉	3.6151	138.3
Q9	3.2814	◉	3.2810	162.5
Q10	3.7772	◉	3.7764	197.1
Q11	4.2577	◉	4.2566	190.5
Q12	2.5208	◉	2.5203	131.5

○ go set ○ cooperation

save setting | resume setting

Fig. 2. An example of a HyperCard, which controls all magnets of RIPS. After input a magnetic rigidity and pushing a button "set", clicking a button "go set" currents of all magnets are set. Every card gives information on the positions of devices to be controlled graphically.

Table 1. Devices under control.

Target chamber	a profile monitor for a primary beam (single-wire type) a Faraday cup a beam viewer (ZnS) and targets a collimator for defining acceptance angle an incident angle monitor for a primary beam
F1 chamber	a profile monitor for a primary beam a collimator for defining momentum acceptance a collimator for selecting several different momenta a position sensitive gas counter (PPAC)
F2 chamber	a profile monitor for a primary beam a Faraday cup a position sensitive gas counter (PPAC) a silicon detector for ΔE measurement a collimator for defining image of a secondary beam
others magnets	a primary beam stopper in D1 magnet 2 dipole magnets 12 quadrupole magnets 4 sextapole magnets beam swinger

Figure 1 is the flow chart of the control system. To control the devices we use an Unix-Melcom60-CIM-DIM system, the same as the control system for RIKEN Ring Cyclotron.[2] For easy control we have developed a man-machine interface, using a Macintosh. For communication between the Unix system and the Macintosh through an RS232C port, we use a HyperCard with a hypertalk (Macintosh application) on the Macintosh. Using the HyperCard, we can also see the location of every device as a picture on Macintosh screen. Figure 2 shows an example of the man-machine interface part.

References

1) T. Kubo, M. Ishihara, N. Inabe, T. Nakamura, H. Okuno, K. Yoshida, H. Kumagai, S. Shimoura, K. Asahi, and I. Tanihata: This Report, p. 96.
2) H. Takebe, T. Wada, M. Kase, T. Kambara, and H. Kamitsubo: "Control system of the RIKEN Ring Cyclotron", Control system Workshop, Tsukuba, Nov. (1987).

RIKEN Accel. Prog. Rep. **24** (1990)

III-5-7. Yield Study of Radioactive Beams of RIPS

N. Inabe, T. Kubo, T. Nakamura, H. Okuno, S. Shimoura, K. Asahi
K. Yoshida, H. Kumagai, I. Tanihata, and M. Ishihara

The yield of radioactive beams in radioactive beam line, RIPS,[1] have been measured on the achromatic second focal plane of RIPS for ^{18}O (100 MeV/u), ^{15}N(112 MeV/u)+^{9}Be(1.1 g/cm^2) reactions. Target thickness was selected to give an optimal yield.

A beam was identified from the energy loss in SSD and time-of-flight (TOF) between a parallel plate avalanche counter (PPAC) and RF of the Ring Cyclotron. Figure 1 shows an example of a ΔE-TOF plot for particle identification, magnet rigidity being set at 3.73 Tm, that is, match to that of ^{14}B in the reaction $^{18}O+^{9}Be$. This figure shows good separation of each beam. To get the yield of every radioactive beam, the effiency of PPAC and the dead time of a computer should have been corrected.

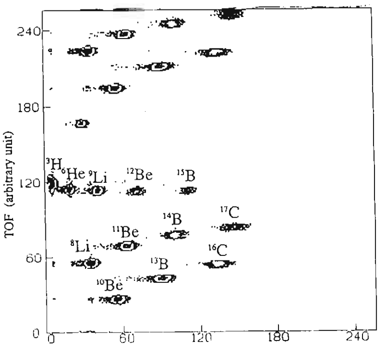

Fig. 1. Particle identification spectrum in the ^{18}O+Be (1.1 g/cm^2) reaction at 100 MeV/u. A horizontal axis is energy loss in a 500 μm SSD and a vertical axis is TOF between PPAC and RF. Both scales are arbitrary.

Table 1 summarizes the yield of each radioactive beam per 1pnA and the ratios of each radioactive beam to a primary beam, comparing with those of obtained at LISE in GANIL.[2] The yields of neutron rich nuclei radioactive beams of RIPS are more than 100 times of that of LISE at GANIL. One reason is that RIPS has a large angular and momentum acceptance ($\Delta\Omega$=5 msr, $\Delta p/p=\pm3\%$), the other is that RIPS has a large maximum rigidity (5.76 Tm-this value is corresponding to the rigidity of about 100 MeV/u ^{11}Li) to collect neutron rich radioactive beams even in the ~100 MeV/u region where kinematical focusing is better in projectile fragmentation and a production target is thicker.

Table 1. Yields of secondary beams of RIPS.

Reaction	Fragments	pps/paA$^{a)}$	I/I_0	I/L_0 at LISE^{P}
100 MeV/u ^{18}O	^{16}C	1.4×10^{5}	2.2×10^{-5}	2×10^{-6} $^{d)}$
+	^{14}B	1.1×10^{4}	1.8×10^{-6}	2×10^{-8} $^{d)}$
1.1 g/cm^2 Be	^{15}B	4.9×10^{3}	7.8×10^{-7}	2×10^{-9} $^{c)}$
	$^{12}B_e$	1.3×10^{4}	2.1×10^{-6}	10^{-8} $^{c)}$
	$^{14}B_e$	7.5×10 $^{b)}$	1.2×10^{-8} $^{b)}$	
	^{9}Li	3.7×10^{4}	5.9×10^{-6}	2×10^{-8} $^{c)}$
	^{11}Li	3.5×10^{2}	5.6×10^{-8}	2.5×10^{-10} $^{f)}$
	$^{8}H_e$	2.7×10^{3} $^{b)}$	4.3×10^{-7} $^{b)}$	
112 MeV/u ^{15}N	^{13}B	1.5×10^{4} $^{c)}$	2.4×10^{-6} $^{c)}$	
+	$^{11}B_e$	9.8×10^{3} $^{c)}$	1.6×10^{-6} $^{c)}$	
1.1 g/cm^2 B$_e$	$^{12}B_e$	7.3×10^{3}	1.2×10^{-6}	
	^{9}Li	3.8×10^{4}	6.1×10^{-6}	
	^{11}Li	4.2×10^{2}	6.8×10^{-8}	

$\Delta B\rho/B\rho=6\%$, $\Omega=5$ msr.
data presented in RIKEN IN2P3 symp. (1987) by R. Bimbot.
a) particles/s/particle-nA. b) $\Delta B\rho/B\rho=4.2\%$. c) $\Delta B\rho/B\rho=2\%$.
d) 65 MeV/u ^{18}O+567 mg/cm^2 Be, $\Delta B\rho/B\rho=3.4\%$, $\Omega=1$ msr.
e) 45 MeV/u ^{18}O+187 mg/cm^2 Be, $\Delta B\rho/B\rho=3.4\%$, $\Omega=1$ msr.
f) 45 MeV/u ^{22}Ne+417 mg/cm^2 Ta, $\Delta B\rho/B\rho=3.4\%$, $\Omega=1$ msr.

Because the usual intensity of the primary beam from RRC is 100pnA, we expect that we get about 270 kcps for ^{8}He, 35 kcps for ^{11}Li and 7.5 kcps for ^{14}Be from these yield measurements. From this result, we confirm the possibility to study neutron drip-line nuclei through secondary reactions.

References

1) T. Kubo, M. Ishihara, N. Inabe, T. Nakamura, H. Okuno, K. Yoshida, H. Kumagai, S. Shimoura, K. Asahi, and I. Tanihata: This Report, p. 96.
2) R. Bimbot: Proc. RIKEN-IN2P3 Symp. on Heavy-Ion Collisions, Shimoda, p. 48 (1987).

RIKEN Accel Prog. Rep. **24** (1990)

III-5-8. Performance of Isotopic Separation in RIPS

T.Nakamura, T.Kubo, S.Shimoura, H.Okuno, N.Inabe, K.Yoshida, H.Kumagai, I.Tanihata, K.Asahi, and M.Ishihara

To study the performance of isotopic separation in a radioactive beam line, RIPS,[1] we have carried out an experiment on the production of radioactive fragments ^{14}B and ^{16}C, using 100 MeV/u ^{18}O beams from RIKEN Ring Cyclotron. The target used was a 277 mg/cm beryllium plate.

Fragments ^{14}B and ^{16}C were selected according to the condition shown in Table 1. Particle identification for these isotopes was performed by measuring the energy loss in a 400-μm silicon detector at the achromatic focal plane (F2) and a time of flight between a PPAC (parallel plate avalanche counter) located at F2 and RF signals of RIKEN Ring Cyclotron. Figure 1 shows beam profiles at F2 and Fig. 2 the projection to the horizontal direction, which are observed by the PPAC. The left focusing image corresponds to ^{14}B and the right one ^{16}C. The displacement and the size of images (FWHM) of two images are also shown in Fig. 2. The displacement is consistent with the designed value of dispersion in the second stage in RIPS (described as D_2), which is 375 cm. The value of D_2 is used for determining mass dispersion D_A by

Table 1. The experimental condition for studying isotopic separation in RIPS. $B\rho_1$, the magnetic rigidity for the first stage, which is optimized for ^{14}B; $B\rho_2$, the magnetic rigidity for the second stage, which is optimized for ^{14}B and ^{16}C; d_0, the thickness of the degrader in the central ray; λ, a parameter in the range formula;[2] R_0, ranges in the degrader.

Magnets	$B\rho_1$	4.02	(T·m)
	$B\rho_2$	3.67	(T·m)
Degrader	$d_0 = 1.365$ g/cm² Aluminum		$\lambda = 3.48$
Isotope		^{14}B	^{16}C
	R_0(g/cm²)	5.15	4.81
	d_0/R_0	0.265	0.284

$$D_A = D_2 \frac{d_0/R_0}{1-d_0/R_0}\frac{1-\lambda}{\lambda} \qquad (1)$$

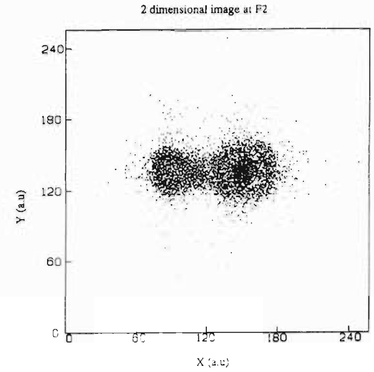

Fig. 1. 2-Dimensional profile of F2 detected by PPAC, tuned for ^{15}B (left) and ^{16}C (right).

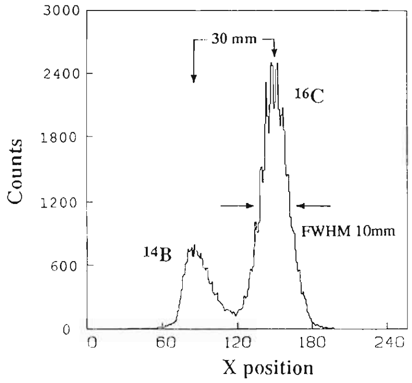

Fig. 2. Horizontal projection of the profile of F2 (Fig. 1), tuned for ^{15}B (left) and ^{16}C (right).

The mass resolving power is thus obtained as

$$|A/\Delta A| = 1.1 \times 10^2 \qquad (2)$$

We may conclude that resolving power $|A/\Delta A| \geq 100$ is achieved without any second order correction.

References

1) T. Kubo *et al.*: This Report p. 96.
2) K.-H. Schmidt, E. Hanelt, H. Gaissel, G. Muenzenberg, and J.P. Dufour: *Nucl. Instrum. Methods*, **A260**, 287 (1987).

RIKEN Accel. Prog. Rep. 24 (1990)

III-5-9. Test Experiment of the GARIS/IGISOL

K. Morita, T. Nomura, A. Yoshida, T. Inamura, M. Koizumi,
M. Fujioka, T. Shinozuka, H. Miyatake, K. Sueki, H. Kudo,
Y. Nagai, K. Yoshimura, and T. Toriyama

We constructed an isotope separator on-line (ISOL) at the E1 experimental hall of the RIKEN Ring Cyclotron (RRC) facility. Since the ISOL consists of a gas-filled recoil isotope separator (GARIS) and an ion-guide type isotope separator on-line (IGISOL), we call the system as GARIS/IGISOL. The GARIS/IGISOL will provide us with short-lived isotopes which will be produced by nuclear reactions with high-energy heavy-ion beams from RRC for the study of spectroscopic features of these isotopes. The construction and the general specifications of the system were reported in Ref. 1.

The GARIS consists of three magnets of a D-Q-Q configuration. The shape of the pole piece of a D-magnet and the geometrical setup of magnets are shown in Fig. 1 together with a beam trajectory obtained by first order calculation. The characteristics of the system as a magnetic spectrograph are listed in Table 1. Solid angular acceptances were measured with use of ^{241}Am α-source, and their values are listed also in Table 1.

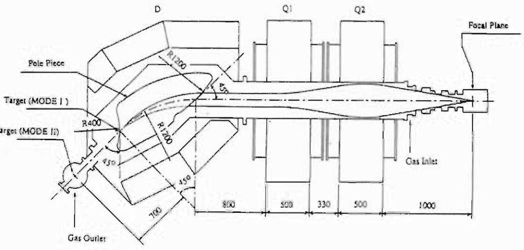

Fig. 1. Geometrical setup of GARIS. A trajectory calculated is shown.

Table 1. Characteristics of GARIS as a spectrograph.

	Mode I	Mode II
Target position	Pole boundary	Center of the scattering chamber
Total length of the trajectory	4.07 m	4.77 m
Trajectory length in the magnetic field	1.94 m	1.94 m
Dispersion	0.20 cm/%	0.78 cm/%
Angular acceptance (horizoltal)	±87.5 mrad	±81.3 mrad
Angular acceptance (vertical)	±78.5 mrad	±68.5 mrad
Solid angle (design value)	12.8 msr	11.2 msr
(measured value)	16.3 msr	12.1 msr
Magnification (horizontal)	0.57	0.74
Magnification (vertical)	1.47	1.51

The efficiency of GARIS was measured by comparing the activity yields on a catcher detector at the focal plane of the GARIS with those on catcher foils at about 5 cm behind targets. Absolute efficiencies (in the entire energy-range of the reaction products) were found to be 15±1% for the ^{169}Tm (^{40}Ar, xn) (E(^{40}Ar)=5 MeV/u) reaction (fusion reaction), 5.3±0.4% for the ^{181}Ta (^{40}Ar, αxn) (E(^{40}Ar)=6 MeV/u) reaction, and 0.5±0.1% for the ^{nat}W(^{14}N, X)^{169}Hf(E(^{14}N)=35 MeV/u) reaction (target fragmentation). The efficiencies strongly depend not only on the angular distributions of the reactions but also the energy distributions of the recoiled products. The efficiencies of GARIS for recoiled products of more than 18 MeV were found to be 30±3% for the fusion reaction, and 12±2% for the (HI, αxn) reaction.

The parameters of the ion optics of IGISOL were tuned with an ^{40}Ar^{1+} ion beam and $^{128-136}$Xe^{1+} ion beams produced by discharge between needles set inside a thermalization chamber which contains helium added with a small amount of argon or xenon gas. The mass resolving power ($A/\Delta A$) obtained by these tuning were found to be about 120 for Ar-ion and about 250 for Xe-ions when the helium gas pressure was 100 mbar.

The efficiency of IGISOL was measured by ^{141}Pr(^{40}Ar, xn)$^{181-x}$Ir reactions under various experimental conditions. Recoiled Ir isotopes were collected with GARIS, then injected into the thermalization chamber of IGISOL, and then stopped there. The isotopes passed through the exit hole of the chamber with a helium gas-flow and were separated from helium atoms with a skimmer, ions were then accelerated to 30 keV with an electrostatic field. The accelerated ions were then collected on the surface of a silicon surface barrier detector set inside a beam tube just before an analyzer magnet of IGISOL. β-Rays and α-particles emitted from the Ir isotopes were detected with the detector, and the effi-

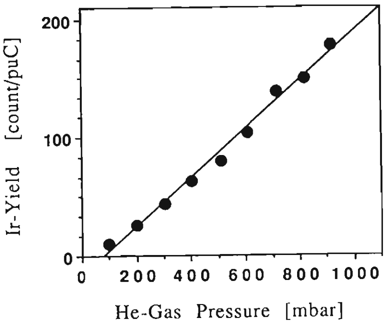

Fig. 2. Extraction yields versus helium gas pressure in the thermalization chamber.

ciency of IGISOL was measured. About 1% of isotopes injected into IGISOL were extracted when pressure was 900 mbar. The dependence of the extracted yield on helium gas pressure is shown in Fig. 2. The extracted yield increases almost linearly with the increase in the gas pressure below 900 mbar.

References

1) K. Morita *et al.*: Proc. Int. Symp. on Heavy Ion Physics and Nuclear Astrophysical Problems, Tokyo July, p. 271 (1988).

RIKEN Accel. Prog. Rep. **24** (1990)

III-5-10. Velocity Distribution of IGISOL Ion Beams

M. Koizumi, M. Azuma, T. Inamura, T. Ishizuka, H. Katsuragawa,
S. Matsuki, K. Morita, T. Murayama, I. Nakamura, M. Nakaoka,
K. Shimomura, I. Sugai, M. Takami, K. Valli, and A. Yoshida

GARIS/IGISOL at RIKEN consists of an ion-guide isotope separator on-line (RIKEN IGISOL) constructed in tandem with a gas-filled recoil isotope separator (GARIS). The design of this system was described in a previous report.[1] This system is potentially powerful in separating refractory elements as well as short-lived species because the separation time is of the order of one millisecond, and equal separation efficiency is obtained for isotopes of any chemical elements. Therefore, we are interested in making collinear laser spectroscopy for isotopes of a wide range of elements using this system. It has been estimated from mass resolution measurements that the energy spread of IGISOL ion beams is 100 eV or more,[2,3] which corresponds to about a 1-GHz resolution at fwhm for $^{40}Ar^{1+}$. The resolution is not sufficient enough for doing laser spectroscopy; about 500 MHz or less is desirable.

Since the energy spead has so far been estimated indirectly from mass resolution, it is desirable to carry out a direct measurement of the velocity distribution of IGISOL ion beams. We have measured the Doppler broadening of a resonance linewidth in a metastable atomic state of $^{40}Ar^{1+}$ (611.6 nm ($3d'^2G_{9/2} \rightarrow 4p^2F_{7/2}$) transition)[4] to observe the velocity distribution of ion beams. A schematical setup is shown in Fig. 1. The energy of ions were 30 keV, and the pressure in a helium gas cell was 20 mbar. A resonance spectrum measured with 150° incidence is shown in Fig. 2. The fwhm is 0.68 GHz, which corresponds to an energy spread of 44 eV. The fwhm of laser induced fluorescence (LIF) spectra systematically measured at three incident angles (30°, 90° and 180°) are plotted as a function of the skimmer voltage in Fig. 3. The divergence of the ion beam is deduced from the measurement at 90°, and the velocity distribution from that at 180°. The fwhm measured at 30° has both contributions. The broadening caused by beam divergence increases with increasing skimmer potential. Although the broadening caused by velocity distribution also increases with an increase in the skimmer potential, it is smaller than that by beam divergence. A typical value of the Doppler broadening caused by only velocity distribution (collinear (180°) at a skimmer potential of 500 V and a pressure of 20 mbar) was 1.25 GHz in fwhm, which corresponds to an energy spread of 120 eV. Since the gas pressure is too low to stop most of the recoil products, a series of measurements are now in progress at higher pressures.

We conclude that the linewidth in the LIF spectrum is narrower at lower skimmer potential. One way to reduce the velocity spread of ion beams in order to get a better resolution in LIF measurements is to select a part of the total velocity distribution by using slits set behind a magnetic analyzer. The spectrum in Fig. 2 was measured in this way. By this method, however, we lose a certain amount of ions for the measurements. The other possibility to reduce the veloc-

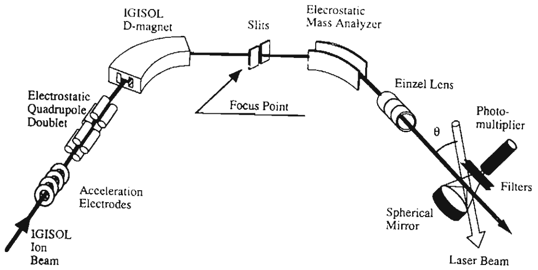

Fig. 1. Schematic setup of an LIF experiment.

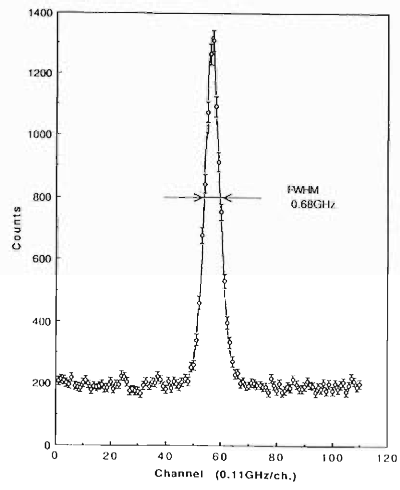

Fig. 2. LIF excitation spectrum of the metastable state in 30-keV Ar^{1+} ions at 150° to a laser beam. The resonance was observed at 16330.96 cm^{-1}.

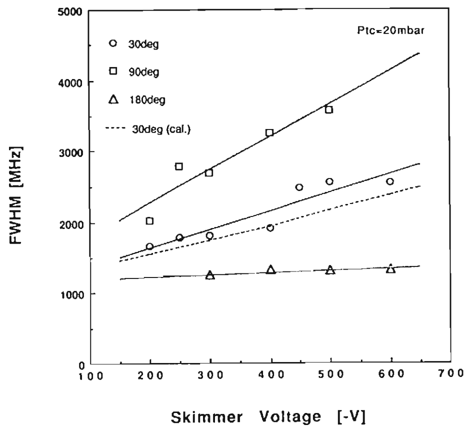

Fig. 3. Skimmer potential dependence of the fwhm of an LIF spectrum at three incident angles of a laser beam to an ion beam: 30°, 90°, and 180°. The dashed line shows fwhm at 30° calculated from 90° and 180° measurements.

ity spread without losing ion intensity is to apply an electrostatic lens system Squeezer[5] between an exit hole of the thermalization chamber of IGISOL and a skimmer. Installation of the Squeezer to our system is now in progress.

References

1) K. Morita, T. Inamura, K. Valli, T. Nomura, J. Tanaka, H. Miyatake, K. Sueki, Y. Hatsukawa, M. Fujioka, T. Shinozuka, T. Taguchi, H. Kudo, Y. Nagai, T. Tomiyama, H. Hama, M. Yoshii, and K. Furuno: *RIKEN Accel. Prog. Rep.*, **21**, 155 (1987).
2) J. Ärje: Research Report No. 3/86, Department of Physics, University of Jyväskylä (1986).
3) M. Yoshii, H. Hama, K. Taguchi, T. Ishimatsu, T. Shinozuka, and M. Fujioka, J.Ärje: *Nucl. Instrum. Methods*, **B26**, 410 (1987).
4) N. Schmidt: Private communication.
5) A. Iivonen, R. Saintola, and K. Valli: *Phys. Scr.*, **42**, 133 (1990).

RIKEN Accel. Prog. Rep. **24** (1990)

III-5-11. Resonance Ionization Spectroscopy with IGISOL

H. Backe, T. Inamura, M. Koizumi, and K. Morita

The knowledge of spins, electromagnetic moments, and radii of nuclei far from stability is important in understanding cold nuclear matter. A great variety of nuclides far from stability can be produced by heavy-ion-induced reactions. A very powerful tool to study the above-mentioned basic properties of these nuclei is laser spectroscopy: The various techniques, including ultrahigh resolution collinear laser spectroscopy, were recently reviewed by Otten.[1] However, since these methods require intensities larger than 10^4/s, their potential use for studies of heavy-ion-induced reaction products with very weak intensities is somewhat limited. (A photon-ion coincidence techniques may be an alternative way to overcome this problem.[2]) We therefore propose to use a new laser spectroscopic method, which is based on very sensitive laser resonance ionization spectroscopy[3,4] in an optical buffer gas cell in combination with the detection of resonantly ionized radioactive atoms using IGISOL.[5] In the following we shortly describe the principle of this method.

The beams of radioactive nuclides, which are collected and guided with GARIS,[5] are stopped in a buffer gas cell that is filled with helium of a few hundred millibars. It is expected that more than 20% of the incoming ions come to rest as neutral atoms and are available for resonance ionization spectroscopy (RIS). The remainder of the ions is transported in a suitable auxiliary electrostatic field to the walls of the cell where they are absorbed. At the end of an accelerator burst the auxiliary electrostatic field is switched off, and two or three tunable dye lasers are fired to resonantly ionize the neutral atoms in the buffer gas cell. The dye lasers may be pumped with an excimer laser (pulse width 20 ns, repetition rate 500 Hz) or a copper vapor laser (pulse width 20 ns, repetition rate 6000 Hz). The created ions are transported to the exit hole by a gas flow and guided to the section of skimmer and extraction electrodes; the acceleration potential of the IGISOL system will be varied from several kV to 80 kV.[5] The mass separated ions are detected at the focal plane with a position sensitive microchannel plate detector. (See Ref. 5 for details.)

The use of the IGISOL system as a detector for RIS has the advantage that it serves as a highly sensitive isotope identifier for even long-lived isotopes to which the radioactive decay detected resonance ionization spectroscopy (RADRIS)[6] cannot be applied. This offers the unique possibility of disentangling complex overlapping hyperfine structures of neighboring isotopes.

The resolution is limited by the laser bandwidth which is typically 1.2 GHz with a Lambda Physik dye laser (with an intra-cavity etalon), the Doppler broadening of about 1 GHz at room temperature and the broadening due to the pressure in the gas cell that will amount to a few hundred megahertzs. The expected resolution of about 1.5 GHz is not so good as the collinear laser spectroscopy. This is, unfortunately, the price to be paid for the ultrahigh sensitivity of RIS in the buffer gas. It should be mentioned, however, that cooling the gas cell and the use of an external narrow band laser oscillator may reduce the linewidth significantly.

References

1) E.W. Otten: "Treatise on Heavy-Ion Physics," (ed. D.A. Bromley), Plenum Press, New York, **Vol. 8**, p. 517 (1989).
2) D.A. Eastham, P.M. Walker, J.R.H. Smith, J.A.R. Griffith, D.E. Evans, S.A. Wells, M.J. Fawcett, and I.S. Grant: *Opt. Commun.*, **60**, 293 (1986).
3) G.S. Hurst, M.G. Payne, S.D. Kramer, and J.P. Young: *Rev. Mod. Phys.*, **51**, 767 (1979).
4) V.S. Letokhov: "Laser Photoionization Spectroscopy," Academic Press Inc., New York (1987).
5) K. Morita, T. Inamura, K. Valli, T. Nomura, J. Tanaka, H. Miyatake, K. Sueki, Y. Hatsukawa, M. Fujioka, T. Shinozuka, K. Taguchi, H. Kudo, Y. Nagai, T. Toriyama, H. Hama, M. Yoshii, and K. Furuno: *RIKEN Accel. Prog. Rep.*, **21**, 155 (1987).
6) H. Backe, Th. Blonningen, M. Dahlinger, U. Doppler, I. Klaft, W. Lauth, A. Scherrer, P. Schwamb, G. Schwickert, W. Theoblad, Z. Zahn, U. Othmer, and N. Trautmann: a contributed paper to the 5th Int. Symp. on Resonance Ionization Spectroscopy and Its Applications, Varese, Italy, Sept. (1990).

RIKEN Accel. Prog. Rep. **24** (1990)

III-5-12. Status Report of the RIKEN Swinger-Magnetic Analyzer with Rotators and Twisters (SMART)

H. Ohnuma, Y. Fuchi, K. Hatanaka, S. Hayakawa, T. Ichihara, M. Ishihara,
M. Kase, S. Kato, T. Kubo, S. Kubono, M. Ohura, H. Okamura,
H. Orihara, H. Sakai, H. Shimizu, Y. Tajima, M.H. Tanaka,
H. Toyokawa, Y. Yano, Y. Yashiro, H.Y. Yoshida and M. Yosoi

A swinger and a magnetic analyzer with rotators and twisters (SMART) have been installed in the experimental area E4 and are currently tested with beams from RRC.

The magnetic analyzer consists of three quadrupoles and two dipoles (PQ1-PQ2-PD1-PQ3-PD2), as described in previous reports,$^{1)}$ and the swinger has two dipoles and two quadrupoles (WD1-WQ1-WQ2-WD2). Results of the field measurements of these magnets, carried out in February and March this year, are described in a separate report.$^{2)}$

A target chamber and other vacuum chambers were installed in May. The entrance window of the target chamber has sliding membrane which moves together with the beam swinger when the incident beam direction is changed. Three sets of defining slits of the spectrometer can be inserted behind the target chamber. The vacuum chambers are designed in such a way as to facilitate small angle (including 0°) measurements. Several beam-stoppers are prepared for this purpose, one attached to the target chamber, one between PQ1 and PQ2, two inside the PD1 vacuum chamber, and one at the exit of PD1. After wiring control cables, they have been tested for vacuum and mechanical movements.

The first beam was led through the twister and the swinger onto a target in June 24, 1990. A 135 MeV ^{14}N beam was successfully transported giving a spot size of about 3 mm in diameter on a target.

Further tests of the system were carried out in July and August using a 140 MeV deuteron beam. Achromatic mode of the beam transport was used, and the alignment of the beam axis was checked using several beam-profile monitors along the beam line and two scintillator targets, one at the target position and the other at the 0° exit of the PD1 vacuum chamber. The beam spot was found to remain unchanged, as expected from optics calculations, when the swinger was rotated along with the twister.

After beam alignment, a faint beam was brought down to the first and the second focal planes to test the performance of the focal plane detectors. Scattered deuterons were also observed with the focal plane detectors. Figure 1 shows a reproduction of rays traced with single-wire proportional counters in the second focal plane. A thick bundle of rays represents deuterons elastically scattered from a 20 μm thick gold target. The overall energy resolution was about 1/1,000 after correcting for abberations, almost equal to the energy resolution of the beam in the achromatic mode. In addition, neutron time-of-flight spectra were taken with a 8.6-m flight path as reported elsewhere.$^{3)}$ Further tests of the system are under way.

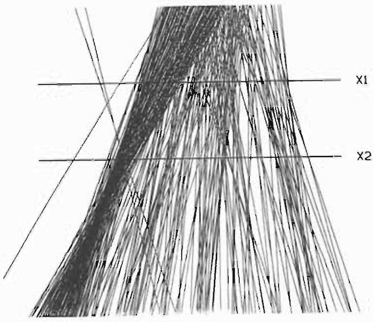

Fig. 1. Rays of deuterons reproduced from raw data obtained with SWPC in the second focal plane. A thick bundle of rays corresponds to deuterons elastically scattered from a 20 μm thick gold target.

References

1) H. Ohnuma *et al.*: *RIKEN Accel. Prog. Rep.*, **21**, 164 (1987); **22**, 148 (1988).
2) Y. Tajima *et al.*: This Report, p. 109.
3) M. Orihara *et al.*: This Report, p. 121.

RIKEN Accel Prog. Rep. **24** (1990)

III-5-13. Field Measurements of the SMART Magnets

Y. Tajima, K. Hatanaka, S. Hayakawa, T. Ichihara, M. Kase, S. Kato, H. Ohnuma,
M. Ohura, H. Okamura, H. Orihara, H. Shimizu, H. Takebe, H. Toyokawa,
Y. Yano, Y. Yashiro, H.Y. Yoshida and M. Yosoi

The magnets of the SMART (a swinger and a magnetic analyzer with rotators and twisters) system[1] were installed in the experimental area E4 in December 1989, and wiring and piping were completed by the end of January 1990.

The magnetic analyzer consists of three quadrupoles and two dipoles (PQ1-PQ2-PD1-PQ3-PD2), and the swinger has two dipoles and two quadrupoles (WD1-WQ1-WQ2-WD2). In addition, there is a twister consisting of seven quadrupoles.

Field measurements of these magnets were carried out in February and March this year. A photograph of the field measurement device is shown in Fig. 1. Its movement was controlled by a PC9801 computer, and the data were stored on magnetic disks. A hole probe used in the measurements was calibrated against an NMR probe at the central region of the dipole magnets to obtain absolute values of magnetic field strength.

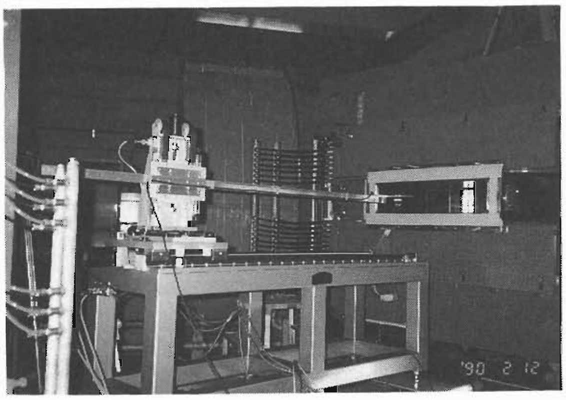

Fig. 1. Field measurement device set for the exit of the dipole magnet PD1 of the spectrometer.

Figure 2 shows sample field distributions of the first dipole of the spectrometer PD1 at different excitations. The maximum fields of the dipole magnets are found about 10% higher than the designed values, indicating iron material used for these magnets are of better quality than originally intended. The effective boundary of the PD1 magnet is about 3 cm inside the physical boundary at the maximum field, coming closer at lower fields. That for the PD2 magnet is about 1 cm outside.

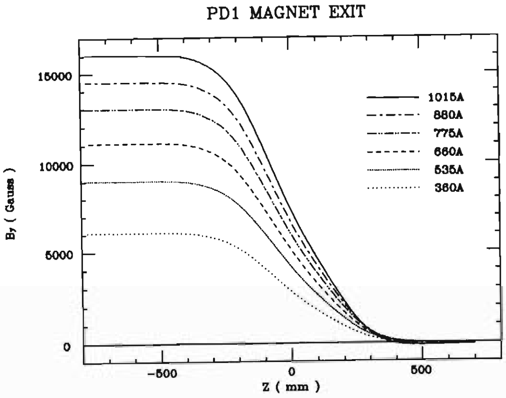

Fig. 2. Sample field distributions of the PD1 magnet.

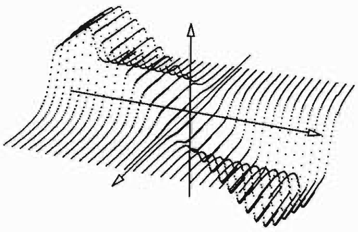

Fig. 3. Three-dimensional display of the field distribution of the quadrupole magnet PQ1.

The three-dimensional display of the field distribution of the first quadrupole magnet of the spectrometer PQ1 is shown in Fig. 3. Good quadrupole fields are realized over a large volume, although the present quadrupole magnets do not have a four-fold symmetry around the axis.

References

1) H. Ohnuma *et al.*: *RIKEN Accel. Prog. Rep.*, **21**,164 (1987); **22**, 148 (1988).

RIKEN Accel. Prog. Rep. **24** (1990)

III-5-14. Test for Dispersive-Mode Beam Transport to the SMART Spectrograph

T. Ichihara, K. Hatanaka, H. Ohnuma, M. Yosoi, Y. Tajima, Y. Yashiro,
H. Toyokawa, M. Ohura, H. Orihara, S. Kubono, M.H. Tanaka, Y. Fuchi,
H. Okamura, H. Sakai, H. Shimizu, S. Hayakawa, and M. Ishihara

The spectrograph SMART was installed in the spring of 1990 in the E4 experiment room in the RIKEN Accelerator Research Facility. After the installation we started systematic diagnosis and development using a beam from the Ring Cyclotron. Figure 1 shows the schematic diagram of the spectrograph SMART. We have so far succeeded in obtaining some test spectra of light-ion and heavy ion direct reactions with proper particle identifications using a deuteron beam of 70 MeV/A and a ^{15}N beam of 70 MeV/A.

One of the most important requirements in operating the SMART spectrograph with high resolution is the dispersion matching of a beam transport system and a spectrograph analyzer system. The momentum resolving power of the SMART spectrograph is anticipated to be $p/\delta p=13{,}000$, while the momentum resolution of the beam extracted from the Ring cyclotron is expected to be 0.1% ($p/\delta p=1{,}000$). Without dispersion matching, we can expect the momentum resolution of SMART spectrograph of about $p/\delta p=1{,}000$ owing to a finite momentum spread of a beam itself. In order to get more high resolution, we need to

(1) achieve dispersion matching with the beam transport system and/or

(2) cut a part of beam by the slit in the beam transport system.

In principle, dispersion matching is archived by setting a beam matrix at the counter position in the spectrograph to "achromatic"; thus the

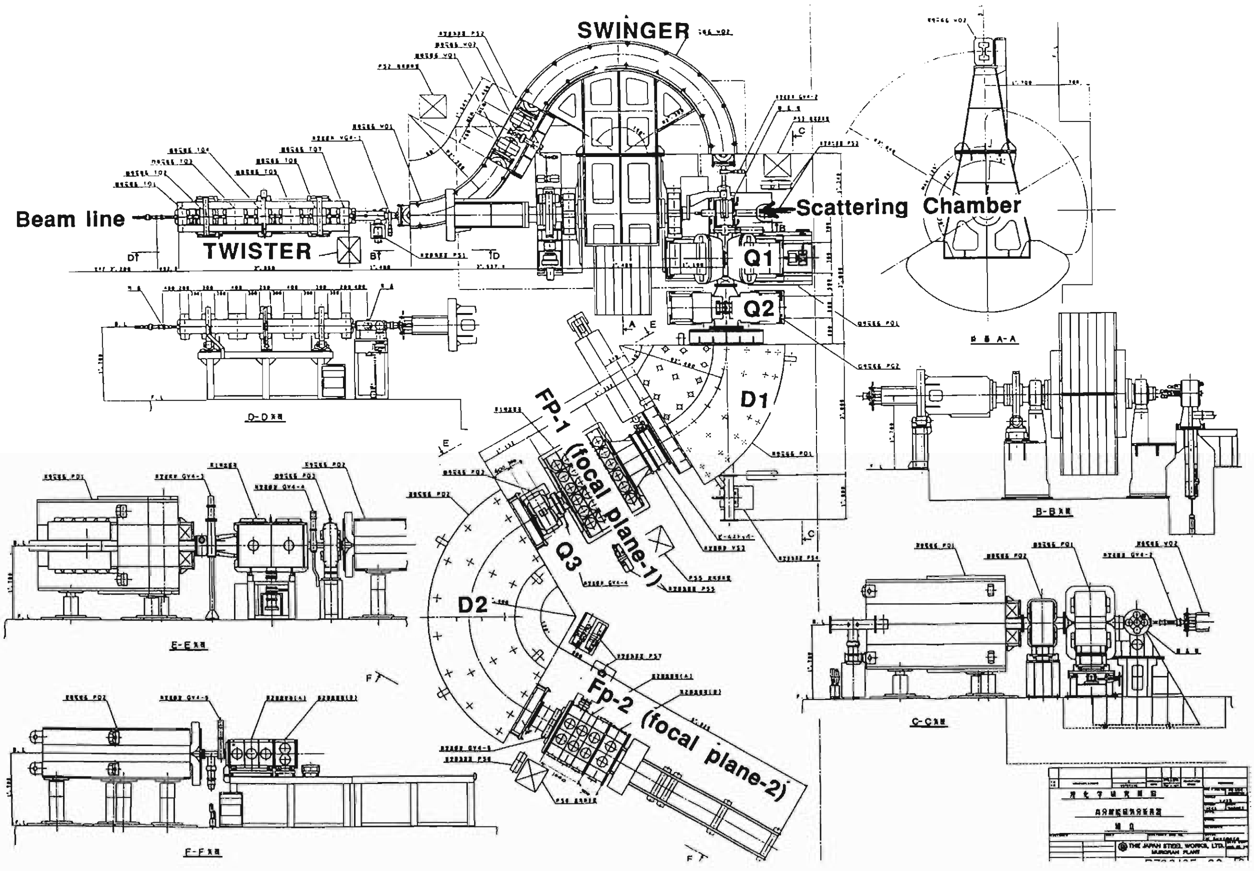

Fig. 1. Schematic layout of the spectrograph SMART.

deviation of the momentum of the primary beam is canceled at the counter position. The condition for the dispersion matching is given by

$$M_{11}R_{16}(\Delta p/p)+M_{16}(\Delta pi/pi)=0$$

where M and R are matrixes of the Spectrograph and the beam transport system, and p and pi are the momentum of the beam transport system. The first order matrix of the SMART spectrograph is as follows. (in unit of program "transport")

```
  0.53456   0.00000   0.00000   0.00000   0.00000  -7.61619
 18.56271   1.87056   0.00000   0.00000   0.00000 -38.84659
  0.00000   0.00000   1.41005  -0.04861   0.00000   0.00000
  0.00000   0.00000  19.76055   0.02797   0.00000   0.00000
-12.06111  -1.42467   0.00000   0.00000   1.00000   9.05130
  0.00000   0.00000   0.00000   0.00000   0.00000   1.00000
```

For a typical experiment of elastic scattering and charge exchange reactions at forward angles, a beam matrix R_{16} required at the target position is

$$R_{16}=-M_{16}/M_{11}=14.2\text{ m}.$$

Therefore we need a dispersion of beam (R_{16}) of about +14.2 m at the target position in order to archive dispersion matching.

In order to achieve this dispersion at the target position, we calculated beam transport matrixes from the accelerator to the target. In order to implement the calculation to the actual beam transport system, careful turning for Q-magnets was carried out. The turning was repeated by inserting and removing thin foils in the first focal point (A01) of an extracted beam to change the momentum dispersion of the beam and measuring the horizontal displacement of the beam position at each beam profile monitor comparing to the transport calculation. The beam transport calculation is usually started at A01, which is the first focal plain after extraction from the accelerator. We also estimated the dispersion of the beam at the focal point A01, assuming the dispersion of a beam in the Ring Cyclotron during acceleration to be $R_{16}=-2.0$ m at A01.

As a result, we obtained a beam spot at the target with this dispersive mode transport. The size of the beam spot at the target was 1.5 mm (vertical)×20 mm (horizontal). The large horizontal size is mainly due to the large dispersion of the beam (14 m) and finite momentum distributions of the beam (0.1%).

We have adjustable slits at the focal point (A11b) in the beam transport system just after the first 90 degree bending magnet (DAA1, DMD1). In this dispersive-mode transport, since the dispersion of the beam at this slit is relatively large (5.7 m), we can reduce the momentum width of the beam by this slit. Table 1 shows the spot size of the beam observed at the target position in contrast to the slit width at the Allb position. We have also mentioned the calculated momentum and energy width of the beam in the table. We can obtain a proper beam spot size and the width of the momentum by adjusting the beam spot.

Table 1. Beam spot size observed at the SMART target position in contrast to the slit opening widths at the Allb position. The momentum and energy width calculated for a beam is also mentioned together. (Beam is ^{15}N 70 MeV/A)

A11b SLIT (H) (Dispersion=5.7m)	spot size on target(H) (Dispersion=13.2m)	ΔP	ΔE (at 1.05GeV)
Full open	20mm	0.15%	3.2MeV
+−6.5mm	15mm	0.12%	2.4MeV
+−3.5mm	10mm	0.08%	1.6MeV
+−1.0mm	4mm	0.03%	0.6MeV

Finally we got a beam spot size of 3 mm FWHM in the horizontal direction at the focal plane counter (a single wire drift chamber which has a 10 cm×50 cm effective area) of the spectrograph when the A11b slits were set at ±6.5 mm and beam spot size at the target was 15 mm in this transport. Therefore the dispersion matching is almost archived in this case, while there is a little error in the turning of desperation.

We are now developing a method of further fine turning of beam desperation, utilizing counters in the spectrograph to archive the ultimate resolution of this spectrograph. Systematical and intensive diagnosis for the optics of this spectrograph is also required to enable the tracing back of ray. The development of a Cathode Readout Drift Changer (CRDC) is also in progress as a high resolution focal plain counter.

RIKEN Accel Prog. Rep. **24** (1990)

III-5-15. Detector System for Secondary Reactions of Unstable Nuclei

T. Nakamura, S. Shimoura, T. Kubo, N. Inabe, I. Tanihata, and M. Ishihara

The radioactive beam line RIPS[1)] is expected to open a way of the study of unstable nuclei through secondary nuclear reactions. One of our interests is the observation of a soft giant dipole resonance of light neutron-rich nuclei such as ^{11}Li or ^{11}Be.[2)] Another interest is the study of a variety of excited states of exotic nuclei by using inverse reactions of (d,p) or (n,p) as secondary reactions. To study the excited states of unstable nuclei, invariant mass spectroscopy provides a powerful and direct method because the excited states of these nuclei are often particle unbound and the resolution of excitation energies dose not suffer from the energy broadening of radioactive nuclear beams. A detector system including an analyzing magnet is now being designed and will be constructed at the end of the beam line RIPS to facilitate the experiments by the invariant-mass-reconstruction method. Here we summarize the outline of the system.

Figure 1 shows a schematic view of the system, which consists of an analyzing magnet, MWPC's (PBT1, PBT2, PAT1 and PAT2), a plastic scintillator (SBT), a drift chamber (DC), a hodoscope for charged particles (HAT), and a hodoscope for neutrons (NEUT).

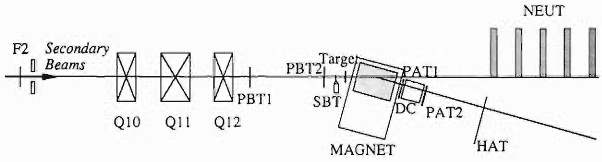

Fig. 1. Detector system for secondary nuclear reaction experiments. PBT1, PBT2, MWPC's before targets; SBT, Scintillator before targets; PAT1, PAT2, MWPC's after targets; DC, a drift chamber; HAT, a hodoscope for charged particles; Neut, a hodoscope for neutrons.

The analyzing magnet is of a C-type with a gap of 250 mm; its poles are determined to be 850 mm in length and 700 mm in width. The maximum bending power $B \cdot L$ is 1.3 T·m, where B denotes the maximum magnetic field and L the effective length of the magnet. Under the condition, one can bend 100-A-MeV ^{10}Be up to 20 degrees. The angular acceptance for charged particles is determined to be 200 mrad in the horizontal direction and 150 mrad in the vertical direction.

PBT1 and PBT2 are 2-dimensional readout type MWPC's with a 1 mm wire spacing. They are used for determining reaction points by measuring the positions and angles of incident radioactive nuclear beams.

SBT is used to define incident radioactive beams and as a TOF counter.

PAT1 and PAT2 are 1-dimensional (horizontal) readout type MWPC's with a 1.5 mm wire spacing. They are located at the exit of the magnet and the exit of DC for excluding beam events from trigger events.

DC is used as a tracking chamber of the analyzing magnet and has 5 planes for determining the horizontal position and 4 planes for determining the vertical position.

HAT is used as the start counter for DC and for measuring the time of flights of charged particles.

NEUT is composed of 5 walls of 940×980 mm^2 sensitive areas, each of which includes 16 plastic scintillators (BC-408) (see Fig. 2). It observes energies of neutrons by a TOF method and observes the tracks as well. The resolution of position detection is expected to be less than 6 cm (FWHM), which corresponds to the angular resolution of 10 mrad.

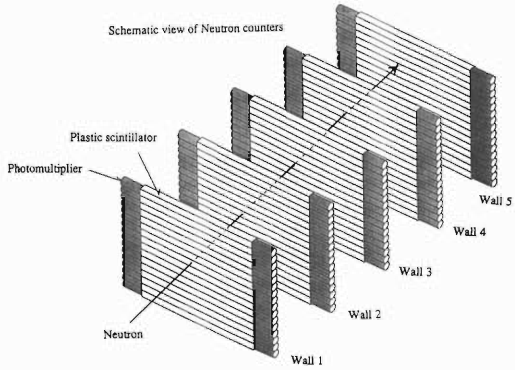

Fig. 2. System for detecting neutrons (NEUT) composed of 5 walls, each of which has 16 plastic scintillators with 32 photomultipliers.

We estimated the resolution of the excitation energy. As an example, for 80-A-MeV ^{11}Be with excitation energy of 5.5 MeV decaying into ^{10}Be and a neutron, the resolution of the excitation energy is estimated as less than 700 keV.

References

1) T. Kubo *et al.*: This Report p. 96.
2) T. Kobayshi, S. Shimoura, I. Tanihata, K. Katori, K. Matsuta, T. Minamisono, K. Sugimoto, W. Mueller, D.L. Olson, T.J.M. Symons, and H. Wieman: *Phys. Lett.*, **B232**, 51 (1989).

RIKEN Accel. Prog. Rep. **24** (1990)

III-5-16. Identification of Intermediate-Mass Fragments with Counter Telescopes

K. Ieki and N. Iwasa

For the identification of the mass and atomic number of heavy particles emitted in heavy-ion reactions, a simple formula[1] has been successfully used for the measurements with counter telescopes. In medium-energy heavy-ion reactions, however, fragments with high atomic numbers are often emitted; accordingly the energy loss in a ΔE counter becomes large and the formula gives wrong results. Thus, using a computer code for the energy loss calculation in the ΔE counter for various ions, we have developed a new formula with a wider dynamic range both in energy ($4 \leq E/A \leq 100$ MeV/u) and atomic number ($Z \leq 40$). The particle identification (PI) is approximated by

$$\mathrm{PI} \propto (E + \Delta E)^n - E$$

$$n = a + b \log(E/(E + \Delta E)).$$

The values of the PI are found to be nearly proportional to $M^{0.724}Z^2$, where M and Z are the mass and atomic number of a fragment.

We applied this formula to the measurement of intermediate-mass fragments produced in the reaction ^{84}Kr + ^{27}Al at 10.6 MeV/u performed at RIKEN Ring Cyclotron. Intermediate-mass fragments are detected with telescopes, consisting of ΔE(30 μm) − E(1 mm) surface-barrier detectors. A particle identification spectrum displayed in Fig. 1 is obtained by using the above formula with $a = 1.745$ and $b = 0.0635$. The discrimination of fragments in the atomic number is achieved up to $Z = 40$.

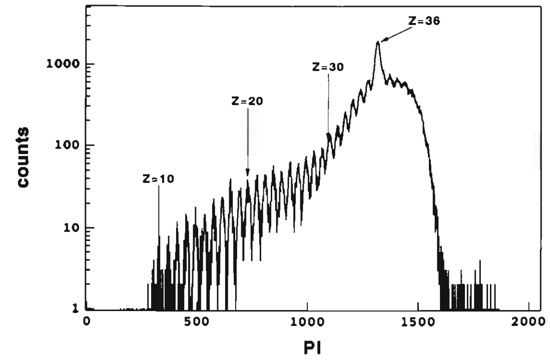

Fig. 1. A typical particle-identification spectrum obtained by using the formula with $a = 1.745$ and $b = 0.0635$ (see text). The abscissa denotes the channel number proportional to $\mathrm{PI}^{1/2.724}$.

The present formula is simple enough to use in an on-line monitoring in the measurement of intermediate-mass fragments.

References

1) T. Nomura: *IPCR Cyclotron Prog. Rep.*, **11**, 81 (1977); T. Shimoda *et al.*: *Nucl. Instrum. Methods*, **165**, 261 (1979).

RIKEN Accel. Prog. Rep. **24** (1990)

III-5-17. Improvement of Position Determination for Two-Dimensional Position-Sensitive Silicon Detector

K. Ieki, M. Kurokawa, T. Takei, N. Iwasa,
Y. Ando, T. Motobayashi, and H. Murakami

In a previous report,[1] we proposed a simple formula to determine the position for two-dimensional position-sensitive silicon detectors (PSD). The formula converts four charge signals Q_i (i=1,2,3,4) from the electrodes located at four corners, $(x,y) = (1,1), (-1,1), (-1,-1)$, and $(1,-1)$, into the incident position (X,Y).

We performed a further test for other two PSD's manufactured by Hamamatsu Photonics Co. and by Intertechnique. The PSD's have an active area of 37 × 37 mm^2. The structure of the electrodes of the two PSD's was similar to the previous one.[1] Their thicknesses were about 400 and 490 μm, and their surface resistances were about 700 and 900 Ω□, respectively. The test was carried out by using collimated light pulses from a LED shooting 82 positions of the PSD.

Conversion was done successfully with an improved formula:

$$X=\frac{A+B}{1+\sqrt{1-A^2-B^2}}$$

$$Y=\frac{B-A}{1+\sqrt{1-A^2-B^2}}$$

$$A=\frac{S_2-S_4}{S_2+S_4}$$

$$B=\frac{S_3-S_1}{S_3+S_1}$$

$$S_1=Q_i^{-\frac{2}{n}}$$

where n is a dimensionless parameter. This formula gives better position resolution than the previous one. The parameter n which gives the best position linearlity was 0.59 and 1.50 for Hamamatsu and Intertechnique PSD's, respectively. An overall good position linearlity was obtained except for the edge regions of the Intertechnique PSD.

References
1) M. Ogiwara *et al.*: *RIKEN Accel. Prog. Rep.*, **22**, 174 (1988); K. Ieki *et al.*: *Nucl. Instrum. Methods*, **A297**, 312 (1990).

RIKEN Accel. Prog. Rep. **24** (1990)

III-5-18. Energy Loss Straggling of High Energy Heavy Ions in a Silicon Detector

K. Nagata, N. Hasebe, H. Murakami, A. Nakamoto,
H. Murakami,* T. Kashiwagi, T. Nakasugi,**
J. Kikuchi, T. Doke, and T. Kohno

Energy loss distributions are measured of an 80 MeV/u ^{40}Ar beam in a Si (Li) detector of 2.8 ㎜ in thickness and 15 ㎝ in diameter. The width of the energy loss distributions is narrowest when the particle incident angle is 10° to the silicon detector.

The width of the energy loss distribution is determined by the gaussian width, electronics noise, detector thickness nonuniformity, and channeling effect. The electronics noise is negligible in a heavy ion energy loss measurement, because of the energy loss is enormously large relative to an electronics noise level. In a preliminary experiment, performed at the RIKEN Ring cyclotron to measure the particle channeling effect in a silicon detector, we observed the energy loss distributions of particle incident angle 0°, 10°, and 20° to the horizontal axis (X-axis) of the detector. Figure 1 shows the experimental energy loss distributions of 80 MeV/u ^{40}Ar ions in a 2.8 ㎜ thick silicon detector. The theoretical gaussian FWHM and experimental FWHM are shown in Table 1.

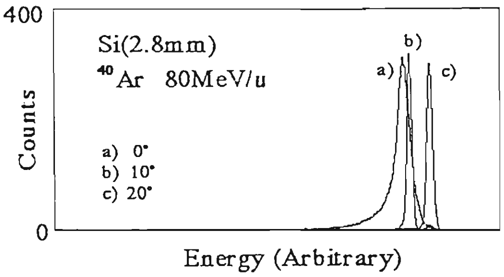

Fig. 1. Energy loss distributions of 80MeV/u ^{40}Ar ions measured in a 2.8 ㎜ thick silicon detector. a), b), and c) correspond to a), b), and c) of Table 1.

Table 1. Comparison of theoretical gaussian FWHM and experimental FWHM.

Incident Angle	FWHM (%)	
	Exp.	Theor.
a) 0°	4.46	0.445
b) 10°	1.53	0.434
c) 20°	1.73	0.397

The distribution width is narrowest at an incident angle of 10°. The absorber materials between the beam exit and the detector are Mylar of 0.20 ㎜, air of 300 ㎜, and Al of 0.04 ㎜. The beam energy spreads caused by these materials are approximately 0.2%. If the energy loss resolutions are limited by the thickness nonuniformity of the detector, the thickness nonuniformity is estimated as ~1.47% (~0.041 ㎜). If we tilt the detector 10° to the beam not only horizontally but also vertically, the FWHM observed will agree with the calculation.

---

* Ehime University.
** Waseda University.

RIKEN Accel. Prog. Rep. **24** (1990)

III-5-19. Responses of Large Position-Sensitive Detectors to Heavy Ion Beams

C. Kato, T. Imai, A. Yoneda, H. Kato, K. Munakata, and T. Kohno

Position sensitive detectors (PSD) play an important role in the high-resolution observation of cosmic-ray heavy ions in space. We are preparing a cosmic-ray heavy ion telescope having a very large geometric-factor. The telescope will be put into a geosynchronous orbit on board the Engineering Test Satellite (ETS-VI) in 1993.[1] The objectives of our observation are elemental and isotopic abundance of galactic cosmic rays (GCR) and solar energetic particles (SEP) up to Fe nuclides. The position information entering the telescope is used to detemine the pathlength in a ΔE detector, which is very important value in a $\Delta E \times E$ method for particle identification.

The two-dimentional charge division type PSD has an effective area of 62 mm × 62 mm. Although some performances of the PSD for low energy heavy ions (stopping in the detector) from 160 cm

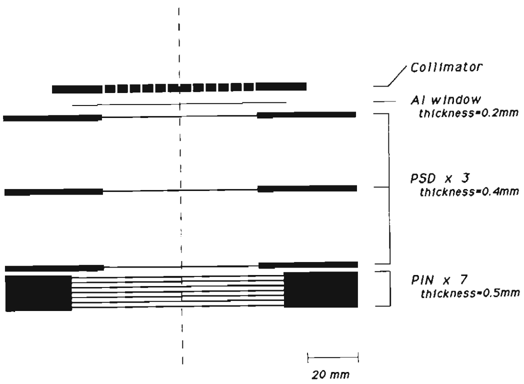

Fig. 1. Detector array for the experiment. An Al film of 0.2 mm in thickness is used for a light shield. Behind three PSDs there are even PIN type energy detectors of 0.5 mm in thickness. This assembly is a front part of the flight model telescope.

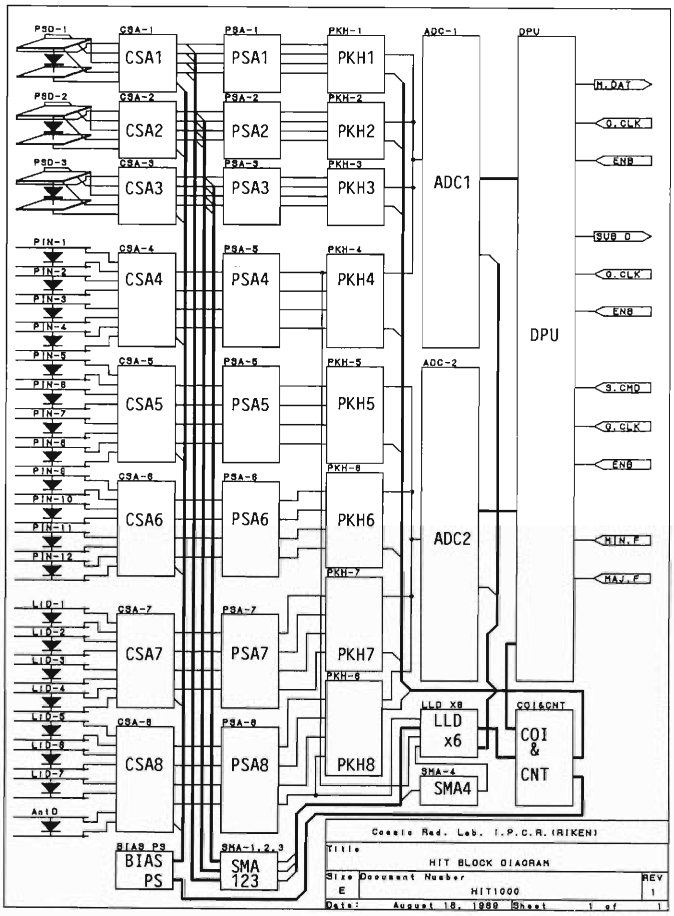

Fig. 2. Block diagram of the telescope system of the flight model. The micro processor part was simulated with a personal computer.

cyclotron have already been reported,[2,3] we need to measure characteristics using penetrated higher energy beam which can be partly simulated to cosmic rays. We here report performances of the PSDs for penetrated heavy ions, using RIKEN Ring Cyclotron. The detector array shown in Fig. 1 was irradiated with an Ar-beam of 95 MeV/u. This detector array basically simulates the flight model assembly, but has small number of signals because of the limits of the number of hvbrid-IC. Different from flight models, four signals from the third PSD are connected to one signal to get energy information only. We used no vacuum chamber to set the telescope, but lead a beam to the atmosphere through a 250 micron thick mylar window from the vacuum system. The distance from the window to the telescope was about 30 cm.

The signal processing system including analog and digital circuits is shown in Fig. 2 for the flight model. The pulse shaping time of the main amplifier is 10 μs. In this experiment, we simulated the digital processing part after the ADCs (telemetry part of the satellite system) by another circuit. These digital circuits have essentially no important role for the resolution of the telescope. We used two 50-m long glass fiber cables to transmit and receive signals from the beam point to the control room located just under the E-1 beam site. We used a personal computer with magneto-optical-disk to control ther telescope and to take data in the control room.

In front of the first PSD, we placed a 3-mm thick brass collimator with 1-mm φ holes on the 13 × 13 lattice points at 5 mm intervals. Since the range of the Ar-beam in brass is much less than 3 mm, only ions passing through the holes can hit PSDs.

In Fig. 3 we show an example of the positions observed corresponding to each hole of the collimator. The positions were calculated by a simple equation shown in Ref. 2. Apparent non-uniformity of the total counts in each hole upon the whole area of PSD depends on the beam profiles during the data taking time period of about 5 hours. In Fig. 4 we illustrate the differences between the calculated position (curve fitted center of each hole) and the real position (center of the 1 mm φ hole) of the collimator with vectors. At the lattice points where there are no vector counts were too low to be detected owing to beam profiles.

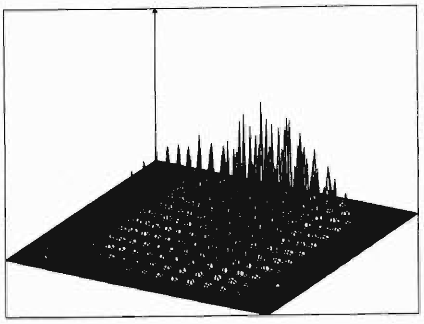

Fig. 3. Three dimensional expression of the position data behind the collimator as described in the text.

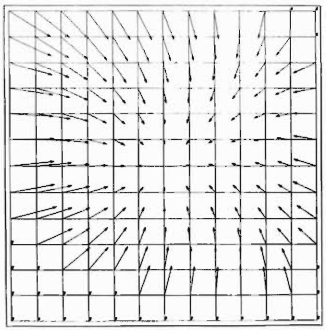

Fig. 4. Position deformation distribution of one PSD. Each vector represents the difference between obtained position and real position of the collimator.

Figure 4 indicates a general shrink of positions toward the center of the detector. In order to 'demodulate' the observed position data in space to correct values, we should carry out similar measurements with various beams.

References

1) T. Kohno: *Space Sci. Rev.*, **51**, 185 (1989).
2) T. Kohno *et al.*: *RIKEN Accel. Prog. Rep.*, **21**, 152 (1987).
3) K. Munakata *et al.*: *ibid.*, **22**, 168 (1988).

RIKEN Accel. Prog. Rep. **24** (1990)

III-5-20. Test of Si Photodiodes for Scintillation of Liquid Xe by Heavy Ions

T. Doke, T. Takahashi, J. Kikuchi, E. Aprile, A. Hitachi, T. Kashiwagi,
N. Ishida, H. Ichinose, K. Masuda, and K. Sumorok*

Liquid xenon (LXe) is a good scintillator for radiation detection and is now considered to be used in nuclear and particle physics. A scilicon photodiode (Si-PD) is suitable for the detection of the scintillation light (170 nm) from LXe because it has fast response and high detection efficiency for the light and works at low temperature and in a magnetic field. We have measured the response of a Si-PD for large energy deposition in LXe by using heavy ions from RIKEN Ring Cyclotron.

The apparatus is a double vacuum chamber, the inner is a container of LXe and the outer is for thermal insulation. The beam windows are a 200-micron SUS foil and a 40-micron Havar foil. The incident ions entered and stopped in LXe after passing through a Ti window of the beam line, 10 cm air, and then the chamber windows. A thin (100 microns) plastic scintillator was sometimes used to obtain a beam trigger. The ions used were 135 MeV/n N, 80 MeV/n Ar, and 100 MeV/n Al.

Xe gas was purified by passing through an Oxisorb purifier with a flow rate of 5 *l*/min and then liquefied in the chamber. The LXe temperature was kept at −75°C with dry ice. The photon detector is a surface-barrier Si-PD made at Waseda University. A mesh-type gold electrode is used to ensure a good transparency of the surface for 170 nm photons. Charge signals from the diode were processed with a preamplifier (fast or slow), a shaper, and an ADC. The waveforms of the signals were also observed with an oscilloscope.

Table 1 shows the energy deposited in LXe, the number of photons incident to the diode surface, the charge collected in PD, a practical quantum efficiency for the LXe scintillation, and the energy resolution, obtained for various ions. The peaking times of signals are also listed. The collected charge was calibrated by a known capacitor and voltages of standard pulses. In the measurement with Ar ions, the capacitor was not calibrated, so that the collected charge (in parentheses) may be incorrect. In other cases, the practical efficiencies, defined as the number of the collected electrons divided by the number of incident photons, were about 0.25. With a peaking time of 20–45 ns, the resolution got better by improving the apparatus and electronics. In conclusion, an energy resolution better than 0.5% r.m.s. was obtained for the energy deposition of 2.5 GeV.

Table 1. Test results of a Si photodiode for LXe scintillation.

Incident ion	Energy in LXe	Incident photon	Collected electron	Practical efficiency	Resolution r.m.s.	Peaking time
N	1.64 GeV	$2.6x10^7$	$6.7x10^6$	0.26	0.60 %	1 μs
N	1.64 GeV	$2.6x10^7$	$6.1x10^6$	0.23	1.2 %	45 ns
Ar	2.65 GeV	$5.2x10^7$	$(2.9x10^7)$	(0.56)	(0.69 %)	20 ns
Al	2.47 GeV	$6.1x10^7$	$1.4x10^7$	0.22	0.48 %	20 ns

---

* Massachusetts Institute of Technology.

RIKEN Accel. Prog. Rep. **24** (1990)

III-5-21. Response of a CsI(Tl) Scintillator to Charged Particles of Energies around 80 MeV/u

M. Kurokawa, T. Motobayashi, K. Ieki, H. Murakami, Y. Ando, N. Iwasa,
T. Takei, C. Perrin, F. Merchez, S. Kox, D. Rebreyend, S. Kubono,
M. Ishihara, S. Shimoura, T. Kubo, and N. Inabe

The response of a CsI(Tl) scintillator to charged particles (p, α, ^{11}B, ^{12}C, ^{13}N, and ^{14}O) of energies around 80 MeV/u was studied. The experiment was carried out using secondary beams from the RIPS facility of the RIKEN Ring Cyclotron. A 4×4×10 cm^3 crystal was coupled to a photomultiplier tube (PMT). Anode pulses from PMT were sent to two charge sensitive ADCs, because the light output has two time components (fast and slow). One ADC is gated from 0 to 0.4 μs to pick up the fast component of the scintillation light (S1) and the other ADC is gated from 1.7 to 5.7 μs to pick up the slow component (S2).

Figure 1 shows the relation between the particle energies and the light output S1 and S2, respectively. In general, the light output of a heavier particle is smaller than that of a lighter particle. This phenomenon is known as "quenching" for various scintillators. We found one exception in the response to protons as shown in Fig. 1(a). The light output of the proton is smaller than that of α particle. This is due to the low probability of recombination of electrons and holes induced by such high energy protons.[1)]

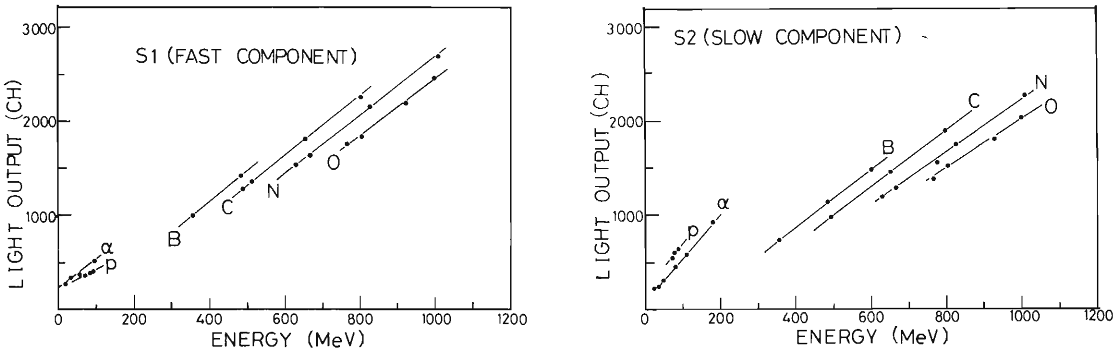

(a) (b)

Fig. 1. Relations between particle energies and light outputs S1 (a) and S2 (b).

References
1) R.B. Murray and A. Meyer: *Phys. Rev.*, **122**, 815 (1961).

RIKEN Accel. Prog. Rep. **24** (1990)

III-5-22. Identification of Charged Particles using Phoswich Detector

Y. Futami, T. Nakagawa, K. Yuasa-Nakagawa, Y. Honjo, T. Mizota,
Y.H. Pu, H. Fujiwara,* H. Toyokawa, and S.M. Lee

As a part of a 4π experiment project, we have been developing a Phoswich detector system which consists of BaF_2 + Plastic Scintillator Phoswich detectors. Here we report the results of the detector's response to charged particles. In the case of BaF_2, particle identification can be achieved by using a pulse shape discrimination technique[1] because the integration of the fast decay component of a light pulse due to scintillation in the BaF_2 crystal depends on incident particles.[2-4] In our Phoswich detector (Fig. 1), a piece of a plastic scintillator is added in front of the BaF_2 crystal. As a result, the identification of charged particles with the two-dimensional plot of the fast component of a total light output pulse versus the total light output would be improved because of a good energy loss measurement of the incident particles by the contribution to the fast component from the plastic scintillator. The detector was tested with ^{11}B (32–66 MeV), ^{12}C (35–80 MeV), ^{16}O (40–99 MeV), ^{28}Si (72–121 MeV), and ^{35}Cl (100–126 MeV) beams produced by the 12 MV UD Tandem Accelerator of Tsukuba University. The detector was placed at an angle of 20° to the beam direction and was exposed to particles scattered by a gold foil. The output signal from the PMT anode was observed to consist of a fast component (plastic's light output and BaF_2's fast component) superimposed on a slow component from BaF_2. By putting a fast gate (50 ns) and a total gate (1.5 μs) on the signal the two components were integrated respectively to give the two light outputs L_{fast} and L_{total}. Several plastic scintillators of different thicknesses were tested. The data are under analysis. Figure 2 shows the FWHM of the fast and total light outputs. The FWHM of the total light output is almost constant, but that of the fast ligh output increases as the atomic number (Z) of the incident particle becomes large.

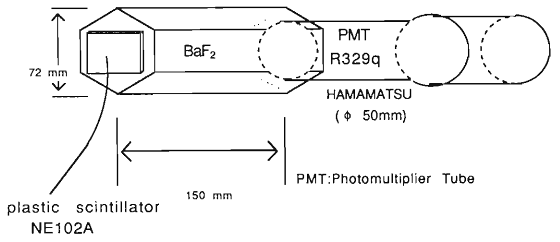

Fig. 1. Schematic view of the BaF_2 + Plastic Scintillator Phoswich detector.

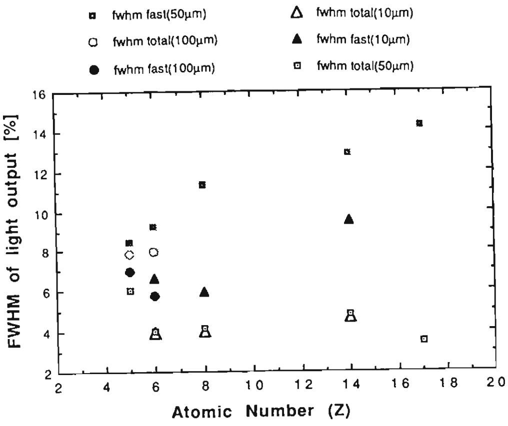

Fig. 2. FWHM[%] of the light output, $L.Z$ is the Atomic Number of the incident particle elastically scattered by a gold target. FWHM[%] is *fwhm*[ch] of the incident particle's peak divided by the peak value L[ch] (FWHM[%] = *fwhm*[ch]/L[ch]). The value in the parenthesis is the thickness of the plastic scintillator.

References

1) T. Murakami *et al.*: *Nucl. Instrum. Methods*, **A253**, 163 (1986).
2) K. Wisshak and F. Käppeler: *ibid.*, **227**, 91 (1984).
3) S. Kubota *et al.*: *ibid.*, **A242**, 291 (1986).
4) E. Dafni: *ibid.*, **A254**, 54 (1987).

---

* SANYO electric, Ltd.

RIKEN Accel. Prog. Rep. **24** (1990)

III-5-23. A Test for SMART Neutron Detectors

H. Orihara, K. Hatanaka, T. Ichihara, M. Ishihara, S. Kato, H. Ohnuma, M. Ohura,
H. Okamura, H. Sakai, H. Shimizu, Y. Tajima, H. Toyokawa,
Y. Yano, Y. Yashiro, H.Y. Yoshida, and M. Yosoi

The SMART system,1) with its beam swinger magnets, allows neutron angular distribution measurements at the maximum flight path of 22 m. A test neutron time-of-flight (TOF) measurement was carried out during a SMART diagnostic run in July–August, 1990, using a 140 MeV deuteron beam and a 1 mm thick Al target. A cylindrical NE213 liquid scintillator detector, 20 cm in diameter and 5 cm in thickness, was placed at 8.6 m from the target. Stop signals were taken from the RF of the injector AVF cyclotron.

Figures 1(a) and (b) show a raw TOF spectrum and a TOF spectrum gated by neutron events, respectively. Neutron-gamma discrimination was made with a pulse-shape discriminator. The raw spectrum shows a sharp peak due to gamma flash, and a broad neutron peak due to deuteron breakup.

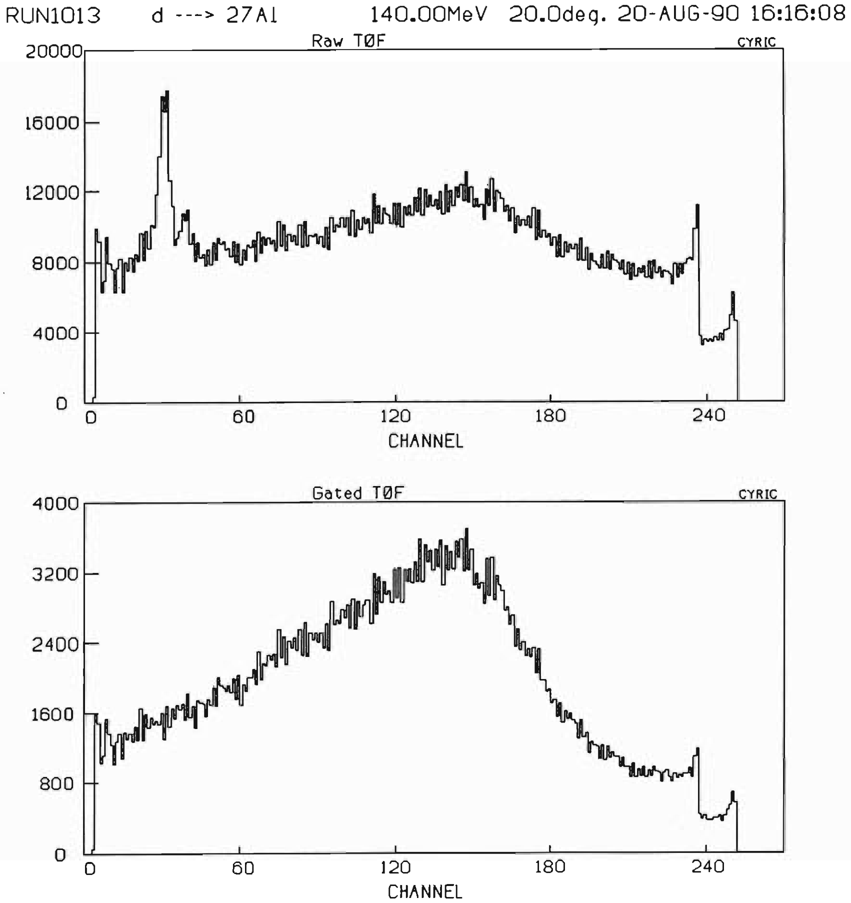

Fig. 1. Time-of-flight spectra (a) without and (b) with the neutron gate. The full range corresponds to 80 ns. A sharp peak is due to gamma flash. The energy of the center of the broad peak is about 70 MeV, indicating this peak is due to breakup neutrons.

Pulse-height spectra corresponding to various slices of flight times ard shown in Fig. 2. One can identify a plateau extending to the heighest puse-height region due to the H(n,p) events, a bump due to the ^{12}C(n,p) events, and a steep rise toward the low pulse-height region due to the ^{12}C(n,α) and ^{12}C(n,n')3α events.

The threshold for the neutron detection was set at about 35 MeV during the test run. The dynamic range was limited by the natural burst of the beam, which was 12.5 MHz. A beam chopper is necessary to obtain a wider dynamic range and a higher efficiency with the maximum flight path of 22 m.

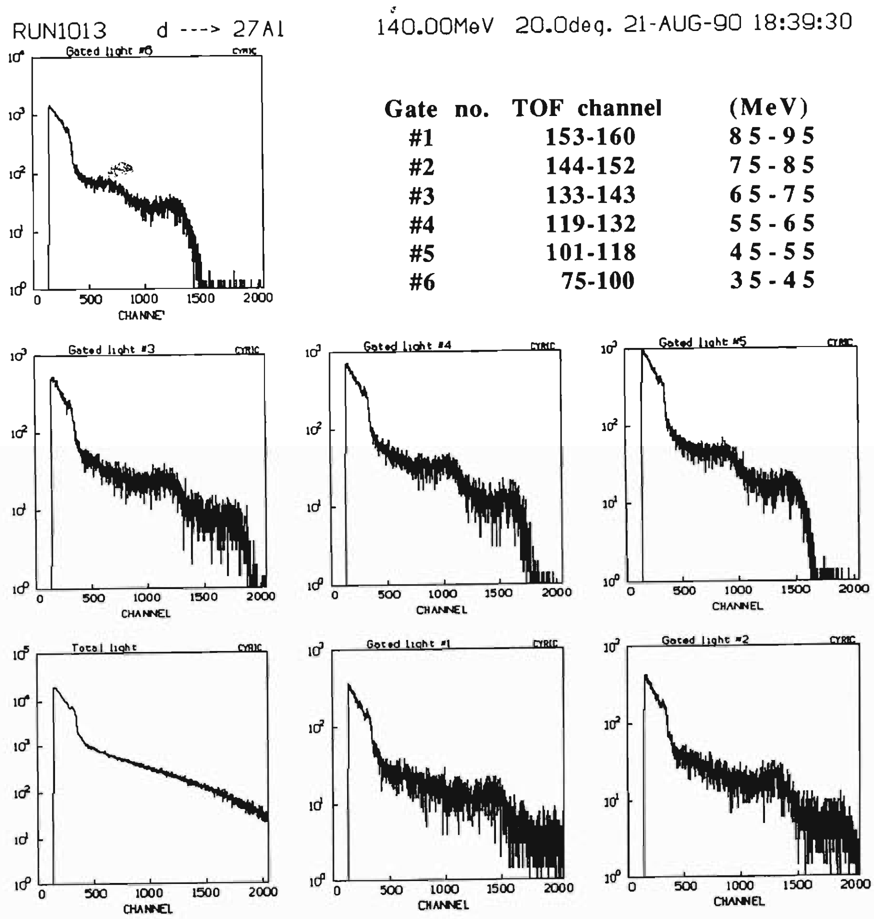

Gate no.	TOF channel	(MeV)
#1	153-160	85-95
#2	144-152	75-85
#3	133-143	65-75
#4	119-132	55-65
#5	101-118	45-55
#6	75-100	35-45

Fig. 2. Pulse height spectra gated by neutron events. Each spectra corresponds to the TOF gate indicated.

References

1) H. Ohnuma *et al.*: *RIKEN Accel. Prog. Rep.*, **21**, 164 (1987); *ibid.*, **22**, 148 (1988).

RIKEN Accel. Prog. Rep. **24** (1990)

III-5-24. Data Acquisition System at the RIKEN Ring Cyclotron

T. Ichihara, T. Inamura, and M. Ishihara

The general description of the data Acquisition System at the RIKEN Ring Cyclotron is described in a previous progress report[1] and IEEE transaction.[2] In this report, we will describe the update status of the system. Figure 1 shows overview.

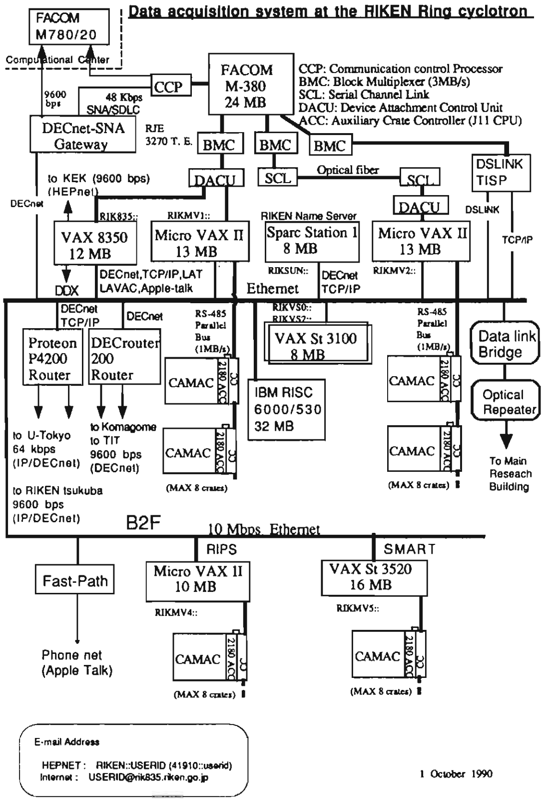

Fig. 1. Overview of the data acquisition system at the RIKEN ring cyclotron.

(1) On-Line Data acquisition System

Currently, five Micro VAX's are used for the on-line experiments of the Ring Cyclotron. The node names are:

RIKMV1:: Micro VAX II (1F counting room)

RIKMV2:: Micro VAX II (1F counting room)

RIKMV3:: Micro VAX II (Liniac Counting room)

RIKMV4:: Micro VAX II (B2F RIPS Counting room)

RIKMV5:: VAX Station 3520 (B2F SMART Counting room).

We can perform independent measurements and counter tests without interference. Now a new version of the data-taking program supports multi-crate parallel-readout using multi J11's (Starbursts). The throughput of the data taking is increased by using this parallel readout features. Currently there is a problem in DMA transfer of VAX Station 3520, resulting from the incompleteness of Q22 bus of the VAX-Stations 3520. This will be fixed soon. In order to increase the security, these on-line VAX's are connected to the RIKEN internal network and cannot access directly outside from RIKEN.

(2) Off-Line Data Processing System-1 (VAX/VMS)

The following VAX's are available in off-line data analysis.

RIKEN:: (virtual node name of the cluster)

RIK835:: VAX-8350 (Internet: rik835. riken. go. jp)

RIKVS0:: VAX STATION 3100 M38

RIKVS1:: VAX Station II/GPX

RIKVS2:: VAX Station 3100 M38

RIKSNA:: DEC net/SNA Gateway (to FACOM M-380, 780)

Theses computers are connected by LAVAC (Local Area VAX Clusters) using Ethernet. They are also connected to HEPNET (DECnet) and TISN (DECnet/IP) Internet and reachable from all over the word. (see Session 6 for detail)

(3) Off-line data processing system-2 (FACOM MSP)

Following FACOM MSP Main Frames are available at the RIKEN Accelerator Facility.

FACOM M-380 (RIKEN Accelerator Research Facility)

FACOM M-780/20 (RIKEN Computational Center)

These two FACOM's are connected by NJE using DSLINK on the Ethernet. These two FACOM's are also connected to DECnet/SNA Gateway and, and therefore 3270 full-screen terminal emulations and file transfer using RJE (Remote Job Entry) are available from VAX. Now we can login to FACOM M-380 and M-780 from any terminals for VAX and FACOM's. In addition, recently FACOM MSP supports TCP/IP on MSP, and now telnet clients and ftp clients are available on FACOM MSP. CLS (Cartilage Library System) on FACOM M-380 is now used to store large size Histograming data and also raw data. MTL (Magnetic Tape Library) is also available at FACOM M-780 to store large data.

(4) RISC work Stations

The following RISC (Reduced Instruction Set Computer) work Stations are installed at the facility.

Fujitsu	SPARC Station 1
IBM	Power station 530 (RS/6000)

SPARC Station 1 is used as a primary name server of the RIKEN domain in the TCP/IP connections. DECnet is also implemented to the SPARC Station. IBM Power station 530 is a very fast (13 MFLOPS, 35 MIPS) workstations for various purpose calculations for the accelerator.

(5) Apple Talk

Recently three Fast Path 4 and two Turbo net Star Couplers are installed in the Accelerator facility for interconnections of Macintoshes, Apple laser writes, VAX's. For the local connection, we use PhoneNet. Alisa Talk Software on VAX-8350 enables printing to any Apple laser writer from VAX and is very convenient. Currently there are about 10 Apple talk zones in RIKEN.

(6) Wide Area Network

Our Facility is connected to the world-wide network of HEPNET (High Energy Physics Network) / SPAN (Space Physics Analysis network) as Area 40, which is a part of DECnet Internet, and TISN internet (Tokyo University International Science Network) which is a part of "The Internet" (NSFnet, DARPA, MILnet etc.).

In order to support a wide area network connection, we are now supporting following 6 leased lines at the accelerator facility.

64 k bps (DECnet/IP) to the University of Tokyo, Faculty of Science

9600 bps (DECnet) to KEK (National High Energy Physics Laboratory)

9600 bps (DECnet/IP) to RIKEN Life Science Tsukuba Center

9600 bps (DECnet) to RIKEN Komagome bunsho (SOR group)

9600 bps (DECnet) to Tokyo Institute of Techology, Faculty of Science

9600 bps (DDX-80) to NTT DDX. (Dial in from the telephone).

In order to connect to the TISN internet, we use Proteon P4200 Router which supports the DECnet packet and IP packet routing simultaneously and Fujitsu-Sparc Station 1 as a primary name server. Modems, DSU's and Routers are connected to a non-stopping CVCF Power supply with a battery and a generator backup to minimize the down time of the network. We are now using DECnet Phase IV and it will be changed to phase V soon. BITNET has also been connected to the FACOM M-780 (JPNRKNCC) at the RIKEN Computational Center and FACOM M-380 (JPNRKNAF) at the RIKEN accelerator research facility recently via Rikkyo-University. Junet has also been changed from the public telephone line to the TISN line and now the most traffics of Junet use a high speed (64 kbps) digital leased line between RIKEN and the University of Tokyo.

The address of the electric mail of the general users of the RIKEN Ring Cyclotron VAX-8350 is as follows.

(HEPnet/SPAN) RIKEN::USERID (or 41910::USERID)

(Internet/BITnet) USERID@RIK835. RIKEN. GO. JP

References

1) T. Ichihara *et al.*: *RIKEN Accel. Prog. Rep.*, **21**, 149 (1987); **22**, 144 (1988).

2) T. Ichihara *et al.*: *IEEE Trans. Nucl. Sci.*, **36**, 1628 (1989).

RIKEN Accel. Prog. Rep. **24** (1990)

III-5-25. High Speed Serial Data Link for PC-9801

J. Fujita

Personal computers are used in various fields of experiments such as CAD, network terminals or local data collection systems of measurements. It is often necessary to transfer real time data at a high speed to remote systems. The high-speed data transfer can be realized by a conventional parallel wire method, but requires many wires. This problem can be solved by using serial data transfer, but the bit rate must be increased by a factor equal to the number of bits per data fields. For example, an 8-bits parallel system operating at 10 MHz needs a serial data transmission capability of more than 80 Mbps (8 MBytes/s). Serial data link, which consists of Am7968 transmitter and Am7969 receiver chips, possesses data throughput of more than 100 Mbps (about 10 Mbytes/s). A data link interface board, using these chips and optical fiber components, is made for a personal computer PC-9801 and tested.

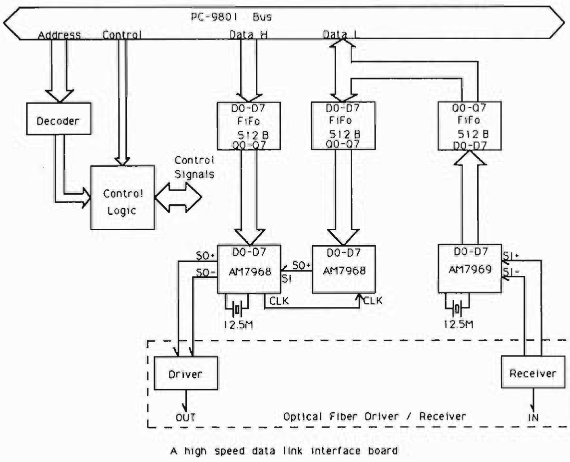

Fig. 1. A high speed data link interface board.

The block diagram of the test circuit is shown in Fig. 1. An optical fiber part of the data link surrounded by a broken line is constructed on a small separate board outside the interface board. The fiber ports are composed of an LED HFBR-1402, a light to voltage converter HFBR-2406, and their related circuits. Fast ECL signals between the data link chips and the fiber circuits are linked with four short RG-174/U cables.

The Am7968 transmitter has two operating modes of local and cascade. The local mode consists of a single transmitter communicating with a single receiver over serial mediums. The cascade mode consists of two or more daisy-chained (cascade) transmitters driving a equal number of receivers over a single serial medium. Two Am7968 transmitters are cascaded to send a two-byte word over a single serial line. In the cascade operation two bytes of data are loaded in parallel through the computer data bus simultaneously. The transmitter connected to the serial medium is referred to as the primary, and is operated in a local mode. The daisy-chained transmitter which supplies serial data to the primary is referred to as the upstream, and is operated in a cascade mode. Word data are written by a processor into transmitting FiFo memories of 512 bytes in size before transfer. Data transfer is began by address-ing a certain memory location. Once transmitting starts, the stocked quantity of data is continuously sent through the cascade over the serial medium without intervention of the processor in the manner of DMA operation until an empty flag of the FiFo memory locks the automatic cycle. The flag status is also sensed by the processor so that next data can be preset into the FiFo regardless of state of the serial medium. Idle time between transmitting data bytes is filled with SYNC bytes.

An Am7969 receiver monitors the serial link, selects only data bytes out of a serial pattern, and writes it into the receiving FiFo memory of 512 bytes in size, the contents of which are read by the processor through DATA L or lower 8 bits on the 16 bits data bus. As the cascade mode is not yet supported in the Am7969 receiver unlike the Am7968 transmitter, each data byte must be stored into the single FiFo memory in turn immediately after receipt. The access time of the receiving FiFo is 25 ns, half of that of the transmitting FiFo of 50 ns.

The FiFo memories and data link control logic are allocated at even addresses from c0000H to c000aH in hexadecimal the locations of which are unused part of user's ROM area in the computer.

The serial data throughput of about 9 Mbytes/s is obtained in a self-back test done by mutually tying fiber input and output ports with a single optical fiber cable of 5 m long. This value is limited by an internal logic of the chained transmitters; however the test shows that the interface can serve sufficiently as a high-speed serial data link between remote computer systems.

RIKEN Accel. Prog. Rep. **24** (1990)

III-6. Material Analysis

1. Measurement of the Surface Angle of a Non-Flat Target from the L/K X-ray Yield Ratio for Quantitative PIXE Analysis

K. Maeda, Y. Sasa, M. Takami, and M. Uda

PIXE (particle induced X-ray emission) method is capable of analyzing multiple elements in a small area in an arbitrary atmosphere, under vacuum or even non-vacuum, without destructing target materials. The method is, therefore, being extensively used in the fields of art, archaeology, and materials science, where the objects should be kept unimpaired during analysis.

For quantitative analysis by X-ray spectrometries, exact values of the incident angle of emerging beams (θ) and the take-off angle of emitted X rays (ϕ) are required for correcting matrix effects such as self-absorption. In general, the surfaces of objects are flattened prior to analysis and the angles, θ and ϕ, are regularized for that purpose. Such a treatment, however, can not be applied to the objects in the above-mentioned fields. Therefore, we have developed a simple, convenient technique to measure the surface angle (and hence, θ and ϕ) of a non-flat target by utilizing the yield ratio of L X rays and K X rays originated from one and the same element. The technique is based on the fact that the self-absorption factors for L and K X rays are quite different from each other. We examined the utility of this technique, choosing a bronze block of a known bulk composition (Cu : Sn : Pb=7 : 2 : 1 by weight) as a typical model target.

Figure 1 shows representative PIXE spectra obtained from the bronze target placed at different surface angles with respect to the incident beam direction. The target was excited, in air of 1 atm, with a beam of 1.16 MeV protons regulated to a 0.7 mm × 2.0 mm rectangle spot. X rays emitted from the target were detected with a Si(Li) detector through a composite absorber made of 0.5 mm-thick polyethylene and 8 μm-thick Co films. The detector was located at a fixed angle of 135° with respect to the incident beam direction.

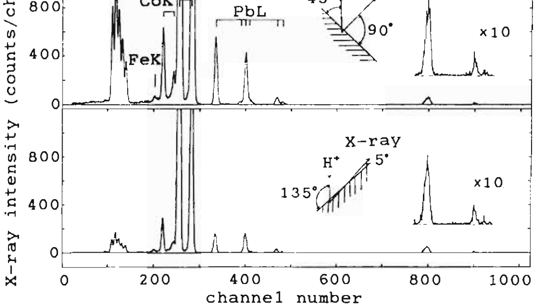

Fig. 1. PIXE spectra obtained from a bronze target (bulk composition Cu : Sn : Pb=7 : 2 : 1 by weight).

As shown in Fig. 1, the L/K X-ray yield ratio for Pb varied drastically with the surface angle of the target. The relationship between the surface angle and the L/K X-ray yield ratio shows no appreciable changes even when the composition of the target changes considerably, as seen from Fig. 2. Thus, rough values of θ and ϕ may be obtained from the observed L/K X-ray yield ratio in the absence of exact data on the composition of a target. Using these values as a first approximation, we are able to determine the exact values of θ and ϕ and the composition of the target after a few iterations.

Although we report here only the case of bronze, the technique is applicable to any target if the following requirements are fulfilled: (1) two kinds of X rays originated from one element are simultaneously detectable; (2) they are absorbed quite differently by the target itself, *e.g.*, Kα and Kβ of Zn from brass.

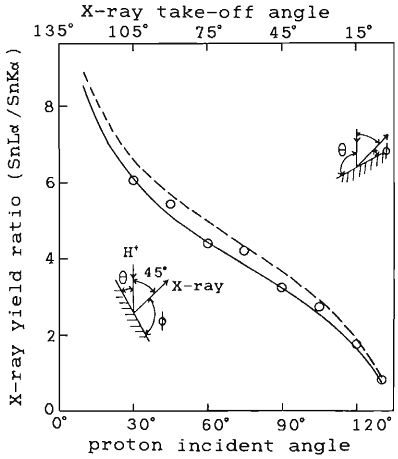

Fig. 2. Sn Lα/Kα X-ray yield ratio.
○, observed (bulk composition Cu : Sn : Pb=7 : 2 : 1); ——, calculated* for target of composition Cu : Sn : Pb=7 : 2 : 1; -----, calculated* for target of composition Cu : Sn : Pb=18 : 1 : 1. (* using the computer program PIXAN given by E. Clayton (PIXAN: The Lucas Heights PIXE Analysis Computer Package AAEC/M113, Australian Atomic Energy Commission, 1986))

RIKEN Accel. Prog. Rep. **24** (1990)

III-6-2. PIXE Analysis under Non-Vacuum Operation

Y. Sasa, K. Maeda, and M. Uda

(1) Improvement of Apparatus

A distinctive feature of a particle induced X-ray emission (PIXE) method is the attainability of trace element analysis on a small area (~ mm^2) in any arbitrary enviroments (external PIXE). This period, the existing PIXE apparatus was improved to be compatible with the operations under non-vacuum conditions. The modified part is schematically shown in Fig. 1. At the down stream end of an ion beam line, an Al exit pipe (3 mm I.D. × 150 mm length) was set and its top was sealed with a 6 μm thick Al foil. An ion beam from a vacuum chamber is transported into a non-vacuum room through the foil. The distance betweem the Al exit foil and a target is set to be 10.0 mm. When operation is carried out in the ordinary atmosphere, the maximum energy of a H^+ ion beam obtainable in this alignment is 1.16 MeV, in contrast with the maximum 1.6 MeV in vacuum operation. The modified machine was successfully used for the determination of trace elements in the materials which are highly sensitive to the change of enviroments and the substances having size beyond the vacuum chamber.

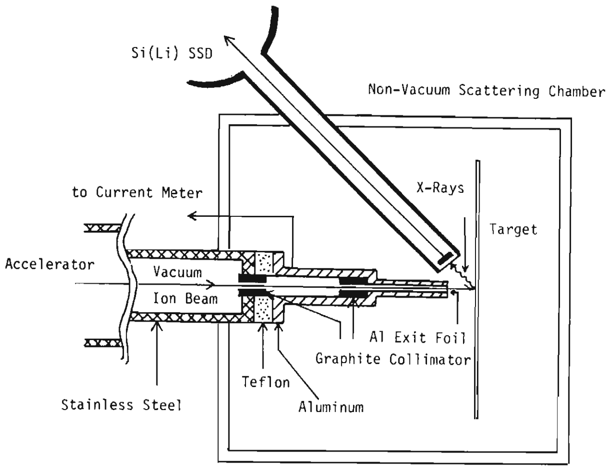

Fig. 1. Schematic view of modified part of PIXE machine compatible with non-vacuum operations.

(2) Applications of External PIXE

We can observe the differences in the clearness of characters printed on the sutras dedicated in the 11th and 14th centuries, which were found in the ceil of Koyasan temple. We inspected trace element contents on these characters by the external PIXE method, but detected no meaningful difference in the concentration of elements of $Z > 13$. This suggests the clearness difference may be attributed to light elements, mainly organic substances. On some sutra, red letters or spots were marked, and from these marks we detected high contents (~ 100 ppm) of Hg and S. Thus the red patterns were judged to contain cinnabar (HgS_2).

The characters on the sutras kept in bronze cases excavated in Seburi-mura, Saga-Prefecture, in 1986, are written with dark red-brownish chinese ink. Sutra researchers conjectured the coexistence of cinnabar or Bengara (Fe_2O_3) in the ink, accordingly. However, no sign of Hg species in the detection limit (~ ppm) and no difference in a Fe content, compared to references, were recognized by PIXE analysis.[1]

The chemical compositions (in weight) of traces (~ 5 mg) of rust collected from a bell-shaped bronze (doutaku) excavated from Hosoe-cho, Shizuoka-Prefecture, in Feb. 1990, were estimated by the PIXE method as 1.00: 0.92: 0.52: 0.11: 0.13 for Cu, Sn, Pb, As, and Sb, respectively. These results suggest that the selective dissolution of Cu and Sn in the bronze had been proceeded under ground by rain waters.

Trace element analysis on the coloring matters of wood block patterns (ukiyoe) printed in the latter Edo period is now in process. Reproduction and reappearance of original colored pictures are subjects of great interest.

References

1) Y. Sasa and K. Maeda: "X-ray spectroscopic analysis on sutra excavated from Seburiyama-kyouzuka", Res. Reports on Excavated Treasures of Seburi-mura, Ed. by Educational Committee of Seburi-mura, SAGA-Pref., **2**, 19 (1990).

RIKEN Accel. Prog. Rep. **24** (1990)

IV. NUCLEAR DATA

1. Status Report of the Nuclear Data Group

A. Hashizume, Y. Tendow, Y. Ohkubo, K. Kitao, and K. Sueki

The Nuclear Data Group has continued its activities$^{1)}$ on the following four items.

(1) Compilation of charged-particle induced reaction cross section data. We are concerned with the reactions of which products are used for mediobiological applications. The cross sections of the reactions producing the following isotopes were compiled in the EXFOR file: ^{11}C, ^{13}N, ^{15}O, ^{18}F, ^{28}Mg, ^{52}Fe, ^{67}Ga, ^{68}Ge, ^{68}Ga, ^{74}As, ^{77}Br, ^{82}Br, ^{77}Kr, ^{81}Rb, ^{82m}Rb, ^{111}In, ^{123}Xe, ^{123}Cs, ^{127}Xe, ^{123}I, ^{124}I, and ^{125}I nuclei.$^{1)}$ In producing these isotopes, impurities are produced by competing reactions. We also compiled the reaction cross sections for various combinations of incident particles and target nuclei to produce these impurities.

An effort was made to complete the collection of the data$^{2-4)}$ on the production of ^{82}Sr, ^{68}Ge, ^{68}Ga, and ^{111}In nuclides. We almost have completed a set of data files of the cross sections of the reactions producing these nuclides. A collection of data and a review on the cross sections on ^{123}I, ^{123}Xe, ^{123}Cs were completed. The results were published from IAEA (International Atomic Energy Agency).$^{5)}$ For further publication, we are trying to make graphs for all cross sections we concern.

Using a computer code for least squares fittings developed last year, experimental excitation functions which produce ^{67}Ga and ^{85}Rb were fitted. Besides linear polynominal and exponent functions, a function representing level densities has been tried for these fittings.

The compilation of the integrated and differential reaction cross-section data originated in Japan in the EXFOR files is continued.

(2) We continue to evaluate the details of collected cross-section data on the ^{12}C(p, pn)^{11}C, ^{27}Al(p, 3pn)^{24}Na, ^{63}Cu(p, 2n)^{62}Zn, and ^{65}Cu(p, n)^{65}Zn reactions to propose standard cross sections for monitor reactions.

(3) For the mass chain evaluation of nuclear structure data, the evaluation of the nuclear structure data on the $A=177$ mass chain is in progress. The deadline of this evaluation is the end of this year.

(4) The references of annual reports and quarterly reports published in Japan during 1989 were compiled in the form of Nuclear Structure References Coding. This work is connected to a consignment research from Japan Atomic Energy and the compilation of recent reference files at Brookhaven National Laboratory (BNL). We have responsibility for the compilation of references published in Japan and all references published in 1987 and 1988 were sent to the BNL Data Center. All compiled references are published periodically as 'recent references' in Nuclear Data Sheets.

References

1) A. Hashizume, Y. Tendow, Y. Ohkubo, K. Kitao, and K. Sueki: *RIKEN Accel. Prog. Rep.*, **23**, 100 (1989).
2) Y. Tendow, A. Hashizume, Y. Ohkubo, and K. Kitao: This Report, p. 129.
3) K. Kitao, A. Hashizume, Y. Tendow, and Y. Ohkubo: This Report, p. 130.
4) A. Hashizume, Y. Tendow, K. Kitao, and Y. Ohkubo: This Report, p. 131.
5) A. Hashizume, Y. Tendow, and K. Kitao: INDC (JPN)-144/L, Oct. (1990) (published from International Atomic Energy Agency).

RIKEN Accel. Prog. Rep. **24** (1990)

IV-2. Cross Section Data for ^{68}Ge Production

Y. Tendow, A. Hashizume, Y. Ohkubo, and K. Kitao

The nuclide ^{68}Ge($T_{1/2}$ = 270.8 d) decays to ^{68}Ga($T_{1/2}$ = 67.629 m) by electron capture, and ^{68}Ga decays by 89% positron emission and 11% electron capture and emits weak γ-rays (3%). Thus, a ^{68}Ge-^{68}Ga system provides a useful generator of positron emitters which could be applied to medical diagnosis with positron computer tomogragh for the localization of malignant human tumors. The short-lived positron emitter ^{68}Ga is separated from ^{68}Ge by milking at any time when a diagnosis is required in hospitals having no cyclotron facilities.

Only a few cross sections measured for ^{68}Ge production are found in the literature. The reaction types, incident energy ranges, and maximum cross sections for the excitation functions measured up to the present are summarized in Table 1.

Table 1. Cross Sections for ^{68}Ge Production.

Reaction	Energy (MeV)	σ max (mb at MeV)	Reference
^{69}Ga (p, 2n)	13 - 56	465 (at 20)	1)
^{71}Ga (p, 4n)	36 - 56	137 (at 43)	1)
^{70}Ge (p, p2n)	24 - 64	100 (at 37)	2)
^{64}Zn (α, γ)	9.4 - 15.6	0.771 (at 11.3)	3)
	10.5 - 16.5	0.9 (at 16.5)	4)
^{66}Zn (α, 2n)	17 - 26	180 (at 26)	3)
	19 - 37	154 (at 31)	5)
^{58}Ni (^{16}O, 2pα)	50 - 70	204 (at 70)	6)
Y (p, spall)	593	6.75	7)
Rb (p, spall)	593	7.80	7)
Br (p, spall)	593	11.1	7)
As (p, spall)	593	10.7	7)
Rb+Br (p, spall)	800	19	8)

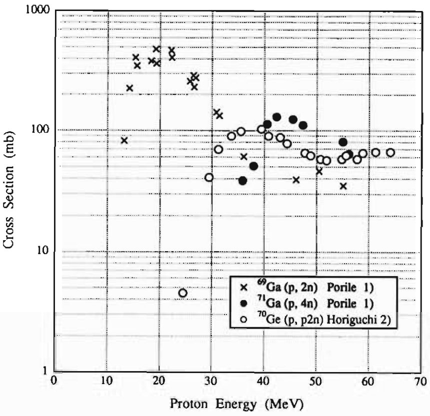

Fig. 1. Excitation functions for Ga(p. xn) and Ge(p, pxn) reactions.

As for the proton-reaction cross section, Porile *et al.*[1] measured for ^{69}Ga(p, 2n), ^{71}Ga(p, 4n) reactions and Horiguchi *et al.*[2] for ^{70}Ge(p, p2n) reaction (Fig. 1). The cross section for (p, xn) reaction, in contrast to the (p, pxn), falls rapidly from the maximum as the proton energy increases. Therefore, in order to obtain large thick target yields, the (p, pxn) reaction would be advanta-geous over the (p, xn) reaction when higher energy proton beams are available.

Nagame *et al.*[5] measured corss sections for the ^{66}Zn(α, 2n) reaction using natural zinc targets. Ruddy *et al.*[3] also measured cross sections for the same reaction in a lower energy part of excitation.

Grütter[7] measured spallation cross sections on As, Br, Rb, and Y targets at a proton energy of 593 MeV.

References

1) N.T. Porile, S. Tanaka, H. Amano, M. Furukawa, S. Iwata, and M. Yagi: *Nucl. Phys.*, **43**, 500 (1963).
2) T. Horiguchi, H. Kumahora, H. Inoue, and Y. Yoshizawa: *Int. J. Appl. Radiat. Isot.*, **34**, 1531 (1983).
3) F.H. Ruddy and B.D. Pate: *Nucl. Phys.*, **A127**, 305 (1969).
4) N.T. Porile: *Phys. Rev.*, **115**, 739 (1959).
5) Y. Nagame, M. Unno, H. Nakahara, and Y. Murakami: *Int. J. Appl. Radiat. Isot.*, **29**, 615 (1978).
6) J.J. Simpson, P.O. Tjøm, and I. Espe, G.B. Hagemann, B. Herskind, and M. Neiman: *Nucl. Phys.*, **A287**, 362 (1977).
7) A. Grütter: *Int. J. Appl. Radiat. Isot.*, **33**, 725 (1982).
8) B.L. Cohen and E. Newman: *Phys. Rev.*, **99**, 718 (1955).

RIKEN Accel. Prog. Rep. **24** (1990)

IV-3. On the Production Cross Sections of ^{82}Sr

K. Kitao, A. Hashizume, Y. Tendow, and Y. Ohkubo

We have reviewed the status of production of strontium-82, as the parent of ^{82}Rb, by charged-particle induced reaction. ^{82}Rb is an important positron emitting nuclide used to study on the blood flow through heart, brain, *etc.*[1] The half-life of ^{82}Rb is short (1.27 m), but that of its parent ^{82}Sr is moderately long (25.0d). Thus, ^{82}Rb can be separated from ^{82}Sr by milking.

For production of ^{82}Sr, ^{nat}Kr(α, xn), ^{nat}Kr (^{3}He, xn), ^{85}Rb(p, 4n), and ^{nat}Mo(p, spall)[2] reactions have been suggested to be practical production methods, although heavy-ion induced reactions, such as ^{71}Ge(^{12}C, xn), are used in the field of nuclear physics. In these reactions, Tarkanyi *et al.*[3] pointed out that at present the most effective method is the spallations. Tarkanyi *et al.*[4] carried out experimental investigations, using high energy ^{3}He and α-particle induced reactions on natural krypton gas.

Recently, some commercial radiopharmaceutic suppliers have used highly enriched ^{124}Xe gas as the target for production of ^{123}I. As compared with the purchasing cost of this gas, that of enriched ^{80}Kr gas is very low.

Thus, we recommend the use of enriched ^{80}Kr and the (α, 2n) reaction for the production of ^{82}Sr. This method is most advantageous in considering the size of cyclotron and the radiation protection for workers engaged in the production of radiopharmaceuticals.

No experimental examination has been made of the cross sections of the ^{80}Kr (α, 2n) reaction. We calculated these cross sections by using a code ALICE/Livermore 82 (see Fig. 1). From these calculations, we expect that the reaction gives a resonable large yield for ^{82}Sr production and small one for ^{83}Sr, a main impurity.

Table 1. List of measured ^{82}Sr production cross sections.

Reaction	Particle energy (MeV)	Ref.	Note
^{85}Rb(p,4n)	32-70	5)	99.78%en. ^{85}RbCl
^{90}Zr(p,3p6n)	80-86	6)	97.7%en. ^{90}ZrO$_2$, CY*
Rb(p,spall)	800	7)	RbBr, CY
Kr(^{3}He,xn)	11-33	3)	
	20-90	4)	
Kr(α,xn)	11-33	3)	
	20-120	4)	
^{80}Kr(^{3}He,n)	25.4	8)	70.1%en. ^{80}Kr
^{82}Kr(^{3}He,3n)	12-34	9)	72.9%en. ^{82}Kr
^{83}Kr(^{3}He,4n)	12-34	9)	73.1%en. ^{83}Kr

* CY = cumulative yield

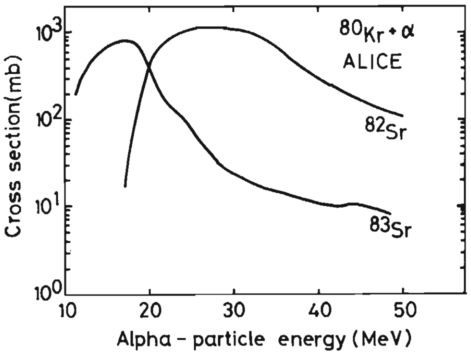

Fig. 1. Calculated excitation functions ^{80}Kr(α, 2n)^{82}Sr and ^{80}Kr(α, n)^{83}Sr.

References

1) T. Jones: *Appl. Radiat. Isot.*, **38**, 171 (1987).
2) K.E. Thomas: *Radiochim. Acta*, **37**, 137 (1984).
3) F. Tarkanyi *et al.*: *Appl. Radiat. Isot.*, **39**, 135 (1988).
4) F. Tarkanyi *et al.*: *ibid.*, **41**, 91 (1990).
5) T. Horiguchi *et al.*: *Int. J. Appl. Radiat. Isot.*, **31**, 141 (1982).
6) M.V. Kantelo and J.J. Hogan: *Phys. Rev.*, **C14**, 64 (1976).
7) P.M. Grant *et al.*: *Int. J. Appl. Radiat. Isot.*, **33**, 415 (1982).
8) W.P. Alford *et al.*: *Nucl. Phys.*, **A330**, 77 (1979).
9) F. Tarkanyi *et al.*: *Radiochim. Acta*, **43**, 185 (1988).

RIKEN Accel. Prog. Rep. **24** (1990)

IV-4. Nuclear Reaction Data for the Production of ^{111}In

A. Hashizume, Y. Tendow, K. Kitao, and Y. Ohkubo

Because of the decay characteristics ($t_{1/2}=2.83$ d, EC, $E_\gamma=171$ keV (90%) and 245 keV (94%)), ^{111}In is suitable in studing slow *in vivo* process. This radionuclide is very useful for locating and imaging certain tumours, visualization of the lymphatic system. Among many kinds of combinations of targets and incident particles, the common reactions utilized so far for the production of ^{111}In are tabulated in Table 1. In the column 3, the maximum cross sections were shown and in the column 4 incident particle energies which give the maximum cross sections.

^{111}Cd(p, n)^{111}In reaction: Five authors[1-5] reported on the cross sections of the ^{111}Cd(p, n)^{111}In reaction. As shown in Fig. 1, from the threshold to 7 MeV incident energy, there is an agreement between Blaser's results[1] and with Otozai's.[4] There is also an agreement between Wing[3] and Skakun.[5] However, a discrepancy is found between the results obtained by Blaser and by Otozai and those by Wing and by Skakun. A precaution for beam contamination was reported by Wing, but not by others. It is difficult therefore to judge which correct is. By using an Alice code, calculation was made by changing initial exciton numbers. As shown in Fig. 1, 2n+2p excitons give the best agreement on cross sections above 18MeV of incident proton energies.

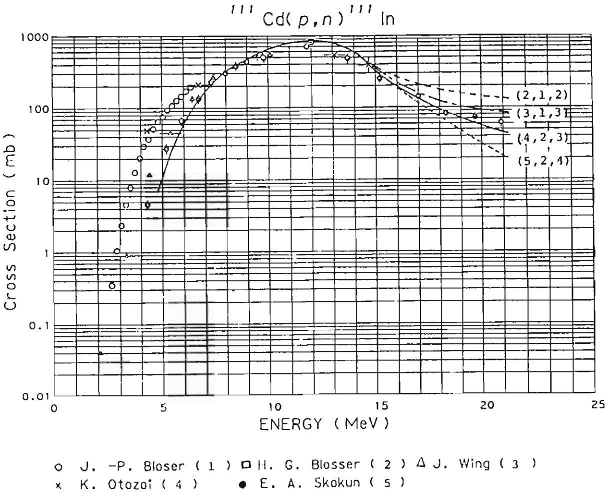

Fig. 1. Excitation function for the ^{111}Cd(p, n)^{111}In reaction. The curves calculated by an Alice code with different exciton numbers are shown.

Table 1. Cross sections for ^{111}In production.

Type of reaction	Q value (MeV)	Maximum σ (mb)	Energy (MeV)	Energy range studied (MeV)	References
^{111}Cd(p, n)^{111}In	− 1.62	700	12	3-21	1),2),3),4),5)
^{112}Cd(p, 2n)^{111}In	−11.02	1,000	21	9-37	4), 5)
^{109}Ag(^{4}He, 2n)^{111}In	−14.03	1,000	25	14-38	6), 7), 8)

^{109}Ag(α, 2n)^{111}In reaction: This reaction was studied by Bleuler,[6] Fukushima,[7] and Chaubey.[8] There are reasonable agreement between the cross sections measured by Fukushima and by Chaubey in the incident energy region of 10 to about 20 MeV. However, in the 21 to 24 MeV region, Chaubey's data are about 25% lower than Fukushima's. Bleuler's results obtained from 14 to 18 MeV agree with those of Fukushima. Chaubey reported that a preequilibrium studied by geometry-dependent hybrid model with 2n+2p+0h gives a good fit to the experimental data.

Other reactions: Yields obtained by the ^{110}Cd(d, n)^{111}In, ^{111}Cd(d, 2n)^{111}In and ^{109}Ag(^{3}He, n)^{111}In reactions were reported. However, we have found so far no cross section measurements on these reactions.

References

1) J.-P. Blaser, F. Boehm, P. Marmler, and D.C. Peaslee: *Helv. Phys. Acta*, **24**, 3 (1951).
2) H.G. Blosser and T.H. Handley: *Phys. Rev.*, **100**, 1340 (1955).
3) J. Wing and J.R. Huizenga: *ibid.*, **128**, 280 (1962).
4) K. Otozai, S. Kume, A. Mito, H. Okamura, R. Tsujino, Y. Kanchiku, T. Katoh, and H. Gotoh: *Nucl. Phys.*, **80**, 335 (1966).
5) E.A. Skakun *et al.*: *Izv. Akad. Nauk. SSSR*, **39**, 24 (1975).
6) E. Bleuler, A.K. Stebbins, and D.J. Tendam: *Phys. Rev.*, **90**, 460 (1953).
7) S. Fukushima, S. Kume, H. Okamura, K. Otozai, K. Sakamoto, Y. Yoshizawa, and S. Hayashi: *Nucl. Phys.*, **69**, 273 (1965).
8) A.K. Chaubey, M.K. Bhardwaj, R.P. Gautam, R.K.Y. Singh, M.A. Ansari, I.A. Rizvi, and H. Signh: *Appl. Radiat. Isot.*, **41**, 401 (1990).

RIKEN Accel. Prog. Rep. **24** (1990)

IV-5. Cross Sections Calculated by an ALICE Code in the A=50−60 Region

A. Hashizume, Y. Tendow, and K. Kitao

In Order to know the applicability of a hybrid model to the calculations of cross sections induced by charged particle reactions, an Alice Livermore code was tested in the mass region A=50−67, and the results were compared with experiment. The purposes of these calculations are to obtain the best combination of parameters to reproduce experimental results and to know the limit of its reproducibilities. Calculations were performed with a FACOM M780 computer. In this mass region, several attempts have been made to analyze excitation functions; however, it was sometimes difficult to fit calculated results to experiment.

In this study, p, d, ^{3}He, and α-particles were chosen as incident ions. The calculations of cross sections were made for 41 targets in the energy region up to 100MeV of incident particles. Experimental data were collected from the literature. When data were given only by figures, we got numerical data from the figures with an aid of a digitizer.

In the reactions which follow complete compound reactions, absolute peak values and peak widths can reproduce the experimental results fairly well for p or α-particle incident. However, in the energy region where a pre-compound process is dominant, the results of calculation depend sensitively on the number of excitons, and can hardly reproduce the absolute value and slope of curves of experimental results. It should be pointed out that the energy spectra of emission particles are needed to decide the number of initial excitons. In Fig. 1, the results of calculations on the ^{65}Cu(p, n)^{65}Zn reactions are shown. Experimental data are taken from Ref. 1. The results of ^{54}Fe(p, p2n)^{52}Fe and ^{65}Cu(α, 2n)^{67}Ga are shown in Fig. 2 and 3, respectively.

For d- and ^{3}He-induced reactions, it is difficult to deduce general conclusion because less experimental results have been reported than those for p or α-particle induced reactions. In addition, large discrepancies between calculation and experiment were observed in some reactions. Calculations for parameter search are still performing for these reactions.

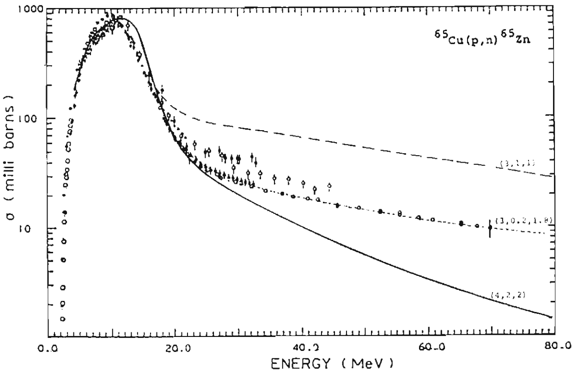

Fig. 1. Excitation function of ^{65}Cu(p, n)^{65}Zn reaction. The number of exciton is shown by a symbol (a_1, a_2, a_3), where a_1 is the initial exciton number, a_2 is the initial excited neutron number and a_3 is the initial excited proton number.

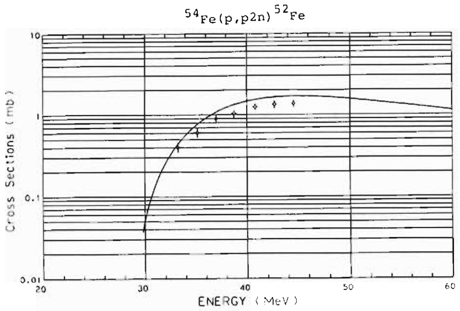

Fig. 2. Excitation function of ^{54}Fe(p, p2n)^{52}Fe and the calculated curve.

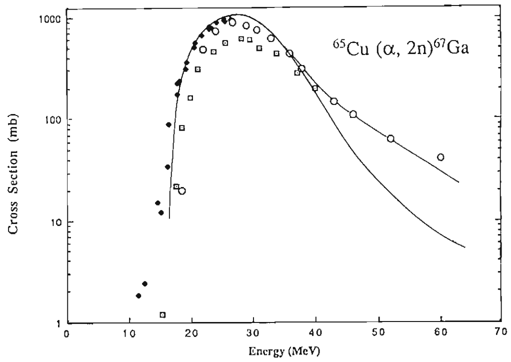

Fig. 3. Excitation function of ^{65}Cu(α, 2n)^{67}Ga and the calculated curves.

References

1) A. Hashizume, Y. Tendow, Y. Ohkubo, and K. Kitao: *RIKEN Accel. Prog. Rep.*, **21**, 186 (1987).

RIKEN Accel. Prog. Rep. **24** (1990)

V. DEVELOPMENT OF ACCELERATOR FACILITIES

1. Ion Accelerator Development

1. Test-Bench Performance of ECR Ion Source (NEOMAFIOS)

E. Ikezawa, Y. Miyazawa, M. Hemmi, Y. Chiba, T. Chiba,
M. Kase, M. Fujimaki, T. Aihara,* T. Ohki,* and H. Hasebe*

An ECR (Electron Cyclotron Resonance) ion source NEOMAFIOS[1)] developed by the ion source development group of C.E.N.-G. (Centre d'Etudes Nucleaires de Grenoble) in France has the features of a small size and low power consumption owing to the permanent magnets (FeNdB) used for both the hexapole field and mirror field. We purchased a set of NEOMAFIOS to replace the PIG source presently used in RILAC because the narrow space of RILAC and the limited power supply capacity of the ion source site. Figure 1 shows the schematic drawing of the source and Table 1 shows its main parameters.

The performance test of NEOMAFIOS was carried out from March to July 1990 on a test bench capable of analyzing charge-states. Operations with 8 gaseous and 25 solid elements were tried and optimum operational parameters were searched for several ion species. In a usual operation, an RF power of less than 400 W is enough and the operating pressure is $3 \times 10^{-7} - 1 \times 10^{-6}$ Torr at the extraction electrode. Ion charge-state spectra were mesured with one to several sets of operational parameters for each element. Figure 2 shows a typical spectrum obtained with Pb.

Table 1. Main parameters of the source.

Magnetic parameters	
Material of permanent magnet	FeNdB
Magnetic field on axis	0.21–0.52 T
Electric power	0 kW
Microwave parameters	
RF frequency	8 GHz
RF power injection	Axial
RF power	1.7 kW max
Final tube (Klystron)	Thomson TH-2461
Electric power consumption	5 kVA
Vacuum window	Al_2O_3
Dimensions	
Chamber diameter	66 mm
Chamber length	148 mm
Ion outlet bore	10 mm
Extraction electrode bore	16 mm
Extraction gap	45 mm
Extraction voltage	10 kV

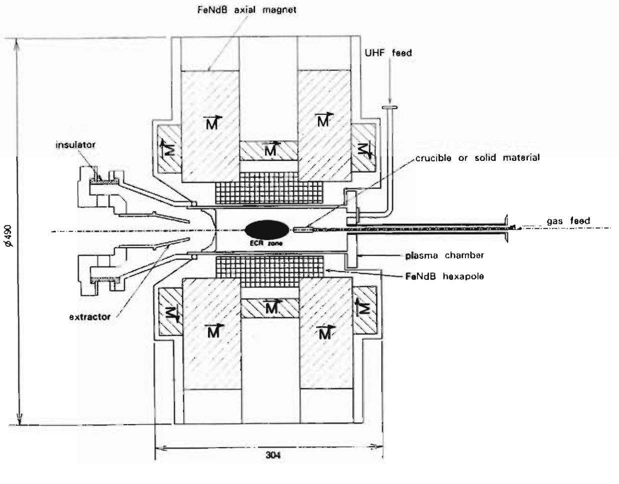

Fig. 1. Schematic drawing of the source.

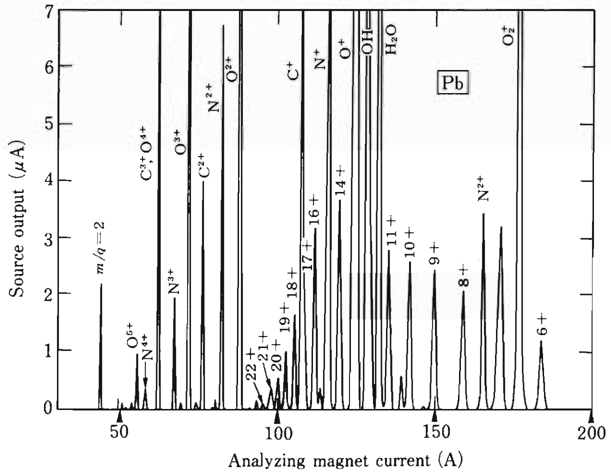

Fig. 2. Charge-state spectrum with Pb optimized at an 18+ peak. RF power, 270 W; Beam extraction voltage, 10 kV; Mixing gas, O_2.

---

* Sumijyu Accelerator Service, Ltd.

Table 2. Output currents of the source.

ECRIS (NEOMAFIOS) Ion Currents (e μ A)																								
Ion	Gas	Charge state																						Remarks
		1+	2+	3+	4+	5+	6+	7+	8+	9+	10+	11+	12+	13+	14+	15+	16+	17+	18+	19+	20+	21+	22+	
^{4}He	He	500	210																					
^{12}C	CO_2,He	75	57		18	2.3																		
^{14}N	N_2	90	95	63	50	30	2.8																	
^{16}O	O_2		85	65		15	6.0	0.25																
^{20}Ne	Ne	215	96	82	65	35	6.5																	
^{40}Ar	Ar,O_2		75	55	50		30	24	26	10		0.7	0.1											
^{84}Kr	Kr,O_2				17.5	16			17	11.5	9.0	6.8		3.7		1.2		1.0		0.5				
^{129}Xe	Xe,O_2				10	11	11	13.5	14	10	6.6		3.8	3.1	2.5	2.2		1.3	1.1		0.4			
^{24}Mg	O_2	30				35		30																MgO, ϕ 4, rod
^{27}Al	O_2		22	34	33		15	6.0	2.0	0.1														Al_2O_3, ϕ 4, rod
^{28}Si	He			15		33				1.0														SiO_2, ϕ 3, rod
^{40}Ca	O_2		72	70	55		36	27	26.5	25.5		5.5	1.0											CaO, ϕ 5.7, rod
^{48}Ti	O_2		**5.2**			15		14			6.5	4.4		0.3										Ti, ϕ 2, rod
^{51}V	O_2		**2.5**		7.5	12	12	12	10	7.5	4.8	2.4	1.0											V, ϕ 1, 2 rods
^{52}Cr	O_2		9		27	30	32.8	25.5	15	8.3	5.8	3.6	2.0		0.3									Cr, ϕ 2, rod
^{55}Mn	O_2				51	68	60	42	19	9	4	2.6	0.8											ϕ 4, T. crucible
^{56}Fe	O_2,He					15	15			11.3	8.2	4.6	3.0	1.0										Fe, ϕ 1, rod
^{58}Ni	O_2,He		4.0	4.8	5.2	8.0	12	13.5	14	11	8.0		1.7	0.75	0.25									Ni, ϕ 1, 2 rods
^{59}Co	He		**3.6**	7.0	15.6	26	25.6	19	11	6.0	2.2													Co, ϕ 1, 2 rods
^{63}Cu	O_2			9.0		17	19	17	15		6.5	4.0												ϕ 4, Ta crucible
^{64}Zn	He		**27**	32		35	34	26		8.3	0.4													ϕ 4, Ta crucible
^{74}Ge	O_2	1.3	**1.8**	3.0		4.3	5.5	6.3	6.0	4.6	2.6	1.3	0.5	0.27										ϕ 4, Ta crucible
^{90}Zr	O_2				1.0		1.7	1.9	2.6	4.2	4.5	5.0	6.5		2.6		0.8							Zr, ϕ 2, rod
^{93}Nb	O_2			11	19	23	13	9.5	7	7	7	5	3	1.7	0.6									Nb, ϕ 3, rod
^{98}Mo	O_2		**2.0**		3.8	5.0		7.5		3.5	3.5	3.0		0.65										Mo, ϕ 2, rod
^{107}Ag	He			1.2	2.6	5.2		8.4	8.7	9.0	7.3	6.5	4.9	2.5	1.6	1.2	0.9	0.4						Ag, ϕ 3, rod
^{115}In	O_2			10	21	31	24	22	16	13.5	10.5	7.5	5.3	4.5	3	2	1.2	0.6	0.2					ϕ 4, Ta crucible
^{120}Sn	O_2,He				3.0	5.2	5.7	6.6	10	7.0		4.2	2.7	1.8	1.0		0.2							ϕ 4, Ta crucible
^{181}Ta	O_2					8.5		18	19	19		14	12		8.2		5.5	5.0	4.3	3.0	2.0	1.1	0.6	Ta, ϕ 1, rod
^{184}W	O_2					0.9	1.0	1.4	1.7	2.4			4.0		3.0		1.5	0.9	0.5	0.2				W, ϕ 1, rod
^{197}Au	O_2—						13.7		19.2	16.5	13.7		10.0	6.0		4.3	4.0	2.6	1.5	0.8	0.4	0.3		ϕ 4, Ta crucible
^{208}Pb	O_2						7.7	10	13.8	13.3	10.8	8.3			5.2		3.5		1.7	1.0	0.5	0.3	0.1	ϕ 4, Ta crucible
^{209}Bi	He						3.3		8.3	10.0	8.7	7.6	5.6		5.6		3.6	2.3	1.4	0.87	0.45	0.32	0.1	ϕ 4, Ta crucible

NEOMAFIOS showed very steady operation in ion production of gaseous elements, and the plasma chamber scarcely needs cleaning. Three methods were examined to insert a solid material into the plasma: a pure metal rod (1–3 mm in diameter and 50 mm in length), an oxide ceramics rod (3–5.7 mm in diameter and 40 mm in length), and a power contained in a small tantalum crucible (4 mm in diameter, 0.3 mm in thickness, and 50 mm in length). Ions of most solid elements can be produced with one of these methods. For ferromagnetic materials such as Fe, Ni, and Co, the samples were made of two twisted wires (each 1 mm in diameter) in order to overcome bending moment due to the magnetic force. Results of the test are summarized in Table 2.

The ECR ion source took 6–12 hours to restore steady operation once the plasma chamber was exposed to the atmosphere. We will have to consider about it in beam time arrangements when we use such ion species that require cleaning of the plasma chamber.

The RILAC beam service with the ECR ion source will start in the middle of January 1991.

References

1) G. Melin *et al.*: Proc. Int. Conf. on Physics of Multiply Charged Ions and Int. Workshop on E.C.R. Ion Sources, Grenoble, France, p. 673 (1988).

RIKEN Accel. Prog. Rep. **24** (1990)

V-1-2. Improvements of the RIKEN Ring Cyclotron Control System

M. Kase, I. Yokoyama, M. Nagase, and Y. Yano

In the past year, the control system (using a MELCOM 350/60[1]) of RIKEN Ring Cyclotron was improved mainly in its man-machine interface. Two sets of new colour graphic displays (Mitsubishi M4328N) were added into an operational console desk. Compared to old ones (M4328), they draw a brighter picture rapidly with higher resolution, displaying mainly a graphic data of beam measurements such as beam turn patterns inside the cyclotron, beam profiles, and trends of beam intensities. A colour hard copy is available for new displays.

A rotary encoder system was introduced as a new input device replacing partly existing touch panels. It promises a real-time-like control of a quadrupole magnet, for example, when a beam spot on a target point is adjusted finely. Three sets of encoders were installed in a small box with a light cable, and they can be used anywhere around the console desk.

Softwares were also inproved and adapted to the new hardwares. Programs "TPMAGY" and "REC00" were newly developed for controlling magnet power supplys with both a touch panel and a rotary encoder. In "TPMAGY", an operator can search easily and quickly a magnet to be controlled out of about 700 elements with the aid of other program for beam diagnosis.

Figure 1 shows an example of the flow of programs communicating with each other via memory on GCA (Grobal Common Area). "TPMAGY" gets information about the position where the last measurement with a beam profile monitor was done by other program "TPPF", that is, where an operator should turn his intention. "TPMAGY" then can make a selection list, on a touch panel screen, of up-to-date magnets arranged from this position toward the upstream beam line, referring to the data base on GCA. Three magnets are selected by a touch action, and their data are stored on GCA. When an operator actuates one of rotary encoders, "REC00", started by "TPMAGY", feels it, and makes a command to change a current of the corresponding magnet. Since "REC00" has no output function except for storing the result of its action one by one on GCA, it can make a quick response to rotary encoder. At the end of access by "REC00", "TPPF" starts, by itself, the next measurement at the same position and displays the result of the access on a graphic screen. This correlative program flow makes the operation simpler and faster.

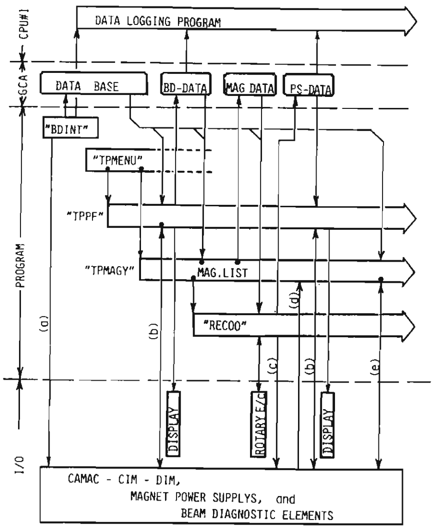

Fig. 1. Example of the flow chart of programs communicating with each other via GCA memory. At the beginning of operation, a program "BDINT" installs the data base of power supplys and beam diagnostic elements on GCA, (f), and initializes the CAMAC-CIM-DIM system,[1] (a). After that, "TPPF" and "TPMAGY" are started. The arrow expresses program's access, and arrows with a small solid circle on their end are triggered by a touch panel action; (b), measurement of profile monitor; (d), periodical status read; (c) and (e), the current setting.

The data written by these programs on GCA are transferred periodically to other computer (CPU#3) and stored in its logging file. These stored data would be useful in the future operations.

References

1) T. Wada, J. Fujita, I. Yokoyama, T. Kambara, and H. Kamitsubo: *Sci. Papers I.P.C.R.*, **79**, 28 (1985).

RIKEN Accel. Prog. Rep. **24** (1990)

V-1-3. Development of a LNA Laser for Polarized ^{3}He Ion Source of Injector AVF Cyclotron

A. Minoh, T. Fujisawa, and Y. Taniguchi

For the polarized ^{3}He ion source of the Injector AVF Cycrotron, we studied a 1083 nm laser$^{1-3)}$ of lanthanum neodymium hexaaluminate (LNA) excited with an Ar laser (514 nm). Its fluorescence spectrum exhibits two peaks, and the yield of 1054 nm light is higher than that of 1082 nm.$^{2)}$ The laser oscillation at the 1054 nm should be suppressed in a cavity to obtain the 1083 nm laser oscillation.

In order to study the condition of the laser oscillation at 1083 nm, a simple laser cavity is set up as shown in Fig. 1. The crystal *c*-axis is set in the longitudinal direction and a lens L1 whose focal length of 4 cm focuses an Ar laser beam on the LNA crystal where the 1083 nm laser radiation is focused with mirrors M1 and M2. The mirror M1 reflects 100% of the 1083 nm light and 90% of the 1054 nm suppressing the undesirable 1054 nm oscillation,* and the reflectivity of M2 is 98% for both lights. All the mirrors and lenses are antireflection coated. We investigate two laser rods of single crystals of 5 mm in diameter and 20 mm in length; in one (LNA10) made by Union Carbide Co. Ltd., a Nd concentration is 10 atomic percent and in the other (LNA15) made by Synthetic Crystal Product Co. Ltd. 15%. The crystal ends are polished perpendicular to the cylinder axis and antireflection coted. The LNA10 crystal absorbs 70% of incident light and the LNA15 80%.$^{3)}$

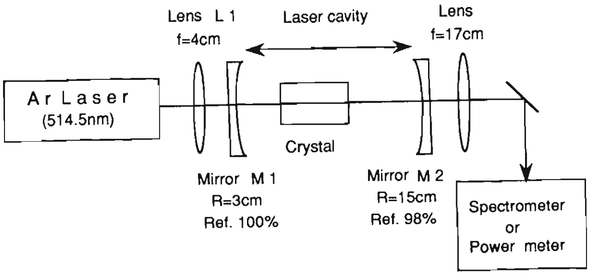

Fig. 1. Test cavity used for the LNA laser pumped by an Ar$^+$ laser.

Figure 2 shows spectra of fluorescence of Nd^{3+} in LNA and laser oscillation at 1083 nm. The width of the peak of laser oscillation is estimated as 100GHz. The laser must be tuned in the atomic transition line of ^{3}He(2S → 2P) whose Doppler width is 2GHz. A 0.1mm air-gap etalon is set in the cavity to reduce the width of the laser oscillation.

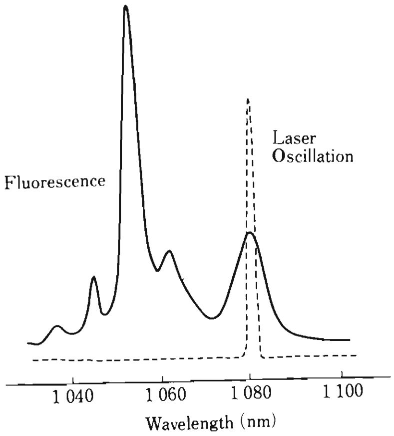

Fig. 2. Fluorescence spectrum of Nd^{3+} in LNA and laser oscillation.

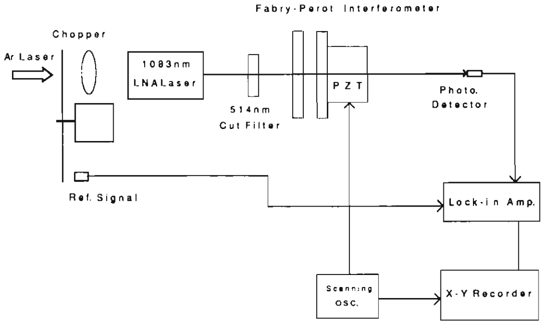

Fig. 3. Experimental setup to measure a spectral width of laser oscillation.

The width of the spectrum is measured with a Fabry-Perot interferometer as shown in Fig. 3. The width is reduced to 30 GHz and the output power is lager than a half of the power without the air-gap etalon. In order to reduce the width of the laser spectrum to 2GHz, we will add an air-gap etalon whose gap is controlled by an external signal because the laser frequency must be automatically tuned in the transition frequency of ^{3}He.

Figure 4 shows the output power of 1083 nm laser oscillation as a function of the excitation power. The power conversion efficiency of LNA15 is 4% at a pumping power of 1.4W and that of LNA10 about 3%. The efficiencys are about a half of that obtained by Schearer.$^{4)}$ The efficiency is strongly depend on the reflectivity of M2 (98%). We will test other mirrors whose reflectivity are less than 98% in order to get higher output power.

---

* This method to suppress of an desirable osscillation is proposed by one of the authors (A. Minoh).

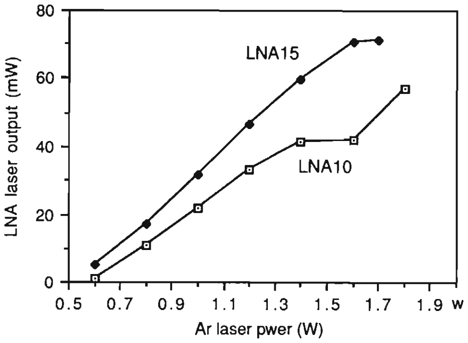

Fig. 4. Output power of the LNA laser as a function of the pumping power.

References

1) T. Fujisawa, A. Minoh, Y. Taniguchi, S. Ishii, K. Hatanaka, and Y. Oshiro: *RIKEN Accel. Prog. Rep.*, **22**, 222 (1988).
2) A. Minoh, T.Fujisawa, and Y. Taniguchi: *ibid.*, **23**, 113 (1989).
3) T. Fujisawa, A. Minoh, Y. Taniguchi, and K. Hatanaka: Int. Workshop on Polarized Ion Source and Polarized Gas Jet. Tukuba, Japan, Feb. 12–17(1990).
4) L.D. Schearer, M. Leduc, D. Vivien, A. Lejus and J. Thery: *IEEE. J. Quantum Electron.*, **QE-22,** 713 (1986).

RIKEN Accel. Prog. Rep. **24** (1990)

V-1-4. RIKEN (Japan)-RAL (U.K.) Collaboration on Muon Science Research

K. Nagamine, T. Matsuzaki, and K. Ishida

In order to promote fundamental studies as well as applications of scientific research using unstable elementary particle called muons (μ^+, μ^-; with life time of 2.2 μs), RIKEN has now started an international collaboration program with the Rutherford Appleton Laboratory (RAL), the largest science research laboratory in U.K. The agreement has been signed between RIKEN and SERC in September 29, 1990.

The goal of the research program is to develop various types of muon science, whose prominent examples are as follows: (a) muon catalyzed fusion, fundamental understandings and application toward energy resources; (b) non-destructive element analysis, application to various sciences including medical diagnostics; (c) muon spin rotation, relaxation and resonance, application to characterizations of new materials including high T_c superconductors.

In order to realize these muon science experiments, RIKEN has already started to construct a new muon generating beam channel as well as experimental facilities at the accelerator laboratory called ISIS at RAL which contains a proton synchrotron producing the strongest pulsed protons in the world. The beam channel contains a large solid-angle pion collector, a large superconducting solenoid where pion decays into muon under a strong confinement field and an advanced muon collector with an electrostatic separator removing background particles and an rf magnetic kicker to feed muon pulses into two experimental ports simultaneously. The construction of the beam channel will be carried out in the period from 1990 to 1993, followed by the construction of basic experimental instruments such as a set-up for muon catalyzed fusion experiment. For all of these purposes, the Japanese government approved for RIKEN the first 40% of the total budget of 1.7 billion yen for the fisical 1990-1992. The proposed layout is shown in Fig. 1.

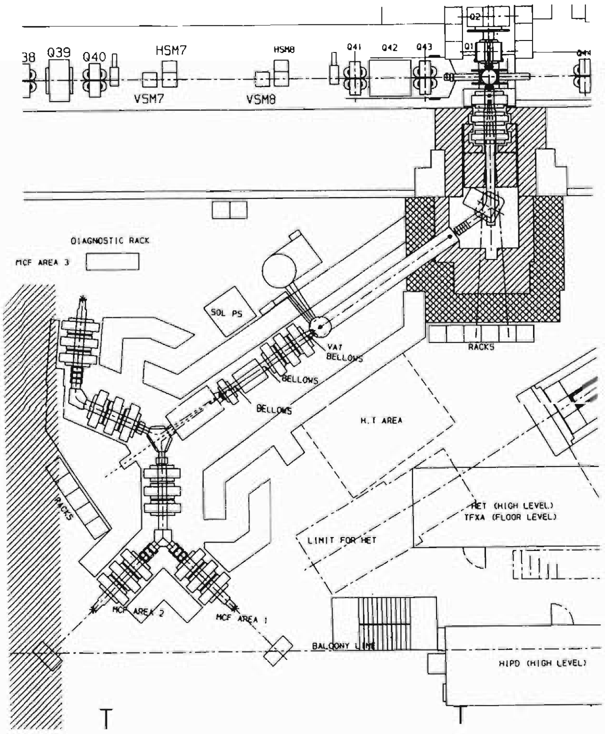

Fig. 1. Proposed layout for the RIKEN-RAL muon beem channel.

RIKEN Accel. Prog. Rep. **24** (1990)

V-2. Synchrotron Radiation Source Development

1. Status of the Synchrotron Radiation Project

H. Kamitsubo

The design study of the 8 GeV synchrotron radiation source, which was named SPring-8 last year, had been pursued in the past two years and the lattice structure of the 8 GeV storage ring was almost established. R&D work on vacuum chambers, magnets, and RF cavities have been performed. On the other hand the design study of an injector linac and a synchrotron has been done by the group of the Japan Atomic Energy Research Institute (JAERI).

The injector consists of two linacs and a synchrotron. A 250 MeV linac is used to produce positrons which are accelerated up to 1 GeV by the main linac. The first acceleration tube of the main linac has a large acceptance for positrons. The synchrotron, which accelerates electrons (positrons) from 1 GeV to 8 GeV, is of FODO type and has 40 cells. Main parameters of the injector are given in Table 1.

Table 1. Major Parameters of Injectors.

Injector Linacs			Synchrotron		
RF frequency	2856	MHz	Injection Energy	1	GeV
Klystron Power	35	MW	Maximum Energy	8	GeV
Repetition Rate	60	Hz	Repetition Rate	1	Hz
Main Linac			Radiation Loss per Turn	11.5	MeV
Injection Energy	120	MeV	Nominal Tune (ν_x / ν_y)	11.73/8.78	
Final Energy	1	GeV	Beam Emittance	195	nmrad
Max. Current (e^-)	300	mA	Chromaticity (ζ_x / ζ_y)	-15.3/-12.7	
(e^+)	10	mA	Momentum Compaction	9.51×10^{-3}	
Emittance	<1.5	mmrad	Bending Magnet		
Energy Spread	< +1.5	%	Field (1GeV / 8GeV)	0.106/0.85	T
Positron Linac			Bending Radius	31.4	m
Electron Energy	250	MeV	Damping Time		
Max. Current (e^-)	10	A	(1GeV, $\tau_x / \tau_y / \tau_z$)	937/938/469	msec
Conversion Target	Ta		(8GeV, $\tau_x / \tau_y / \tau_z$)	1.8/1.8/0.9	msec
Target Thickness	~10	mm	RF System		
Positron Energy	120	MeV	Frequency	508.58	MHz
Positron Current	10	mA	Harmonic Number	672	
			Voltage(8GeV)	17.1	MV
			Quantum Lifetime	> 10	s

The storage ring is designed to have 40 straight sections of 6.5 m long and 4 long straight sections of 30 m long. The design procedure of this ring is as follows: Firstly we designed a low emittance ring which has a 48-fold symmetric strucure and consists of 48 cells. The unit cell is of a Chasmann-Green type and consists of two bending magnets, ten quadrupoles, and seven sextupoles. The straight section is 6.5 m in length and the circumference of the ring is 1436 m. As we are thinking to operate the ring in a so-called hybrid mode, that is, in an operating mode that β functions have high and low values alternately at the neighbouring straight sections. We could find a very good low emittance lattice structure having 24 superperiod.

We then introduced 4 straight cells by removing two bending magnets in the unit cell. The beam-dynamical properties of this ring are essentially the same as those of the original one. The emittance of this ring is a little higher than the original one because the total number of bending magnets decreases. The parameters of this ring is given in Table 2.

Finally we rearrange quadrupoles and sextupoles in a straight section and convert it to a long straight section. We have not yet optimized the final procedure, but the preliminary result of the calculations shows that a ring having a large dynamic aperture and low emittance can be realized.

Prototypes of the bending, quadrupole, and sextupole magnets were made and their field distributions were measured. By taking the results into account, the final design of these magnets were finished. In R&D work we designed a combined-type sextupole magnet which can produce horizontal and vertical fields independently for small correction of the beam

Table 2. Major Parameters of the Storage Ring.

Energy	8	GeV
Current (multi-bunch)	100	mA
Current (singl bunch)	5	mA
Circumference	1435.95	m
Dipole magnet field	0.665	T
Bending radius	40.098	m
Number of cells	48 (44+4)	
Straight section length	6.4	m
Natural emittance	6.89	πnmrad
Critical photon energy	28.32	keV
Tune ν_x	51.22	
ν_y	16.16	
Synchrotron tune	0.0102	
Momentum compaction	$1{:}49x10^{-4}$	
Natural chromaticity	-113.17 -43.32	
Energy loss in the arc	9.04	MeV/rev
Energy spread	0.108	%
Damping time τ_x	8.473	
τ_z	8.481	msec
τ_e	4.242	msec
Harmonic number	2436	
RF voltage	17	MV
RF frequency	508.58	MHz

direction. In the final design, however, we decided to separate the sextupole and dipole magnet to reduce the construction cost.

A cold model of an RF cavity was fabricated and high frequency characteristics were measured. On the basis of the result of the investigation on the cold model, a klystron test facility and two prototypes of the RF cavity are fabricated to perform a high power test. The R&D work on the vacuum chambers is continued.

The site of the SR facility was decided at Harima Science Park City in Hyougo Prefecture and ground preparation started in March. The site will be available for us in 1992. The plan of the campus is shown in Fig. 1. The final design of the storage ring building is under way and its construction will start in the fall of the next year.

The research program at the SPring-8 is discussed in the user organization and JAERI-RIKEN user group. A conceptual design of the front-end part of a beam line is in progress.

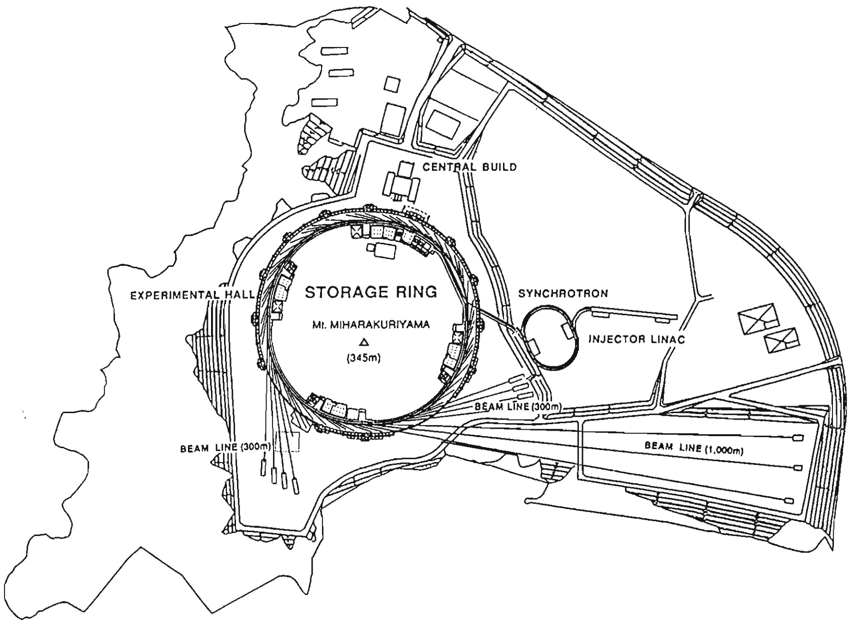

Fig. 1. Site and general layout of the SPring-8.

The construction of the magnets and the injector linac was authorized and will start this fiscal year.

RIKEN Accel. Prog. Rep. **24** (1990)

V-2-2. Design Modification of the Lattice of the SPring-8 Storage Ring

H. Tanaka and M. Hara

Last year, magnet arrangement and specification were finalized in consideration of the spacing of equipment. The terms of them were modified as follows.

(1) Each length of quadrupoles and sextupoles was 10–30% shortened.
(2) Bending magnet strength was changed from 0.665 T to 0.679 T.
(3) All combined type sextupole magnets were divided into correctors and conventional sextupole magnets.

For the new magnet arrangement and specification, the strength of each magnet was optimized again, because above modifications affect beams as the systematic magnetic errors. The optics whose horizontal and vertical tunes are respectively 51.22 and 16.16 was selected as the best one from the viewpoint of beam stability. We show new lattice functions, dynamic aperture, momentum dependence of tunes, and horizontal amplitude dependence of tunes in Figs. 1–4, respectively.

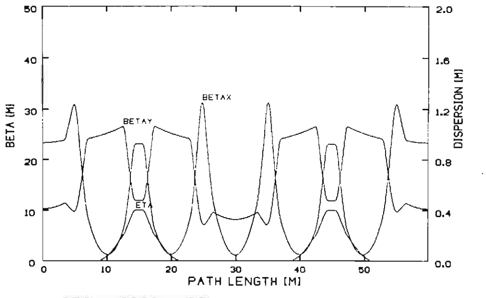

Fig. 1. Lattice functions of 1/24 ring.

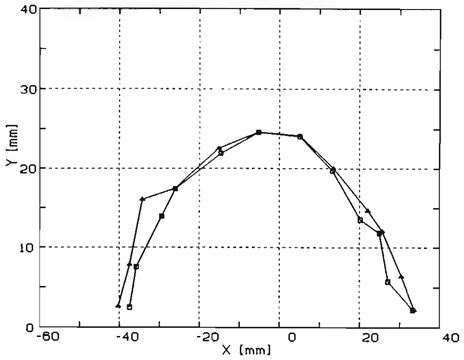

Fig. 2. Dynamic aperture without errors. Open sqares and triangles represent the dynamic aperture for one unit cell and one superperiod (ring), respectively.

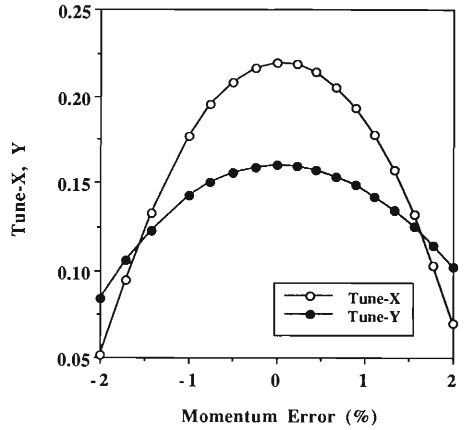

Fig. 3. Momentum dependence of tunes. Open and filled circles represent respectively horizontal and vertical tuneshifts.

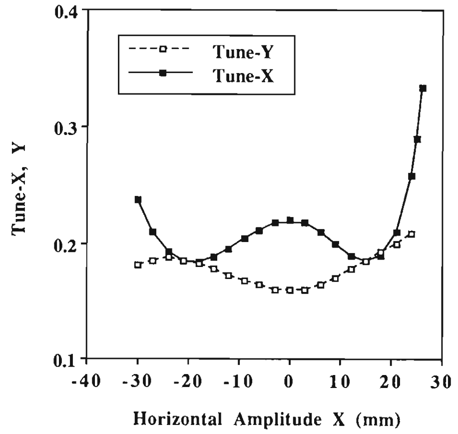

Fig. 4. Amplitude dependence of tunes. Open and filled squares represent horizontal and vertical tuneshifts.

We have also investigated the strength variation of each magnet within the expected operation range to determine the maximum field strength of each magnet. As the operation range, tune space surrounded with $51 < \nu_x < 54$ and $16 < \nu_x < 20$ was determined based on the nmrad-order emittance and the structure resonances arising from the sextupole magnets. Furthermore, nine operation points were selected considering the accidental resonances, and optics was designed in each operation point to minimize nonlinearity and chromaticities. The main parameters of the designed optics and the maximum strength of each magnet are shown in Table 1.

Table 1. Optics parameters.

	HLC1	HLC2	HLC2B	HLC3	HLC4	HLC5	HLC6	HLC7	HLC8	HLC9	**Maximum**
Emittance	7.37	7.18	6.96	6.97	5.55	6.36	6.3	6.23	5.81	5.62	**Absolute Val.**
(nmrad)											
Tune-X	50.78	51.22	51.22	51.22	53.22	52.22	52.22	52.22	53.22	53.22	
Tune-Y	17.84	16.16	16.16	19.16	20.16	17.16	18.16	20.16	16.16	17.16	
Chrom-X	-112.835	-115.034	-115.665	-119.21	-151.86	-128.372	-130.992	-134.136	-142.123	-146.127	
Chrom-Y	-45.179	-40.561	-40.003	-40.769	-36.673	-35.759	-40.677	-36.817	-42.199	-44.177	
Dapt (mm)			37.5		30		30				
Quad.(1/m2)											
Q1 (0.35m)	-0.271006	-0.2676974	-0.2804218	-0.324116	-0.4293008	-0.45	-0.3738486	-0.5100997	-0.3993006	-0.3849753	**-0.51009971**
Q2 (0.97m)	0.39115138	0.39626132	0.39820044	0.41345984	0.453587	0.4488201	0.42954855	0.46278188	0.43421758	0.42931603	**0.46278188**
Q3 (0.51m)	-0.4200039	-0.4421373	-0.4384298	-0.4465654	-0.473576	-0.4329687	-0.4380724	-0.4275559	-0.3976053	-0.3986581	**-0.473576**
Q4 (0.41m)	-0.599187	-0.6002218	-0.6005168	-0.6006863	-0.5689327	-0.5641903	-0.5725541	-0.577045	-0.5959445	-0.5958499	**-0.60068627**
Q5 (0.51m)	0.63459914	0.63486642	0.63494261	0.63498646	0.62670983	0.62546122	0.62766224	0.6288387	0.63376034	0.6337359	**0.63498646**
Q6 (0.51m)	0.63459914	0.63486642	0.63494261	0.63498646	0.62670983	0.62546122	0.62766224	0.6288387	0.63376034	0.6337359	**0.63498646**
Q7 (0.41m)	-0.599187	-0.6002218	-0.6005168	-0.6006863	-0.5689327	-0.5641903	-0.5725541	-0.577045	-0.5959445	-0.5958499	**-0.60068627**
Q8 (0.51m)	-0.6111753	-0.5641996	-0.5639839	-0.6085078	-0.6477088	-0.6147593	-0.6376664	-0.6406061	-0.6038247	-0.6188258	**-0.6477088**
Q9 (0.97m)	0.62993686	0.61076948	0.6131862	0.63670642	0.6567255	0.63433075	0.64253921	0.65693364	0.62980984	0.64382442	**0.65693364**
Q10 (0.35m)	-0.558958	-0.4682987	-0.4772537	-0.5960309	-0.6262088	-0.5371429	-0.5695372	-0.6687368	-0.492766	-0.5668234	**-0.66873677**
Q1L (0.35m)	-0.2697424	-0.2679152	-0.2802094	-0.3275172	-0.430755	-0.4499966	-0.3743248	-0.5102091	-0.398446	-0.3854678	**-0.51020911**
Q2L (0.97m)	0.39136039	0.39639031	0.39836897	0.41522999	0.4540551	0.44910214	0.4291701	0.46460469	0.43522917	0.42938506	**0.46460469**
Q3L (0.51m)	-0.4213736	-0.4424384	-0.4407436	-0.45123	-0.4742785	-0.4345252	-0.4394947	-0.4349822	-0.4004257	-0.3988237	**-0.4742785**
Q4L (0.41m)	-0.6014747	-0.6047839	-0.6029004	-0.6012575	-0.5731277	-0.5658337	-0.5760398	-0.5827213	-0.5982215	-0.5953164	**-0.60478393**
Q5L (0.51m)	0.63408259	0.63585901	0.63559198	0.63484484	0.6277234	0.62413605	0.62993574	0.62572757	0.6345072	0.63357767	**0.63585901**
Q6L (0.51m)	0.63408259	0.63585901	0.63559198	0.63484484	0.6277234	0.62413605	0.62993574	0.62572757	0.6345072	0.63357767	**0.63585901**
Q7L (0.41m)	-0.6014747	-0.6047839	-0.6029004	-0.6012575	-0.5731277	-0.5658337	-0.5760398	-0.5827213	-0.5982215	-0.5953164	**-0.60478393**
Q8L (0.51m)	-0.6140763	-0.5646396	-0.5659702	-0.6116985	-0.6495088	-0.6182566	-0.6394865	-0.6407294	-0.6067203	-0.6276984	**-0.64950875**
Q9L (0.97m)	0.63069924	0.6108467	0.61380912	0.63671407	0.65720184	0.63607749	0.64243699	0.65566835	0.62938104	0.64514699	**0.65720184**
Q10L(0.35m)	-0.5583546	-0.4682029	-0.4790422	-0.5916446	-0.6277359	-0.5364398	-0.569886	-0.6335672	-0.4924942	-0.5667397	**-0.63356715**
Sext.(1/m2)											
S1 (0.30m)			3.90425		3.89212502		3.79978212				**3.90425**
S2 (0.30m)			-4.3		-3.3034221		-3.8933542				**-4.3**
S3 (0.30m)	-4.1419007	-4.0274434	-3.9593631	-4.2041257	-4.5380338	-4.3609077	-4.3136708	-4.5324001	-3.9470107	-3.9594442	**-4.53803378**
S4 (0.50m)	7.45602048	7.29383773	7.125668	7.45658514	7.73011839	7.6263767	7.58107588	7.71036944	7.03669422	7.004448	**7.730118393**
S5 (0.30m)	-4.1419007	-4.0274434	-3.9593631	-4.2041257	-4.5380338	-4.3609077	-4.3136708	-4.5324001	-3.9470107	-3.9594442	**-4.53803378**
S6 (0.30m)			-2.384615		-2.6588116		-3.4947048				**-3.49470479**
S7 (0.30m)			4.284888		4.54678647		4.5				**4.54678647**

RIKEN Accel. Prog. Rep. 24 (1990)

V-2-3. Study of Linear Coupling Compensation for the Storage Ring of SPring-8 (2)

H. Tanaka and M. Hara

Linear coupling compensation in the storage ring of SPring-8 has been investigated. In previous work,[1,2] we presented a new linear coupling compensation scheme based on a lowest-order perturbation treatment and simulated its effect. To confirm the validity of our approach, we investigated coupling ratio distributions along the ring under four error conditions shown in Table 1, by two methods.[3] One is called an indirect method, in which the coupling ratio is calculated with the maximum amplitudes of betatron oscillations and uncoupled beta functions. The other is called a direct method, in which the coupling ratio is directly calculated from the ratio of phase space areas. If the perturbation treatment is a good approximation, the coupling ratio should be almost constant along the ring, and the results obtained by both methods should be consistent with each other. As a result of this study, we found that the perturbation treatment is not always valid in our ring, and also its validity is strictly limited. Results are summarized below.

Table 1. Error condition used in this study.

Error level	Displacement error (mm)	Tilt error (mrad)	Field error (%)	Residual rms COD (mm)
1	0.05	0.5	0.05	< 0.04
2	0.10	0.5	0.05	< 0.06
3	0.15	0.5	0.05	< 0.075
4	0.20	0.5	0.05	< 0.10

(1) Linear coupling becomes so strong at error levels above 0.15 mm random rms displacement error (error level 3 in Table 1) and this phenomena can not be well described by the perturbation treatment. That is, the coupling ratio much depends on the azimuthal position at these strong error conditions. We show the realistic coupling ratio distributions and those induced by small skew fields, which are will explained by the perturbation treatment, in Figs. 1 and 2, respectively.

(2) By a simple compensation scheme with two skew quadrupoles and one observation point, presented in previous study, the strength of linear coupling can be reduced to about one-fourth. But to keep the coupling ratio lower than 10% at every insertion device, the error condition must be under the error level 2, which is severe for the magnet alignment. In Figs. 3 and 4, we show respectively the difference between the distributions calculated by the two methods after the compensation and the realistic coupling ratio distributions. From these

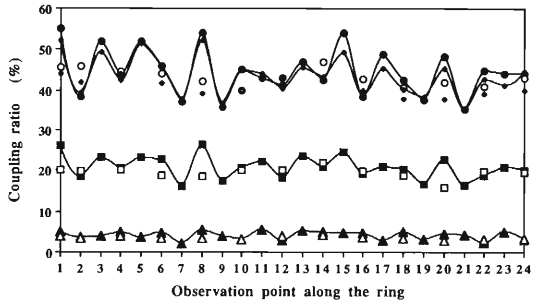

Fig. 1. Typical result of the coupling ratio distributions along the ring before compensation. White and black colors denote the values obtained respectively, by the direct method and by the indirect method. Triangle, square, diamond, and circle represent the error levels 1, 2, 3, and 4, respectively.

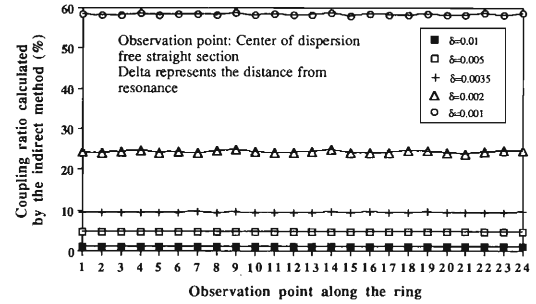

Fig. 2. Typical result of the coupling ratio distributions along the ring for the model cases well explained by perturbation treatment.

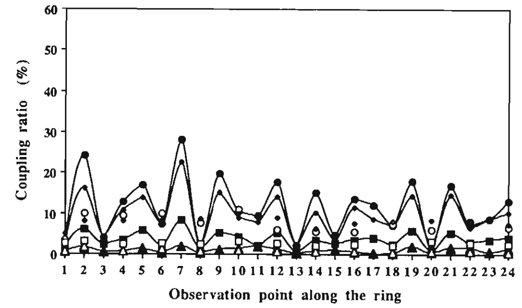

Fig. 3. Typical result of the coupling ratio distributions along the ring after compensation. White and black colors denote the values obtained respectively, by the direct method and by the indirect method. Triangle, square, diamond, and circle represent the error levels 1, 2, 3, and 4, respectively.

figures, we can see that two skew quadrupoles for the compensation markedly distort the optics above the error level 3.

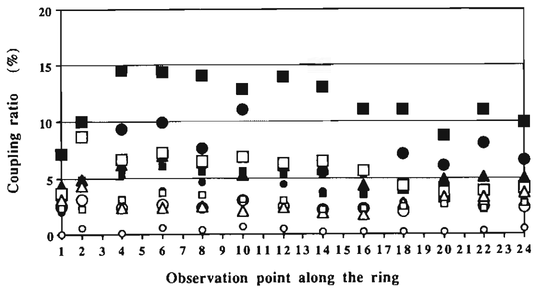

Fig. 4. Coupling ratio distributions along the ring after compensation. White and black colors denote the error level 4 and 2, respectively. Triangle, large and small squares, and large and small circles represent 5 different rings.

(3) For such a ring with strong linear coupling, many points for emittance observation and skew magnets should be necessary for sufficient compensation, because one observation point can't represent the whole ring. Furthermore, the coupling ratios can be precisely obtained only by the direct method.

References

1) H. Tanaka, K. Yoshida, R. Nagaoka, K. Tsumaki, and M. Hara: *RIKEN Accel. Prog. Rep.*, **23**, 122 (1989).

2) H. Tanaka, R. Nagaoka, K. Yoshida, K. Tsumaki, and M. Hara: 7th Symp. on Accel. Sci. and Technol., Osaka, Japan, p. 299 (1989).

3) H. Tanaka and M. Hara: Presented at 2nd EPAC, Nice, France (1990).

RIKEN Accel. Prog. Rep. **24** (1990)

V-2-4. Lattice Parameter Distortions at Insertion Devices

H. Tanaka, Y. Ishii,* and M. Hara

From the viewpoint of photon beam characteristics[1,2] and the design of photon beam lines, lattice parameter distortions at insertion devices (IDs) should be reduced. To find the magnitude of the distortions, we calculate the lattice parameters: closed orbit distortion (COD), beta functions, and dispersion functions, at the center of every dispersion free straight section. Momentum and magnetic errors are considered for the calculation.

Table 1(a). Lattice parameter distortions for the high β dispersion-free straight section.

High β dispersion free straight section

	COD		Beta function	Dispersion functions	
	Displacement (mm)	Angle (mrad)	(%)	Displacement (m)	Angle (mrad)
• Maximum values of 30 rings					
Horizontal	-0.157	-0.049	43	-0.104	+0.005
Vertical	-0.205	-0.053	25	-0.071	-0.007
• Rms values of 30 rings					
Horizontal	0.035	0.008	11.3	0.028	0.0014
Vertical	0.074	0.014	7.3	0.025	0.0024

Table 1(b). Lattice parameter distortions for the low β dispersion-free straight section.

Low β dispersion free straight section

	COD		Beta function	Dispersion functions	
	Displacement (mm)	Angle (mrad)	(%)	Displacement (m)	Angle (mrad)
• Maximum values of 30 rings					
Horizontal	-0.626	+0.170	44	+0.024	+0.022
Vertical	+0.356	+0.067	26	+0.049	+0.009
• Rms values of 30 rings					
Horizontal	0.058	0.014	10.6	0.007	0.006
Vertical	0.146	0.024	7.5	0.017	0.003

Table 2. Calculation conditions and results of the increment of beam divergence.

Calculation condition		
Horizontal emittance (mrad)	7×10^{-9}	
Vertical emittance (mrad)	7×10^{-10}	
Horizontal beta function (m)	22.01 (High β)	1.13 (Low β)
Vertical beta function (m)	10.0 (High β)	4.96 (Low β)
Momentum spread (%)	0.1	
Increment of beam divergence Δε/ε (%)		
• High β dispersion free straight section		
Horizontal Δε/ε	7.0 (for $\Delta\varepsilon_{max}$),	0.5 (for $\Delta\varepsilon_{rms}$)
Vertical Δε/ε	72.0 (for $\Delta\varepsilon_{max}$),	8.9 (for $\Delta\varepsilon_{rms}$)
• Low β dispersion free straight section		
Horizontal Δε/ε	7.3 (for $\Delta\varepsilon_{max}$),	0.6 (for $\Delta\varepsilon_{rms}$)
Vertical Δε/ε	69.2 (for $\Delta\varepsilon_{max}$),	8.3 (for $\Delta\varepsilon_{rms}$)

(1) Distortions due to magnetic errors: The magnetic errors used here are 0.2 mm alignment errors, 0.5 mrad rotation errors, and 5×10^{-4} field errors. The field errors only include multipole field errors lower than sextupole. We estimate distortions after a normal COD correction procedure.[3,4] COD is corrected to be about 0.1 mm as a rms value at monitors. A calculation is performed for 30 different rings with a computer code, STAT, which is made of the linear calculation part of RACETRACK[5] and a statistic calculation function. The results are shown in Tables 1(a) and 1(b).

The increment of beam divergence at IDs can be predicted from

$$\frac{\Delta\varepsilon_z}{\varepsilon_z} = \frac{(\eta_z \Delta P/P)^2}{\beta_z\ \varepsilon_z} \tag{1}$$

$$z = x,\ y$$

where, ε, η, β, and $\Delta P/P$ are respectively the emittance, spurious dispersion function, beta function, and momentum spread. Calculation conditions and results are shown in Table 2. We find that the vertical increments of beam divergence are markedly large, about 10% at both straight sections and that some dispersion function corrections in vertical plane are necessary at IDs.

The angular spread of circulating beams broaden an undulator spectrum.[1,2] The spread in the vertical plane, δ, is related to a relative spectrum line width by

$$\frac{\Delta\lambda}{\lambda} \approx \gamma^{*2}\delta^2 \tag{2}$$

$$\gamma^* = \frac{1}{\sqrt{1-\left(\beta^2\left[1\frac{1}{2}\left(\frac{K}{\gamma}\right)^2\right]\right)}} \tag{3}$$

where, N, γ, β and K are respectively the number of an undulator period, normalized energy by the electron rest mass, normalized velocity by the velocity of light, and field parameter. The line width is inversely proportional to beta, as shown in Fig. 1, because the angular spread is inversely proportional to the square root beta. Thirty percent reduction in the beta values (maximum beta distortion at the high beta straight section) increases the relative line width due to the angular spread by 40%. Since the line width is determined by the angular spread in the SPring-8 storage ring, the beta reduction

---

*Nuclear Engineeering, Tokyo Institute of Technology.

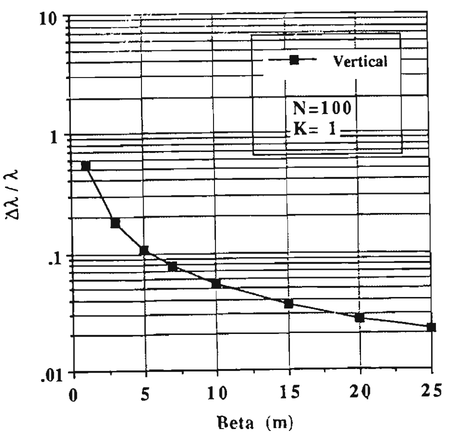

Fig. 1. Relative spectrum line width *v.s.* β functions.

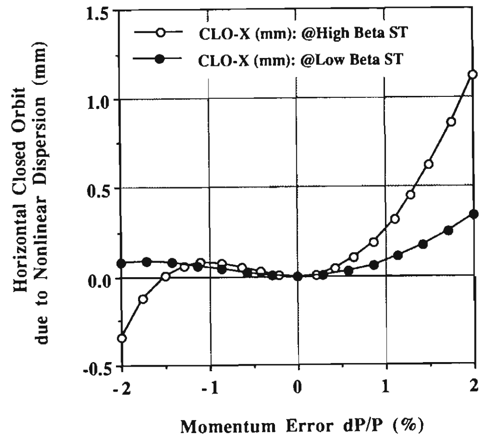

Fig. 2. COD due to a nonlinear dispersion function.

should be recovered at the undulators to suppress the spectrum line width.

On the basis of the results of Table 1(a) and (b), we can estimate a source point deviation. For a displacement and angle error of source point, 1 mm and 0.2 mrad should respectively be considered to design photon beam lines.

(2) Distortions due to the momentum error: Even under an ideal magnetic condition, nonlinear dispersion exists at the dispersion-free straight section The momentum dependent COD at IDs are shown in Fig. 2. If the momentum spread is increased from 0.1% to 1% owing to the microwave instability at a single bunch operation, the increment of horizontal beam divergence at the high beta straight section reaches about 40%. Therefore, the microwave instability should be sufficiently suppressed at a single bunch operation to keep the beam emittance low.

References

1) S. Krinsky: *Nucl. Instrum. Methods*, **172**, 73 (1980).
2) A. Hofmann: *ibid.*, **152**, 17 (1978).
3) H. Tanaka, R. Nagaoka, K. Tsumaki, K. Yoshida, and M. Hara: *RIKEN Accel. Prog. Rep.*, **22**, 231 (1988).
4) H. Tanaka, R. Nagaoka, K. Yoshida, K. Tsumaki, and M. Hara: *ibid.*, p. 235.
5) A. Wrulich: DESY Rep., 84-026 (1984).

RIKEN Accel. Prog. Rep. **24** (1990)

V-2-5. Study of Multipole Field Effects due to Correctors on the Beam Dynamics

H. Tanaka and M. Hara

In the third-generation light source, many quadrupole and sextupole magnets are used to realize low emittance and high beam stability, compared with other kinds of cyclic accelerators. Therefore, it is important for practical design to use a unit cell space, effectively. As an effective space-utilization, there is such an idea as a dipole corrector included in a sextupole magnet. On the other hand, this kind of magnet induces systematic multipole error fields, owing to a pole surface mismatch. In this case, sextupole, decapole, and so on are excited as systematic higher harmonics of a dipole, because the dipole field is generated with a sextupole whose poles are not optimized to a dipole magnetic potential. These error fields excite odd order resonances by first-order of their strengths, which potentially induce unbounded motions. We studied how much these multipole error fields damage beam dynamics.

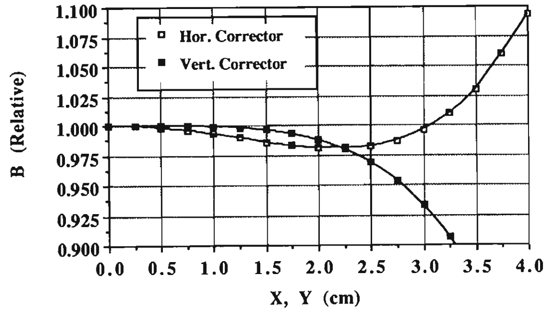

Fig. 1. Distribution of a normalized corrector field.

In Fig. 1[1)] and Table 1, normalized corrector field distributions and strengths of the multipole error fields up to 18-pole are shown. We numerically investigated the systematic multipole error fields' effects on beam dynamics with particle tracking. To easily treat these systematic multipole error fields, we assumed that magnetic fields were not saturated at every points in poles and yoke within an operation range and used a model that the multipole error fields linearly changed according to the dipole field strength. On the basis of the above model, we added a function of correctors with systematic multipole error fields up to 18-pole to RACETRACK.[2)] Strenths of all correctors were determined through a COD correction simulation,[3,4)] in which random conventional errors[3)] corresponding to 0.2 mm rms random misalignment was used.

Table. 1. Multipole coefficients of a horizonal and vertical corrector included in a sextupole magnet.

Horizontal Corrector a_n : Normal Multipole Coefficient		
Dipole	: a_0	$+5.97 \times 10^{-2}$
Sextupole	: a_2	-4.75×10^{-0}
Decapole	: a_4	$+4.77 \times 10^{+3}$
14-pole	: a_6	$+2.89 \times 10^{+5}$
18-pole	: a_8	$-1.08 \times 10^{+7}$

Vertical Corrector b_n : Skew Multipole Coefficient		
Dipole	: b_0	$+6.00 \times 10^{-2}$
Sextupole	: b_2	$+8.00 \times 10^{-2}$
Decapole	: b_4	$-4.81 \times 10^{+3}$
14-pole	: b_6	$-1.16 \times 10^{+5}$
18-pole	: b_8	$-1.67 \times 10^{+8}$

$Bx = \Sigma a_n r^n \sin(n\theta) + \Sigma b_n r^n \cos(n\theta)$

$By = \Sigma a_n r^n \cos(n\theta) - \Sigma b_n r^n \sin(n\theta)$

$x = r \cos(\theta)$, $y = r \sin(\theta)$

a_n, b_n [T/m^n]
L_B(Length of Magnet) = 0.45 m
Br(Magnetic Regidity) = 26.67 T m

As a result of numerical investigation, we found systematic multipole error fields' effects on beam dynamics were not so serious in our ring condition. The results are summarized below.

(1) The systematic multipole error fields scarcely affect the COD correction performance. Maximum and rms COD are almost unchanged by these multipole fields.

(2) Dynamic aperture is inversely proportional to the strengths of the systematic multipole error fields. It is reduced one-forth by expected multipole error fields and reduced only one-half even by error fields, which is ten times stronger than the expected ones. This one-half reduction is comparable to the effect of random conventional errors. The obtained dynamic aperture is shown in Figs. 2–3.

(3) The dynamic aperture with three kinds of errors are shown in Fig. 4, compared with that with only random conventional errors. Combined effects of various errors to the dynamic aperture reduction can't be found. The dynamic aperture appears to be limited by only random conventional errors mainly working on the beams as linear field errors. This fact shows that the random linear field errors con-

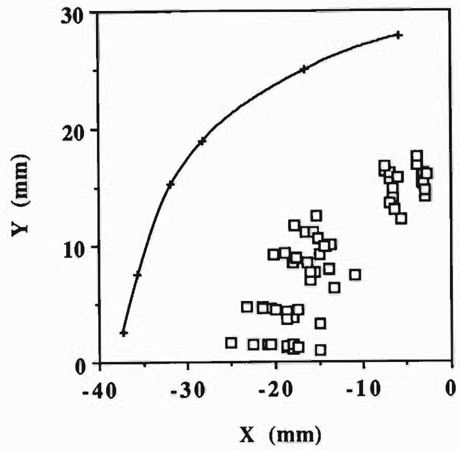

Fig. 2. 8-GeV hybrid lattice dynamic aperture with only random conventional errors. The solid line represents the ideal dynamic aperture; the open squares represent the dynamic aperture with the random conventional errors.

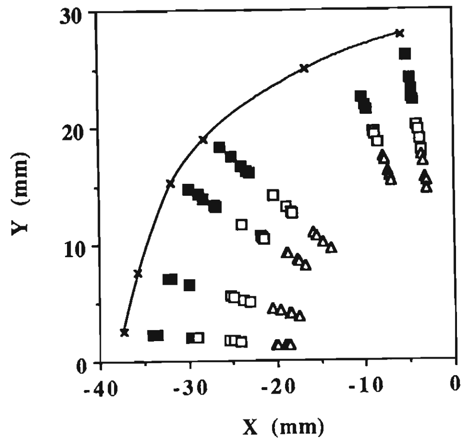

Fig. 3. 8-GeV hybrid lattice dynamic aperture with only systematic multipole error fields. The solid line represents the ideal dynamic aperture; the filled squares represent the dynamic aperture with expected error fields. The open squares and triangles represent respectively the dynamic aperture with error fields five and ten times stronger than an expected one.

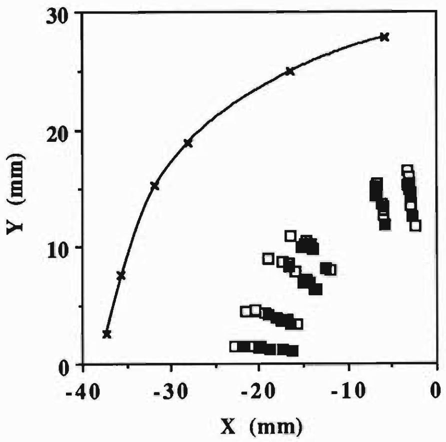

Fig. 4. 8-GeV hybrid lattice dynamic aperture with a -1% constant momentum error, systematic multipole error fields, and random conventional errors. The solid line represents the ideal dynamic aperture; the open and filled squares represent respectively the dynamic aperture with only random conventional errors and three kinds of errors.

sequently generate nonlinear effects greatly more than the systematic multipole error fields. This phenomenon can be explained as follows. The linear field errors break the periodicity of linear functions. This symmetry breaks of the linear functions much enhance the resonance driving terms by the sextupole magnets, which are almost cancelled out with perfect symmetries of linear functions under an ideal condition.

References

1) J. Ohnishi and S. Motonaga: 11th Int. Conf. on Magnet Technology, Tsukuba, Japan, p. 194 (1989).
2) A. Wrulich: DESY Rep., 84-026 (1984).
3) H. Tanaka, R. Nagaoka, K. Tsumaki, K. Yoshida, and M. Hara: *RIKEN Accel. Prog. Rep.*, **22**, 231 (1988).
4) H. Tanaka, R. Nagaoka, K. Yoshida, K. Tsumaki, and M. Hara: *ibid.*, p. 235.

RIKEN Accel. Prog. Rep. 24 (1990)

V-2-6. Calculated Spectral Distributions of On-axis Brilliance from Insertion Devices in the SPring-8

T. Takada and M. Hara

Main light sources in the SPring-8 are insertion devices (IDs) optimized for the storage ring characteristics. The storage ring is designed to have a large number of dispersion-free straight sections for installation of IDs. The target performances of (1) undulator sources are to obtain a high brilliance of 10^{19} (photons/s/mm^2/mrad^2/0.1%b.w.) from the first harmonic radiation in the X-ray region from 10 keV to 20 keV, and those of (2) wiggler sources are to obtain a highflux radiation of 10^{14} (photons / s / mrad (horiz.)/0.1%b.w.) from a multi-pole wiggler (MPW) in the region above 50 keV. We calculated the spectral distributions of on-axis brilliance from typical IDs (undulator and MPW) in the SPring-8.

Table 1. Design parameters of the storage ring for the SPring-8.

Electron / Positron energy	E[GeV]	8
Beam current (multi-bunch)	I[mA]	100
Beam current (single-bunch)	I[mA]	5
Circumference	C[m]	1435.95
Dipole magnetic field	B[T]	0.679
Bending radius	ρ[m]	39.27
Number of cells	N_c	48(44+4)
Length of straight section		
Normal	L[m]	6.5
Long	L[m]	28.1
Natural emittance	ε_n[nm•rad]	6.89
Coupling coefficient	κ[%]	10.0
Horizontal emittance	ε_x[nm•rad]	6.264
Vertical emittance	ε_y[nm•rad]$=0.1\varepsilon_x$	0.626
Critical photon energy	ε_c[keV]	28.91 (λ_c[Å]=0.429)
Energy spread	σ_e/E[%]	0.108
Lorentz factor	γ	15656
Radiation cone of an electron	$1/\gamma$[μrad]	63.87

Design Parameters of the Storage Ring for the SPring-8: The design parameters of the storage ring of the SPring-8 are listed in Table 1. The number of cells are 48, 44 normal cells and 4 straight cells, which are equivalent except for the absence of bending magnets (BMs). The storage ring has 40 normal-length straight sections (6.5 m) and 4 long straight sections (about 30 m) named 'very long straight section', each consists of one normal cell and one straight cell. For the 40 normal-length straight sections, 20 straight sections with a high beta function value (high-β) and 20 low one (low-β) appear alternatively. The high-β straight sections are designated for installing undulators because of a small angular divergence and for beam injection elements. On the other side, the low-β ones are for installing MPW and RF-cavities. In the 4 long straight sections, focusing elements (quadrupole and sextupole magnets) are installed for the first stage, and they are capable of installing 4 IDs separated by the focusing elements. The focusing elements will be rearranged to empty the long area of the long straight sections, so that a long ID with a length of about 20 m can be installed.

Since 1 high-β straight section is occupied by the beam injection elements out of 20 high-β ones, other 19 high-β ones are reserved for installing IDs, mainly undulators. On the other side, since 5 low-β ones are occupied by RF-cavities out of 20 low-β ones, the remaining 15 ones are reserved for installing IDs, mainly MPWs. Besides IDs in the straight sections, 23 BMs will be used as light sources. In summary, 23 BMs, 15 low-β normal-length straight sections, and 19 high-β ones will be available for light sources. To our schedule, 10 beam lines (6 IDs and 4 BMs) will be prepared by the commissioning in 1998.

Design Parameters of typical IDs and BM: The betatron function value, electron beam size, and angular divergence at the straight sections for IDs and at the source points of BM are listed in Table 2. The design parameters of a typical MPW and a typical undulator in the SPring-8 are summarized in Table 3 and 4, respectively. The total lengths of IDs are to be about 4.0 m from the normal-length straight section (6.5 m), since the maximum length available for an ID out of a 6.5 m normal length one is 4 m.

Calculated Spectral Distributions of On-axis Brilliance of the SPring-8: The on-axis peak magnetic field and first harmonic photon energy are plotted in Fig. 1 against the undulator gap width. An undulator with a magnetic period length of 3 cm at 8 GeV ring provides the first harmonic radiation that is tunable in the X-ray region from about 16 keV to 20 keV, corresponding to the change in the magnetic gap width from 3.5 cm to 2.0 cm.

Table 2. Electron beam size and the angular divergence.

Device type	β_x [m]	β_y [m]	σ_x [μm]	σ_y [μm]	$\sigma_{x'}$ [μrad]	$\sigma_{y'}$ [μrad]
Dipole[1)]	1.91	26.25	147.81	128.23	70.76	5.00
MPW[2)]	1.08	8.65	82.13	73.60	76.27	8.51
Undulator[3)]	23.48	10.01	383.49	79.16	16.33	7.91

1) Dipole source is 15 cm apart from the edge.
2) MPW will be installed in the low-β straight section.
3) Undulator will be installed in the high-β straight section.

Table 3. Parameters of a typical MPW.

Magnetic period length	λ_o[m]	0.18
Total length	L[m]	3.96
Number of periods	N	22
On-axis peak magnetic field	B_g[T]	0.952
Critical photon energy of MPW	ε_c[keV]	40.54(λ_c[Å]=0.306)
Deflection parameter	K=93.4B_g[T]λ_o[m]	16.0
First harmonic photon energy on-axis	ε_1[eV]	26.17

Table 4. Parameters of a typical undulator.

Device type	Pure magnet configuration	
Magnetic period length	λ_o[m]	0.03
Total length	L[m]	3.99
Number of periods	N	133
Magnetic gap width range	g[m]	0.02–0.035
On-axis peak magnetic field range	B_g[T]	0.055–0.265
Deflection parameter range	K=93.4B_g[T]λ_o[m]	0.15–0.75
First harmonic photon energy on-axis range	ε_1[keV]	15.8–20.0
Nd-Fe-B permanent magnet characteristics		
Residual magnetic flux density	B_r[T]	1.25
Height of magnet	h[m]=λ_o[m]/2	0.015

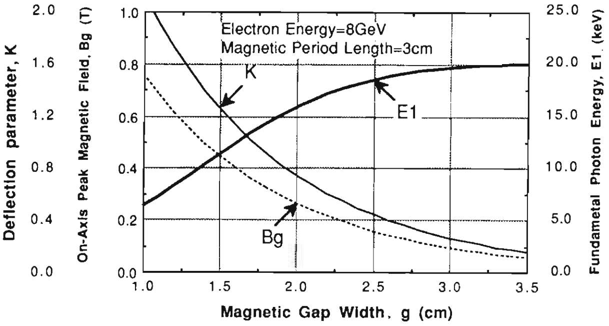

Fig. 1. On-axis peak magnetic field and fundamental photon energy of a pure magnet type undulator as a function of the magnetic gap width. The on-axis peak magnetic field and K parameter are independent of the magnetic gap-width.

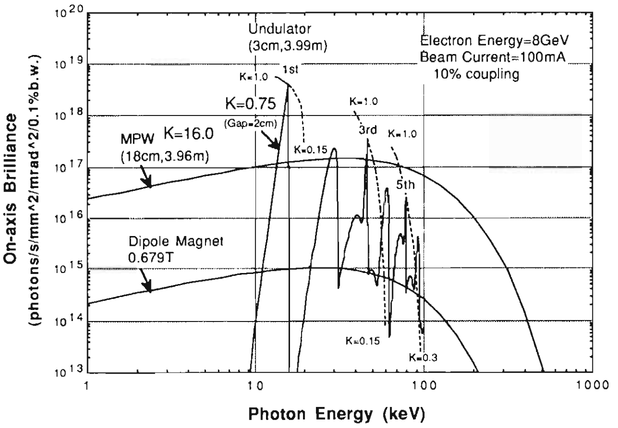

Fig. 2. Spectral distributions of on-axis brilliance calculated as a function of photon energy for BM, typical MPW, and typical undulator. The numbers in parentheses denote the magnetic period length and total length. Dotted lines denote the peaks of 1st, 3rd, and 5th harmonics from the undulator on changing the K parameter (magnetic gap-width) of the undulator.

Calculated spectral distributions of on-axis brilliance are shown in Fig. 2 as a function of photon energy for MPW listed in Table 3 and BM, and as a function of the K parameter (magnetic gap width) for the undulator listed in Table 4. The spectral distribution of on-axis brilliance calculated as a function of photon energy from the undulator with $K=0.75$ corresponding to a magnetic gap width g of 2.0 cm is also shown in Fig. 2; the calculation was performed by using a program 'URGENT'[1)] for generating undulator radiation. In the SPring-8, a brilliance of about 3.7×10^{18} photons/sec/mm^2/mrad^2/0.1%b.w. will be obtained at a first harmonic photon energy of 15.8 keV with $K=0.75$ by using an undulator whose parameters are listed in Table 4. Brilliances of 3.0×10^{17} and 2.5×10^{16} will be obtained at 3rd and 5th harmonics, respectively. The use of MPW will be more advantageous than that of the undulator in the region above 48 keV, which corresponds to the 3rd harmonic photon energy of the undulator described above.

References

1) R.P. Walker: ST/M-88/19, SINCROTRONE TRIESTE (1988).

RIKEN Accel. Prog. Rep. 24 (1990)

V-2-7. Progress in Magnet System for the SPring-8 Storage Ring

J. Ohnishi, S. Motonaga, and H. Takebe

The SPring-8 storage ring has a 1436 m of circumference, containing 48 unit cells of a Chasman-Green type lattice. One unit cell is composed of 2 dipoles, 10 quadrupoles, 7 sextupoles, and 10 steering magnets. Since the field qualities are required to be stringent to store a low emittance beam in the ring and total number of magnets is very large, we designed and built prototypes of dipoles, quadrupoles, and sextupoles. On the basis of the results of field measurements,[1] we have redesigned the magnets. The points of new designs are as follows.

1) We abandoned a plan that some steering magnets are incorporated with sextupole magnets. The principal reasons are simplification of operation and the reduction of a construction cost.

2) Field strengths of quadrupoles and sextupoles are increased and their lengths are shortened in order to make space for locating steering magnets separated from the sextupole magnets.

3) The bore diameters of quadrupoles and sextupoles are reduced to 85 mm and 92 mm, respectively, to save power dissipation and to increase maximum strengths.

4) Maximum field strengths of quadrupoles and sextupoles are increased to 18 T/m, 450 T/m^2, respectively. The geometry of iron poles and yokes was designed so that saturation loss is suppressed lower than 5% for quadrupoles and sextupoles at the nominal field strength. On the other hand, the sizes of a uniformed field region are decreased by 4 mm for quadrupoles and 12 mm for sextupoles.

5) The pole width of dipoles is narrowed to 160 mm from 240 mm in order to reduce the weight and the construction cost. Since this induces a sextupole field more strongly, the fields have to be corrected to widen the uniformed region by attaching end shims.

6) Since the yokes of some quadrupoles and sextupoles are interfered with vacuum tubes for extraction of synchrotron radiation from insertion devices or dipole magnets, we designed them with two types of cross-sections.

Table 1 shows newly designed specifications of dipoles, quadrupoles, and sextupoles. Figure 1 shows the cross section of quadrupoles with smaller yokes and the vacuum chamber. Figure 2 shows its gradient distribution calculated with a 2-D code, LINDA. The real integrated fields are expected to be less uniformed than the 2-D calculation due to a dodecapole field produced at the end of a magnet core; however, it can be corrected with end shims to restore required uniformity. Figure 3 shows the cross section of the sextupole magnet with smaller yokes. Figure 4 shows a field distribution calculated with LINDA.

We have ordered all the magnets to be located in the ring. The first magnet of each type will be

Table 1. Parameters for dipole, quadrupole, and sextupole magnets.

Family		dipole	quadrupole						sextupole		
			Q1,Q10	Q4,Q7	Q3, Q6 Q8	Q2	Q5	Q9	S1,S7	S2,S3 S5,S6	S4
Number of magnets		88	96	96	144	48	48	48	96	192	48
Bore diameter	(mm)	64.04	85	85	85	85	85	85	92	92	92
Effective field length	(m)	2.804	0.35	0.41	0.51	0.97	0.51	0.97	0.30	0.30	0.50
Magnet length	(m)	3.09	0.48	0.54	0.64	1.10	0.64	1.10	0.41	0.37	0.61
Magnet weight	(Kg)	6200	980	1100	1400	2500	2000	3600	510	610	820
Field strength, max	(T, T/m, T/m^2)	0.679	18	18	18	18	18	18	450	450	450
Magnetomotive force	(x10^4 AT)	3.5	1.49	1.49	1.49	1.42	1.49	1.42	0.64	0.64	0.61
Turn numbers per pole		16	28	28	28	28	28	28	24	24	24
Conductor size	(mm)	16 x 26	9 x 16	9 x 16	9 x 16	9 x 16	9 x 16	9 x 16	8 x 8	8 x 8	8 x 8
Hollow size	(mm)	ø11	ø5	ø5	ø5.5	5 x 8	ø5.5	5 x 8	ø3	ø3	ø3.5
Current, max	(A)	1090	531	531	531	508	531	508	266	266	254
Current density	(A/mm^2)	3.40	4.27	4.27	4.42	4.88	4.42	4.88	4.67	4.67	4.67
Conductor resistance	(mW/MAG)	11.6	21.1	23.2	27.5	50.4	27.5	50.4	50.0	50.0	69.0
Voltage drop, max	(V)	12.6	11.2	12.3	14.6	25.6	14.6	25.6	13.3	13.3	17.5
Power dissipation	(KW)	13.8	5.94	6.55	7.75	13.0	7.75	13.0	3.54	3.54	4.45
Cooling circut		2	4	4	4	4	4	4	6	6	6
Water flow	(l/min)	18.1	10.2	9.66	11.6	17.1	11.6	17.1	4.6	4.6	6.0
Pressure drop	(Kg/cm^2)	5	5	5	5	5	5	5	5	5	5
Temperature rise	(°C)	10.8	8.3	9.7	9.5	10.9	9.5	10.9	11.0	11.0	10.7

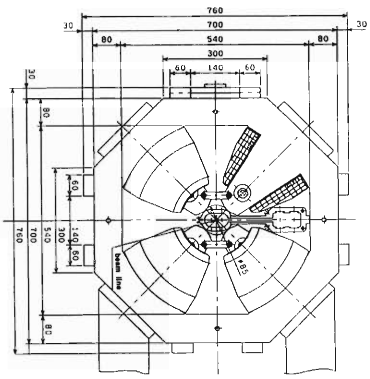

Fig. 1. Cross-sectional view of a newly designed quadrupole magnet.

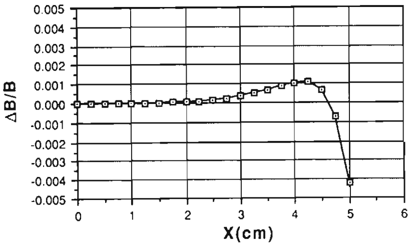

Fig. 2. Field distribution of a quadrupole magnet calculated with a 2-D code LINDA. The Y axis indicates a relative deviation from an ideal quadrupole field at the nominal strength, 18 T/m.

delivered next fall to verify the design. A full-scale manufacturing starts in early 1992.

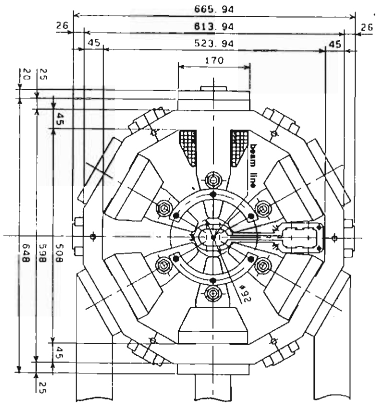

Fig. 3. Cross-sectional view of a newly designed sextupole magnet.

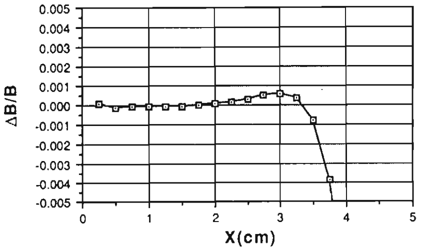

Fig. 4. Field distribution of a sextupole magnet calculated with a 2-D code LINDA. The Y axis indicates a relative deviation from an ideal sextupole field at the nominal strength, 450 T/m^2.

References

1) J. Ohnishi, S. Motonaga, and H. Takebe: This Report, p. 153; 155.

RIKEN Accel. Prog. Rep. 24 (1990)

V-2-8. Magnetic Field Measurements of a Prototype Quadrupole Magnet for the SPring-8 Storage Ring

J. Ohnishi, S. Motonaga, and H. Takebe

The SPring-8 storage ring being designed to be a low emittance machine has a Chasman-Green type Lattice structure with 480 quadrupole magnets.[1] Because the multipole fields of these magnets, produced by the end effect and manufacture imperfection of magnet yokes, cause the reduction in a dynamic aperture, they should be small enough. The tolerance of field gradient uniformity is calculated by tracking simulations as.

$$\frac{|\,\delta\int(dB/dx)\,ds\,|}{|\,\int(dB/dx)\,ds\,|}<5\times10^{-4}$$

$$(\,|\,x\,|<35\mathrm{mm},\quad |\,y\,|<15\mathrm{mm})$$

We constructed a prototype quadrupole magnet and measured the fields to ascertain the design and the production technique. Figure 1 shows a cross section of the prototype quadrupole magnet. It has a core length of 465 mm and a bore diameter of 90 mm. Iron yokes are assembled from four blocks of stacked Si steel plates with a thickness of 0.5 mm. Non-magnetic spacers are put between upper and lower yokes (hatched part in the figure) in order to investigate the effect of symmetry reduction due to cutting magnetic circuits, because some quadrupole magnets have little space for return yokes at this parts through which a synchrotron radiation port goes.

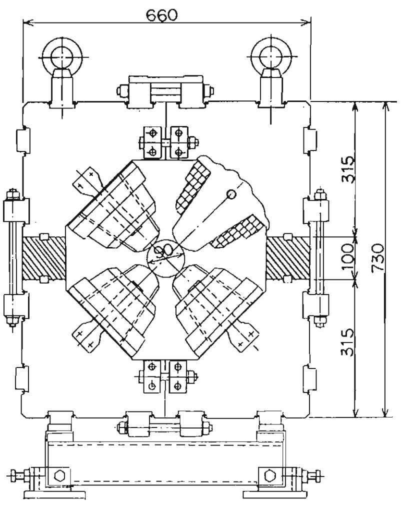

Fig. 1. Cross-sectional view of a prototype quadrupole magnet.

The magnetic fields of the prototype quadrupole were measured with an instrument called "twin flip coils". Figure 2 shows its sensing part in which two coils for fields measuring are fixed. One coil is wound 200 turns on a bobbin with a diameter of 5 mm. This block is supported with a pipe of 1 m long and is flipped in about 0.7 seconds by a stepping motor. The magnetic field and the gradient were measured by integrating output voltages from two coils induced for flipping with a high precision voltmeter (HP3458A) and fields mapping was done by carrying twin coils on a moving table.

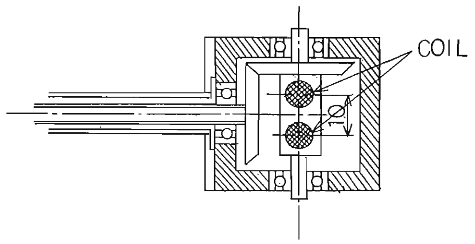

Fig. 2. Sensing part of "twin flip coils" for field measurements of a quadrupole magnet.

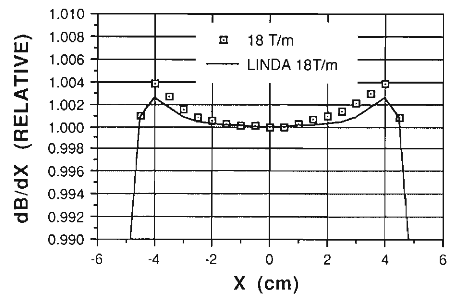

Fig. 3. Transverse field distributions of the prototype quadrupole magnet for measurements and calculation. Each distribution is normalized at $x=0$. The field strengths are nominal about 18 T/m.

Figure 3 shows the transverse distributions of field gradients on the median plane at the centre of the magnet. This measurement and a 2-D LINDA calculation agree within 2×10^{-3}. Figure 4 shows the transverse distributions of integrated gradients calculated by summing up mapped data. The integrated gradients decrease with distance from the center by a dodecapole field produced at the end part, and do not satisfy the required uniformity within the region. This results are not satisfied with the requirement as already indicated. However, the field distribution can be corrected by attaching end shims as the distributions change little for exiting levels. On the other hand, it is found that an octupole field induced due to cutting magnetic circuits is small enough.

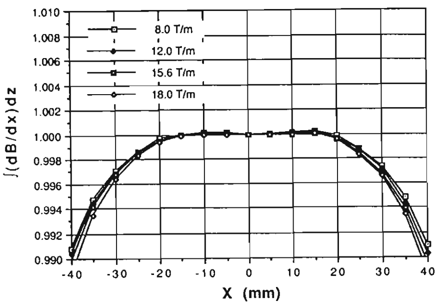

Fig. 4. Transverse distributions of integrated fields of the prototype quadrupole magnet. Integrated fields are calculated from mapped data.

Recently we have finished redesigning[2)] and now ordered all the magnets to be located in the ring.

References

1) M. Hara *et al.*: Proc. 2nd European Particle Accel. Conf., p. 466 (1990).
2) J. Ohnishi, S. Motonaga, and H. Takebe: This Report, p. 151.

RIKEN Accel. Prog. Rep. **24** (1990)

V-2-9. Magnetic Field Measurements of a Prototype Dipole Magnet for the SPring-8 Storage Ring

J. Ohnishi, S. Motonaga, and H. Takebe

The lattice of the SPring-8 storage ring contains 88 dipole magnets.[1] Diviation of field strengths in each dipole causes a closed orbit distortion and ununiformity of field distribution, which signify existence of multipole fields, raises reduction of dynamic aperture. The tolerance of field uniformity is calculated by tracking simulations as

$$\frac{|\delta\int Bds|}{|\int Bds|}<5\times10^{-4}$$

$$(|x|<29\text{ mm},\quad |y|<15\text{ mm})$$

We constructed a prototype magnet for verification of the design and development of a high-accuracy production technique. Figure 1 shows a cross section of the prototype dipole magnet, which has a rectangular configuration and 3.08 m total length including coils. Its iron yoke is stacked from punched Si steel plates of 0.5 mm in thickness.

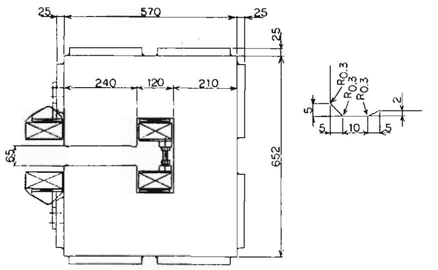

Fig. 1. Cross-sectional view of a prototype dipole magnet.

Magnetic fields of the prototype were measured with a hall probe (SIEMENCE SBV604), which is fixed in a copper block whose temperature is stabilized within ±0.1°C. Calibration is made by a NMR probe and field strengths are calculated in 7th polynomial of output voltage. The field mapped data are taken by carrying a hall probe on a moving table (4 m×0.2 m×0.2 m) controlled with a personal computer through a GP-IB bus.

Figure 2 shows transverse field distributions on the median plane for some longitudinal positions. Distributions measured are in good agreement with a calculation using LINDA. The difference in distributions in the z position, produced by geometrical gap error, is small enough to affect integrated fields. Figure 3 shows a transverse distribution of integrated fields on the median plane. Data were taken at intervals of 20mm in the longitudinal direction and integrated fields were calculated by summing up mapped data. A sextupole field due to an effect of edge fields is induced fairly strongly as shown in the figure. An influence of the field distributions to beam is being investigated in detail.

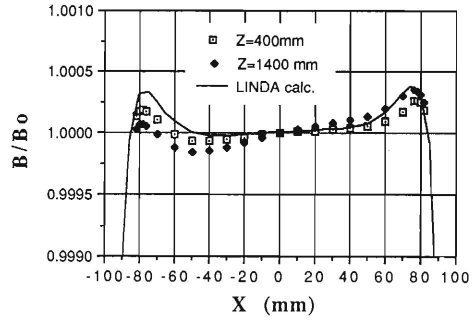

Fig. 2. Transverse field distributions of a prototype dipole magnet for measurements and calculation. Each distribution is normalized at $x=0$. The field strength is nominal about 0.665 T.

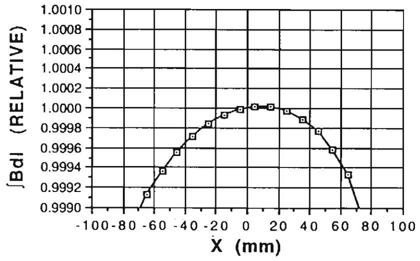

Fig. 3. Transverse distribution of integrated fields of a prototype dipole magnet. Integrated fields are calculated from mapped data.

In practical magnets, a pole width is narrowed to be 160 mm from 240 mm in order to reduce the cost. As a sextupole field is strengthened in such a case, we shall correct edge fields with end shims.

Recently we have finished design modification[2] and ordered all magnets to be located in the ring.

References
1) M. Hara *et al.*: Proc. 2nd European Particle Accel. Conf., p. 466 (1990).
2) J. Ohnishi, S. Motonaga, and H. Takebe: This Report, p. 151.

RIKEN Accel. Prog. Rep. **24** (1990)

V-2-10. Design of a Power Supply System for SPring-8 Storage Ring Magnets

H. Takebe, S. Motonaga, J. Ohnishi, and N. Kumagai

Fundamental design for an SR magnet power supply system (PS) was achieved and reported already.[1] Lattice parameters are slightly changed and the magnet design are modified. The maximum currents and the PS arrangement are changed. Tables 1 - 4 show magnet types, PS names, maximum currents, cable resistances and lengths, power consumptions, PS cubicle DAC and VME chassis numbers. Divided cubicle num bers for eight types of Q-magnets (Q-1,-3,-4, -5,-6,-7,-8,-10) are decreased to two from four, though the maximum voltages are less than 600 V. The Q magnets in the long straight sections have auxiliary power supply units in order to adjust the current in a range of few percent (instead of the bypass control circuits). For the correction of beam orbit distortion, effected by an insertion device (ID), Q1-3 and Q8-10, beside ID, have also auxiliary power supply units (1 - 4 %).

Tables 1-4. Required parameters for B, Q, Sx, St-magnets and power supplies.

Table 1. Dipole magnet

Magnet Name	PS Name	length (m)	Curr. (A)	Rm Ω	Cable km	Cable mm2	Cable Ω	Loss kW	Mx.Cur. (A)	V (PS) *V	Power (kW)	No. of PS	Tot.Po. (kW)	Total DAC
B	BP	2.804	1090	1.113	3.170	800	0.074	88.3	1145	1359	1556	1	1597	1

Table 2. Quadrupole magnet (Bypass Type)

Magnet Name	PS Name	length (m)	Max (A)	Rm Ω	Cable km	Cable mm2	Cable Ω	Loss kW	Mx.Cur. *(A)	V (PS) *V	Power (kW)	No. Cubic	Tot.Po. (kW)	Total DAC
QD1	QP1	0.35	531	0.506	2.300	400	0.108	60.5	557.6	342.4	190.9	2	392	50
QF2	QP2	0.97	508	0.605	1.150	400	0.054	54.9	533.4	351.5	187.5	4	792	52
QD3	QP3	0.51	531	0.660	2.300	400	0.108	60.5	557.6	428.2	238.8	2	488	50
QD4	QP4	0.41	531	0.557	2.300	400	0.108	60.5	557.6	370.8	206.8	2	424	50
QF5	QP5	0.51	531	0.660	2.300	400	0.108	60.5	557.6	428.2	238.8	2	488	50
QF6	QP6	0.51	531	0.660	2.300	400	0.108	60.5	557.6	428.2	238.8	2	488	50
QD7	QP7	0.41	531	0.557	2.300	400	0.108	60.5	557.6	370.8	206.8	2	424	50
QD8	QP8	0.51	531	0.660	2.300	400	0.108	60.5	557.6	428.2	238.8	2	488	50
QF9	QP9	0.97	508	0.605	1.150	400	0.054	54.9	533.4	351.5	187.5	4	792	52
QD10	QP10	0.35	531	0.506	2.300	400	0.108	60.5	557.6	342.4	190.9	2	392	50
								594				24	5168	504

Table 2-A. Bipass of Q magnet

Magnet Name	PS Name	length (m)	Main *(A)	Bipass Current (%)	Bipass Current (A)	Bipass Current (W)	No.of Bipass	Power (kW)	Bipass (kW)	Total (kW)
QD1	QP1	0.35	558	4.0	22.3	221	24	5.3	10.60	403
QF2	QP2	0.97	533	1.0	5.3	118	12	1.41	5.65	798
QD3	QP3	0.51	558	1.0	5.6	71.1	24	1.71	3.41	491
QD4	QP4	0.41	558	1.0	5.6	61	24	1.46	2.93	427
QF5	QP5	0.51	558	1.0	5.6	71.1	24	1.71	3.41	491
QF6	QP6	0.51	558	1.0	5.6	71.1	24	1.71	3.41	491
QD7	QP7	0.41	558	1.0	5.6	61	24	1.46	2.93	427
QD8	QP8	0.51	558	1.0	5.6	71.1	24	1.71	3.41	491
QF9	QP9	0.97	533	1.0	5.3	118	12	1.41	5.65	798
QD10	QP10	0.35	558	4.0	22.3	221	24	5.3	10.60	403
								23.2	52.0	5220.0

Table 3. Sextupole magnet

Magnet Name	PS Name	Length m	Curr. (A)	Rm Ω	Cable km	Cable mm2	Cable Ω	Loss kW	Mx.Cur. *(A)	V (PS) *V	Power (kW)	No. Cubicle	Tot.Po. (kW)	DAC No.
S1	SP1	0.30	266	2.400	4.260	185	0.431	30.6	279.3	790.7	221	1	227	1
S2	SP2	0.30	266	2.400	4.260	185	0.431	30.6	279.3	790.7	221	1	227	1
S3	SP3	0.30	266	2.400	4.260	185	0.431	30.6	279.3	790.7	221	1	227	1
S4	SP4	0.50	254	3.312	4.260	185	0.431	27.7	266.7	998.3	266	1	271	1
S5	SP5	0.30	266	2.400	4.260	185	0.431	30.6	279.3	790.7	221	1	227	1
S6	SP6	0.30	266	2.400	4.260	185	0.431	30.6	279.3	790.7	221	1	227	1
S7	SP7	0.30	266	2.400	4.260	185	0.431	30.6	279.3	790.7	221	1	227	1
								211				7	1633	7

Table 4. Correction magnet

Magnet Name	PS Name	Length m	Curr. (A)	Rm Ω	Cable km	Cable mm2	Cable Ω	Loss kW	Mx.Cur. (A)	V (PS) V	Power (kW)	No. Cubicle	Tot.Po. (kW)	DAC No.
VS	CP1	0.15	3.0	1.900	0.506	2	4.731	0.04	3.0	19.9	0.06			
VS	CP2	0.20	3.0	2.900	0.506	2	4.731	0.04	3.0	22.9	0.07			
HS	CP3	0.20	3.0	3.300	0.506	2	4.731	0.04	3.0	24.1	0.07			
HS	CP4	0.20	3.0	3.300	0.506	2	4.731	0.04	3.0	24.1	0.07			
VHS	CP5	0.20	3.0	3.300	0.506	2	4.731	0.04	3.0	24.1	0.07			
	CP6	0.20	3.0	3.500	0.506	2	4.731	0.04	3.0	24.7	0.07			
VS	CP7	0.15	3.0	1.900	0.506	2	4.731	0.04	3.0	19.9	0.06	16	48.96	576
VS	CP8	0.20	3.0	2.900	0.506	2	4.731	0.04	3.0	22.9	0.07			
HS	CP9	0.20	3.0	3.300	0.506	2	4.731	0.04	3.0	24.1	0.07	(12Cell/4PS)		
HS	CP10	0.20	3.0	3.300	0.506	2	4.731	0.04	3.0	24.1	0.07			
VHS	CP11	0.20	3.0	3.300	0.506	2	4.731	0.04	3.0	24.1	0.07			
	CP12	0.20	3.0	3.500	0.506	2	4.731	0.04	3.0	24.7	0.07			
								8.06				16	48.96	576
												VME	kW	DAC
					Total			902 kW				48	8499	1088

A cabling route between the magnet and PS was decided. Cables for large current magnets (B, Q, and Sx) are led along the upper cable rack on the SR machine cave as shown in Fig. 1. Other cables for steering (correction) magnets and Q's auxiliary PS units are led on the outer rack. The total cable lengths of B, Q, and Sx magnets are 3.1, 2.3, and 4.2 km, respectively. The ratio of the cable length inside the machine cave to the total length is 33 %. An average length of steering magnet cables are about 506 m. Total power consumption for the magnet PS is 8.5 MW. The total power consumption for the cables is 902 kW and that inside the machine cave is 300 kW.

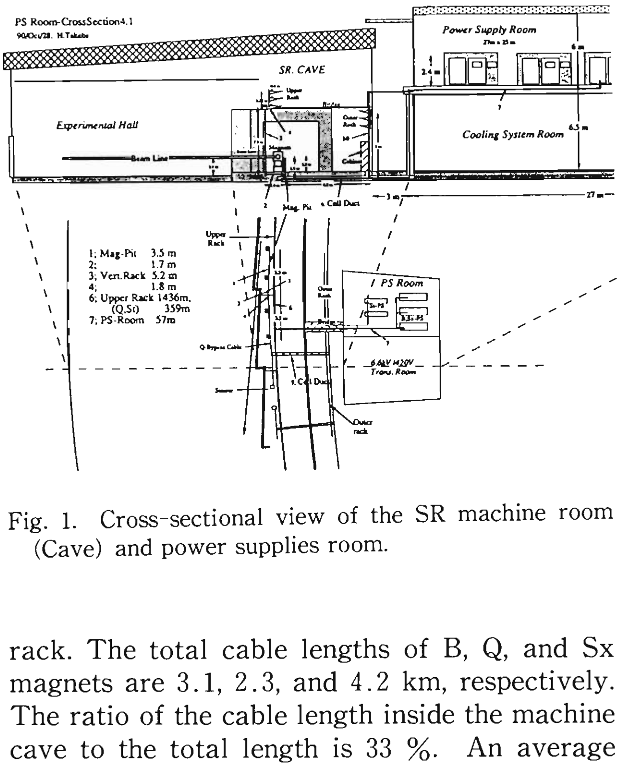

Fig. 1. Cross-sectional view of the SR machine room (Cave) and power supplies room.

The total number of the magnet parameters, which correspond to the DAC numbers, is 1,088. In order to reduce the number of the VME chassis, PS cabinets, must be consists of multiple PS units. Thirty-six steering magnet PS units are enclosed and controlled by one PS system. And twelve auxiliary PS units for the Q-magnets are similar system (see Table 2A and Table 4). In

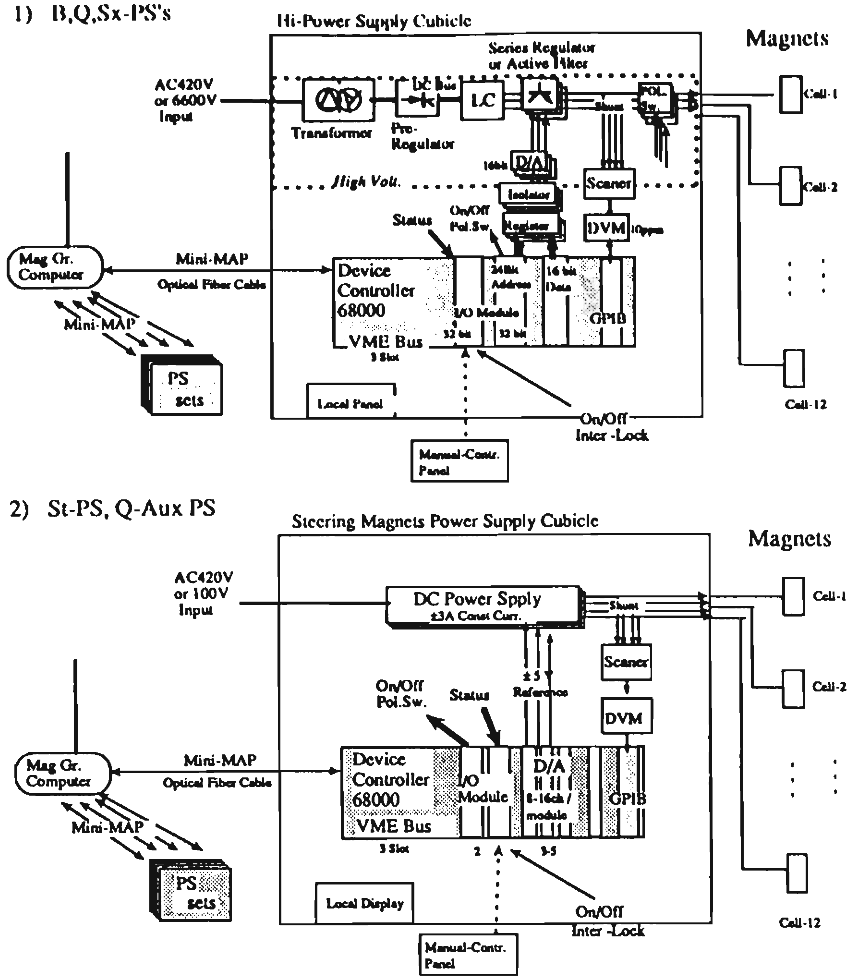

Fig. 2. Block diagram of the power supply system. A VME controller and DAC control interfaces are investigated.

order to reduce the manufacturing cost for the PS interface, a control and an interface system are investigated. Figure 2 shows control diagrams of the PS. High powered PS's (B, Q, Sx) are controlled by a floated DAC's through 16 bit isolators (photo-couplers) as seen in Fig. 2-1. Other PS systems (Co-PS, St-PS) are controlled by an analog reference voltage given by a 12-14 bit VME DAC module (see Fig. 2-2) or a VME remote I/O card.

References

1) H. Takebe, S. Motonaga, and H. Kamitsubo: *RIKEN Accel. Prog. Rep.*, **23**, 165 (1989).

RIKEN Accel. Prog. Rep. **24** (1990)

V-2-11. Bump Magnet of SPring-8

H. Miyade, H. Takebe, and S. Motonaga

On injection of a beam, a bump orbit is formed around the injection section; the orbit is parallel to the reference orbit and has an amplitude of 13.34 mm. The bump orbit is formed by four bump magnets installed at the positions shown in Fig. 1. Two of the four are installed in the both ends of the injection section (BP2, BP3) and the other two are beside bending magnets (BP1, BP4).

The magnets are excited in two operation patterns shown in Fig. 2. In a 1-Hz mode the magnets are energized once a second, and in a 60-Hz mode 8 times a second with repetitions of 60 Hz. Each pulse has a trapezoid form with a 4 μs in width, a 1 μs rise time, and a 2 μs flat top.

To reduce an eddy current, the magnet core is made of ferrite and the vacuum chamber is made of ceramic.

Cross sectional views and main parameters of

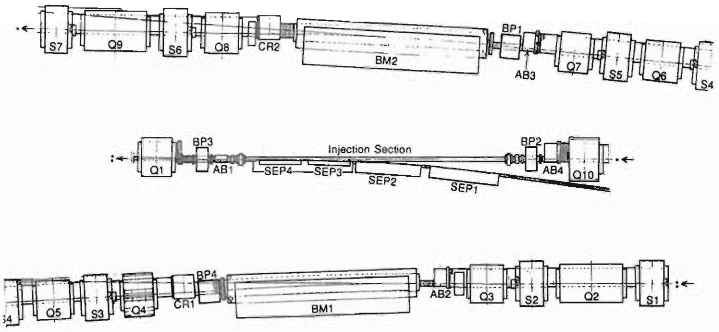

Fig. 1. Arrangement of bump magnets. BP, Bump Magnet; BM, Bending Magnet; Q, Quadrupole Magnet; S, Sextupole Magnet; SEP, Septum Magnet; AB, Absorber; CR, Crotch.

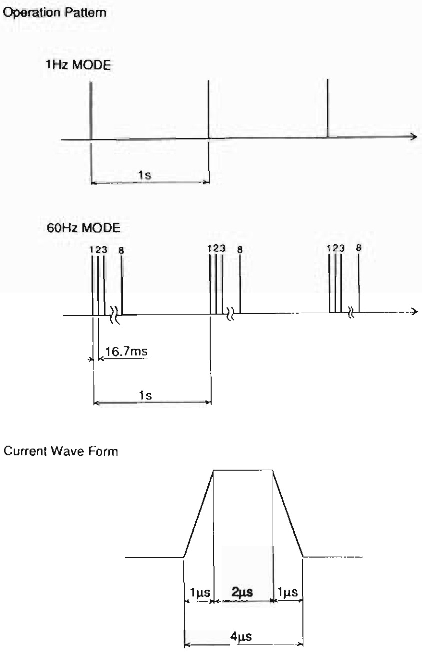

Fig. 2. Operation pattern and current wave form of bump magnets.

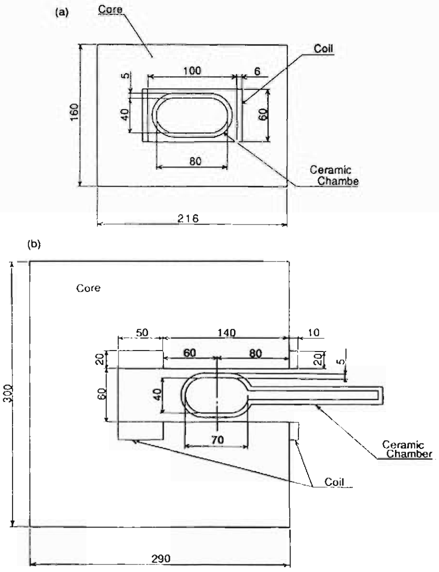

Fig. 3. Cross sectional views of bump magnets. (a), BP1, BP2, BP3; (b), BP4.

Table 1. Main parameters of bump magnets.

	BP1	BP2	BP3	BP4
Number	1	1	1	1
Kick Angle (mrad)	2.093	0.547	0.547	2.093
Core Length (mm)	300	200	200	350
Effective Length (mm)	285	190	190	335
Peak Field (T)	0.196	0.077	0.077	0.167
Number of Turns	2	1	1	2
Inductance (μH)	2.5	0.42	0.42	4.1
Peak Current (A)	4680	3670	3670	3980
Pulse Width (μs)	4	4	4	4
Rise Time (μs)	1	1	1	1
Flat Top (μs)	2	2	2	2

the bump magnets are shown in Fig. 3 and Table 1, respectively. The magnets BP1, BP2, and BP3 are of a window-frame type. The magnet BP4 is installed upstream of a crotch, so the vacuum chamber of BP4 has a slot through which a photon beam comes; the cross section of BP4 is C-shaped.

RIKEN Accel. Prog. Rep. 24 (1990)

V-2-12. Measurement of a 508 MHz Model Coupler for the SPring-8 Storage Ring

K. Inoue, Y. Kawashima, T. Nakamura, and M. Hara

In the SPring-8 storage ring, eight 508.58 MHz cavities are located in each of four 6.5-m straight sections with low-betatron functions. The RF power generated by a CW klystron is fed to the eight single-cell cavities through input couplers. Thus a total of 32 couplers are needed during operation.

The input coupler consists of an adaptor from a waveguide to a coaxial line, an RF window for vacuum seal, and a loop antenna. We decided following design policies of the input couplers for the SPring-8 storage ring.

(1) A total of voltage standing wave ratio is within 1.05.

(2) A multipactoring discharge on the RF window is reduced as low as possible.

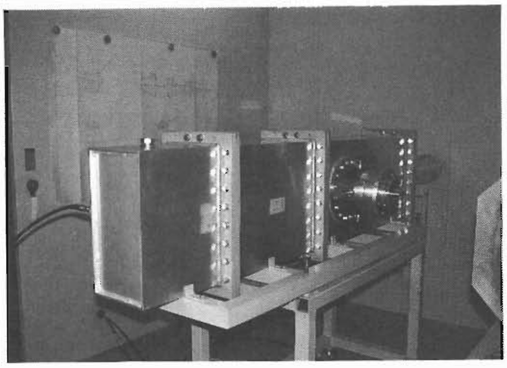

Fig. 1. Photograph of the model coupler.

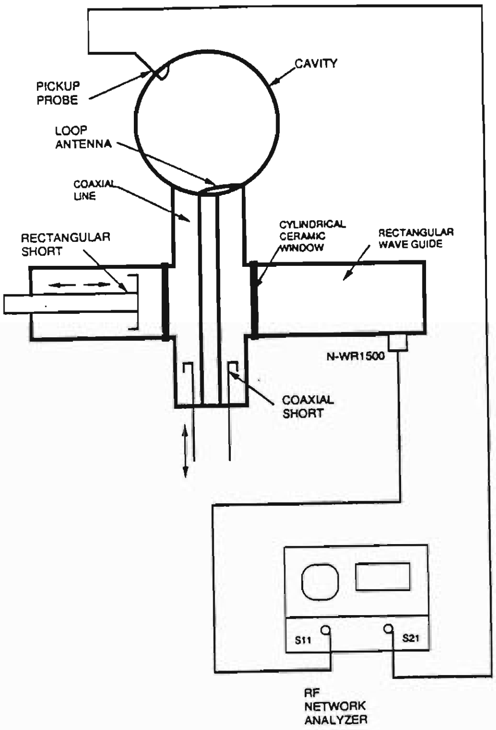

Fig. 2. Schematic cross section of the model coupler.

According to these policies, we have fabricated a model coupler shown in Fig. 1 to study its RF characteristics. A schematic cross section of the model coupler is shown in Fig. 2. It includes a WR1500 rectangular waveguide, an adaptor from the waveguide to a WX152D coaxial line, a cylindrical RF window, and a loop antenna. We have adopted a cylindrical RF window, 152 mm in diameter, 193 mm long, 5 mm thick, made of 95% alumina ceramics, which is successfully used for KEK TRISTAN APS cavities operating at 508 MHz,[1] and located it at the transition from the waveguide to the coaxial line. The end plates of the rectangular waveguide and the coaxial line are movable. The direction of the loop antenna was adjusted by rotating the coaxial line. RF characteristics were measured by a reflection and transmission method with a network analyzer. Figure 3 shows a preliminary result of the resonance characteristics of the model cavity[2] when the model coupler is

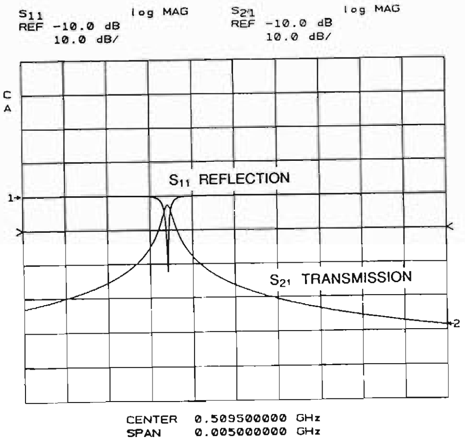

Fig. 3. Measured resonance of the 508 MHz model cavity.

mounted on a coupler port.

We are planning to measure its RF characteristics in detail and carry out high power tests using a 1-MW klystron³⁾.

References

1) M. Akemoto and T. Yamazaki: "High Power Input Coupler for the Tristan APS Cavity", Proc. 7th Symp. Accel. Sci. Technol. (Osaka, Japan) (1989).
2) K. Inoue, T. Kusaka, Y. Kawashima, T. Nakamura, and M. Hara: This Reort p. 162.
3) K. Inoue, Y. Kawashima, T. Nakamura, and M. Hara: This Report p. 166.

RIKEN Accel. Prog. Rep. **24** (1990)

V-2-13. Measurement of a 508 MHz Model Cavity for the SPring-8 Storage Ring

K. Inoue, T. Kusaka,* Y. Kawashima, T. Nakamura, and M. Hara

In the SPring-8 storage ring, it is necessary to reduce the intrinsic higher-order mode impedances of cavities. We designed a spherically shaped cavity.[1]

A model cavity was fabricated to examine its RF characteristics. Cross section of the model cavity is shown in Fig. 1. The resonant frequency in a TM010 mode was designed to be 508.58 MHz in the model cavity. Because the resonant frequency change due to an input coupler port was calculated to be −1.48 MHz, the resonant frequency of the axially-symmetric structure was designed to be 510.06 MHz. The equatorial radius of the model cavity was designed to be 254.7 mm, and the resonant frequency change corresponding to a machining error of ±0.1 mm was ∓0.217 MHz from SUPERFISH[2] calculations. The resonant frequency in the air was calculated to 509.924± 0.217 MHz, because the model cavity is tested in the atmosphere. The fabrication process of the model cavity was divided into two steps as follows, and RF characteristics were measured in each process.

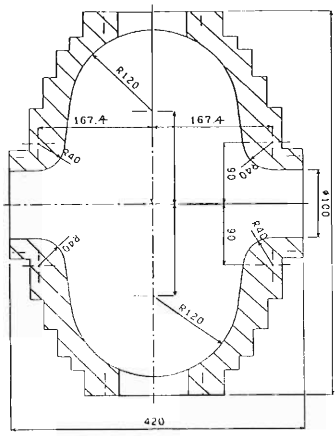

Fig. 1. Cross section of the model cavity.

In the first step, the model cavity machined out of 5052 aluminum alloy has four ϕ22 mm holes for measuring probes. Resonant frequencies and Q-values were measured by a reflection method with a network analyzer. Twenty resonant modes were observed below 1.5 GHz. The resonant frequency in the TM010 mode was 509.965 MHz and agreed well with a calculated value. The Q-value of the TM010 mode was 23580, 84% of the calculated value. The electric and magnetic field distributions for intrinsic higher-order modes were measured by a perturbation method.[3,4] A metal sphere, a teflon sphere, a metal disk, and a metal needle were used as perturbing objects. The results are shown in Fig. 2 and agree well with MAX3D[5] calculations. The geometrical factor R/Q (R: shunt impedance) also agrees well with calculated values as shown in Table 1.

Table 1. Comparison of R/Q values measured in several resonant modes with calculation.

Mode	R/Q(Ω *or* Ω/*m*)	
	Measured	Calculated
TM010	160.026	151.129
TE111	40.392	72.702
TM110	260.464	228.713
TM011	67.191	65.122
TM111	290.557	310.505

In the second step, additional four ports were machined in the model cavity. These ports were prepared for an input coupler, two frequency tuners, and a damping coupler which suppresses high-order modes. The Q-value of the TM010 mode at a frequency of 508.58 MHz with an input coupler and three frequency tuners was 21400, which was 76.5% of a calculated value.

We are planning to fabricate a prototype cavity and carry out high power tests using a 1-MW klystron.[6]

References

1) T. Kusaka, T. Yoshiyuki, T. Moro, and M. Hara: *RIKEN Accel. Prog. Rep.*, **22**, 265 (1988).
2) K. Halback and R.F. Holsinger: *Particle Accelerators.*, **7**, 213 (1976).
3) Y. Yamazaki, K. Takata, and S. Tokumoto: KEK 80-8, AUG. (1980).
4) L.C. Maier, Jr. and J.C. Slater: *J. Appl. Phys.*, **23**, 1 (1952).
5) M. Hara, T. Wada, K. Mitomori, and F. Kikuchi: *RIKEN Accel. Prog. Rep.*, **20**, 199 (1986).

---

* Kobe Steel, Ltd.

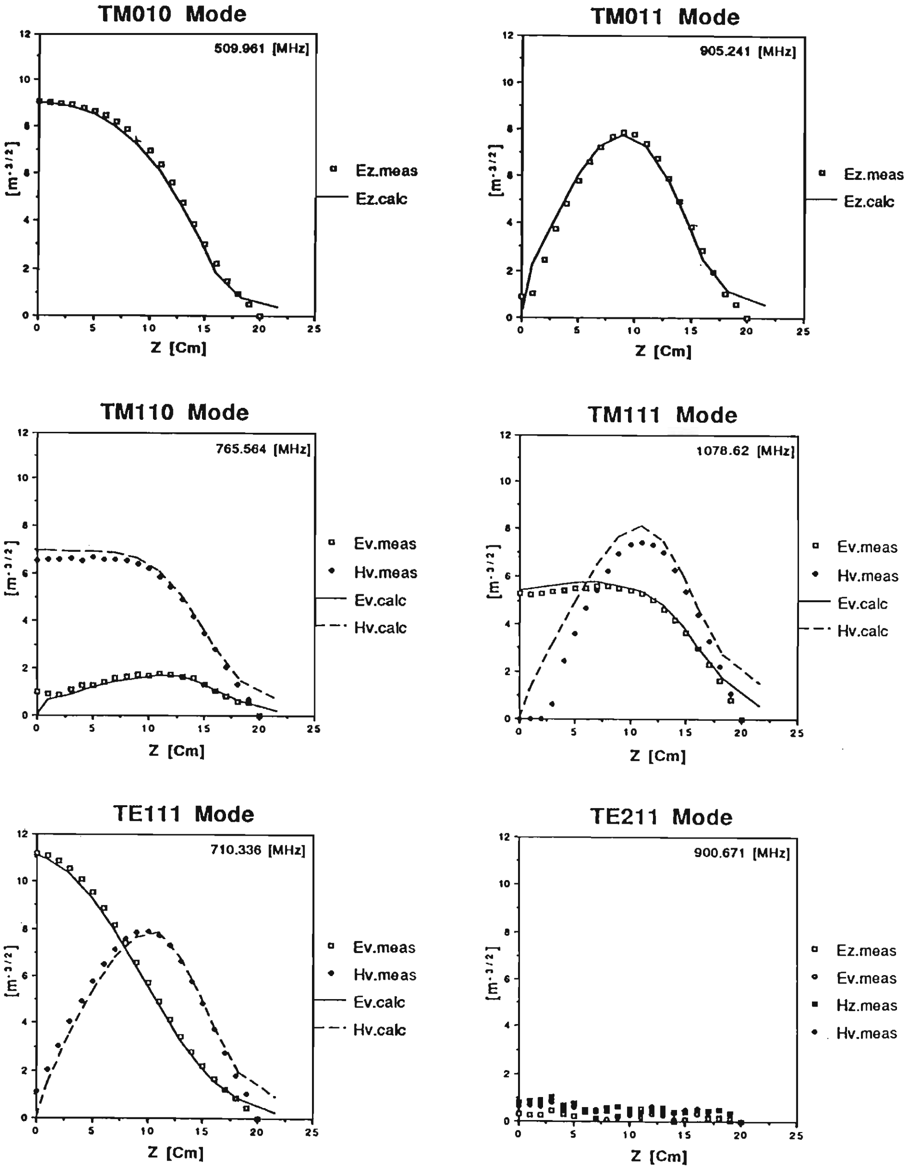

Fig. 2. RF characteristics measured with the model cavity with an axially-symmetric structure.

6) K. Inoue, Y. Kawashima, T. Nakamura, and M. Hara: This Report, p. 166.

RIKEN Accel. Prog. Rep. **24** (1990)

V-2-14. Design of the Prototype Cavity for the SPring-8 Storage Ring

K. Inoue, Y. Kawashima, T. Nakamura, and M. Hara

Single-cell cavities consisting of 32 pieces with a frequency of 508.58 MHz are installed on the straight lines of 6.5 m in length in the SPring-8 storage ring. We have made a cold model cavity and measured its RF properties.[1] Results are consistent well with calculation and confirmed to be well fitted to the RF feature expected. Furthermore, to examine high power RF, we newly designed a prototype cavity. The design principles are listed below.

1) Two plungers for a frequency tuner are mounted opposite to each other to suppress the symmetry breaking for the distribution of an electro-magnetic field in the cavity as small as possible. Their installed lengths from the inside surface of the cavity is decided to be 10 mm, and one of them is movable and the other is fixed.

2) A coupling coefficient for an input coupler should be 1 because the prototype cavity has no beam loading.

3) Under above two conditions, the diameter at the equator of the cavity is 510.2 mm, corresponding to a resonant frequency of 508.58 MHz.

4) Even if a shift from the resonant frequency happens for thermal deformation due to the energy loss on the surface of the cavity estimated as 100 kW, a frequency tuner can recover 508.58 MHz. The temperature of the inside surface of the cavity that has a structure easily being cooled down must be kept constant everywhere.[2]

In order to examine the influences of the different processes for joining two copper plates in making a cavity on an RF and a vacuum, two methods using diffusion bonding and electron beam welding are adopted. Both cavities are made of oxygen-free high-conductivity copper (OFHC). Their cross sections made by two different methods are shown in Fig. 1(a) and (b). The type (a) is made by the diffusion-bonding method using a copper plate of 40 mm in thickness. One side of the cavity (right-hand side from the bonding place in Fig. 1(a)) is made from 6 copper plates welded by the above method, the other consists of 3 copper plates. Five ports for an input coupler, two frequency tuners, a damping coupler, and an RF pick-up probe are made in a bigger copper block. Furthermore, some vacuum flanges are attached. Two blocks are then bonded after precise machining. By this method, they are bonded with less insert metal.

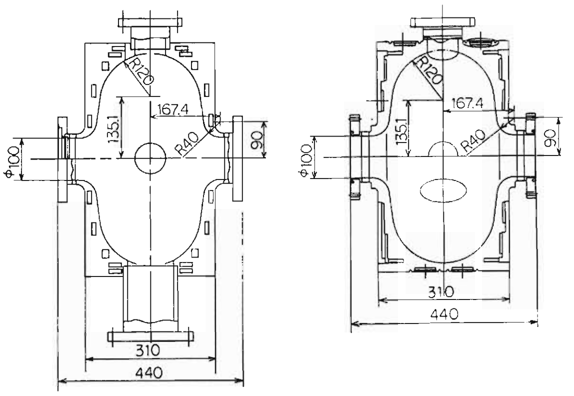

Fig. 1. Two cavities made through different processes; type (a) is made by the diffusion method. (b) is shaped the inside of copper blocks, then two blocks are joined.

On the other hand, in type (b), after two OFHC blocks are shaped into designed forms, they are connected at the equator to each other. In connection, temperature is suppressed below 60°C, to make thermal displacement small.

As an input coupler, we adopt the 508.58 MHz-input coupler developed for KEK TRISTAN MR.[3] The RF window shown in Fig. 2 is made of cylin-

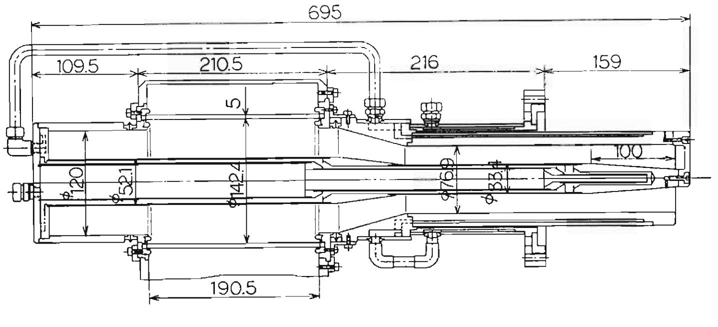

Fig. 2. Cross section of a cylindrical RF window.

drical ceramic. We are also designing another disk-type RF window.

We will test both cavities by using a 1 MW-Klystron, which is being constructed at RIKEN,[4] and then design a practical cavity for the SPring-8.

References

1) K. Inoue, T. Kusaka, Y. Kawashima, T. Nakamura, and M. Hara: This Report, p. 162.
2) T. Kusaka, K. Inoue, T. Yoshiyuki, and M. Hara: *RIKEN Accl. Prog. Rep.*, **23** 156 (1989).
3) M. Akemoto, and T. Yamazaki: "High power input coupler for the TRISTAN APS cavity", Proc. 7th Symp. Accel. Sci. and Technol., (Osaka, Japan, 1989).
4) K. Inoue, Y. Kawashima, T. Nakamura, and M. Hara: This Report, p. 166.

RIKEN Accel. Prog. Rep. **24** (1990)

V-2-15. Test Stand of a Klystron for the SPring-8 Storage Ring

K. Inoue, Y. Kawashima, T. Nakamura, and M. Hara

A test stand consisting of a klystron and its waveguide is being constructed in the cyclotron-physics experimental building. The klystron generates about 1 MW radiofrequency (RF) power in continuous wave (CW). This is also the same model as that to be installed in the ring site of the SPring-8 and supplies a 508.58 MHz RF power to RF cavities for a storage and a synchrotron rings. In order to investigate characters of the klystron and, furthermore, take various data for the final design work of RF cavities, various studies are carried out.

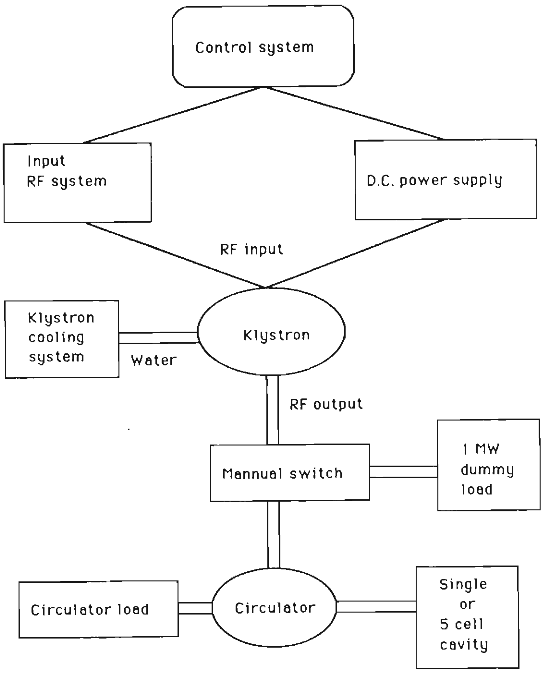

Fig. 1. Block diagram of the test stand for the klystron and the RF cavity.

The block diagram of the test stand is shown in Fig. 1 and its side view in the building in Fig. 2. The specifications of the klystron are listed in Table 1. As a cooling system for the collector parts of the klystron, vapor cooling has been used, but we improved it to more powerful water cooling. The klystron unit has three operation modes, a storage-ring, a synchrotron, and a pulse modes. The first one is a constant amplitude and continuous wave mode. In the second one, the output power level is modulated in accordance with a pattern required for a synchrotron acceleration at a repetition of 1 Hz. The pulse one generates a pulsed RF power of a 10 μs-1 ms width and is used for aging the klystron and cavities.

In order to protect the klystron from an accident, for example, when a load is short-circuited, a crowbar works within 6 μs. Once the crowbar is triggered, the cathode voltage is short-circuited at least 20 ms long until the vacuum circuit breaker (VCB) on an AC power line is off.

The input system of the klystron comprises a signal generator, a preamplifer, a circulator with a load, and an amplitude and phase monitor.

To handle up to a 1.2 MW power level between the klystron and a cavity, the WR1500 (15″×7.5″) rectangular waveguide made of the

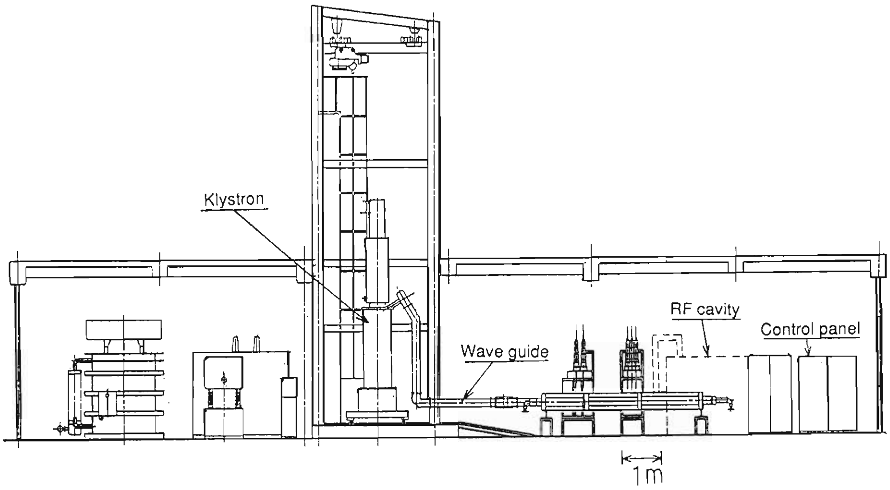

Fig. 2. Layout of the test stand in the building.

Table 1. Relevant parameters of the klystron.

Company	Toshiba
Type	E3786
Frequency	508.58 MHz
Heater power	23.0*A* × 11.2*V*
Anode vol.	64.5 kV
/current	2.2 mA
Cathode vol.	95 kV
/beam current	19.95 A
Drive power	3.8 W
RF power	1.2 MW
Efficiency	63.4%

6063-T5 aluminum is used. The electrical and thermal conductivities are 3.2×10^7 mhos/m and 1.95 W/cm°C, respectively. Air is flowed inside the waveguide for cooling.

In the first stage, the studies on the performance of the klystron and the waveguide system propagating RF power of more than 1 MW from the klystron are examined by using a water cooled dummy load of 1 MW rating. And then RF cavities are installed. There are two type RF cavities. One is single-cell for a storage ring and the other consists of 5 cells for a synchrotron. Their input couplers and tuners are tested with or without RF power from the klystron. The test stand is to be completed early 1991.

RIKEN Accel. Prog. Rep. **24** (1990)

V-2-16. All-Metal Gate Valve with an RF Contact

S. Yokouchi, K. Yagi,* K. Yoshida,* T. Ohbayashi,* and S.H. Be

We manufactured an all-metal gate valve with an RF contact on trial. Table 1 gives main specifications of the gate valve. The gate valve at the open position is shown in Fig. 1. The present valve body was made of stainless-steel, but that to be used in the practical SR ring is made of aluminum-alloy except a part of valve seats and disks. A technique is employed, which provides an enclosed evacuated space between double seals, thereby reducing the pressure difference across the seals and decreasing the leak rate of the seals. In the open position, the RF contact which has the same geometry as the beam chamber can bring about a direct electrical connection between two body flanges. Applying the thrusting force of an actuator to cam parts, which are connected to a carrier and two disks by a link mechanism (see Fig. 2), the sealing force between the seats and disks coated with silver is amplified by $F/F_0>1$. The further amplification of the sealing force is obtained by pushing the disks with a small arc to tapered seats polished like a mirror (see Fig. 3). The deformation amount of the valve disks and seats due to the sealing force is within an elastic limit.

Table 1. Main specification.

Pressure range	10^{-11}~760 Torr
Leak rate	less than 1×10^{-10}Torr·l/s
body and valve seal part*	
Materials	
Main parts	SUS304
RF contact	Be-Cu
Others	Al-alloy
Compressed air pressure	5~7 kgf/cm^{2}G
Bakeout temperature	150°C
Flange dimension	JVIS 003 NB100 Bakeable Flange

* Differential pressure on the valve seal is 1 atm in either direction.

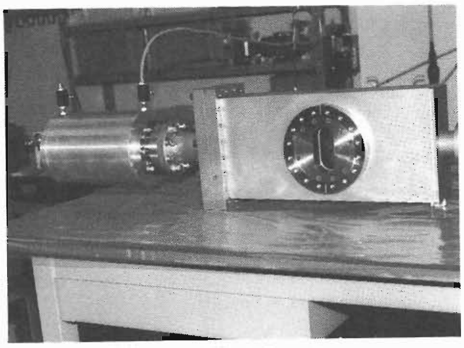

Fig. 1. Outside view.

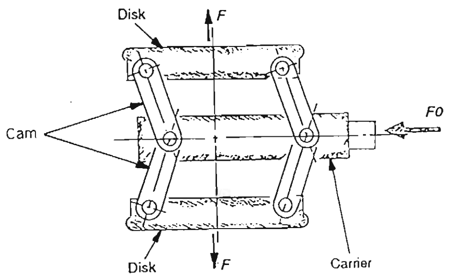

Fig. 2. Amplification mechanism of sealing force.

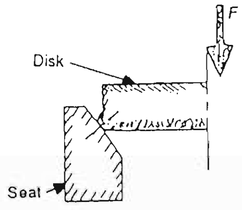

Fig. 3. Valve seal part.

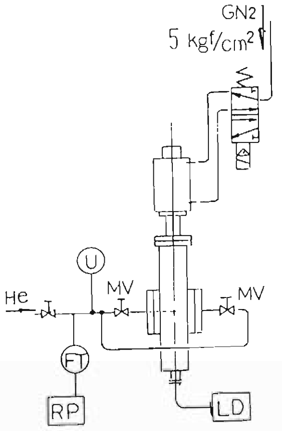

Fig. 4. Test system.

To investigate the leakage reliability at seals, we actuated the valve 1,000 times using the test system as shown in Fig. 4. The results show that the performance is not yet satisfied completely because there are a leak of the order of 10^{-8} Torr·l·s^{-1} over several times during actuations of these first 1,000 times. However, the present leak rate can be reduced to less 1×10^{-10} Torr·l·s^{-1} by evacuating the enclosed space between double seals.

To improve fluctuation of the leak rate to 1×10^{-10} Torr·l·s^{-1}, we are planning an investigation of the relation between the sealing pressure and the leak rate.

---

* Osaka Vacuum, Ltd.

RIKEN Accel. Prog. Rep. 24 (1990)

V-2-17. Pumping Speed of NEG Strips Distributed in a 4 m-Long Vacuum Chamber

S. Yokouchi, T. Nishidono, S.R. In,* H. Daibo, K. Watanabe, and S.H. Be

We measured the pumping speeds of NEG (St 707) strips distributed in a 4 m-long Al-alloy vacuum chambers[1)] manufactured for the R & D of the Spring-8. The NEG strips were installed in the straight section chamber (SSC) in four rows and in the bending magnet chamber (BMC) in two rows. The effective length per row is 360 cm both in SSC and in BMC. The total effective surface areas of the NEG strips in SSC and BMC are 7,776 and 3,888 cm^2, respectively.

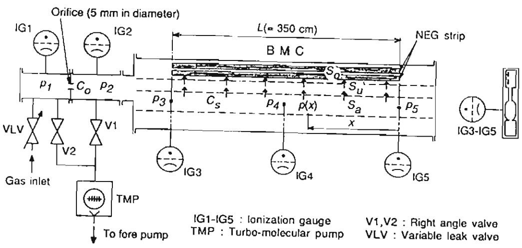

Fig. 1. Schematic diagram of the measurement setup for BMC. $p(x)$ is the pressure at x in Torr, S_a the average pumping speed at the beam chamber per unit length in $l \cdot s^{-1} cm^{-1}$, S_u the pumping speed of the NEG strip per unit length in $l \cdot s^{-1} cm^{-1}$, S_o the pumping speed of the NEG strip per unit area in $l \cdot s^{-1} cm^{-2}$, C_s the conductance of the slot per unit length in $l \cdot s^{-1} cm^{-1}$, L the length of the distributed NEG strip in cm, C_o the conductance of the orifice in $l \cdot s^{-1}$, and p_1, p_2, p_3, p_4, and p_5 the pressure measured at IG1, IG2, IG3, IG4, and IG5 in Torr, respectively.

Figure 1 shows the schematic diagram of the measurement setup for BMC. The base pressure was in the range of 10^{-10} Torr after a bakeout at 140°C for 40 hours. The NEG strips were activated at 450°C for 25 hours before measurements for H_2. For CO, the activation was performed at 450°C for 50 minutes before measurements. We calculated the average pumping speed, S_a, from

$$S_a = Q_o / \int_0^L p(x)\, dx \qquad (1)$$

where Q_0 is the throughput injected to the chamber in Torr·$l \cdot s^{-1}$, and can be obtained from $Q_o = C \times (P_1 - P_2)$. Since it is difficult to know the true $p(x)$, we assumed $p(x) = p_5 \times f(x) \times \cosh(kx)$, where $k = (1/L) \cosh^{-1}(p_3/p_5)$, and $f(x)$ is the quadratic determined by p_3, p_4, and p_5. Finally, we got S_0 from

$$S_o = (1/S_a - 1/C_s)^{-1} (350/360)/n/5.4 \qquad (2)$$

where n is the number of NEG strips.

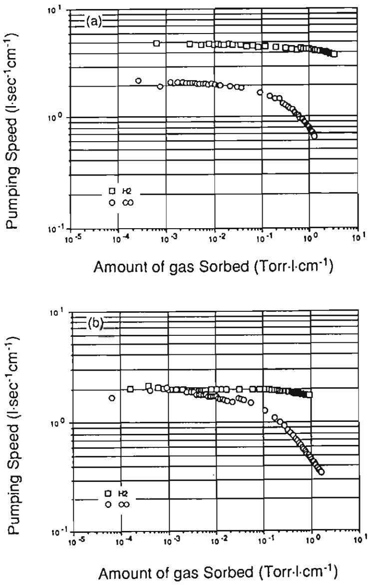

Fig. 2. Average pumping speeds per unit length for H_2 and CO at the beam chambers of (a) SSC and (b) BMC.

Figures 2 (a) and (b) show the average pumping speeds for H_2 and CO at the beam chambers of SSC and BMC, respectively. Using these results and Eq. 2, we obtained normalized pumping speeds of the NEG strips in SSC and BMC for H_2 and CO as shown in Fig. 3 (a) and (b). The pumping

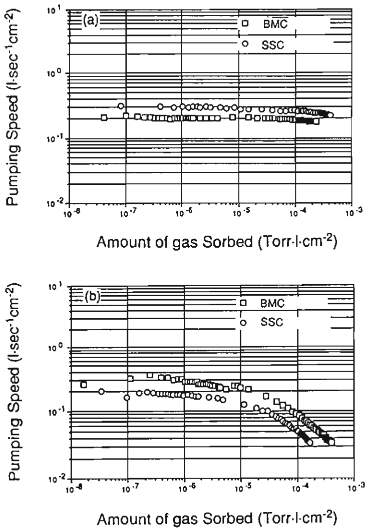

Fig. 3. Pumping speeds per unit area of the NEG strips in SSC and BMC for (a) H_2 and (b) CO.

---

* On leave of absence from KAERI, Korea.

speeds for H_2 is fairly constant because of the well known bulk-diffusion.[2)] On the other hand, the pumping speeds for CO decrease rapidly with an increase in the amount of sorbed CO.[3)] The dependence of the pumping speed on the amount of sorbed gas is similar to that of a short piece of NEG strip[4)] for both H_2 and CO. However, the pumping speed for H_2 is rather lower than that of the NEG strip piece. For CO, the maximum pumping speed is lower than that of the NEG strip piece by one order. This disagreement is a problem remaining unsolved.

References

1) S. Yokouchi, H. Sakamoto, T. Nishidono, Y. Morimoto, and S.H. Be: *J. Vac. Soc. Jpn.*, **33**, 258 (1990).
2) R.J. Knize and J.L. Cecchi: *J. Appl. Phys.*, **54**, 3183 (1983).
3) C. Benvenuti and F. Francia: *J. Vac. Sci. Technol.*, **6**, 2528 (1988).
4) Y.P. Lee, S. Yokouchi, Y. Morimoto, H. Sakamoto, T. Nishidono, N. Hinago, and S.H. Be: *J. Vac. Soc. Jpn.*, **33**, 154 (1990).

RIKEN Accel. Prog. Rep. **24** (1990)

V-2-18. Experimental Device for Measurement of Photon Induced Gas Desorption

K. Watanabe, S.R. In, S. Yokouchi, K. Yano, and S.H. Be

Gases desorbed by photodesorption influence electron beam lifetimes in a storage ring. In fact, it was reported that as an electron beam is injected into the storage ring chamber, the pressure increases from 10^{-11} Torr to 10^{-6} Torr and the lifetime becomes a few minutes. The photodesorption is said to be caused by primary photons (synchrotron radiation), secondary photons (reflect light and fluorescence), secondary electrons (photoelectron, Compton electron and Auger electron), and so on. However, the mechanism of the photodesorption has not been clear. Recently, Trickett[1] suggested that an outgassing rate is not proportional to a photocurrent, but is proportional to a fluorescent flux. Further, our calculations show that photodesorption yield η, which is the number of desorbed molecules per photon, is independent of the critical photon energy.[2]

To investigate the dependence of outgassing on fluorescence and photoelectron, and the dependence of η on critical photon energy, we are planning experiments. Figure 1 shows the experimental apparatus. Synchrotron radiation with a critical photon energy of 26 keV is adjusted with a horizontal collimator and a vertical collimator to be 5×5 mm^2 in cross section. As shown in Fig. 2, the test chamber is a cylindrical tube of 60 mm in diameter and 300 mm in length. The chamber is made of oxygen free copper, which is considered to be used as an absorbing material. The chamber is cooled with water to reduce thermal desorption when the chamber is irradiated with synchrotron radiation. The flange attached to the port for the measurement of fluorescence is installed at one end of the test chamber; a beryllium window of 1 mm in thickness is installed at the end of the port. The fluorescence passing through a hole of 1 mm in diameter on a lead shield is detected by a solid-state detector. In this experiment, we pay attention to the fluorescence of absorption edge energy, 8.98 keV, of the copper K shell, because synchrotron radiation is mostly attenuated by a photoelectric effect. Further, the fluorescence yield of the copper K shell has somewhat a large value, 0.374. The outgassing rate is measured by a throughput method. The gas species are observed by a quadrupole mass analyzer.

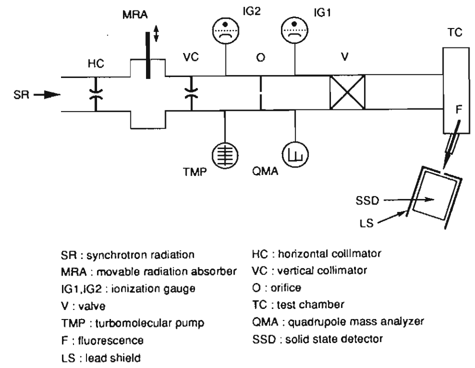

Fig. 1. Schematic drawing of the experimental apparatus.

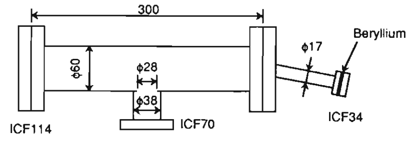

Fig. 2. Test chamber.

References

1) B. Trickett: Proceedings of SR Vacuum Workshop, RIKEN, p.428 (1990).
2) S.R. In and S.H.Be: This Report, p. 178.

RIKEN Accel. Prog. Rep. **24** (1990)

V-2-19. Vacuum Characteristics of a NEG Wafer Module

S.R. In, T. Maruyama,* Y.P. Lee,** S. Yokouchi, and S.H. Be

We have studied the vacuum characteristics of a St 707 non-evaporable getter (NEG) wafer module, which is the basic structure element of the lumped NEG pump (LNP) for the crotch of the SPring-8 storage ring. The main purposes of the unit NEG module experiment are to study the physical properties of NEG and to consider the geometrical effect of the wafer module configuration.

Figure 1 schematically shows the experimental apparatus for measuring the pumping speed of the NEG wafer module. A standard test dome which has an orifice between two chambers was used. The base pressure of the experimental chamber was in the lower 10^{-10} Torr range.

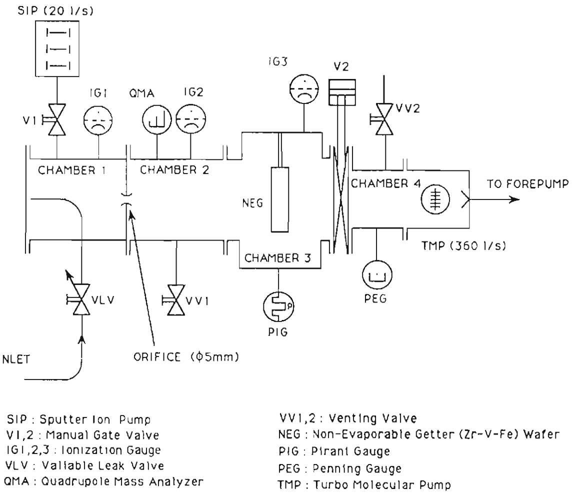

Fig. 1. Schematic diagram of experimental setup for NEG wafer module.

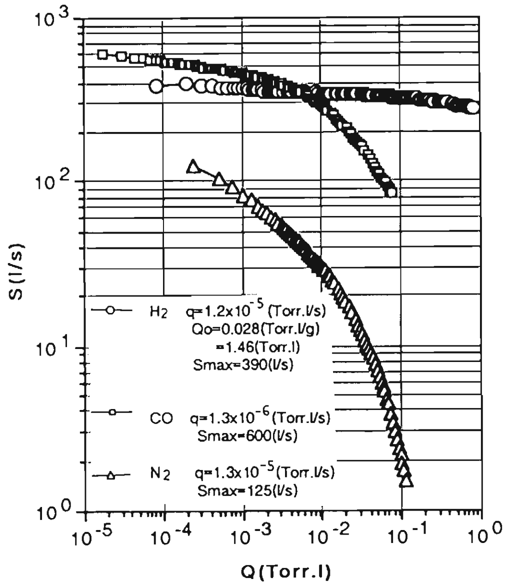

Fig. 2. Pumping speeds of NEG wafer module for H_2, CO, and N_2 as a function of sorption amount of each gas.

Activation of NEG was carried out at the flat-top temperature of 450°C for sufficient time. Activation followed by H_2 injection was continued until the initial gas quantity, Q_0, sorbed per unit mass of NEG reached a desired level, though the dependence of the pumping speed on Q_0 is very weak. Q_0 of H_2 was obtained from the NEG temperature and the chamber pressure by Sievert's law.[1]

Activation for other gases such as CO and N_2 was performed not to reduce Q_0's of these gases, but to enhance the diffusion of sorbed molecules into the bulk of NEG and make its surface fresh. One-hour-activation at 450°C was usually sufficient to reproduce preceding conditions.

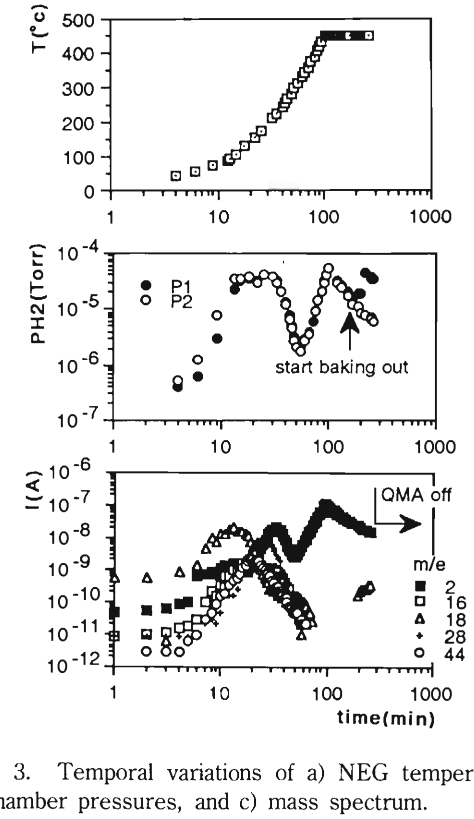

Fig. 3. Temporal variations of a) NEG temperature, b) chamber pressures, and c) mass spectrum.

---

* Osaka Vacuum Ltd.

** RIST, Pohang, Korea.

The measurement of a pumping speed was performed at room temperature. The pumping speed, $S(l/s)$, was obtained by a throughput method. The total gas quantity, $Q(\mathrm{Torr}\cdot l)$, sorbed in NEG was obtained by integrating the gas injection rate, q $(\mathrm{Torr}\cdot l/s)$, with respect to time.

Figure 2 shows the S-Q relationships for H_2, CO, and N_2. The maximum S's are 390(l/s), 600 (l/s), and 125(l/s), respectively. S for H_2 is almost constant owing to the diffusion into the bulk, while those for CO and N_2 decrease quickly as the NEG surface becomes saturated with sorbed gases. The NEG surface of the wafer module was almost saturated with CO or N_2 of about 10^{-1}–10^{0} $(\mathrm{Torr}\cdot l)$.

The variation in the mass spectrum obtained with a quadrupole mass analyzer (QMA) with time during activation is shown in Fig. 3. Although the peak heights of mass 16, 18, 28, and 44 increase at first due to initial contamination on the NEG surface, that of 2 becomes dominant because of the high diffusion rate of hydrogen atoms to the NEG surface from the bulk at elevated temperature, and increase of the H_2 desorption rate.

The calculation of S by a Monte Carlo method in parallel with the distributed pump model, using a sticking coefficient obtained in the NEG strip experiment,[2)] is now in progress.

References

1) J. Briesacher, N. Toyoda, C. Boffito, and F. Doni: *Ultra Clean Technol.*, **1**, 49 (1990).
2) Y.P. Lee, S. Yokouchi, Y. Morimoto, H. Sakamoto, T. Nishidono, and S.H. Be: *RIKEN Accel. Prog. Rep.*, **23**, 141 (1989).

RIKEN Accel. Prog. Rep. **24** (1990)

V-2-20. Performance Test of Lumped NEG Pump

S.R. In,* T. Maruyama,** S Yokouchi, and S.H. Be

In the vacuum system of SPring-8, synchrotron radiation produced in bending magnets is mostly intercepted by crotches and absorbers. To protect other vacuum components from severe inrush of the photo-desorbed particles from the crotches and absorbers, a proper pumping system of sufficient pumping speed and capacity must be prepared. A Lumped NEG Pump (LNP) was manufactured and tested to examine such requirement.

Structure of LNP A proto-type LNP[1)] consists of 14 St 707 non-evaporable getter (NEG) wafer modules installed concentrically in a cylindrical housing made of Al-alloy. The inner virtual surface made by 14 wafer modules forms a strong adsorbing cylindrical channel of which diameter and length are all 250 mm. The diameter of the pumping port is 200 mm, and the total weight of the LNP is about 45 kgf.

Performance test of LNP Figure 1 shows a schematic diagram of the experimental setup. Figure 2 indicates the pumping speeds of the LNP for H_2, CO, N_2 and CO_2. CO is more reactive with the NEG material and, consequently, has a higher sticking coefficient than H_2. However the pumping

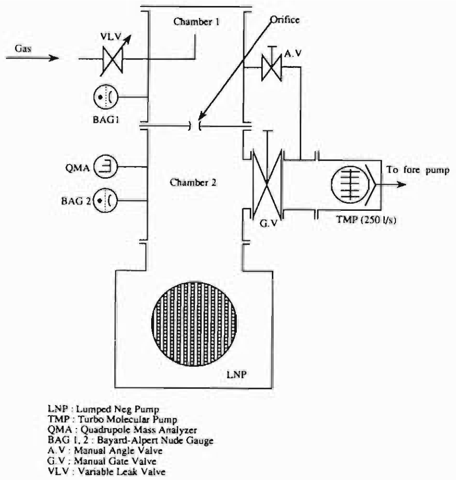

Fig. 1. Schematic diagram of the experimental setup for the LNP.

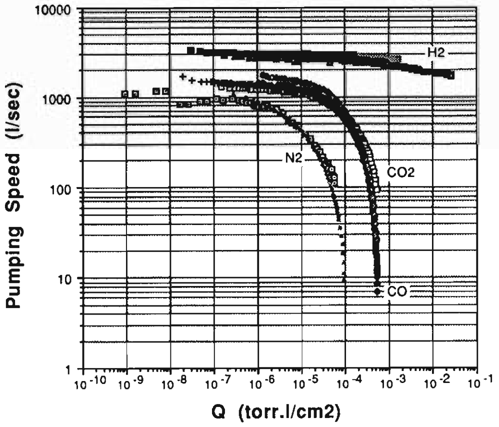

Fig. 2. Pumping speeds of the LNP for H_2, CO, N_2, and CO_2 as a function of the sorption amount of each gas.

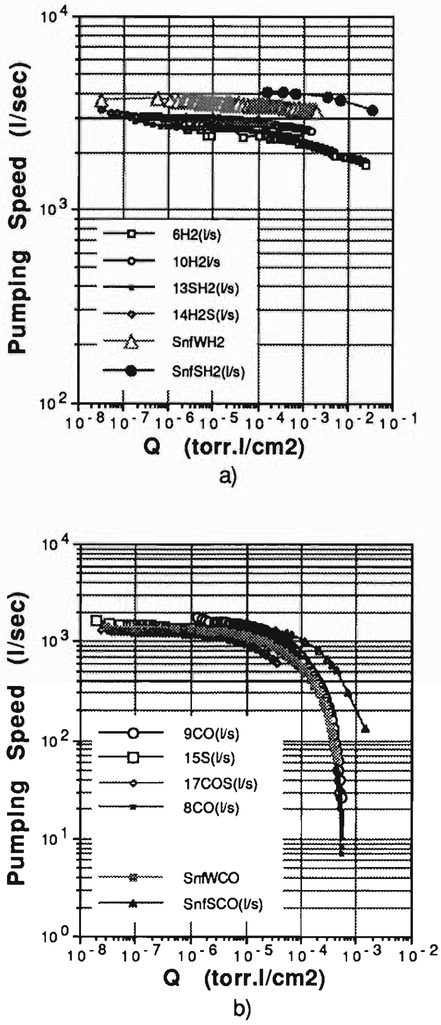

Fig. 3. Comparison of measured pumping speeds of the LNP for a) H_2 and b) CO with calculated pumping speeds using the data of 1 wafer module experiment.

---

* On leave from KAERI, Dajeon, Korea.

** Osaka Vacuum Ltd.

speed of H_2 is higher than that of CO in the LNP structure because NEG strips are folded into a highly integrated form in the LNP, and the pumping speed depends strongly on the conductance as well as the sticking coefficient. In Fig. 3 the pumping speeds of the LNP for H_2 and CO calculated from the data obtained with 1 wafer module are compared with the observed pumping speeds of the LNP. In this calculation, we took into account the distributed characteristics of the LNP pumping channel, and conductance to the pump entrance. Figure 3 shows slight but allowable discrepancies between the two values.

The chamber pressure during activation was in the range of 10^{-6} – 10^{-7} Torr, depending on the amount of H_2 sorbed in the NEG. The maximum temperature of the Al-alloy housing was controlled easily just below 150°C even without water cooling. This scheme of activation had an additional benefit that the pump housing and the adjacent chamber could be baked out at a time with activation. The influence of desorbed gas molecules from a baked wall on the resultant pumping speed of the LNP after activation was tolerable. Figure 4 shows the temperature variations at several positions in the LNP and the test chamber during activation of NEG. In a typical control mode for the NEG temperature, the power consumption of the LNP was about 1.1 kW at the temperature rise stage, and about 700 W at a flat-top temperature of 450°C.

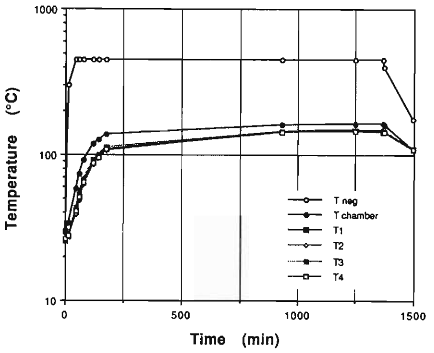

Fig. 4. Temporal variations in the temperature of the LNP and the test chamber.

References

1) S. Yokouchi, Y. Yamano, T. Nishidono, Y. Morimoto, Y.P. Lee, and S.H. Be: *RIKEN Accel. Prog. Rep.*, **23**, 138 (1989).

RIKEN Accel. Prog. Rep. **24** (1990)

V-2-21. Alteration of the Cracking Pattern of CO_2 with CO Generated on the Hot Filaments of the Pressure Gauges

S.R. In,* T. Maruyama,** and S.H. Be

A residual gas analyzer is used to determine the kinds of gas molecules contained in a vacuum system. However measured mass spectra confuse us occasionally with many unexpected mass peaks of various fragment ions produced in the reaction volume of the analyzer. Since a gas analyzer has its specific cracking pattern for a gas species, we can identify the mass number and calculate the gas composition. If there are other reactions producing undesired molecules, however, we face difficulties in confirmation of gas species.

Figure 1 shows time dependence of the relative peak heights of mass 28 and 44 during the measurement of the pumping speed for CO_2 in a test chamber of a non-evaporable getter (NEG) wafer module.[1] This figure indicates that the CO concentration is changed inversely with the variation in the pumping speed of the NEG for CO. Hot filaments inevitably used in the pressure gauges are considered to be main sources of spurious reactions.[2] The change in the peak height ratio of mass 28 to 44 as given in Fig. 2 was obtained in the experiment programmed to examine possible sources, including a quadrupole mass analyzer (QMA), extracter gauge (EXTR), sputter ion pump (SIP), and NEG, for the CO generation. From this figure we can recognize that the filament of QMA is one of the most probable CO sources.

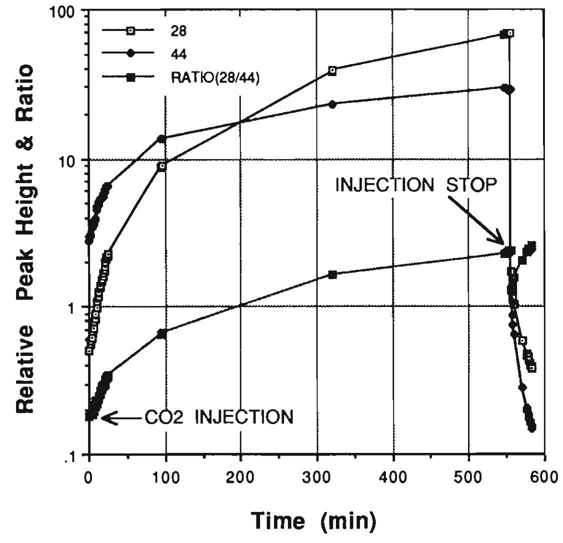

Fig. 1. Temporal evolutions of the relative peak heights of the mass 28 and 44.

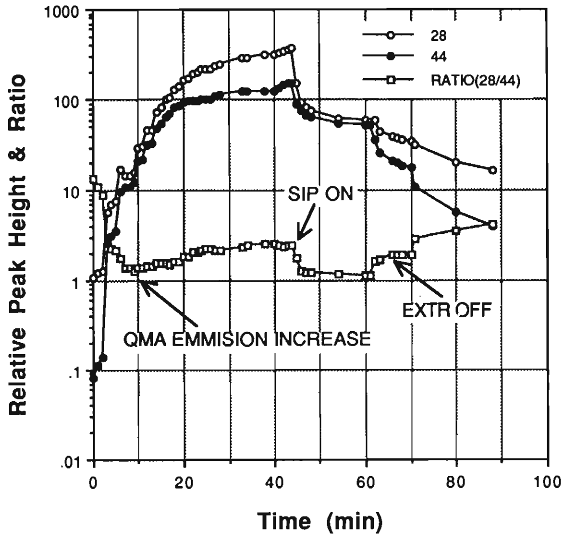

Fig. 2. Variations in the ratio of a 28 peak and a 44 peak during a preprogrammed experiment of CO_2 injection.

To measure the rate of CO generation we utilized a standard test chamber containing no NEG. Typical experimental conditions and some selected results are summarized in Table 1. The rate of the CO pressure change is represented as the total generation rate of CO minus the effective pumping speed for CO. In the steady state the CO generation rate is obtained by multiplying the peak height ratio of 28 to 44 by the pumping speed for CO. Consequently we obtain the CO generation rates of 0.2 *l*/s for the QMA filament with 1 mA emission current, 0.3 *l*/s for 5 mA emission current, and 0.5 *l*/s for the BA gauge filament. In conclusion, if the effective pumping speed for CO in an experiment system is at least a few tens of *l*/s like the situation of the LNP test chamber, we can confidently use the measured pumping speed for CO_2.

---

* On leave from Korea Atomic Energy Research Institute, Dajeon, Korea.

** Osaka Vacuum, Ltd.

Table 1. CO generation rates on the hot filaments.

Exp. Conditions						I_f (10^{-12}A)		CO generation rate (l/s)		
		B.A	QMA	Ie (mA)	GAS	44	28			
(1)		○	○	1	×	1.0	3.8	BA + QMA (2)−(1) ; 0.7	I	BA
(2)		○	○	1	○	19.7	12.2			
(3)	i)	×	○	1	×	0.51	0.715	QMA (3)ii−(3)i ; 0.2	II	I)−II); 0.5
	ii)	×	○	1	○	28.6	3.77			
(4)	i)	×	○	5	×	74.4	104.4	(4)ii−(4)i ; 0.3		
	ii)	×	○	5	○	2500	510			

○ : Turn on or Injection
× : Turn off or no Injection

References

1) S.R. In, T. Maruyama, Y.P. Lee, S. Yokouchi, and S.H. Be: This Report, p. 172.
2) P.E. Gear: *Vacuum*, **26**, 3 (1975).

RIKEN Accel. Prog. Rep. **24** (1990)

V-2-22. Estimation of the Photo-Desorption Yield of OFHC Absorber

S.R. In* and S.H. Be

Gas molecules desorbed from oxygen free high purity copper (OFHC) absorbers by interacting with synchrotron radiation are major constituents of residual gas of the SPring-8 storage ring during a beam-on operation. The desorption rate is influenced by many factors such as beam energy, beam current, incidence angle, material conditions at the surface and in the bulk of absorber, and history of machine operation. Therefore, theoretical estimation of the photo-desorption yield and application of the experimental results to a practical system are not easy. However we should evaluate the quantitative effect of the photo-desorption to provide the requirements for material selection and pumping system design.

The photo-desorption rate is obtained by multiplying a photo-desorption yield by a photon incident rate. The latter depends only on the machine parameters and is easily given, but the evaluation of the former is considerably difficult, because the photo-desorption yield depends on both machine and material parameters. Fortunately, however, it has been revealed that the photo-desorption yield is nearly independent of a photon energy spectrum. Hence, we can conveniently use the results on other systems of machine parameters different from ours.

Figure 1 shows a rearranged and combined graph of the photo-desorption yield η obtained from two separate experiments in the different range of critical photon energy.[1,2] Variation in η is less than expected one, and η can be considered approximately constant over the most range of the critical photon energy. On this premise we estimate the photo-desorption yield of a crotch made of OFHC under the operational conditions of SPring-8 by using experimental data[3] obtained in PF at KEK with an OFHC sample. η is expressed as [photon dose]$^{-2/3}$, where the photon dose is a function of beam energy multiplied by accumulated beam current, D[A.H]. Thus, $\eta = AD^{-2/3}$, where A is a constant determined by a specific beam energy and experimental data. The photo-desorption yields obtained by this procedure for H_2 and CO are approximately $7 \times 10^{-5}D^{-2/3}$ and $5 \times 10^{-6}D^{-2/3}$, respectively, under the normal conditions of SPring-8.

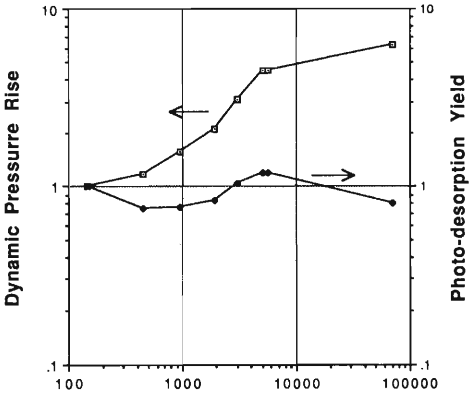

Fig. 1. Combined curve of the photo-desorption yield *vs.* the critical photon energy.

The photo-desorption rate, consequent chamber pressure rise, depletion of the pumping capacity of a non-evaporable getter (NEG), and resulting pumping speed reduction of a lumped NEG pump (LNP) can be calculated by using the photo-desorption yield given above and other machine parameters. An activation schedule of NEG is decided as a final step. The procedures for determining the activation schedule of the LNP are as follows: (1) calculation of the desorption rate $q(t)$ for H_2 and CO, (2) calculation of the sorbed amount $Q(t)$, (3) estimation of the pumping speed $S_p(t)$ from $S_p(Q)$ or the sticking coefficient $s(Q)$ curves, (4) estimation of the pressure rise $\Delta P(t)$ and/or base pressure $p(t)$, (5) evaluation of the activation intervals using proper criteria. We are considering the activation schedules for several types of the LNP under the practically expected conditions of SPring-8.

References

1) H. Halama: Proc. SR. Vac. Work., RIKEN, p. 405 (1990).
2) O. Grobner, J.M. Laurent, and A.G. Mathewson: Proc. EPAC, Nice (1990).
3) M. Kobayashi: Proc. SR. Vac. Work., RIKEN, p. 347 (1990).

---

* On leave from Korea Atomic Energy Research Institute, Dajeon, Korea.

RIKEN Accel. Prog. Rep. **24** (1990)

V-2-23. Equilibrium Characteristics of NEG in LNP

S.R. In,* T. Maruyama,** and S.H. Be

Base pressures of a chamber for testig a lumped NEG pump (LNP) were usually in the medium of 10^{-11} Torr range. However the chamber pressure increased even up to 10^{-5} Torr range during an activation of non-evaporable getter (NEG) because of large sorption-capacity of the LNP for hydrogen. A long activation period is anticipated to attain a low hydrogen sorption level, considering a limited pumping speed in a practical machine. In order to design a supplement pumping system appropriately and make a reasonable operation schedule for a vacuum system employing NEG as a main pump, we need detailed information on the equilibrium characteristics of the NEG material especially during the activation.

H_2 is absorbed into the NEG forming a metastable compoud which can be easily decomposed at elevated temperature. The surface concentration of hydrogen is in equilibrium with external gas pressure. We can not measure the equilibrium pressure itself, but we figure out it by measuring the gas pressure around NEG. By changing an effective pumping speed for outgassed molecules from the NEG during activation we can estimate the relationship between measured pressure and equilibrium pressure. As a conclusion, accurate equilibrium pressure is obtained from the pressure in the lower chamber of the LNP test system.[1] Measured chamber pressure at the temperature above about 300°C follows Sievert's law, and varies linearly in the Log$P$-$1/T$ graph.

Figure 1 shows a typical chamber pressure variation recorded in the temperature rise and fall stages during NEG activation. Calculated parameter B from this figure is slightly larger than that recommended by maker. Figure 2 indicates the change in the chamber pressure at the flat-top temperature of 450°C. The vertical axis is the inverse square root of the measured chamber pressure. The gradient of the line is a function of initial pressure P_i and α, where α is the characteristics time taken to reduce the pressure to a quarter of the initial value. We should determine actual parameters of the vacuum system so that α becomes a reasonable value.

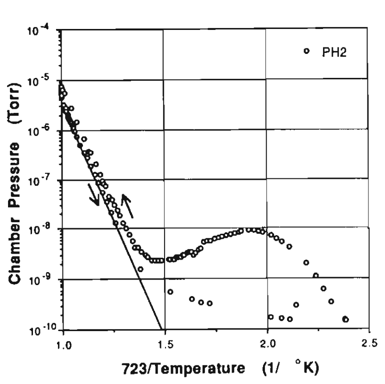

Fig. 1. Variation in the chamber pressure as a function of NEG temperature.

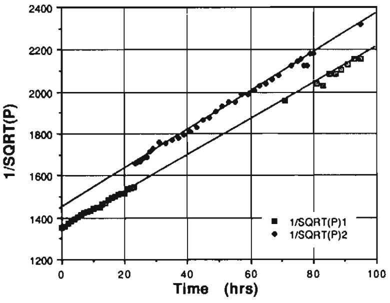

Fig. 2. Time dependence of the chamber pressure at the flat-top temperature of 450°C.

As the effective pumping speed, during NEG activation changes, the chamber pressure and net outgassing rate are also changed; outgassing rate q for opening the gate valve in the LNP test system is expressed as $AsC_0(P_{eq}\text{-}P)$, and q' for closing the valve is given as $AsC_0(P_{eq}\text{-}P')$. Therefore the sticking coefficient s is calculated by known values of the total NEG area A, unit orifice conductance C_0, pressures P and P' measured for two situations, and calculated outgassing rates q and q', though the true P_{eq} is stil unknown. On this principle the sticking coefficient for H_2 is calculated to be about 0.004, which is almost the same as that estimated by comparing data of pumping speed measurements and a Monte Carlo calculation.[2]

References

1) S.R. In, T. Maruyama, S. Yokouchi, and S.H. Be: This Report, p. 174.
2) S.R. In and S.H. Be: *ibid.*, p. 180.

---

* On leave from KAERI, Dajeon, Korea.
** Osaka Vacuum Ltd.

RIKEN Accel. Prog. Rep. **24** (1990)

V-2-24. Monte Carlo Simulation in the LNP Structure

S.R. In,* T. Wada, and S.H. Be

Three types of non-evaporable getters (NEG's), *i.e.*, a NEG strip, NEG wafer module, and lumped NEG pump (LNP) comprising several NEG wafer modules, have distinct pumping charatceristics even though they are made of the same material. If we know geometrical influences of the NEG cofigurations, we can accurately estimate the pumping speed of a specified pump structure, using known sticking coefficients as universal parameters. A distributed pump model and Monte Carlo simulation are generally used to solve such a problem.

The pumping speed is expressed as a multiplication of a pumping probability at the top plane and an orifice conductance of the pump entrance port. The pumping probability depends on the sticking coefficient of NEG and the practical geometry of the whole pump system. The Monte Carlo method is an effective tool of calculating the pumping probability. In a Monte Carlo program diffuse reflections and sticking probabilities are treated as random processes. The pumping probability is obtained as a ratio of the total counts of absorption to the total counts of incidence of test particles.

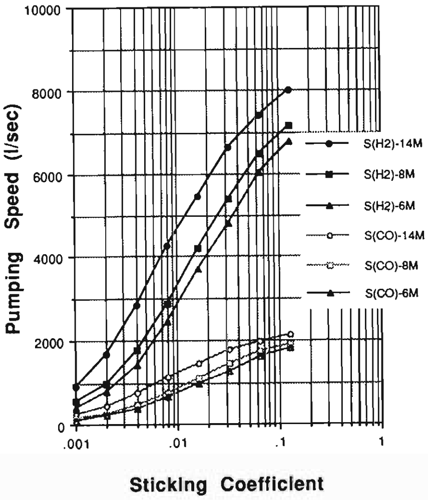

Fig. 1. Calculated pumping speeds of the LNP's with different configurations for H_2 and CO as a function of the sticking coefficient.

Figure 1 shows the pumping speed of the LNP for H_2 and CO calculated as a function of the sticking coefficient. By comparing with typical experimental data of the pumping speed, the sticking coefficients of NEG used in the LNP are roughly estimated at 0.004 for H_2 and 0.03 for CO. The sticking coefficient for H_2 was directly measured in the experiment of the equilibrium characteristics of the LNP[1] to be about 0.004. This indicates that the calculating model used and the experimental conditions are consistent with each other. A few examples of the pumping speeds calculated for different configurations of the NEG modules in the LNP are also shown in Fig. 1. Because the conductances to the pumping port are almost the same for all the configurations, the pumping speeds of the LNP are not linearly proportional to the number of NEG modules used in the LNP, especially for heavy molecules. The pumping speeds of the LNP with 6 NEG modules for H_2 and CO are about 50% and 70% of those with 14 NEG modules.

The intrinsic pumping speed of a pump is defined as the pumping speed measured with a test chamber of infinite size. In a Monte Carlo calculation such a situation is easily prepared, but actual pumping speeds can not be measured without using a test chamber of finite size. The difference between the two chambers is in the degree of random for the incident directions of gas particles. An average cosine for the chamber of finite size is larger than 1/4, indicating that the particles incident upon the pumping port prefer the forward direction. The Monte Carlo simulation shows that the pumping speed must be measured at the position above the entrance plane of the pump. The influence of the orifice diameter is not clear yet.

References

1) S.R. In, T. Maruyama, and S.H. Be: This Report, p. 179.

---

* On leave from KAERI, Dajeon, Korea.

RIKEN Accel. Prog. Rep. 24 (1990)

V-2-25. Thermal Load Test of the Absorber for the Crotch with an Electron Beam

S. Takahashi, Y. Morimoto,* S. Yokouchi, and S.H. Be

A crotch for the SPring-8 has two absorbers (AB1, AB2), which get high thermal load (~26.7 kW/cm^2) from the synchrotron radiation (SR). Therefore, the absorbers should be designed to withstand such a high power-density. We are carring out thermal analysis especially for AB1, because the power density at AB1 is higher than that at AB2.[1,2] The results showed that the inside conditions of an inlet cooling channel such as boiling conditions and the temperature of cooling channel walls, and the temperature gradient on the absorber are mainly influenced by the total power, and that the temperature of the surface irradiated directly with SR is dominated by the power density which strongly affects thermal fatigue of absorber materials. To confirm whether these results are really realistic, we are preparing an thermal load test of AB1 with electron beams.

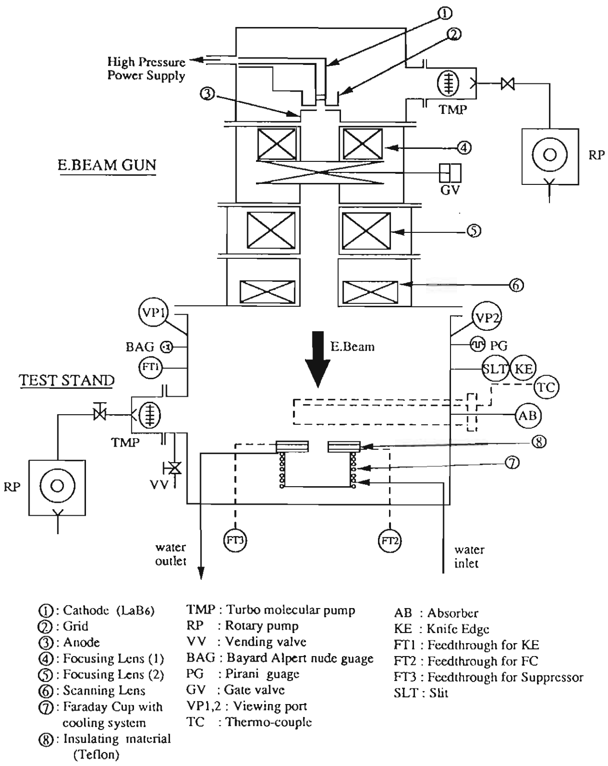

Fig. 1. Schematic diagram of the test device.

The test device shown in Fig. 1 consists of an electron beam gun (E.B. Gun) and a test stand. The main specifications of the E.B. Gun are given in Table 1. The test stand made of stainless steel (SUS304) is equipped with a Faraday cup (FC) for the measurement of electron beam currents. To suppress secondary electrons generated by bombarding an electron beam in FC, a negative bias voltage is applied to the entrance of FC.

Table 1. Specification of the E.B. Gun.

Item	Specification
Model	EB 10/30 (Rearranged Type ; IHI)
Beam Power	Max. 5kW
Acc. Voltage	Max. 30kV
Beam Current	Max. 160mA
Cathode	LaB$_6$ Dia. : 6mm

An absorber (AB), which has two cooling channels (inlet and outlet) and six holes for thermocouples as shown in Fig. 2, is installed at 300 mm below the bottom of the E.B. Gun. AB is irradiated over a length of 18 mm with a scanning E.B. scanned by using lens of E.B. Gun at a frequency of 500 Hz. The scanning irradiation of the E.B. at 500 Hz corresponds to a realistic SR irradiation.

The total power of SR received by AB1 in the real storage ring is about 1.2 kW. A corresponding total power of an electron beam is obtained at a beam current of 40 mA and an accelerating voltage of 30 kV. To find a beam current profile

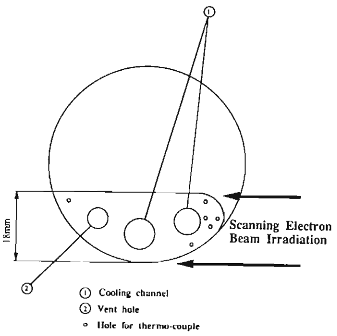

Fig. 2. Cross sectional view of the absorber. It is irradiated with a scanning electron beam, and thermal distribution is measured with six thermo couples.

---

* Kobe Steel, Ltd.

at the location of AB1 for thermal load tests we did a beam dynamical analysis.

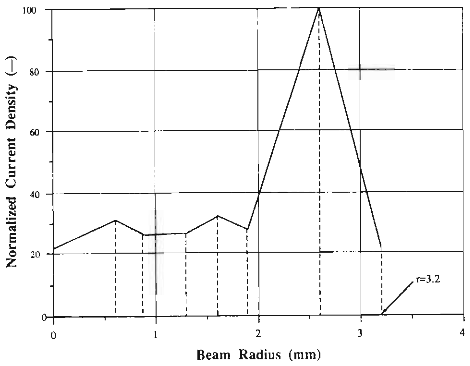

Fig. 3. Beam current profile obtained from a beam orbital analysis.

A typical beam current profile obtained from the analysis is shown in Fig. 3, which shows that the beam diameter at the location of AB is 6.4 mm. This value is larger than that expected because of a low accelerating voltage. To carry out an experiment similar to a practical SR, the scanning width of E.B. is to be reduced to below 1 mm with a slit made of tungsten, as shown in Fig. 4. We have to increase the current of E.B. to the value at which a beam power passing through the slit (the slashed area in Fig. 4) is 1.2 kW. Therefore, if we utilize the slit of $W = 0.1$ cm, the power density for 18 mm scanning is 6.7 kW / cm^2. For the same power density ($\sim$26.7 kW/cm^2) as the practical one, $W = 0.025$ cm is required. Problems are whether such a small slit width can be machined accurately, and whether the total power of a beam passing through the slit of $W = 0.025$ cm can be 1.2 kW with this E.B. Gun (Maximum total power=5 kW). Therefore, for the time being, our experiments are focused on the investigation of the inside conditions of cooling channels and the temperature gradient on the absorber by using a slit of $W = 0.1$ cm. A thermal analysis under actual experimental conditions will be performed in parallel with the experiments.

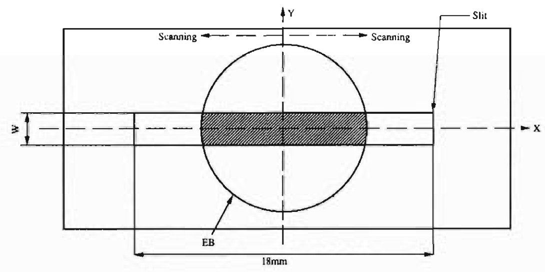

Fig. 4. Relation between E.B. and a slit width.

References

1) Y. Morimoto, S. Yokouchi, H. Sakamoto, S.H. Be, and T. Shirakura: *RIKEN Accel. Prog. Rep.*, **22**, 292 (1988).
2) Y. Morimoto, T. Shirakura, K. Konishi, and S.H. Be: This Report, p. 183.

RIKEN Accel. Prog. Rep. 24 (1990)

V-2-26. Thermal Analysis of a Crotch for the SPring-8 Storage Ring

Y. Morimoto,* T. Shirakura,* K. Konishi,* and S.H. Be

In the SPring-8 storage ring, the photon power density deposited at a crotch located just downstream of a bending magnet reaches approximately 35 kW/cm^2. This high power density causes high metal wall temperature and, as a result, high thermal stress.

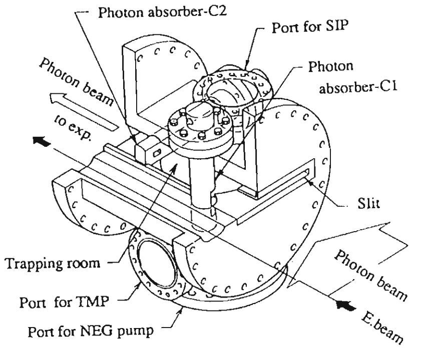

Fig. 1. Isometric view of a crotch.

A photon beam is stopped at two kinds of photon absorbers (ABS-C1 and C2) installed in the crotch. (see Fig. 1) ABS-C1 receives photons of a power density higher than ABS-C2. Therefore we pay more attention to the analysis of ABS-C1. Three models for ABS-C1 (model C1-1, C1-2, and C1-3) and one model for ABS-C2 (model C2-1) are considered. Models C1-1 and C2-1 are basic models whose shapes are the same as those of ABS-C1 and C2 which have been manufactured for a prototype crotch. Models C1-2 and C1-3 are alternative ones to decrease wall temperature and thermal stress. Model C1-2 has a fin plate for promoting a heat transfer area at the place where maximum temperature would be observed. Model C1-3 has two surfaces inclined with respect to a photon beam to reduce the power density. One of the two surfaces is vertically rotated and another is horizontally rotated to the direction of the outside of the ring, so that reflected photons and gas molecules would not tend to come into an electron beam channel.

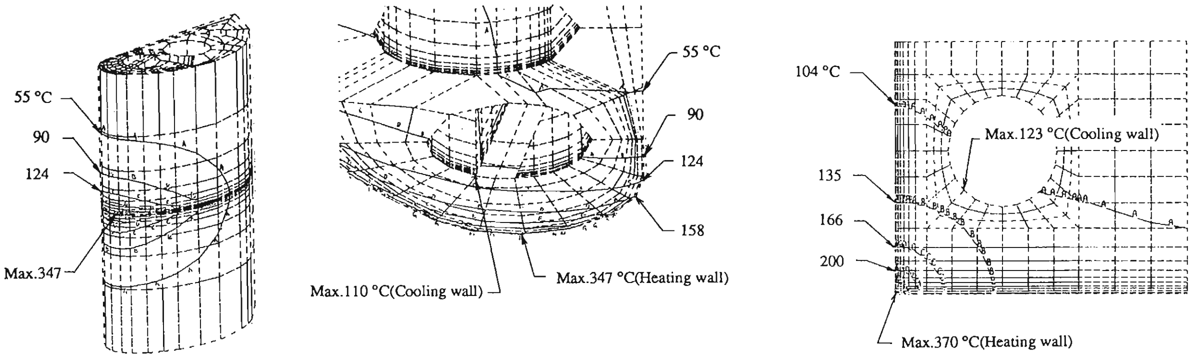

(a) Model C1-2 (OFHC-Class 1)

(b) Model C2-1(OFHC-Class 1)

Fig. 2. Temperature distributions computed for model C1-2 (OFHC-Class1) and model C2-1 (OFHC-Class1).

Table 1. Computed thermal stress and Tresca's equivalent stress σ_{eq}.

Model	Material	Max.thermal stress(kg/mm^2) X direct.	Y direct.	Z direct.	σ_{eq}(kg/mm^2)
C1-1	OFHC-Class 1	-37.4	-12.4	-23.7	-25.0
	GlidCop AL-35	-49.6	-14.5	-28.1	-35.1
C1-2	OFHC-Class 1	-30.4	-7.2	-17.1	-23.2
	GlidCop AL-35	-39.9	-9.3	-23.1	-30.6
C2-1	OFHC-Class 1	-	-	-	-

Thermal analysis was made using a finite element program ANSYS developed by Swanson Analysis Systems, Inc. Figure 2 shows results of calculations for temperature distributions, and Table 1 shows those of calculations for thermal stress. These thermal stress should be judged using a criteria for the fatigue failure due to the thermal cycles during normal operating procedures. The fatigue failure data are commonly plotted on an S-N diagram shown in Fig. 3. The design curve in the S-N diagram is decided using

---

* Kobe Steel, Ltd.

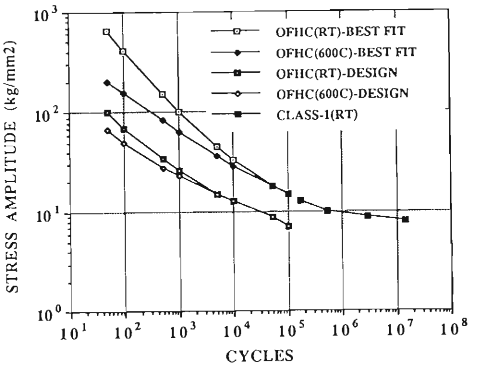

Fig. 3. Fatigue failure strength of OFHC subjected to the cycles of alternating tension and compression.

the safety factor 2 for stress and 20 for cycles in accordance with ASME Boiler and Pressure Vessel Code Sect. III and Sect. VIII Div. 2.

If Tresca's equivalent stress of 30.6 kg/mm^2, which is obtained in model C1-2 for GlidCop AL-35, is estimated from this design curve, the design life would be 5000 cycles. It corresponds a ten-year life, assuming that electrons are injected to the storage ring twice a day. (2 cycles/day × 250 days/year × 10 years = 5,000 cycles). The analysis for model C1-3 is in progress.

RIKEN Accel. Prog. Rep. **24** (1990)

V-2-27. Heated Water Bakeout System

S. Takahashi, S. Yokouchi, T. Nishidono, K. Watanabe, and S.H. Be

We are considering to bake out alluminum alloy chambers for the SPring-8 by means of a heated-water bakeout system (HBS). An exisiting prototype vacuum chambers has been baked out with SUS304 sheathed heaters installed on the chamber surfaces. NEG strips installed in the chamber was activated while cooling the chamber with two channels of 10 mm in diameter.[1)]

Advantages of the proposed system are compared with an existing method as follows:

1) Bakeout and NEG activation can be performed simultaneously.
2) The chamber temperature during bakeout and NEG activation can be controlled easily and uniformly without a risk of overheating.

Figure 1 shows the cross-sectional view of a straight chamber. There are two cooling channels of 10 mm in diameter at the pumping chamber side, and one racetrack-shaped channel (12 mm × 16 mm) at the opposite side. A new type bending chamber have four cooling channels of 10 mm in diameter. As shown in Fig. 2, the region of one cell is baked out with one unit of HBS in view of easy control.

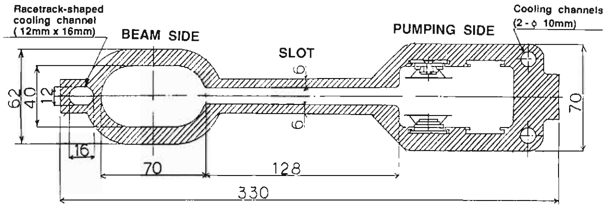

Fig. 1. Cross sectional view of the straight chamber.

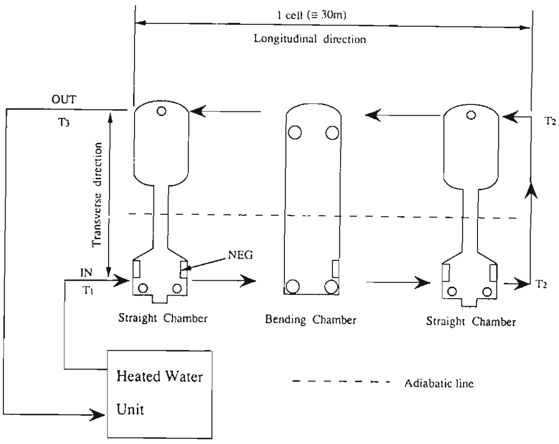

Fig. 2. Cooling water flow for one cell.

We are investigating how to keep the temperature of chambers uniformly at about 150°C in both longitudinal and transverse directions simultaneous with activation of NEG. Table 1 gives power parameters measured actually with existing prototype chambers. To decrease transverse thermal gradient, cooling channels are connected in series, as shown in Fig. 2. Because the slot between a beam and the pumping chamber has high thermal resistance due to its low thickness, we assume an adiabatic line (dotted) at which heat exchange between both chambers would be isolated, as shown in Fig. 2. As the power required for bakeout of the beam chamber is close to that at the pumping chamber side, we should supply a half of the total power of a chamber to the beam chamber side. We further assume that a part of heat generated during NEG activation is utilized for the bakeout of the pumping chamber.

Table 1. Power parameters measured actually with existing prototype chambers.

Q_1	Power required for bakeout	SC : 1.36kW/4m BC : 1.81kW/4m
Q_2	Heat generated during NEG activation	SC : 4.1kW/3.5m $\times 4^{\text{lines}}$ BC : 2.4kW/3.5m $\times 2^{\text{lines}}$

Calculations are performed as follows:

1) Heat Balance

① For the pumping chamber side

$$Q_2 - Q_1/2 = \pi/4 \cdot 1^2 \times v \times N \times \rho \times (T_2 - T_1) \times k$$

② For the beam chamber side

$$Q_1/2 = \pi/4 \cdot 1.4^2 \times v \times N \times \rho \times (T_2 - T_3) \times k$$

2) Heat Transfer between chamber and heated water

① For the pumping chamber side

$$Q_2 - Q_1/2 = h \times A \times \Delta T$$

② For the beam chamber side

$$Q_1/2 = h \times A \times \Delta T$$

Q_1 : required power for bakeout (W)
Q_2 : heat generated during NEG activation (W)
v : water velocity (cm/s)
N : number of cooling channels (—)
ρ : density (at 150°C) = 0.916 kg/cm^3
k : conversion factor = 4.33 J/g·K
A : heat transfer area (cm^2)
h : heat transfer coefficient (W/cm^2·°C)
= $0.023\ (Re)^{0.8}(Pr)^{0.4} \times \lambda/d$
ΔT: temperature difference between heated water and channel's wall of a chamber (°C)
λ : thermal conductivity (at 150°C)
= 0.587 kcal/m·hr·°C
Pr : Plandtl number (at 150°C) = 1.15

The calculations give $T_1=141.6$°C and $T_3=145.3$°C for $v=1.5$ m/s and $T_2=150$°C (see Fig. 2). As a result, ΔT's for the pumping and beam chamber side are 0.30°C and 1.59°C, respectively. This means that the temperature of the chamber wall is almost the same as that of heated water. Thus the maximum thermal gradients of the chamber for the longitudinal direction and the transverse direction are 8.4°C/30m and 3.7°C, respectively. A total pressure loss for a system of one cell is about 1.01 kg/cm^2, and a required flow is approximately 1000 l/h.

Figure 3 shows a rough layout of a unit of HBS. At first, since the vapor pressure of water at 150°C is about 5.9 kg/cm^2·G, the hydraulic pressure of hot water should be increased up to about 7 kg/cm^2·G. After that, to increase the temperature up to about 150°C, the water is transferred to the heater by a pump. A heat exchanger is used when the heater is overheated or in case of emergency. The heater power and the cooling valve will be adjusted to keep the temperature T_1 at a predetermined value.

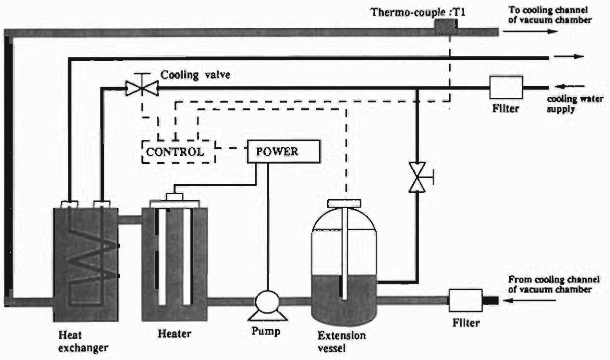

Fig. 3. Diagram of the Heated Water Bakeout System.

We are planning to test and evaluate the performance of HBS, using a 5 m prototype straight chamber (Fig. 1).

References

1) H. Sakamoto, T. Bizen, S. Yokouchi, Y. Morimoto, T. Nishidono, Y.P. Lee, and S.H. Be: *RIKEN Accel. Prog. Rep.*, **23**, 145 (1989).

RIKEN Accel. Prog. Rep. **24** (1990)

V-2-28. Sensitivity Calibration of Nude Ionization Gauges for Several Gases Using a Spinning Rotor Gauge

H. Daibo, S.R. In, S. Takahashi, S. Yokouchi, and S.H. Be

The calibration system used in the present experiments is shown schematically in Fig. 1. A welded bellows is inserted between the calibration chamber and the turbo-molecular pump (TMP). The calibration chamber has six ports; one is used for installation of spinning rotor gauge (SRG) and others are for the calibrating gauge heads.[1] Because there are no baffles between the ports, only one gauge head can be calibrated at a time. During 3 months we calibrated 15 (9 BA's and 6 EXTR's) gauge heads for N_2, H_2, CO, and CO_2.

Figures 2 and 3 summarize the absolute and relative sensitivities of the calibrating gauge heads measured using SRG as a pressure standard. In an extreme case there is even an 80% deviation in the absolute sensitivity. However the scattering patterns of the sensitivity data of the gauge heads for different working gases are almost identical. Consequently, as shown in Fig. 3, the plots of the relative sensitivities, normalized to that of N_2, exhibit minute dispersion. We accordingly skipped the calibration procedures for all gases except N_2 in some gauge heads which have two filaments.

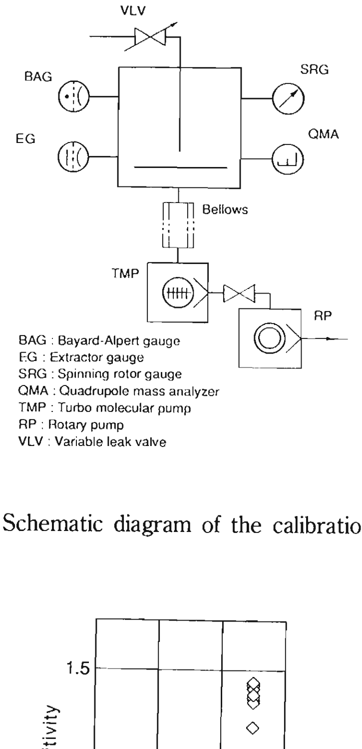

Fig. 1. Schematic diagram of the calibration setup.

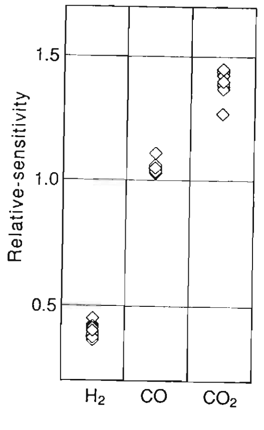

Fig. 2. Absolute sensitivities of the gauge heads for N_2, H_2, CO, and CO_2.

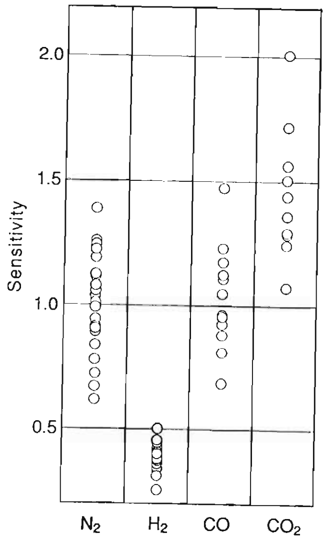

Fig. 3. Relative-sensitivities of the gauge heads for H_2, CO, and CO_2.

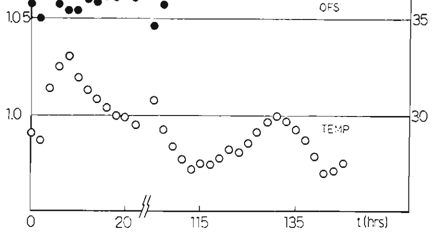

Fig. 4. Temporal evolutions of the offset and temperature of SRG.

Because the ambient temperature of the laboratory was not controlled accurately, the temperatures of the SRG components have changed to a certain extent during a calibration cycle. But temperature variation of a few degrees did not affect seriously the residual drag (offset) of SRG. Figure 4 shows the changes of SRG offset and the temperature of SRG mounting flange. In Fig. 4, we can not find that the change in the offset value is strongly related with the temperature variation. Then this change may be thought as a statistical fluctuation.

The vibration level during the calibration work was in the range of 0.005–0.01 G(0.03–0.05 μm) after utilizing a damper for the rotary pump, and any definite correlation between the actual vibration level and the offset of SRG could not be revealed. Even when TMP was installed directly in the calibration chamber without the bellows, this vibration level was within the same range.

References

1) H. Daibo, Y.P. Lee, S. Yokouchi, T. Nishidono, Y. Morimoto, and S.H. Be: *RIKEN Accel. Prog. Rep.*, **23**, 153 (1989).

RIKEN Accel. Prog. Rep. **24** (1990)

V-2-29. Vacuum Characteristics of a Mixed Pumping System

H. Daibo, S. Yokouchi, T. Nishidono, K. Watanabe, and S.H. Be

We measured the ultimate pressures of a straight-section chamber (SSC) and a bending magnet chamber (BMC) in which NEG strip, SIP, TSP and turbo-molecular pump (TMP) were installed.

The total active length and surface area of the NEG strip of SSC are 1440 cm and 7776 cm^2, and those of BMC, 720 cm and 3888 cm^2, respectively. Normal pumping speeds of SIP and TMP are 110 *l*/s and 300 *l*/s, respectively. The schematic diagram of the setup for the measurement of pressure is shown in Fig. 1.

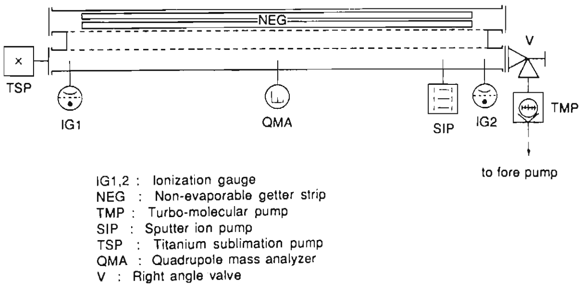

Fig. 1. Schematic diagram of the setup for the measurement of SSC.

The pressure variation in SSC vs the pumping time is shown in Fig. 2. After evacuation for 145 h we carried out bakeout of the chamber and activation of the NEG strip simultaneously ((1) in Fig. 2), and at their last stage we performed pre-conditioning for SIP and TSP (2). After that, we got the ultimate pressures of 7.4×10^{-9} Pa and 1.3×10^{-8} Pa with the NEG strip and TMP (3). However, the pressures with only NEG strip were increased up to 1.6×10^{-6} Pa and 2.0×10^{-6} Pa (4) with a build-up of CH_4 ($M/e=16$), as shown in Fig. 3 a), which could not be pumped out by the NEG strip. We obtained the ultimate pressures of 6.2×10^{-9} Pa and 8.9×10^{-9} Pa with the NEG strip and SIP (5), and measured a mass spectrum (Fig. 3 b). Although TSP was finally flashed (6), the pressure was not lowered (7) below that with the NEG strip and SIP.

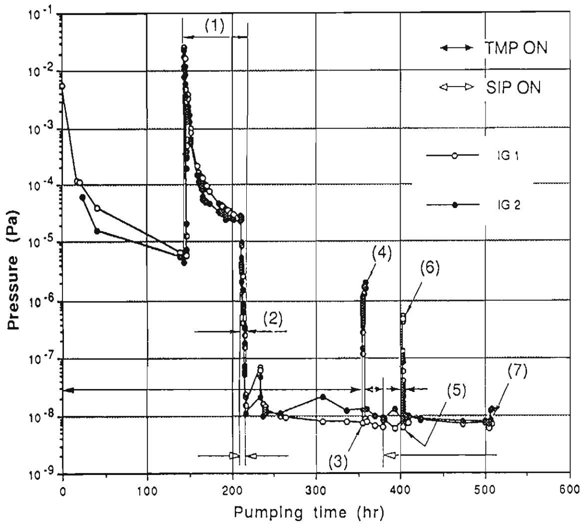

Fig. 2. Pressure variation *vs.* pumping time of SSC.

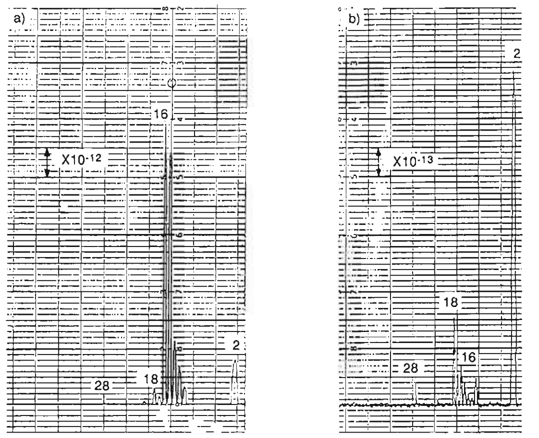

Fig. 3. Pressure variation *vs.* pumping time of BMC.

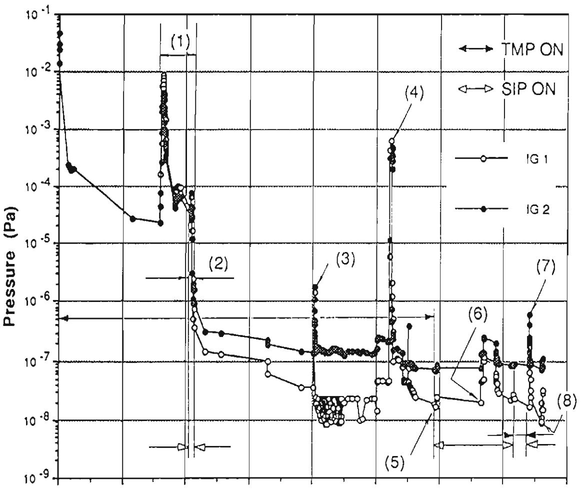

Fig. 4. Mass spectrum obtained when the chamber was evacuated a) with the only NEG strip, and b) with the NEG strip and SIP.

The pressure variation in BMC vs the pumping time is shown in Fig. 3. After evacuation for 160 h we carried out bakeout of the chamber ((1) in Fig. 4), and at its last stage we performed preconditioning for SIP (2). After evacuation for 400 h we performed pre-conditioning for TSP (3). After evacuation for 540 h we carried out activation for the NEG strip (4). After that, we got the ultimate pressures of 1.7×10^{-8} Pa and 7.0×10^{-8} Pa with NEG strip and TMP (5). However, the pressures with NEG strip and SIP were not lowered (6) below that with the NEG strip and TMP. For BMC, the ultimate pressure also was not influenced by TSP (7). Finally we obtained the ultimate pressures 9.4×10^{-9} Pa and 7.4×10^{-8} Pa with the NEG strip, SIP, and TSP (8).

RIKEN Accel. Prog. Rep. 24 (1990)

V-2-30. Manufacture of a Complicated Ceramic Chamber and Its Joining Methods to an Aluminum-alloy Chamber

T. Nishidono, S. Yokouchi, H. Daibo, T. Toga,* and S.H. Be

We are considering to use alumina ceramic chambers to prevent eddy current generating on the surface of the chamber used in fast bump magnets.[1] Since the material of normal vacuum chambers in SPring-8 is aluminum-alloy, joining of ceramics to aluminum metals is required.

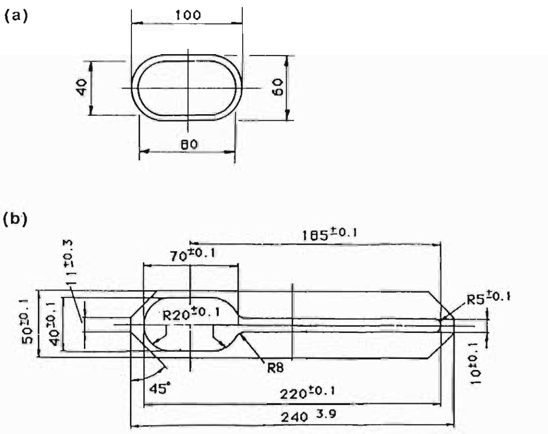

Fig. 1. Cross-sectional view of ceramic chambers. (a) for No. 1, No. 2, and No. 3 bump magnet. No. 2 and No. 3 are 200 mm in length; No. 1 is 300 mm in length. (b) for No. 4 bump magnet, 350 mm in length.

The cross-sectional views of two different ceramic chambers designed for SPring-8 are shown in Fig. 1. A ceramic chamber of a simple geometry as shown in Fig. 1 (a) can be manufactured easily, and direct joining of ceramics to aluminum (Al)-alloy is feasible by using an existing technique. However the manufacture of a complicated chamber of 35 cm in length and 26 cm in width as shown in Fig. 1 (b) is difficult, and the joining of this chamber to Al-alloy one is not easy either. Therefore its manufacture technique is required to be established.

A manufacture process of the ceramic chamber is shown in Fig. 2. An important subject in the process is to improve a manufacture accuracy. A particular attention is paid to the joining method because the joint must be stronger and leak-tight. For the complicated ceramic chamber, direct joining to stainless-steal (SUS) or Al-alloy is impossible because of thermal stress caused by large thermal expansion mismatch between the two. A joining process of ceramics to Al-alloy is shown in Fig. 3. To minimize the stress in the seal or ceramics, SUS of a different expansion coefficient can be jointed with a graded seal.

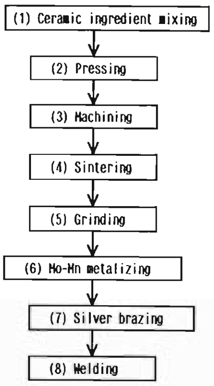

(2) with hydrostaic press.
(4) at~ 1650 ℃
(6) Ni electroplating after Mo-Mn metalizing.
(7) 10 min. at 830 ~850 ℃ in vacuum furnace.
(8) TIG welding.

Fig. 2. Fabrication process of a ceramic chamber.

The seal consists of Fe-Ni-Co alloy (KOVAR) segment, which have a slightly different expansion and forms a zone of gradual transition with

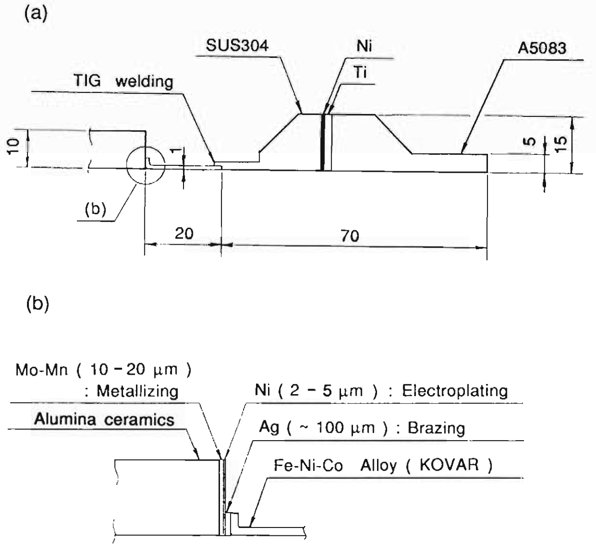

Fig. 3. (a) Geometry of a transition piece; (b) detail of the joining area of a KOVAR piece.

---

* KYOCERA Corporation.

high and low expansion. Using the graded seal, the ceramics can be joining to SUS, as shown in Fig. 3 (b). After that TIG (tungsten inert gas) welding is performed between KOVAR and SUS, and then SUS is jointed to Al-alloy by an explosion bonding method using nickel and titanium as insert metal. As KOVAR is corrosive under a radiation circumstance, the surface of KOVAR is coated electrically with nickel. The weakest joint part is between KOVAR and ceramics. The joining strength is estimated to be in the range of 5-10 kg/mm^2, because the strain due to the difference in thermal expansions between two mother materials remains.

References

1) H. Miyade, H. Tanaka, J. Ohnishi, and S. Motonaga: Proc. 7th Symp. on Accel. Sci. and Technol., p. 169 (1989).

RIKEN Accel. Prog. Rep. **24** (1990)

V-2-31. Mounting of a Straight Section Vacuum Chamber with Slide Guides

T. Nishidono, T. Bizen,* H. Daibo, Y. Suzuki,* and S.H. Be

We manufactured a new chamber mount, namely a slide guide, and mounted a straight-section chamber with ribs for suppressing chamber deformation. An end of the chamber is fixed and allows no chamber motion in any direction before and after bakeout.

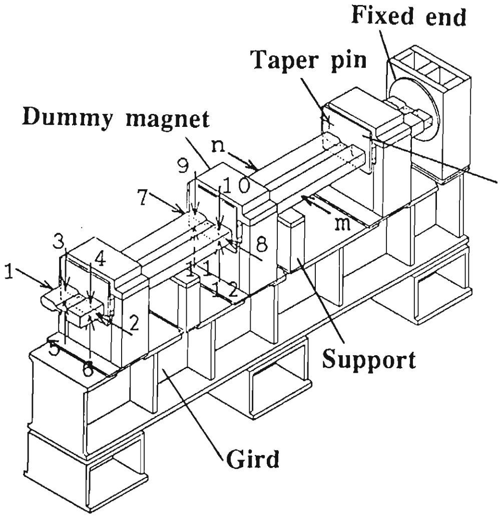

Fig. 1. Schematic diagram of the experimental model chamber with slide guides. The points of measurement are denoted by numbers.

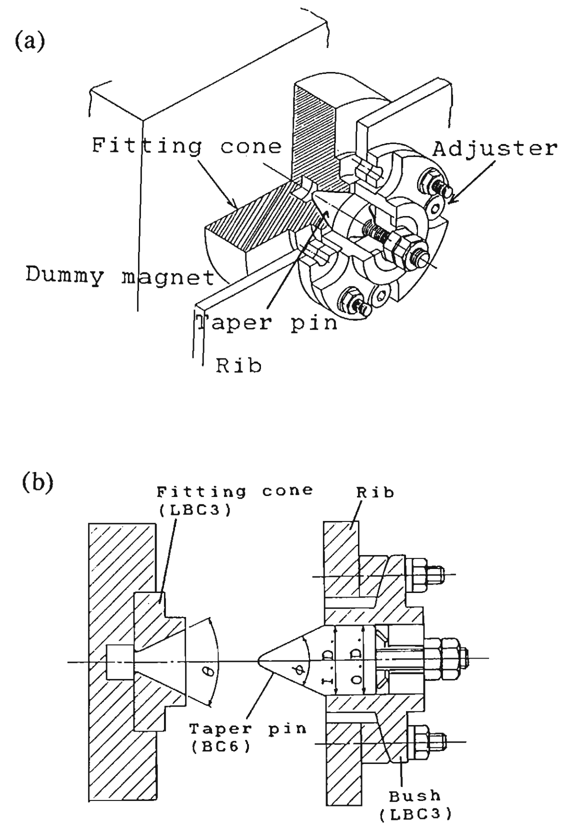

		I.D.	O.D.	ϕ	θ
Designed value		$20^{+0.013}_{-0}$	$20^{+0}_{-0.09}$	50° ±10″	50° ±10″
Measured value	Pin 1	20.005	19.995	49° 59′ 55″	50° 00′ 05″
	Pin 2	20.005	19.992	49° 59′ 58″	50° 00′ 05″
	Pin 3	20.005	19.998	49° 59′ 50″	49° 59′ 58″

Fig. 2. Schematic diagram of the slide guide. (a), Mechanism of the slide guide; (b), Dimensions of fitting parts.

An experimental model chamber with three slide guides and their structures are shown in Figs. 1. and 2, respectively. A solid lubricant of copper alloys is applied to taper pins (BC6) and fitting cones (LBC3). The chamber is positioned by a taper pin inserted tightly in a fitting cone at room temperature. During bakeout, the taper pin is released by thermal expansion of the chamber. Therefore the chamber motion is allowed in any direction during bakeout, but the chamber returns to the original positions of each bake cycle. This chamber mount is capable of releasing a large force caused by the displacement of the chamber on heating.

The displacements of the chamber were measured with 1 μm scale dial gauges set in the transverse sections of the chamber.

The maximum temperature difference between points m and n in Fig. 1. during bakeout was 10 °C, which caused a 600 μm-deformation at the end of the chamber. The taper pins were perfectly released during bakeout and fit on after bakeout. Figure 3 (a) shows the displacements of the chamber. The displacements of the chamber and a gird were less than 42 μm and 12 μm on each point of the measurements, respectively. Moreover the displacement of dummy magnets was negligibly small, compared with other deformations. This means that the position of a beam position monitor (BPM) is ensured within an

---

* Ishikawajima-Harima Heavy Industries Co., Ltd.

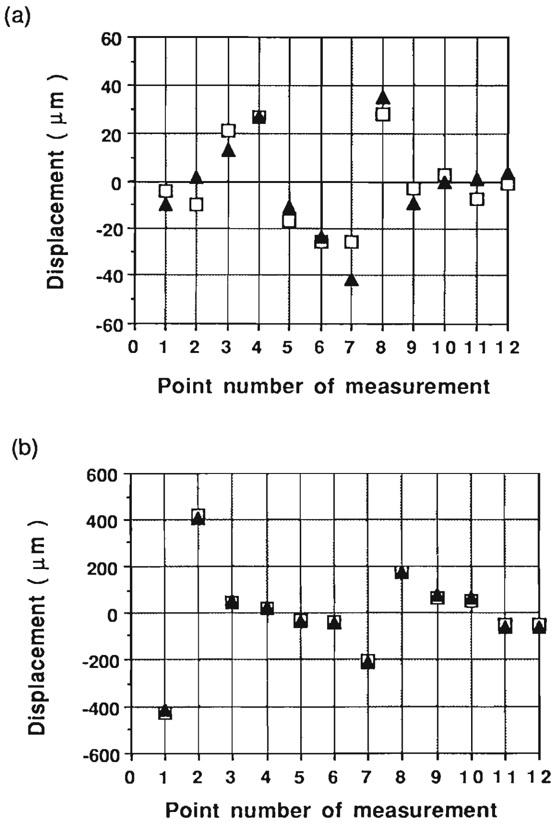

Fig. 3. Displacements of the chamber from the initial installation position (a) with and (b) without slide guides. □, 1st bakeout; ▲, 2nd bakeout.

accuracy of 62 μm even with a measurement error of 8 μm. This result with slide guides is to be compared with the result without the slide guides. The result without the slide guides is shown in Fig. 3 (b). The maximum displacement from the initial installation position was more than 400 μm in the horizontal direction after first bakeout, which was invariant after second bakeout. The displacement of the vartical direction was less than tens of micrometers after bakeout because supports suppressed the downward displacement.

To confirm the reliability of chamber deformations before and after bakeout, detailed tests are in progress. From the results of the preliminary tests, we conclude that the slide guide satisfies the restorability of BPM with an accuracy to within 62 μm.

RIKEN Accel. Prog. Rep. 24 (1990)

V-2-32. Bellows Assembly with RF Sliding Finger Shielding

T. Nishidono, T. Bizen,* H. Daibo, Y. Suzuki,* and S.H. Be

In the design of a bellows assembly, a special effort must be made to minimize its RF impedance, because, in a storage ring, the maximum beam current depends greatly on the impedance. Therefore the bellows assembly is to be designed with no change in the cross-section as much as possible by shielding with RF fingers. Furthermore the bellows assembly should have some tolerance for the variation in the longitudinal direction of the vacuum chamber caused by thermal expansions and contractions due to baking and temperature fluctuations of the cooling water and ambient air. In addition, the assembly should compensate manufacturing tolerance and alignment errors in the longitudinal and transverse direction. Alignment errors are considered to be ±2.5 mm in the longitudinal directiton and up to ±1 mm in the transverse direction.

The length of slide fingers and their contact forces must be chosen so as to ensure a good electrical connection between the fingers and the inner surface of the chamber. Since the vacuum chamber with a slot to be used in the SPring-8 storage ring has a different structure from the chambers in an existing storage ring, bellows assemblies which have been using so far are not suitable to our storage ring. Therefore we are now developing a bellows assembly as shown in Fig. 1.

To make a large contact force, we designed the sliding fingers which contact the inclined inner surface of chambers with half cylindrical contact projections. The sliding fingers will be made of a beryllium copper alloy (JIS C1720P-1/4H) of high electrical conductivity, high strength, and nonmagnetism. Depending on a temperature in use, a residual stress of the alloy is relaxed with a time at high temperature: 80% after 5000 hours bakeout at 150 °C. A relationship between the stress relaxation and a Larson-Miller parameter is given in Fig. 2, which shows that the stress relaxation must be considered at the initial stage of design.

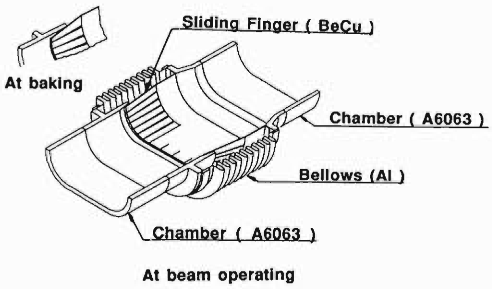

Fig. 1. Schematic diagram of a sliding finger for the bellows.

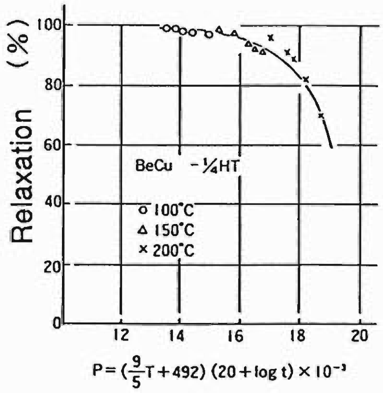

Fig. 2. Relationship between stress relaxation and a Larson-Miller parameter.

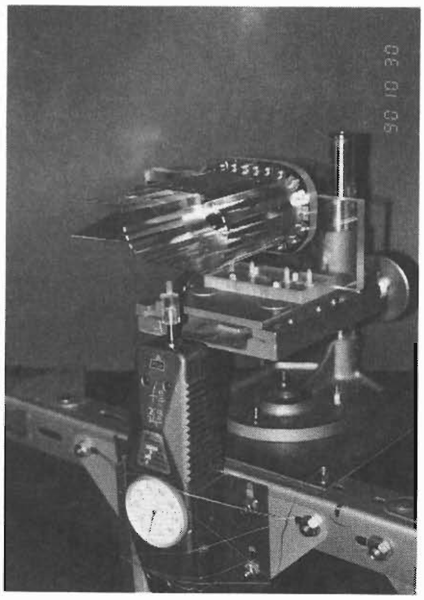

Fig. 3. Photograph of a model of a sliding finger.

---

* Ishikawajima-Harima Heavy Industries Co., Ltd.

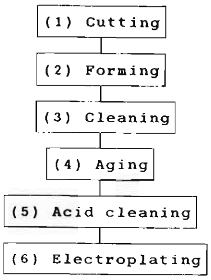

(1) with wire electrical discharge machining
(3) with 1,1,1-trichlorethane
(4) 340 °C x 3 hr in N_2 gas
(5) in H_2SO_4
(6) with silver

Fig. 4. Manufacturing process of a sliding finger.

We manufactured a new bellows assembly, and measured the contact force and resistance, using a simple instrument shown in Fig. 3. The sliding fingers were made of 0.5-mm thick Be-Cu sheet metal by a process shown in Fig. 4, and coated with silver to 3 μm in thickness to decrease contact resistance. Figure 5 shows a schematic diagram of the fingers. Preliminary experimental results of the contact force are in the range of 30 g to 50 g at narrow fingers and 150 g at wide ones, compared with contact forces calculated are 42 g and 345 g, respectively. The total contact resistance of 43 fingers is 0.8 mΩ. The results do not satisfy our requirements; therefore a new design to increase the contact force is in progress.

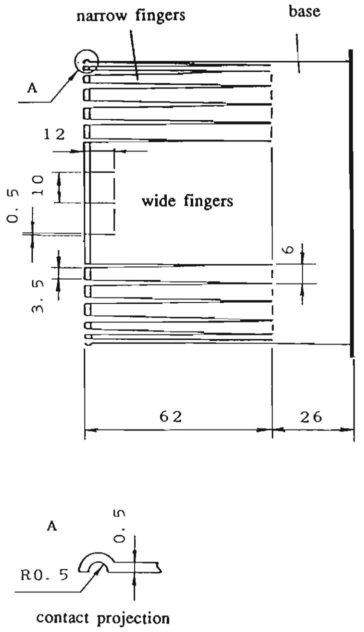

Fig. 5. Schematic diagram of the model of a sliding finger.

RIKEN Accel. Prog. Rep. **24** (1990)

V-2-33. Problems for Improvement of Existing Aluminum-Alloy Flange

T. Nishidono, S. Yokouchi, H. Daibo, N. Takagi,* and S.H. Be

An aluminum-alloy flange, which is planned to be used in the SPring-8 storage ring, is required to be leakless even after many cycles of baking at 150°C.

To pursue the origin of leakage, we inspected the surfaces of flange edges in detail of two types of conflat flanges which have been using for particle accelerators so far. Table 1 shows the specifications of two types of the flanges. The surface was investigated with a scanning electron spectroscope (SEM) and optical microscope. Figure 1 shows expanded sectional views of flange edges photographed with the optical microscope with a magnifying power of 12.5. We observed.: 1, Si segregation on the surface.; 2, Existence of lines of a pitch of 4–16μm drawn by machining.; 3, Non-uniformity of the sealing surface, *i.e.*, average roughness of 0.24–3μm; 4, Non-uniformity of TiN and CrN film of 1–2μm thick. 5, Existence of pits of 8–16μm, of cracks of 8–80μm width and spherical projections. To improve the reliability of leakage, these items are problems to be improved. According to our experience of using them, type A seems to be more leakless than type B.[1]

Table 1. Specifications of aluminum-alloy flanges.

		TYPE A	TYPE B	Notes
Flange	Seal	Knife edge seal (Conflat seal)	Knife edge seal (Conflat seal)	
	Material	Al-Si alloy	Al-Cu alloy	
	Tensile Strength	43 kg/mm^2 31 kg/mm^2	44 kg/mm^2 36 kg/mm^2	Representative value At room temp. At 150 ℃
	Yield Strength	35 kg/mm^2 31 kg/mm^2	33 kg/mm^2 32 kg/mm^2	Representative value At room temp. At 150 ℃
	Coefficient of thermal expansion	20.5 $\times 10^{-6}$	22.3 $\times 10^{-6}$	Representative value
	Surface treatment	TiN	CrN, CrC	Ion plating
	Surface Roughness	R_{max} 1.9 μm	R_{max} 0.2 μm	Measured value
Gasket	Material	Pure Al	Pure Al	
	Hardness	Hv 38 ~39	Hv 43 ~48	Measured value

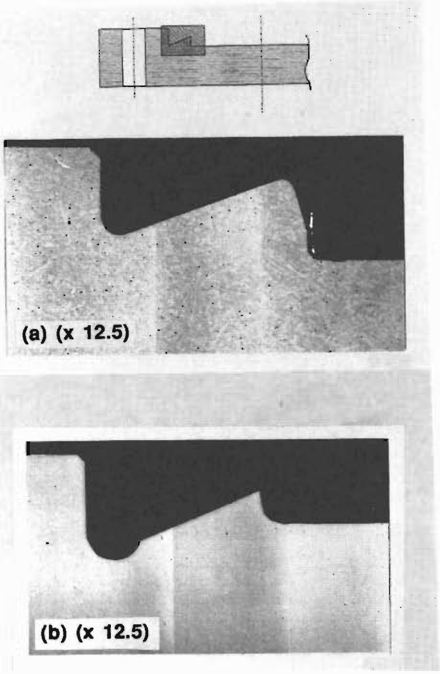

Fig. 1. Photographs of knife edge of aluminum-alloy flanges. (a) at type A flange (× 12.5); (b) at type B flange (× 25).

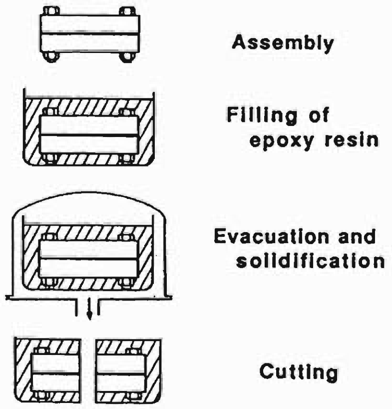

Fig. 2. Fabrication process of the cut sample of fastened flange.

---

* ULVAC Corporation.

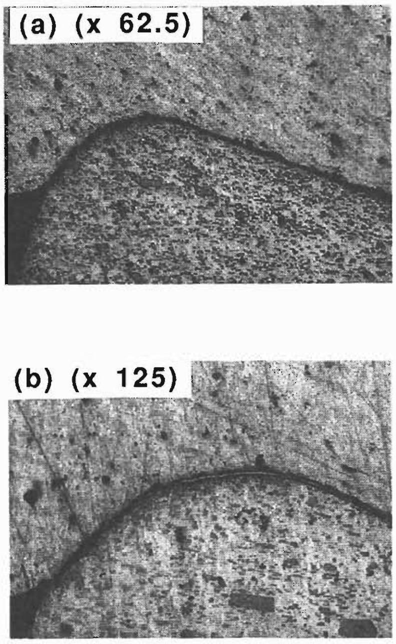

Fig. 3. Cross-sectional views of fastened type A flange.

To investigate the relationship between the sealing mechanism and geometry of a knife edge, we photographed the cross-sectional view of a cut sample of fastened type A flanges (see Fig. 3.). The sample was fabricated by the process as shown in Fig. 2. Figure 3 shows that only the top area of a knife edge touches to a gasket. Improvement to be touched over the whole area is required. Moreover we are still inspecting the same items on the type B flange.

Finally, materials of the flange, bolt, and gasket, and the geometry of a knife edge are very important factors for high vacuum sealing.

References

1) T. Nishidono, S. Yokouchi, Y. Morimoto, Y. Sakamoto, Y.P. Lee, and S.H. Be: *J. Vac. Soc. Jpn.*, **33**, 241 (1990).

RIKEN Accel. Prog. Rep. 24 (1990)

V-2-34. Bending Fabrication of a Vaccum Chamber

T. Nishodono, T. Bizen,* Y. Suzuki,* and S.H. Be

A circulating electron beam in a storage ring reduces electromagnetic fields in vacuum system components such as chamber, bellows, and gate valve. When a straight chamber is used in a bending magnet section, the break of symmetrical electromagnetic fields might drive a transverse instability for an electron beam, because a curved beam causes an offset in respect to the center of the beam chambers transversally. Therefore chambers in the bending magnet section should be curved along beam orbits.

To ascertain the feasibility of bending the complicated chamber to be used in bending magnet section of the SPring-8 storage ring, we built a bending magnet chamber by means of stretch forming. Figure 1 shows the schematics of a stretch former, and Fig. 2 the photograph of a bending test. In this test we used an existing forming block of 23-m curvature radius for an another chamber to save the building cost of the bending magnet chamber.

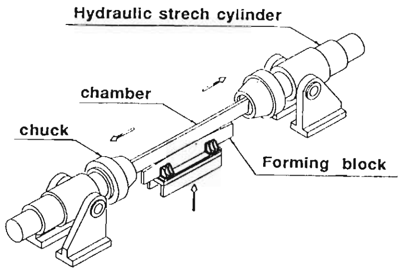

Fig. 1. Schematic diagram of a stretch former.

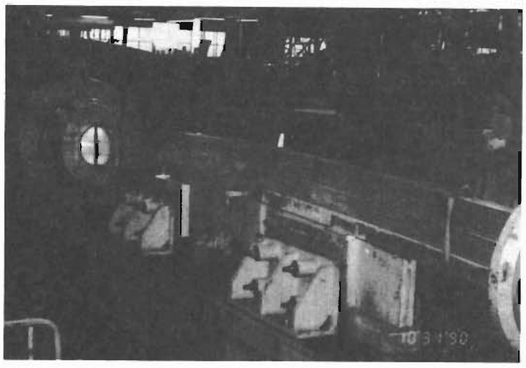

Fig. 2. Photograph of the test.

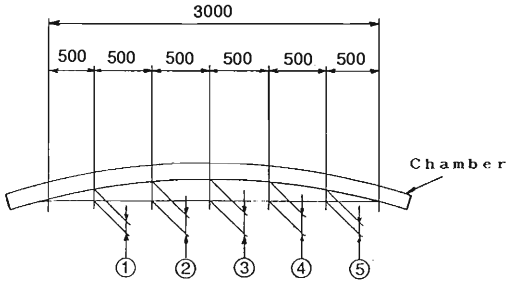

Points of measurement	①	②	③	④	⑤
22.539 m radius	* 27.8	* 44.5	* 50.0	* 44.5	* 27.8
Chamber 1	16.8	27.0	30.2	26.7	16.1
Chamber 2	22.6	35.8	40.7	36.4	22.7
Chamber 3	22.1	35.3	39.7	35.3	22.1

* calculated value

Fig. 3. Bending radius of the chamber after stretch forming.

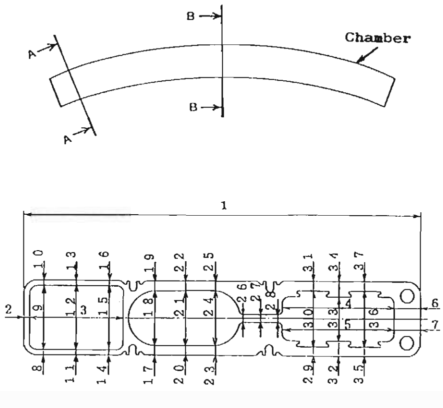

No	Section A	Section B	No	Section A	Section B
1	−0.10	0.0	20	+0.01	0.0
2	+0.05	+0.14	21	−0.10	−0.40
3	−0.10	+0.10	22	−0.02	−0.01
4	0.0	−0.20	23	+0.02	−0.02
5	−0.10	−0.10	24	−0.10	−0.50
6	−0.10	0.0	25	+0.01	−0.04
7	+0.10	0.0	26	−0.20	−0.50
8	+0.07	+0.04	27	−0.30	−0.70
9	0.0	+0.60	28	−0.30	−0.60
10	+0.06	+0.12	29	+0.08	−0.12
11	−0.03	+0.03	30	−0.20	−0.60
12	0.0	0.0	31	+0.02	+0.08
13	+0.03	+0.05	32	+0.03	−0.05
14	0.0	+0.03	33	−0.10	−0.30
15	+0.10	0.0	34	−0.01	−0.02
16	0.0	+0.02	35	−0.09	−0.01
17	0.0	+0.06	36	0.0	−0.20
18	0.0	−0.10	37	+0.02	−0.02
19	+0.05	+0.06			

Fig. 4. Deformations of the cross-sections of the chamber.

---

* Ishikawajima-Harima Heavy Industries Co., Ltd.

The chambers were built along the forming block with approximately 80 ton tensile force after elongating by one percent of the total length of the chamber with a hydraulic stretch cylinder beforehand. The test results are shown in Figs. 3 and 4, which reveal that curvature values measured at five points along the bending chamber are not in agreement with calculated ones, but the deformations of the chamber cross-section are within 100 μm except for a few points. We conclude therefore that the bending chamber of 40-m curvature radius to be used in the SPring-8 storage ring will be built by adjusting the curvature radius of the forming block and tensile force.

RIKEN Accel. Prog. Rep. **24** (1990)

V-2-35. Mounts of the Straight Section Vacuum Chamber with Leaf Springs

T. Nishidono, T. Bizen,* H. Daibo, Y. Suzuki,* and S.H. Be

A chamber mount with leaf springs is one of the positioners for a beam position monitor (BPM). Leaf springs are discussed whether they are used for the chamber mount or not, but the data on their restorability are insufficient for deciding to use them. We have fabricated leaf springs for mounting a model chamber and have been testing their restorability.

The experimental chamber with leaf springs is shown in Fig. 1. Each leaf spring is composed of five layers of 1-mm thick stainless-steel plates. The displacements of the chamber were measured with 1 μm scale dial guages set on the transverse sections of the chamber. The leaf springs suppress the displacement in the horizontal and vertical directions, but deflect in the longitudinal direction when the chamber expands by bakeout. The displacement in the downword direction is also suppressed by a support.

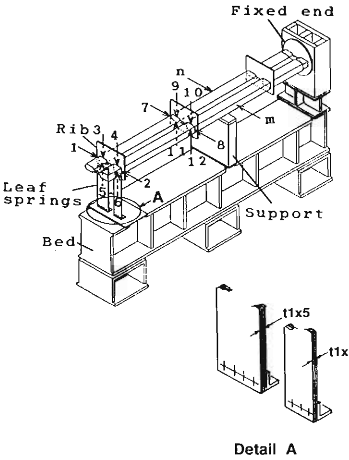

Fig. 1. Schematic diagram of the experimental chamber with leaf springs. The points of measurement of displacement and temperature are denoted by numbers and alphabets, respectively.

Figure 2 shows the temperature of the chamber during bakeout. The maximum temperature difference between point m and n in Fig. 1. was 10°C. Figure 3 shows the displacements of the chamber from the first installation position. The absolute value of the displacement was less than 20 μm on each point of the measurement, indicating that the restorability of the BPM are within 30 μm ever with a measurement error of 8 μm.

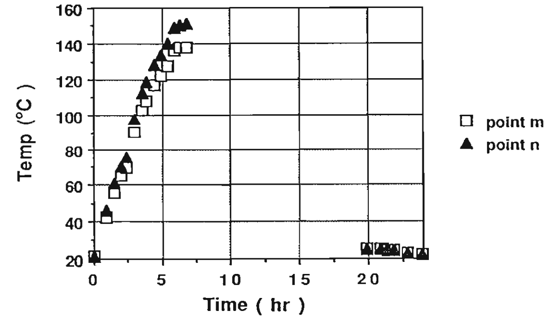

Fig. 2. Relationship between the surface temperature of the chamber and the baking time.

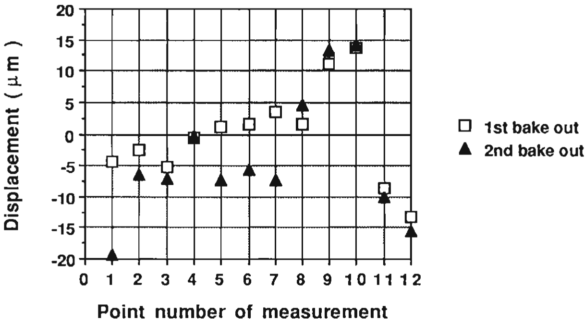

Fig. 3. Displacements of the chamber from the first installation position. Measured at room temperature after baking.

We noticed that the leaf springs ensured a highly accurate restorability, but were deflected downword at the first setting because of chamber's weight. We continue the test to solve this problem and design for the SPring-8 with careful consideration.

---

* Ishikawajima-Harima Heavy Industries Co., Ltd.

RIKEN Accel. Prog. Rep. 24 (1990)

V-2-36. Design of the Control System for the SPring-8

T. Wada

The SPring-8 accelerator complex consists of four linacs, a synchrotron, and a storage ring. As the accelerator equipments are distributed geographically and functionally over the entire accelerator site (about 900 m × 700 m), a distributed control system will be most appropriate for the facility. In designing this system, it is very important to determine the specifications of hardware (H/W) such as, number, hierarchy structure, linking, and installation places of the processors. The software (S/W) system is also very important, since recently the cost of S/W has become higher than that of H/W. Computer-aided S/W development tools (CAxx) will be introduced, where possible, in all stages of development of application programs.

For control system design, the following conditions are taken into account:

Distributed processors and local area network (LAN):

Easy Operation:

1) The operator's console should be small and simple, minimizing the number of parameters on regular display.
2) Centralization of operation.
3) Unification of operation and display format.
4) Voice alarm system.

Safety:

Provision of both a H/W and S/W interlock system. All accelerator equipment should have individual internal interlock systems. In some instances, a cross-equipment interlock is required, for example between the vacuum and RF system.

Reduction of Human Laboun:

Standard and fixed-order operations are performed automatically by computers. Operators only perform such operations in which high level judgement is required.

Expansibility:

1) Accommodate an increase in and modification of accelerator equipments.
2) Accommodate additional computers or interface H/W.
3) Link with other system such as a radiation safety control system, an experimental system, or a computer center.

Noise immunity:

In order to prevent malfunctions of equipment, or deterioration of exchanged information by equipment, optical fiber cables are adopted for long distance signal transfer, and even in short distance communications opto-coupled devices are adopted. Signals of TTL level are not appropriate for transmission between equipment and interface systems.

Radiation:

Selection of the appropriate location for installation of control devices or cables.

Adoption of specially produced cables or devices.

Easy Maintenance:

Adoption of standard modules for H/W and S/W.

Creation of comprehensive documentation and on-line HELP systems.

Reduction of Computer Load:

Introduction of microprocessors or programmable controllers at the lowest hierarchy levels.

Easy programming:

Standardization:

Central management of S/W and database:

The control system consists of a central control system, a program developing system, and several local control systems for each accelerator. These local systems and central control system are linked through computer networks. Each local system consists of a host computer, several front-end processors (FEP) and an operator's console. Figure 1 shows schematically the computers and their interconnecting network.

At the lower hierarchy level, some FEP's are linked. These FEP's are microprocessors such as VME (Versa Module European) crate systems and programmable controllers. At equipment levels, integrated microprocessors are used. Microprocessors are especially useful for driving motors and the acquisition of beam diagnostic data.[1] When high data processing speed is required, such as by a fast digital feedback system, a VXI system has been selected, since the data transmission rate of the VXI bus is much higher than that of the VME bus. Engineering workstations (EWS) are used as operator's consoles, which permit X-window operation.

As is shown in Fig. 1, a so called multi-media LAN (FDDI-3) is adopted for backbone control, with full- and mini-MAP (Manufacturing Automation Protocol) LAN's for real-time control. Voice signals and TV signals are also transmitted on FDDI cables. MAP has two advantages over Ethernet (TCP/IP). One is that messages are exchanged by the token-passing method. Hence, even under heavy traffic conditions, real-time response can be maintained. The other is that mini-MAP bypasses

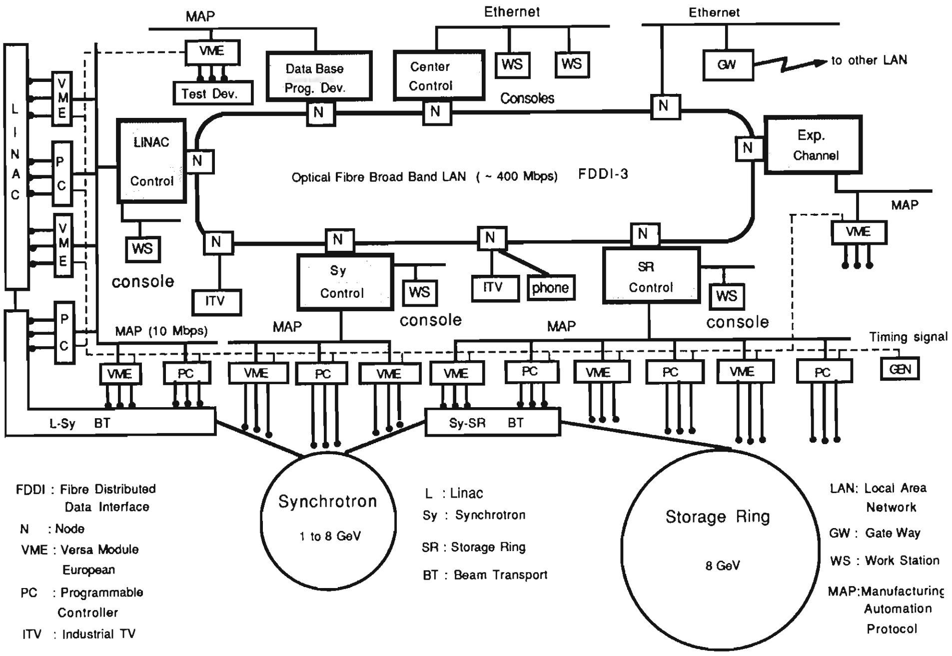

Fig. 1. Schematic diagram of computers and the inter-connecting network.

the middle four (3–6) of the seven layers of OSI (Open System Interconnection, which is a standardized protocol system for computer network). Thereby quick response is achieved.

UNIX and VMS are presently the most popular operating systems. VMS is very powerful, but can only be run on VAX computers. UNIX, on the other hand, is nearly machine independent and has been implemented in many different computers. It is powerful for program development and communication between computers. Although the early version of UNIX had few real-time functions, it has subsequently been improved. One example is the RIKEN ring cyclotron control system, in which UNIX and real-time operating systems coexist in the same computer.[1] For lower level computers, such as VME, real-time operating systems are adopted. The programs are, therefore, developed in UNIX and later down loaded to real time control computers or written on EPROM's (erasable programmable read-only memory).

The timing system supplies synchronization pulses to the gun, linac, booster pulsed magnets, storage ring pulsed magnets, beam position monitoring system, and control-room instruments. It also provides pulses for use by experimenters. Pulses driven from booster magnetic field trigger the linac RF system and electron gun to fill a selected booster bucket. The timing signals are lead directly to delay modules in the FEP's.

References

1) T. Wada, H. Takebe, J. Fujita, T. Kambara, and H. Kamitsubo: "Control System of the RIKEN Ring Cyclotron", presented at the Control Conference, at Villars in Switzerland, 28 Sep.–2 Oct. (1987).

RIKEN Accel. Prog. Rep. **24** (1990)

V-2-37. Design of the Beam Diagnostic System for the SPring-8 Storage Ring

S. Sasaki and Y. Yamamoto

Overall design of the beam diagnostic system for the storage ring of SPring-8 project has been performed. The primary purpose of the beam diagnostic system is obtaining information of the behavior of the electron beam during the commissioning of the machine, user experimental runs, and machine studies for accelerator physics. The information will be fed back to operation conditions of the storage ring.

The components of the system listed in Table 1 are described in some detail. Since detailed design parameters are not yet decided, only qualitative or semi-quantitative descriptions are presented.

Table 1. Components of the beam diagnostic system.

Device	Number	Purpose or quantities to be measured
DCCT	1	Average stored current
CT/WCM	1 or more	Beam intensity of a bunch
Screen monitors		Beam position of the first turn after injection
Beam position monitors	432	Beam position of the stored beam
Beam loss monitors	surround the ring	Occurrence and rough position of beam losses
Perturbing electrodes	1	Excitation of coherent oscillations, suppression of instabilities
Strip line electrodes	1	Directional coupling monitor
Synchrotron Radiation monitoring system	2 for B 2 for I.D.	Beam profile, angular distributions, emittance and tune, bunch length
Synchrotron Radiation beam line stabilization systems	each beam line	Stabilization of the photon beam line axes

(1) *Direct Current Current Transformer (DCCT):* An average stored current will be measured with a direct current current transformer (DCCT), whose dynamic range should cover the range from about 10 μA for the minimum sensitivity to above 100 mA for the maximum operating current.

(2) *Current Transformer (CT) or Wall Current Monitor (WCM):* The intensity of each bunch could be seen through one of these monitors on an oscilloscope display, if the monitor has enough bandwidth. No detailed time structures within a bunch will be observed because of the attenuations of the high frequency component of signals.

(3) *Screen monitors:* Fluorescent screens will be installed at the injection point and several other places around the storage ring. They will be driven and positioned with air cylinders to be inserted into the electron orbit. Electrons or positrons supplied by successive injection cycles, with a repetition rate of 1 Hz, will illuminate the screens and provide information on the beam positions of the first turn of the injection, in a destructive way.

(4) *Beam Position Monitors (BPMs):* Measurement of position of the stored beam will be done with capacitive coupling button pickup electrodes in a non-destructive way. This type of monitors will be the main monitors during normal operations.

From the view point of beam dynamics and the closed orbit correction scheme which we are going to adopt, it is desirable that beam position signals can be obtained for one single passage of a bunch. Also, for stable multiple passages, the averaged signals should be able to be detected in better position resolution. The single pass processing of the singal is especially desirable during the commissioning. If the monitors can record every single passage of a pulse consisting of a group of a few bunches, then the phase space mapping can be obtained with an appropriately placed pair of position monitors.

The required position measurement accuracy is about 1 mm for single passage of a pulse signal, and within 100 μm for multiple passage signals. The 100-μm accuracy of the position measurements with BPMs is required for correcting the closed orbit within the accuracy of 100 μm. The accuracy will be mainly determined by electronic noise errors arising from the signal processing electronics circuits for the single pass measurements, and by mechanical positional uncertainty of mounting the monitor vacuum chambers to the magnets for the multiple pass measurement. We expect the position resolution determined by the electronic noise of the signal processing electronics circuits for the multiple pass measurements to be less than 50 μm.

A super heterodyne method is adopted for the singal processing electronics.[1] For single pass measurements, a bandwidth is required to be wide enough for covering the revolution frequency, 208.8 kHz. The central frequency of the first band pass filter will be the same as f_{rf}, which is 508.58 MHz, and the intermediate frequency will be 50 MHz with a bandwidth of about 2 MHz, *i.e.*, ten times the revolution frequency.

(5) Beam loss monitors: Beam losses can be observed by detecting γ-rays produced by bremsstrahlung of electrons hitting vacuum chamber walls and others. One of these monitors can identify the rough position of the beam loss. Gas ionization chambers filled with dried air or plastic fiber scintillators with lead converters surrounding the whole circumference of the storage ring will be used as loss monitors.

(6) Perturbing electrodes (RFKO): The perturbing electrodes, which are also called RFKO (Radio Frequency Knock Out) electrodes, are driving electrode generating an A.C. magnetic field on the electron orbit so as to excite coherent oscillations or suppress instabilities. Betatron tunes will be measured by exciting coherent oscillations with these electrodes.

(7) Strip line electrode: Strip line electrodes will be used as directional coupling monitors. This type of monitors can be designed so that the frequency response is flat up to high frequencies.[2)]

(8) Synchrotron radiation monitoring systems[3)]*:* Information about the behavior of an electron beam can be deduced from synchrotron radiation emitted from the bending magnets and insertion devices. Detailed design of SR monitoring systems depends on several factors such as the wavelength of radiation which is used for observation, radiation source characteristics (a bending magnet or an insertion device).

In general, for deducing information from synchrotron radiation, following devices will be used: a telescope or a pinhole for focusing the profile of an electron beam, a TV camera to record the profile, one dimensional and two dimensional photodiode arrays for recording the profile and for oscillation frequency analysis when the resonance is excited by the strip line electrodes, and a streak camera to measure the bunch length.

Emittance will be measured from the electron beam profiles or angular distributions with the synchrotron radiation monitoring systems at certain points whose betatron functions will have been already measured by some other methods.

(9) Photon beam stabilization: Various kinds of sources will cause a long term drift and/or vibrations of photon beam lines. The long term drift will be suppressed with a global closed orbit distortion correction supervised by the central control system of the storage ring. Vibrations with much higher frequency components will be suppressed with a local feedback scheme. The high frequency end of the feedback will be limited mainly by the effect of an eddy current in the vacuum chamber.

Further studies on photon beam position monitors and their precision, sensitivity, frequency response, and stability, as well as feedback electronics and feedback algorithms are necessary.

References

1) J. Hinkson, J. Johnston, and I. Ko: Proc. of 1989 IEEE particle accel. conf., March 20–23, 1989, Chicago, IL, USA, 1507 (1989).
2) "1-2 GeV Synchrotron radiation source, conceptual design report, July 1986" Lawrence Berkeley Laboratory, University of California, Berkeley, California 94720, USA, 103 (1986).
3) T. Katsura: "OHO'86", Proc. of KEK accel. summer school, Oho, Tsukuba, Ibaraki, Japan III-12 (in Japanese), (1986).

RIKEN Accel. Prog. Rep. **24** (1990)

VI. Radiation Monitoring

1. Neutron Dose Around an Iron Beam Stopper

T. Shikata, N. Nakanishi, S. Nakajima, S. Fujita, K. Ikegami, and T. Kosako

Shielding calculations[1] have been carried out for determining an operation mode of RIKEN Ring Cyclotron to keep the radiation below tolerable level in the key areas of the facility. It is important to confirm the results from experiments, and to make clear the energy- and angular-distrubution of neutrons ejected from a beam stopper for design of a neutron shielding. However, we have only a few data on the neutron production by interactions of heavy ions of several hundreds of million electron volts per nucleon with beam-stopping materials.

We carried out a preliminary experiment on the angular distributions of high-energy neutrons ejected from a cubic iron beam stopper of 15 mm in thickness, by collision with nitrogens of 135 MeV/nucleon. The measurements were performed at polar angles of 0°, 25°, 45°, 70°, 110°, and 135° with respect to the beam by a shadow bar method using a "rem counter", Studsvik 2202D. The shield used was a polyethylene slab of 45 cm in thickness, which was placed only at the front of the rem counter. The measurements were also carried out without the shield. The distance between source and detector was 4 m.

Although the response function of the rem counter is not given above 20 MeV in its manual, Suzuki *et al.*[2] reported that neutrons of above 20 MeV contribute as much as 40% to the dose rate measured by the rem counter outside the thick shield of the high-energy proton accelerator with 12 GeV at KEK. The dose for source neutrons with less than several tens of million electron volts decrease drastically with decreasing energy when the polyethylene shield is used. Neutrons of less than several million electron volts ejected from a beam stopper may be distributed isotropically. Therefore, the angular distribution of high-energy neutrons may be known roughly from the measurement of the dose rate with and without a shielding. The results are shown in Fig. 1. Above several tens of million electron volts, detection efficiency increases with increasing thickness of the polyethylene shield. The greatly decreased dose rates due to the shield with smaller polar angle indicate that they correspond to neutrons mainly up to several tens of million electron volts and that these neutrons has a peak in the forward direction and occupy a comparatively large portion of the energy distribution. The values measured with the shield show contributions from neutrons with higher energies and rather a few backscattered neutrons.

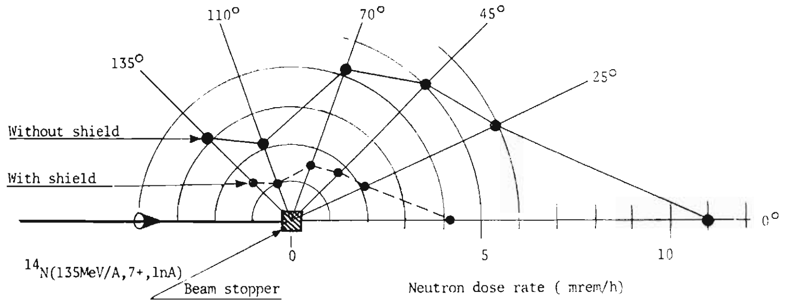

Fig. 1. Dose rates measured with a rem counter with and without a 45 cm polyethylene shield in front of it.

Neutron dose rates outside a concrete wall were also measured in the direction of 90°. The results are about 1/50 of these calculated (not for nitrogen, but for carbon of 135 MeV/nucleon). Even if the decrease of the rem counter response is taken into account for neutrons above 20 MeV, the caculated value is overestimated. The reason may be ascribed mainly to the inaccuracy in neutron energy spectrum from the source and/or in the neutron cross sections used in the calculations. Therefore, exact measurement of the energy spectrum produced in the beam stopper should be necessary.

References

1) T. Shikata, N. Nakanishi, T. Kosako, and S. Fujita: Unpublished.
2) T. Suzuki, M. Numajiri, Y. Oki, T. Miura, S. Miura, H. Tawara, S. Ban, H. Hirayama, K. Kondo, and L. Moritz: Proc. 2nd Intern. Symp. Advanced Nuclear Energy Research, Mito, Jan., p.213 (1990).

RIKEN Accel. Prog. Rep. **24** (1990)

VI-2. Residual Activities in the Ring Cyclotron Facility

S. Fujita, T. Takagi, S. Okamoto, N. Nakanishi,
I. Sakamoto, T. Inamura, and H. Kamitsubo

Residual activities were measured at various points in the Ring Cyclotron Facility.

From June 18 to 24, an experiment was carried out with a $^{14}N^{7+}$ beam of 135 MeV/u in the experimental vault E4. However, because water leakage was found at a part of north side dee of the AVF cyclotron at the last day of the experiment, the acceleration chamber was opened. On June 27, residual activities in the AVF cyclotron

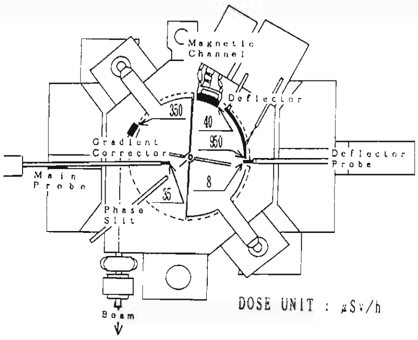

Fig. 1. Detection points around the injector AVF cyclotron. Dose rates are indicated in units of μSv/h.

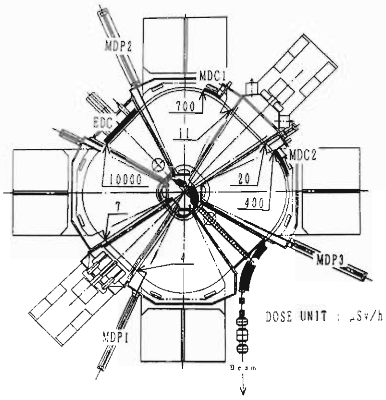

Fig. 2. Detection points around RIKEN Ring Cyclotron. EDC, an electrostatic deflection channel; MDC1, a magnetic deflection channel 1; MDC2, a magnetic deflection channel 2; MDP1, a main differential probe 1; MDP2, a main differential probe 2; MDP3, a main differential probe 3. Numerals indicated are dose rates in units of μSv/h.

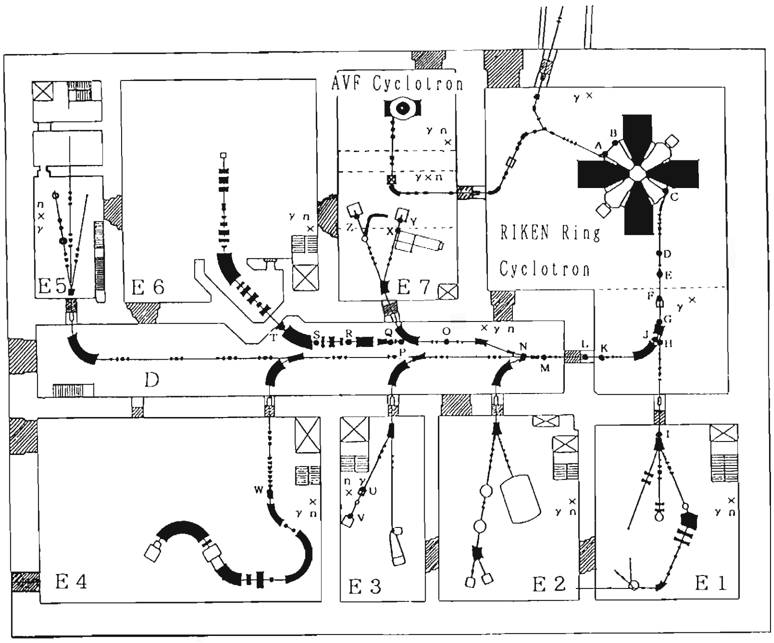

Fig. 3. Layout of RIKEN Ring Cyclotron facility as of 1990. Monitoring positions are denoted by ×. Detection points of residual activity on the beam lines are denoted by alphabets.

were measured with a portable ionization chamber (AE-133/Λ_1 manufactured by Applied Engineering Inc., Japan). The measurements were made for three days after the stop of machine operation. The results are shown in Fig. 1 together with detection points. The dose rates of the deflector increased about 25 times than that of a previous report,[1] depending on the positions.

Table 1. Summary of residual activities measured along the beam lines. Alphabets indicate detection points (see Fig. 3).

Detection point	Ionization chamber survey meter(μSv/h)	Date
A	100	May. 26
B	40	May. 26
C	120	May. 26
D	120	May. 26
E	250	May. 26
F	65	May. 26
G	40	May. 26
H	30	May. 26
I	20	Jul. 25
J	200	May. 26
K	40	May. 26
L	500	May. 26
M	40	May. 26
N	150	May. 26
O	700	May. 26
P	200	May. 26
Q	45	May. 26
R	1000	May. 26
S	900	Mar. 28
T	600	May. 26
U	26	Jun. 21
V	150	Jun. 21
W	28	Aug. 02
X	250	Jun. 25
Y	300	Jun. 25
Z	45	May. 07

From August 1 to 3, last experiments in the spring term were carried out with an $^{40}Ar^{16+}$ beam of 80 MeV/u in the experimental vault E2.

A routine overhaul was made in August, and the dose rates due to residual activities of the Ring Cyclotron was measured on Aug. 24. The results are shown in Fig. 2 together with detection points. The dose rates of EDC increased about 165 times than that of a previous report,[2] depending on the positions.

We also measured those of MDC1 and MDC2 at the occasion of the overhaul after three-year separation.

In this period, January to December, residual activities were measured along the beam lines to the experimental vault E6 with a portable ionization chamber. The detection points above 20μSv/h are shown in Fig. 3. Table 1 summarizes the detected dose rates with measured date. There were several points above 500μSv/h in the beam disturibution corridor. It suggested large beam loss at experiments of RIPS. In the areas above 20μSv/h, we have posted a notice saying 'Dose equivalent of this area is XXX μSv/h', in order to make people keep off the area.

References

1) S. Fujita, I. Sakamoto, T. Inamura, and H. Kamitsubo: *RIKEN Accel. Prog. Rep.*, **23**, 173 (1989).
2) S. Fujita, I. Sakamoto, T. Inamura, and H. Kamitsubo: *ibid.*, **22**, 307 (1988).

RIKEN Accel. Prog. Rep. **24** (1990)

VI-3. Leakage Radiation Measurements in the Ring Cyclotron Facility

S. Fujita, N. Nakanishi, T. Shikata, K. Ikegami, T. Takagi, S. Okamoto, I. Sakamoto, T. Inamura, and H. Kamitsubo

The radiation safety control system has work-

Table 1. Dose rates of neutron leakage radiation from a target point A in extended experimental vault E5 (see Figs. 1-a,b).

Measured point	Dose rates (μSv/h)	Measured point	Dose rates (μSv/h)
a	0.56	g	0.002
b	0.34	h	0.006
c	0.033	i	125
d	0.002	j	14
e	0.010	k	0.125
f	1.80		

Table 2. Dose rates of neutron leakage radiation from a target point B in the beam distribution corridor. (see Figs.1- a,b,c.) A letter "A" stands for the neutron dose rate meter of 2202D Studsvik No.83064; "B" for 2202D of Studsvik No.89006; "C" for 2202D of Studsvik No. 86032; and "D" for NSN1001 of Fuji electric.

Measured point	Detector name	Count rates (C/3min)	Dose rates (μSv/h)
(1)	B	0	0
(2)	A	0	0
(3)	C	2	0.03
(4)	C	17	0.22
(5)	C	89	1.15
(6)	B	184	3.10
(7)	A	38	0.64
(8)	C	4	0.05
(9)	B	2	0.03
(10)	B	0	0
(11)	C	0	0
(12)	B	0	0
(13)	C	0	0
(14)	B	0	0
(15)	A	0	0
(16)	C	3	0.04
(17)	C	42	0.54
(18)	C	6	0.08
(19)	C	34	0.44
(20)	B	9	0.15
(21)	B	5	0.08
(22)	B	22	0.37
(23)	B	110	1.85
(24)	B	6	0.10
(25)	B	82	1.38
(26)	C	15	0.19
(27)	B	0	0
(28)	B	0	0
(29)	D	-	0.002
(30)	D	-	0.002
(31)	D	-	0.020
(32)	D	-	0.018
(33)	D	-	0.029
(34)	D	-	0.006
(35)	D	-	0.055
(36)	D	-	0.040
(37)	D	-	0.029
(38)	D	-	0.059
(39)	D	-	0.030
(40)	D	-	0.006

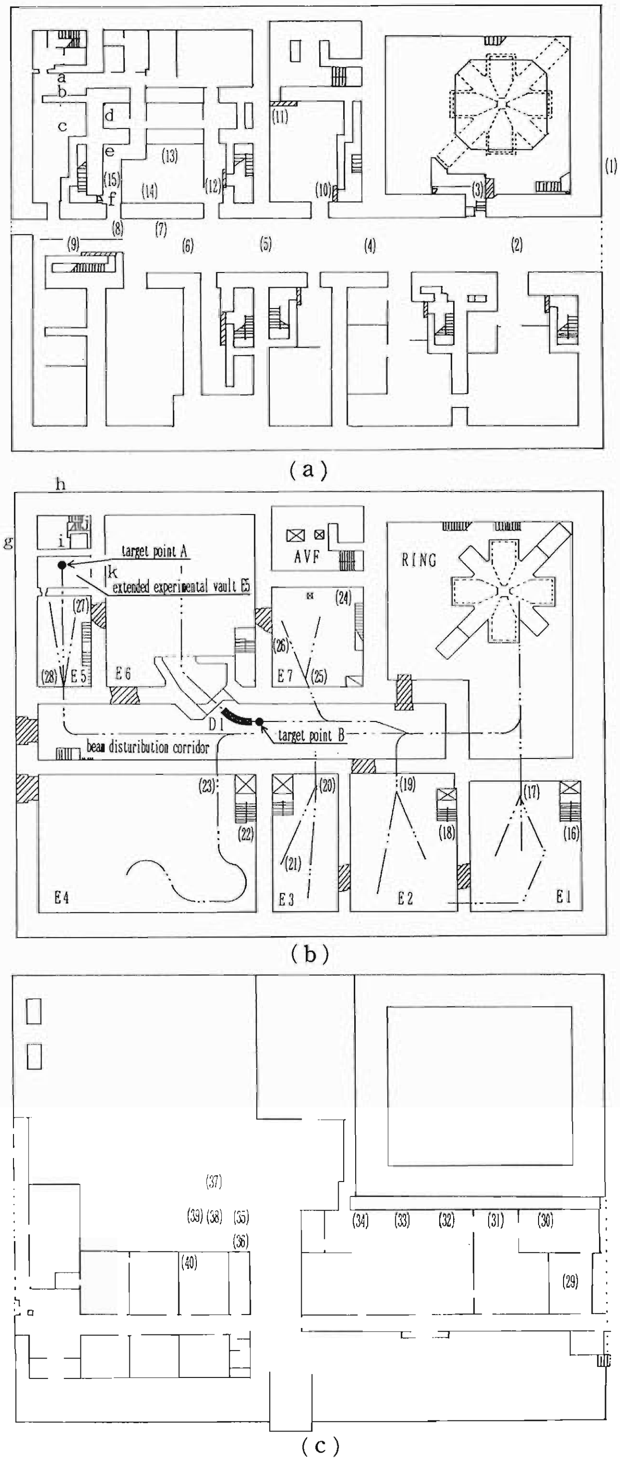

Fig. 1. Layout of RIKEN Ring Cyclotron facility as of 1990. a : Plan view of basement 2th floor; b : Plan view of basement 1th floor; c : Plan view of first floor. Leakage radiation doses measuring points are denoted by alphabets and the number in the parentheses.

ed steadily this year, performing radiation monitoring continuously and automatically. A new beam line became available in a newly extended experimental vault E5.

On June 14, an experiment was carried out with a 135 MeV/u $^{12}C^{6+}$ beam at a particle intensity of 1 pnA in the experimental vault E5, where leakage radiation was measured with neutron dose rate meters 2202D of Studsvik. In Fig. 1-a and b are shown a target point A and detection points of leakage radiation alphabetically. Results are summarized in Table 1.

Although the points *i* and *j* showed high radiation levels, nobody can enter the stair room, because it was closed during experiments.

On March 22 an experiment was carried out with a 100 MeV/u $^{18}O^{8+}$ beam at a particle intensity of 44pnA in the experimental vault E6. The beam was stopped at a target point B in the beam disturibution corridor located in front of the dipole magnet D1.

Leakage radiation of neutrons was measured with four neutron dose rate meters, three 2202D's of Studsvik and an NSN1001 of Fuji electoric. 2202D's were used with pulse counters because of their low sensitivity to neutrons; NSN1001 was used alone because of its high sensitivity. Figure 1- a, b, and c show the target point B and a position where leakage radiation was measured. Results are summarized in Table 2. The radiation level in the controlled area is well below the safety limit (1mSv/week), and the level outside the controlled area is below the safety limit (0.3mSv/week).

This period, January through December, no leakage of gamma rays and neutrons was detected with environmental monitors set outside the building.

RIKEN Accel. Prog. Rep. 24 (1990)

VI-4. Routine Monitoring of the Cyclotron, RILAC, TANDETRON, and the Personal Monitoring of RIKEN Accelerator Workers

I. Sakamoto, S. Fujita, M. Yanokura, T. Kobayashi, K. Ogiwara,
T. Katou, Y. Matsuzawa, M. Miyagawa, S. Kagaya,
H. Katou, M. Iwamoto, and I. Kohno

1. Routine Monitoring of the Cyclotron, RILAC, and TANDETRON

Routine radiation monitoring was carried out for the cyclotron, RILAC, and TANDETRON from January to December, 1990, aspects of leakage radiation from the cyclotron are described in a succeeding report.[1]

(1) Contamination in the cyclotron building: Surface contamination has been kept below 10^{-1} Bq/cm^2 on the floors of the cyclotron building.

When radioactive substances were handled in the hot laboratory and chemical laboratories, the air in a draft chamber was activated; the radioactivity at the exit of the chamber was of the order of 10^{-6}–10^{-8} Bq/cm^3.

(2) Drainage: Radioactivities in the drain water from the cyclotron and the linac buildings were found to be of the order of 10^{-4}–10^{-3} Bq/cm^3. The total activity in aqueous effluents was 14 kBq.

(3) Radiation monitoring for RILAC and TANDETRON: The leakage radiation during operation of RILAC was measured outside the linac building every three months. No leakage of γ rays and neutrons from the linac building was detected. No contamination due to residual activities was found on the floor of control area and in conditioned air in the linac building.

X-ray monitoring was carried out for TANDETRON, when an aluminum target was bombarded with 1.6 MeV H^+ ions of 1 nA. No leakage X-rays were detected around TANDETRON and outside the TANDETRON room.

2. Personal monitoring of RIKEN accelerator workers

The number of RIKEN accelerator workers increased to 1.3 times that in the preceding period.

The external exposure doses were measured by using γ ray and neutron film badges. The doses received by accelerator workers from January to December, 1990, are shown in Table 1. The external doses were detected for 11 persons: four RILAC operators, four nuclear chemists, and three other researchers. The collective dose owing to thermal and fast neutron exposures was below the detection limit.

Table 1. Annual external exposure doses received by RIKEN accelerator workers from January to December, 1990.

Workers	Number of persons				Collective dose (mSv)
	Dose undetectable	0.1-1 (mSv)	>1 (mSv)	Total	
Accelerator physicists and Operators #	40	4	0	44	0.9
Nuclear physicists	163	0	0	163	0
Researchers in other fields	196	7	0	203	1.6
TANDETRON workers	17	0	0	17	0
Health physicists	7	0	0	7	0
Total	423	11	0	434	2.5

Operators: For Ring Cyclotron, Cyclotron, and RILAC.

Average annual dose per person, 0.006 mSv; Maximum individual annual dose, 0.6 mSv.

References

1) I. Sakamoto, S. Fujita, and I. Kohno: This Report, p. 212.

RIKEN Accel. Prog. Rep. **24** (1990)

VI-5. Leakage-Radiation Measurements in the Cyclotron Building

I. Sakamoto, S, Fujita, and I. Kohno

Leakage radiation was measured at various points is the cyclotron building in March 1990, when a target placed on the beam line No. 2 was bombarded with 18-MeV helium-3 ions at a beam intensity of 3 μA.

γ-Ray dose rates were measured with an ionization chamber survey meter, and dose-equivalent rates for fast and slow neutrons were measuered with "rem counter"*. The results are shown in Fig. 1.

The leakage doses measured monthly during January—April, 1990, with γ-ray and neutron film badges placed at two positions (points A and B in Fig. 1) on the underground passage shown in Table 1.

Of the dose values measured every month at point A, the maximum total dose of 10.2 mSv was observed in March, when the values for γ-rays, thermal and fast neutrons were 7.8, 0.3, and 2.1 mSv, respectively.

High fast-neutron doses observed at point A in March, and at point B in February, and March were 2.1, 4.7, and 8.5 mSv, respectively. The increase in the neutron dose at point B was due to high intensity irradiation on the beam line No. 4, where a target was bombarded with 22-MeV helium ions at a beam intensity of 100 nA; beam intensities cyclotron users frequently use on this beam line was 7-8 nA. The high fast-neutron doses at point A were due mainly to activation analysis and radioisotope production carried out on the beam line No. 2 during this periods.

Operating conditions		Dose unit	
E(^{3}He)	: 18 MeV	γ Ray	: μSv/h
Beam line	: No. 2	Neutron	: μSv/h (underlined value)
Target	: GaAs		

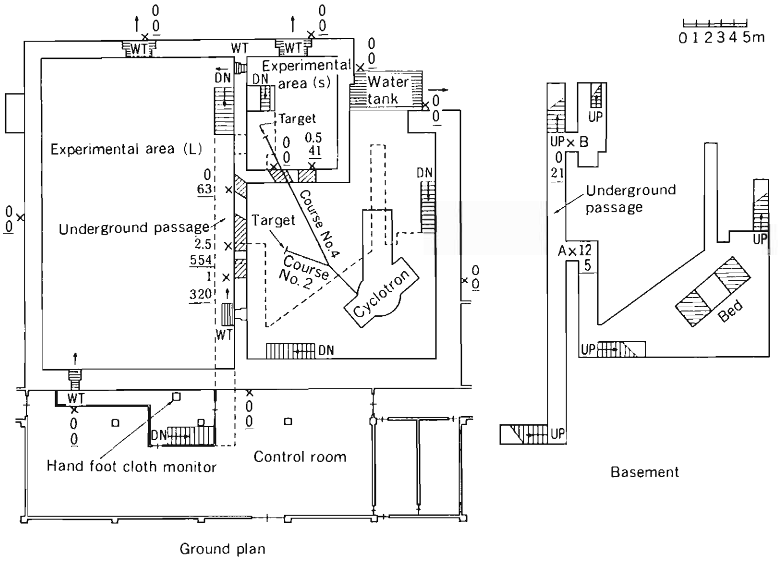

Fig. 1. Leakage radiations (neutrons and γ rays) in the cyclotron building.

---

* A Neutron Rem Counter NSN1 manufactured by Fuji Electric Co., Ltd. Japan.

Table 1. Leakage-radiation doses (1 cm dose-equivalent in mSv) on the underground passage of the cyclotron building during January-April, 1990.

Month	Point A*				Point B*			
	γ rays (mSv)	Thermal neutrons (mSv)	Fast neutrons (mSv)	Total (mSv)	γ rays (mSv)	Thermal neutrons (mSv)	Fast neutrons (mSv)	Total (mSv)
Jan. 90'	2. 1	0. 1	0. 9	3. 1	0	0	0. 2	0. 2
Feb.	0. 4	0	0. 3	0. 7	0. 8	0	4. 7	5. 5
Mar.	7. 8	0. 3	2. 1	10. 2	1. 4	0. 1	8. 5	10. 0
Apr.	4. 5	0. 1	1. 5	6. 1	0	0	0	0
Total	14. 8	0. 5	4. 8	20. 1	2. 2	0. 1	13. 4	15. 7

* See Fig. 1

VII. LIST OF PUBLICATIONS

1. Accelerator development and accelerator physics

1) Y.P. Lee, S. Yokouchi, Y. Morimoto, H. Sakamoto, T. Nishidono, N. Hinago, and S.H. Be: "The Performance Characteristics of a St 707 Non-Evaporable Getter Strip for SPring-8", J. Vac. Soc. Jpn., **33**, 154 (1990).
2) T. Nishidono, S. Yokouchi, Y. Morimoto, H. Sakamoto, Y.P. Lee, and S.H. Be: "Test of Aluminium Alloy Flange", *ibid*., p. 241.
3) S. Yokouchi, H. Sakamoto, T. Nishidono, Y. Morimoto, Y.P. Lee, Y. Hirano, and S.H. Be: "Manufacture of the Al-alloy Vacuum Chamber for SPring-8", *ibid*., p. 258.
4) Y. Morimoto, S. Yokouchi, H. Sakamoto, T. Nishidono, Y.P. Lee, and S.H. Be: "Manufacture of Crotch for SPring-8", *ibid*., p. 262.
5) S.H. Be, S. Yokouchi, Y. Morimoto, H. Sakamoto, T. Nishidono, Y.P. Lee, and Y. Oikawa: "The Conceptual Design of Vacuum System for SPring-8", *ibid*., p. 266.
6) T. Fujisawa, K. Ogiwara, S. Kohara, Y. Oikawa, I. Yokoyama, M. Nagase, and Y. Chiba: "The Radiofrequency System of the RIKEN Ring Cyclotron", Nucl. Instrum. Methods in Phys. Res. A, **292**, 1 (1990).
7) Y. Yano: "RIKEN Heavy Ion Accelerator Facility", Proc. 2nd Int. Symp. on Advanced Nucl. Energy Res., p. 353 (1990).
8) J. Ohnishi and S. Motonaga: "Design of the Sextupole Magnet for an 8 GeV Storage Ring", Proc. 11th Int. Conf. on Magnet Technol., **1**, 194 (1990).

2. Nuclear physics and nuclear instrumentation

1) K. Soutome, T. Maruyama, and K. Saito: "Relativistic σ-ω Model at Finite Temperature in Thermo Field Dynamics", *Nucl. Phys. A*, **507**, 731 (1990).
2) M. Yasue, M.H. Tanaka, T. Hasegawa, K. Nisimura, H. Ohnuma, H. Shimizu, K. Ieki, H. Toyokawa, M. Iwase, J. Iimura, H. Yoshida, T. Nakagawa, A. Soto, T. Niizeki, J. Takamatsu, Y. Takahashi, T. Tohei, H. Orihara, T. Suehiro, S.I. Hayakawa, K. Ogawa, M. Igarashi, and R.J. Peterson: "Structure of ^{14}C Studied by the $^{14}\mathrm{C}(p, d)^{13}\mathrm{C}$ Reaction", *ibid*., **509**, 141 (1990).
3) M. Yasue, M.H. Tanaka, T. Hasegawa, K. Nisimura, S. Kubono, H. Ohnuma, H. Shimizu, K. Ieki, H. Toyokawa, M. Iwase, J. Iimura, H. Yoshida, T. Nakagawa, A. Soto, T. Niizeki, J. Takamatsu, Y. Takahashi, T. Tohei, H. Orihara, T. Suehiro, S.I. Hayakawa, and M. Igarashi: "Systematic Enhancement for the $^{14}\mathrm{C}(p, t)^{12}\mathrm{C}$ Reaction Leading to the $T=0$ States", *ibid*., **510**, 285 (1990).
4) H. Ohnuma, N. Hoshino, K. Ieki, M. Iwase, H. Shimizu, H. Toyokawa, T. Hasegawa, K. Nisimura, M. Yasue, M. Kabasawa, T. Nakagawa, T. Tohei, H. Orihara, S. Hayakawa, K. Miura, T. Suehiro, S.K. Nanda, D. Dehnhard, and M.A. Franey: "The $^{16}\mathrm{O}(p, p')$ Reactions at 35 MeV", *ibid*., **514**, 273 (1990).
5) M. Gong and M. Tohyama: "Time-Dependent Density Matrix Theory I. Damping of Small Amplitude Motion", *Z. Phys*., **A335**, 153 (1990).
6) M. Gong, M. Tohyama, and J. Randrup: "Time-Dependent Density Matrix Theory II. Mass Dispersion in Damped Nuclear Reactions", *ibid*., p. 340.
7) M. Tohyama: "Landau's Collision Term in Time-Dependent Density Matrix Formalism", *ibid*., p. 413.
8) J.A. Casado, S. Daté, C. Merino, and C. Pajares: "Small p_T Particle Production in the Dual Parton Model", *Z. Phys*., **C46**, 129 (1990).
9) W.P. Liu, T. Kubo, H. Kumagai, T. Nakagawa, T. Suzuki, M. Yanokura, I. Tanihata, T. Ito, T. Kashiwagi, J. Kikuchi, H. Yamaguchi, T. Doke, H. Murakami, T. Yanagimachi, and N. Hasebe: "Identification of Projectile Fragments Using Position Sensitive Silicon Detectors", *Nucl. Instrum. Methods in Phys. Res*., **A287**, 476 (1990).
10) T. Nakagawa, I. Tanihata, and K.

Yuasa-Nakagawa: "Timing Properties of a New Type Time Pick-up Detector", *ibid.*, **290**, 136 (1990).

11) K. Ieki, M. Ogiwara, Y. Ando, N. Iwasa, H. Murakami, and T. Motobayashi: "A New Method of Position Determination for a Two-dimentional Position-Sensitive Detector", *ibid.*, **A297**, 312 (1990).
12) T. Kubo, M. Ishihara, N. Inabe, T. Nakamura, H. Okuno, K. Yoshida, H. Kumagai, S. Shimoura, K. Asahi, and I. Tanihata: "The Projectile Fragment Separator at RIKEN Ring Cyclotron Facility", Proc. 1st Int. Conf. on Radioactive Nuclear Beams, World Scientific, Singapore, p. 563 (1989).
13) T. Kubo, and M. Ishihara: "The Status and Perspective of RIKEN Projectile Fragment Separator", Proc. 2nd IN2P3-RIKEN Symp. on Haeavy-Ion Collisions, World Scientific, Singapore, eds. B. Heusch, M. Ishihara, p. 40 (1990).
14) S.M. Lee, T. Nakagawa, K. Yuasa-Nakagawa, S.C. Jeong, Y.H. Pu, T. Mizota, Y. Futami, K. Ieki, T. Sugimitsu, B. Heusch, and T. Matsuse: "Production Mechanism of Intermediate Mass Fragments from Hot Nuclie", *ibid.*, p. 155.
15) Y. Abe, N. Carjan, M. Ohta, and T. Wada: "Decay Dynamics of Hot Nuclei", *ibid.*, p. 169.
16) T. Suzuki: "Inclusive π^- Production in Heavy-Ion Collisions below 100 A MeV", *ibid.*, p. 355.
17) W. Bohne, H. Morgenstern, K. Grabisch, T. Nakagawa, and S. Proschitki: "Critical Excitation Energy in Fusion-Evaporation Reaction", *Phys. Rev.*, **C41**, 41 (1990).
18) A. Ohnishi, H. Horiuchi, and T. Wada: "Nucleon Momentum Distribution in Colliding Nuclei and Potential between Excited Nuclei Studied with the Vlasov Equation", *ibid.*, p. 2147.
19) K. Ieki, J. Iimura, M. Iwase, H. Ohnuma, H. Shimizu, H. Toyokawa, K. Furukawa, H. Kabasawa, T. Nakagawa, T. Tohei, H. Orihara, S. Hayakawa, T. Hasegawa, K. Nishimura, M. Yasue, K. Miura, T. Suehiro, and M.A. Franey: "Density Dependent Interaction Applied to Low-Multipole (p, p') and (p, n) Transitions in Light Nuclei", *ibid.*, **42**, 457 (1990).
20) J. Pēter, J.P. Sullivan, D. Cussol, G. Bizard, R. Brou, M. Louvel, J.P. Patry, R. Regimbart, J.C. Steckmeyer, B. Tamain, E. Crema, H. Doubre, K. Hagel, G.M. Jin, A. Pēghaire, F. Saint-Laurent, Y. Cassagnou, R. Legrain, C. Lebrun, E. Rosato, R. MacGrath, S.C. Jeong, S.M. Lee, Y. Nagashima, T. Nakagawa, M. Ogihara, J. Kasagi, and T. Motobayashi: "Strong Impact Parameter Dependence of Pre-Equilibrium Particle Emission in Nucleus-Nucleus Reactions at Intermediate Energies", *Phys. Lett.*, **B237**, 187 (1990).
21) K. Yoshida, J. Kasagi, H. Hama, M. Sakurai, M. Kodama, K. Furutaka, K. Ieki, W. Galster, T. Kubo, and M. Ishihara: "Excitation Energy Dependence of the Giant Dipole Resonance in Hot Nuclei", *ibid.*, **245**, 7 (1990).
22) J.P. Sullivan, J. Pēter, D. Cussol, G. Bizard, R. Brou, M. Louvel, J.P. Patry, R. Regimbart, J.C. Steckmeyer, B. Tamain, E. Crema, H. Doubre, K. Hagel, G.M. Jin, A. Pēghaire, F. Saint-Laurent, Y. Cassagnou, R. Legrain, C. Lebrun, E. Rosato, R. MacGrath, S.C. Jeong, S.M. Lee, Y. Nagashima, T. Nakagawa, M. Ogihara, J. Kasagi, and T. Motobayashi: "Disappearance of Flow as a Function of Impact Parameter and Energy in Nucleus-Nucleus Collisions", *ibid.*, **249**, 8 (1990).
23) K. Nagamine, T. Matsuzaki, K. Ishida, Y. Watanabe, S. Sakamoto, M. Iwasaki, Y. Miyake, K. Nishiyama, E. Torikai, H. Kurihara, H. Kudo, M. Tanase, M. Kato, K. Kurokawa, M. Sugai, M. Fujie, and H. Umezawa: "X-ray Observation of α-Sticking Phenomena in Muon Catalyzed Fusion for High Density D-T Mixture with High T_2 Concentration", Proc. Int. Symp. on Muon Catalyzed Fusion μCF-89, Oxford, RAL-90-022, p. 27 (1990).
24) K. Nagamine: "Ultra-Slow μ^- Production via Muon Catalyzed Fusion", *ibid.*, p. 49.

3. Atomic and solid-state physics

1) T. Tonuma, H. Kumagai, T. Matsuo, and H. Tawara: "Coincidence Measurements of Slow Recoil Ions with Projectile Ions in 42-MeV Ar^{q+}-Ar Collisions", *Phys. Rev A*, **40**, 6238 (1989).
2) H. Tawara, T. Tonuma, H. Kumagai,

and T. Matsuo: "Production of Recoil Ne^{i+} Ions Accompanied by Electron Loss and Capture of 1.05-MeV/amu Ne^{q+i} ($q=2$, 4, 6, 8, and 10) Ions", *ibid.*, **41**, 116 (1990).

3) H. Fukuda, T. Ishihara, and S. Hara: "Hyperradial Adiabatic Treatment of du+t Collisions at Low Energies", *ibid.*, p. 145.

4) I. Shimamura, C.J. Noble, and P.G. Burke: "Complex Quantum Defects of Superexcited Rydberg States of H_2", *ibid.*, p. 3545.

5) T. Mizogawa, Y. Awaya, T. Kambara, Y. Kanai, M. Kase, H. Kumagai, P.H. Mokler, and K. Shima: "Foil-Thickness Dependence of Projectile K-Satellite X-Ray Yields in the L-Shell Nonequilibrium Region", *ibid.*, **42**, 1275 (1990).

6) I. Shimamura: "Energy Loss by Slow Electrons in Polar Gases", *ibid.*, p. 1318.

7) I. Shimamura and T. Fujimoto: "State Densities and Ionization Equilibrium of Atoms in Dense Plasmas", *ibid.*, p. 2346.

8) H. Ichinose, T. Doke, A. Hitachi, J. Kikuchi, K. Masuda, H. Matsui, E. Otobe, E. Shibamura, and T. Takahashi: "Energy Resolution for 1 MeV Electrons in Liquid Argon Doped with Allene", *Nucl. Instrum. Methods in Phys. Res. A*, **295**, 354 (1990).

9) T. Kobayashi, O. Mishima, M. Iwaki, H. Sakairi, and M. Aono: "Crystallographic Polarity of Idiomorphic Faces on a Cubic Boron Nitride Single Crystal Determined by Rutherford Backscattering Spectroscopy", *Nucl. Instrum. Methods B*, **45**, 208 (1990).

10) K. Tanaka, E. Yagi, N. Masahashi, Y. Mizuhara, K. Tatsumi, and T. Takahari: "Lattice Location B Atoms in $Ni_{0.75}$ $Al_{0.15}$ $Ti_{0.10}$ Intermetallic Compounds as Observed by the Channelling Method", *ibid.*, p. 471.

11) T. Kobayashi, S. Takekawa, K. Shigematsu, T. Takahashi, M. Iwaki, H. Sakairi, H. Takahara, and M. Aono: "Ion Irradiation Effect in a Bi-Sr-Ca-Cu-O Oxide Superconductor", *ibid.*, p. 480.

12) K. Kawatsura, M. Sataka, H. Naramoto, Y. Nakai, Y. Yamazaki, K. Komaki, K. Kuroki, Y. Kanai, T. Kambara, Y. Awaya, and N. Stolterfoht: "Angular Momentum Distribution of Autoionizing Rydberg States Produced by 64 MeV S Ions in Collisions with C Foils", *ibid.*, **48**, 103 (1990).

13) A. Koyama, H. Ishikawa, Y. Sasa, K. Maeda, O. Benka, and M. Uda "Incident-Angle Dependence of Peak Energies of Al and Si LVV Auger Electrons for Ar^{12+} Ion Impact", *ibid.*, p. 608.

14) M. Tachibana, H. Adachi, T. Mukouyama, Y. Hibino, Y. Sasa, K. Fuwa, and M. Uda: "Intensity Analysis of F K Satellite Spectra of NaF and KF", *ibid.*, **49**, 15 (1990).

15) V. Zoran, A. Enulescu, I. Piticu, G. Wintermeyer, T. Kambara, M. Gabr, and R. Schuch: "Enhanced Double Ionization of the $3d\sigma$ Molecular Orbital at Small Impact Parameters", *Phys. Rev. Lett.*, **64**, 527 (1990).

16) J. Kawai, M. Takami, and C. Satoko: "Multiplet Structure in Ni K_β X-Ray Fluorescence Spectra of Nickel Compounds", *ibid.*, **65**, 2193 (1990).

17) T. Tonuma, H. Kumagai, T. Matsuo, and H. Tawara: "Multiple Ionization Process Studied with Coincidence Technique between Slow Recoil Ion and Projectile Ion in 42 MeV Ar^{q+}-Ar Collisions", *Chinese J. Atom. Molec. Phys.*, **7**, 1603 (1990).

18) I. Shimamura: "Muon-Catalyzed Fusion and Muonic Molecules", *ibid.*, p. 1623.

19) H. Tawara, T. Tonuma, H. Kumagai, and T. Matsuo: "Multiply Charged Carbon Ions and Their Production Mechanisms in MeV/amu Ar^{q+} ($q=14-4$) + CH_4 Collisions", *Phys. Scr.*, **42**, 434 (1990).

20) H.A. Sakaue, Y. Kanai, K. Ohta, M. Kushima, T. Inaba, S. Ohtani, K. Wakiya, H. Suzuki, T. Takayanagi, T. Kambara, A. Danjo, M. Yoshino, and Y. Awaya: "Autoionisation of C^{4+}(21nl') Measured by Electron Spectroscopy in Collisions of C^{6+} with He", *J. Phys.*, **B23**, L401 (1990).

21) R. Schuch, E. Justiniano, M. Schulz, P.H. Mokler, S. Reusch, S. Datz, P.F. Dittner, J. Giese, P.D. Miller, H. Schoene, T. Kambara, A. Müller, Z. Stachura, R. Vane, A. Warczak, and G. Wintermeyer: "RTE of Hydrogen-Like and Lithium-Like Ions", The Physics of Electronic and Atomic Collisions, American Institute of Physics, New York, p. 562 (1990).

22) S. Ohtani, M. Kimura, and Y. Awaya: "Reports on Workshop on Atomic Physics at the Advanced Photon

Source", *J. Jpn. Soc. Synchrotron Radiat. Res.* (in Japanese) **3**, 329 (1990).

23) P.G. Burke and I. Shimamura: "Theory of Electron- and Photon-Molecule Collisions", Molecular Processes in Space, eds. T. Watanabe, I. Shimamura, M. Shimizu, and Y. Itikawa, Plenum, New York, p. 17 (1990).

4. Radiochemistry, radiation chemistry and radiation biology

1) T. Miyazaki, Y. Hayakawa, K. Suzuki, M. Suzuki, and M. Watanabe: "Radioprotective Effects of Dimethylsulfoxide in Golden Hamster Embryo Cells Exposed to Gamma Rays at 77 K. I. Protection from Lethal, Chromosomal and DNA Damages", *Radiat. Res.*, **124**, 66 (1990).
2) M. Watanabe, M. Suzuki, K. Suzuki, Y. Hayakawa, and T. Miyazaki: "Radioproductive Effects of Dimethylsulfoxide in Golden Hamster Embryo Cells Exposed to Gamma Rays at 77 K. II Protection from Lethal, Chromosomal and DNA Damages", *ibid*., p. 73.
3) K. Tazaki, W.S. Fyfe, and S.J. Van Der Gaast: "Growth of Clay Minerals in Natural and Synthetic Glasses", *Clays and Clay Minerals*, **37**, 348 (1989).
4) K. Tazaki, W.S. Fyfe, K. Fukushima, and A. Fukami: "Wet-to-dry Transition of Smectite as Revealed by Humidity-Con-trolled Electron Microscopy", *ibid*., **38**, 327 (1990).
5) S. Ambe and F. Ambe: "^{119}Sn-Emission Mössbauer Studies on ^{119m}Te and ^{119}Sb in S, Se, and Te", *Bull. Chem. Soc. Jpn.*, **63**, 3260 (1990).
6) Y. Kobayashi, M. Katada, H. Sano, T. Okada, K. Asai, M. Iwamoto, and F. Ambe: "^{99}Ru, ^{61}Ni, ^{57}Fe, and ^{119}Sn Mössbauer Studies of Heusler Alloys Containing Ruthenium", *Hyperfine Interact.*, **54**, 585 (1990).
7) K. Nakagawa, A. Ejiri, K. Kimura, and M. Nishikawa: "Density Effect on Photoionization Process in Supercritical Xenon Fluids Doped with TMAE (tetrakis-dimethylaminoethylene)", *Phys. Scr.*, **41**, 140 (1990).
8) K. Tazaki, W.S. Fyfe, K.C. Sahu, and M. Powell: "Observations on the Nature of Fly Ash Particles", *FUEL*, **68**, 727 (1989).
9) M. Watanabe, K. Suzuki, and S. Kodama: "Karyotypic Change with Neo-Plastic Conversion in Morphologically Transformed Golden Hamster Embryo Cells Induced by X-Rays", *Cancer Research*, **50**, 760 (1990).
10) K. Tazaki, T. Mori, T. Nonaka, and S. Noda: "Mineralogical Investigation of Microbially Corroded Concrete", *Clay Sci.* (Nendo Kagaku), (in Japanese), **30**, 91 (1990).
11) K. Suzuki, M. Suzuki, K. Nakano, I. Kaneko, and M. Watanabe: "Analysis of Chromatid Damages in G_2 Phase Induced by Heavy-Ions and X-Rays", *Int. J. Radiat. Biol.*, **58**, 781 (1990).
12) Y. Itoh, M. Takai, H. Fukushima, and H. Kirita: "The Study of Contamination of Carbon, Boron, and Oxygen in LEC-GaAs", *Mat. Res. Soc. Symp. Proc.*, **163**, 1001 (1989).
13) T. Takahashi and F. Yatagai: "Effects of Heavy Ions and HZE Particles on *B. Subtilis* Spores", *Biol. Sci. Space* (in Japanese), **4**, 166 (1990).

5. Material Analysis

1) K. Maeda, Y. Sasa, H. Kusuyama, Y. Yoshida, and M. Uda: "PIXE Analysis of Hnman Spermatozoa Isolated from Seminal Plasma", *Nucl. Instrum. Methods*, **B49**, 228 (1990).
2) Y. Sasa, K. Maeda, and M. Uda; "Application of PIXE Analysis to Materials Science", *ibid*., p. 569.
3) Y. Sasa and K. Maeda: "X-Ray Spectroscopic Analysis on Sutra Exavated from Sebriyam-Kyouzuka", Research Reports of Seburi-mura, Ed. by Educational Committee of Seburi-mura, SAGA-pref., (in Japanese), **2**, 19 (1990).
4) Y.P. Lee, T. Nishidono, S. Yokouchi, Y. Morimoto, and S.H. Be: "Surface Analysis of an Al-Mg-Si Vacuum Chamber for SPring-8", *Sci. Papers I.P.C.R.*, **84**, 1 (1990).

VIII. LIST OF PREPRINTS

(1987—1990)

RIKEN-AF-NP

58 Isao Tanihata; March, 1987, "On the Possible Use of Secondary Radioactive Beams".

59 Isao Tanihata; April, 1987, "Nuclear Structure Studies Using High-Energy Radioactive Nuclear Beams".

60 Isao Tanihata, T. Kobayashi, O. Yamakawa, S. Shimoura, K. Ekuni, K. Sugimoto, N. Takahashi, T. Shimoda, and H. Sato; July, 1987, "Measurement of Interaction Cross Sections Using Isotope Beams of Be and B, and Isospin Dependence of the Nuclear Radii".

61 K. Asahi, M. Ishihara, T. Shimoda, T. Fukuda, N. Takahashi, K. Katori, K. Hanakawa, T. Itahashi, Y. Nojiri, T. Minamisono, N. Ikeda, S. Shimoura, and A. Nakamura; September, 1987, "Production of Spin Polarized ^{15}C in Heavy-Ion Reaction and Measurement of g-Factor for the $1/2^+$ ground State".

62 M. Oshima, E. Minehara, S. Kikuchi, T. Inamura, A. Hashizume, M. Matsuzaki, and H. Kusakari; October, 1987, "Rotational Perturbation to the Natural-Parity Rotational Band of ^{163}Dy"

63 S. Ymaji, H. Hofmann, and R. Samhammer; November, 1987, "Selfconsistent Transport Coefficients for Average Collective Motion at Moderately High Temperatures"

64 Isao Tanihata; November, 1987, "Nuclear Structure Studies Using Beams of Radioactive Nuclei".

65 S. Takeuchi, K. Shimizu, and K. Yazaki; November, 1987, "Exchange Current Arising from Quark Degrees of Freedom".

66 T. T. Inamura; March, 1988, "Lasers in Nuclear Physics".

67 I. Tanihata; June, 1988, "Nuclear Studies eith Radioactive Beams".

68 M. Matsuo, F. Sakata, T. Marumori, and Y. Zhuo; July, 1988, "Master Equaions in the Microscopic Theory of Nuclear Collective Dynamics INS-Rep.-696".

69 F. Sakata, M. Matsuo, T. Marumori, and Y. Zhuo; Sep, 1988, "Master Equaions in the Microscopic Theory of Nuclear Collective Dynamics". INS-Rep.-703

70 S. Yamaji, H. Hofmann, and R. Samhammer; Feb, 1989, "Selfconsistent Transport Coefficients for Damped Motion".

71 T. Nakagawa, I.Tanihata, and K. Nakagawa; April, 1989, "Timing Property of a New Type Time Pick-up Detector".

72 W. P. Liu, T. Kubo, H. Kumagai, T. Nakagawa, T. Suzuki, M. Yanokura, I. Tanihata, T. Ito, T. Kashiwagi, J. Kikuchi, H. Yamaguchi, T. Doke, H. Murakami, T. Yanagimachi, and N. Hasebe; April, 1989, "Identification of projectile Fragments using Position sensitive Silicon detectors".

73 R. Samhammer, H. Hofmann, and S. Yamaji; May, 1989, "Self-Consistent Transport Tensors for Collective Motion in Several Dimensions".

74 K. Soutome,T. Maruyama, and K. Saito; June, 1989, "Relativistic sigma-omega Model at Finite Temperature in Thermo Field Dynamics".

75 M. Oshima, M. Matsuzaki, S. Ichikawa, H. Iimura, H. Kusakari, T. Inamura, A. Hashizume, and M Sugawara; June, 1989, "Electromagnetic transition probabilities in the natural-parity rotational band of 173Tb".

76 T. Kobayashi, S. Shimoura, I. Tanihata, K. Katori, K. Matsuta, T. Minamisono, K. Sugimoto, W. Muller, D. L. Olson, T. J. M. Symons, and H. Wieman; June, 1989, "Electromagnetic Dissocoation and Soft Giant Dipole Resonance of Neutron Dripline Nuclei 11Li".

77 M. Sano; July, 1989, "Strangeness production in high-enrgy nuclear collisions"

78 I. Tanihata; August, 1989, "Reactions Using High Energy Beams of Radio Active Nuclei".

79 S. Yamaji; October, 1989, "Nuclear Collective Motion: Markovian or not?"

80 Isao Tanihata; October, 1989, "A Systematics of the Nuclear Radii and Neutron Halo"

81 M. Fukuda, K. Asahi, T. Ichihara, N. Inabe, M. Ishihara, T. Kubo,H. Kumagai, T. Nakagawa, I. Tanihata, M. Adachi, M. Koguchi; November, 1989, "Measurment of Reaction Cross Sections Using 11Be Beam".

82 S. Shimoura,I. Tanihata,T. Kobayashi,K. Matsuta, K. Katori,K. Sugimoto,D.L. Olson,W.F.J. Muller,H.H. Wieman; December, 1989, "Energy Dependence of Interaction Cross Sections".

83 T. Kubo,M. Ishihara,N. Inabe,T. Nakamura,H. Okuno,S. Shimoura,K. Yoshida,K. Asahi,H. Kumagai,I. Tanihata; December, 1989, "The Projectile Fragment Separator at RIKEN Ring Cyclotron Facility".

84 K. Asahi, K. Matsuta, K. Takeyama, K.H. Tanaka,Y. Nojiri, and T. Minamisono; December, 1989, "Half-life and Branching Rations of the 13O Beta Decay".

85 K. Asahi, M. Ishihara, H. Takanashi, M. Koguchi, M. Adachi, M. Fukuda, N. Inabe, D. Mikolas, D. Morrissey, D. Beaumel, T. Ichihara, T. Kubo,T. Shimoda, H. Miyatake, and N. Takahashi; December, 1989, "SPIN-POLARIZED RADIOACTIVE ISOTOPE BEAMS FROM INTERMEDIATE ENERGY HEAVY ION COLLISION".

86 K. Asahi, M. Ishihara, T. Ichihara, M. Fukuda, T. Kubo,Y. Gono, A.C. Mueller, R. Anne, D.Bazin, D. Guillemaud-Mueller, R. Bimbot, W.D. Schmidt-Ott, and J. kasagi; January, 1990, "OBSERVATION OF SPIN-ALIGNED SECONDARY FRAGMENT BEAMS OF 14B".

87 K. Asahi, M. Ishihara, N. Inabe, T. Ichihara,T. Kubo, M. Adachi, H. Takanashi, M. Kouguchi, M. Fukuda, D. Mikolas, D.J. Morrissey, D. Beaumel, T. Shimoda, H. Miyatake, and N. Takahashi; January, 1990, "New Aspect of Intermediate Energy Heavy Ion Reactions: Large Spin Polarization of Fragments".

88 T. Inamaura; February, 1990, "Nuclear Structure Study through the Electromagnetic Interaction".

89 T. Suzuki, M. Fukuda, T. Ichihara, N. Inabe, T. Kubo, T. Nakagawa, K. Yoshida, I. Tanihata, T. Kobayashi, T. Suda, S. Shimoura, and M. Fujiwara; March, 1990, "Anomalous Slope Factor of Inclusive π-Spectrum in 41 A MeV Heavy Ion Collision"

90 K.Yoshida, j.Kasagi, H.Hama, M.Sakurai M.Kodama, K.Furutaka, W.Galster, T.Kubo,and M.Iahihara; March, 1990, "Excitation Energy Dependence of Giant Dipole Resonance on Hot Nuclei*".

91 I. Tanihata; March, 1990, "Study of Exotic Nuclei with Radioactive Beams".

92 K.Nakagawa; June, 1990, "Property of the Fast Timing Detector using an Electron Multiplier".

93 I.Tanihata; June, 1990, "Structure of Neutron-Rich Nuclei Studied by Radioactive Beams Neutron halo Soft E1 excit ms ==Neutron halo Soft E1 excitation== ".

94 M.Sano and M.Wakai; August, 1990, "Strangeness Production in High-Energy Nuclear Collisions".

95 H.Toki,Y.Sugahara,D.Hirata,B.V.Carlson and I.Tanihata ; August, 1990, "Properties of Nuclei far from the Stability Line in the Relativistic Hartree Theory ".

96 Kouichi SOUTOME and Shuhei YAMAJI Mitsuo SANO: October , 1990, "COULOMB DISSOCIATION OF 11Li".

97 Kensuke Kusaka; October, 1990, "Effective Theory of Qcd For Deconfinement and chiral Phase transitions at finite temperature".

98 T.suzuki,M.fukuda,T.ichihara,N.inabe,T.kubo,T.nakagawa,K.yoshida ,I.tanihataT.kobayashi,T.suda,S.simoura,M.fujiwara; October, 1990, "NAGATIVE PION PRODUCTION IN SUBTHRESHOLD HEAVY ION COLLISIONS".

99 D.Hirata, H.Toki, T.Watabe, I.Tanihata, and B.V.Garlson; January, 1991, "Relativistic Hartree Theory for Nuclei Far from stability Line".

IX. PAPERS PRESENTED AT MEETINGS

1. Accelerator development and accelerator physics

1) S. Yokouchi: "Vacuum System for SPring-8 Storage Ring and Test Experience", SR Vacuum Workshop, Wako, Mar. (1990).
2) S. Motonaga, J. Ohnishi, and H. Kamitsubo: "Design of Magnets for the 8 GeV Storage Ring", Spring Meet. Am. Phys. Soc., Washington, U.S.A., Apr. (1990).
3) J. Ohnishi, S. Motonaga, H. Takebe, and H. Kamitsubo: "Progress in Magnet Systems for the SPring-8", 3rd Annu. Meet. Synchrotron Radiat. Soc. Jpn., Osaka, Apr. (1990).
4) H. Miyade, H. Tanaka, J. Ohnishi, and S. Motonaga: "Development of the Eddy Current Type Septum Magnet for the Beam Injection into SPring-8 Storage Ring", 1990 Spring Meet. Phys. Soc. Jpn., Osaka, Apr. (1990).
5) H. Miyade, H. Tanaka, J. Ohnishi, S. Motonaga, and M. Hara: "Study of the Injection Devices for SPring-8", 3rd Meet. of the Jpn. Soc. for Synchrotron Radiat. Res., Osaka, Apr. (1990).
6) S. Motonaga, J. Ohnishi, and H. Takebe: "Design of Magnets for the 8 GeV Storage Ring", European Particle Accel. Conf., Nice, June (1990).
7) S. Yokouchi, T. Nishidono, Y. Morimoto, H. Daibo, Y.P. Lee, S.R. In, and S. H. Be: "Vacuum Performance Characteristics of 4 m-Long Vacuum Chamber with NEG Strip for SPring-8", *ibid*.
8) K. Inoue, I. Takeshita, and M. Hara: "Design of the RF System for the SPring-8 Storage Ring", 15th Linear Accelerator Meet. in Jpn., Sapporo, Sep. (1990).
9) J. Ohnishi, Y. Ishii, S. Motonaga, and H. Takabe: "Field Measurements of Prototype Magnets for SPring-8", 1990 Fall Meet. Phys. Soc. Jpn., Nara, Sep. (1990).
10) T. Nakagawa: "Gas Mixing Effect on ECR Ion Source", *ibid*.
11) Y. Yano: "RIKEN Heavy Ion Accelerator Facility", 4th China-Japan Joint Symp. on Accelerators for Nucl. Sci. and Their Applications, Beijing, Oct. (1990).
12) K. Yagi, T. Ohbayashi, K. Yoshida, S.H. Be, and S. Yokouchi: "Performance Test of All-Metal Gate Valve With RF Contact", 31th Vacuum Symp. of Vacuum Soc. Jpn., Osaka, Oct. (1990).
13) T. Maruyama, S.R. In, Y.P. Lee, S. Yokouchi, and S.H. Be: "Pumping Performance Characteristics of NEG Wafer Module", *ibid*.
14) S. Yokouchi, T. Nishidono, H. Daibo, S. R. In, K. Watanabe, Y. Hirano, and S.H. Be: "Vacuum Characteristics of Al-Alloy Chamber with NEG Strips", *ibid*.
15) S.R. In, H. Daibo, T. Maruyama, S. Yokouchi, S. Takahashi, and S.H. Be: "Sensitivity Calibration of Ionization Gauges for Various Gases Using SRG", *ibid*.
16) S.R. In, T. Maruyama, S. Yokouchi, and S.H. Be: "Manufacture and Performance Test of Lumped NEG Pump", *ibid*.
17) T. Nakagawa, T. Kageyama, E. Ikezawa, M. Hemmi, and Y. Miyazawa: "Recent Development RIKEN ECR Ion Sources", 10th Int. Workshop on ECR Ion Sources, Knoxville, Nov. (1990).
18) S.H. Be. S. Yokouchi, Y. Morimoto, T. Nishidono, Y.P. Lee, S.R. In, H. Daibo, and Y. Oikawa: "Vacuum System Design for SPring-8, and a Series of Test and Evaluation", Vacuum Design of Synchrotron Light Source, Argonne, Nov. (1990).
19) S. Yokouchi, S.R. In, T. Nishidono, H. Daibo, and S.H. Be: "Vacuum Performance of Vacuum Chamber with NEG Strips of 8 and 16 m", *ibid*.
20) Y. Morimoto, S. Yokouchi, and S.H. Be: "Design of the Crotch for SPring-8", *ibid*.
21) S.R. In, T. Maruyama, S. Yokouchi, and S.H. Be: "Performance and Characteristics of Lumped NEG Pump", *ibid*.

2. Nuclear physics and nuclear instrumentation

1) T. Kohno, K. Munakata, T. Imai, A. Yoneda, M. Matsuoka, T. Doke, J. Kikuchi, T. Kashiwagi, K. Nishijima, N. Hasebe, H. Murakami, A. Nakamoto, T. Yanagimachi, K. Nagata, and H.J. Crawford, "Calibration Test of a Cos-

mic Ray Heavy Ion Telescope by Accelerator Beam", 21th Int. Cosmic Ray Conf., Adelaid, Australia, Jan. (1990).

2) T. Wada: "Resonating-Group-Method Study of ^{3}He-Nucleus Elastic Scattering", RCNP Workshop on Polarization in Nucl. Reaction, Ibaraki, Jan. (1990).
3) T. Inamura: "Velocity Distribution Measurements of IGISOL Ion Beams by Means of Collinear Laser Spectroscopy", Workshop of Nucl. Chem. and Nucl. Phys. Using a Reactor, Kumatori, Jan. (1990).
4) T. Inamura: "Nuclear Laser Spectroscopy", Workshop on Cyclotron Cascade Project, Osaka, Jan. (1990).
5) K. Soutome, S. Yamaji, and M. Sano: "Coulomb Dissociation of ^{11}Li", RIKEN Symp. on Unstable Nuclei, Wako, Feb. (1990).
6) M. Sakai, Y. Fujita, M. Imamura, K. Omata, Y. Gono, S. Ohya, T. Muto, T. Miura, and S. Chojnacki: "Mono-Energetic Electron Production in e^{+} + Th Interaction", 45th Annu. Meet. Phys. Soc. Jpn., Toyonaka, Mar. (1990).
7) T. Wada, Y. Abe, and N. Carjan: "Induced Fission Studied with Multi-Dimensional Langevin Equation", *ibid.*
8) H. Ichinose, T. Doke, J. Kikuchi, A. Hitachi, H. Matsui, K. Masuda, E. Shibamura, and T. Takahashi: "Energy Resolution for 1 MeV Electrons in Liquid Argon Detectors (II)", *ibid.*
9) K. Ishida, T. Matsuzaki, K. Nagamine, H. Kitazawa, Y. Miyake, and E. Torikai: "Surface Muon Production in Heavy-Ion Reactions", *ibid.*
10) H. Matsui, T. Doke, J. Kikuchi, H. Ichinose, T. Nakasugi, E. Shibamura, and K. Masuda: "Observation of Rare Gas Liquid Scintillation by Si Detectors", 37th Meet. Jpn. Soc. Appl. Phys. and Related Soc., Asaka, Mar. (1990).
11) K. Ishida, T. Matsuzaki, K. Nagamine, H. Kitazawa, Y. Miyake, and E. Torikai: "High Acceptance Axisymmetric Secondary Beam Course Producing Surface Muon Beam from Heavy Ion Reactions", 18th INS Int. Symp. on Phys. with High-Intensity Hadron Accelerators", Tokyo, Mar. (1990).
12) K. Ishida, T. Matsuzaki, R. Kadono, and K. Nagamine: "Muon Paroduction at RIKEN Ring Cyclotron and Future Plans for Muon Science", RIKEN Symp. Applications of Nucl. Methods to Chem., Wako, Mar. (1990).
13) K. Ishida: "Subthreshold Pion Production", TARN2 Workshop, Tanashi, Mar. (1990).
14) T. Inamura: "Laser Facilities for Nuclear Physics and Recent Results Obtained at RIKEN", Am. Chem. Soc. 199th Natl. Meet., Boston, Apr. (1990).
15) K. Ishida, T. Matsuzaki, K. Nagamine, H. Kitazawa, Y. Miyake, and E. Torikai: "Surface Muon Paroduction in Medium-Energy Heavy-Ion Reaction at RIKEN", 5th Int. Conf. on Muon Spin Rotation, Relaxation and Resonance, Oxford, Apr. (1990).
16) S.M. Lee, T. Nakagawa, K. Yuasa-Nakagawa, S.C. Jeong, Y.H. Pu, T. Mizota, Y. Futami, K. Ieki, T. Sugimitsu, B. Heusch, and T. Matsuse: "Effects of Sequential Decay in Nuclear Fragment Distributions of Complex Fragments for ^{84}Kr + ^{27}Al at 10.6 MeV/u", Int. Workshop on Nucl. Dynamics, Erba, Apr. (1990).
17) S.M. Lee, T. Nakagawa, K. Yuasa-Nakagawa, S.C. Jeong, Y.H. Pu, T. Mizota, Y. Futami, K. Ieki, T. Sugimitsu, B. Heusch, and T. Matsuse: "Production Mechanism of Intermediate Mass Fragments from Hot Nuclei", 2nd IN2P3-RIKEN Symp. on Heavy-Ion Collisions, Obernai, France, Apr. (1990).
18) T. Kubo and M. Ishihara: "The Status and Perspective of RIKEN Projectile Fragment Separator", *ibid.*
19) T. Suzuki: "Subthreshold Pion Production at 42 MeV/u", 45th Spring Meet. Phys. Soc. Jpn., Toyonaka, Apr. (1990).
20) Y. Futami, Y. Honjo, M. Shinohara, A. Mochizuki, S.C. Jeong, H. Fujiwara, T. Mizota, and S.M. Lee: "Cold Fusion by the Pressurized Gas Method", *ibid.*
21) S. Daté, J. Casado, C. Merino, and C. Pajares: "Small p_T Particle Production in High Energy Heavy Ion Collisions", *ibid.*
22) S. Yamaji and H. Hofmann: "Nuclear Collective Motion; Markovian or Not?", Int. Conf. on Nucl. Phys. in Honor of Akito Arima, Santa-Fe, May (1990).
23) K. Soutome, S. Yamaji, and M. Sano: "Coulomb Dissociation of ^{11}Li", *ibid.*
24) Y. Watanabe, S. Sakamoto, K. Ishida, T. Matsuzaki, P. Strasser, and K. Nagamine: "New Insights in Muon

Transfer Reaction of (μd)+He", Int. Conf. on Muon Catalyzed Fusion, Wien, May (1990).

25) K. Nagamine, T. Matsuzaki, K. Ishida, S. Sakamoto, Y. Watanabe, M. Iwasaki, Y. Miyake, K. Nishiyama, E. Torikai, H. Kurihara, H. Kudo, M. Tanase, M. Kato, M. Sugai, M. Fujie, K. Kurosawa, S. Okane, and H. Umezawa: "X-ray Observation of α-Sticking Phenomena in Muon Catalyzed Fusion for Liquid and High T Concentration D-T Mixture", *ibid*.

26) K. Nagamine, P. Strasser, and K. Ishida: "Proposal for Slow μ^- Production via Muon Catalyzed Fusion", *ibid*.

27) K. Ishida, T. Matsuzaki, and K. Nagamine: "Large Solid Angle Superconducting Coil and Solenoid Muon Channel for Future μ CF Experiment", *ibid*.

28) T. Suzuki: "Pion Production in Heavy-Ion Collisions below 100-MeV/u Nuclear Physics Seminar", Brookheaven Natl. Lab., New York, July (1990).

29) K. Ishida: "Muon Beam Course Using Large Solid Angle Solenoidal Lens Focusing", KAON Workshop, Vancouver, July (1990).

30) K. Morita, A. Yoshida, T. Inamura, M. Koizumi, T. Nomura, J. Tanaka, Y. Nagai, T. Toriyama, K. Yoshimura, M. Fujioka, T. Shinozuka, K. Sueki, and H. Kudo: "Status Report on the RIKEN GARIS/IGISOL", 3rd Workshop on Ion Guide Based Isotope Separation, Leuven, Sep. (1990).

31) M. Koizumi, K. Azuma, T. Inamura, T. Ishizuka, H. Katsuragawa, S. Matsuki, K. Morita, T. Murayama, I. Nakamura, M. Nakaoka, K. Shimomura, I. Sugai, M. Takami, and A. Yoshida: "The Velocity Distribution of the IGISOL Ion Beams", *ibid*.

32) S. Daté: "Simulator Version of Multichain Model", 10th Int. Seminar on High Energy Phys. Problems-Relativistic Nucl. Phys. and Quantum Chromodynamics, Dubna, Sep. (1990).

33) S. Daté: "Can We Create High-density Nuclear Matter in Heavy Ion Collisions?", Int. Workshop on High Density Nucl. Matter, Tsukuba, Sep. (1990).

34) J. Murakami, M. Oshima, H. Kusakari, M. Sugawara, Y. Gono, K. Morita A. Yoshida, and H. Kumagai: "γ-Decay of 10^+ Isomers in $N=78$ Isotones and Coulomb Excitation of Unstable Nuclei", 1990 Fall Meet. Phys. Soc. Jpn., Nara, Sep. (1990).

35) N. Inabe, S. Shimoura, T. Nakamura, H. Okuno, H. Okamura, H. Sakai, T. Kubo, T. Nakagawa, H. Kumagai, I. Tanihata, and M. Ishihara: "Measurements of Energy and Target Dependence of Total Interactions Cross Sections for ^{11}Li and ^{14}Be", *ibid*.

36) M. Koizumi, M. Azuma, T. Inamura, T. Ishizuka, H. Katsuragawa, K. Shimo mura, I. Sugai, T. Takami, M. Nakaoka, I. Nakamura, M. Matsuki, T. Murayama, K. Morita, and A. Yoshida: "The Velocity Distribution of IGISOL Ion Beams", *ibid*.

37) T. Takei, T. Motobayashi, C. Perrin, F. Merchez, S. Kox, D. Rebreyend, K. Ieki, H. Murakami, Y. Ando, N. Iwasa, M. Kurokawa, M. Ishihara, T. Ichihara, T. Kubo, N. Inabe, S. Shimoura, and S. Kubono: "Coulomb Breakup Reactions of ^{14}O and ^{13}N at 90 MeV/u", *ibid*., Oct.

38) T. Motobayashi, C. Perrin, F. Merchez, S. Kox, D. Rebreyend, K. Ieki, H. Murakami, Y. Ando, N. Iwase, T. Takei, M. Kurokawa, M. Ishihara, T. Ichihara, T. Kubo, N. Inabe, S. Shimoura, and S. Kubono: "^{12}C-3α Breakup Reaction at 35 and 90 MeV/u", *ibid*.

39) M. Kurokawa, T. Motobayashi, C. Perrin, F. Merchez, S. Kox, D. Rebreyend, K. Ieki, H. Murakami, Y. Ando, N. Iwasa, T. Takei, M. Ishihara, T. Ichihara, T. Kubo, N. Inabe, S. Shimoura, and S. Kubono: "Response of CsI(Tl) Scintillators to Charged Particles at around 100 MeV/u", *ibid*.

40) K. Shimomura, S. Hattori, T. Kohmoto, Y. Fukuda, T. Murayama, T. Inamura, S. Morinobu, M. Kondo, and S. Matsuki: "Nuclear Polarization of Recoil Implanted ^{164}Tm with Radiation-Dectected Optical Pumping in Solids", *ibid*.

41) Y. Watanabe, S. Sakamoto, K. Nagamine, K. Ishida, T. Matsuzaki, and P. Strasser: "Muon Transfer Reaction in Liquid Deuterium with ^{4}He Impurity", *ibid*.

42) K. Ishida, T. Matsuzaki, R. Kadono, A. Matsushita, K. Nagamine, H. Kitazawa, Y. Miyake, and E. Torikai: "Target Dependence of Surface Muon Production in Heavy-Ion Reactions", *ibid*.

43) K. Nagamine, K. Ishida, P. Strasser, and

E. Torikai: "Ultra-Slow μ^- Production via Muon Catalyzed Fusion", *ibid.*

44) K. Shimomura, T. Nakamura, H. Okuno, M. Koizumi, S. Hamada, N. Inabe, I. Ogawa, K. Suzuki, H. Sunaoshi, Y. Funakoshi, M. Wada, T. Murayama, T. Shinozuka, T. Kubo, T. Kohmoto, K. Asahi, T. Inamura, M. Ishihara, M. Fujioka, and S. Matsuki: "Production of Neutron Rich Si Isotopes via Ar + Be Reaction and Their Structure Study with Radiation-Detected Optical Pumping in Solids", *ibid.*

45) T. Nakamura, T. Kubo, N. Inabe, H. Okuno, K. Yoshida, S. Shimoura, K. Asahi, H. Kumagai, I. Tanihata, and M. Ishihara: "Performance of a New Projectile-fragment Separator RIPS", *ibid.*

46) H. Okuno, K. Asahi, T. Nakamura, M. Adachi, H. Miyatake, T. Shimoda, N. Takahashi, T. Ichihara, N. Inabe, T. Kubo, D. Mikolas, D. Morrissey, D. Beaumel, and M. Ishihara: "Polarization Measurements ^{12}B and ^{13}B in the Reaction ^{15}N(112MeV/u) + ^{197}Au", *ibid.*

47) T. Kubo: "Nuclear Physics Experiments at RIKEN Ring Cyclotron", *ibid.*

48) K. Masuda, E. Shibamura, T. Doke, J. Kikuchi, T. Kashiwagi, H. Ichinose, T. Nakasugi, T. Ito, A. Hitachi, S.S. Gau, M. Gaudreau, K. Sumorok, and E. Aprile: "Silicon Photodiodes for Detection of Rare Gas Liquid Scintillation", *ibid.*

49) K. Soutome, S. Yamaji, and M. Sano: "Dissociation of ^{11}Li", *ibid.*

50) N. Iwasa, K. Ieki, T. Takei, T. Kato, and Y. Nunoya: "Particle Identification of Heavy Ions ($Z \leqq 36$) Using Couter Telescopes", *ibid.*

51) T. Kubo, M. Ishihara, N. Inabe, T. Nakamura, H. Okuno, K. Yoshida, H. Kumagai, S. Shimoura, K. Asahi, and I. Tanihata: "The Projectile Fragment Separator at RIKEN Ring Cyclotron Facility", 1st Int. Conf. on Radioactive Nucl. Beams, Berkeley, Oct. (1990).

52) K. Ishida: "Future Muon Facility (Japanese Hadron Paroject)", Workshop on Pulsed Muons at LAMPF, Los Alamos, Oct. (1990).

53) S. Yamaji, H. Hofmann, and A.S. Jensen: "Selfconsistent Transport Theory of Nuclear Collective Motion", Yukawa Inst. Workshop on New Trend in Nucl. Collective Motion, Kyoto, Oct. (1990).

54) K. Soutome, S. Yamaji, and M. Sano: "Coulomb Dissociation of ^{11}Li", Tamura Workshop on Nucl. Reaction Dynamics, Austin, Nov. (1990).

3. Atomic and solid-state physics

1) T. Mizogawa, Y. Awaya, Y. Isozumi, S. Ito, and R. Katano: "A New Read-Out Method of Two-Dimensional Position Sensitive Counter", 5th Symp. on Ionizing Radiat. Detectors and Dosimetry, Tsukuba, Jan. (1990).

2) K. Kobayashi, S. Namba, T. Fujihana, and M. Iwaki: "Collision Effects on Ion Beam Induced Crystallization of Aluminum Nitride", 2nd Int. Symp. on Adv. Nucl. Energy Res.-Evalution by Accellerat., Mito, Jan. (1990).

3) K. Ishida, T. Matsuzaki, and K. Nagamine: "Present Status and Prospect of Materials Science Studies", RIKEN Symp. Studies on Materials Sci., Atomic Processed, Nucl. Chem. and Radiobiol. by RIKEN Ring Cyclotron, Wako, Jan. (1990).

4) Y. Awaya: "The RIKEN-JAERI 8-Gev Synchrotron Radiation Project-SPring-8", Workshop on Atomic Phys. at the Adv. Photon Source, Argonne, Mar. (1990).

5) K. Kobayashi, S. Namba, T. Fujihana, T. Kobayashi, and M. Iwaki: "Effects of N-Implantation on Formation of AlN Thin Film (VI)", 37th Spring Meet. Jpn. Soc. Appl. Phys., Asaka, Mar. (1990).

6) Y. Kanai, H.A. Sakaue, K. Ohta, M. Kushima, T. Inaba, S. Ohtani, K. Wakiya, H. Suzuki, T. Takayanagi, T. Kambara, A. Danjo, M. Yoshino, and Y. Awaya: "Electron Spectroscopy of Doubly-Excited Helium-Like Ions", Int. RIKEN Symp. on High-Energy Ion-Atom Collisions, Wako, Mar. (1990).

7) P.H. Mokler, Ch. Kozhuharov, S. Reusch, Th. Stöhlker, J. Ullrich, Y. Awaya, T. Kambara, A. Stachura, A. Szymanski, A. Warczak, R.E. Livingston, A. Müller, R. Schuch, and M. Schulz: "Resonant Transfer and Excitation", *ibid.*

8) T. Kambara, Y. Awaya, Y. Kanai, T. Mizogawa, A. Hitachi, K. Kuroki, and K. Shima: "Electron Capture and Loss Processes in the 26 MeV/u Ar + C System", *ibid.*

9) T. Watanabe: "History of Ion-Atom

Collision Research in Japan—A Report from the Far-East—", *ibid*.

10) K. Kawatsura, M. Sataka, Y. Yamazaki, K. Komaki, Y. Kanai, H. Naramoto, K. Kuroki, T. Kambara, Y. Awaya, Y. Nakai, J.E. Hansen, I. Kadar, and N. Stolterfoht: "Zero-degree Electron Spectroscopy by Using High-Energy Heavy Ions (III)", 45th Annu. Meet. Phys. Soc. Jpn., Toyonaka Mar. (1990).

11) Y. Kanai, T. Kambara, T. Mizogawa, A. Hitachi, K. Shima, and Y. Awaya: "Charge-State Distributions of 26-MeV/u Ar Ions after Passage through Foil", *ibid*.

12) T. Kambara, Y. Awaya, Y. Kanai, A. Hitachi, T. Mizogawa, and K. Kuroki: "Cross Section of Radiative Electron Capture for 26 MeV/u Ar^{18+} + C Collisions", Toyonaka, *ibid*.

13) H.A. Sakae, K. Ohta, M. Kushima, T. Inaba, Y. Kanai, S. Ohtani, K. Wakiya, T. Takayanagi, H. Suzuki, A. Danjo, M. Yoshino, T. Kambara, and Y. Awaya: "Ejected Electron Spectrum from N^{4+**} (1s2lnl') formed by N^{6+}(1s)+He Collisions", *ibid*.

14) E. Yagi: "Behaviour of Kr Atoms Implanted into Al", *ibid*.

15) T. Mitamura, M. Terasawa, K. Kawatsura, E. Yagi, H. Iwasaki, K. Koterasawa, and Y. Nakai: "Ion Beam Analysis of Austenitic Stainless Steel Single Crystals", *ibid*.

16) M. Mogi, T. Mukouyama, H. Adachi, Y. Sasa, M. Tachibana, Y. Hibino, K. Fuwa, and M. Uda: "On the Mechanism of Chemical Effect on F K Satellites", *ibid*.

17) M. Tachibana, T. Mukouyama, H. Adachi, Y. Sasa, Y. Hibino, M. Mogi, K. Fuwa, and M. Uda: "On the Mechanism of Chemical Effect of F K Satellites (II)", *ibid*.

18) H. Ishikawa, A. Koyama, and Y. Sasa: "Excitation of Convoy-like Electrons by Impact of Glancing-Angle Incident Fast Heavy-Ions III", 1990 Spring Meet. Phys. Soc. Jpn., Osaka, Apr. (1990).

19) T. Iitaka, A. Koyama, and H. Ishikawa: "Acceleration of Convoy Electrons by Heaby-ions Impact", *ibid*.

20) Y. Awaya: "Electron Spectroscopy at RIKEN ECR Ion Source", Phys. of Highly Charged Ions, Abisko, Sweden, May (1990).

21) E. Yagi: "Study on the State of Hydrogen in Metals by Means of Ion Channelling Method", 133 Committee of Jpn. Soc. for Promotion of Sci., Tokyo, May (1990).

22) I. Shimanura: "Resonance States of Muonic Molecules and Muon-Catalyzed Fusion", Workshop on Plasma Spectroscopy and Atomic Processes, Nagoya, May (1990).

23) Y. Sakamoto, H. Kokai, T. Uchiyama, S. Komuro, K. Yano, and Y. Iimura: "Formation of Metal Oxide Films by Using Oxygen ECR Plasma", C-MRS Int. '90, Beijing, June (1990).

24) T. Kambara: "K-X-Ray-Scattered Particle Coincidence Measurements in Heavy Ion Collisions", Joint US/Japanese Seminar on Excitation by Exotic and Highly Charged Ions, Anchorage, June (1990).

25) Y. Awaya: "Radiative Electron Capture Cross Sections for 26 MeV/u Ar Ions on Carbon", *ibid*.

26) H. Fukuda, T. Watanabe, I. Shimamura, and L. Végh: "Scattering Angle Dependence of Ionization in Ion-Atom Collisions", *ibid*.

27) J. Kawai, T. Konishi, and Y. Gohshi: "A New Interpretation of the Broadening of Ge $K\alpha_1$ X-Ray Emission Lins of Iron Oxides", 15th Int. Conf. on X-Ray and Inner-Shell Processes, Knoxville, July (1990).

28) J. Kawai, K. Maeda, Y. Sasa, M. Takami, and M. Uda: "Charge Transfer Peak in the Ni $L\alpha$ X-Ray Spectra", *ibid*.

29) K. Fujima, Y. Naito, T. Watanabe, Y. Awaya, and T. Kambara: "The m-Level Dependence of Inner-Shell Excitation by Heavy-Ion Atom Collisions", *ibid*.

30) T. Papp, Y. Awaya, A. Hitachi, T. Kambara, Y. Kanai, and T. Mizogawa: "High-Resolution L X-ray Angular Distrubution Measurement on Terbium", *ibid*.

31) M.R. Harston, D.F. Measday, P. Weber, S. Stanislaus, D. Armstrong, A. Noble, D. Horvath, and K. Aniol: "Negative Pion Capture and Transfer in Molecular Systems", 15th Meet. of the Soc. for Atomic Collision Res., Tokyo, Aug. (1990).

32) Y. Zou: "Lifetime of Ti XIII Measured by Beam Foil Method", *ibid*.

33) T. Niizeki: "A Concept of the Beam Line for Atomic Physics at SPring-8", 6th

Workshop on Studies of Atomic Phys. and Correlated Topics at SPring-8, Wako, Aug. (1990).

34) Y. Awaya: "Reports on the Recent Activities of Atomic Physics Sub-Group at *Users Group for Advanced X-Ray Source*", *ibid.*

35) Y. Awaya: "Reports of Fifteenth International Conference on X-Ray and Inner-Shell Processes", *ibid.*

36) Y. Kanai, H.A. Sakaue, D.S. Ohtani, K. Wakiya, H. Suzuki, T. Takayanagi, T. Kambara, M. Yoshino, and Y. Awaya: "Electron Spectroscopy of Doubly-Excited Helium-Like Ions", 5th Int. Conf. on the Phys. of Highly-Charged Ions, Giessen, (1990).

37) T. Kambara, Y. Awaya, Y. Kanai, R. Dörner, and H. Schmidt-Böcking: "Azimuthal Angular Dependence of K-X-Ray Emission in Swift Ne^{7+}-Ne Collisions", *ibid.*

38) H. Tawara, T. Tonuma, H. Kumagai, T. Matsuo, and H. Shibata: "Multiply Charged Ions and Cluster Ions Produced form Frozen CO_2 and H_2O Targets in Energetic, Heavy Ion Collisions", *ibid.*

39) Y. Awaya, A. Hitachi, T. Kambara, Y. Kanai, T. Mizogawa, and T. Papp: "Angular Distribution of the X-Rays of 1 MeV/amu Argon Beams Passing through Carbon Foil", 4th Workshop on High-Energy Ion-Atom Collision Processes, Debrecen, Sep. (1990).

40) H. Fukuda, L. Vĕgh, I. Shimamura, and T. Watanabe: "Singly Ionizing Proton-He Collisions at Very Small Scattering Angles", *ibid.*

41) E. Yagi: "Behaviour of Krypton Atoms Implanted into Aluminium as Investigated by a Channelling Method", NATO Adv. Res. Workshop on Fundamental Aspects of Inert Gases in Solids, Bonas, France, Sep. (1990).

42) K. Kobayashi, T. Fujihara, and M. Iwaki: "Correlation Between Energy Deposition and AIN Crystal Growth Induced by Ion Implantation", 7th Int. Conf. on Ion Beam Modification of Materials, Knoxvill, Sep. (1990).

43) M.R. Harston, D.F. Measday, P. Weber, S. Stanislaus, D. Armstrong, D. Horvath, and K. Aniol: "Negative Pion Capture and Transfer in Molecular Systems", 3rd Japan-UK Seminar on the Theory of Atomic Collisions, Tsukuba, Sep. (1990).

44) H. Fukuda, I. Shimamura, L. Vĕgh, and T. Watanabe: "Singly and Highly Differential Cross Sections for Ionization of Helium Atoms by Proton Impact", *ibid.*

45) K. Tanaka, N. Masahashi, Y. Mizuhara, K. Tatsumi, T. Takahari, and E. Yagi: "Study on Lattice Location of B Atoms in $Ni_{0.75}Al_{0.15}Ti_{0.10}$ Intermetallic Compounds by a Channelling Method", 1990 Fall Meet. Jpn. Inst. Metals, Sendai, Sep. (1990).

46) K. Yano and H. Oyama: "Mass Analysis of Charged Particles in ECR Hydrogen Plasma in Contact with Graphite", 1990 Fall Meet. Jpn. Soc. Appl. Phys., Iwate, Sep. (1990).

47) T. Uchiyama, H. Kokai, Y. Sakamoto, S. Komura, K. Yano, and Y. Iimura: "Plasma Chemical Modification of Wall Surface of UHV Vessel (I)", *ibid.*

48) Y. Yamazaki, K. Komaki, T. Azuma, K. Kawatsura, Y. Kanai, T. Kambara, and Y. Awaya: "Emission of Secondary Electrons from Thin Foils Bombarded by Relativistic Heavy-Ions", 1990 Fall Meet. Phys. Soc. Jpn, Gifu, Oct. (1990).

49) T. Sekioka, M. Terasawa, and Y. Awaya: "Characteristics of Kingdon-Type Ion trap", *ibid.*

50) K. Ando, Y. Zou, T. Kambara, Y. Awaya, T. Tonuma, S. Kohmoto, and S. Tsurubuchi: "Life Time of Ti XIII Measured by Beam Foil Method", *ibid.*

51) Y. Yamazaki, K. Komaki, T. Azuma, K. Kuroki, K. Kawatsura, Y. Kanai, T. Kambara, and Y. Awaya: "Secondary Electron Emission from Thin Foils by Relativistic Heavy Ions", *ibid.*

52) Y. Zou, K. Ando, S. Kohmoto, T. Kambara, Y. Awaya, T. Tonuma, T. Niizeki, and S. Tsurubuchi: "Beam-Foil Lifetime Study of Neon-Like Ti^{12+}", *ibid.*

53) S. Ito, Y. Isozumi, R. Katano, N. Maeda, Y. Awaya, and T. Mizogawa: "Development of High Pressure Position Sensitive Proportional Counter for X-Ray Measurements", *ibid.*

54) E. Yagi: "Behaviour of Kr Atoms Implanted into Al", *ibid.*

55) S. Sato, I. Hashimoto, H. Yamaguchi, E. Yagi, and M. Iwaki: "Random Motion of He Bubbles in Al", *ibid.*

56) M. Tachibana, T. Mukouyama, H. Adachi, Y. Sasa, Y. Hibino, M. Mogi, K. Fuwa, and M. Uda: "Chemical Effect

on F K Satellites (I)", *ibid.*

57) M. Mogi, T. Mukouyama, H. Adachi, Y. Sasa, M. Tachibana, Y. Hibino, K. Fuwa, and M. Uda: "Chemical Effect on F K Satellites (II)", *ibid.*

58) H. Fukuda, I. Shimamura, L. Végh, and T. Watanabe: "Kinetic Energies of Recoil Ions in Ionization Processes", *ibid.*

59) M.R. Harston, I. Shimamura, and M. Kamimura: "Electron Screening Effect on Muonic Molecules dtu", *ibid.*

60) T. Tonuma, H. Kumagai, T. Matsuo, and H. Tawara: "Multiple Ionization Process Studied with Coincidence Technique between Slow Recoil Ion and Projectile Ion in 42 MeV Ar^{q+}-Ar Collisions", 3rd Joint Japan-China Seminar on Atomic and Molecular Phys. Taian, China, Oct. (1990).

61) I. Shimamura: "Muon-catalyzed Fusion and Muonic Molecules", *ibid.*

62) E. Yagi: "Recent Topics on Lattice Defects in Solids in Relation to Ion Beam-Solid Interaction", 30th Domestic Meet. on Lattice Defects., Inuyama, Oct. (1990).

63) K. Kobayashi, T. Fujihana, and M. Iwaki: "Effects of Ne and Ar Gas Ion Implantation Composition and Crystal Structure in AlN_x Thin Films", 6th Symp. on Surface Layer Modification by Ion Implantation, Tokyo, Nov. (1990).

64) E. Yagi: "Lattice Location Study on Hydrogen in Metals by Means of a Channelling Method", 13th Werner-Brandt Workshop on the Interaction of Charged Particles with Matter, Nara, Nov. (1990).

65) H. Ishikawa, Y. Sasa, A. Koyama, A. Misu, T. Iitaka, Y.H. Ohtsuki, and M. Uda: "Convoy Electron Excitation by Glancing-Angle Incident Heavy-Ion Impact on Thick Metal Targets", *ibid.*

66) K. Kobayashi, T. Fujihana, and M. Iwaki: "Effects of Noble Gas Ion Implantation on the Properties of AlN_x Thin Films", 10th Meet. Surface Anal. Soc., Tokyo, Dec. (1990).

4. Radiochemistry, radiation chemistry and radiation biology

1) T. Takahashi: "Present Status of Bioligical and Medical Studies at RIKEN Ring Cyclotron", RIKEN Symp. Studies on Mat. Sci. Atomic Processes, Nucl. Chem. and Radiobiol. by RIKEN Ring Cyclotron, Wako, Jan. (1990).

2) K. Yoshida, T. Takahashi, and K. Nakano: "Fabrication of Through-holes on Polymer Films by Ions from RIKEN Ring Cyclotron", 8th Track Detector Symp., Tokyo, Mar. (1990).

3) H. Kumagai, K. Nakano, K. Hatanaka, F. Yatagai, A. Hitachi, H. Ichinose, I. Kaneko, T. Takahashi, Y. Suzuki, K. Watanabe, T. Kosaka, K. Kasai, and T. Kanai: "Dosimetry at RIKEN Ring Cyclotron Biology Facility", 37th Spring Meet. Jpn. Soc. Appl. Phys. and Related Soc., Asaka, Mar. (1990).

4) K. Kimura, F. Sano, and S. Yanagisita: "Development of a Ion-track Scope and Stopping-Power Dependent Luminescence of Helium", 45th Annu. Meet. Phys. Soc. Jpn., Toyonaka, Mar. (1990).

5) Y. Kobayashi, T. Okada, M. Iwamoto, F. Ambe, M. Watanabe, M. Katada, and H. Sano: "^{99}Ru Mössbauer Spectroscopy on Halogen Adducts of Ruthenocene", 2nd RIKEN Symp. on Appl. of Hyperfine Techniques to Chem., Wako, Mar. (1990).

6) M. Iwamoto, Y. Kobayashi, T. Okada, N. Sakai, I. Kohno, F. Ambe, K. Mishima, K. Kubo, Y. Sakai, T. Tominaga, M. Nakada, Y. Watanabe, K. Endo, H. Nakahara, and H. Sano: "Emission Mössbauer Spectroscopy of ^{57}Fe Using ^{57}Mn as the Source Nuclide", *ibid.*

7) Y. Ohkubo, Y. Yanagida, Y. Kobayashi, F. Ambe, and K. Asai: "Perturbed Angular Correlation and Emission Mössbauer Spectroscopy of ^{99}Ru in α-Fe_2O_3 Using ^{99}Rh as the Source Nuclide", *ibid.*

8) Y. Itoh and H. Tachi: "Lattice Defect in GaAs Crystals by Positron Annihilation", *ibid.*

9) K. Asahi, M. Adachi, H. Okuno, M. Ishihara, T. Kubo, Y. Ohkubo, Y. Kobayashi, M. Iwamoto, and F. Ambe: "Application of Spin Polarized Oxygen-13 Beam to Chemistry", *ibid.*

10) H. Kusawake, T. Saito, N. Takahashi, H. Baba, Y. Ohkubo, and A. Shinohara: "Angular-Momentum Effect in Heavy Ion-Induced Fusion Reactions", 59th Spring Annu. Meet. of the Chem. Soc. of Jpn. Yokohama, Apr. (1990).

11) M. Furukawa, E. Taniguchi, M. Narita, A. Shinohara, S. Kojima, Y. Ohkubo, Y.

Kobayashi, M. Iwamoto, S. Ambe, F. Ambe, T. Saito, H. Kusawake, and S. Shibata: "Radiochemical Studies of Reaction Products Induced by Intermediate-Energy Heavy Ions", *ibid*.

12) M. Watanabe, K. Suzuki, N. Sakakibara, and K. Watanabe: "Cytoskeltal Changes in Preneoplastic and Neoplastic Syrian Hamster Embryo Cells Induced by X-rays", Workshop on Syrian Hamster Embryo Cell Transformation, The Natl. Toxicology Program (NIEHS), Wintergreen, May (1990).

13) T. Takahashi, F. Yatagai, and K. Izumo: "Microdosimetric Considerations of Effects of Heavy Ions on *E. coli* K-12 Mutants", 28th Plenary Meet. Committee on Space Res., The Hague, June (1990).

14) K. Tazaki: "Daiagenetic Mineral Transformations and Hydrothermal Alterations", Leg 126 Post-Cruise Conf. Hawaii Inst. of Geophysics, Hawaii, July (1990).

15) M. Minami, M. Aratani, M. Yanokura, and M. Yuyatani: "Measurement of Diamondlike Carbon Films by Heavy-ion Probe Rutherford Scattering Analysis", 27th Annu. Meet. on Radioisotopes in the Phys. Sci. and Industries, Tokyo, July (1990).

16) M. Yuyatani, M. Aratani, M. Yanokura, and M. Minami: "Rutherford Scattering Analysis Applied to Hydrogen Isotopes and Metals in the Electrodes", *ibid*.

17) W.S. Fyfe, Kazue Tazaki, and Koichi Tazaki: "Environmental Education; The Need for an Holistic Approach to the System Sun-living Cell-Earth", Int. Cong. of Ecology, Yokohama, Aug. (1990).

18) K. Tazaki: "Dinosaur Egg Shell—A Mineralogical Observation by Electron Microscope", Lecture Meet. on Dinosaur —RIKEN Phys. and Chem. Colloquim, Wako, Aug. (1990).

19) K. Kimura, J. Wada, and M. Arai: "Stopping-Power Dependent Luminescence of Condensed Helium by a Techique of the Track-dept Resolved Measurement", 1990 Fall. Meet, Phys. Soc. Jpn., Gifu, Oct. (1990).

20) K. Kimura, J. Wada, and M. Arai: "Depthresolved Emission Spectra near Termination of Ion-Track Termination", 33th Meet. Radiat. Chem. Jpn., Sendai, Oct. (1990).

21) K. Kimura, M. Arai, and J. Wada: "Fast Emission Decay Measurement for Heavyion Excitation; Effect of High-density Excitation on Auger Free Emission of BaF2", *ibid*.

22) T. Takahashi, F. Yatagai, N. Miyabe, M. Ueno, A. Maruyama, K. Izumo, and T. Kosaka: "Analytical Formula of the Dose around the Path of an Ion and Its Application", 33th Annu. Meet. Jpn. Radiat. Res. Soc., Sendai, Oct. (1990).

23) H. Ohara, T. Kanai, H. Itsukaichi, K. Fukutsu, K. Eguchi, H. Sato, F. Yatagai, and T. Takahashi: "Biological Effect of Carbon Ions from RIKEN Ring Cyclotron; Relation between RBE and LET", *ibid*.

24) K. Tazaki, F.G. Ferris, R.G. Wiese, and W.S. Fyfe: "Bacterial Mineralization in Cherts", Int. Symp. on Biomineralization, Odawara, Oct. (1990).

25) K. Tazaki: "Clays and Environmental Geology", Clay Sci. Assoc. of Jpn. 34th Annu. Meet. Kagoshima, Oct. (1990).

26) S. Ambe, Y. Ohkubo, M. Iwamoto, and Y. Kobayashi: "Preparation of No-Carrier-Added Cd* and Ag* and Their Chemical Behavior", 34th Symp. Radiochem., Tokyo, Oct. (1990).

27) T. Takahashi and Y. Itoh: "Defects in GaAs Crystals Studied by Positron", *ibid*.

28) H. Kusawake, T. Saito, N. Takahashi, H. Baba, Y. Ohkubo, and A. Shinohara: "Angular-Momentum Effect in Heavy Ion-Induced Fusion Reactions", *ibid*.

29) M. Furukawa, E. Taniguchi, M. Narita, A. Shinohara, S. Kojima, T. Saito, H. Kusawake, Y. Ohkubo, F. Ambe, and S. Shibata: "Yields of Nuclear Reaction Products Induced by 95 MeV/u-^{40}Ar Ions", *ibid*.

30) A. Shinohara, E. Taniguchi, M. Narita, M. Furukawa, S. Kojima, T. Saito, H. Kusawake, Y. Ohkubo, F. Ambe, and S. Shibata: "Heavy-Ion Reactions of Copper with Intermediate-Energy ^{14}N and ^{40}Ar Ions", *ibid*.

31) Y. Kobayashi, T. Okada, F. Ambe, M. Watanabe, M. Katada, and H. Sano: "^{99}Ru Mössbauer Spectroscopy on Halogen Adducts of Ruthenocene Derivatives", *ibid*.

32) J. Nakamura, N. Yamada, K. Asai, Y. Kobayashi, and F. Ambe: "^{121}Sb Möss-

bauer Spectroscopy on MnSb", *ibid.*

33) T. Nagamine, J. Honda, Y. Kobayashi, I. Endo, F. Ambe, Y. Teratani, and A. Hirata: "A Study on A Photoresponsive Enzyme; The Valency Change in Iron Atoms during Photoirradiation", *ibid.*

34) M. Aratani, M. Yanokura, M. Minami, I. Chu, and T. Kobayashi: "Heavy-Ion Probe Rutherford Scattering Applied to Pathological Samples", *ibid.*

35) M. Ohkubo, I. Sugai, M. Minami, M. Yuyatani, M. Yanokura, and M. Aratani: "Development of Carbon Stripper Foils with Institute for Nuclear Study", *ibid.*

36) A. Kaburagi, M. Minami, K. Onoue, I. Sugai, M. Yanokura, and M. Aratani: "Analysis of Contamination Processes during Vacuum Deposition of Thin Films", *ibid.*

37) M. Yanokura, A. Kaburagi, M. Minami, and M. Aratani: "Spreading Application of Heavy-Ion TOF-RS", *ibid.*

38) M. Furukawa, Y. Taniguchi, M. Narita, A. Shinohara, S. Kojima, T. Saito, H. Kusawake, Y. Ohkubo, F. Ambe, and S. Shibata: "Target Dependence of Nuclear Reaction Product Yield by 95 MeV/u—^{40}Ar Irradiation", *ibid.*

39) A. Shinohara, Y. Taniguchi, M. Narita, M. Furukawa, S. Kojima, T. Saito, H. Kusawake, Y. Ohkubo, F. Ambe, and S. Shibata: "Cu+^{14}N, ^{40}Ar Nuclear Reaction in Intermediate Energy Region", *ibid.*

40) K. Asahi, M. Adachi, H. Okuno, Y. Ohkubo, T. Nakamura, H. Inabe, T. Kubo, M. Iwamoto, E. Yagi, Y. Kobayashi, J. Kura, A. Yoshida, J. Nakamura, F. Ambe, M. Ishihara, W.-D. Schmidt-Ott, and K. Asai: "Material Science Using Spin-Polarized Unstable Light Nuclei as a Probe", *ibid.*

41) S.Y. Chen, S. Ambe, Y. Ohkubo, M. Iwamoto, Y. Kobayashi, N. Takematsu, and F. Ambe: "Adsorption of Metal Elements on Clay Minerals, Sea Sediments, and Iron Oxide", *ibid.*

42) Y. Ohkubo, Y. Kobayashi, K. Harasawa, T. Okada, F. Ambe, and K. Asai: "Time Differential γ-ray Perturbed Angular Correlation and Emission Mössbauer Spectroscopy of ^{99}Ru in Fe_3O_4 Using ^{99}Rh as the Source Nuclide", *ibid.*

43) Y. Ohkubo, Y. Kobayashi, Y. Yanagida, M. Iwamoto, F. Ambe, and K. Asai: "Measurements of γ-ray Perturbed Angular Correlation and Emission Mössbauer Effects for ^{99}Ru in α-Fe_2O_3 Using ^{99}Rh as a Source Nuclide", *ibid.*

44) M. Nakada, Y. Watanabe, K. Endo, H. Nakahara, H. Sano, K. Mishima, K. Kubo, Y. Sakai, T. Tominaga, M. Iwamoto, Y. Kobayashi, K. Asai, T. Okada, N. Sakai, I. Kono, and F. Ambe: "Emission Mössbauer Spectroscopy of ^{57}Fe with ^{57}Mn as the Source Nuclide", *ibid.*

45) M. Iwamoto, Y. Kobayashi, S.Y. Chen, Y. Ohkubo, M. Yanokura, S. Ambe, and F. Ambe: "Separation by Heating Under Reduced Pressure of Multi-Tracers Produced in an Target by Heavy-Ion Irradiation", *ibid.*

46) T. Takahashi and Y. Itoh: "Defects in GaAs Crystals Studied by Positrons", *ibid.*

47) M. Aratani, M. Yanokura, M. Minami, I. Chu, and T. Kobayashi: "Heavy-Ion Probe Rutherford Scattering Applied to Pathological Samples", *ibid.*

48) M. Ohkubo, I. Sugai, M. Minami, S. Yuyatani, M. Yanokura, and M. Aratani: "Development of Carbon Stripper Foil with Long Lifetime", *ibid.*

49) A. Kaburagi, M. Minami, M. Yanokura, M. Aratani, K. Onoe, and I. Sugai: "Analysis of Contamination Processes during Vacuum Deposition of Thin Films", *ibid.*

50) M. Watanabe, M. Suzuki, K. Suzuki, and K. Watanabe: "Premature Chromosome Condensation (PCC) Technique for Detecting Genotoxicity of Inter-phase Cells", 7th CAAT Symp., Baltimore, Nov. (1990).

51) F. Ambe: "Accelerator Facilities and Several Applications to Physical and Chemical Research in RIKEN", RIKEN Symp. on Spreading Appl. of Meterial Characterization Using Heavy-ion Linear Accelerator, Wako, Nov. (1990).

52) M. Minami: "Application of Heavy Ion Rutherford Scattering to Carbon Materials", *ibid.*

53) A. Kaburagi: "Application of Heavy Ion Rutherford Scattering to Metal Thin Foils", *ibid.*

54) M. Aratani: "Combination of Heavy Ion Rutherford Scattering and Time-Of-Flight Mass Spectroscopy—A Perspective—", *ibid.*

55) Y. Qiu, T. Kobayashi, H. Tsukagoshi, M. Minami, M. Aratani, and M. Yanokura: "Application of Heavy-Ion Probe Rutherford Scattering to the Analysis of Rare Elements in Biological Materials", 14th Annu. Meet. Jpn. Neurosci. Soc., Kyoto, Dec. (1990).

5. Material analysis

1) N. Takaura, K. Maeda, Y. Sasa, and M. Uda: "Quantitative Analysis of Doped Zn into GaAs by Ion Induced X-Ray Emission Analysis (PIXE)", 37th Spring Meet. Jpn. Soc. Appl. Phys., Asaka, Mar. (1990).
2) N. Takaura, K. Maeda, Y. Sasa, and M. Uda: "Lower Detection Limits of Impurities in the Si by Ion Induced X-Ray Emission Analysis", 1990 Fall Meet. Jpn. Soc. Appl. Phys., Morioka, Sep. (1990).
3) K. Maeda, Y. Sasa, M. Uda, and M. Takami: "Measurement of Surface Angle of Non-flat Target via L/K X-Ray Intensity Ratio and Its Application to PIXE Analysis", 27th Meet. for X-ray Chem. Anal. Jpn., Suita, Oct. (1990).

X. SUBJECTS UNDER CONTRACT

(Jan.–Dec. 1990)

1) "Radiochemical Analysis of ^{16}O, ^{14}N, and ^{12}C in Si Crystal and GaAs"	H. Kirita Japan Chemical Analysis Center
2) "Radiation Damage of Solar Cells"	T. Saga Sharp Co., Ltd.
3) "Improvement of Thyristors by Proton Irradiation"	K. Tomii Semiconductor R&D Lab., Matsushita Electric Work Co., Ltd.
4) "Improvement of Thyristors by Proton Irradiation"	H. Akiyama LSI Lab., Mitsubishi Electric Co., Ltd.
5) "Improvement of Thyristors by Proton Irradiation"	M. Kitagawa and A. Ohsawa Toshiba Co., Ltd.
6) "Improvement of Thyristors by Proton Irradiation"	Y. Shimizu Hitachi Co., Ltd.
7) "Improvement of Thyristors by Proton Irradiation"	K. Muraoka and S. Sasaki Toyo Electric Co., Ltd.

XI. LIST OF SEMINARS

(Jan.-Dec. 1990)

Radiation Lab., Cyclotron Lab., Linear Accelerator Lab.

1) R. Seki, California State Univ. (USA), 17 January
   "Understanding Nuclear Force as Soliton Interaction"

2) H. Toki, Tokyo Metropolitan Univ. (Tokyo), 14 February
   "Δ-Isobar Excitation in (^{3}He, t) Reactions"

3) H.G. Backe, Mainz Univ. (Germany), 28 February
   "Optical Spectroscopy of Fission Isomers"

4) Y. Sakuragi, Osaka City Univ. (Osaka), 22 March
   "Recent Topics on Polarized Heavy Ions"

5) J. Žofka, Nuclear Physics Institute Řež Prague (Czechoslovakia), 22 March
   "Recent Development in Hypernuclear Physics"

6) L. Bimbot, IPN Orsay (France), 27 March
   "Subthreshold Pion Production"

7) R.N. Boyd, Ohio State Univ. (USA), 10 April
   "Lectures in Nuclear Astrophysics"

8) T. Wada, RIKEN, 25 April
   "Induced Fission Studied with Multi-Dimensional Langevin Equation"

9) S. Kox, ISN Grenoble (France), 9 May
   "Total Reaction Cross Sections Measured for Stable and Exotic Heavy Ions in the Intermediate Energy Range"

10) D. Rebreyend, ISN Gernoble (France), 25 May
   "Source Size Measurements in Heavy Ion Reactions from Light Particle Correlations"

11) M. Tohyama, Kyorin Univ. (Tokyo), 6 June
   "Time-Dependent Density Matrix and its Applications"

12) M. Sakai, Institute for Nuclear Study (Tokyo), 13 June
   "Electron Spectra in the e^+ + Th Interaction"

13) E.K. Hulet, Univ. of California (USA), 6 July
   "Fission of Heavy Actinide Elements"

14) K. Kaki, Tokyo Institute of Technology (Tokyo), 11 July
   "Multiple Scattering Contributions to the RIA Optical Potential"

15) T. Sasakawa, Tohoku Univ. (Miyagi), 18 July
   "Recent Development in the Study of the Three Nucleon System"

16) U.G. Meissner, Bern Univ. (Switzerland), 4 August
   "The Pion in QCD"

17) K. Ikeda, Niigata Univ. (Niigata), 6 September
   "Structure of Unstable Nuclei and a New Type of Resonance Modes"

18) K. Kusaka, RIKEN, 17 September
   "Schematic Model of QCD Phase Transition"

19) K. Niita, Giessen Univ. (Germany), 22 October
   "Subthreshold Particle Production in Heavy Ion Collisions"

20) G. Hagemann, The Niels Bohr Institute (Denmark), 31 October
   "Study on Band Crossing"

21) B. Mottelson, NORDITA (Denmark), 29 November
   "Physics of Superdeformation"

22) N. Carjan, CEN Bordeaux (France), 4 December
   "Two-Dimensional Langevin Approach to Nuclear Fission"

23) D. Napoli, Legnalo-Padova (Italy), 10

December
"Subbarrier Transfer Reactions with the Legnaro Recoil Mass Spectrometer (LMS)"

24) T. Udagawa, Univ. of Texas at Austin (USA), 25 December
"Subbarrier Fusion Reactons"

Atomic Processes Lab.

1) R. Srivastava, Univ. Roorkee (India), 26 January
"Application of Distorted-Wave Approach to Electron-Atom (Ion) Scattering"

2) U. Safranova, Inst. Spectroscopy (USSR), 18 May
"Spectroscopy of High Ionized Atom in Hot Plasmas"

3) L. Vainshtein, Lebedev Physical Inst. (USSR), 18 May
"Using of K-Matrix for Channel Interaction Problem"

4) D. Habs, Max Planck Inst. für Kernphysik, (Germany), 2 November
"Experiments with Heavy Ion Cooler Ring in Heidelberg"

5) A.M. Ermolaev, Univ. Durham (U.K.), 17 October
"Atomic Physics with Low Energy Antiprotons"

Metal Physics Lab.

1) R. Fleming, Univ. of British Columbia (Canada), 9 October
"Muonium Reactions in Gases"

2) R. Fleming, Univ. of British Columbia (Canada), 11 October
"Muonium Reactions on Powder Surfaces"

3) A. Schenck, ETH (Switzerland), 3 December
"Study of Heavy Fermion Systems Using Muon Probes"

4) A Zubarev, Tashikent Univ. (USSR), 18 December
"New Theory on α-sticking in Muon Catalyzed Fusion and Complex Energy of dHe μ Resonance"

Radiochemistry Lab.

1) Zhang Guilin, The Shanghai Institute of Nuclear Research (China), 5 December
"Ion Implantation Mössbauer Spectroscopy"

Synchrotron Radiation Facility Design Group

1) K. Kasahara, National Research Center for Disaster Prevention (Tsukuba), 3 April
"Ground Investigation by Artifitial Earthquake"

2) S. Liu, IHEP (China), 19 April
"The Consideration of JLC Control"

3) T. Kobari and M. Matsumoto, Hitachi, Ltd., (Tsuchiura), 1 June
"An Investigation on Photo-Desorption at PF"

4) D.D. Bhawalkar, CAT (India), 11 July
"Synchrotron Radiation Facility in India"

5) K. Odaka, Hitachi Ltd., (Tsuchiura), 20 July
"Measurement of Thermal Gas Desorption Rate"

6) Y. Kojima, Mitsubishi Electric Corporation (Tokyo), 20 September
"Superconducting Cavity Dvelopment at KEK"

7) G. Hirata, Denken Seiki Co., Ltd. (Tokyo), 3 October
"Earth and Ground for Noise Reduction and Safety"

8) H. Winick, Stanford Synchrotron Radiation Laboratory (USA), 12 October
"Present Status in SPEAR and PEP"

XII. LIST OF PERSONNEL

Steering Committee

AMBE Fumitoshi 安部文敏
CHIBA Yoshiaki 千葉好明
HASHIZUME Akira 橋爪 朗
ISHIHARA Masayasu 石原正泰
KATSUMATA Koichi 勝又紘一
KOHNO Isao 河野 功
MIYAZAWA Yoshitoshi 宮沢佳敏
TAKAMI Michio 高見道生
YANO Yasushige 矢野安重
AWAYA Yohko 粟屋容子
HANAOKA Fumio 花岡文雄
INAMURA Takashi 稲村 卓
KAMITSUBO Hiromichi 上坪宏道*
KIRA Akira 吉良 爽
MATSUOKA Masaru 松岡 勝
NAGAMINE Kanetada 永嶺謙忠
TANIHATA Isao 谷畑勇夫

---

* Chairman

Cyclotron Operation and Maintenance Group

FUJITA Shin 藤田 新
KAGEYAMA Tadashi 影山 正
OGIWARA Kiyoshi 荻原 清
IKEGAMI Kumio 池上九三男
KOHARA Shigeo 小原重夫
TAKEBE Hideki 武部英樹

Linac Operation and Maintenance Group

CHIBA Yoshiaki 千葉好明
IKEZAWA Eiji 池沢英二
KASE Masayuki 加瀬昌之
YANOKURA Minoru 矢野倉 実
HEMMI Masatake 逸見政武
INOUE Toshihiko 井上敏彦
MIYAZAWA Yoshitoshi 宮沢佳敏

Scientific and Engineering Personnel

Cosmic Radiation Laboratory

IMAI Takashi 今井 喬
MUNAKATA Kazuoki 宗像一起
KOHNO Tsuyoshi 河野 毅

(Visitors)
HASEBE Nobuyuki 長谷部信行 (Fac. Gen. Educ., Ehime Univ.)
MURAKAMI Hiroyuki 村上浩之 (Fac. Sci., Rikkyo Univ.)
NAGATA Katsuaki 永田勝明 (Fac. Eng., Tamagawa Univ.)
NAKAMOTO Atsusi 中本 淳 (Fac. Sci., Rikkyo Univ.)
NISHIJIMA Kyoshi 西嶋恭司 (Sci. Eng. Res. Lab., Waseda Univ.)
YANAGIMACHI Tomoki 柳町朋樹 (Fac. Sci., Rikkyo Univ.)

(Student)
KASHIWAGI Toshisuke 柏木利介 (Sci. Eng. Res. Lab., Waseda Univ.)

Cyclotron Laboratory

BE Suck Hee 裵 碩喜
FUJISAWA Takashi 藤沢高志
DATÉ Schin 伊達 伸
FUJITA Jiro 藤田二郎

FUJITA Shin 藤田 新
HARA Masahiro 原 雅弘
INABE Naohito 稲辺尚人
KAGEYAMA Tadashi 影山 正
KOHARA Shigeo 小原重夫
NAGASE Makoto 長瀬 誠
NAKAJIMA Shunji 中島諄二
OGIWARA Kiyoshi 荻原 清
SAITOU Motozou 斎藤始三
SHIKATA Takashi 四方隆史
TAKEBE Hideki 武部英樹
YAMAJI Shuhei 山路修平
YOKOYAMA Ichiro 横山一郎

GOTO Akira 後藤 彰
IKEGAMI Kumio 池上九三男
INAMURA Takashi 稲村 卓
KAMITSUBO Hiromichi 上坪宏道
MORITA Kosuke 森田浩介
NAKAGAWA Takahide 中川孝秀
NAKANISHI Noriyoshi 中西紀喜
OOTA Sigemi 太田滋生
SASAKI Shigeki 佐々木茂樹
SOUTOME Kouichi 早乙女光一
WADA Takeshi 和田 雄
YANO Yasushige 矢野安重

(Visitors)
ABE Yasuhisa 阿部恭久 (Res. Inst. Fundam. Phys., Kyoto Univ.)
ARAI Eiichi 新井栄一 (Res. Lab. Nucl. Reactors, Tokyo Inst. Technol.)
BACKE H.G. (Dep. Phys., Mainz Univ.)
EJIRI Hiroyasu 江尻宏泰 (Dep. Phys., Osaka Univ.)
FUJIOKA Manabu 藤岡 学 (Cyclotron Radioisot. Cent., Tohoku Univ.)
FUJITA Yoshitaka 藤田佳孝 (Dep. Phys., Osaka Univ.)
FUKUMOTO Sadayoshi 福本貞義 (KEK)
FURUNO Kohei 古野興平 (Inst. Phys. Tandem Accel. Cent., Univ. Tsukuba)
HATANAKA Kichiji 畑中吉治 (RCNP, Osaka Univ.)
HATSUKAWA Yuichi 初川雄一 (JAERI, Tokai)
HIRAO Yasuo 平尾泰男 (Natl. Inst. Radio. Sci.)
HORIUCHI Hisashi 堀内 昶 (Dep. Phys., Kyoto Univ.)
HORIGUCHI Takayoshi 堀口隆良 (Dep. Phys., Hiroshima Univ.)
IKEDA Kiyomi 池田清美 (Dep. Phys., Niigata Univ.)
IKEGAMI Hidetsugu 池上栄胤 (RCNP, Osaka Univ.)
INOUE Makoto 井上 信 (RCNP, Osaka Univ.)
ISHIZUKA Takeo 石塚武男 (Dep. Phys., Saitama Univ.)
IWAMOTO Akira 岩本 昭 (Japan Atomic Energy Res. Inst.)
IWASHITA Yoshihisa 岩下芳久 (Inst. Chem. Res., Kyoto Univ.)
KANMURI Tetsuo 冠 哲夫 (Dep. Phys., Osaka Univ.)
KATAYAMA Ichirou 片山一郎 (RCNP, Osaka Univ.)
KATORI Kenji 鹿取謙二 (Dep. Phys., Osaka Univ.)
KATSURAGAWA Hidetsugu 桂川秀嗣 (Dep. Phys., Toho Univ.)
KAWAI Mitsuji 河合光路 (Dep. Phys., Kyushu Univ.)
KIKUCHI Fumio 菊池文男 (Coll. Arts Sci., Univ. Tokyo)
KISHIMOTO Teruo 岸本照夫 (Dep. Phys., Univ. Tsukuba)
KOBAYASHI Shinsaku 小林晨作 (Dep. Phys., Kyoto Univ.)
KOHMOTO Susumu 河本 進 (Univ. Electro-Commun.)
KOHMOTO Toshiro 河本敏郎 (Dep. Phys., Kyoto Univ.)
KONDO Michiya 近藤道也 (RCNP, Osaka Univ.)
KOSAKO Toshiso 小佐古敏荘 (Atomic Energy Res. Cent., Univ. Tokyo)
KUDOU Hisaaki 工藤久昭 (Dep. Chem., Niigata Univ.)
KUROYANAGI Tokihiro 黒柳登喜大 (Dep. Phys., Kyushu Univ.)
LEE Sang-Moo 李 相茂 (Dep. Phys., Univ. Tsukuba)
MARUMORI Toshio 丸森寿夫 (Dep. Phys., Univ. Tsukuba)
MATUKI Seishi 松木征史 (RCNP, Osaka Univ.)
MINOWA Tatsuya 箕輪達哉 (Dep. Phys., Toho Univ.)
MIURA Iwao 三浦 岩 (RCNP, Osaka Univ.)
MIYATAKE Hiroari 宮武宇也 (Fac. Sci., Osaka Univ.)
MURAKAMI Tetsuya 村上哲也 (Dep. Phys., Kyoto Univ.)
MURAYAMA Toshiyuki 村山利幸 (Tokyo Univ. Mercantil Marine)

NAGAI Yasuki 永井泰樹 (Dep. Appl. Phys., Tokyo Inst. Technol.)
NAKAHARA Hiromichi 中原弘道 (Dep. Chem., Tokyo Metrop. Univ.)
NAKAI Koji 中井浩二 (KEK)
NAKAMURA Ichiro 中村市郎 (Dep. Phys., Saitama Univ.)
NAKAMURA Takashi 中村尚司 (Cyclotron Radioisot. Cent., Tohoku Univ.)
NIITA Koji 仁井田浩二 (Dep. Phys., Univ. of Giessen, Germany)
NOMURA Toru 野村 亨 (Inst. Nucl. Study, Univ. Tokyo)
OGATA Hiroshi 小方 寛 (RCNP, Osaka Univ.)
ONISHI Naoki 大西直毅 (Dep. Phys., Coll. Gen. Educ., Univ. Tokyo)
SAKAI Hideyuki 酒井英行 (Fac. Sci., Univ. Tokyo)
SASAGAWA Tatsuya 笹川辰弥 (Dep. Phys., Tohoku Univ.)
SATO Kenichi 佐藤憲一 (Dep. Phys., Tohoku Coll. Pharm.)
SHIKAZONO Naoki 鹿園直基 (JAERI, Tokai)
SHINOZUKA Tsutomu 篠塚 勉 (Cyclotron Radioisot. Cent., Tohoku Univ.)
SUEKI Keisuke 末木啓介 (Inst. Nucl. Study, Univ. Tokyo)
SUGAI Isao 菅井 勲 (Inst. Nucl. Study, Univ. Tokyo)
TAGISHI Yoshihiro 田岸義宏 (Tandem Accel. Cent., Univ. Tsukuba)
TAKADA Kenjiro 高田健次郎 (Dep. Phys., Kyushu Univ.)
TAKEMASA Tadashi 武政尹士 (Dep. Phys., Saga Univ.)
TAKIGAWA Noboru 滝川 昇 (Dep. Phys., Tohoku Univ.)
TAMAGAKI Ryozo 玉垣良三 (Dep. Phys., Kyoto Univ.)
TANAKA Jinichi 田中仁市 (Inst. Nucl. Study, Univ. Tokyo)
TOHYAMA Mitsuru 遠山 満 (Dep. Phys., Kyorin Univ.)
TOMIMASU Takio 富増多喜男 (Electro Tech. Lab.)
TORIYAMA Tamotsu 鳥山 保 (Dep. Appl. Phys., Tokyo Inst. Technol.)
TSUNEMOTO Hiroshi 恒元 博 (Natl. Inst. Radiol. Sci.)
VALLI K. (Dep. Phys., Jyvaskyla Univ., Finland)
WAKAI Masamichi 若井正道 (Dep. Phys., Osaka Univ.)
YAMANOUCHI Mikio 山内幹雄 (Tandem Accel. Cent., Univ. Tsukuba)
YAMAZAKI Takashi 山崎 魏 (RCNP, Osaka Univ.)
YOSHIDA Nobuaki 吉田宣章 (Dep. Phys., Univ. Tokyo)
YOSHIDA Shiro 吉田思郎 (Dep. Phys., Tohoku Univ.)
YOSHINAGA Naotaka 吉永尚孝 (Comput. Cent., Univ. Tokyo)

(Students)
AZUMA Mitsuhiro 東 光弘 (Dep. Phys., Toho Univ.)
FUKASHIRO Yasuyuki 深代康之 (Dep. Phys., Tohoku Univ.)
HAMADA Shingo 濱田真悟 (Dep. Nucl. Eng., Kyoto Univ.)
HIRASAWA Junichirou 平澤淳一郎 (Dep. Appl. Phys., Tokyo Inst. Technol.)
KOBAYASHI Takayuki 小林貴之 (Dep. Chem., Tokyo Metrop. Univ.)
KOIZUMI Mitsuo 小泉光生 (Dep. Phys., Hiroshima Univ.)
KOSUGA Hiroyuki 小菅洋之 (Dep. Phys., Toho Univ.)
MARUYAMA Toshiki 丸山敏毅 (Dep. Phys., Kyoto Univ.)
MUROYA Shin 室谷 心 (Dep. Phys., Waseda Univ.)
NAKAOKA Masaya 中岡正哉 (Dep. Phys., Saitama Univ.)
NISHINAKA Ichiro 西中一郎 (Dep. Chem., Tokyo Metrop. Univ.)
OGAWA Izumi 小川 泉 (Dep. Phys., Kyoto Univ.)
SHIMOMURA Koichiro 下村浩一郎 (Dep. Phys., Kyoto Univ.)
SUNAOSHI Hitoshi 砂押 仁 (Dep. Phys., Tohoku Univ.)
SUZUKI Katsuhiro 鈴木勝博 (Dep. Phys., Kyoto Univ.)
WADA Michiharu 和田道治 (Dep. Phys., Tohoku Univ.)
YOSHIMURA Katsumi 吉村克巳 (Dep. Appl. Phys., Tokyo Inst. Technol.)

Linear Accelerator Laboratory

CHIBA Toshiya 千葉利哉
FUJIMAKI Masaki 藤巻正樹
KASE Masayuki 加瀬昌之
KUMAGAI Hidekazu 熊谷秀和
SUZUKI Takeshi 鈴木 健
TONUMA Tadao 戸沼正雄
YANOKURA Minoru 矢野倉 実
CHIBA Yoshiaki 千葉好明
HEMMI Masatake 逸見政武
KUBO Toshiyuki 久保敏幸
MIYAZAWA Yoshitoshi 宮沢佳敏
TANIHATA Isao 谷畑勇夫
WADA Takahiro 和田隆宏
YOSIDA Koichi 吉田光一

(Visitors)
BAI Xi Xiang 白 希祥 (Inst. Atomic Energy, China)
FUJIWARA Ichiro 藤原一郎 (Inst. Atomic Energy, Kyoto Univ.)
FUJIWARA Mamoru 藤原 守 (RCNP, Osaka Univ.)
ITO Noriaki 伊藤憲昭 (Dep. Cryst. Mater., Nagoya Univ.)
KATORI Kenji 鹿取謙二 (Fac. Sci., Osaka Univ.)
KIKUCHI Jun 菊地 順 (Sci. Eng. Res. Lab., Waseda Univ.)
KIMURA Kikuo 木村喜久雄 (Fac. Sci., Kyushu Univ.)
KOBAYASHI Toshio 小林俊雄 (KEK)
SAKAI Hideyuki 酒井英行 (Fac. Sci., Univ. Tokyo)
SUDA Toshimi 須田利美 (Fac. Sci., Tohoku Univ.)
SUGAWARA Masahiko 菅原昌彦 (Fundam. Sci., Chiba Inst. Technol.)
YAMAGUCHI Hiromi 山口裕美 (Sci. Eng. Res. Lab., Waseda Univ.)

(Students)
ABE Kenichi 阿部健一 (Fac. Sci., Osaka Univ.)
ITO Tatsuya 伊藤達也 (Sci. Eng. Res. Lab., Waseda Univ.)

Radiation Laboratory

GONO Yasuyuki 郷農靖之
ICHIHARA Takashi 市原 卓
IZUMO Koichi 出雲光一
NOMURA Izumi 野村和泉
TENDO Yoshihiko 天道芳彦
HASHIZUME Akira 橋爪 朗
ISHIHARA Masayasu 石原正泰
KONNO Satoshi 金野 智
TAKAHASHI Tan 高橋 旦
YOSHIDA Atsushi 吉田 敦

(Visitors)
ABE Yasuhisa 阿部恭久 (Res. Inst. Fundam. Phys., Kyoto Univ.)
ADACHI Minoru 足立 實 (Dep. Appl. Phys., Tokyo Inst. Technol.)
ANDO Yoshiaki 安藤嘉章 (Dep. Phys., Rikkyo Univ.)
APRILE Elena (Columbia Univ.)
ASAHI Koichiro 旭 耕一郎 (Fac. Sci., Tokyo Inst. Technol.)
DOKE Tadayoshi 道家忠義 (Sci. Eng. Res. Lab., Waseda Univ.)
ENDO Saburo 遠藤三郎 (Fac. Eng., Sci. Univ. Tokyo)
FUCHI Yoshihide 渕 好秀 (Inst. Nucl. Study, Univ. Tokyo)
FUJIOKA Manabu 藤岡 学 (Dep. Phys., Tohoku Univ.)
FUKUDA Mitsunori 福田光順 (Fac. Sci., Osaka Univ.)
FUKUDA Tomokazu 福田共和 (Inst. Nucl. Study, Univ. Tokyo)
HASEGAWA Takeo 長谷川武夫 (Inst. Nucl. Study, Univ. Tokyo)
HITACHI Akira 月出 章 (Sci. Eng. Res. Lab., Waseda Univ.)
ICHIMURA Munetake 市村宗武 (Coll. Arts Sci., Univ. Tokyo)
IEKI Kazuo 家城和夫 (Fac. Sci., Rikkyo Univ.)
IJIRI Kenichi 井尻憲一 (Radioisot. Cent., Univ. Tokyo)
ISHIKAWA Masanobu 石川雅紀 (Tokyo Univ. Fisheries)
KASAGI Jirota 笠木治郎太 (Fac. Sci., Tokyo Inst. Technol.)
KASAI Kiyomi 笠井清美 (Natl. Inst. Radiol. Sci.)

KATO Norihisa 加藤哲久 (Dep. Phys., Kyushu Univ.)
KATO Seigo 加藤静吾 (Fac. Educ. Yamagata Univ.)
KATORI Kenji 鹿取謙二 (Fac. Sci., Osaka Univ.)
KAWAKAMI Hirokane 川上宏金 (Inst. Nucl. Study, Univ. Tokyo)
KAWASHIMA Hideo 川島英雄 (Inst. Nucl. Study, Univ. Tokyo)
KIKUCHI Jun 菊池 順 (Sci. Eng. Res. Lab., Waseda Univ.)
KITAHARA Yoshitaka 北原義孝 (Hoya Corp.)
KITAO Kensuke 喜多尾憲助 (Natl. Inst. Radiol. Sci.)
KOMAGATA Kazuyuki 駒形和行 (Asahi Glass Co., Ltd.)
KOX Serge (ISN, Grenoble, France)
KUBONO Sigeru 久保野 茂 (Inst. Nucl. Study, Univ. Tokyo)
KUBOTA Shinzou 窪田信三 (Fac. Sci., Rikkyo Univ.)
KUSAKARI Hideshige 草刈英榮 (Fac. Educ., Chiba Univ.)
LEE Sang Mu 李 相茂 (Inst. Phys., Univ. Tsukuba)
MAEDA Kazushige 前田和茂 (Coll. Gen. Educ., Tohoku Univ.)
MASUDA Kimiaki 増田公明 (Saitama Coll. Health)
MERCHEZ F. (ISN, France)
MIYATAKE Hiroari 宮武宇也 (Coll. Gen. Educ., Osaka Univ.)
MORINAGA Haruhiko 森永晴彦 (Sec. Phys. Tech. Univ. München)
MOTOBAYASHI Tohru 本林 透 (Fac. Sci., Rikkyo Univ.)
MÜLLER Alex (Inst. Phys. Nucl., Orsay, France)
MURAKAMI Takeshi 村上 健 (Dep. Phys., Tokyo Inst. Technol.)
NAGAI Yasuki 永井泰樹 (Fac. Sci., Tokyo Inst. Technol.)
NAGASHIMA Yasuo 長島泰夫 (Dep. Phys., Univ. Tsukuba)
NAKAYAMA Shintaro 中山信太郎 (Coll. Gen. Educ., Tokushima Univ.)
OGAWA Masao 小川雅生 (Fac. Sci., Tokyo Inst. Technol.)
OHNUMA Hajime 大沼 甫 (Fac. Sci., Tokyo Inst. Technol.)
OKAMURA Hiroyuki 岡村弘之 (Fac. Sci., Univ. Tokyo)
ORIHARA Hikonojo 織原彦之丞 (Cyclotron and Radioisot. Cent., Tohoku Univ.)
OSHIMA Masumi 大島眞澄 (Japan Atomic Energy Res. Inst.)
OSHIRO Takashi 尾城 隆 (Tokyo Univ. Fisheries)
OYAIZU Michihiro 小柳津充広 (Inst. Nucl. Study, Univ. Tokyo)
PERRIN Claude (ISN, France)
REBREYEND D. (ISN, France)
RUAN (GEN) Jian-zhi 阮 建治 (Dep. Phys., Rikkyo Univ.)
SAKAGUCHI Harutaka 坂口治隆 (Dep. Phys., Kyoto Univ.)
SAKAI Mitsuo 坂井光夫 (Inst. Nucl. Study, Univ. Tokyo)
SATO Hiroshi 佐藤 鉱 (Seikei Univ.)
SCHMIDT-OTT Wolf-Dieter (II Phys. Inst., Univ. Goettingen, Germany)
SHIBAMURA Eido 柴村英道 (Saitama Coll. Health)
SHIMIZU Hajime 清水 肇 (Fac. Educ., Yamagata Univ.)
SHIMODA Tadashi 下田 正 (Coll. Gen. Educ., Osaka Univ.)
SHIMOURA Susumu 下浦 享 (Fac. Sci., Univ. Tokyo)
SHIRATO Shoji 白土釥二 (Dep. Phys., Rikkyo Univ.)
SHIROYAMA Masaki 城山正樹 (Asahi Glass Co., Ltd.)
TAKADA Eiichi 高田栄一 (Natl. Inst. Radiol. Sci.)
TAKAHASHI Noriaki 高橋憲明 (Coll. Gen. Educ., Osaka Univ.)
TAKIGAWA Noboru 滝川 昇 (Dep. Phys., Tohoku Univ.)
TANAKA Masahiko 田中雅彦 (Inst. Nucl. Study, Univ. Tokyo)
TAO Kazuyuki 垰 和之 (Radioisot. Cent., Univ. Tokyo)
TOKI Hiroshi 土岐 博 (Dep. Phys., Tokyo Metrop. Univ.)
TOYOKAWA Hidenori 豊川秀訓 (Inst. Phys., Univ. Tsukuba)
XU Hushan 徐 瑚珊 (Inst. Mod. Phys., Acad. Sin. China)
YAMAYA Takashi 山屋 堯 (Dep. Phys., Tohoku Univ.)
YASUE Masaharu 安江正治 (RCNP, Osaka Univ.)
YATO Osamu 矢頭 治 (Inst. Radiat. Breeding, NIAR)

YOSHIDA Kazuo 吉田和夫 (Hoya Corp.)
YOSHINAGA Naotaka 吉永尚孝 (Saitama Univ.)
YOSOI Masaru 與曽井 優 (Fac. Sci., Tokyo Inst. Technol.)

(Students)
FUJIWARA Hideaki 藤原英明 (Inst. Phys., Univ. Tsukuba)
FUNATSU Yoshinori 船津義徳 (Fac. Sci., Univ. Tokyo)
FURUTAKA Kazuyoshi 古高和禎 (Fac. Sci., Tokyo Inst. Technol.)
FUTAMI Yasuyuki 二見康之 (Inst. Phys., Univ. Tsukuba)
HIRENZAKI Satoru 比連崎 悟 (Fac. Sci., Tokyo Metrop. Univ.)
HONJO Yoshio 本城義夫 (Inst. Phys., Univ. Tsukuba)
ICHINOSE Hideo 市之瀬秀夫 (Sci. Eng. Res. Lab., Waseda Univ.)
ISHIDA Nobumichi 石田伸道 (Sch. Sci. Eng., Waseda Univ.)
ISHIDA Satoru 石田 悟 (Fac. Sci., Univ. Tokyo)
ITO Tatsuya 伊藤達也 (Sci. Eng. Res. Lab., Waseda Univ.)
ITO Tomoyuki 伊藤朋行 (Sci. Eng. Res. Lab., Waseda Univ.)
IWASA Naohito 岩佐直仁 (Dep. Phys., Rikkyo Univ.)
KURA Jumpei 蔵 純平 (Fac. Sci., Tokyo Inst. Technol.)
KUROKAWA Meiko 黒川明子 (Dep. Phys., Rikkyo Univ.)
KUWAHARA Kōta 桑原宏太 (Sch. Sci. Eng., Waseda Univ.)
MARUYAMA Akiko 丸山晶子 (Japan Women's Univ.)
MIYABE Noriko 宮部規子 (Japan Women's Univ.)
MIZOTA Takeshi 溝田武志 (Inst. Phys., Univ. Tsukuba)
MORIKAWA Tsuneyasu 森川恒安 (Fac. Sci., Hiroshima Univ.)
NAKAMURA Takashi 中村隆司 (Fac. Sci., Univ. Tokyo)
OHNISHI Hiroko 大西裕子 (Coll. Agric. Vet. Med., Nihon Univ.)
OHNO Mariko 大野真理子 (Radioisot. Cent., Univ. Tokyo)
OHURA Masaki 大浦正樹 (Tohoku Univ.)
OKUNO Hiroki 奥野広樹 (Fac. Sci., Univ. Tokyo)
PU Y.H. 蒲 越虎 (Inst. Phys., Univ. Tsukuba)
TAJIMA Yasuhisa 田島靖久 (Fac. Sci., Tokyo Inst. Technol.)
TAKEI Taro 武井太郎 (Dep. Phys., Rikkyo Univ.)
UENO Miyuki 上野美幸 (Japan Women's Univ.)
YAJIMA Akira 矢嶋 亨 (Fac. Sci., Tokyo Inst. Technol.)
YASHIRO Yoshinori 矢代義徳 (Fac. Sci., Tokyo Inst. Technol.)
YOON Chong Cheor 尹 鐘哲 (Fac. Sci., Tokyo Inst. Technol.)
YOSHIDA Akira 吉田 晃 (Sci. Eng. Res. Lab., Waseda Univ.)
YOSHIDA Hiroshi 吉田浩司 (Fac. Sci., Tokyo Inst. Technol.)
YUASA-NAKAGAWA Keiko 中川恵子 (Inst. Phys., Univ. Tsukuba)

Atomic Processes Laboratory

ANDO Kozo 安藤剛三
FUKUDA Hiroshi 福田 宏
KANAI Yasuyuki 金井保之
SHIMAMURA Isao 島村 勲
AWAYA Yohko 粟屋容子
KAMBARA Tadashi 神原 正
NISHIDA Masami 西田雅美
WATANABE Tsutomu 渡部 力

(Visitors)
AZUMA Toshiyuki 東 俊行 (Coll. Arts Sci., Univ. Tokyo)
DANJO Atsunori 壇上篤徳 (Dep. Phys., Niigata Univ.)
ERMOLAEV Alex (Univ. Durham, England)
FUJIMA Kazumi 藤間一美 (Fac. Eng., Yamanashi Univ.)
HABS Dietrich (Max Planck Inst. for Nucl. Phys., Germany)
HARA Shunsuke 原 俊介 (Inst. Phys., Univ. Tsukuba)
HARSTON Michael R.

HINO Ken-ichi 日野健一 (Univ. Electro-Commun.)
HITACHI Akira 月出 章 (Inst. Sci. Technol., Waseda Univ.)
ICHIMIYA Ayahiko 一宮彪彦 (Dep. Eng., Nagoya Univ.)
ISHII Keishi 石井慶之 (Dep. Eng. Sci., Kyoto Univ.)
ISOZUMI Yasuhito 五十棲泰人 (Inst. Chem. Res., Kyoto Univ.)
ITO Shin 伊藤 真 (Radioisot. Res. Cent., Kyoto Univ.)
ITOH Yoh 伊藤 陽 (Fac. Sci., Josai Univ.)
IWATA Yasushi 岩田康嗣 (Coll. Arts Sci., Univ. Tokyo)
KARASHIMA Shosuke 唐島照介 (Dep. Electron. Eng., Tokyo Univ. Sci.)
KAWATSURA Kiyoshi 川面 澄 (Kyoto Inst. Technol.)
KOBAYASHI Nobuo 小林信夫 (Dep. Phys., Tokyo Metrop. Univ.)
KOIKE Fumihiro 小池文博 (Sch. Med., Kitasato Univ.)
KOIZUMI Tetsuo 小泉哲夫 (Dep. Phys., Rikkyo Univ.)
KOMAKI Ken-ichiro 小牧研一郎 (Coll. Arts Sci., Univ. Tokyo)
KUROKI Kenro 黒木健郎 (Natl. Res. Inst. Police Sci.; Inst. Phys. Coll. Arts Sci., Univ. Tokyo)
MATSUO Takashi 松尾 崇 (Dep. Pathol., Tokyo Med. Dent. Univ.)
MATSUZAWA Michio 松澤通生 (Dep. Eng. Phys., Univ. Electro-Commun.)
MIZOGAWA Tatsumi 溝川辰巳 (Nagaoka Coll. Technol.)
OHTANI Shunsuke 大谷俊介 (Inst. Laser Sci., Univ. Electro-Commun.)
OKUNO Kazuhiko 奥野和彦 (Dep. Phys., Tokyo Metrop. Univ.)
SATO Hiroshi 佐藤浩史 (Dep. Phys., Ochanomizu Univ.)
SEKIOKA Tsuguhisa 関岡嗣久 (Himeji Inst. Technol.)
SHIBATA Hiromi 柴田裕実 (Res. Cent. Nucl. Sci. Technol., Univ. Tokyo)
SHIMA Kunihiro 島 邦博 (Tandem Accel. Cent., Univ. Tsukuba)
SHIMAKURA Noriyuki 島倉紀之 (Gen. Educ. Dep., Niigata Univ.)
SPÄDTKE Peter (GSI, Germany)
SUZUKI Hiroshi 鈴木 洋 (Dep. Phys., Sophia Univ.)
TAKAGI Shoji 高木祥示 (Dep. Phys., Toho Univ.)
TAWARA Hiroyuki 俵 博之 (Natl. Inst. Fusion Sci.)
TERASAWA Mititaka 寺沢倫孝 (Himeji Inst. Technol.)
TSURUBUCHI Seiji 鶴淵誠二 (Fac. Technol., Tokyo Univ. Agric. Technol.)
WAKIYA Kazuyoshi 脇谷一義 (Dep. Phys., Sophia Univ.)
YAMAZAKI Yasunori 山崎泰規 (Coll. Arts Sci., Univ. Tokyo)
YOSHINO Masuhiro 吉野益弘 (Lab. Phys., Shibaura Inst. Technol.)
ZOU Yaming (Jiao Tong Univ., China)

(Students)
INABA Takayuki 稲葉貴之 (Inst. Laser Sci., Univ. Electro-Commun.)
KAKUTANI Nobukazu 角谷暢一 (Coll. Arts Sci., Univ. Tokyo)
KUSHIMA Masahiro 久嶋真博 (Dep. Phys., Sophia Univ.)
NABESHIMA Takayuki 鍋島貴之 (Dep. Phys., Sophia Univ.)
NAKAMURA Nobuyuki 中村信行 (Dep. Phys., Sophia Univ.)
SAKAUE Hiroyuki 坂上裕之 (Dep. Phys., Sophia Univ.)

Metal Physics Laboratory

ISHIDA Katsuhiko 石田勝彦
KOYAMA Akio 小山昭雄
MATSUZAKI Teiichiro 松崎禎市郎
YAGI Eiichi 八木栄一
KADONO Ryosuke 門野良典
MATSUSHITA Akira 松下 明
NAGAMINE Kanetada 永嶺謙忠

(Visitors)
FUJIOKA Manabu 藤岡 学 (Cyclotron Radioisot. Cent., Tohoku Univ.)
MINAMISONO Tadanori 南園忠則 (Fac. Sci., Osaka Univ.)

MIYAKE Yasuhiro　三宅康博　(Meson Sci. Lab., Univ. Tokyo)
TANAKA Koki　田中幸基　(Nippon Steel Corp.)
TORIKAI Eiko　鳥養映子　(Fac. Eng., Yamanashi Univ.)

(Student)
ISHIKAWA Hiroshi　石川　浩　(Fac. Sci., Sci. Univ. Tokyo)

Magnetic Materials Laboratory

OKADA Takuya　岡田卓也
SAKAI Nobuhiko　坂井信彦

Plasma Physics Laboratory

OYAMA Hitoshi　大山　等
YANO Katsuki　矢野勝喜

(Visitor)
SAKAMOTO Yuichi　坂本雄一　(Electr. Eng. Dep., Toyo Univ.)

Semiconductor Laboratory

(Visitor)
AONO Keiko　青野桂子　(Coll. Lib. Arts, Kitasato Univ.)

Inorganic Chemical Physics Laboratory

AMBE Shizuko　安部静子
MAEDA Kuniko　前田邦子
TAKAMI Michio　高見道生
KAWAI Jun　河合　潤
SASA Yoshihiko　佐々嘉彦

(Visitors)
FUKUDA Yukio　福田行男　(Coll. Lib. Arts, Kobe Univ.)
ISHII Keizo　石井慶造　(Cyclotron Radioisot. Cent., Tohoku Univ.)
KUSUYAMA Hiroyuki　楠山弘之　(Saitama Med. Sch.)
MUKOYAMA Takashi　向山　毅　(Inst. Chem. Res., Kyoto Univ.)
UDA Masayuki　宇田応之　(Dep. Mater. Sci. Eng., Waseda Univ.)

Radiochemistry Laboratory

AMBE Fumitoshi　安部文敏
ITOH Yoshiko　伊東芳子
KOBAYASHI Yoshio　小林義男
ARATANI Michi　荒谷美智
IWAMOTO Masako　岩本正子
OHKUBO Yoshitaka　大久保嘉高

(Visitors)
ASAI Kichizo　浅井吉蔵　(Univ. Electro-Commun.)
BABA Hiroshi　馬場　宏　(Fac. Sci., Osaka Univ.)
CHEN Shaoyong　陳　紹勇　(South China Sea Inst. Oceanol.)
ENDO Kazutoyo　遠藤和豊　(Fac. Sci., Tokyo Metrop. Univ.)
FURUKAWA Michiaki　古川路明　(Fac. Sci., Nagoya Univ.)
GARG Amar Nath　(Nagpur Univ., India)
IMAI Masato　今井正人　(Komatsu Electronic Metals Co., Ltd.)
IMURA Ryo　井村　亮　(Cent. Res. Lab., Hitachi, Ltd.)
KATADA Motomi　片田元己　(Fac. Sci., Tokyo Metrop. Univ.)
KATO Hajime　加藤　一　(Fac. Educ., Yamanashi Univ.)

KOJIMA Sadao 小島貞男 (Nucl. Med. Cent., Aichi Medical Univ.)
KUBO Kenya 久保謙哉 (Fac. Sci., Univ. Tokyo)
KUBOTA Takeshi 久保田 剛 (Inst. Mater. Sci., Univ. Tsukuba)
OKADA Shigenobu 岡田繁信 (R/D Eng., Shimadzu Corp.)
OOHIRA Shigeo 大平重男 (Nikkei Techno Res. Co., Ltd.)
SAITO Kazuo 斉藤和男 (Toshiba Corp., R&D Cent.)
SAITO Tadashi 斎藤 直 (Fac. Sci., Osaka Univ.)
SHIBATA Seiichi 柴田誠一 (Inst. Nucl. Study)
SHINOHARA Atsushi 篠原 厚 (Fac. Sci., Nagoya Univ.)
SUGAI Isao 菅井 勲 (Inst. Nucl. Study, Univ. Tokyo)
TAKAHASHI Naruto 髙橋成人 (Fac. Sci., Osaka Univ.)
TAKAI Mikio 高井幹夫 (Fac. Eng. Sci., Osaka Univ.)
TAZAKI Kazue 田崎和江 (Fac. Sci., Shimane Univ.)
TOMINAGA Takeshi 富永 健 (Fac. Sci., Univ. Tokyo)
WATANABE Yasuo 渡辺裕夫 (Fac. Sci., Tokyo Metrop. Univ.)
YOKOYAMA Akihiko 横山明彦 (Fac. Sci., Osaka Univ.)
ZHANG Guilin 張 桂林 (Shanghai Inst. Nucl. Res., China)

(Students)
HAYANO Syuichi 早野修一 (Fac. Sci., Osaka Univ.)
KIRIU Masaru 桐生 大 (Fac. Sci., Osaka Univ.)
KOBAYASHI Hiroshi 小林 洋 (Fac. Sci., Osaka Univ.)
KUSAWAKE Hiroaki 艸分宏昌 (Fac. Sci., Osaka Univ.)
MINAMI Masaki 南 正樹 (Dep. Metal Eng., Shibaura Inst. Technol.)
MISHIMA Kenji 三嶋謙二 (Fac. Sci., Univ. Tokyo)
MIYAUCHI Takahiro 宮内貴宏 (Fac. Sci., Osaka Univ.)
MURAYAMA Koujiro 村山浩二郎 (Fac. Sci., Nagoya Univ.)
NAKADA Masami 中田正美 (Fac. Sci., Tokyo Metrop. Univ.)
NAKAMURA Jin 中村 仁 (Univ. Electro-Commun.)
NARITA Midori 成田 緑 (Fac. Sci., Nagoya Univ.)
SHINTAI Junichirou 新帯淳一朗 (Fac. Sci., Nagoya Univ.)
TAKESAKO Kazuhiro 竹迫和浩 (Fac. Sci., Osaka Univ.)
TANIGUCHI Eugene 谷口勇仁 (Fac. Sci., Nagoya Univ.)
YANAGIDA Yasuo 柳田保雄 (Fac. Sci., Toho Univ.)
YOSHIDA Ryusho 吉田龍晶 (Fac. Sci., Nagoya Univ.)

Chemical Dynamics Laboratory

KIMURA Kazuie 木村一宇

(Visitor)
ITO Yasuo 伊藤泰男 (Res. Cent. Nucl. Sci. Technol., Univ. Tokyo)

(Students)
ARAI Masaru 新井 勝 (Dep. Phys., Chuo Univ.)
WADA Jiro 和田次郎 (Dep. Phys., Chuo Univ.)

Radiation Biology Laboratory

HANAOKA Fumio 花岡文雄
YATAGAI Fumio 谷田貝文夫
KITAYAMA Shigeru 北山 滋

(Visitors)
ANDO Kohichi 安藤興一 (Natl. Inst. Radiol. Sci.)
BAVERSTOCK Keith F. (Radiobiol. Unit, Med. Res. Counc., U.K.)

FUKUMURA Akifumi 福村明史 (Natl. Inst. Radiol. Sci.)
HASHIMOTO Shozo 橋本省三 (Fac. Med., Keio Univ.)
HOSHINO Kazuo 星野一雄 (Natl. Inst. Radiol. Sci.)
ITOH Hisao 伊東久夫 (Fac. Med., Keio Univ.)
KANAI Tatsuaki 金井達明 (Natl. Inst. Radiol. Sci.)
KAWACHI Kiyomitsu 河内清光 (Natl. Inst. Radiol. Sci.)
KAWASHIMA Katsuhiro 川島勝弘 (Natl. Inst. Radiol. Sci.)
KIMOTO Masafumi 木元正史 (Natl. Inst. Radiol. Sci.)
KOBAYASHI Yasuhiko 小林泰彦 (Japan. Atomic Energy Res. Inst.)
KOHNO Toshiyuki 河野俊之 (Natl. Inst. Radiol. Sci.)
KOIKE Sachiko 小池幸子 (Natl. Inst. Radiol. Sci.)
KOSAKA Toshifumi 小坂俊文 (Dep. Vet. Radiol., Nihon Univ.)
McINTYRE Cindy L. (Radiobiol. Unit, Med. Res. Counc., U.K.)
MINOHARA Shinichi 蓑原伸一 (Natl. Inst. Radiol. Sci.)
NAKAI Hirokazu 中井弘和 (Dep. Agric., Shizuoka Univ.)
OHARA Hiroshi 大原 弘 (Natl. Inst. Radiol. Sci.)
SOGA Fuminori 曽我文宣 (Inst. Nucl. Study, Univ. Tokyo)
SUDO Michio 須藤美智雄 (Natl. Inst. Radiol. Sci.)
TAKATUJI Toshihiro 高辻俊宏 (RI Cent., Nagasaki Univ.)
WATANABE Hiroshi 渡辺 宏 (Japan Atomic Energy Res. Inst.)
WATANABE Masami 渡辺正己 (RI Cent., Fac. Med., Yokohama City Univ.)
YAMASHITA Shoji 山下昌次 (Natl. Saitama Hospital)

(Student)
SUZUKI Masao 鈴木雅雄 (RI Cent., Fac. Med., Yokohama City Univ.)

Safety Control Affairs Office

KAGAYA Satoru 加賀屋 悟
KATOU Takeo 加藤武雄
MATSUZAWA Yasuhide 松沢安秀
SAKAMOTO Ichiro 坂本一郎
USUBA Isao 薄葉 勲
KATOU Hiroko 加藤博子
KOHNO Isao 河野 功
MIYAGAWA Makoto 宮川真言
SHINOHARA Shigemi 篠原茂己

Surface Characterization Center

IWAKI Masaya 岩木正哉
SAKAIRI Hideo 坂入英雄
KOBAYASHI Takane 小林 峰

(Visitor)
FUJIHANA Takanobu 藤花隆宣 (Advanced Technology Inc.)

(Student)
KOBAYASHI Kenzo 小林健三 (Fac. Eng. Sci., Osaka Univ.)

Laser Science Research Group

NAMBA Susumu 難波 進

Synchrotron Radiation Facility Design Group

BE Suck Hee 裵 碩喜
KAMITSUBO Hiromichi 上坪宏道
MATSUI Sakuo 松井佐久夫
HARA Masahiro 原 雅弘
KAWASHIMA Yoshitaka 川島祥孝
MOTONAGA Syoshichi 元永昭七

NAGAOKA Ryutaro 長岡隆太郎
OIKAWA Yoshifumi 老川嘉郁
TAKEBE Hideki 武部英樹
TANAKA Hitoshi 田中 均
WATANABE Kowashi 渡辺 剛
OHNISHI Jun-ichi 大西純一
SASAKI Shigeki 佐々木茂樹
TAKESHITA Isao 竹下勇夫
WADA Takeshi 和田 雄

(Visitors)
DAIBO Hidemi 大保秀実 (Hitachi, Ltd.)
IN Song Ryul 印 相烈 (Korea At. Energy Res. Inst.)
INOUE Kouji 井上浩司 (Kobe Steel, Ltd.)
KUMAGAI Keiko 熊谷桂子 (Fuji Electric Co., Ltd.)
KUSAKA Takuya 日下卓也 (Kobe Steel, Ltd.)
MIYADE Hiroki 宮出宏紀 (Sumitomo Heavy Ind., Ltd.)
MORIMOTO Yoshihide 森本佳秀 (Kobe Steel, Ltd.)
NISHIDONO Toshirou 西殿敏朗 (Ishikawajima-Harima Heavy Ind. Co., Ltd.)
SHIMIZU Akira 清水 明 (Irie Koken Co., Ltd.)
TAKADA Takeo 高田武雄 (Shin-Etsu Chemical Co., Ltd.)
TAKAHASHI Sunao 高橋 直 (Kobe Steel, Ltd.)
TSUMAKI Kouji 妻木孝治 (Hitachi, Ltd.)
YAMAMOTO Yuichi 山本雄一 (Mitsubishi Electric Corp.)
YOKOUCHI Shigeru 横内 茂 (Osaka Vacuum Ltd.)
YOSHIYUKI Takeshi 吉行 健 (Toshiba Corp.)

(Students)
ASADA Eriko 浅田恵利子 (Coll. Hum. Sci., Nihon Univ.)
HASEGAWA Jun 長谷川 潤 (Fac. Sci. Eng., Chuo Univ.)
HIRANO Yoshiki 平野芳樹 (Coll. Hum. Sci., Nihon Univ.)
ISHII Yasuyuki 石井保行 (Nucl. Eng., Tokyo Inst. Technol.)
ITOH Kiwamu 伊藤 研 (Coll. Hum. Sci., Nihon Univ.)
YAMAGUCHI Hitoshi 山口仁史 (Coll. Hum. Sci., Nihon Univ.)

AUTHOR INDEX

RIKEN Accelerator Progress Report

理化学研究所加速器年次報告　第24巻（1990）

印刷　平成3年（1991）3月20日
発行　平成3年（1991）3月29日
発行者　理化学研究所
代表者　小田稔
〒351-01　埼玉県和光市広沢2番1号
電話（0484）62－1111
編集者　理化学研究所加速器研究施設運営委員会
印刷所　勝美印刷株式会社
〒112　東京都文京区小石川1丁目3番7号

定価 5,000円
（消費税別）

理化学研究所

埼玉県　和光市　広沢